Journal of Heat Transfer

Published Monthly by ASME

VOLUME 129 • NUMBER 4 • APRIL 2007(pp.405-606)

SPECIAL ISSUE ON COMPUTATIONAL HEAT TRANSFER CELEBRATING SUHAS PATANKAR'S 65TH BIRTHDAY

GUEST EDITORIAL

RESEARCH PAPERS

Review Paper

Model Development

Turbine Blade Cooling

Micro/Nanoscale Heat Transfer

Processes Equipment and Devices

(Contents continued on inside back cover)

This journal is printed on acid-free paper, which exceeds the ANSI Z39.48-1992 specification for permanence of paper and library materials. ∞™
♻ 85% recycled content, including 10% post-consumer fibers.

Editor, **YOGESH JALURIA (2010)**
Assistant to the Editor, **S. PATEL**

Associate Editors
Gautam Biswas, Indian Inst. of Tech., Kanpur (2009)
Louis C. Burmeister, Univ. of Kansas (2008)
Minking Chyu, Univ. of Pittsburgh (2009)
Suresh V. Garimella, Purdue Univ. (2007)
A. Haji-Sheikh, Univ. of Texas at Arlington (2008)
Anthony M. Jacobi, Univ. of Illinois (2008)
Yogendra Joshi, Georgia Inst. of Tech. (2008)
Satish G. Kandlikar, Rochester Inst. of Tech. (2007)
Jay M. Khodadadi, Auburn Univ. (2007)
Jose L. Lage, Southern Methodist Univ. (2008)
Sai C. Lau, Texas A&M Univ. (2009)
Ben Q. Li, Univ. of Michigan, Dearborn (2009)
Raj M. Manglik, Univ. of Cincinnati (2009)
Chang H. Oh, Idaho National Lab. (2007)
Ranga Pitchumani, Univ. of Connecticut (2007)
Ramendra P. Roy, Arizona State Univ. (2007)
Jamal Seyed-Yagoobi, Illinois Inst. of Tech. (2009)
Bengt Sunden, Lund Inst. of Tech., Sweden (2008)
Walter W. Yuen, Univ. of California–Santa Barbara (2008)

Past Editors
V. DHIR
J. R. HOWELL
R. VISKANTA
G. M. FAETH
K. T. YANG
E. M. SPARROW

HEAT TRANSFER DIVISION
Chair, **RODNEY DOUGLASS**
Vice Chair, **TIM TONG**
Past Chair, **MICHAEL JENSEN**

PUBLICATIONS COMMITTEE
Chair, **BAHRAM RAVANI**

OFFICERS OF THE ASME
President, **TERRY E. SHOUP**
Executive Director,
VIRGIL R. CARTER
Treasurer,
THOMAS D. PESTORIUS

PUBLISHING STAFF

Managing Director, Publishing
PHILIP DI VIETRO

Manager, Journals
COLIN McATEER

Production Coordinator
JUDITH SIERANT

Production Assistant
MARISOL ANDINO

Transactions of the ASME, Journal of Heat Transfer (ISSN 0022-1481) is published monthly by The American Society of Mechanical Engineers, Three Park Avenue, New York, NY 10016. Periodicals postage paid at New York, NY and additional mailing offices.
POSTMASTER: Send address changes to Transactions of the ASME, Journal of Heat Transfer, c/o THE AMERICAN SOCIETY OF MECHANICAL ENGINEERS, 22 Law Drive, Box 2300, Fairfield, NJ 07007-2300.
CHANGES OF ADDRESS must be received at Society headquarters seven weeks before they are to be effective. Please send old label and new address.
STATEMENT from By-Laws. The Society shall not be responsible for statements or opinions advanced in papers or ... printed in its publications (B7.1, Para. 3).
COPYRIGHT © 2007 by The American Society of Mechanical Engineers. For authorization to photocopy material for internal or personal use under those circumstances not falling within the fair use provisions of the Copyright Act, contact the Copyright Clearance Center (CCC), 222 Rosewood Drive, Danvers, MA 01923, tel: 978-750-8400, www.copyright.com. Request for special permission or bulk copying should be addressed to Reprints/Permission Department.
Canadian Goods & Services Tax Registration #126148048

(**Contents continued**)

Journal of Heat Transfer **Volume 129, Number 4** **APRIL 2007**

TECHNICAL BRIEFS

ERRATUM

The ASME Journal of Heat Transfer is abstracted and indexed in the following:

Applied Science and Technology Index, Chemical Abstracts, Chemical Engineering and Biotechnology Abstracts (Electronic equivalent of Process and Chemical Engineering), Civil Engineering Abstracts, Compendex (The electronic equivalent of Engineering Index), Corrosion Abstracts, Current Contents, E & P Health, Safety, and Environment, Ei EncompassLit, Engineered Materials Abstracts, Engineering Index, Enviroline (The electronic equivalent of Environment Abstracts), Environment Abstracts, Environmental Engineering Abstracts, Environmental Science and Pollution Management, Fluidex, Fuel and Energy Abstracts, Index to Scientific Reviews, INSPEC, International Building Services Abstracts, Mechanical & Transportation Engineering Abstracts, Mechanical Engineering Abstracts, METADEX (The electronic equivalent of Metals Abstracts and Alloys Index), Petroleum Abstracts, Process and Chemical Engineering, Referativnyi Zhurnal, Science Citation Index, SciSearch (The electronic equivalent of Science Citation Index), Theoretical Chemical Engineering

Journal of Heat Transfer

Guest Editorial

Foreword to the Special Issue on Computational Heat Transfer

It is our great pleasure to present this Special Issue of the Journal of Heat Transfer which is being published in honor of Professor Suhas V. Patankar's 65th birthday in 2006. This issue not only highlights Professor Patankar's seminal contributions to computational heat transfer and fluid dynamics (CFD) research and pedagogy, but also gives us an opportunity to review the current status and future prospects of CFD.

We may argue about when CFD really began, whether it was with Lewis Richardson's work on the computation of creeping flow in 1910, or with the publication of the landmark paper by Courant, Friedrichs, and Lewy in *Mathematische Annalen* in 1928, or with Harlow and Fromm's 1965 *Scientific American* article, "*Computer Experiments in Fluid Dynamics*." There is little doubt though, that the last 40 years have been an exhilarating time for CFD. Professor Patankar has been an integral part of the evolution of modern CFD, and one of its most significant architects.

Professor Patankar was born on February 22, 1941 in Pune, India. He obtained his B.E and M.Tech degrees from Pune University. He obtained his Ph.D. from Imperial College, London in 1967 under Professor Brian Spalding, marking the beginning of a long and fruitful collaboration. He taught at the Indian Institute of Technology, Kanpur, from 1967 to 1970. He returned to Imperial College in 1970, and working with Professor Spalding, published a series of papers, including their landmark 1972 paper describing the SIMPLE algorithm, one of the most cited papers in the thermal-fluid sciences literature. Professor Patankar taught at the University of Waterloo in 1973–1974, and joined the Department of Mechanical Engineering at the University of Minnesota in 1974, which became his home for over 25 years until his retirement in 2000. He founded the CFD company Innovative Research Inc. in 1987, and now serves as its President.

Professor Patankar's career spans the arc of modern CFD, from its modest beginnings in the 1960s, to its near-ubiquity as an industrial analysis and design tool a scant 40 years later. The great majority of the computational work done in the 1950s and 1960s addressed either Euler flows or creeping flows. Professor Patankar's Ph.D. thesis on the computation of two-dimensional boundary layers marks one of the earliest attempts to resolve boundary layer growth through the use of a flow-conforming mesh. The generalization of 2D boundary layer computations to three-dimensional parabolic situations necessitated the invention of the SIMPLE algorithm in 1972 to compute pressure in incompressible flows. The remarkable computational economy afforded by SIMPLE facilitated the simulation of surprisingly complex fluid flows through the 1970s and 1980s, despite the relative paucity of computer resources. Over the years, the SIMPLE algorithm and its variants have become the mainstay of a vast variety of elliptic incompressible flow calculations, and today form the core solver engine of most commercial finite volume CFD codes.

Another critical advance in popularizing CFD was the development of boundary-fitted and unstructured finite volume schemes to address complex geometries. The path to their development was not straightforward, however. Early pressure-based schemes such as SIMPLE employed staggered storage of pressure and velocity to overcome difficulties with the occurrence of spurious pressure modes. To translate these staggered schemes to body-fitted meshes, grid-following co- and contravariant velocity systems had to be used. Professor Patankar and his students, as well as other researchers, developed this class of techniques in the early 1980s. However, these methods were still geometrically too cumbersome, and co-located or nonstaggered schemes were invented. Here too, Professor Patankar and his students developed one of the earliest co-located pressure-velocity formulations in the literature in 1980–1981, and variants and extensions of these ideas can again be found in many commercial CFD solvers today.

Ultimately, body-fitted meshes were themselves judged too inflexible for commercial use, and the remarkable expansion of CFD into the industrial arena could not occur without the development of unstructured finite volume techniques. Here too, Professor Patankar's imprint is clear. In the early 1980s, he and his students developed a class of unstructured finite volume techniques combining ideas of scalar conservation with finite-element-like shape functions. Triangular and quadrilateral elements were addressed in their early work. These techniques, called the control-volume finite element methods (CVFEMs), inspired the invention of cell-based unstructured finite volume solvers in the 1980s and early 1990s, which sought to simplify the geometric complexity of CVFEMs, and to generalize them to the arbitrary polyhedral cells necessary for true flexibility. These advances, combined with advances in solid modeling and unstructured mesh generation, finally made CFD versatile enough for routine industrial use.

Over the years, CFD textbooks and undergraduate and graduate curricula were developed to support the ever-expanding need for CFD practitioners in industry. Professor Patankar's contributions to CFD pedagogy are also significant. His excellence as a teacher is legendary. His 1980 textbook, *Numerical Heat Transfer and Fluid Flow*, remains to this day a model of simplicity and clarity, and one of most coherent explications of the finite volume technique ever written.

With all the success that CFD has enjoyed, what opportunities for future work remain? The greatest opportunities are, of course, afforded by the continuing expansion in computational resources. With the advent of petascale computing, many of the computational economies that drove the invention of SIMPLE and its variants may no longer be necessary. Thus, more robust (albeit more storage-intensive) pressure-velocity coupling schemes are already being developed and may soon become the mainstay of commercial solvers. Robust handling of more challenging physics, addressing turbulence, multiphase flows, chemically reacting flows, and other complexities, are necessary. In particular, simulation of turbulence has been radically improved through direct numerical simulation (DNS) and large eddy simulation (LES) of turbulence that provide spatially- and temporally-resolved calculations of the unsteady flowfield and do not require the modeling of the entire spectrum of turbulent fluctuations. LES tools are now increasingly being integrated into many commercial solvers, and it is anticipated that these tools will be further refined and utilized to a significantly greater extent by industry and academia in the next decade. Simulation itself will become more ubiquitous, significantly more multiphysics, multiscale, and design-oriented, and less and less the purview of experts. These trends inevitably demand better quantification of error and uncertainty propagation, and the development of expert systems to guide users.

The special issue consists of 17 full-length papers and five technical briefs representing a spectrum of topics in CFD from new methodologies and model developments to applications ranging from nano- to macro-thermal-fluid systems. The first paper in the issue is a review paper by Professor Patankar's students and associates and reviews the developments in CFD methodology, from SIMPLE-based methods to control-volume-based finite element methods (CVFEMs), in which Professor Patankar had a defining role. The remaining papers in the issue are contributed papers that have all been rigorously reviewed according to the Journal Heat Transfer standards.

We appreciate the overwhelming support of the heat transfer community, and the contributions of many experts in the CFD area that have made the special issue possible. On behalf of all the students and associates of Professor Patankar, we would like to thank him for introducing us to CFD and providing us the education and training that have helped us to build our own paths in industry or academia. We would also like to thank Professor Jaluria and the Journal of Heat Transfer for graciously agreeing to produce a special issue on computational heat transfer and fluids in honor of Professor Patankar.

On the occasion of Professor Suhas Patankar's 65th birthday, we ask you to join us in acknowledging his seminal contributions to CFD, and wishing him many more happy years of computing.

S. Acharya

J. Murthy

S. Acharya
Department of Mechanical Engineering,
Louisiana State University,
Baton Rouge, LA 70803

B. R. Baliga
Department of Mechanical Engineering,
McGill University,
Montreal, Quebec, Canada H3A 2K6

K. Karki
Innovative Research Inc.,
3025 Harbor Lane, Suite 300,
Plymouth, MN 55447

J. Y. Murthy
School of Mechanical Engineering,
Purdue University,
West Lafayette, IN 47907

C. Prakash
GE Aircraft Engines,
30 Merchant St.,
Princeton Hill P20,
Cincinnati, OH 45246

S. P. Vanka
Department of Mechanical Science
and Engineering,
University of Illinois, Urbana-Champaign,
Urbana IL 61801

Pressure-Based Finite-Volume Methods in Computational Fluid Dynamics

Pressure-based finite-volume techniques have emerged as the methods of choice for a wide variety of industrial applications involving incompressible fluid flow. In this paper, we trace the evolution of this class of solution techniques. We review the basics of the finite-volume method, and trace its extension to unstructured meshes through the use of cell-based and control-volume finite-element schemes. A critical component of the solution of incompressible flows is the issue of pressure-velocity storage and coupling. The development of staggered-mesh schemes and segregated solution techniques such as the SIMPLE algorithm are reviewed. Co-located storage schemes, which seek to replace staggered-mesh approaches, are presented. Coupled multigrid schemes, which promise to replace segregated-solution approaches, are discussed. Extensions of pressure-based techniques to compressible flows are presented. Finally, the shortcomings of existing techniques and directions for future research are discussed. [DOI: 10.1115/1.2716419]

Keywords: numerical methods, finite volume, pressure-based, fluid flow, multigrid, incompressible, compressible

1 Introduction

Over the last decade, computational fluid dynamics (CFD) has become a staple of industrial design and analysis. CFD analysis is now common in applications as diverse as automotive aerodynamics and underhood cooling, chemical and materials processing, electronics cooling, food processing, and in the pharmaceuticals, aerospace and power generation sectors. With the widespread availability of inexpensive computational power, it is now routine for the industrial design engineer to run simulations involving millions of degrees of freedom, and to address an enormous range of physics, including, for example, laminar and turbulent single and multiphase flows, rheologically complex flows, chemical reactions and combustion, participating radiation, and flow and heat transfer in porous media. The rapid spread of CFD is all the more impressive because it has happened over a relatively short time frame of about 40 years. A central element has, of course, been the exponential increase in computer power. An equally important element has been the development of computational algorithms that could exploit this power. The seminal work of Harlow and co-workers [1,2] in the 1950s and 1960s, the development of pressure-based solution techniques by Patankar and Spalding [3], the computation of Euler flow over a complete aircraft by Jameson and co-workers [4], and the emergence of computational techniques for complex geometries, are important landmarks in the development of CFD as an industrial tool.

In addition to the development of modern computer-aided design software and powerful structured and unstructured mesh generation techniques, a central factor in the success of CFD has been the development of robust solution kernels for incompressible flows. Solution techniques for Euler and viscous compressible flows, suitable for the aerospace and defense industries, had long been the focus of CFD development. However, incompressible flows form a large percentage of industrial flows, and efficient and robust techniques to address them were developed through the 1960s and 1970s using pressure-based finite-volume methods. The earliest finite-volume methods were formulated for regular meshes [5], and employed sequential pressure-based solution algorithms, such as SIMPLE [3]. The robustness and efficiency of this class of techniques allowed the solution of a wide variety of two- and three-dimensional viscous flows despite relatively meager computational resources ([6,7], for example). By the 1980s, efforts were underway to expand the reach of finite-volume methods to body-fitted and block-structured meshes [8–10]. Eventually, versatile unstructured finite-volume methods were developed by the 1990s [11–15]. Their deployment in commercial software marked the transition of CFD from use by relatively small numbers of experts to widespread use by industrial analysts and designers. The generalization to unstructured meshes also required a shift away from staggered-mesh techniques [5], which could not easily be implemented in an unstructured framework, to co-located and equal-order pressure-velocity storage approaches [12,16,17]. Widespread availability of inexpensive memory also spurred the development of fast multigrid solution techniques [18–20] to replace low-memory sequential procedures such as SIMPLE, and the extension and refinement of these techniques to the unstructured framework continues apace [21]. Over the years, extensions of pressure-based formulations to compressible flows ([22–24], for example) and the development of auxiliary models for heat transfer, turbulence, chemical reactions, and other physics, have broadened the application base of CFD.

Contributed by the Heat Transfer Division of ASME for publication in the JOURNAL OF HEAT TRANSFER. Manuscript received December 31, 2006; final manuscript received January 7, 2007. Review conducted by Yogesh Jaluria.

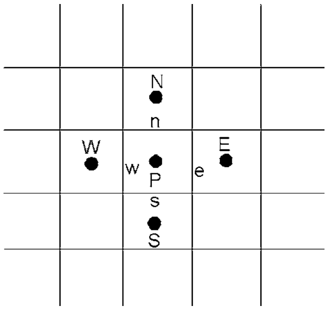

Fig. 1 Control volume around *P* and associated nomenclature

In this paper, we review the development of finite-volume techniques for incompressible flows. We first present the basic finite-volume discretization in Sec. 2. We review the development of staggered-grid methods and sequential solution techniques such as the SIMPLE algorithm and its variants in Sec. 3. Co-located storage schemes are reviewed in Sec 4. Section 5 discusses finite-volume schemes for complex geometries, and Sec. 6 reviews the extension of pressure-based methods for compressible flows. We present an overview of coupled solution techniques that seek to supplant sequential procedures in Sec. 7. The paper closes with an assessment of the state-of-the-art, and makes some recommendations for future work.

2 Basic Finite-Volume Method

The basic finite-volume method begins with the generic scalar transport equation governing the transport of mass, momentum, energy, and other transported scalars [5]

$$\frac{\partial}{\partial t}(\rho\phi) + \nabla \cdot (\rho \boldsymbol{V}\phi) = \nabla \cdot \Gamma_{\phi} \nabla \phi + S_{\phi} \tag{1}$$

Here, ρ is the mass density, ϕ the transported scalar, $\boldsymbol{V}$ the velocity vector, Γ_{ϕ} the diffusion coefficient, and S_{ϕ} the source term. For simplicity, we consider a rectangular geometry, which is discretized into rectangular control volumes or cells, as shown in Fig. 1. The values of ϕ, ρ, and Γ_{ϕ} are stored at cell centroids. Integrating Eq. (1) over the control volume ΔV associated with cell P and over the time step Δt in the manner described in [5] yields

$$\frac{(\rho\phi)_P - (\rho\phi)_P^o}{\Delta t}\Delta V + \left(\rho u \phi - \Gamma\frac{\partial\phi}{\partial x}\right)_e A_e - \left(\rho u \phi - \Gamma\frac{\partial\phi}{\partial x}\right)_w A_w + \left(\rho v \phi - \Gamma\frac{\partial\phi}{\partial y}\right)_n A_n - \left(\rho v \phi - \Gamma\frac{\partial\phi}{\partial y}\right)_s A_s = S_{\phi}\Delta V \tag{2}$$

Here, A_e, A_w, A_n, and A_s represent the cell-face areas in Fig. 1. Equation (2) represents the conservation of ϕ over the control volume P. Convective and diffusive fluxes are evaluated at the cell-face centroids (e,w,n,s). A variety of first-order and second-order discretizations suitable for structured meshes have been published [5,25–27] to relate cell-face values of ϕ and its spatial gradients to the value of ϕ at the cell centroids. Extensions to yet higher-order schemes is possible, but would require higher-order quadratures in making the transition from Eq. (1) to Eq. (2). A first-order implicit time integration has been employed in Eq. (2) with unsuperscripted variables representing the current (unknown) time level, and the superscript "*o*" representing the previous time level; however, higher-order time stepping schemes are easily admitted as well. The discretization procedure yields a set of coupled algebraic equations relating the cell-centered value ϕ_P to that of its neighbors *nb* (*E*, *W*, *N*, *S* in Fig. 1). Thus

$$a_P\phi_P = \sum_{nb=E,W,N,S} a_{nb}\phi_{nb} + b_P \tag{3}$$

The nominally linear algebraic set represented by Eq. (3) can be solved using a variety of direct and iterative techniques, though iterative techniques have traditionally been preferred because of their low memory requirements and operation count. Since the mesh in Fig. 1 admits line structure, line-based solvers such as the line-by-line tri-diagonal matrix algorithm (LBL-TDMA) [5] are preferred. Patankar [5] has described sequential iterative procedures for solving multiple nonlinear coupled transport equations like Eq. (1), whereby each governing equation is discretized and solved over the domain in turn. Such an approach is low in memory requirements, and linear in the number of solution variables, and has formed the mainstay of many general-purpose solvers. However, the loose inter-equation coupling implicit in a sequential procedure can lead to divergence when governing equations are strongly dependent on each other. The coupling between the momentum and continuity equations presents a particular difficulty and may be addressed by coupled solvers such as those described in Sec. 7.

The principle of conservation embodied in Eq. (2) can be used not only for the rectangular control volumes shown in Fig. 1, but for any closed volume. This idea forms the basis of unstructured discretizations based on arbitrary polyhedra [11–15]. However, as shown in Sec. 5, a number of scheme-specific details must be worked out. For example, with unstructured meshes, neither the line-based higher-order discretization schemes in [25] nor line-based linear solvers [5] can easily be used.

3 Semi-Implicit Calculation Procedures: SIMPLE and Variants

The incompressible continuity and momentum equations can, in principle, be cast into the form of Eq. (1) and discretized as in Sec. 2, with the resulting algebraic equation sets being solved sequentially and iteratively. However, for incompressible flows, a central problem is encountered if sequential procedures are used [5]. If we identify the continuity equation as an equation for density, and each momentum equation as an equation for the corresponding velocity, we may devise a sequential solution procedure for their solution. However, density is constant in incompressible flows, and cannot be used as a solution variable. Pressure, which is the appropriate solution variable, does not appear explicitly in the continuity equation, and is not related to density through an equation of state. In sequential pressure-based schemes, this problem is solved by developing a pressure equation through appropriate manipulation of the discrete continuity equation, as discussed in this section.

Since its conception in 1972, the SIMPLE (Semi-Implicit Method for the Pressure Linked Equations) algorithm of Patankar and Spalding [3] has been extensively used to solve the coupled pressure-velocity equations in incompressible flow problems. Over the years, a number of modifications to the SIMPLE algorithm have been proposed; the two most popular approaches with improved convergence properties have been the SIMPLE-Consistent (SIMPLEC) scheme of Van Doormaal and Raithby [28] and the SIMPLE-Revised (SIMPLER) scheme of Patankar [5]. Issa and coworkers have proposed the PISO (Pressure-Implicit with Splitting of Operators) algorithm [29,30] which is a noniterative time-marching procedure. In this section, we will briefly describe the SIMPLE approach, and some of its variants, and point out the pros and cons of these approaches.

3.1 Finite-Volume Discretization. The differential equations expressing the conservation of momentum and mass are special cases of Eq. (1). The momentum equation may be written by replacing ϕ in Eq. (1) by the velocity component u_i in the ith coordinate direction. The continuity equation may be written assuming ϕ to be unity [5]. Thus

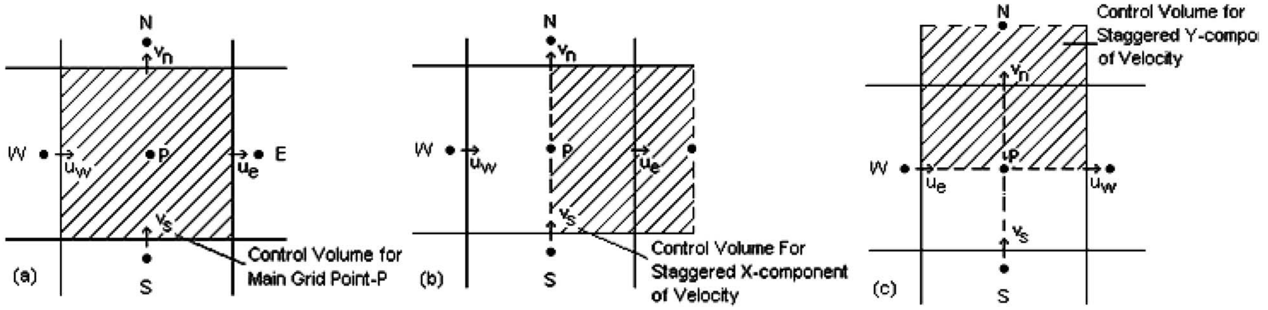

Fig. 2 Staggered grid arrangement (*a*) control-volume for scalars and pressure, (*b*) control-volume for *u*, and (*c*) control-volume for *v*

$$\frac{\partial}{\partial t}(\rho u_i) + \boldsymbol{\nabla}\cdot(\rho \boldsymbol{V} u_i) = -\boldsymbol{\nabla} p + \boldsymbol{\nabla}\cdot(\mu\,\boldsymbol{\nabla}\, u_i) + S_c + S_P u_i \tag{4}$$

$$\frac{\partial \rho}{\partial t} + \boldsymbol{\nabla}\cdot(\rho \boldsymbol{V}) = 0 \tag{5}$$

Here, u_i represents the velocity components u and v of the velocity vector $\boldsymbol{V}$, p is the pressure, μ is the dynamic viscosity, and $(S_c + S_P u_i)$ is the linearized source term [5]. The pressure does not appear explicitly in the continuity equation, but is specified indirectly through the requirement of mass conservation.

In the Patankar-Spalding method [3,5], the finite-volume scheme described in Sec. 2 is used to discretize the continuity and momentum equations. In solving incompressible flow equations, a staggered grid (Fig. 2(*a*)) is frequently used to eliminate the possibility of checkerboarded pressure and velocity fields [2,3]. Colocated or nonstaggered storage schemes have also been developed [12,16,17] and are discussed in Sec. 4.

If a staggered-grid arrangement is used (Fig. 2), the resulting discretized equations for u_e and v_n are

$$(a_e + \rho\Delta V/\Delta t)u_e = \sum_{nb} a_{nb}u_{nb} + A_e(p_p - p_E) + S_c\Delta V + \frac{\rho^o \Delta V}{\Delta t}u_e^o \tag{6}$$

$$(a_n + \rho\Delta V/\Delta t)v_n = \sum_{nb} a_{nb}v_{nb} + A_n(p_p - p_N) + S_c\Delta V + \frac{\rho^o \Delta V}{\Delta t}v_n^o \tag{7}$$

The expressions for the coefficients a_e, a_n, and a_{nb} depend on the choice of the profile approximations (or differencing scheme) in each coordinate direction.

Equations (6) and (7) represent the finite-volume analogs of the unsteady momentum equations; steady-state results can be obtained by marching in time. If only steady-state solutions are of interest, it is not necessary to obtain converged results of the system of algebraic equations at each time step. Therefore, at each time step, the coefficients need be calculated only once, based on the previous time step solution, and a partially converged result for the system of equations obtained. The results approach steady-state values through successive time-stepping. This approach is termed the *time-marching* procedure in this section.

An alternative approach, which uses an iterative method, is to start with the steady-state form of Eqs. (6) and (7) and to solve these equations in an iterative framework using under-relaxation. These under-relaxed discretized equations have the form

$$a_e\left(1 + \frac{1-\lambda}{\lambda}\right)u_e = \Sigma a_{nb}u_{nb} + A_e(p_p - p_E) + S_c\Delta V + \frac{1-\lambda}{\lambda}a_e u_e^* \tag{8}$$

$$a_n\left(1 + \frac{1-\lambda}{\lambda}\right)v_n = \Sigma a_{nb}v_{nb} + A_n(p_p - p_N) + S_c\Delta V + \frac{1-\lambda}{\lambda}a_n v_n^* \tag{9}$$

where λ is the under-relaxation factor, and u_e^*, v_n^* indicate results from the previous iteration. Successive solution of Eqs. (8) and (9), with the coefficients updated at each iteration, results in the steady-state solution.

In the discussion that follows, the discretized momentum equations (Eqs. (6) and (7) or Eqs. (8) and (9)) are first re-written for convenience as

$$\tilde{a}_e u_e = \Sigma a_{nb}u_{nb} + A_e(p_p - p_E) + b_e \tag{10}$$

$$\tilde{a}_n v_n = \Sigma a_{nb}v_{nb} + A_n(p_p - p_N) + b_n \tag{11}$$

3.2 SIMPLE Algorithm. For a guessed pressure field p^*, the velocities u^* and v^* satisfy

$$\tilde{a}_e u_e^* = \Sigma a_{nb}u_{nb}^* + A_e(p_p^* - p_E^*) + b_e \tag{12}$$

$$\tilde{a}_n v_n^* = \Sigma a_{nb}v_{nb}^* + A_n(p_p^* - p_N^*) + b_n \tag{13}$$

If Eqs. (12) and (13) are subtracted from (10) and (11), the fully implicit velocity correction (u', v') equations are obtained as

$$\tilde{a}_e u_e' = \Sigma a_{nb}u_{nb}' + A_e(p_p' - p_E') \tag{14}$$

$$\tilde{a}_n v_n' = \Sigma a_{nb}v_{nb}' + A_n(p_p' - p_N') \tag{15}$$

where

$$u' = u - u^*, \quad v' = v - v^* \quad \text{and} \quad p' = p - p^* \tag{16}$$

In the SIMPLE algorithm, the velocity correction equations are obtained by dropping the $\Sigma a_{nb}u_{nb}'$ and $\Sigma a_{nb}v_{nb}'$ terms on the right side of Eqs. (14) and (15), resulting in

$$u_e = u_e^* + d_e(p_p' - p_E') \quad \text{and} \quad v_n = v_n^* + d_n(p_p' - p_N') \tag{17}$$

where

$$d_e = \frac{A_e}{\tilde{a}_e} \quad \text{and} \quad d_n = \frac{A_n}{\tilde{a}_n} \tag{18}$$

To obtain the discretized equation for the pressure correction, Eq. (17) is substituted into the discretized continuity equation for the control volume around the main grid point:

$$(\rho_p - \rho_p^o)\Delta V/\Delta t + \rho_e u_e A_e - \rho_w u_w A_w + \rho_n v_n A_n - \rho_s v_s A_s = 0 \tag{19}$$

The resulting pressure-correction equation has the following form (see Fig. 2 for notation)

$$a_p p'_p = a_E p'_E + a_W p'_W + a_N p'_N + a_S p'_S + b \tag{20}$$

Detailed expressions for the coefficients may be found in [5]. Equations (10), (11), and (20) may be solved using standard iterative linear solvers, as described in Sec. 2.

The SIMPLE algorithm consists of the following steps:

1. Guess the pressure field p^*.
2. Solve the momentum equations (Eqs. (12) and (13)) to obtain u^* and v^*.
3. Solve p' equation (Eq. (20)) and update pressure by $p = p^* + \lambda_p p'$, where λ_p is an under-relaxation factor.
4. Update velocity u_e and v_n using the velocity-correction equations (Eq. (17)).
5. Repeat steps 2 and 4 until convergence (each pass of this algorithm constitutes one time step in the *time-marching* formulation and one iteration in the *iterative formulation*).

3.3 SIMPLEC Algorithm. The SIMPLEC algorithm follows the same general steps as the SIMPLE algorithm with the primary difference being in the formulation of the velocity-correction equation. In this approach, $u'_e \Sigma a_{nb}$ is subtracted from both sides of Eq. (14) and the term $\Sigma a_{nb}(u'_{nb} - u'_e)$ on the right side of the equation is neglected. A similar operation is performed on the v' equation. This approximation of dropping $\Sigma a_{nb}(u'_{nb} - u'_e)$ is an improvement over dropping $\Sigma a_{nb} u'_{nb}$ as in the SIMPLE method, since the difference term $(u'_{nb} - u'_e)$ is likely to be smaller than u'_{nb} alone. The resulting velocity-correction equations have the same form as that of Eq. (17) but with d_e and d_n re-defined as

$$d_e = \frac{A_e}{\tilde{a}_e - \Sigma a_{nb}} \qquad d_n = \frac{A_n}{\tilde{a}_n - \Sigma a_{nb}} \tag{21}$$

The pressure-correction equation is exactly the same as that described earlier (Eq. (20)) with the *d*-coefficients being computed from Eq. (21) rather than from Eq. (15). The overall iterative solution algorithm is identical to that described for SIMPLE.

3.4 SIMPLER Algorithm. In developing the SIMPLER procedure, it was recognized that the pressure-correction equation in the SIMPLE algorithm, in view of the approximation that $\Sigma a_{nb} u'_{nb} = \Sigma a_{nb} v'_{nb} \cong 0$, was responsible for the slow convergence of the pressure field. While SIMPLEC alleviated the magnitude of this approximation, the p' equation was still based on the neglect of the $\Sigma a_{nb}(u'_{nb} - u'_e)$ term. The SIMPLER algorithm derives a pressure equation that does not require the aforementioned approximations made in the SIMPLE and SIMPLEC methods. This is done by first defining pseudo-velocities $\hat{u}_e$ and $\hat{v}_n$ as

$$\hat{u}_e = \frac{\Sigma a_{nb} u_{nb} + b_e}{\tilde{a}_e} \quad \text{and} \quad \hat{v}_n = \frac{\Sigma a_{nb} v_{nb} + b_n}{\tilde{a}_n} \tag{22}$$

Thus, Eqs. (10) and (11) are re-expressed as

$$u_e = \hat{u}_e + d_e(p_p - p_E) \quad \text{and} \quad v_n = \hat{v}_n + d_n(p_p - p_N) \tag{23}$$

where d_e and d_n are defined by Eq. (18). Substituting Eq. (23) into Eq. (19) leads to an equation for the pressure

$$a_p p_p = a_E p_E + a_W p_W + a_N p_N + a_S p_S + b \tag{24}$$

Detailed expressions for the coefficients may be found in [5]. Equation (24) is a better approximation for the pressure p than that obtained from the corresponding p' equation (Eq. (20)) in the SIMPLE algorithm.

3.5 PISO Algorithm. The PISO algorithm, proposed by Issa [29], is a time-marching procedure, with a predictor step and one or more corrector steps during each time step. Issa et al. [30] recommend that the equations first be recast in an incremental form in order to minimize the computing effort and reduce storage requirements. For convenience in notation, the converged solution at the previous time step is denoted by a superscript n, while the solutions at the present time step are denoted by a superscript * at the predictor level, ** at the first corrector level, and *** at the second corrector level.

Equation (10) can be expressed implicitly as

$$\tilde{a}_e u_e^* = \Sigma a_{nb} u_{nb}^* + A_e(p_P^n - p_E^n) + b_e^n \tag{25}$$

and then, updated by

$$\tilde{a}_e u_e^{**} = \Sigma a_{nb} u_{nb}^* + A_e(p_p^* - p_E^*) + b_e^n \tag{26}$$

Subtracting Eq. (25) from Eq. (26) gives the increment equation

$$u_e^{**} = \hat{u}_e + d_e(p_p^* - p_E^*) \tag{27}$$

where

$$\hat{u}_e = u_e^* - d_e(p_p^n - p_E^n) \tag{28}$$

and d_e is given by Eq. (18). Similar equations can be derived for u_w^{**}, v_n^{**}, and v_s^{**}. Equation (25) is the velocity-predictor equation, while Eq. (27) represents the first corrector step for velocity. Substitution of Eq. (27) into the continuity equation (19) leads to the pressure equation, which is exactly of the same form as Eq. (24) with the $\hat{u}$ and $\hat{v}$ in the coefficients given by Eq. (28) instead of Eq. (22). This equation is the predictor equation for pressure.

The next set of corrector equations can be derived by expressing Eq. (10) as

$$\tilde{a}_e u_e^{***} = \Sigma a_{nb} u_{nb}^{**} + A_e(p_p^{**} - p_E^{**}) + b_e^n \tag{29}$$

and subtracting Eq. (26) from the above equation. This results in a second corrector equation for velocity

$$u_e^{***} = \hat{u}_e + d_e(p_p^{**} - p_E^{**}) \tag{30}$$

where

$$\hat{u}_e = u_e^{**} + \{\Sigma a_{nb}(u_{nb}^{**} - u_{nb}^*)\}/\tilde{a}_e - d_e(p_p^* - p_E^*) \tag{31}$$

Similar equations can be derived for u_w^{***}, v_n^{***}, and v_S^{***}.

To derive the pressure-corrector equation, equations of the form (30) are substituted into the discretized continuity equation, and again a system of equations represented by Eq. (24) is obtained. This equation represents the pressure-corrector equation.

The PISO algorithm can be described by the following steps:

1. Using the previous time step solution (u^n, v^n, p^n), calculate the coefficients of the momentum equations (such as Eq. (25)) and solve this system of implicit equations. This represents the predictor step for velocity.
2. Using this predicted velocity, calculate coefficients of pressure equation (24) and solve for the pressure field. This is the predictor step for the pressure.
3. Correct the velocity field using the explicit equation, Eq. (27). This is the first corrector step for velocity.
4. Using the corrected velocities, calculate the coefficients of the pressure equation in the corrector step and solve the implicit system of equations to obtain an updated pressure field.
5. Using the corrected pressure field, re-evaluate the velocity field using the explicit equation, Eq. (30). This is the second corrector step for the velocity.
6. March to the next time step.

3.6 Performance Assessment. In attempting to provide an assessment of how the various methods perform, it should be noted that only general conclusions can be drawn based on reported studies [31], and that the quantitative performance of the methods varies from one problem to another. In general, both SIMPLEC and SIMPLER exhibit improved convergence characteristics over SIMPLE. However, both SIMPLEC and SIMPLER show comparable behavior, and the work requirement per iteration or time step is lower for SIMPLEC. The PISO algorithm exhibits good convergence properties, particularly for problems where the scalar equation is not strongly coupled with the momentum equation. As an example of comparative performance, Fig. 3 shows a compari-

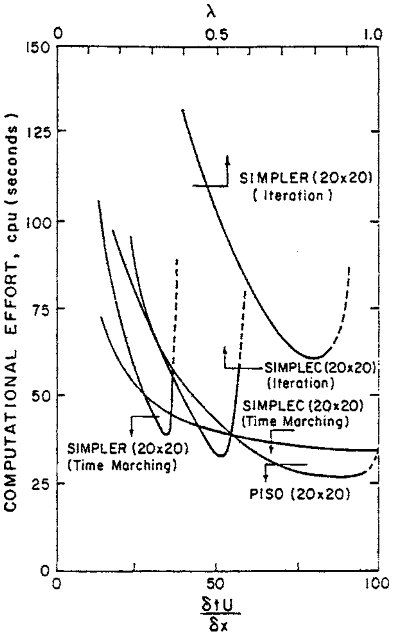

Fig. 3 Comparison of SIMPLER, SIMPLEC, and PISO for turbulent flow in a sudden expansion geometry (from Jang et al. [31])

son of the computational effort associated with SIMPLER, SIMPLEC, and PISO on a single processor for turbulent flow in an axisymmetric sudden expansion geometry on a very coarse grid (for illustrative purposes). Results are shown with the schemes cast in both an iterative framework and a time-stepping framework. It can clearly be seen that SIMPLEC and PISO show better performance from a computational effort perspective. Results with SIMPLE are not shown since they are considerably inferior. On co-located grids, the convergence of the continuity equation is poor for both SIMPLE and SIMPLER, which have been formulated using a correction proposed by Rhie and Chow [17]; the SIMPLEM (SIMPLE-Modified) approach of Moukalled and Acharya [32] shows improved convergence. This is illustrated in Fig. 4, which shows the comparison between SIMPLER with the Rhie and Chow correction (Fig. 4(*a*)) and SIMPLEM (Fig. 4(*b*)) for a driven cavity. If attention is focused on the residual of the momentum equations, it can be seen that the SIMPLEM algorithm provides improved convergence

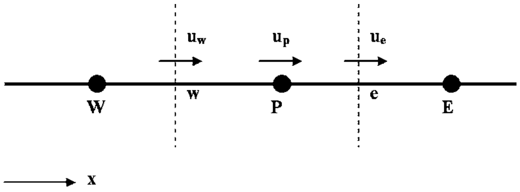

Fig. 5 Nomenclature for co-located storage scheme

characteristics.

In general, though there are modest differences in their performance, the algorithms comprising the SIMPLE family perform robustly, and impose relatively low memory and computational overhead, making them suitable solver engines for a wide variety of industrial CFD problems. However, the performance of this type of sequential solution procedure deteriorates when velocity and pressure fields are tightly coupled to each other by strong body forces, such as those resulting from rotation, swirl, or buoyancy. For these, coupled multigrid solution techniques, such as those described in Sec. 7, promise more robust performance.

4 Co-located Storage Schemes

The term “co-located” refers to methods in which both velocity and pressure are solved for at the same set of nodes, which are typically located at the centers of control volumes. In contrast, in the staggered-grid formulation used in Sec. 3, pressure is stored at the center and velocities at the faces of the control volumes.

The underlying issues behind staggered and co-located methods can be discussed via a simple one-dimensional situation sketched in Fig. 5. The two flow variables to be solved for are the velocity u and pressure p. Following the widely recognized nomenclature of [5], point P represents a typical grid node, points E and W are the neighbors of P, and points e and w are located on the faces of the control volume surrounding P. The discretized momentum and continuity equations read

$$a_P u_P = \sum_{nb} a_{nb} u_{nb} - \Delta V_P \left(\frac{dp}{dx}\right)_P \tag{32}$$

$$A_e u_e = A_w u_w \tag{33}$$

Here, a_P and a_{nb} represent discretization coefficients; A_e, A_w are the face areas, and ΔV_P represents the volume of the control vol-

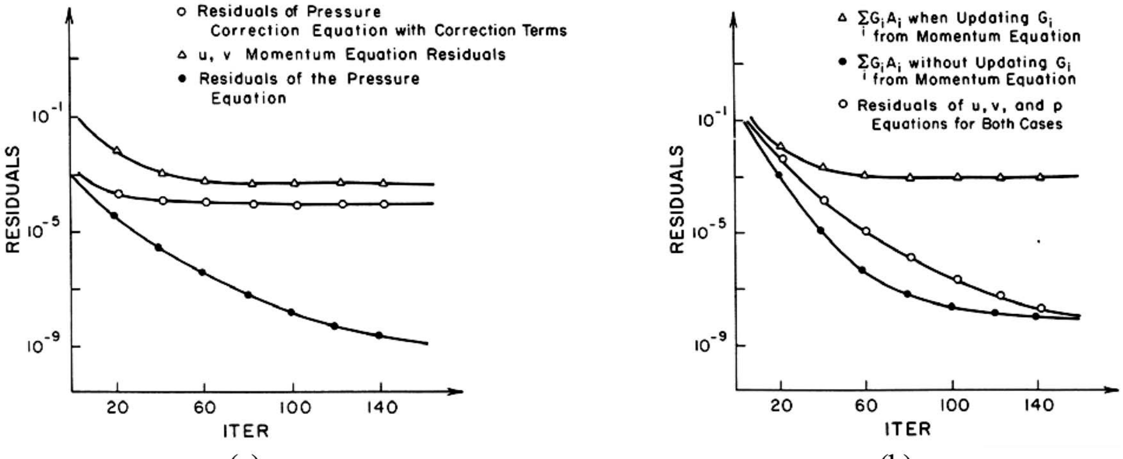

(a)

(b)

Fig. 4 Comparison of (*a*) SIMPLER with Rhie and Chow correction and (*b*) SIMPLEM for flow in a driven cavity Re=100 (from Moukalled and Acharya [32])

ume. Incompressible flow is assumed in the derivation of Eq. (33) for simplicity.

As explained in [5], two problems arise with a simple-minded co-located approach. First, assuming linear pressure variation between nodes, Eq. (32) results in u_P being driven by the pressure difference between *alternate* nodes W and E; that is, by $(p_W - p_E)$. As a consequence, since the numerical model only involves pressure differences between *alternate* nodes, spurious checkerboarded pressure fields can arise. The second problem arises from the continuity equation. Assuming a linear variation of velocity between nodes (and assuming $A_e = A_w$ for simplicity), Eq. (33) implies $u_W = u_E$. Thus, the numerical model only involves velocity differences between *alternate* nodes resulting in the possibility of checkerboarded velocity fields.

None of the above problems arises in a staggered-grid formulation, where pressure is stored at the primary nodes located at the center of control volume (W, P, E), while velocity is computed at control volume faces (w, e). The momentum discretization equation is now written for u_e, and it involves a pressure difference between *adjacent* nodes P and E; that is, $(p_P - p_E)$. As a result, checkerboarded pressure fields cannot arise. Furthermore, since the continuity equation is directly applied to face velocities u_e and u_w without any interpolation whatsoever, checkerboarded velocity fields cannot arise.

Due to the desirable attributes stated above, many early CFD codes employed the staggered-grid formulation, and the method has served us well. However, a limitation of the formulation is that it cannot easily be extended to general nonorthogonal curvilinear grids, and/or to unstructured-mesh methods, which are needed to handle complex geometries. As an example, consider the control-volume finite element method (CVFEM) of [11], which is described in Sec. 5. Here, for triangular elements, control volumes are constructed by joining the centroid of the elements to the midpoint of the sides. Clearly, for such a method, a staggered-grid formulation would be extremely tedious (perhaps impossible) to work out.

The above limitations of the staggered-grid approach prompted a search for co-located methods in late 1970s and early 1980s. This effort resulted in the following formulation that is widely used today [12,16,17,33]. The method is briefly described below.

We re-write Eq. (32) in the following alternate form

$$u_P = \hat{u}_P - D_P^u \left(\frac{dp}{dx} \right)_P \tag{34}$$

where

$$\hat{u}_P = \left(\sum_{nb} a_{nb} u_{nb} \right) \Big/ a_P \quad D_P^u = \frac{\Delta V_P}{a_P} \tag{35}$$

Equation (34) can be generalized to the following expression

$$\tilde{u} = \hat{u} - D^u \left(\frac{dp}{dx} \right) \tag{36}$$

We can now talk of a velocity field $\tilde{u}$ that is linked to the primary velocity field u by Eq. (36) through the artifact of the field $\hat{u}$, the pressure gradient (dp/dx), and the variable D^u.

The basic idea behind the co-located method of [12,16,17,33] lies in applying the continuity equation to the $\tilde{u}$ field instead of the primary u field. Thus, while Eq. (32) continues to be the discretized momentum equation, the continuity equation now reads

$$\tilde{u}_e = \tilde{u}_w \tag{37}$$

where

$$\tilde{u}_e = \hat{u}_e - D_e^u \left(\frac{dp}{dx} \right)_e \quad \tilde{u}_w = \hat{u}_w - D_w^u \left(\frac{dp}{dx} \right)_w \tag{38}$$

The values of $\hat{u}$ and D^u at the faces e and w are obtained by a suitable interpolation of values at the nodes (for example, $\hat{u}_e = f\hat{u}_P + (1-f)\hat{u}_E$, where f is an interpolation factor). However, and this is the critical point, the pressure gradients appearing in Eq. (38) are obtained using pressure differences between *adjacent* nodes. Thus

$$\left(\frac{dp}{dx} \right)_e = \frac{(p_E - p_P)}{(x_E - x_P)} \quad \left(\frac{dp}{dx} \right)_w = \frac{(p_P - p_W)}{(x_P - x_W)} \tag{39}$$

Equations (37)–(39) can be combined to get the desired equation that relates pressure at the point P to pressure at neighbors E and W.

Due to the use of Eq. (39), the numerical model now involves pressure differences between *adjacent* nodes and hence checkerboarded pressure fields are filtered out. Likewise, since the continuity equation (Eq. (37)) involves *adjacent* velocities (albeit for the $\tilde{u}$ field), checkerboarded velocity fields are prevented. Thus, we have a co-located method that is not afflicted by any of the problems described at the beginning of this section.

The co-located method described above is also sometimes called *momentum interpolation*. It has become an industry standard and is the basis of several commercial codes in use today. For simplicity, we have limited the discussion here to a one-dimensional situation; details of extension to multiple dimensions in the context of finite-volume and control volume finite-element formulations may be found in [12,16,17,33].

Even though it is being used widely, the above co-located method has subtle features that are not entirely desirable. It is important that these features be understood and appropriate caution exercised by code developers and users. Two of these features are briefly discussed below. A more detailed discussion may be found in [16,33].

(1) Suppose a term (λu_P) is added to both the left- and right-hand sides of the discretized momentum equation (Eq. (32)). This operation does not alter Eq. (32) itself. However, $\hat{u}_P$ and D_P^u are modified and now read

$$\hat{u}_P = \left(\lambda u_P + \sum_{nb} a_{nb} u_{nb} \right) \Big/ (a_P + \lambda) \quad D_P^u = \frac{\Delta V_P}{(a_P + \lambda)} \tag{40}$$

Because $\hat{u}$ and D^u have changed, the $\tilde{u}$ field that enters the continuity equation also changes. As a result, the overall numerical model is altered and a different velocity and pressure solution results. The fact that the addition of a term (λu_P) to both sides of Eq. (32) changes the overall solution is definitely not desirable. For instance, the term (λu_P) could be introduced to under-relax Eq. (32). Our final solution would then depend on the under-relaxation factor λ. A similar problem would arise if there were momentum source terms that were linearized as $(S = A + Bu_P)$. In this case, different solutions would result depending on the linearization process used to compute A and B. Another situation to consider is unsteady flow where a term such as (λu_P) represents the transient term with λ being inversely proportional to time step Δt. As can be seen, with the above formulation, the final steady-state solution would depend on the time step Δt chosen, something that is clearly undesirable. A similar problem would arise in parabolic flows where the fully developed solution would depend on the marching step size.

The above difficulty is a consequence of the fact that $\hat{u}$ and D^u depend on the particular form of the momentum equation (Eq. (32)) chosen. Fortunately, however, this also gives us a means of circumventing the problem. For instance, just for the purpose of defining $\hat{u}$ and D^u, one may work with Eq. (32) in its nonunder-relaxed form and shift the (λu_P) term to the right-hand side. Doing so would clearly evade the problems mentioned in the previous paragraph.

(2) The second difficulty with the above co-located method stems from the fact that we are now working with two loosely coupled velocity fields of which one (u) is driven by the momentum and the second $(\tilde{u})$ is driven by continuity. Consider a one-

dimensional incompressible situation in which the velocity is determined entirely by continuity. The co-located method will then deliver the right velocity field $\tilde{u}$. However, there is no guarantee that the field u will satisfy continuity. Indeed, in the presence of an arbitrary distribution of source terms in the momentum equation, the u field can be at great variance from that required by continuity. The severity of this problem further depends on the numerical formulation employed and how the source terms are discretized. The problem is more severe in a traditional finite-volume approach because the source terms are assumed uniform over the control volumes while the pressure gradient is uniform over the region between the nodes. In contrast, the problem is less severe (or nonexistent) in a finite-element type formulation where uniform source terms and pressure gradients are both defined over the elements.

In summary, co-located approaches have many advantages, including extension to methods for complex geometries. However, they have some undesirable features, as discussed here, and the severity of these problems depends on the details of the implementation, and on whether cell-based or node-based formulations are being used. Though some solutions to these problems have been proposed in [16,33], there is definitely room for further development and improvement, and such efforts are surely welcome.

5 Schemes for Complex Geometries

5.1 Staggered Body-Fitted-Mesh Methods. The prediction of fluid flow in complex geometries requires the use of boundary-fitted grids, which may be either structured or unstructured. The use of structured body-fitted meshes allows the use of pressure-velocity staggering, and several publications in the 1980s employed these formulations to avoid the difficulties with co-located formulations discussed in Sec. 4. In this section, we briefly review these techniques, addressing orthogonal and nonorthogonal meshes in turn.

Orthogonal Grids. The staggered-grid method for a general orthogonal grid is a straightforward extension of the basic method for standard coordinate systems [5]. The velocity components normal to the control-volume faces are chosen as the dependent variables and one velocity component is stored at each face. These velocity components do not have fixed directions. Consequently, the corresponding momentum equations involve additional curvature terms, such as Coriolis and centrifugal forces; these terms reflect the fact that linear momentum is conserved in a straight line and not along a grid line. Thus, the additional features introduced by a general orthogonal grid are the calculation of geometric quantities (for example, lengths, areas, and volumes) and the momentum source terms due to grid curvature. For examples of calculation methods based on orthogonal grids, see Pope [34], Rastogi [35], and Raithby et al. [36].

Nonorthogonal Grids. For many arbitrary shaped domains, the construction of an orthogonal grid becomes difficult or impossible and a nonorthogonal grid must be used. Staggered-grid methods for nonorthogonal grids differ primarily in the choice of the velocity components used as the dependent variables in the momentum equations. The available choices include the Cartesian velocity components and the grid-oriented curvilinear (covariant and contravariant) velocity components. For Cartesian velocity components, the momentum equations are simple; for the curvilinear velocity components, they are quite complex and involve curvature terms because the base vectors for these components do not have fixed directions. The expressions for the curvature terms involve Christoffel symbols and can be obtained using tensor algebra (for example, [37,38]). Karki and Patankar [10,39] have proposed an alternative algebraic procedure based on a locally fixed coordinate system for their evaluation. The mathematical derivation of this algebraic procedure has been given by Davidson and Hedberg [40].

Some of the early staggered-grid methods for nonorthogonal grids were straightforward extensions of the basic method developed for the Cartesian coordinate system. These methods (for example, [41]) store one Cartesian velocity component at a control-volume face. Such methods are suitable only for grids that do not deviate significantly from the reference Cartesian grid and encounter difficulties when the grid lines turn by 90 degrees. A more general method can be developed by storing *all* Cartesian velocity components at each face of a control volume [8]. Such a formulation, however, involves extra computational effort to solve for the additional velocity components even in the regions where the grid is orthogonal or nearly orthogonal. In an alternative arrangement [42], all Cartesian velocity components are stored at the centers of the control volumes and the pressures at the corners. However, this arrangement leads to a weak coupling between the velocity and pressure fields and also involves extra computational effort.

The use of grid-oriented velocity components as the primary dependent variables in the momentum equations leads to calculation methods with wider applicability. In these formulations, only one velocity component need be stored at a control-volume face. The preferred choices for the velocity components are the physical covariant (directed along the grid line) and contravariant (directed normal to the control-volume face) components. Each choice of velocity component offers certain advantages and disadvantages. For the covariant velocity component, the pressure term involves only the pressures at the two grid points straddling the velocity component. However, the calculation of mass fluxes at the control-volume faces involves covariant components at the neighboring locations and requires interpolation. For the contravariant velocity component, on the other hand, the pressure term involves transverse gradients, but no interpolation is required to calculate the mass fluxes. Thus, there is no clear advantage in choosing one velocity component over the other, and methods based on both components are available. For representative methods based on contravariant velocity components, see Refs. [37,38,43–45]; for methods based on covariant components, see Refs. [10,39,40,46]. As discussed above, the momentum equations for grid-oriented velocity components involve curvature terms. These terms can be calculated using either tensor algebra or a simpler algebraic procedure proposed by Karki and Patankar [10,39]. Among the reference methods cited here, the tensor algebra approach has been used in Refs. [37,38] and the algebraic procedure in [40,43–46].

Although staggered-grid methods are widely used for the calculation of fluid flow in complex geometries, they have certain disadvantages. The use of staggered grids leads to tedious programming, especially for three-dimensional geometries. The discretization of curvature terms in the momentum equations requires that the grid be smooth. When grid-oriented velocity components are used as the primary variables, transformation to Cartesian velocity components is required to calculate auxiliary quantities such as production terms in turbulence models or viscous terms for non-Newtonian rheologies. Finally, the generation of good-quality nonorthogonal grid becomes difficult for very complex geometries. Because of these disadvantages, the use of unstructured grids is gaining popularity.

5.2 Control-Volume Finite-Element Methods. Control-volume finite-element methods (CVFEMs) are formulated by amalgamating and extending concepts that are native to finite-volume methods (FVMs) and finite-element methods (FEMs) [5,11,47,48]. Thus, CVFEMs could be regarded as FEMs based on the subdomain-type (or control-volume-based) method of weighted residuals, and they could also be thought of as element-based *vertex-centered* FVMs [49,50].

For CVFEMs, staggered-mesh schemes of the type discussed in Sec. 3 are not workable. Instead, two approaches have been taken: (i) unequal-order formulations in which a sparser grid and a lower-order interpolation is used for pressure than that for the

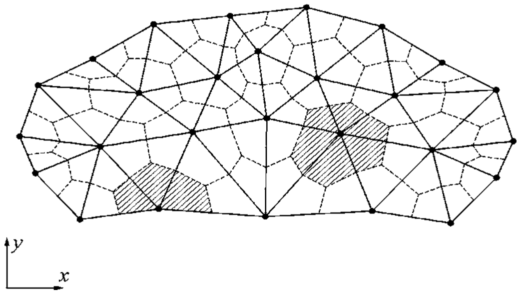

Fig. 6 CVFEM discretization of a planar two-dimensional calculation domain

velocity components [11,47], and (ii) the equivalent of the co-located momentum-interpolation scheme described in Sec. 4 [12,17,51]. Unequal-order formulations are afflicted by the following disadvantages [49]: (i) the need to use two sets of control volumes or elements makes the specification and calculation of geometric information unwieldy; (ii) mass conservation is not strictly satisfied over the momentum control volumes; and (iii) accurate solutions of flows involving high Reynolds numbers or large pressure gradients could require excessively fine grids due to the lower-order interpolation of pressure. Thus, co-located formulations based on the momentum-interpolation scheme have become the methods of choice in computational fluid dynamics, especially when unstructured grids are employed. An overview of the typical steps involved in the formulation of CVFEMs is presented in this section in the context of a co-located, equal-order, primitive-variables version of the method, formulated for the solution of steady, planar, two-dimensional problems involving incompressible fluid flow and heat transfer.

Domain Discretization. The discretization of an irregular-shaped planar two-dimensional calculation domain is shown in Fig. 6. First, the domain is discretized into three-node triangular elements: the solid lines and black dots show the edges and vertices of such elements, respectively, in Fig. 6. The centroid of each triangular element is then joined to the midpoints of its sides, as shown by the dashed lines in Fig. 6. These dashed lines divide each triangular element into three *equal* areas (regardless of the shape of the triangular element), and, collectively, these areas form nonoverlapping contiguous control volumes of polygonal cross section, each associated with a node in the finite-element mesh: the hashed regions in Fig. 6 indicate two such control volumes, and the associated details are shown in Figs. 7(*a*) and 7(*b*). In *co-located* CVFEMs, the nodes are the storage locations of *all* dependent variables of interest.

Integral Conservation Equations. Let $\boldsymbol{J}$ denote the flux vector for combined diffusion and advection of a generic scalar transport variable ϕ, as in Eq. (1). Then

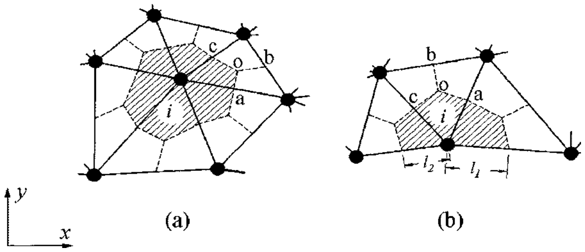

Fig. 7 CVFEM grid and related nomenclature: (*a*) internal node and (*b*) boundary node

$$\boldsymbol{J} = (-\Gamma_\phi \partial\phi/\partial x + \rho u \phi)\boldsymbol{i} + (-\Gamma_\phi \partial\phi/\partial y + \rho v \phi)\boldsymbol{j} \qquad (41)$$

In this expression, $\boldsymbol{i}$ and $\boldsymbol{j}$ are unit vectors in the x and y Cartesian coordinate directions, respectively. Cartesian velocity components u and v are used here, in contrast to the co- and contravariant velocity formulations discussed in Sec. 5.1.

With reference to the control volume V_i associated with any node i, akin to those shown in Figs. 7(*a*) and 7(*b*), and under steady-state conditions, an integral equation expressing the conservation of ϕ in the presence of diffusion, advection, and volumetric rate of generation (or source term) S_ϕ can be cast in the following form [49]

$$\left[\int_a^o \boldsymbol{J}\cdot\boldsymbol{n}ds + \int_o^c \boldsymbol{J}\cdot\boldsymbol{n}ds - \int_{iaoc} S_\phi dV\right] + [\text{similar contributions from other elements associated with node } i] + [\text{boundary contributions, if applicable}] = 0 \qquad (42)$$

where $\boldsymbol{n}$ is a unit vector normal to the differential length element ds, pointing outward with respect to the control volume associated with the node i.

Interpolation Functions. The derivation of algebraic approximations to the contributions of each element to integral conservation equations akin to Eq. (42) requires the specification of appropriate interpolation functions for the diffusion coefficients, mass density, source terms, and the dependent variables. In each triangular element, the values of Γ_ϕ and ρ at the centroid are assumed to prevail over the corresponding element. The source term S_ϕ is linearized, if required, and expressed in the following general form [5]: $S_\phi = G^{S_\phi} + E^{S_\phi}\phi$. In *each* element, the *nodal* values of G^{S_ϕ} and E^{S_ϕ} are assumed to prevail over the portions of the corresponding control volumes.

In the calculation of mass flow rates across the control volume faces, the mass-conserving velocity components in the x and y directions are denoted by u^m and v^m, respectively, and the corresponding velocity vector is given by $\boldsymbol{V}^m = u^m\boldsymbol{i} + v^m\boldsymbol{j}$. The mass-conserving velocities are interpolated using a special momentum-interpolation scheme borrowed from the work of Prakash and Patankar [12], in order to prevent spurious pressure and velocity oscillations. Some details of this scheme are given in Sec. 4, and additional details are available in [52]. The pressure p is interpolated linearly within each element.

In the derivation of algebraic approximations to the surface integrals of diffusion fluxes in Eq. (42), the gradients of the dependent variable inside each triangular element are approximated using linear interpolation functions. With linear interpolation of ϕ and the piecewise constant (centroidal value prevailing) interpolation of Γ_ϕ, to ensure that the algebraic approximations of the diffusion transport terms contribute positively to the coefficients in the discretized equations, every element must be an acute-angle triangle (that is, each vertex angle must be $\leqslant \pi/2$ radians). Venditti [53] has presented a proof of this sufficient condition.

For the derivation of algebraic approximations to the surface integrals of advection fluxes in Eq. (42), Baliga and Patankar [11] recommend a flow-oriented upwind scheme (FLO), constructed by borrowing ideas from the works of Spalding [54] and Raithby [55]. In this scheme, ϕ is assumed to vary exponentially in the direction of the element-average mass-conserving velocity vector and linearly in the direction normal to this vector. Furthermore, when an element-based Peclet number Pe_Δ approaches zero, this function becomes fully linear. In problems that involve acute-angle triangular elements and relatively modest values of Pe_Δ, the FLO scheme performs well and produces accurate solutions; related references are given in [49,52]. However, when large gradients of the dependent variable occur within an element or obtuse-angle triangular elements are used in problems with large values of Pe_Δ, the FLO scheme can lead to undesirable negative contributions of the advection transport terms to the coefficients in the

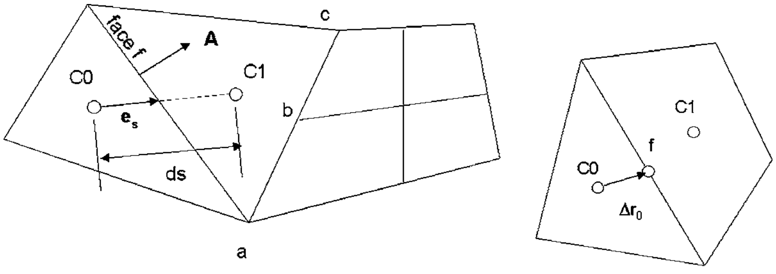

(a) (b)

Fig. 8 (***a***) **Nomenclature for cell-based finite volume scheme and (*b*) geometry for higher-order interpolation**

discretized equations. Masson et al. [56] have proposed a mass-weighted skew upwind scheme (MAW) that overcomes this difficulty. However, this MAW scheme, which is an adaptation of the positive-coefficient schemes of Schneider and Raw [57] and Saabas and Baliga [58], is only first-order accurate. Recently, Tran et al. [59] have proposed a second-order extension of this MAW scheme, but it is not bounded; with the incorporation of suitable limiters, this scheme could prove very useful.

Discretized Equations. The discretized equations are obtained by first deriving algebraic approximations to the element contributions and the boundary contributions, if applicable, to Eq. (42), and then assembling these contributions appropriately [52]. With reference to Fig. 7(*a*), such an equation for node *i* can be cast in the following general form

$$a_i^{\phi}\phi_i = \sum_{nb} a_{nb}^{\phi}\phi_{nb} + b_i^{\phi} \tag{43}$$

The integral momentum conservation equations are formulated in terms of Cartesian velocity components. Except for the presence of integrals of the pressure gradients, they are identical in form to the integral conservation equation for ϕ. The discretized approximations of these equations can be cast in the following forms

$$a_i^u u_i = \sum_{nb} a_{nb}^u u_{nb} + b_i^u + [-\overline{(\partial p/\partial x)}_{V_i}]V_i \tag{44}$$

$$a_i^v v_i = \sum_{nb} a_{nb}^v v_{nb} + b_i^v + [-\overline{(\partial p/\partial y)}_{V_i}]V_i \tag{45}$$

The terms $\overline{(\partial p/\partial x)}_{V_i}$ and $\overline{(\partial p/\partial y)}_{V_i}$ are volume-averaged values of the pressure gradients in the various elements associated with node *i*, and V_i is the volume of the control volume surrounding this node [52]. The integral mass conservation equation applied to the control volume surrounding node *i* in Fig. 7(*a*) is obtained from Eq. (42) by replacing the advection-diffusion flux $\boldsymbol{J}$ by the mass flux $\rho\boldsymbol{V}^m$, and setting the source term S_ϕ to zero. An algebraic approximation of this equation using the momentum-interpolation scheme for the mass-conserving velocity components yields the discretized equation for pressure. With reference to node *i* in Fig. 7(*a*), this equation can be cast in the following form [52]

$$a_i^p p_i = \sum_{nb} a_{nb}^p p_{nb} + b_i^p \tag{46}$$

Solution of the Discretized Equations. A sequential iterative variable adjustment procedure, formulated by Saabas and Baliga [58] by borrowing ideas from the SIMPLER procedure of Patankar [5], is used to solve the nonlinear coupled sets of discretized equations for *u*, *v*, *p*, and ϕ. Full details of this procedure are available in Baliga and Atabaki [52]. In each of the overall iterations of this procedure, sets of linearized, decoupled, discretized equations are solved sequentially. If a structured grid is used, each of these sets of discretized equations can be solved using an iterative line-by-line TDMA [5]. If an unstructured grid is used, an iterative point-by-point successive over-relaxation method can be used to solve these equations [53]. Implementation of techniques to accelerate the convergence of these iterative linear equation solvers is highly recommended, especially for the solution of the discretized pressure equations. In particular, the additive-correction multigrid method with adaptive volume agglomeration proposed by Elias et al. [60] has been found to be very useful [53]. Implementation of coupled multigrid schemes, akin to those discussed in Sec. 7 of this paper, would also be very useful.

In summary, a basic outline of a co-located, equal-order, CVFEM for solving steady, planar, two-dimensional, incompressible fluid flow and heat transfer problems has been presented in this section. An adaptation of this CVFEM for the solution steady, two-dimensional, axisymmetric problems is available in the work of Masson and Baliga [56].

Examples of the applications of the aforementioned steady, two-dimensional CVFEMs to a variety of test problems are available in the works of Baliga and Patankar [11], Prakash and Patankar [12], and Masson and Baliga [56,61]. Unstructured-grid, *h*-adaptive versions of these methods and their application to test problems are discussed in the work of Venditti [53]. Three-dimensional CVFEMs based on tetrahedral elements and examples of their applications to test problems are available in the works of LeDain-Muir and Baliga [62], Saabas and Baliga [58], and Costa et al. [63]. Examples of CVFEMs for the prediction of unsteady fluid flow and their applications to test problems involving gas-solid particle flows over a wide range of concentration are available in the work of Masson and Baliga [61]. A second-order MAW scheme implemented in a two-dimensional CVFEM and its application to test problems are discussed in the recent work of Tran et al. [59]. As was mentioned earlier, this second-order MAW scheme seems very promising, but recent tests with it have shown that it is not bounded. An extension of this MAW scheme to three-dimensional formulations, along with suitable limiters (to ensure that it is bounded), would greatly enhance the usefulness of CVFEMs.

5.3 Cell-Based Finite-Volume Methods.

In contrast to CVFEMs, cell-based finite-volume schemes enforce the conservation principle on the element itself (referred to as a cell), rather than on a control volume constructed around the vertices, such as in Fig. 7(*a*) [14,15,64,65]. In a cell-based formulation, the domain is discretized into arbitrary unstructured convex polyhedral cells, as shown in Fig. 8(*a*). General nonconformal interfaces, such as the face *abc* are admitted automatically by considering the cell *C1* to be four-sided. In addition, hybrid meshes composed of cells with different shapes are admitted. This generality in cell shape is achieved by eschewing finite-element like shape functions for interpolation. The solution variable ϕ, as well as ρ and Γ_ϕ in Eq. (1)

are stored at the cell centroid.

Integrating Eq. (1) over the control volume *C0* in Fig. 8(*a*), yields the cell-balance equation

$$\left[\frac{\partial}{\partial t}(\rho\phi)\right]_0 \Delta V_0 + \sum_f F_f\phi_f = \sum_f D_f + S_\phi \Delta V_0 \tag{47}$$

Here, F_f is the mass flow rate out of the cell *C0* across face f, ΔV_0 is the volume of the cell *C0*, and D_f is the diffusive transport through the face f into the cell *C0*. The unsteady and source terms are dealt with in the manner described in [64]. We turn now to the diffusion and convection terms.

Diffusion Term. The diffusion term at the face is given by

$$D_f = \Gamma_{\phi f} \nabla \phi \cdot \boldsymbol{A} \tag{48}$$

Here, $\boldsymbol{A}$ is the outward-pointing area vector for the face f in Fig. 8(*a*), and $\Gamma_{\phi f}$ is the diffusion coefficient evaluated at the face f. In the absence of element-based shape functions, in order to write an implicit discretization of Eq. (48) in terms of the cell values ϕ_0 and ϕ_1 in Fig. 8(*a*), the diffusion term is written as [64]

$$D_f = \Gamma_{\phi f} \frac{(\phi_1 - \phi_0)}{ds} \frac{\boldsymbol{A}\cdot\boldsymbol{A}}{\boldsymbol{A}\cdot\boldsymbol{e}_s} + S_f$$

$$S_f = \Gamma_{\phi f}\left(\bar{\nabla}\phi\cdot\boldsymbol{A} - \bar{\nabla}\phi\cdot\boldsymbol{e}_s\frac{\boldsymbol{A}\cdot\boldsymbol{A}}{\boldsymbol{A}\cdot\boldsymbol{e}_s}\right) \tag{49}$$

Here, $\bar{\nabla}\phi$ is the average gradient of ϕ at the face, and is taken as the arithmetic average of the gradient in the cells *C0* and *C1*. The diffusion term D_f is seen to consist of two terms: the primary term, represented by the first term in the D_f expression and the secondary gradient term, S_f. For orthogonal meshes $\boldsymbol{A}$ and $\boldsymbol{e}_s$ are parallel to each other (see Fig. 8(*a*)), and the secondary term goes to zero. The primary term is treated implicitly in terms of the cell-centroid values ϕ_0 and ϕ_1, and contributes to the coefficient matrix in the discrete equations, while the secondary gradient term is treated explicitly. If a general cell-shape-independent way can be found to evaluate the cell gradient $\nabla\phi$, a powerful technique for complex geometries may be devised.

Convective Term. The convective term in Eq. (47) requires the evaluation of the face value ϕ_f at the face f in Fig. 8(*a*). A simple first-order upwind approximation to it may be found using

$$\phi_f = \phi_0 \quad \text{if } F_f \geqslant 0$$

$$\phi_f = \phi_1 \quad \text{if } F_f < 0 \tag{50}$$

Here, F_f is the mass flow rate out of cell *C0* through face f. Higher-order schemes for the face value may be found using, for example, upwind approximations such as [64]

$$\phi_f = \phi_0 + (\nabla\phi)_0 \cdot \Delta\boldsymbol{r}_0 \tag{51}$$

The vector $\Delta\boldsymbol{r}_0$ is shown in Fig. 8(*b*); Eq. (51) assumes that cell *C0* is the upwind cell. The gradient in cell *C0*, i.e., $(\nabla\phi)_0$, may be limited using standard limiters to prevent overshoots and undershoots [66]. It is important to note that line-based higher-order schemes, such as that in [25], cannot easily be applied. The development of higher-order schemes for unstructured meshes remains an active area of research.

Gradient Calculation. Cell gradients of ϕ are necessary to evaluate the secondary gradient S_f in Eq. (49), and also to devise higher-order convection schemes. Cell-based finite-volume schemes are distinguished from CVFEMs in that the cell gradient $(\nabla\phi)_0$ is not found from element-based shape functions, which are typically specific to particular element shapes, and are not easily generalizable to arbitrary polyhedra. Instead, cell-based schemes have employed either a gradient-theorem approach or a least-squares approach for finding $(\nabla\phi)_0$ [66]. In the least-squares approach, the gradient at the cell centroid is evaluated such that it reconstructs the solution in the neighborhood of the cell in a least-squares sense. For example, for cell *C0* in Fig. 9, we wish to find a gradient $(\nabla\phi)_0$ such that it reconstructs the cell-centroid value at each of the neighboring cells C_j $(j=1,2,3,4)$. By assuming a locally linear variation of ϕ, we may write

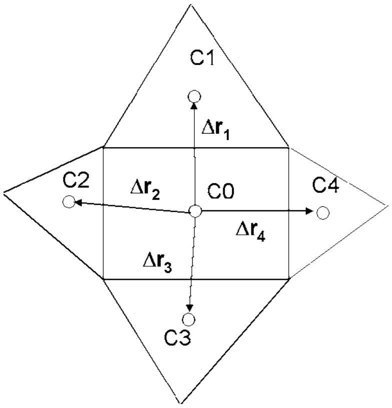

Fig. 9 Nomenclature for least-squares interpolation to find cell gradients in cell-based finite volume scheme

$$\phi_0 + (\nabla\phi)_0 \cdot \Delta\boldsymbol{r}_j = \phi_j \tag{52}$$

The unknowns in 2D are the two components of the gradient: $(\partial\phi/\partial x)_0$ and $(\partial\phi/\partial y)_0$. However, the number of available equations is greater than 2, since an equation similar to Eq. (52) may be written for all neighbors j in Fig. 9, leading to an over-determined system. Physically, this means that a single linear profile cannot exactly reconstruct *all* neighboring cell values j. Instead, we use a least-squares procedure that finds $(\partial\phi/\partial x)_0$ and $(\partial\phi/\partial y)_0$ such that the root mean square value of the difference between the reconstructed and actual neighbor values is minimized, that is, we minimize the residual R defined as

$$R = \sum_j R_j \quad R_j = \Delta x_j \left(\frac{\partial\phi}{\partial x}\right)_0 + \Delta y_j \left(\frac{\partial\phi}{\partial y}\right)_0 - (\phi_j - \phi_0) \tag{53}$$

This technique poses no restrictions on cell shape or connectivity.

Solution of Discrete Equations. As with CVFEMs, the discrete equation set resulting from cell-based finite-volume schemes is sparse and unstructured, and line-based solution techniques cannot be used. Algebraic multigrid methods have been devised for the solution of linear unstructured algebraic sets, and by using intelligent agglomeration schemes, have been shown to work well for a variety of problems, including those with high degrees of geometric anisotropy, as well as anisotropy in fluid properties [67]. Gradient-search techniques, such as the preconditioned conjugate gradient method, have also been found to work well for these unstructured systems [68–70].

Computation of Fluid Flow. Unlike finite-volume schemes for structured meshes, staggered storage of pressure and velocity is not tenable; furthermore, unequal-order storage and interpolation is also not easily done with cell-based finite-volume schemes. Thus, co-located storage schemes, which store pressure and velocity at cell-centroids, are the only viable option. As with CVFEMs, Cartesian velocity components are the primary solution variables. Extensions of [17] to cell-based unstructured schemes have been published in [15] and form the basis of a number of commercial solvers. The shortcomings of co-located schemes discussed in Sec. 4 also apply here, and further research in this area is warranted.

In summary, cell-based finite-volume schemes enforce conservation on the element or cell directly, rather than on auxiliary

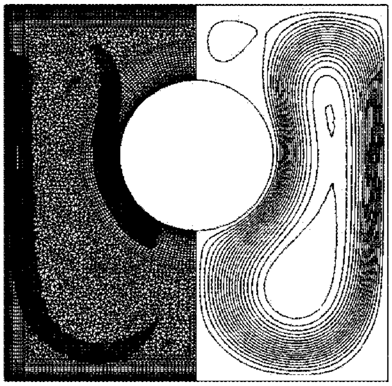

Fig. 10 Hybrid mesh adapted to velocity magnitude (left), and streamlines (right) for laminar natural convection over a hot cylinder located in a square box

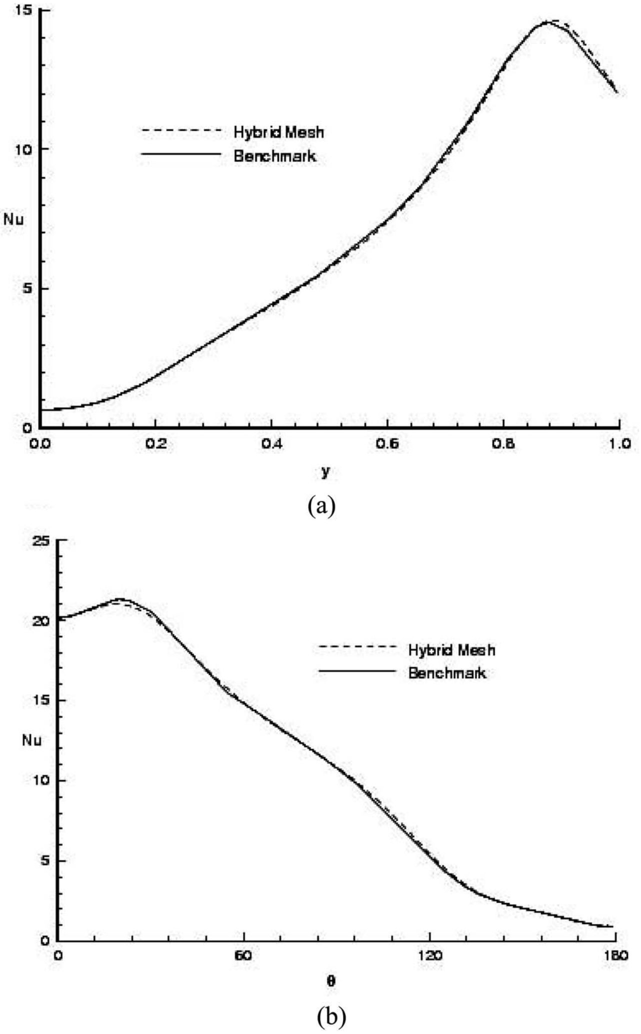

(a)

(b)

Fig. 11 Nusselt number along (*a*) cold wall, and (*b*) hot wall (Rayleigh number = 10^6 and Prandtl number = 0.1) [15], and comparison with benchmark solution of Demirdzic et al. [71]

control volumes constructed around element vertices. Because care is taken to devise discretization and gradient calculation procedures that are independent of cell shape, great geometric flexibility results. Thus, nonconformal meshes, with non-coincident vertices such as that in Fig. 8(*a*), are easily admitted. This allows not only for hanging-node mesh adaptation, but also the computation of flows involving sliding meshes, such as those occurring during rotor-stator interaction. It also eases the task of mesh generation by allowing the user to create nonconformal mesh blocks.

As an illustration, laminar natural convection around a hot cylinder located in a square box is shown in Fig. 10 [15]. A hybrid mesh of triangles and quadrilaterals adapted to the rising plume is shown on the left half of Fig. 10; typical streamlines are shown on the right half. Fig. 11(*a*) shows the cold (vertical) wall Nusselt number. Fig. 11(*b*) shows the Nusselt number on the hot cylinder, with θ being angle measured from the stagnation point. The comparison in Fig. 11 is with the benchmark solution of Demirdzic et al. [71]; good agreement is found despite the use of a coarser mesh. Applications of cell-based finite-volume schemes to combustion, radiation and other physics are now ubiquitous, and some examples may be found in [72,73]. Nevertheless, fruitful areas for future research remain. The development of robust higher-order schemes, fast and robust coupled solvers of the type discussed in Sec. 7, efficient linear solvers, as well as more accurate co-located schemes, all remain open areas for research.

6 Pressure-Based Methods for Compressible Flow

So far, we have focused on pressure-based methods for predicting incompressible flows. In this section, we discuss the extension of these methods to compressible flows. Traditional numerical methods [74–78] for compressible flows regard density as the dependent variable of the continuity equation and extract pressure from density via an equation of state. These *density-based* methods become inaccurate and inefficient at low Mach numbers, where density is a weak function of pressure. They are not applicable to incompressible flows unless ideas such as preconditioning [77] are introduced. Pressure-based methods, in which pressure is the primary variable and density is obtained from the equation of state, do not have any such limitations and are uniformly valid for incompressible and compressible flows, including those with shocks. Consequently, there is great interest in developing pressure-based methods that work across the range of Mach numbers.

To formulate pressure-based methods for compressible flows, it is instructive to analyze the role of pressure. In incompressible flows, density is independent of pressure, and pressure influences only the velocities, through the momentum equations. In this limit, the continuity equation represents a constraint equation for calculating pressure: when the correct pressure distribution is substituted in the momentum equations, the resulting velocities satisfy the mass conservation. For highly compressible flows, on the other hand, velocity is nearly independent of pressure, and pressure influences only the density, through the equation of state. Now the continuity equation can be considered as the equation for density. In a unified treatment that bridges these two limiting cases, pressure must be allowed to play a dual role: it should influence both density and velocities. In addition, the continuity equation should be interpreted as a constraint for calculating pressure. The correct pressure field is the one that produces velocities and densities that together satisfy mass conservation.

The governing equations for compressible flows are the continuity equation, the momentum equations, and the energy equation, supplemented by an equation of state. The treatment of the momentum and energy equations is identical to the procedure presented in Secs. 2 and 3 in the context of incompressible flows and is not repeated here. The pressure or pressure-correction equations, however, must be modified. These details are presented next.

Pressure-Correction Equation for Compressible Flows. The pressure-correction equation is derived for a steady, two-dimensional situation by using a grid in the Cartesian coordinate system, as shown in Fig. 1. The formulation is valid for both staggered and nonstaggered (or co-located) grid arrangements and can easily be extended to complex geometries.

The discretized continuity equation for the control volume around grid point P is given by

$$[(\rho u)_e A_e - (\rho u)_w A_w] + [(\rho v)_n A_n - (\rho v)_s A_s] = 0 \tag{54}$$

To proceed further, two important issues must be addressed: linearization of the mass flux terms and the value of density at a control-volume face (density interpolation).

Linearization of the Mass Flux Terms. For a linearization to be applicable to both incompressible and compressible flows, it must allow both velocity and density to play an active role. This is accomplished by linearizing the mass flux (ρu) as follows [5,22–24,39]

$$\rho u = (\rho u)^* + \rho^* u' + \rho' u^* \tag{55}$$

where the second-order term $\rho' u'$ has been neglected. In the above equation, the starred quantities denote the currently available values and the primed quantities are the changes caused by a change in pressure.

To obtain an equation in terms of a pressure correction, the changes in velocity and density are related to the change in pressure via a truncated form of the momentum equation (similar to that used for incompressible flows) and the equation of state, respectively. The velocity corrections are related to the pressure corrections via relations such as

$$u'_e = d_e(p'_P - p'_E) \tag{56}$$

The density correction is related to the pressure correction as

$$\rho' = Kp' \tag{57}$$

where

$$K = \frac{\partial \rho}{\partial p} \tag{58}$$

The quantity K represents a measure of the influence of pressure on density and is calculated from the equation of state. Its value depends on the process (for example, isentropic or isothermal) assumed in evaluating the partial derivative in Eq. (58). The choice of K does not affect the final results; it only influences the approach to convergence. For incompressible flows, density is independent of pressure, and thus, $K=0$.

By combining Eqs. (55)–(57), we get the following expression for $(\rho u)_e$

$$(\rho u)_e = (\rho u)_e^* + \rho_e^* d_e(p'_P - p'_E) + u_e^* \rho'_e \tag{59}$$

Density Interpolation. Equation (59) involves density and density correction at the control-volume face. These quantities must be interpolated from their grid-point values. The density interpolation scheme must satisfy two important requirements:

(a) In conjunction with the differencing scheme for the pressure gradient term, it should lead to a pressure or pressure-correction equation that exhibits the correct Mach number dependence: the character of the equation should be elliptic for subsonic flows and hyperbolic for supersonic flows.

(b) It should provide for a smooth transition from subsonic to supersonic flows.

In compressible flows the continuity equation acts as a transport equation for density. Thus, the interpolation schemes for the dependent variable in a general convection-diffusion equation (Eq. (1)) are also applicable for density, but with the Mach number taking the role of the Peclet number. The simplest, and most robust, choice is to take the face value of density as the value at the upstream grid point [5,22–24,39]. Thus, assuming $u_e > 0$, we have

$$\rho_e = \rho_P$$

$$\rho'_e = \rho'_P = K_P p'_P \tag{60}$$

Now the equation for $(\rho u)_e$ can be written as

$$(\rho u)_e = (\rho u)_e^* + \rho_P^* d_e(p'_P - p'_E) + u_e^* K_P p'_P \tag{61}$$

This expression contains a diffusion-like term (that involving d_e) and a convection term (that involving u_e). It is instructive to examine the ratio of the coefficients of the diffusion and convection terms in Eq. (61)

$$\frac{\rho_P d_e}{u_e K_P} \sim \mathrm{M}^{-2} \tag{62}$$

The ratio $(\rho_P d_e / u_e K_P)$ is proportional to the inverse of the square of Mach number M. At low Mach numbers, the diffusion term is dominant, and the mass flux is controlled by the pressure difference across the control-volume face. As the Mach number increases, the convection term becomes progressively more dominant, and the mass flux is controlled increasingly by the upstream pressure. Thus, the resulting pressure or pressure-correction equation exhibits the correct Mach number dependence, with a smooth transition between the subsonic and supersonic regimes.

Although the use of the upwind scheme for density interpolation leads to a robust formulation, it introduces excessive numerical diffusion and leads to smearing of shock waves. Solution accuracy can be improved by using high-resolution schemes for interpolating density (see [79,80], for example).

If we substitute expressions such as Eq. (61) for mass fluxes in Eq. (54), we obtain the following pressure-correction equation

$$a_P p'_P = a_E p'_E + a_W p'_W + a_N p'_N + a_S p'_S + b \tag{63}$$

where

$$a_E = A_e[\rho_e^* d_e + \max(-u_e^*,0)K_E] \tag{64a}$$

$$a_W = A_w[\rho_w^* d_w + \max(u_w^*,0)K_W] \tag{64b}$$

$$a_N = A_n[\rho_n^* d_n + \max(-v_n^*,0)K_N] \tag{64c}$$

$$a_S = A_s[\rho_s^* d_s + \max(v_s^*,0)K_S] \tag{64d}$$

$$\begin{aligned} a_P = {} & A_e[\rho_e^* d_e + \max(u_e^*,0)K_P] + A_w[\rho_w^* d_w + \max(-u_w^*,0)K_P] \\ & + A_n[\rho_n^* d_n + \max(v_n^*,0)K_P] + A_s[\rho_s^* d_s + \max(-v_s^*,0)K_P] \end{aligned} \tag{64e}$$

$$b = (\rho u)_w^* A_w - (\rho u)_e^* A_e + (\rho v)_s^* A_s - (\rho v)_n^* A_n \tag{64f}$$

The appearance of the compressible form of the pressure-correction equation is identical to that of its incompressible counterpart [5]. There are, however, important differences. The discretization coefficients now have both diffusive and convective parts, and the central coefficient a_P is no longer the sum of the neighboring coefficients. Because of the latter property, pressure is not a relative variable in compressible flows; its absolute levels are fixed by boundary conditions. (Note that, for $K=0$, this equation reverts to the incompressible pressure-correction equation.)

The solution algorithms for incompressible flows, presented in earlier sections, can be extended to compressible flows by replacing the incompressible pressure-correction equation by its compressible counterpart. The pressure corrections are now used to correct densities, in addition to pressures and velocities. In algorithms that involve multiple pressure or pressure-correction equations, the pressure corrections used to correct pressures are also used to correct densities [10,39].

So far, for simplicity, we have formulated the compressible pressure-correction method using a Cartesian grid. The basic procedure, however, is equally applicable to complex (structured and unstructured) grids (for example, [10,39,79–87]). Furthermore, it can easily be extended to control-volume-based finite-elements methods [88,89].

In the above formulation, the density and velocity are taken as independent variables, and the density correction leads to the convection terms in the pressure-correction equation. In an alternative approach [90,91], the composite variable (ρu), which represents momentum per unit volume, is taken as the dependent variable. The resulting pressure-correction equation contains only diffusive terms; consequently, it remains elliptic at all speeds and does not exhibit hyperbolic behavior at high Mach numbers. To remedy this defect, the hyperbolic nature of the flow is simulated by using a retarded pressure or density, an approach that was originally proposed for solution of the transonic potential flow equation [92,93]. The specification of boundary conditions in compressible flows depends on the local Mach number. For complete details, see Karki [39] and Ferziger and Peric [94].

7 Acceleration of Pressure-Based Schemes Using Multigrid Techniques

7.1 Motivation. The above-described SIMPLE and its variants were all originally based on a single-grid solution concept. The use of a single grid to solve the governing flow equations is well established. It is flexible, robust, and convenient. However, a primary difficulty with single-grid procedures is their rate of convergence. The rate of convergence of single-grid schemes is acceptable when very coarse grids are used to discretize the governing equations. Such was the case in the early days of CFD, when available computer memory prohibited the use of fine grids, whether using density-based or pressure-based techniques. However, computational fluid dynamics has now progressed from the "demonstration of ability" phase to the "practical use" phase in which accurate answers are required. Hence, in industry, the current state of art is to use very fine grids in order to accurately represent the geometry as well as to reduce discretization errors. It is not uncommon nowadays to use grids that may consist of $(1-10)\times 10^6$ finite-volumes to represent the flow domain. In such cases, the SIMPLE algorithm and its variants often fail to converge rapidly. Even with the advent of parallel computers of teraflop speed, the design cycle time is considered untenably long.

The convergence of the SIMPLE algorithm can be accelerated in a number of ways. These include a better formulation of the pressure-correction scheme, a more efficient solution of the linear equations of momentum and pressure/pressure-correction, and treatment of the inter-equation coupling such as among the turbulence, chemical species, and momentum/continuity equations. The entire set of equations is highly nonlinear and coupled. Any one of the equations can slow down the convergence of the entire set. Hence, all couplings and nonlinearities must be carefully resolved before fast convergence to high accuracy is achieved.

For quite some time, multigrid methods [95–99] have been demonstrated to be among the fastest converging solvers for a set of linear equations. In a number of works (for example, [100,102,103], the multigrid procedure has been demonstrated to accelerate the convergence of the SIMPLE algorithm and its variants. While the demonstrations have been done primarily in relatively simple flows (model problems), there is potential in the concept to be applied to complex industrial flows. When developed, such a procedure can provide high-fidelity solutions to many industrial flows in optimal computer times. It is expected that reductions of CPU time by a factor of 5–10 can be achieved over current commercial software. We provide here some details of such a possibility, and also review previous works.

7.2 Overview of Multigrid Techniques. The motivation for multigrid methods stems from the poor rate of convergence of traditional iterative solvers for the low-frequency components of the error. In the initial iterations, the high-frequency components of the error decrease rapidly, providing a fast rate of convergence. However, the remaining error is "smooth," that is, of low frequency. Multigrid techniques are based on the premise that such slowly convergent errors can be made to converge fast by eliminating them on coarser grids. Hence, the concept in multigrid methods is to detect the poor rate of convergence and then interpolate low-frequency errors to a coarse grid. The errors are then resolved on the coarse grid using the same (or a similar) discretization operator. The corrections obtained are subsequently interpolated back to the finer grid to correct the fine-grid solution previously computed. The solution on the finer grid is further iterated to remove newly created high-frequency errors. A similar procedure can be followed for multiple coarse grids when the finest grid contains a large number of nodes/elements. The coarsest grid must be small enough that a direct solver can be used inexpensively.

The three main components in a multigrid procedure are the solution scheme (called the relaxation scheme), interpolation procedures called restriction and prolongation, and the cycling procedure, which decides the manner in which the grids are visited. When nonlinear equations are encountered, a variant of the correction scheme called the full approximation scheme, which works with the solution rather than the corrections is more appropriate [104,105]. When these are combined in an ideal multigrid procedure, grid-independent convergence rates are achieved. The total work count can be made to vary as $O(N)$. Therefore, multigrid methods are very attractive for solving practical fluid flow, heat and mass transfer problems.

7.3 Previous Works With Multigrid Pressure-Based Solvers. Several researchers have previously attempted to enhance the SIMPLE algorithm with the multigrid technique. These include Sivaloganathan and Shaw [100], Shyy et al. [101], Hortmann et al. [102], Smith et al. [20], and Lange et al. [103]. The principal components of all these procedures are similar. The differences stem from the details in the use of the multigrid cycling scheme, the variant of the SIMPLE algorithm and the problems studied. In a series of works, Vanka and co-workers [18,19,106–108] used a relaxation procedure called the symmetric coupled Gauss-Seidel scheme, the origins of which can be traced to the simultaneous variable adjustment procedure [109] developed at Imperial College, London, prior to the SIMPLE algorithm. The coupled solver avoids the use of the pressure/pressure-correction equation as it solves the continuity equation in its primitive form (Eq. (19)). The coupled concept can also be used along a line [110] and in conjunction with the multigrid idea. The coupled procedure is a factor of 2 or so faster than the decoupled (i.e., sequential) procedure. However, when more complex linear solvers are used, decoupled whole-field solvers are found to perform better.

For complex geometries, multigrid implementations of both staggered and co-located (see Sec. 4) versions of the SIMPLE algorithm have been published [111,112] using grid-following co- and contravariant velocities as dependent variables. For unstructured grids, Jyotsna and Vanka [113] implemented a multigrid procedure based on the control-volume finite-element method (CVFEM) ([11,12]; see Sec. 5). They demonstrated a significant acceleration over the single-grid algorithm for driven cavity flows in square, semi-circular, and triangular cavities.

Multigrid versions of coupled and decoupled (sequential) solvers have also been developed for turbulent and reacting flows [114,115]. However, success in such extensions has not been as expected. The coupling of turbulence equations with the momentum and continuity equations on the coarser grids has not been entirely successful. One approach followed is the solution of the turbulence equations only on the finest grid and restricting the turbulent viscosity to the coarser grids. However, such a strategy did not give the expected grid-independent rate of convergence, but was still faster than decoupled strategies. Similarly, the equations for species transport with chemical reactions had to be solved only on the finest grid. Only the density was restricted to coarser grids. The procedure was applied to the study of flow in a

Table 1 Comparison of the performance of segregated single-grid and multigrid schemes for jet impingement flows [117]

Case (120×20×36) grid	Work units		CPU time (s)	
	Segregated Single-grid	Multigrid, three levels	Segregated Single-grid	Multigrid, three levels
Laminar cold jets	98.1	87.8	271.5	135.5
Laminar hot jets	118.4	57.4	362.1	143.0
Turbulent cold jets	242.5	219.5	975.3	719.4
Turbulent hot jets	287.1	150.0	1108.8	482.8

ramjet combustor by Vanka et al. [116].

Table 1 shows a performance comparison of segregated single-grid and segregated multigrid solvers for cold and hot gas jet impingement in laminar and turbulent flows [117]. Table 2 compares the performance of a coupled solution procedure implemented using both single- and multigrid frameworks for laminar and turbulent dilution jet flows; details may be found in [117]. Acceleration due to the use of the multigrid procedure is clearly evident.

7.4 Future Prospects. In order to accelerate practical flows using multigrid techniques, several advances need to be made. It is now accepted in the CFD community that unstructured grids provide the highest flexibility and ease of representing a practical flow. Furthermore, the grid system should not have any constraints of being nested in a hierarchical series. Hence, for a general purpose problem, the finest grid that is suited to the problem must be first determined. All boundary conditions must be prescribed on this grid, which should then be coarsened progressively. The concept best suited for this is agglomeration [118–120]. An agglomeration-based procedure consists of combining several cells around a vertex to make a macro-cell. A consistent multigrid sequence can then be constructed for visiting such macro-cells and resolving the low-frequency errors. Koobus et al. [118] first proposed the agglomeration multigrid algorithm for the Euler equations. A finite-volume cell-vertex method was developed and demonstrated for flow over an airfoil. However, for viscous terms involving second derivatives, it is necessary to scale the fluxes by a ratio representing the characteristic length scales. Mavriplis and colleagues [119,120] have developed several practices to accelerate compressible flow solvers for external aerodynamic flows. Both Euler and Navier-Stokes equations were considered. For thin boundary layers, directional agglomeration [121], which is analogous to semi-coarsening, was developed to preferentially coarsen in directions normal to the boundary layers. Recently, Lambropoulos et al. [122] used a Jacobian-based time-marching scheme for unstructured grids and accelerated it through agglomeration multigrid and parallel processing. All the above works were limited to high-speed flows for which a density-based method with time-marching was used in conjunction with agglomeration multigrid acceleration. However, no previous works have addressed the pressure-based approach, which is used mostly for low-speed flows.

The agglomeration multigrid method has some similarities with two other techniques proposed for accelerating convergence of the solution of sets of linear equations. The first one is additive correction multigrid (ACM) [60,123]. ACM is based on the concept of adding constant corrections to groups of equations that can be combined to form a “macro” equation. An additive correction multigrid scheme for the Navier-Stokes equations has been published in [124]. The algebraic multigrid method (AMG) [125] is another similar technique that has been developed as a black-box multigrid method. However, AMG is developed to be less dependent on the origin of the linear equations, and hence can be applied to equations obtained from any field without any underlying partial-differential equation. The works of Webster [126,127] are the only ones to our knowledge that have used a coupled (block) AMG on unstructured grids. Because of the lack of a grid structure and only heuristic arguments of coarsening, it is not clear how the entire set of equations can be coarsened.

The solution of the coupled set of equations for flow, turbulence, heat transfer, and chemical species poses a greater challenge. A coupled solution of the turbulence and chemical species equations along with the momentum and continuity equations is not well convergent even if direct solvers are used [128]. Hence, it is necessary to decouple the individual physics, and couple them through the properties such as turbulent viscosity and density. In such a case, formulation of the coarse grid equations is not very obvious. Restricting the frozen turbulent viscosity and density has in the past been shown to slow down the asymptotic rate of convergence after a certain (low) residual has been reached [116]. Further research is needed to accelerate this slow convergence. Another area of research is the proper imposition of “wall functions” in turbulent flow modeling. The wall functions are very local on the finest grid, and as such, coarsening them or imposing them on the coarse grids can give rise to inconsistent formulations. These issues should be resolved in future research.

8 Comparison With Other Approaches

Like finite-volume methods, finite-element methods have also seen rapid development during the last few decades [50]. Though they originally addressed structural mechanics problems, finite element methods today covers the same thermal-fluids applications as FVM, and also form the basis of popular commercial solvers. Galerkin-based discretization procedures [50] are widely used, and differ from the finite-volume approach described here in that they do not employ the conservation principle as the basis of the

Table 2 Comparison of the performance of coupled single-grid and multigrid schemes for dilution jet flows [117]

Problem (64×32×32) grid	Single-grid, iterations	Single-grid, CPU (s)	Multigrid, three levels, iterations	Multigrid, three levels, CPU (s)
Laminar isothermal dilution jet	299	177.9	54	82.5
Laminar non-isothermal dilution jet	523	405.2	150	249.5
Turbulent isothermal dilution jet	555	930.3	150	383.2

discretization. As a consequence, unlike FVM, conservation is only satisfied only if sufficiently fine meshes are used. In other respects, finite-volume and finite-element methods have followed nearly parallel paths in their evolution. As with FVM, discretization schemes for convection-dominated flows were a subject of intense research in 1970s and 1980s [12,129]. Early FEM implementations employed direct solvers [130], but there, too, segregated solvers are now widely used for incompressible flows [131]. The issue of spurious pressure modes also appears in the FEM literature, and there, too, equal-order interpolation methods, analogous to the co-located techniques discussed here, have been developed to address them [132,133]. Once the discrete equation set has been derived, the solution techniques for the algebraic equations are independent of the discretization principle itself, and thus, multigrid schemes, gradient search schemes, and other approaches are all equally applicable. The mathematical formulation of finite element methods makes the extension to higher-order formulations somewhat simpler, and higher-order spectral element schemes, for example, are easier to develop using FEM [134]. Also, since nearly all structural mechanics solvers today employ FEM, a seamlessly coupled solver spanning fluid and solid domains may be somewhat easier to write with FEM. On the other hand, the great geometric flexibility afforded by FVM formulations supporting arbitrary polyhedral cells, is more difficult to match within an FEM framework.

An emerging contender for complex geometries is the class of meshless methods [135–139] which avoid the creation of both surface and volume elements, and require, for the most part, only the creation of mesh points and information about local proximity. Since a large proportion of the time required for CFD calculation is consumed by mesh generation at present, meshless methods promise to significantly reduce the human time required for industrial problem solving. Meshless methods also promise easy solution adaptivity and hold particular promise for problems with time-evolving fronts such in crack-propagation or shocks. However, though the human time required for mesh generation is reduced with meshless methods, the time required for geometry creation is the same, and computation time may be significantly larger due to the penalty imposed by numerical quadrature, and the use of direction solution techniques in some implementations [139]. For flow computation, the method is still evolving, and must be tested against a variety of compressible and incompressible laminar and turbulent flow problems. Ultimately, the success of meshless methods will depend on whether the mesh-generation burden of FVM and FEM is relieved by the development of fast, good-quality automatic mesh-generation schemes that do not require significant user intervention.

9 Closure

In this paper, the history and evolution of pressure-based finite-volume methods have been reviewed. Finite-volume methods have made a remarkable transition from their inception in the 1960s to their widespread use in commercial codes today. This transition has been facilitated not only because of the ubiquity of inexpensive computing power, but by the ever-expanding ability of this class of techniques to address real-world problems.

Despite this remarkable success, a number of improvements remain to be made. As computer memory becomes less and less of a bottleneck, sequential solution procedures like SIMPLE, which were conceived with computational and storage efficiency in mind, must inevitably give way to more powerful coupled techniques that promise to be faster, but which impose a storage penalty. This transition is already underway to some degree, but fundamental algorithmic advances are necessary to develop robust fully coupled procedures that cover important physics such as turbulence and chemical reactions. The disparate time and spatial scales of these phenomena pose particular challenges for coupled procedures. The promised increase in speed through faster-converging coupled techniques is especially critical for design and optimization, where large parametric spaces must be explored.

Accuracy remains an enduring issue with finite-volume schemes. Though there appear to be no insurmountable conceptual bottlenecks, nearly all published finite-volume schemes are of second-order accuracy. Industrially driven CFD typically does not demand ultra-high-order schemes at present because of other unresolved uncertainties, typically in turbulence modeling, physical properties and boundary conditions. However, as large-eddy simulations and direct numerical simulations of turbulence become more common, it will be necessary to create more flexible frameworks which will admit schemes of higher order. How to devise such schemes within an unstructured mesh framework remains an open research question.

Extremely complex physics, such as those governing liquid-vapor multiphase flows, remain a challenge today, both in terms of an adequate description of the physics as well as in devising robust algorithms for their solution. Pressure-velocity coupling in this context remains a particular problem. Accurate and efficient solution of complicated time-evolving free surfaces at multiple scales and coupling to appropriate thermodynamic descriptions for phase change are an important area for research.

As the reach of simulation becomes wider, finite-volume techniques must inevitably begin to address multiscale and multiphysics problems. This may take the form of extending finite-volume methods to address new classes of physics, such as those for participating radiation [140–142], stress analysis [14], electromagnetics [143] or nanotechnology [144]. Alternatively, coupling seamlessly to domain-specific techniques may be another useful approach.

Last but not least, verification and validation protocols must continue to be developed and emphasized in CFD code development, along with a quantification of uncertainty in predictions. Without these, CFD in general, and finite-volume methods in particular, may provide broad intuition and heuristic guidance, but cannot provide specific and reliable information.

Nomenclature

a_P, a_{nb} = discretization coefficients
a_e, a_n = discretization coefficients for the u and v staggered momentum equation
A_e, A_w, A_n, A_s = area of faces (e,w,n,s)
$\boldsymbol{A}$ = outward-pointing area vector
b_P = discretization coefficient
D_f = diffusion term for face f
$\boldsymbol{e_s}$ = unit vector along line joining cell centroids
F_f = mass flow rate through face f
$\boldsymbol{J}$ = flux vector
M = Mach number
$\boldsymbol{n}$ = unit normal
p = pressure
p' = pressure correction
S_ϕ = source term
S_f = secondary gradient term at face f
t = time
$\hat{u}, \hat{v}$ = pseudo-velocities
$\tilde{u}$ = continuity-satisfying velocity field in co-located scheme
u^m, v^m = continuity-satisfying velocities in CVFEM
u, v = Cartesian velocity components
u', v' = velocity corrections
$\boldsymbol{V}$ = velocity vector
x, y = Cartesian coordinates

Greek Symbols

ρ = density
ρ' = density correction
ϕ = transport variable
μ = dynamic viscosity

λ = under-relaxation coefficient
Γ_ϕ = diffusion coefficient
ΔV = volume of control volume
Δt = time step

Subscripts and Superscripts

e, w, n, s = associated with cell face indices
E, W, N, S = associated with cell neighbors
f = associated with cell face
nb = associated with neighbor cell
P = associated with cell P
* = prevailing value
0 = associated with cell $C0$
$\max(a,b)$ = maximum of a and b

References

[1] Harlow, F. H., and Fromm, J. E., 1965, "Computer Experiments in Fluid Dynamics," Sci. Am., **212**, pp. 104–110.
[2] Harlow, F. H., and Welch, J. E., 1965, "Numerical Calculation of Time-Dependent Viscous Incompressible Flow of Fluid With Free Surface," Phys. Fluids, **8**, pp. 2182–2189.
[3] Patankar, S. V., and Spalding, D. B., 1972, "A Calculation Procedure for Heat, Mass and Momentum Transfer in Three-Dimensional Parabolic Flows," Int. J. Heat Mass Transfer, **15**, pp. 1767–1806.
[4] Jameson, A., Baker, T. J., and Weatherill, N. P., 1986, "Calculation of Inviscid Flow over a Complete Aircraft," AIAA 24th Aerospace Sciences Meeting, Reno, Nevada, January 6–9, AIAA-86-0103.
[5] Patankar, S. V., 1980, *Numerical Heat Transfer and Fluid Flow*, Hemisphere Publishing Corporation, Washington D.C.
[6] Patankar, S. V., Pratap, V. S., and Spalding, D. B., 1974, "Prediction of Laminar Flow and Heat Transfer in Helically Coiled Pipes," J. Fluid Mech., **62**, p. 539–551.
[7] Patankar, S. V., Ivanovic, M., and Sparrow, E. M., 1979, "Analysis of Turbulent Flow and Heat Transfer in Internally Finned Tubes and Annuli," ASME J. Heat Transfer, **101**, pp. 29–37.
[8] Maliska, C. R., and Raithby, G. D., 1984, "A Method for Computing Three-Dimensional Flows Using Non-orthogonal Boundary-Fitted Coordinates," Int. J. Numer. Methods Fluids, **4**, 519–537.
[9] Shyy, W., Tong, S. S., and Correa, S. M., 1985, "Numerical Recirculating Flow Calculation Using a Body-Fitted Coordinate System," Numer. Heat Transfer, **8**, pp. 99–113.
[10] Karki, K. C., and Patankar, S. V., 1986, "Calculation Procedure for Viscous Incompressible Flows in Complex Geometries," Numer. Heat Transfer, **14**, pp. 295–307.
[11] Baliga, B. R., and Patankar, S. V., 1983, "A Control-Volume Finite Element Method for Two-Dimensional Incompressible Fluid Flow and Heat Transfer," Numer. Heat Transfer, **6**, pp. 245–261.
[12] Prakash, C., and Patankar, S. V., 1985, "A Control-Volume-Based Finite-Element Method for Solving the Navier-Stokes Equations Using Equal-Order Velocity-Pressure Interpolation," Numer. Heat Transfer, **8**, pp. 259–280.
[13] Schneider, G. E., and Raw, M. J., 1987, "Control-Volume Finite Element Method for Heat Transfer and Fluid Flow Using Co-Located Variables -1. Computational Procedures," Numer. Heat Transfer, **11**, pp. 363–390.
[14] Demirdzic, I., and Muzaferija, S., 1995, "Numerical Method for Coupled Fluid Flow, Heat Transfer and Stress Analysis Using Unstructured Moving Meshes With Cells of Arbitrary Topology," Comput. Methods Appl. Mech. Eng., **125**, pp. 235–255.
[15] Mathur, S. R., and Murthy, J. Y., 1997, "A Pressure-Based Method for Unstructured Meshes," Numer. Heat Transfer, Part A, **31**, pp. 195–216.
[16] Hsu, C. F., 1981, "A Curvilinear-Coordinate Method for Momentum, Heat and Mass Transfer in Domains of Irregular Geometry," Ph.D. thesis, University of Minnesota, Minneapolis.
[17] Rhie, C. M., and Chow, W. L., 1983, "A Numerical Study of the Turbulent Flow Past an Isolated Airfoil With Trailing Edge Separation," AIAA J., **21**, pp. 1525–1532.
[18] Vanka, S. P., 1986, "Block-Implicit Multigrid Solution of Navier-Stokes Equations in Primitive Variables," J. Comput. Phys., **65**, pp. 138–158.
[19] Vanka, S. P., 1986, "Block-Implicit Multigrid Calculation of Two-Dimensional Recirculating Flows," Comput. Methods Appl. Mech. Eng., **59**, pp. 29–48.
[20] Smith, K. M., Cope, W. K., and Vanka, S. P., 1993, "Multigrid Procedure for Three-Dimensional Flows on Non-orthogonal Collocated Grids," Int. J. Numer. Methods Fluids, **17**, pp. 887–904.
[21] Jyotsna, R., and Vanka, S. P., 1995, "Multigrid Calculation of Steady, Viscous Flow in Triangular Cavity," J. Comput. Phys., **122**, 107–117.
[22] Patankar, S. V., 1971, "Calculation of Unsteady Compressible Flows Involving Shocks," Report No. UF/N/A/4, Imperial College, London.
[23] Van Doormal, J. P., Raithby, G. D., and McDonald, B. H., 1987, "The Segregated Approach to Predicting Viscous Compressible Flows," ASME J. Turbomach., **109**, pp. 268–277.
[24] Karki, K. C., and Patankar, S. V., 1989, "Pressure Based Calculation Procedure for Viscous Flows at All Speeds in Arbitrary Configurations," AIAA J., **27**, pp. 1167–1174.
[25] Leonard, B. P., 1979, "A Stable and Accurate Convective Modeling Procedure Based on Quadratic Upstream Interpolation," Comput. Methods Appl. Mech. Eng., **19**, pp. 59–98.
[26] Hirsch, C., 1990, *Numerical Computation of Internal and External Flows: Computational Methods for Inviscid and Viscous Flows*, Wiley, New York.
[27] Laney, C. B., 1998, *Computational Gas Dynamics*, Cambridge University Press, Cambridge, U.K.
[28] Van Doormaal, J. P., and G. D. Raithby, 1984, "Enhancements of the SIMPLE Method for Predicting Incompressible Fluid Flows," Numer. Heat Transfer, **7**, pp. 147–163.
[29] Issa, R. I., 1982,"Solution of the Implicit Discretized Fluid Flow Equations by Operator Splitting," Mechanical Engg. Report, FS/82/15, Imperial College, London.
[30] Issa, R. I., Gosman, A. D., and Watkins, A. P., 1986, "The Computation of Compressible and Incompressible Recirculating Flows by a Non-Iterative Implicit Scheme," J. Comput. Phys., **62**, pp. 66–82.
[31] Jang, D. S., Jetli, R., and Acharya, S., 1986, "Comparison of the PISO, SIMPLER and SIMPLEC Algorithms for the Treatment of the Pressure-Velocity Coupling in Steady Flow Problems," Numer. Heat Transfer, **10**(3), pp. 209–228.
[32] Moukalled, F., and Acharya, S., 1989, "Improvements to Incompressible Flow Calculation on a Non-Staggered Curvilinear Grid," Numer. Heat Transfer, Part B, **15**(2), pp. 131–152.
[33] Prakash, C., 1981, "A Finite Element Method for Predicting Flow Through Ducts With Arbitrary Cross-Sections," Ph.D. thesis, University of Minnesota, Minneapolis.
[34] Pope, S. B., 1978, "The Calculation of Turbulent Recirculating Flows in General Orthogonal Coordinates," J. Comput. Phys., **26**, pp. 197–217.
[35] Rastogi, A. K., 1984, "Hydrodynamics in Tubes Perturbed by Curvilinear Obstructions," ASME J. Fluids Eng., **106**, pp. 262–269.
[36] Raithby, G. D., Galpin, P. F., and Van Doormaal, J. P., 1986, "Prediction of Heat and Fluid Flow in Complex Geometries Using General Orthogonal Coordinates," Numer. Heat Transfer, **9**, pp. 125–142.
[37] Demirdzic, I., Gosman, A. D., Issa, R. I., and Peric, M., 1987, "A Calculation Procedure for Turbulent Flows in Complex Geometries," Comput. Fluids, **15**, pp. 251–273.
[38] Segal, A., Wesseling, P., Van Kan, J., Oosterlee, C. W., and Kassels, K., 1992, "Invariant Discretization of the Incompressible Navier-Stokes Equations in Boundary Fitted Co-ordinates," Int. J. Numer. Methods Fluids, **15**, pp. 411–426.
[39] Karki, K. C., 1986, "A Calculation Procedure for Viscous Flows at All Speeds in Complex Geometries," Ph.D. thesis, University of Minnesota, Minneapolis.
[40] Davidson, L., and Hedberg, P., 1989, "Mathematical Derivation of a Finite-Volume Formulation for Laminar Flow in Complex Geometries," Int. J. Numer. Methods Fluids, **9**, pp. 531–540.
[41] Shyy, W., Tong, S. S., and Correa, S. M., 1985, "Numerical Recirculating Flow Calculation Using a Body-Fitted Coordinate System," Numer. Heat Transfer, **8**, pp. 99–113.
[42] Vanka, S. P., Chen, C.-J., and Sha, W. T., 1980, "A Semi-Implicit Calculation Procedure for Flow Described in Body-Fitted Coordinate Systems," Numer. Heat Transfer, **3**, pp. 1–19.
[43] Joshi, D. S., and Vanka, S. P., 1991, "Multigrid Calculation Procedure for Internal Flows in Complex Geometries," Numer. Heat Transfer, Part B, **20**, pp. 61–80.
[44] Kelkar, K. M., and Choudhury, D., 1993, "Numerical Method for the Computation of Flow and Scalar Transport Using Non-Orthogonal Boundary-Fitted Coordinates," Numer. Heat Transfer, Part B, **24**, pp. 391–414.
[45] He, P., and Salcudean, M., 1994, "A Numerical Method for 3D Viscous Incompressible Flows Using Non-Orthogonal Grids," Int. J. Numer. Methods Fluids, **18**, pp. 449–469.
[46] Melaen, M. C., 1992, "Calculation of Fluid Flows With Staggered and Nonstaggered Curvilinear Nonorthogonal Grids—The Theory," Numer. Heat Transfer, Part B, **21**, pp. 1–19.
[47] Baliga, B. R., 1978, "A Control-Volume-Based Finite Element Method for Convective Heat and Mass Transfer," Ph.D. thesis, University of Minnesota, Minneapolis.
[48] Baliga, B. R., and Patankar, S. V., 1980, "A New Finite Element Formulation for Convection-Diffusion Problems," Numer. Heat Transfer, **3**, pp. 393–409.
[49] Baliga, B. R., 1997, "Control-Volume Finite Element Methods for Fluid Flow and Heat Transfer," in *Advances in Numerical Heat Transfer*, J. W. Minkowycz and M. E. Sparrow, eds., Taylor & Francis, New York, Vol. 1, Chap. 3, pp. 97–135.
[50] Zienkiewicz, O. C., and Taylor, R. L., 2000, *The Finite Element Method Vol. 3 Fluid Dynamics*, 5th ed., McGraw-Hill, London.
[51] Peric, M., Kessler, R., and Scheuerer, G., 1988, "Comparison of Finite-Volume Numerical Methods With Staggered and Co-Located Grids," Comput. Fluids, **16**, pp. 389–403.
[52] Baliga, B. R., and Atabaki, N., 2006, "Control-Volume-Based Finite-Difference and Finite-Element Methods," in *Handbook of Numerical Heat Transfer*, 2nd ed., J. W. Minkowycz, M. E. Sparrow, and Y. J. Murthy eds., John Wiley & Sons, New York, Chap. 6.
[53] Venditti, D. A., 1998, "An h-Adaptive Control-Volume Finite Element Method for Steady, Two-Dimensional Fluid Flow and Heat Transfer," M.Eng. thesis, McGill University, Montreal, Quebec, Canada.
[54] Spalding, D. B., 1972, "A Novel Finite-Difference Formulation for Differential Expressions Involving Both First and Second Derivatives," Int. J. Numer. Methods Eng., **4**, pp. 551–559.

[55] Raithby, G. D., 1976, “Skew Upstream Difference Schemes for Problems Involving Fluid Flow,” Comput. Methods Appl. Mech. Eng., **9**, pp. 153–164.

[56] Masson, C., and Baliga, B. R., 1994, “A Control-Volume Finite Element for Dilute Gas-Solid Particle Flows,” Comput. Fluids, **23**, pp. 1073–1096.

[57] Schneider, G. E., and Raw, M. J., 1986, “A Skewed Positive Influence Coefficient Upwind Procedure for Control-Volume-Based Finite Element Convection-Diffusion Computation,” Numer. Heat Transfer, **9**, pp. 1–26.

[58] Saabas, H. J., and Baliga, B. R.,1994, “A Co-Located Equal-Order Control-Volume Finite Element Method for Multidimensional, Incompressible Fluid Flow—Part I: Formulation,” Numer. Heat Transfer, Part B, **26**, pp. 381–407.

[59] Tran, L. D., Masson, C., and Smaïli, A., 2006, “A Stable Second-Order Mass-Weighted Upwind Scheme for Unstructured Meshes,” Int. J. Numer. Methods Fluids, **51**, pp. 749–771.

[60] Elias, S. R., Stubley, G. D., and Raithby, G. D., 1997, “An Adaptive Agglomeration Method for Additive Correction Multigrid,” Int. J. Numer. Methods Eng., **40**, pp. 887–903.

[61] Masson, C., and Baliga, B. R., 1998, “Simulation of Gas-Solid Particle Flows Over a Wide Range of Concentration,” Int. J. Numer. Methods Fluids, **28**, pp. 1441–1479.

[62] Ledain-Muir, B., and Baliga, B. R., 1988, “Solution of Three-Dimensional Convection-Diffusion Problems Using Tetrahedral Elements and Flow-Oriented Upwind Interpolation,” Numer. Heat Transfer, **9**, pp. 253–272.

[63] Costa, V. A. F., Oliveira, L. A., and Figueiredo, A. R., 1995, “A Control-Volume-Based Finite Element Method for Three-Dimensional Incompressible Turbulent Fluid Flow, Heat Transfer and Related Phenomena,” Int. J. Numer. Methods Fluids, **21**, pp. 591–613.

[64] Mathur, S. R., and Murthy, J. Y., 2000, “Unstructured Finite Volume Methods for Multi-Mode Heat Transfer,” in *Advances in Heat Transfer*, J. W. Minkowycz and M. E. Sparrow eds., Taylor and Francis, New York, Vol. II pp. 37–70.

[65] Davidson, L., 1996, “A Pressure Correction Method for Unstructured Meshes With Arbitrary Control Volumes,” Int. J. Numer. Methods Fluids, **22**, pp. 265–281.

[66] Murthy, J. Y., Minkowycz, W. J., Sparrow, E. M., and Mathur, S. R., 2006, “Survey of Numerical Methods,” *Handbook of Numerical Heat Transfer*, 2nd ed., J. W. Minkowycz, M. E. Sparrow, and Y. J. Murthy eds., John Wiley & Sons, New York, Chap. 1.

[67] Hutchinson, B. R., and Raithby, G. D., 1986, “A Multigrid Method Based on the Additive Correction Strategy,” Numer. Heat Transfer, **9**, pp. 511–537.

[68] Van den Vorst, H. A., and Sonneveld, P., 1990, “CGSTAB: A More Smoothly Converging Variant of CGS,” Technical Report, Delft University of Technology, Delft, The Netherlands.

[69] Van den Vorst, H. A., 1992, “BI-CGSTAB: A Fast and Smoothly Converging Variant of BI-CG for the Solution of Non-Symmetric Linear Systems,” SIAM (Soc. Ind. Appl. Math.) J. Sci. Stat. Comput., **13**, pp. 631–644.

[70] Saad, Y., and Schultz, M. H., 1986, “GMRES: A Generalized Residual Algorithm for Solving Non-Symmetric Linear Systems,” SIAM (Soc. Ind. Appl. Math.) J. Sci. Stat. Comput., **7**, pp. 856–869.

[71] Demirdzic, I., Lilek, Z., and Peric, M., 1992, “Fluid Flow and Heat Transfer Test Problems for Non-Orthogonal Grids,” Int. J. Numer. Methods Fluids, **15**, pp. 329–354.

[72] Murthy, J. Y., and Mathur, S. R., 2001, “Unstructured Mesh Methods for Combustion Problems,” in *CFD in Industrial Combustion*, E. C. Baukal and X. Li, eds., CRC Press, Boca Raton, FL, pp. 61–94.

[73] Murthy, J. Y., and Mathur, S. R., 1998, “Finite Volume Method for Radiative Heat Transfer Using Unstructured Meshes,” J. Thermophys. Heat Transfer, **12**(3), pp. 313–321.

[74] Beam, R. M., and Warming, R. F., 1978, “An Implicit Factored Scheme for Compressible Navier-Stokes Equations,” AIAA J., **16**, pp. 393–402.

[75] MacCormack, R. W., 1982, “A Numerical Method for Solving Equations of Compressible Viscous Flows,” AIAA J., **20**, pp. 1275–1281.

[76] Ni, R. H., 1982, “A Multiple Grid Scheme for Solving the Euler Equations,” AIAA J., **20**, pp. 1565–1571.

[77] Choi, D., and Merkle, C. L., 1985, “Application of Time-Iterative Schemes to Incompressible Flows,” AIAA J., **23**, 1518–1524.

[78] Kwak, D., Chang, J. L. C., Shanks, S. P., and Chakravarthy, S. R., 1986, “A Three-Dimensional Incompressible Navier-Stokes Flow Solver Using Primitive Variables,” AIAA J., **24**, 390–396.

[79] Issa, R. I., and Javareshkian, M. H., 1998, “Pressure-Based Compressible Calculation Method Utilizing Total Variation Diminishing Schemes,” AIAA J., **36**, pp. 1652–1657.

[80] Moukalled, F., and Darwish, M., 2001, “A High-Resolution Pressure Based Algorithm for Fluid Flow at All Speeds,” J. Comput. Phys., **168**, pp. 101–133.

[81] Demirdzic, I., Lilek, Z., and Peric, M., 1993, “A Collocated Finite Volume Method for Predicting Flows at All Speeds,” Int. J. Numer. Methods Fluids, **16**, 1029–1050.

[82] Marchi, C. H., and Maliska, C. R., 1994, “A Nonorthogonal Finite-Volume Method for the Solution of All Speed Flows Using Co-located Variables,” Numer. Heat Transfer, Part B, **26**, pp. 293–311.

[83] Shyy, W., and Chen, M. H., 1992, “Pressure-Based Multigrid Algorithm for Flow at All Speeds,” AIAA J., **30**, pp. 2660–2669.

[84] Rincon, J., and Elder, R., 1997, “A High-Resolution Pressure-Based Method for Compressible Flows,” Comput. Fluids, **26** pp. 217–231.

[85] Demirdzic, I., Issa, R. I., and Lilek, Z., 1990, “Solution Method for Viscous Flows at All Speeds in Complex Domains,” in *Notes on Numerical Fluid Mechanics*, P. Wesseling ed., Vieweg, Braunschweig, Vol. 29.

[86] Mathur, S. R., and Murthy, J. Y., 1999, “All Speed Flows on Unstructured Meshes Using a Pressure Correction Approach,” AIAA Paper No. 99-3365.

[87] Lien, F. S., 2000, “A Pressure-Based Unstructured Grid Method for All-Speed Flows,” Int. J. Numer. Methods Fluids, **33**, pp. 355–374.

[88] Karimian, S. M. H., and Schneider, G. E., 1994, “Pressure-Based Computational Method for Compressible and Incompressible Flows,” J. Thermophys. Heat Transfer, **8**, pp. 267–274.

[89] Darbandi, M., and Schneider, G. E., 1997, “Momentum Variable Procedure for Solving Compressible and Incompressible Flows,” AIAA J., **35**, 1801–1805.

[90] Lien, F. S., and Leschziner, M. A., 1993, “A Pressure-Velocity Solution Strategy for Compressible Flow and Its Application to Shock/Boundary-Layer Interaction Using Second-Moment Turbulence Closure,” ASME J. Fluids Eng., **115**, pp. 717–725.

[91] McGuirk, J. J., and Page, G. J., 1990, “Shock Capturing Using a Pressure Correction Method,” AIAA J., **29**, pp. 1751–1757.

[92] Hafez, M., South, J., and Murman, E., 1979, “Artificial Compressibility Methods for Numerical Solutions of Transonic Full Potential Equations,” AIAA J., **17**, pp. 838–844.

[93] Wornom, S. F., and Hafez, M. M., 1986, “Calculation of Quasi-One Dimensional Flows With Shocks,” Comput. Fluids, **14**, pp. 131–140.

[94] Ferziger, J. H., and Peric, M., 1996, *Computational Methods for Fluid Dynamics*, Springer Verlag, Berlin.

[95] Hackbusch, W., and Trottenberg, U., 1982, *Multigrid Methods*, Springer Verlag, Berlin.

[96] Stuben, K., and Trottenberg, U., 1982, *Multigrid Methods: Fundamental Algorithms, Model Problems, Analysis and Applications*, in Lecture Notes in Mathematics No. 960, pp. 1–176, Springer Verlag, Berlin.

[97] Brandt, A., 1984, *Multigrid Techniques: 1984 Guide with Applications to Fluid Dynamics*, GMD Bonn, GMD-Studien Nr. 85.

[98] MGNET: Multigrid Bibliography, maintained by C. C. Douglas, Yale University.

[99] Trottenberg, U., and Oosterlee, C. W., and Schuller, A., 2001, *Multigrid*, Academic Press, New York.

[100] Sivaloganathan, S., and Shaw, G. J., 1988, “A Multigrid Method for Recirculating Flows,” Int. J. Numer. Methods Fluids, **8**(4), p 417–440.

[101] Shyy, W., Chen, M-H., and Sun, C-S., 1992, “Pressure-based Multigrid Algorithm for Flow at all Speeds,” AIAA J., **30**(11), pp. 2660–2669.

[102] Hortmann, M., Peric, M., and Scheurer, G., 1990, “Finite Volume Multigrid Method for the Prediction of Incompressible Flows,” Int. J. Numer. Methods Fluids, **11**, pp. 189–207.

[103] Lange, C. F., Schafer, M., and Durst, F., 2002, “Local Block Refinement With a Multigrid Flow Solver,” Int. J. Numer. Methods Fluids, **38**, pp. 21–41.

[104] Brandt, A., 1977, “Multilevel Adaptive Solutions to Boundary-Value Problems,” Math. Comput., **31**, pp. 333–390.

[105] Henson, V. E., 2003, “Multigrid Methods for Nonlinear Problems: An Overview,” Proc. SPIE, **5016**(1), pp. 36–48.

[106] Vanka, S. P., 1986, “A Calculation Procedure for Three-Dimensional Recirculating Flows,” Comput. Methods Appl. Mech. Eng., **55**, pp. 321–338.

[107] Vanka, S. P., 1986, “Performance of a Multigrid Calculation Procedure in Three-Dimensional Sudden Expansion Flows,” Int. J. Numer. Methods Fluids, **6**, pp. 459–477.

[108] Joshi, D. S., and Vanka, S. P., 1991, “Multigrid Calculation Procedure for Internal Flows in Complex Geometries,” Numer. Heat Transfer, Part B, **20**, pp. 61–80.

[109] Caretto, L. S., Gosman, A. D., Patankar, S. V., and Spalding, D. B., 1973, “Two Calculation Procedures for Steady, Three-Dimensional Flows With Recirculation,” *Proceedings of the 3rd International Conference on Numerical Methods in Fluid Mechanics. II*, pp. 60–68.

[110] Galpin, P. F., Van Doormaal, J. P., and Raithby, G. D., 1985, “Solution of the Incompressible Mass and Momentum Equations by Application of a Coupled Equation Line Solver,” Int. J. Numer. Methods Fluids, **5**(7), pp. 615–625.

[111] He, P., Salcudean, M., Gartshore, I. S., and Nowak, P., 1996, “Multigrid Calculation of Fluid Flows in Complex 3D Geometries Using Curvilinear Grids,” Comput. Fluids, **25**(4), pp. 395–419.

[112] Shyy, W., Sun, C.-S., Chen, M.-H., and Chang, K. C., 1993, “Multigrid Computation for Turbulent Recirculating Flows in Complex Geometries,” Numer. Heat Transfer, Part A, **23**(1), pp. 79–98.

[113] Jyotsna, R., and Vanka, S. P., 1995, “A Pressure-Based Multigrid Procedure for the Navier-Stokes Equations on Unstructured Grids,” *Proceedings of the 1995 Copper Mountain Conference on Multigrid Methods*, Copper Mountain, CO.

[114] Lin, F. B., and Sotiropoulos, F., 1997, “Strongly-Coupled Multigrid Method for 3-D Incompressible Flows Using Near-Wall Turbulence Closures,” ASME J. Fluids Eng., **119**(2), pp. 314–324.

[115] Zheng, X., Liao, C., Liu, C., Sung, C. H., and Huang, T. T., 1997, “Multigrid Computation of Incompressible Flows Using Two-Equation Turbulence Models, Part I-Numerical Method,” ASME J. Fluids Eng., **119**(4), pp. 893–899.

[116] Vanka, S. P., Krazinski, J. L., and Nejad, A. S., 1989, “Efficient Computational Tool for Ramjet Combustor Research,” J. Propul. Power, **5**(4), pp. 431–437.

[117] Wang, G., 1994, “Numerical Simulations of STOVL Hot Gas Ingestion in Ground Proximity Using a Multigrid Solution Procedure,” MS thesis, University of Illinois at Urbana-Champaign, IL.

[118] Koobus, B., Lallemand, M. H., and Dervieux, A., 1994, “Unstructured Volume Agglomeration MG: Solution of the Poisson Equation,” Int. J. Numer. Methods Fluids, **18**, pp. 27–42.

[119] Mavriplis, D. J., and Venkatakrishnan, V., 1995, “A 3D Agglomeration Mul-

tigrid Solver for the Reynolds-Averaged Navier-Stokes Equations on Unstructured Meshes," 33rd Aerospace Sciences Meeting and Exhibit, Jan. 9–12, Reno, NV.

[120] Mavriplis, D. J., 2000, "Viscous Flow Analysis Using a Parallel Unstructured Multigrid Solver," AIAA J., **38**(11), pp. 2067–2076.

[121] Mavriplis, D. J., 1999, "Directional Agglomeration Multigrid Techniques for High-Reynolds-Number Viscous Flows," AIAA J., **37**(10), pp. 1222–1230.

[122] Lambropoulos, N. K., Koubogiannis, D. G., and Giannakoglou, K. C., 2004, "Acceleration of a Navier-Stokes Equation Solver for Unstructured Grids Using Agglomeration Multigrid and Parallel Processing," Comput. Methods Appl. Mech. Eng., **193**, pp. 781–803.

[123] Hwang, Y. H., 1995, "Unstructured Additive Correction Multigrid Method for the Solution of Matrix Equations," Numer. Heat Transfer, Part B, **27**, pp. 195–212.

[124] Sathyamurthy, P. S., and Patankar, S. V., 1994, "Block-Correction-Based Multigrid Method for Fluid Flow Problems," Numer. Heat Transfer, Part B, **25**(4), pp. 375–394.

[125] Brandt, A., McCormick, S. F., and Ruge, J., 1984, "Algebraic Multigrid (AMG) for Sparse Matrix Equations," *Sparsity and its Applications*, D. J. Evans, ed., Cambridge University Press, Cambridge, pp. 257–284.

[126] Webster, R., 1994, "An Algebraic Multigrid Solver for Navier-Stokes Problems," Int. J. Numer. Methods Fluids, **18**, pp. 761–780.

[127] Webster, R., 1996, "An Algebraic Multigrid Solver for Navier-Stokes Problems in the Discrete Second Order Approximation," Int. J. Numer. Methods Fluids, **22**, pp. 1103–1123.

[128] Vanka, S. P., 1985, "Block-Implicit Calculation of Steady Turbulent Recirculating Flows," Int. J. Heat Mass Transfer, **28**(11), pp. 2093–2103.

[129] Yu, C.-C., and Heinrich, J. C., 1986, "Petrov-Galerkin Methods for Time-Dependent Convective Transport Equation," Int. J. Numer. Methods Eng., **23**, pp. 883–901.

[130] Ortega, J. M., and Rheinboldt, W. C., 1980, *Iterative Solution of Nonlinear Equations in Several Variables*, Academic Press, New York.

[131] Haroutunian, V. H., Engelman, M. S., and Hasbani, I., 1993, "Segregated Finite Element Algorithms for the Numerical Solution of Large-Scale Incompressible Flow Problems," Int. J. Numer. Methods Fluids, **17**, pp. 323–348.

[132] Hughes, T. J. R., Franca, L. P., and Becestra, M., 1986, "A New Finite Element Formulation for Computational Fluid Dynamics, V: Circumventing the Babuska-Brezzi Condition: A Stable Petrov-Galerkin Formulation of the Stokes Problem Accomodating Equal-Order Interpolations," Comput. Methods Appl. Mech. Eng., **59**, pp. 85–99.

[133] Tezduyar, T. E., Shih, R., Mittal, S., and Ray, S. E., 1990, "Incompressible Flow Computation With Stabilized Bi-Linear and Linear Equal-Order Interpolation Velocity-Pressure Elements," Technical Report, University of Minnesota Supercomputing Institute Research Report UMSI90/165.

[134] Amon, C. H., 2000, "Spectral Element Methods for Unsteady Fluid Flow and Heat Transfer in Complex Geometries: Methodology and Applications," *Advances in Numerical Heat Transfer*, W. J. Minkowycz and E. M. Sparrow, eds., Taylor and Francis, New York, Vol. 2, Chap. 3, pp. 71–108.

[135] Belytschko, T., Lu, Y. Y., and Gu, L., 1994, "Element-Free Galerkin Methods," Int. J. Numer. Methods Eng., **37**, pp. 229–256.

[136] Duarte, C. A., and Oden, J. T., 1996, "An Hp Adaptive Method Using Clouds," Comput. Methods Appl. Mech. Eng., **139**, pp. 237–262.

[137] Liu, G. R., 2002, *Mesh Free Methods: Moving Beyond the Finite Element Method*, CRC Press, Boca Raton, FL.

[138] Atluri, S. N., and Zhu, T., 1998, "A New Meshless Local Petrov-Galerkin (MPLG) Approach in Computational Mechanics," Comput. Mech., **22**, pp. 117–127.

[139] Pepper, D. W., 2006, "Meshless Methods," *Handbook of Numerical Heat Transfer*, 2nd ed., W. J. Minkowycz, E. M. Sparrow, and J. Y. Murthy, eds., John Wiley and Sons, New York, pp. 225–247.

[140] Raithby, G. D., and Chui, E. H., 1990, "A Finite-Volume Method for Predicting Radiant Heat Transfer in Enclosures With Participating Media," ASME J. Heat Transfer, **112**, pp. 415–423.

[141] Chai, J. S., Lee, H. S., and Patankar, S. V., 1994, "Finite-Volume Method for Radiation Heat Transfer," J. Thermophys. Heat Transfer, **8**(3), pp. 419–425.

[142] Murthy, J. Y., and Mathur, S. R., 1998, "Finite Volume Method for Radiative Heat Transfer Using Unstructured Meshes," J. Thermophys. Heat Transfer, **12**(3), pp. 313–321.

[143] Wang, Z. J., Przekwas, A. J., and Liu, Y., 2002, "A FV-TD Electromagnetic Solver Using Adaptive Cartesian Grids," Comput. Phys. Commun., **148**, pp. 17–29.

[144] Murthy, J. Y., and Mathur, S. R., 2002, "Computation of Sub-Micron Thermal Transport Using an Unstructured Finite Volume Method," ASME J. Heat Transfer, **124**(6), pp. 1176–1181.

An Explicit Algebraic Model for Turbulent Heat Transfer in Wall-Bounded Flow With Streamline Curvature

B. A. Younis
Department of Civil & Environmental Engineering,
University of California,
Davis, CA 95616

B. Weigand

S. Spring

Institut fuer Thermodynamik der Luft- und Raumfahrt,
University of Stuttgart,
70569 Stuttgart, Germany

Fourier's law, which forms the basis of most engineering prediction methods for the turbulent heat fluxes, is known to fail badly in capturing the effects of streamline curvature on the rate of heat transfer in turbulent shear flows. In this paper, an alternative model, which is both algebraic and explicit in the turbulent heat fluxes and which has been formulated from tensor-representation theory, is presented, and its applicability is extended by incorporating the effects of a wall on the turbulent heat transfer processes in its vicinity. The model's equations for flows with curvature in the plane of the mean shear are derived and calculations are performed for a heated turbulent boundary layer, which develops over a flat plate before encountering a short region of high convex curvature. The results show that the new model accurately predicts the significant reduction in the wall heat transfer rates wrought by the stabilizing-curvature effects, in sharp contrast to the conventional model predictions, which are shown to seriously underestimate the same effects. Comparisons are also made with results from a complete heat-flux transport model, which involves the solution of differential transport equations for each component of the heat-flux tensor. Downstream of the bend, where the perturbed boundary layer recovers on a flat wall, the comparisons show that the algebraic model yields indistinguishable predictions from those obtained with the differential model in regions where the mean-strain field is in rapid evolution and the turbulence processes are far removed from local equilibrium. [DOI: 10.1115/1.2709960]

Keywords: turbulence modeling, streamline curvature, heat flux models

1 Introduction

The majority of flows that occur in nature or in engineering practice are turbulent and, more often than not, are "complex" in the sense that they possess features that are absent from classical thin shear layers. These features commonly arise from the interaction of the turbulence field with a body force, e.g., Corioli's, or from its distortion by mean rate of strain components other than the usual shear. The literature is abound with contributions made by S.V. Patankar and his colleagues in the computational modeling of these difficult flows. Examples include their study of flows in curved pipes [1], the comprehensive study they conducted of the requirements of turbulence models for flows in rotating ducts [2], and their prediction of the film cooling of curved surfaces [3,4]. Our focus in this paper is on a subclass of complex flows, namely, those involving streamline curvature in the plane of the mean shear. Examples of this type include flows over aircraft wings and over turbomachinery blades, where the accurate prediction of momentum and heat transfer rates is critical to their safe and efficient design. The effects of streamline curvature on the turbulent stresses and the heat fluxes are well known: these quantities are diminished when the angular momentum of the mean flow increases in the direction of the radius of curvature as would occur in a flow over a convex-curved surface (stabilizing curvature) and are enhanced when the angular momentum decreases with radius [5]. In strong stabilizing curvature, turbulence is effectively extinguished and the flow becomes laminarlike in many of its features [6]. Accounting for these effects in closure models of the type used in practical engineering design invariably involves making the mixing-length or the eddy-viscosity dependent on an appropriately defined Richardson number. This approach, while immensely successful for the class of flows for which the modification has been devised, has in recent years been abandoned in favor of models that account more directly for the effects of curvature on the Reynolds stresses. In these models, the eddy-viscosity assumptions are abandoned and the Reynolds stresses are instead obtained directly either from algebraic nonlinear relationships or from the solution of modeled differential transport equations in which they appear as the dependent variables. Here, again, Patankar's contributions may be cited [3]; specifically, in the use of an explicit algebraic model for the Reynolds stresses that reproduced many features of a flow over a curved surface.

In sharp contrast to the Reynolds stresses, little has hitherto been done on the related problem of modeling the effects of streamline curvature on the turbulent heat fluxes. The usual approach to the modeling of flows with heat transfer is to approximate the unknown turbulent heat fluxes ($-\overline{u_i t}$) using Fourier's law

$$-\overline{u_i t} = \Gamma_t \frac{\partial T}{\partial x_i} \tag{1}$$

and then evaluating the eddy diffusivity (Γ_t) by scaling the eddy viscosity with the turbulent Prandtl number

$$\Gamma_t = \frac{\nu_t}{\sigma_t} = \frac{C_\mu k^2/\epsilon}{\sigma_t} \tag{2}$$

where σ_t is the turbulent Prandtl number, usually assigned a constant value, and k and ϵ are the turbulence kinetic energy and its dissipation rate, respectively. It is tempting to justify the use of Fourier's law on the basis that changes to the turbulent heat fluxes due to curvature will be adequately accounted for via the changes

---

Contributed by the Heat Transfer Division. Manuscript received March 6, 2006; final manuscript received July 31, 2006. Review conducted by Sumanta Acharya.

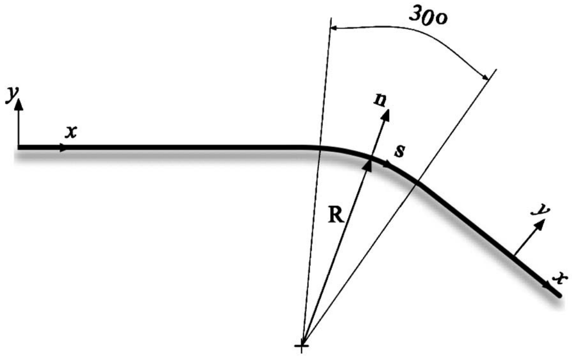

Fig. 1 Flow domain and coordinate systems

to k and ϵ predicted by a curvature-sensitive turbulence model. However, this expectation is not supported by the experimental evidence, which suggests that the heat fluxes are affected by streamline curvature to a greater extent than the Reynolds stresses [7,8]. Thus, in the experiments of Gibson et al. [8], for example, the Stanton number on a mildly curved convex surface, fell by 18% of the flat-plate value compared to a mere 10% drop in the wall skin-friction coefficient. The immediate implication of these findings is that the turbulent Prandtl number, which is normally assigned a constant value when used with Fourier's law, is in fact a strong function of the streamline curvature. This is not a surprising result because it can be shown to arise directly from analysis of the modeled transport equations for the turbulent heat fluxes. One such analysis was conducted by Gibson [9] who invoked local-equilibrium assumptions to convert the differential equation for the turbulent heat fluxes into algebraic expressions. The main conclusion of that study was that the effects of streamline curvature on heat transfer are mainly due to the curvature-dependent terms appearing in the transport equations for the heat fluxes. This conclusion turns out to have far-reaching consequences for the development of an alternative and more rationally based model for these fluxes. To demonstrate this, consider the exact terms that express the rates of production of the two nonzero heat-flux components $\overline{ut}$ and $\overline{vt}$ in a heated boundary layer where only the gradients in the cross-stream direction (n) are important (refer to Fig. 1). These terms are given as [10]

$$P_{\overline{ut}} = -\overline{vt}\left(\frac{\partial U}{\partial n} + \frac{U}{r}\right) - \overline{uv}\frac{\partial T}{\partial n}$$

$$P_{\overline{vt}} = 2\overline{ut}\frac{U}{r} - \overline{v^2}\frac{\partial T}{\partial n} \tag{3}$$

Since the heat fluxes are expected to be proportional to their rates of production, Eqs. (3) show that these fluxes must depend explicitly on the mean rates of strain, including those extra strains that arise from streamline curvature. Such dependence is entirely absent from Fourier's law and this explains, in part, the failure of this model to capture the correct response to curvature. Equations (3) also indicate that a rational model for the heat fluxes must also correctly reflect their explicit dependence on the details of the turbulence structure, as characterized by the components of $\overline{u_iu_j}$, and not just on the scalar turbulent kinetic energy k. This is because the components of the Reynolds-stress tensor are affected by the streamline curvature in ways that cannot be represented by changes in k alone. In the experiments of [11] on a convex-curved boundary layer, for example, the shear stress $\overline{uv}$ was observed to vanish in the presence of finite shear and then reverses sign in the outer layer in response to strong stabilizing-curvature effects. In contrast, k was only marginally reduced under the same conditions.

The purpose of this paper is to report on the development of an algebraic model for the turbulent heat fluxes for curved wall flows that is explicit in these quantities and contains the direct dependence on the mean rates of strain that was identified in [9] as being critical to the success of the model. The motivation for the work is to determine whether such a model, which combines the computational convenience and robustness of Fourier's law with the physics implied in the exact equations, can capture the curvature effects that have hitherto been reproducible only with ad hoc modifications, or with much more complicated closures involving the solution of several differential transport equations. Details of this explicit algebraic model will be presented in Sec. 2. In order to put this model's results into meaningful perspective, comparative predictions were also obtained with the most complete available closure for the turbulent heat fluxes, namely, the one that obtains each heat-flux component from the solution of its modeled differential transport equation. Details of this more complex model, and of the Reynolds-stress transport model used to close the momentum equations, are also provided in Sec. 2. Section 3 presents details of the computational method used for solving the governing equations. Comparisons of model predictions to experimental data from a heated boundary layer with streamline curvature are presented in Sec. 4, followed in Sec. 5 by a summary of the main conclusions.

2 Mathematical Models

2.1 Equations for Mean Velocity and Temperature. The flows where the effects of streamline curvature are most prominent tend to be of the boundary-layer type, where flow reversal is absent and the pressure-gradient effects, although present, are far outweighed by those due to turbulent transport. This is certainly the case in the experiment that will be used later to check the model. The geometry is shown in Fig. 1, which also defines the coordinate systems used. Upstream and downstream of the curved section, the flow develops over a flat wall, and hence, the Cartesian system is appropriate. Over the curved wall, the flow is more conveniently analyzed using the s-n coordinate system, where s is distance measured along the curved surface and n is measured along straight lines normal to s and away from the center of curvature. To the boundary-layer approximation, and for steady, two-dimensional high-Reynolds-number incompressible flows, the equations that describe the conservation of mass, momentum, and energy can be written in the following form:

$$\frac{\partial U}{\partial s} + \frac{\partial hV}{\partial n} = 0$$

$$\frac{\partial U^2}{\partial s} + \frac{\partial hVU}{\partial n} + 2\frac{\overline{uv}}{R} + \frac{UV}{R} = -h\frac{\partial \overline{uv}}{\partial n} - \frac{1}{\rho}\frac{\partial p}{\partial s}$$

$$\frac{h}{\rho}\frac{\partial p}{\partial n} = \frac{U^2}{R}$$

$$\frac{\partial UT}{\partial s} + \frac{\partial hVT}{\partial n} = -h\frac{\partial \overline{vt}}{\partial n} \tag{4}$$

where $h=(1+n/R)$. Note that for a flat wall ($R=\infty$), Eqs. (4) reduce to the familiar Cartesian forms with s and n being equivalent to x and y.

2.2 Algebraic Heat-Flux Model. It is instructive in presenting the new algebraic model for the turbulent heat flux in wall-bounded flows to refer to the *exact* equation for this quantity which, for steady flows, takes the form:

$$\overbrace{U_k\frac{\partial\overline{u_i t}}{\partial x_k}}^{\text{convection}} = \overbrace{-\frac{\partial}{\partial x_k}\left(\overline{u_k u_i t} + \frac{\overline{p' t}}{\rho}\delta_{ik} - \gamma\overline{u_i\frac{\partial t}{\partial x_k}} - \nu\overline{t\frac{\partial u_i}{\partial x_k}}\right)}^{\text{diffusion}}$$
$$\overbrace{-\overline{u_k t}\frac{\partial U_i}{\partial x_k} - \overline{u_k u_i}\frac{\partial T}{\partial x_k}}^{\text{production}} \overbrace{-(\gamma+\nu)\overline{\frac{\partial t}{\partial x_k}\frac{\partial u_i}{\partial x_k}}}^{\text{dissipation}} - \overbrace{\overline{\frac{p'}{\rho}\frac{\partial t}{\partial x_i}}}^{\text{correlations}} \qquad (5)$$

where γ is the thermal molecular diffusivity, ρ is the fluid density, and p' is the fluctuating pressure.

The usual approach to the development of an algebraic model for the turbulent heat fluxes based on Eq. (5) (e.g., [9]) is to invoke local-equilibrium assumptions to eliminate the differential terms representing convection and diffusion of the heat fluxes and to approximate the remaining terms, which contain the unknown turbulence correlations. The outcome is a set of algebraic expressions that is *implicit* in the heat fluxes and whose success depends heavily on the validity of the assumptions made to approximate the last term in Eq. (5). This term, which represents the correlation between the fluctuating pressure field and the gradients of the fluctuating scalars, is particularly difficult to model due to the absence of guiding experimental measurements. An alternative approach to modeling the heat fluxes, and one that does not involve finding approximations to the unknowns in Eq. (5), is to postulate a functional relationship for this quantity in terms of other variables suggested by the exact equation and then use tensor representation theory to derive explicit algebraic relations for the heat fluxes. This approach was first suggested by [13]. Their model reads:

$$-\overline{u_i t} = C_1\frac{k^2}{\epsilon}\frac{\partial T}{\partial x_i} + C_2\frac{k}{\epsilon}\overline{u_i u_j}\frac{\partial T}{\partial x_j} + C_3\frac{k^3}{\epsilon^2}\frac{\partial U_i}{\partial x_j}\frac{\partial T}{\partial x_j}$$
$$+ C_4\frac{k^2}{\epsilon^2}\left(\overline{u_i u_k}\frac{\partial U_j}{\partial x_k} + \overline{u_j u_k}\frac{\partial U_i}{\partial x_k}\right)\frac{\partial T}{\partial x_j} \qquad (6)$$

The values of the coefficients in Eq. (6) were determined by the model originators by reference to the large-eddy simulation (LES) and direct numerical simulation (DNS) results of [13] for scalar diffusion in homogeneous turbulence with uniform shear and constant scalar gradients and are given as $(C_1, C_2, C_3, C_4) = (-0.045, 0.37, -0.0037, -0.023)$.

The main features of this model are immediately apparent: it is algebraic and explicit in the heat fluxes—properties that will significantly simplify its implementation in a numerical algorithm. Moreover, the model contains all the dependences that are required by the exact equation; specifically, the turbulent heat fluxes now depend explicitly on the Reynolds stresses and not merely on the scalar turbulence kinetic energy. They also explicitly depend on the mean rate of strain. Thus, to the boundary-layer approximation in the *s-n* coordinate system, the heat fluxes are obtained as

$$-\overline{ut} = C_2\frac{k}{\epsilon}\overline{uv}\frac{\partial T}{\partial y} + C_3\frac{k^3}{\epsilon^2}\frac{\partial U}{\partial y}\frac{\partial T}{\partial y} + C_4\frac{k^2}{\epsilon^2}\frac{\partial T}{\partial y}P_{\overline{uv}}$$

$$-\overline{vt} = C_1\frac{k^2}{\epsilon}\frac{\partial T}{\partial y} + C_2\frac{k}{\epsilon}\overline{v^2}\frac{\partial T}{\partial y} + C_4\frac{k^2}{\epsilon^2}\frac{\partial T}{\partial y}P_{\overline{v^2}} \qquad (7)$$

where $P_{\overline{v^2}}$ and $P_{\overline{uv}}$ are, respectively, the rates of production of the normal-stress component $\overline{v^2}$ and the shear stress $\overline{uv}$,

$$P_{\overline{uv}} = -\overline{v^2}h\frac{\partial U}{\partial y}\left(1 - \frac{\overline{u^2}}{\overline{v^2}}S\right)$$

$$P_{\overline{v^2}} = 2\overline{uv}\frac{U}{r} \qquad (8)$$

In Eq. (8), S is the curvature parameter, which represents the ratio of the "extra" rate of strain due to streamline curvature to the usual mean shear,

$$S = \frac{U/r}{\partial U/\partial y} \qquad (9)$$

The model of [12] is not applicable in its proposed form in the region close to a solid wall. This was first noted in [14] in their study of axial heat conduction on heat transfer in low Prandtl number fluids. That the model requires adaptation to be applicable in that region can be seen by inspection of the form of Eq. (7) for flat-wall flows. There, the vertical heat flux component is obtained as

$$-\overline{vt} = (C_1 k + C_2\overline{v^2})\frac{k}{\epsilon}\frac{\partial T}{\partial y}$$

Thus, with the values of C_1 and C_2 quoted above, it can be seen that when

$$0.373 < \frac{\overline{v^2}}{k} < 0.0455, \quad \text{i.e., } \overline{v^2}/k < 0.122$$

then $\overline{vt}$ and $\partial T/\partial y$ will be incorrectly predicted to be of the same sign. Now, in wall-bounded flows, $\overline{v^2}/k$ decreases rapidly with distance to the wall. In the direct numerical simulations of [15] obtained in a channel, for example, $\overline{v^2}$ falls below the critical value of 0.122 at $y^+ \approx 24$. Consequently, the original model, when applied in the region $0 < y^+ < 24$, will yield values for $\overline{vt}$ that will be of the opposite sign to those obtained in the direct numerical simulations. The model is thus not expected to perform well close to a rigid wall—a region likely to be significantly affected by streamline curvature effects.

Extension of the model of [12] to near-wall turbulent flows requires making one or more of the coefficients of Eq. (6) dependent on parameters that are strongly sensitive to changes in the turbulence structure that occur in that region. These parameters include the turbulence Reynolds number (Re_t), the turbulence Peclet number (Pe), and the second and third invariants (A_2, A_3) of the Reynolds-stress anisotropy tensor (A_{ij}) and the stress-flatness parameter (A), defined as

$$\mathrm{Re}_t = \frac{k^2}{\nu\epsilon}$$

$$\mathrm{Pe} = \mathrm{Re}_t\,\mathrm{Pr}$$

$$A_{ij} = \frac{\overline{u_i u_j}}{k} - \frac{2}{3}\delta_{ij}$$

$$A_2 = A_{ij}A_{ij}$$

$$A_3 = A_{ij}A_{ij}A_{ij}$$

$$A = 1 - \frac{9}{8}(A_2 - A_3) \qquad (10)$$

Inclusion of Re_t is justified on the basis that this parameter represents the ratio of the turbulent to the molecular shear stresses and its value is thus zero at the wall, thereafter increasing monotonically with distance from it. It is also a scalar quantity and therefore independent of the direction of the wall normal vector. The same is true of Pr whose inclusion is necessitated by the strong dependence of the flow in the viscous sublayer on the nature of the fluid itself. The tensor A_{ij} provides complete but cumbersome characterization of the state of the Reynolds-stress anisotropy. The same state can be characterized by just the two scalar

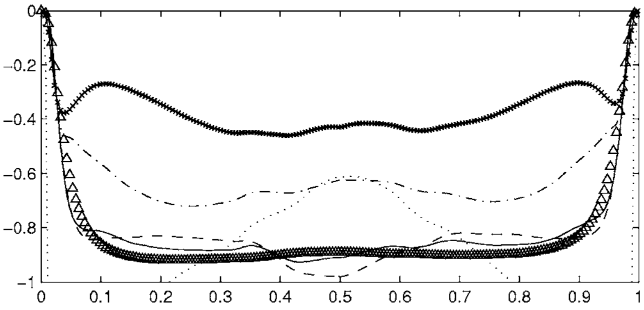

Fig. 2 Heated channel flow (Pr=0.7). Data of Debusschere. Models: solid line, present; dotted line, [31]; dashed line, [32]; dotted-dashed line, [33]; x-x-x, [34].

quantities A_2 and A_3 [16], or by their combination A. Making the model dependent on the invariants of A_{ij} is also required to capture the essentially two-component nature of turbulence very close to the wall.

Detailed analysis of the model's performance in relation to data from a large number of studies of wall-bounded flows using direct numerical simulations [17–20] showed that the model yields acceptable predictions of the heat flux component in the direction of flow, $(\overline{ut})$, but that the normal component $(\overline{vt})$ was in serious error for the reasons already discussed. This was an important finding since, as Eq. (6) suggests, it is only the C_1 coefficient that requires modification in the near-wall region. A straightforward way to accomplish this is to postulate a damping function of the form

$$C_1^* = C_1(1 - e^{-A\beta P_e^{\alpha}}) \tag{11}$$

Close to the wall, Re_t is of order unity, and the correction expressed in Eq. (11) yields a lower value for C_1 than that deduced from the homogeneous data of [13]. Further away, and as Re_t increases, damping is removed, and the value appropriate to high turbulence Reynolds number is recovered. The values of α and β were determined by computer optimization to yield best fit to data for $\overline{vt}$ from a number of direct numerical simulations of heated wall-bounded flows. These included the heated Poiseuille flow simulations of [17,18,21] with values of Prandtl number of 0.71 and 1.0, and the heated Couette flow simulations of [19]. The values that gave the best fit (as determined by the least-squares method) for all these flows were $\alpha=0.1$ and $\beta=1.5$. The model's results obtained with these values are compared to the DNS results of [20] for a heated channel (Fig. 2) and a heated Couette flow (Fig. 3). In both flows, the value of Pr was 0.7 and the Reynolds number (based on half width and bulk mean velocity) of 3000. Also plotted there are predictions obtained with alternative algebraic models. It is clear that the present model provides a very accurate fit to the DNS data over the whole field, and especially close to the wall. Departures from symmetry in the channel-flow results observed in these plots are due to variations in the DNS data used as input to the models.

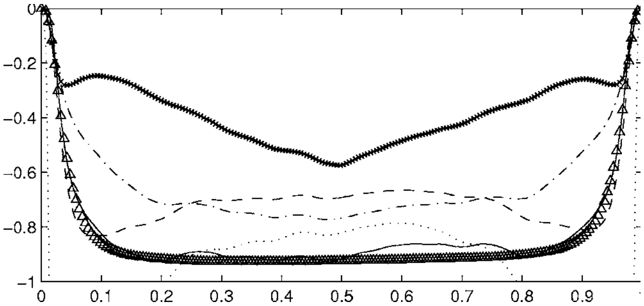

Fig. 3 Heated Couette flow (Pr=0.7). Data of Debusschere (Models: solid line, present; dotted line, [31]; dashed line, [32]; dotted-dashed line, [33]; x-x-x, [34])

2.3 Reynolds-Stress Transport Model. Since the focus of this paper is on modeling the heat fluxes, it is appropriate to seek to represent the Reynolds stresses with the best available turbulence closure in order to provide as accurate a description of the turbulence field as is possible to obtain with a Reynolds-averaged approach. The model chosen for this study is the complete Reynolds-stress transport closure found in previous studies [23,24] to yield acceptable results for curved flows.

In Cartesian-tensor notation, the equations for Reynolds stresses are written as

$$\begin{aligned}\overbrace{U_k\frac{\partial\overline{u_iu_j}}{\partial x_k}}^{\text{Convection:}C_{ij}} &= \overbrace{-\left(\overline{u_iu_k}\frac{\partial U_j}{\partial x_k}+\overline{u_ju_k}\frac{\partial U_i}{\partial x_k}\right)}^{\text{Production:}P_{ij}}\\ &\quad\overbrace{-\frac{\partial}{\partial x_k}\left[\overline{u_iu_ju_k}+\frac{1}{\rho}(\overline{p'u_i}\delta_{jk}+\overline{p'u_j}\delta_{ik})-\nu\frac{\partial\overline{u_iu_j}}{\partial x_k}\right]}^{\text{Diffusion:}D_{ij}}\\ &\quad\overbrace{-2\nu\left(\overline{\frac{\partial u_i}{\partial x_k}\frac{\partial u_j}{\partial x_k}}\right)}^{\text{Dissipation:}\epsilon_{ij}}+\overbrace{\overline{\frac{p'}{\rho}\left(\frac{\partial u_i}{\partial x_j}+\frac{\partial u_j}{\partial x_i}\right)}}^{\text{Redistribution:}\Phi_{ij}}\end{aligned} \tag{12}$$

Following the practices that proved successful in the earlier studies of curved flows, the triple-velocity correlations responsible for turbulent diffusion were modeled with the usual gradient-transport hypothesis

$$-\overline{u_iu_ju_k}=C_s\frac{k}{\epsilon}\overline{u_ku_l}\frac{\partial\overline{u_iu_j}}{\partial x_l} \tag{13}$$

where the ratio k/ϵ defines a characteristic turbulence time scale and C_s is an empirical coefficient taken equal to 0.22.

The difficult pressure-strain correlations term was modeled as a combination of a return-to-isotropy part and a rapid part, with corrections to each to account for the effects of a solid wall in damping the pressure fluctuations in its vicinity, thus,

$$\Phi_{ij}=\Phi_{ij,1}+\Phi_{ij,2}+\Phi_{ij,w} \tag{14}$$

where

$$\Phi_{ij,1}=-C_1\frac{\epsilon}{k}\left(\overline{u_iu_j}-\tfrac{2}{3}\delta_{ij}k\right)$$

$$\Phi_{ij,2}=-C_2\left(P_{ij}-\tfrac{2}{3}\delta_{ij}P_k\right)$$

$$\begin{aligned}\Phi_{ij,w}&=C_1'\frac{\epsilon}{k}\left(\overline{u_ku_m}\mathbf{n}_k\mathbf{n}_m\delta_{ij}-\tfrac{3}{2}\overline{u_ku_i}\mathbf{n}_k\mathbf{n}_j-\tfrac{3}{2}\overline{u_ku_j}\mathbf{n}_k\mathbf{n}_\mathbf{i}\right)f\\ &\quad+C_2'\left(\Phi_{km,2}\mathbf{n}_k\mathbf{n}_m\delta_{ij}-\tfrac{3}{2}\Phi_{ki,2}\mathbf{n}_k\mathbf{n}_j-\tfrac{3}{2}\Phi_{kj,2}\mathbf{n}_k\mathbf{n}_\mathbf{i}\right)f\end{aligned} \tag{15}$$

In Eqs. (15), $\mathbf{n}_\mathbf{i}$ is the wall normal unit vector and f is a function which determines the local strength of wall damping. This is taken here to be proportional to the ratio of a representative size of energy-containing eddy $(k^{3/2}/\epsilon)$ to distance from the wall. The proportionality constant is chosen to give this function a unity value close to the wall.

The coefficients associated with this model have been assigned the values recommended by [24,25] viz. $(C_1,C_2,C_1',C_2')=(3.0,0.3,0.75,0.5)$.

The final approximation needed to close Eq. (12) relates to the term representing dissipation by viscous action. At high values of the turbulence Reynolds number, the dissipative motions are assumed to be isotropic and the dissipation rate of $\overline{u_iu_j}$ is related to ϵ, the dissipation rate of k

$$\epsilon_{ij} = \tfrac{2}{3}\delta_{ij}\epsilon \tag{16}$$

and ϵ is obtained from the solution of the modeled conservation equation

$$\frac{D\epsilon}{Dt} = \frac{\partial}{\partial x_i}\left(C_\epsilon \frac{k}{\epsilon}\overline{u_i u_j}\frac{\partial \epsilon}{\partial x_j}\right) + C_{\epsilon 1}P_k - C_{\epsilon 2}\frac{\epsilon^2}{k} \tag{17}$$

where P_k is the rate of production of turbulence kinetic energy

$$P_k = -\overline{u_i u_j}\left(\frac{\partial U_i}{\partial x_j} + \frac{\partial U_j}{\partial x_i}\right) \tag{18}$$

The coefficients are again assigned the values found by [24,25] most appropriate for the prediction of curved shear flows, viz. $(C_\epsilon, C_{\epsilon 1}, C_{\epsilon 2}) = (0.15, 1.40, 1.80)$.

2.4 Heat-Flux Transport Model. In order to put the algebraic model's results in appropriate context, comparative predictions were also obtained with the more complete but complex model which is based on the solution of a modeled differential transport equation for each heat-flux component. The exact equations have already been presented in the section on the formulation of the algebraic model (Eq. (5)). Here, the modeling assumptions required to close those equations are presented. The term that represents the transport of $\overline{u_i t}$ by turbulent fluctuations is modeled via the usual gradient-transport assumptions with a coefficient of 0.15 as recommended by [26]. The rate of dissipation of the heat fluxes by viscous action vanishes at high turbulence Reynolds numbers and is dropped.

The production terms are exact and are rewritten here for later convenience as

$$P_{it,1} \equiv -\overline{u_k u_i}\frac{\partial T}{\partial x_k} \tag{19}$$

$$P_{it,2} \equiv -\overline{u_k t}\frac{\partial U_i}{\partial x_k} \tag{20}$$

The fluctuating pressure-scalar-gradient correlation term (π_{it}) may be viewed as the counterpart of the pressure-strain term in the $\overline{u_i u_j}$ transport equation and is expected to play an equally important role in accounting for the effects of streamline curvature. This term is usually modeled as the sum of three elements [27]

$$\pi_{it} = \pi_{it,1} + \pi_{it,2} + \pi_{it,w} \tag{21}$$

the separate contributions arising, respectively, from purely turbulence interactions, interactions between the mean strain and fluctuating quantities, and corrections to allow for wall damping. Following [27], these contributions are modeled as follows:

$$\pi_{it,1} = -C_{1t}\frac{\epsilon}{k}\overline{u_i t} \tag{22}$$

$$\pi_{it,2} = -C_{2t}P_{it,2} \tag{23}$$

$$\pi_{it,w} = -C_{t,w}\frac{\epsilon}{k}\overline{u_i t}\mathbf{n_i}\mathbf{n}_k f \tag{24}$$

where f is the wall-damping function previously defined. The coefficients, which are determined by reference to measurements of streamwise and cross-stream flux components in homogeneous shear flows [27], are assigned the values $(C_{1t}, C_{2t}, C_{t,w}) = (2.85, 0.55, 1.2)$.

3 Solution of Equations

The mean-flow and turbulence-closure equations of Sec. 2 were solved simultaneously by means of the EXPRESS code [28]. This is an implicit finite-volume marching integration method which is based largely on another of S. V. Patankar's influential contributions: the GENMIX boundary-layer calculation procedure [29] without which none of the pioneering work on turbulence modeling would have been possible. The main differences in the two procedures are in the choice of transformed coordinates used to cause the computational grid to adapt to match the actual width of the flow thereby ensuring that all the computational nodes remain within the shear layer. In Patankar's method, the dimensionless stream function was used while here it is the physical cross-stream distance nondimensionalized by the local boundary layer width. Second-order accurate spatial discretization is employed. The simulations reported here were obtained with a forward-step size that was limited to 1% of the local boundary layer width, and with 60 nodes that were unevenly distributed in the cross-stream direction. Virtually identical results were obtained with a grid utilizing twice as large a forward-step size and only 30 nodes in the cross-stream direction (the maximum differences in skin-friction coefficient and in the shape factor obtained with the two grids were 0.17% and 0.21%, respectively). Reducing the forward-step size by a factor of five produced no discernible differences.

The solution was started from assumed equilibrium velocity, turbulence, and temperature profiles and was advanced step by step in the direction of flow. At each streamwise location, iterations were performed until the absolute sum of the residuals for all the dependent variables fell to below 10^{-3}. Further reduction in this tolerance produced no change in the predictions.

The experiment chosen to test the model is one in which a turbulent boundary layer develops over a surface of high convex curvature. The flow is strictly partially parabolic in the sense that the effects of the curved surface are sensed some distance upstream due to changes in the pressure field. Moreover, significant radial pressure gradients are set up over the curved surface itself. This flow would be amenable to simulation using another of Patankar's seminal contributions to computational fluid dynamics; namely, the partially parabolic algorithm described in [1]. Here, we adopt a simplified approach made possible by the availability of measurements of the static pressure distribution along the curved surface. An estimate of the radial distribution of static pressure can be obtained from potential flow analysis. Thus, with the assumption of parallel flow, the radial momentum equation reduces to

$$\frac{\partial p}{\partial n} = \rho\frac{{U_p}^2}{r} \tag{25}$$

where U_p is the potential velocity whose radial distribution can be deduced from the condition of zero spanwise vorticity

$$\frac{1}{r}\frac{\partial(rU_p)}{\partial r} - \frac{\partial V_p}{\partial s} = 0 \tag{26}$$

which, again with the assumption of parallel flow, reduces to

$$rU_p = RU_{pw} \tag{27}$$

where w refers to "wall" value.

With this result, Eq. (25) may be integrated to yield p_i, the pressure at location i within the flow

$$p_i = p_{sw} + \frac{1}{2}\rho U_{pw}^2 - \frac{1}{2}\rho U_{pw}^2\left(\frac{R}{r}\right)^2 \tag{28}$$

Finally, by differentiating this expression and by recognizing that the total pressure is conserved there results

$$\left(\frac{\partial p}{\partial s}\right)_i = \left(\frac{R}{r}\right)^2\frac{\partial p_{sw}}{\partial s} - \rho U_{pw}^2\frac{R}{r}\frac{\partial R/r}{\partial s} \tag{29}$$

Equation (29) was used to evaluate the axial pressure gradients in the curved-flow simulations presented here. Experimental values of the wall static-pressure coefficients are plotted in Fig. 4, together with the distribution obtained by curve fitting the experimental measurements using the Akima spline interpolation

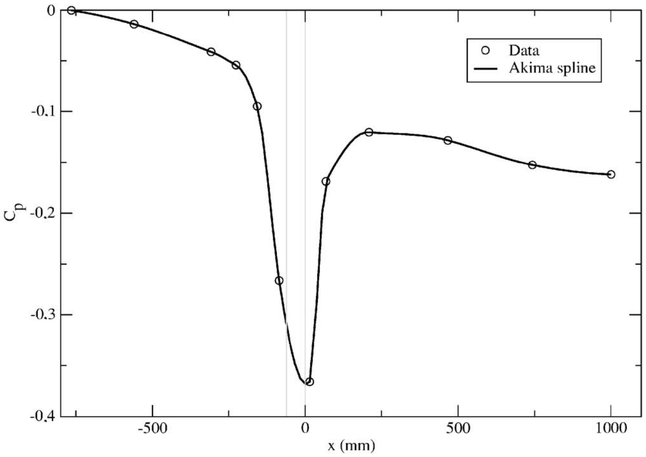

Fig. 4 Streamwise variation of wall static-pressure coefficient; vertical lines signify location of convex bend

scheme. This was the only input from the experiments. The freestream velocity was deduced and the predicted and measured variations of this quantity with streamwise distance are compared in Fig. 5, which provides a convincing demonstration of the ability of this simplified method to capture the radial variation in static pressure induced by the streamline curvature. The use of the Akima spline scheme proved essential to the attainment of smooth variations in freestream velocity.

The boundary conditions were as follows: at the freestream, the cross-stream gradients of all dependent variables were set equal to zero, except for the temperature whose value there was set, as in the experiment being simulated, at 14.6 K below the wall temperature, which was kept constant in the direction of flow. At the wall, integration terminated outside the viscous sublayer and the boundary conditions applied there consisted of specifying the fluxes of momentum and heat at the wall. These were, in turn, deduced from the universal logarithmic laws

$$u^+ = \frac{1}{\kappa}\ln(y^+) + B$$

$$T^+ = \frac{1}{\kappa'}\ln(y^+) + B' \tag{30}$$

where the coefficients were assigned their usual values ($\kappa = 0.41$, $B = 5.0$, $\kappa' = 0.45$, $B' = 3.0$). Fluxes of all the Reynolds-stress components at the nodes closest to the wall were set equal to zero. The dissipation rate was assumed to vary inversely with distance from the wall to the node closest to it. With this assumption, and after neglecting the convection and normal-stress gradients, Eq. (17) reduces to the quadratic equation:

$$\epsilon^2 - \frac{C_{\epsilon 1}}{C_{\epsilon 2}} P_k \epsilon - \frac{C_\epsilon}{C_{\epsilon 2}} \frac{k\overline{v^2}}{y^2} = 0 \tag{31}$$

The solution to this equation yields values for ϵ at the near-wall nodes that were used to provide the boundary conditions there. These values did not generally turn out to be equal to the rate of production of turbulence kinetic energy except away from the convex bend, where the two quantities did, indeed, turn out to be equal.

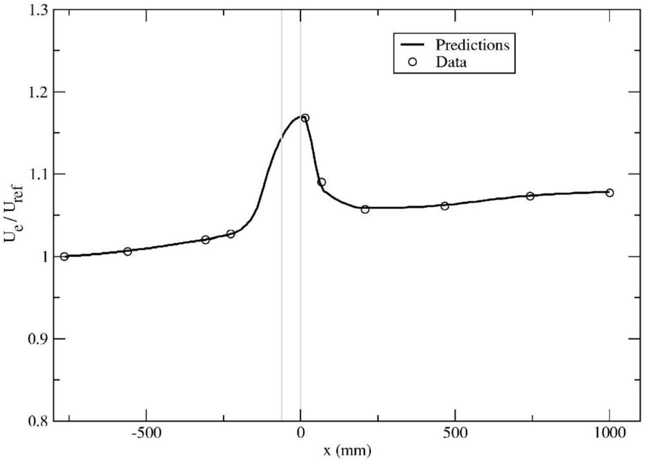

Fig. 5 Predicted and measured variation of freestream velocity (U_e/U_{ref})

4 Results and Discussion

The experimental data used to check the model's performance in a curved, heated, wall-bounded flow are those of [30] obtained in a turbulent boundary layer recovering downstream of a short convex bend. The geometry is shown in Fig. 1. The boundary layer is first developed to equilibrium on a flat plate before encountering the convex bend. The bend had a turning angle of 30 deg and a surface radius of curvature $R = 0.115$ m. At entry to the bend, the ratio of boundary layer thickness (δ) to surface radius of curvature was ~0.19. This ratio provides a useful measure of the strength of curvature effects; its value here is higher than that attained in any other experiment in which the curved flow remained of the boundary layer type. Downstream of this bend, the flow recovers on another flat section.

The measured streamwise variation of the wall static-pressure coefficient C_p $[=(p-p_{\mathrm{ref}})/1/2\rho U_e^2]$ is plotted in Fig. 4 together with the interpolated values used in the predictions. In this and subsequent figures, the distance x is measured from the end of the convex bend. Figure 4 shows that the effects of curvature on this quantity are quite substantial and are felt at significant distance upstream of the bend. Closer to the bend, the pressure initially falls quite rapidly and then rises before finally falling again on the flat recovery section. Thus, quite strong axial pressure gradients are set up, initially favorable, but then adverse though not sufficient to cause flow reversal. The ability of the algorithm for evaluating the pressure gradients described in Sec. 3 is illustrated in Fig. 5, which compares the predicted and measured streamwise variation of the freestream velocity U_e. The response of this parameter to the favorable pressure gradient is quite dramatic with the local freestream velocity initially rising to $1.17U_{\mathrm{ref}}$ immediately on exit from the bend and then falling to $1.057U_{\mathrm{ref}}$ at about ten boundary layer heights downstream from there. These rapid variations are well reproduced by the pressure-gradient algorithm described in Sec. 3. The predicted and measured boundary-layer thickness (δ) are compared in Fig. 6. Measurements of the mean velocity, from which δ was deduced, were obtained using both a flattened stagnation tube and constant-temperature hot wire anemometry with differences of order 3% reported immediately downstream of the bend. The predictions there show an unrealistic spike produced as an artifact of the procedure used to adjust the size of the computational domain to match that of the flow.

The effects of pressure gradient on the measured and the Reynolds-stress model predictions of the skin friction coefficient C_f $[=\tau_w/(1/2)\rho U_e^2]$ are shown in Fig. 7. Following the initial rise in this quantity in response to flow acceleration, C_f drops quite markedly due to stabilizing curvature effects and attains a minimum value some distance after exit from the convex bend. This is obtained in both the measurements and the predictions though somewhat further downstream in the latter. Also plotted in Fig. 7 is the correlation of experimental data for a heated flat-plate boundary layer

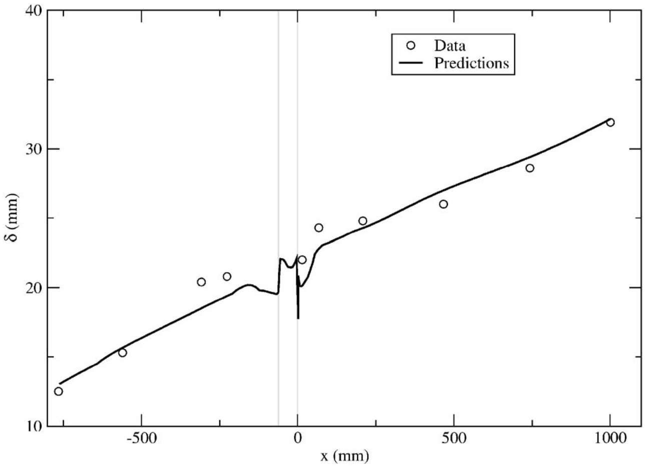

Fig. 6 Predicted and measured variation of boundary layer thickness

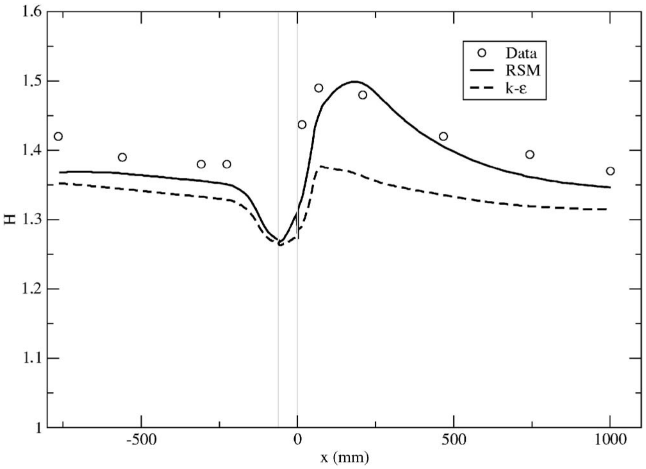

Fig. 8 Predicted and measured shape factor

$$C_f = 0.0592\,\mathrm{Re}_x^{-0.2} \tag{32}$$

Comparisons to this correlation show that both prediction and measurements indicate a fairly rapid recovery in this parameter to flat-plate values. Results obtained with the k-ϵ model are also plotted for comparison. These show fairly accurate response to the favorable pressure gradient but, as expected, almost no sensitivity to convex-curvature effects.

The combined influence of streamwise pressure gradients and streamline curvature on the shape factor $(H=\delta_1/\delta_2)$ is equally pronounced and well represented by the Reynolds-stress transport model. This can be seen from Fig. 8, where the k-ϵ predictions are also included. As expected, the trends in H are opposite to those in C_f: increasing in the bend before recovering to values typical of flat-plate flow.

The predicted and measured mean-velocity profiles are compared in Fig. 9, where they are presented in wall coordinates. Also plotted there is the law of the wall (Eq. (30)), which was used to deduce the wall momentum flux. Agreement for the later stages of flow development is quite satisfactory, but this is not so for $x = 68$ mm, where the predicted profile shows stronger departure from the log law than that shown by the experiments. This departure from the standard log law is consistent with the effects of strong adverse pressure gradients; that the measurements do not also show this is probably due, in part, to the difficulty in obtaining accurate estimates of the wall shear stress using the various techniques listed in Fig. 7.

Figure 10 compares the measured and Reynolds-stress transport model predictions of the shear stress profiles upstream and downstream of the bend. The effects of stabilizing curvature are most prominent in the outer layers where it is seen that the shear stress falls to zero (and actually reverses sign at $x=15$ mm) in a region where the mean rate of strain is finite. In this respect, the present behavior is quite similar to that observed in [11] for an approximately similar ratio of δ/R. Agreement at the stations immediately after the bend is not particularly good due, in part, to the inability of the turbulence model to capture the effects of adverse pressure gradients—a defect it shares with most other closures. The experimental data close to the wall are generally subject to error due to inadequate spatial resolution of the hot wire probe there. The consequences of such error are estimated in [30] to cause underestimation of $\overline{uv}$ by $\sim$12%. This is confirmed by the steep gradients observed in the measured $\overline{uv}$ profiles with respect to the wall values, which are also shown in Fig. 10. This behavior contrasts quite sharply with the predicted profiles that appear to smoothly asymptote toward the wall values.

Attention is now turned to the thermal field and, in particular, to the performance there of the proposed algebraic heat-flux model. Figure 11 compares the predicted and measured axial variation of

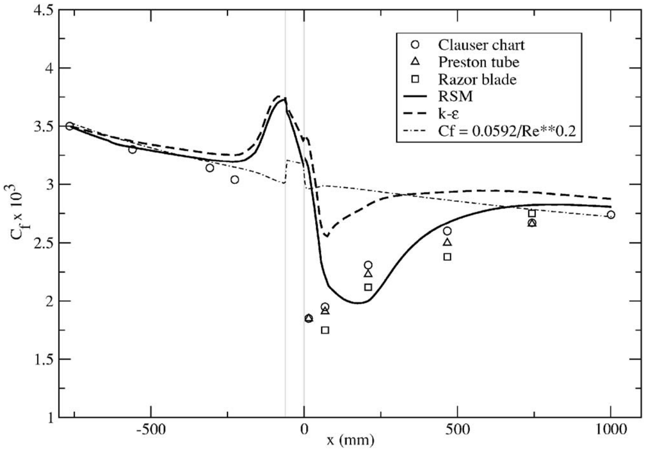

Fig. 7 Predicted and measured streamwise variation of skin-friction coefficient

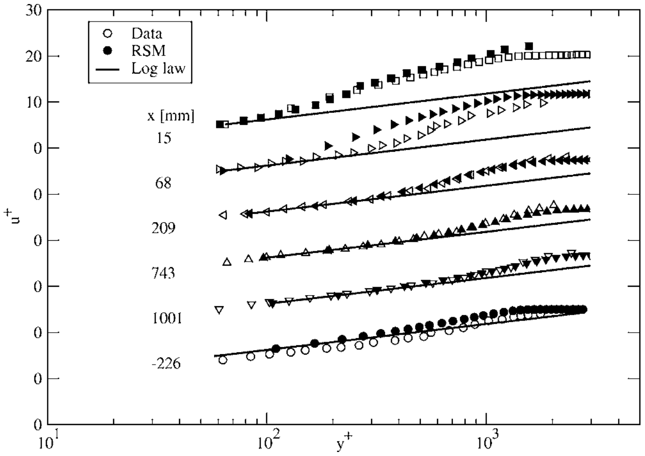

Fig. 9 Mean-velocity profiles in wall coordinates

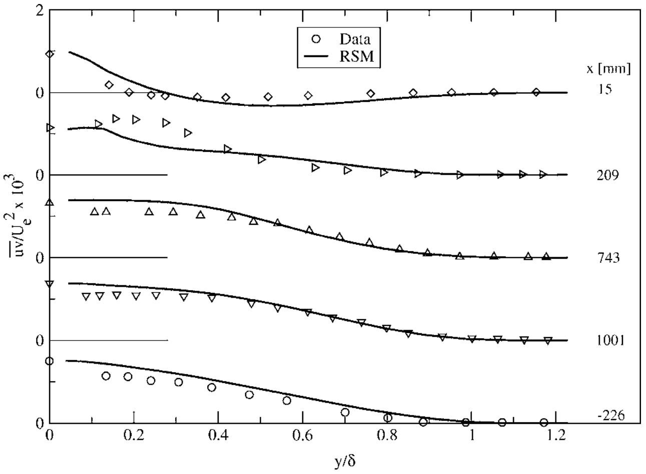

Fig. 10 Predicted and measured profiles of $-\overline{uv}$

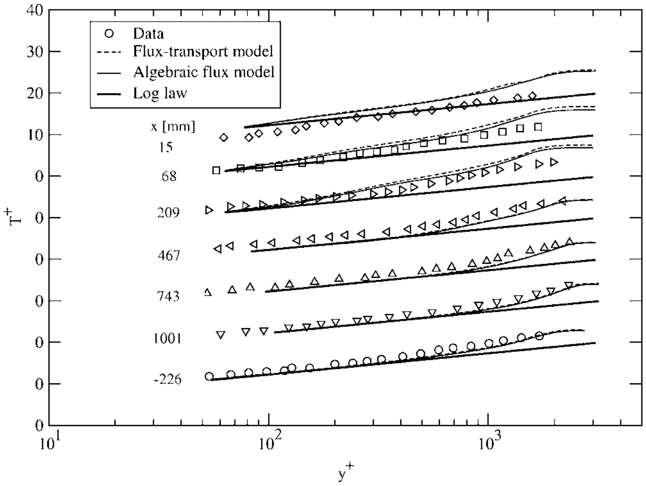

Fig. 12 Mean-temperature profiles in wall coordinates

Stanton number (St). Both results of the algebraic model and heat-flux transport model are included, and these show that the differences between the two models to be almost insignificant. The exception here is on exit from the bend where transport of heat flux by the mean flow, something that cannot be represented by the algebraic model, is expected to be important. Apart from that, both models appear to significantly exaggerate the combined effects of stabilizing curvature that influence the thermal layer directly, and the adverse pressure gradients effects, that enter indirectly via changes to the velocity field. Recovery to flat-plate values is predicted by both models to occur at the same rate. Results obtained with Fourier's law are also plotted and show that this model, as expected, exhibits a poor response to stabilizing curvature effects. This is clear from comparison of this model's result to the conventional experimental correlation for a flat-plate boundary layer

$$\mathrm{St} = 0.0296\,\mathrm{Pr}^{-0.4}\,\mathrm{Re}_x^{-0.2} = 0.5C_f\,\mathrm{Pr}^{-0.4} \qquad (33)$$

The computed and measured temperature distributions, plotted in inner-layer coordinates, are compared in Fig. 12, which also shows the log law (Eq. (30)), which was used to provide the wall heat fluxes. The results of both the algebraic and the flux-transport models are again hardly distinguishable from each other except at $x=68$ mm, where small differences are observed. Both models and the measurements show departures from the flat-wall log law up to $x=209$ mm but then seem to follow this distribution very closely for the remainder of the recovery length.

The predicted and measured profiles of the heat-flux component $\overline{vt}$ are compared in Fig. 13. Here, too, the results of the two models are virtually identical and both appear to overestimate the measurements in a manner which is quite similar to that previously observed for the shear stress (Fig. 10). It would be reasonable to expect that errors in the hot-wire measurement would appear consistently in both $\overline{uv}$ and $\overline{vt}$, and this does, indeed, seem to be the case here. Note the differences between the predicted and measured behavior in the inner-wall region with only the former showing the expected asymptotic approach to the wall heat-flux values.

Figure 14 shows the predicted and measured heat-flux component $\overline{ut}$. This quantity, which would be obtained as zero with Fourier's law, is predicted as being finite with the present algebraic model, albeit with values that significantly underestimate both the measurements and the flux-transport model results. In boundary layer flows, this component plays no part in the computations since diffusion in the streamwise direction is excluded. It does, however, play an important part in buoyant flows, where it enters into the rate of production of turbulence kinetic energy. In such flows additional terms that bring in dependence on gravitational acceleration and temperature variance would appear in the algebraic representation of $\overline{ut}$, and these additional terms are expected to bring about better correspondence between predictions and measurements. The strategy for inclusion of buoyancy-related ef-

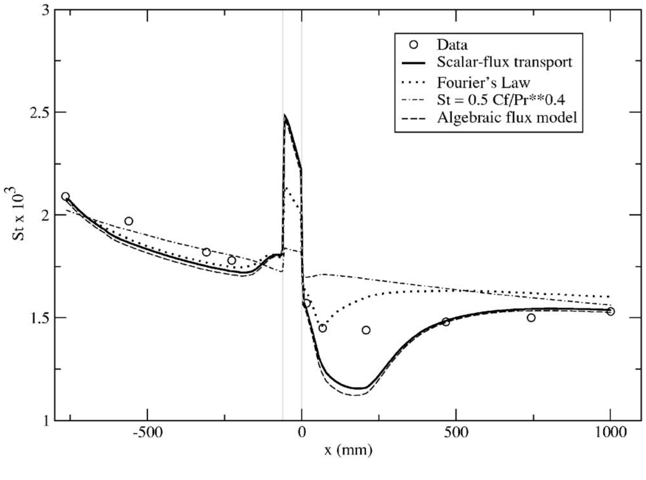

Fig. 11 Predicted and measured variation of Stanton number

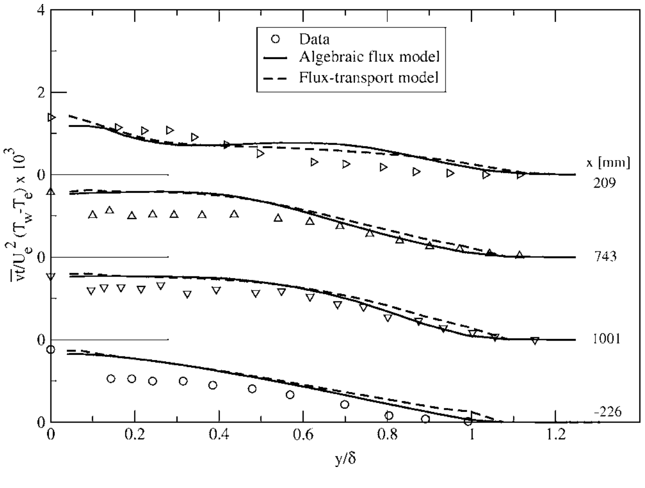

Fig. 13 Predicted and measured profiles of $-\overline{vt}$

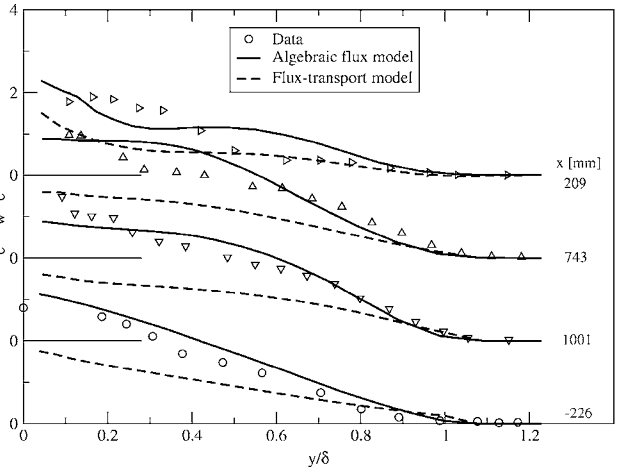

Fig. 14 Predicted and measured profiles of $-\overline{ut}$

fects in the tensor representation approach is given in [12]; validation against buoyant-flow data is the subject of an ongoing study.

5 Closing Remarks

The results presented in this paper suggest that a model for the turbulent heat fluxes, formulated using tensor representation theory, is capable of capturing the pronounced effects of streamline curvature without the ad hoc modifications found necessary with Fourier's law. The model is both algebraic and explicit in the heat fluxes, properties that enhances its usability in engineering prediction methods. Moreover, it allows for all the dependencies that are required by the exact equations for the heat fluxes. Specifically, the heat fluxes are obtained as functions of the Reynolds stresses and of the mean rates of strain, including the extra strains that arise from streamline curvature. Comparisons to data from an experiment on a heated boundary layer that develops over a short region of high convex curvature show the algebraic model to perform just as well as a more complicated and computationally more demanding heat-flux transport model. The results suggest that this model, in the form extended to account for the wall-damping effects, provides a suitable tool for the practical prediction of engineering flows where heat transfer is of importance.

References

[1] Patankar, S. V., Pratap, V. S., and Spalding, D. B., 1975, "Prediction of Turbulent Flow in Curved Pipes," J. Fluid Mech., **67**, pp. 583–595.
[2] Howard, J. H. J., Patankar, S. V., and Bordynuik, R. M., 1980, "Flow Prediction in Rotating Ducts Using Coriolis-Modified Turbulence Models," ASME J. Fluids Eng., **102**(4), pp. 456–461.
[3] Berhe, M. K., and Patankar, S. V., 1999, "Curvature Effects on Discrete-Hole Film Cooling," ASME J. Turbomach., **141**(4), pp. 781–791.
[4] Berhe, M. K., and Patankar, S. V., 1999, "Investigation of Discrete-Hole Film Cooling Parameters Using Curved-Plate Models," ASME J. Turbomach., **141**(4), pp. 792–803.
[5] Rayleigh, T. W. S., 1917, "Dynamics of Revolving Fluids," Proc. R. Soc. London, Ser. A, **93**, pp. 148–154.
[6] Bradshaw, P., 1973, "Effects of Streamwise Curvature on Turbulent Flows," AGARDograph No. 169.
[7] Simon, T. W., and Moffat, R. J., 1979, "Heat Transfer Through Turbulent Boundary Layers—The Effects of Introduction of and Recovery From Convex Curvature," ASME Winter Annual Meeting, New York, ASME Paper No. 79-WA/GT-10.
[8] Gibson, M. M., Verriopoulos, C. A., and Nagano, Y., 1982, "Measurements in the Heated Turbulent Boundary Layer on a Mildly Curved Convex Surface," *Turbulent Shear Flows*, Springer-Verlag, Berlin, Vol. 3.
[9] Gibson, M. M., 1978, "An Algebraic Stress and Heat-Flux Model for Turbulent Shear Flow With Streamline Curvature," Int. J. Heat Mass Transfer, **21**, pp. 1609–1617.
[10] Younis, B. A., and Berger, S. A., 2006, "On Predicting the Effects of Streamline Curvature on the Turbulent Prandtl Number," ASME J. Appl. Mech., **73**, pp. 1–6.
[11] Smits, A. J., Young, S. T. P., and Bradshaw, P., 1979, "The Effect of Short Regions of High Surface Curvature on Turbulent Boundary Layers," J. Fluid Mech., **94**, pp. 209–242.
[12] Younis, B. A., Speziale, C. G., and Clark, T. T., 2005, "A Rational Model for the Turbulent Scalar Fluxes," Proc. R. Soc. London, Ser. A, **461**, pp. 575–594.
[13] Kaltenbach, H.-J., Gerz, T., and Schumann, U., 1994, "Large-Eddy Simulation of Homogeneous Turbulence and Diffusion in Stably Stratified Shear Flow," J. Fluid Mech., **280**, pp. 1–40.
[14] Weigand, B., Schwartzkopff, T., and Sommer, T. P., 2002, "A Numerical Investigation of the Heat Transfer in a Parallel Plate Channel With Piecewise Constant Wall Temperature Boundary Condition," ASME J. Heat Transfer, **124**, pp. 626–634.
[15] Kim, J., Moin, P., and Moser, R., 1987, "Turbulence Statistics in Fully Developed Channel Flow at Low Reynolds Number," J. Fluid Mech., **177**, pp. 133–166.
[16] Pope, S. B., 2000, *Turbulent Flows*, Cambridge University Press, Cambridge, England.
[17] Abe, H., and Kawamura, H., 2002, "A Study of Turbulence Thermal Structure in a Channel Flow Through DNS Up to $\mathrm{Re}_\tau=640$ with $\mathrm{Pr}=0.71$," *Proc. 9th European Turbulence Conference*, University of Southampton, Southampton, pp. 399–402.
[18] Kawamura, H., Ohsaka, K., Abe, H., and Yamamoto, K., 1998, "DNS of Turbulent Heat Transfer in Channel Flow With Low to Medium-High Prandtl Number," Int. J. Heat Fluid Flow, **19**, pp. 482–491.
[19] Kawamura, H., Abe, H., and Shingai, K., 2002, "DNS of Turbulence and Heat Transport in a Channel Flow With Different Reynolds and Prandtl Numbers and Boundary Conditions," *Proc. 3rd Int. Symp. on Turbulence, Heat and Mass Transfer*, Aichi Shuppan, Japan, pp. 15–32.
[20] Debusschere, B., and Rutland, C. J., 2003, "Turbulent Scalar Transport Mechanisms in Plane Channel and Couette Flows," Int. J. Heat Mass Transfer, **47**, pp. 222–242.
[21] Kasagi, N., and Iida, O., 1999, "Progress in Direct Numerical Simulation of Turbulent Heat Transfer," *Proc 5th ASME/JSME Joint Thermal Engineering Conference*, San-Diego, ASME, New York, pp. 1–17.
[22] Gibson, M. M., Jones, W. P., and Younis, B. A., 1981, "Calculation of Turbulent Boundary Layers Over Curved Surfaces," Phys. Fluids, **24**, pp. 386–395.
[23] Gibson, M. M., and Younis, B. A., 1982, "Modeling the Curved Turbulent Wall Jet," AIAA J., **20**(12), pp. 1707–1712.
[24] Gibson, M. M., and Younis, B. A., 1986, "Calculation of Swirling Jets With a Reynolds Stress Closure," Phys. Fluids, **29**, pp. 38–48.
[25] Gibson, M. M., and Younis, B. A., 1986, "Calculation of Boundary Layers With Sudden Transverse Strains," ASME J. Fluids Eng., **108**, pp. 470–475.
[26] Malin, M. R., and Younis, B. A., 1990, "Calculation of Turbulent Buoyant Plumes With a Reynolds-Stress and Heat-Flux Transport Closure," Int. J. Heat Mass Transfer, **33**(10), pp. 2247–2264.
[27] Gibson, M. M., and Launder, B. E., 1978, "Ground Effects on Pressure Fluctuations in the Atmospheric Boundary Layer," J. Fluid Mech., **86**(3), pp. 491–511.
[28] Younis, B. A., 1996, "EXPRESS: Accelerated Parabolic Reynolds Stress Solver," Hydraulics Section Report, City University, London.
[29] Patankar, S. V., and Spalding, D. B., 1970, *Heat and Mass Transfer in Boundary Layers*, Intertext Books, London.
[30] Gibson, M. M., and Servat-Djoo, K., 1989, "Effect of a Short Region of High Convex Curvature on Heat Transfer Through a Turbulent Boundary Layer," Int. J. Heat Fluid Flow, **10**(1), pp. 75–82.
[31] Rubinstein, R., and Barton, J. M., 1991, "Renormalization Group Analysis of Anisotropic Diffusion in Turbulent Shear Flows," Phys. Fluids A, **3**, pp. 415–421.
[32] Rogers, M. M., Mansour, N. N., and Reynolds, W. C., 1989, "An Algebraic Model for the Turbulent Flux of a Passive Scalar," J. Fluid Mech., **203**, pp. 77–101.
[33] Suga, K., and Abe, K., 1999, "Nonlinear Eddy Viscosity Modelling for Turbulence and Heat Transfer Near Wall and Shear-Free Boundaries," Int. J. Heat Fluid Flow, **39**, pp. 455–465.
[34] So, R. M. C., and Sommer, T. P., 1996, "An Explicit Algebraic Heat-Flux Model for the Temperature Field," Int. J. Heat Mass Transfer, **39**, pp. 455–465.

A New Low Reynolds Stress Transport Model for Heat Transfer and Fluid in Engineering Applications

Rongguang Jia
Fluent Inc.,
Lebanon, NH

Bengt Sundén[1]
Division of Heat Transfer,
Lund Institute of Technology,
Lund 22100, Sweden
e-mail: Bengt.Sunden@vok.lth.se

Mohammad Faghri
Department of Mechanical Engineering and
Applied Mechanics,
University of Rhode Island, Kingston, RI

A new Reynolds stress transport model (RSTM) aimed for engineering applications is proposed with consideration of near-wall turbulence. This model employs the Speziale, Sarkar, and Gatski (SSG) pressure strain term, the ω equation, and the shear stress transport (SST) model for the shear stresses at the near-wall region (say, $y^+ < 30$*). The models are selected based on the following merits: The SSG RSTM model performs well in the fully turbulent region and does not need the wall normal vectors; the ω equation can be integrated down to the wall without damping functions. The SST model is a proper two-equation model that performs well for flows with adverse pressure gradient, while most two-equation models can have a good prediction of the shear stresses. A function is selected for the blending of the RSTM and SST. Three cases are presented to show the performance of the present model: (i) fully developed channel flow with* $Re_\tau = 395$*, (ii) backward-facing step with an expansion ratio of 1.2 and* $Re = 5200$ *base on the step height, and (iii) circular impingement with the nozzle-to-wall distance* $H = 4D$ *and* $Re = 20{,}000$*. It is believed that the new model has good applicability for complex flow fields.* [DOI: 10.1115/1.2709957]

1 Introduction

Heat transfer in gas turbine systems involves complex turbulent flows with separation, subsequent reattachment, and stagnation regions in, e.g., ribbed cooling ducts. Accurate modeling of these phenomena is very important because they have a big influence on the fluid flow and heat transfer. To date, however, the most commonly used turbulence models have been eddy-viscosity schemes. Yet, the second-moment closures, also known as the Reynolds stress transport model (RSTM), offer the potential for far more reliable predictions. This is because important production terms are calculated directly from resolved variables, while the production terms of two-equations models are modeled. However, the main difficulties in the RSTMs are the modeling of pressure-strain terms and the near-wall turbulence. The near-wall modeling needs low-Re models, which are critical for heat transfer predictions.

Many available low-Re RSTMs show a problem for flows with separation and reattachment, such as a backward-facing step flow. There exists an unphysical bulge at the reattachment region, as shown in Fig. 1. The streamlines shown in Fig. 1 are predicted by Speziale, Sarkar, and Gatski (SSG) [1] based on the ω equation. The same problem exists for many other low-Re RSTMs according to the authors' and other researchers' practices, e.g., the Launder, Reece, and Rodi (LRR) model [2], the stress-ω model [3]. This is mainly because the overprediction of the gradient of the shear stresses around the reattachment region. Parneix and Durbin's elliptic relaxation procedure [4] can decently resolve this problem. However, it needs six more Poisson equations for obtaining the relaxation factor f_{ij}, whose complexity is beyond the feasibility of most of the industrial applications.

In this paper, a new RSTM aimed for engineering applications in, e.g., ribbed cooling ducts, is proposed with consideration of near-wall turbulence. This model employs the SSG pressure strain term, the ω equation, and the shear stress transport (SST) [5] model for the shear stresses at the near-wall region (say, $y^+ < 30$). The models are selected based on the following merits: the SSG RSTM model performs well at the fully turbulent region and does not need the wall normal vectors; the ω equation can be integrated down to the wall without damping functions. The SST model is a proper two-equation model that performs well for flows with adverse pressure gradient, while most two-equation models can have a good prediction of the shear stresses. A function is selected for the blending of the RSTM and SST.

By the proposed new model, the unphysical bulge at the reattachment region is eliminated. Then the model is applied for the fully developed channel flow and an impingement jet case for flows with stagnation regions.

2 Method

The method is based on solving the Reynolds-averaged Navier Stokes (RANS) equations. The Reynolds stresses are either modeled by the Bousinessq hypothesis or solved directly by transport equations.

2.1 RANS Equations.

$$\frac{\partial U_i}{\partial x_i} = 0 \tag{1}$$

$$\frac{\partial U_i}{\partial t} + \frac{\partial (U_j U_i)}{\partial x_j} = -\frac{1}{\rho}\frac{\partial P}{\partial x_i} + \frac{\partial}{\partial x_j}(2\nu S_{ij} - R_{ij}) \tag{2}$$

$$\frac{\partial T}{\partial t} + \frac{\partial (U_j T)}{\partial x_j} = \frac{\partial}{\partial x_j}\left(\frac{\nu}{\mathrm{Pr}}\frac{\partial T}{\partial x_j} - \overline{t' u_j'}\right) \tag{3}$$

where $S_{ij} = (1/2)[(\partial U_i/\partial x_j) + (\partial U_j/\partial x_i)]$. R_{ij} and $\overline{t' u_j'}$ are the specific turbulent Reynolds stresses and heat fluxes, respectively, and they are modeled in the following sections.

2.2 Turbulence Models. In this paper, the V2F [6], SST [5], and SSG [1] models based on the ω equation are applied. In

---

[1] Corresponding author.

Contributed by the Heat Transfer Division of ASME for publication in the JOURNAL OF HEAT TRANSFER. Manuscript received March 1, 2006; final manuscript received August 9, 2006. Review conducted by Sumanta Acharya.

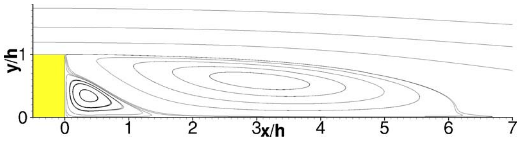

Fig. 1 Predicted streamlines by the SSG-W model for the backward-facing-step case

addition, a new model SSG-SST, based on the SST model and SSG model, is proposed. The V2F model is only for comparison purposes; thus, its equations are not shown here.

2.2.1 SST k-ω Model.

$$\frac{\partial k}{\partial t}+\frac{\partial(U_jk)}{\partial x_j}=\frac{\partial}{\partial x_j}\left[\left(\nu+\frac{\nu_t}{\sigma_k}\right)\frac{\partial k}{\partial x_j}\right]+\widetilde{P_k}-\beta^*k\omega \tag{4}$$

$$\frac{\partial \omega}{\partial t}+\frac{\partial(U_j\omega)}{\partial x_j}=\frac{\partial}{\partial x_j}\left[\left(\nu+\frac{\nu_t}{\sigma_\omega}\right)\frac{\partial \omega}{\partial x_j}\right]+\frac{\gamma}{\nu_t}P_k-\beta\omega^2$$

$$+(1-F_1)2\sigma_{\omega 2}\frac{1}{\omega}\frac{\partial k}{\partial x_j}\frac{\partial \omega}{\partial x_j} \tag{5}$$

where $P_k=-\overline{u_i'u_j'}\partial U_i/\partial x_j=2\nu_tS_{ij}S_{ij}$ is the production of kinetic energy, and $\widetilde{P}_k=\min(P_k,c_l\epsilon)$

$$\nu_t=\frac{a_1k}{\max(a_1\omega,\sqrt{2}SF_2)}$$

$$S=\sqrt{S_{ij}S_{ij}} \tag{6}$$

The Reynolds stresses are modeled as

$$R_{ij}\equiv\overline{u_i'u_j'}=\tfrac{2}{3}k\delta_{ij}-2\nu_tS_{ij} \tag{7}$$

Closure coefficients $\phi=F_1\phi_1+(1-F_1)\phi_2$, where ϕ can be any of the following coefficients, e.g., $\sigma_k=F_1\sigma_{k1}+(1-F_1)\sigma_{k2}$, and F_1 is the blending function:

$$\sigma_{k1}=2,\quad \sigma_{\omega 1}=2,\quad \gamma_1=0.5532,\quad \beta_1=0.075$$

$$\sigma_{k2}=1,\quad \sigma_{\omega 2}=1.168,\quad \gamma_2=0.4403,\quad \beta_2=0.0828$$

$$c_l=10,\quad a_1=0.31\quad \beta^*=0.09 \tag{8}$$

$$F_1=\tanh(arg_1^4)$$

$$arg_1=\min\left[\max\left(\frac{\sqrt{k}}{\beta^*\omega y},\frac{500\nu}{y^2\omega}\right),\frac{4\rho\sigma_{\omega 2}k}{CD_{k\omega}y^2}\right]$$

$$CD_{k\omega}=\max\left(2\rho\sigma_{\omega 2}\frac{1}{\omega}\frac{\partial k}{\partial x_j}\frac{\partial \omega}{\partial x_j},1.0e^{-10}\right) \tag{9}$$

$$F_2=\tanh(arg_2^2)$$

$$arg_2=\max\left(2\frac{\sqrt{k}}{\beta^*\omega y},\frac{500\nu}{y^2\omega}\right) \tag{10}$$

In addition $\epsilon=\beta^*\omega k$ and $l=k^{0.5}/\omega$, $\omega_w=6\nu/\beta_0y_1^2$, where indices w and 1 denote the wall and the first point off the wall, respectively.

2.2.2 SSG Model Based on ω Equation (SSG-ω). We reformulated the SSG [1] model based on the ω equation, because the ω equation can be naturally integrated to the wall

$$\frac{\partial R_{ij}}{\partial t}+\frac{\partial(U_mR_{ij})}{\partial x_m}=\frac{\partial}{\partial x_m}\left[\left(\nu+\frac{\nu_t}{\sigma_k}\right)\frac{\partial R_{ij}}{\partial x_m}\right]+P_{ij}-\frac{2}{3}\beta^*k\omega\delta_{ij}+\Pi_{ij} \tag{11}$$

The ω equation is the same as that in the SST k-ω model, except the calculation of the production term, which is calculated as $P_k=-R_{ij}(\partial U_i/\partial x_j)$.

The diffusion term is modeled using a simple eddy viscosity model,

$$D_{ij}=\frac{\partial}{\partial x_m}\left(\frac{\nu_t}{\sigma_k}\frac{\partial R_{ij}}{\partial x_m}\right) \tag{12}$$

The pressure-strain tensor is modeled as follows:

$$\Pi_{ij}=\Phi_{ij,1}+\Phi_{ij,2} \tag{13}$$

$$\Phi_{ij,1}=-\beta^*k\omega\left[C_{s1}a_{ij}+C_{s2}\left(a_{ik}a_{jk}-\tfrac{1}{3}A\delta_{ij}\right)\right] \tag{14}$$

$$\begin{aligned}\Phi_{ij,2}=&-C_{r1}Pa_{ij}+C_{r2}kS_{ij}-C_{r3}kS_{ij}A^{1/2}\\&+C_{r4}k\left(a_{ik}S_{jk}+a_{jk}S_{ik}-\tfrac{2}{3}a_{kl}S_{kl}\delta_{ij}\right)\\&+C_{r5}k(a_{ik}\Omega_{jk}+a_{jk}\Omega_{ik})\end{aligned} \tag{15}$$

where

$$a_{ij}=\frac{R_{ij}}{k}-\frac{2}{3}\delta_{ij} \tag{16}$$

$$A=a_{ij}a_{ij} \tag{17}$$

Auxiliary Relations:

$$\nu_t=\frac{k}{\omega} \tag{18}$$

$$R_{ij}\equiv\overline{u_i'u_j'},\quad k=\frac{1}{2}R_{kk} \tag{19}$$

$$P_{ij}=-R_{im}\frac{\partial U_j}{\partial x_m}-R_{jm}\frac{\partial U_i}{\partial x_m},\quad P=\frac{1}{2}P_{kk} \tag{20}$$

The constants have the values

C_{s1}	C_{s2}	C_{r1}	C_{r2}	C_{r3}	C_{r4}	C_{r5}
1.7	−1.05	0.9	0.8	0.65	0.625	0.2

2.2.3 SSG-SST Model. The SSG-SST model is based on the SSG-ω model. The only difference is that the shear Reynolds stresses used in the momentum equation are blended from R_{ij} and those from the SST model. Here, the normal stresses are not blended because we want to keep the anisotropy feature of the normal stresses of the RSTM.

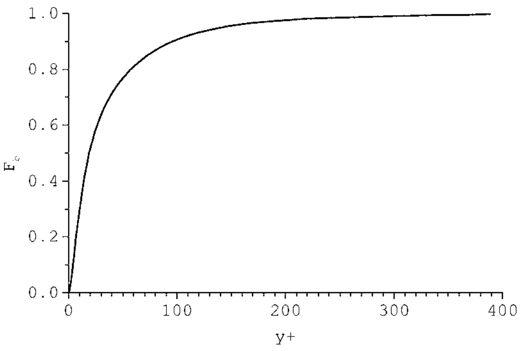

Fig. 2 Plot of the blending function F_b

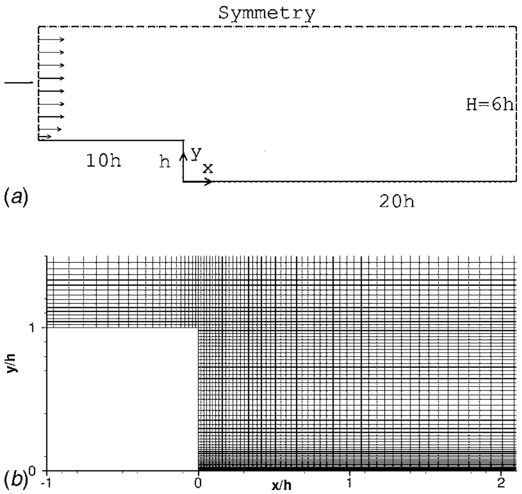

Fig. 3 Computational geometry: (*a*) topology and (*b*) grid around the step

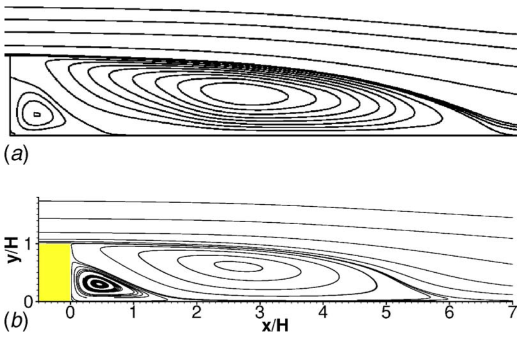

Fig. 4 Streamlines for the backward-facing-step case: (*a*) DNS and (*b*) SSG-SST note: (a) and (b) are scaled the same

$$R_{ij}|_{\text{effect}} = F_b\, R_{ij}|_{\text{SSG}-\omega} + (1 - F_b)\, R_{ij}|_{\text{SST}} \quad i \neq j \tag{21}$$

where F_b is the blending function. Equation (21) is only strictly correct for a Cartesian coordinate system but can be further developed to be valid in any coordinate system. The selection of a blending function is to ensure the asymptotic consistency with the near-wall behavior of the exact equation of motion. In this work, a blending function has been tentatively adopted from the low-Re two-equation model of Abe et al. [7] as

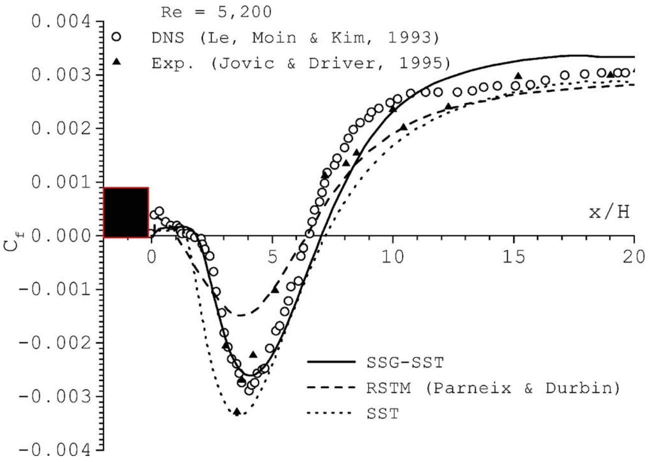

Fig. 5 Friction coefficient of the backward-facing-step case

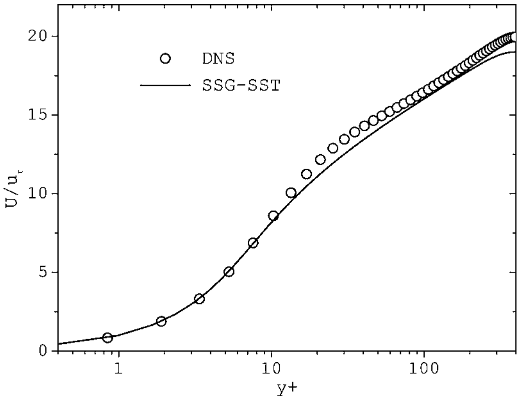

Fig. 6 U-velocity profile of the channel flow case

$$F_b = (1 - e^{-(y^*/14)})^2 (1 + 5\,\mathrm{Re}_t^{-0.75}\, e^{-(\mathrm{Re}_t/200)^2}) \tag{22}$$

where $y^* = (\nu\epsilon)^{0.25} y/\nu$ and $\mathrm{Re}_t = k^2/\epsilon\nu$. Figure 2 shows a typical plot of the blending function F_b versus y^+ for the fully developed channel flow case of $\mathrm{Re}_\tau = 395$. F_b is close to zero at the near-wall region, while it is unity at the fully turbulent region. This blending function has the desirable feature, but some work is needed to reveal its general applicability.

2.2.4 Modeling of Turbulent Heat Fluxes. The turbulent heat fluxes are computed using a simple eddy diffusivity model (SED)

$$\overline{t'u_j'} = -\frac{\nu_t}{\mathrm{Pr}_t}\frac{\partial T}{\partial x_j} \tag{23}$$

where the turbulent Prandtl number is $\mathrm{Pr}_t = 0.89$.

2.3 Numerical Solution Procedure. The computations are

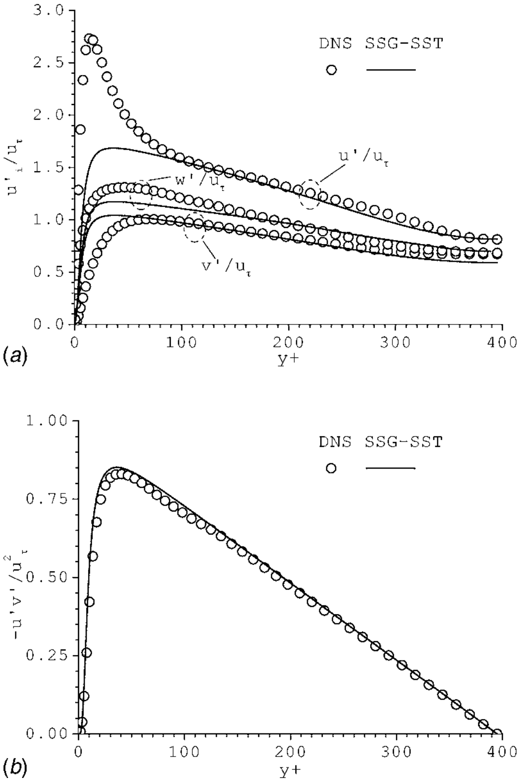

Fig. 7 Reynolds stresses of the channel flow case: (*a*) normal stresses and (*b*) shear stress

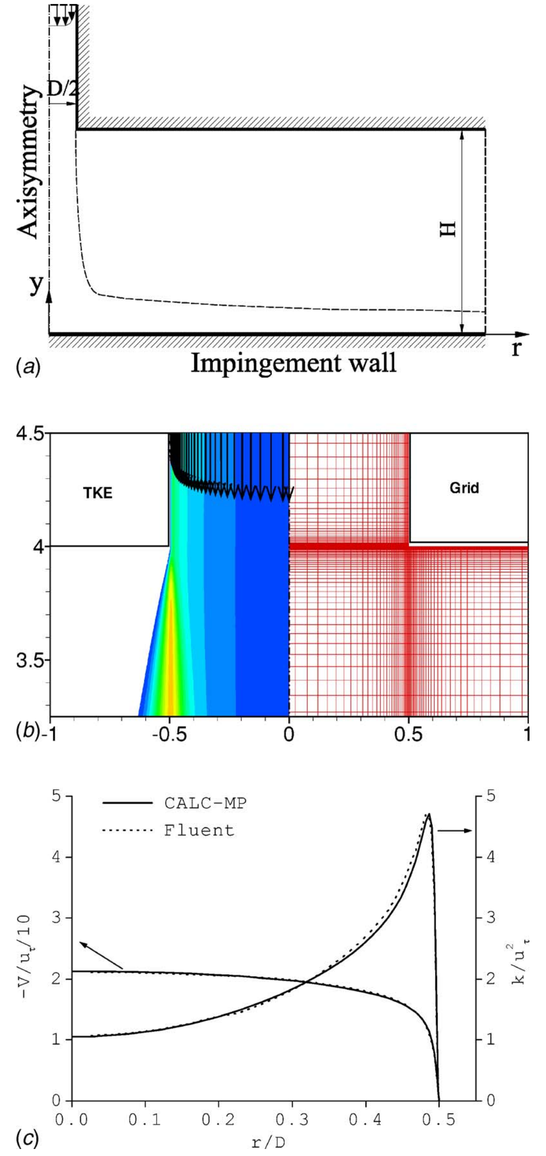

Fig. 8 Inlet profiles of the impingement jet case: (*a*) geometry, (*b*) grid and TKE contours around the jet inlet, and (*c*) inlet profiles

carried out in an in-house multiblock computer code CALC-MP [8] based on the finite volume technique. The code uses a collocated mesh arrangement and employs the improved Rhie and Chow interpolation [9] to calculate the velocities at the control volume faces. The SIMPLEC algorithm couples the pressure and velocity. An algorithm based on TDMA is used for solving the algebraic equations. Coefficients are determined by the QUICK scheme for the momentum equations and the hybrid scheme for all the other discretized equations.

3 Results and Discussion

3.1 Backward-Facing-Step Case. The geometry of the backward-facing-step case is shown in Fig. 3(*a*). The flow is symmetric about the centerline of the channel. As a consequence, we take only half of the channel as the computational domain. The computational region ranges from $x/h=-10$ to 20, $x=0$ being the location of the sudden expansion and h being the step height. The fully developed channel flow inlet is set at $x/h=-10$. The Reynolds number based on the step height h and the inlet bulk velocity is 5000. We checked the solution for grid independence, and a multiblock grid (52×52 and 122×102) is found to give independent results. The focused view of the grid is shown in Fig. 3(*b*).

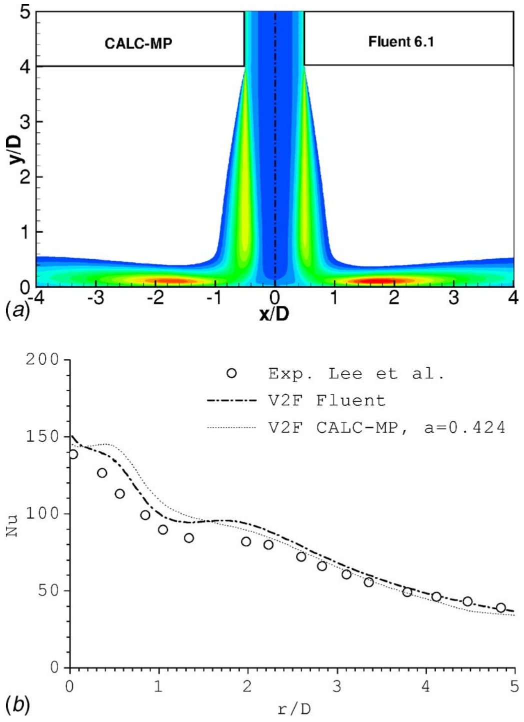

Fig. 9 Comparison between the present solver and FLUENT with the V2F model for the impingement jet case: (*a*) TKE contours and (*b*) Nusselt number

Figure 4 shows the predicted streamlines from DNS of Le et al. [10] and the SSG-SST model. The reattachment is well predicted by the SSG-SST model in comparison to the DNS data, and the unphysical bulge is suppressed. The size of the corner bubble is also in good agreement with the data.

Figure 5 shows the friction coefficient. For comparison purposes, the predicted results by the combined elliptic relaxation procedure of Durbin and the SSG model are also included. Our new model provides an improved prediction of the friction coefficient. After the reattachment, the recovery is also good. The only problem is the small overprediction of the reattachment length, which might be due to the SST model being used for the near-wall shear stresses. By analogy, the model is also good for the prediction of near-wall heat transfer. For the model of Durbin, however, large underprediction can be observed at the back-flow region. This is attributed to the underprediction of the back-flow intensity by Parneix and Durbin [4]. They also stated that "this specific problem seems to be common to every existing second moment closure model, whatever near-wall model is used (low-Re or wall function)." In their study, in addition, the recovery after the reattachment is too slow, which might be linked to the too slow back flow.

The proposed new model obviously works fine for flows with separation and reattachment. We need to further test the model in simpler generic geometries, like the fully developed channel flow.

3.2 Fully Developed Channel Flow Case. The fully developed channel flow is driven by the constant pressure gradient $\partial P/\partial x$, which is balanced by the wall shear stresses. The flow with $\mathrm{Re}_\tau=u_\tau\delta/\nu=395$ is symmetric about the centerline of the channel. As a consequence, we take only half of the channel as the computation domain. Periodic boundary conditions are set in the main flow direction. The results are compared to existing DNS (direct numerical simulation) data.

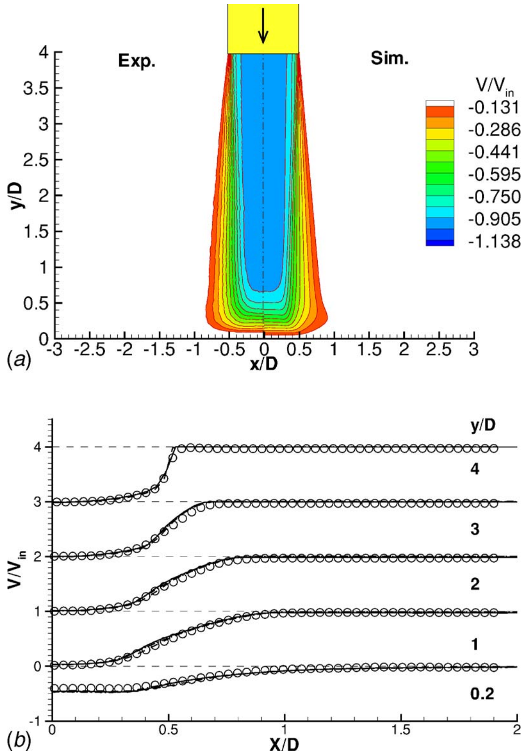

Fig. 10 V-velocity comparison between experiments and present simulations (circle: PIV experiments, solid line: SSG-SST model, dashed line: V2F model, and dashed-dotted line: SST model): (*a*) *V* contours and (*b*) *V* line plots (note: the strictly horizontal lines are axes)

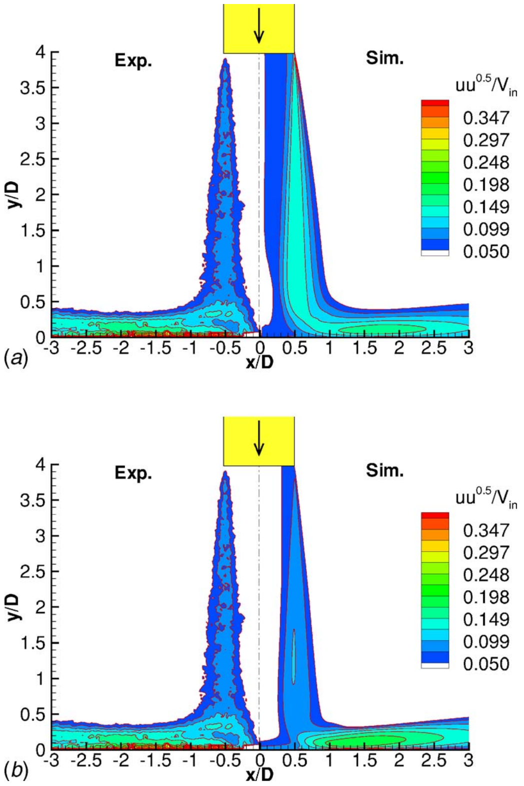

Fig. 11 $\overline{u'u'}$ comparison between experiments and the present simulations: (*a*) V2F and (*b*) SSG-SST

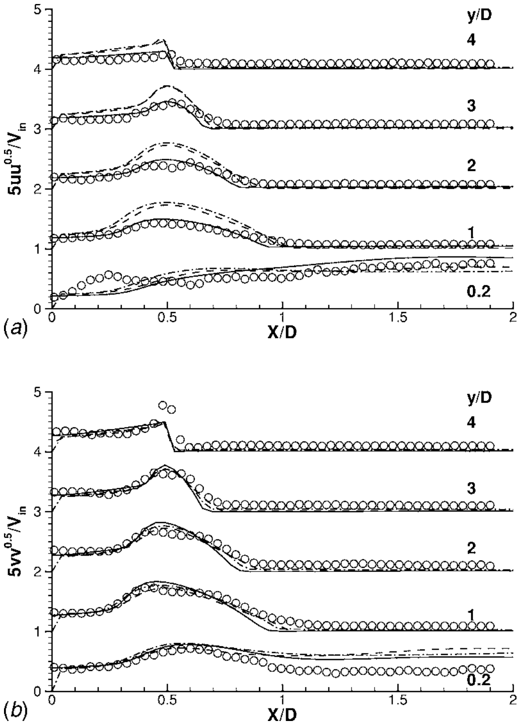

Fig. 12 Line plot comparisons between experiments and the present simulations (legend as in Fig. 10): (*a*) $\overline{u'u'}$ and (*b*) $\overline{v'v'}$

Figure 6 shows the predicted mean velocity profile normalized by the friction velocity. We can see that it is in reasonably good agreement with the DNS data of Moin and Kim [11], although there is a small underprediction.

Figure 7 shows the predicted Reynolds stress profiles normalized by the friction velocity. The shear stress is in good agreement with the DNS data. For the normal stresses, good agreement can be observed at most of the regions. However, in the buffer layer, the main-stream-direction stress $\overline{u'u'}$ is seriously underpredicted. This might be so because the SSG pressure strain model needs a proper near-wall model and the present one might not be appropriate (see also [12]).

Both the backward-facing-step and channel-flow cases are dominated by shear. In Sec. 3.3, a normal strain dominated case is provided, i.e., an axisymmetric impingement jet case.

3.3 Circular Impingement Jet Case. Figure 8(*a*) shows the computational geometry. The nozzle-to-wall distance is kept at 4. Figure 8(*b*) shows the focused view of the computational grid around the jet inlet. The Reynolds number based on the nozzle diameter is 20,000. For this case, we want to validate the implementation of the turbulence models to eliminate the numerical errors. At first, the V2F model is validated versus the commercial software FLUENT 6.1, which also has an implementation of the V2F model. Here, we compare the results from our in-house code CALC-MP and FLUENT 6.1 predictions. At the end of the section, the new proposed model is evaluated against the V2F model and experimental data.

Figure 8(*c*) shows the inlet boundary conditions for the mean velocity and kinetic energy. They are both calculated in separate computations for fully developed pipe flow. A focused view of the turbulent kinetic energy (TKE) contours around the jet inlet is shown in the left-hand side of Fig. 8(*b*). A fully developed profile can be clearly observed.

Figure 9(*a*) shows the predicted turbulent kinetic energy contours by the different implementations of the V2F model. A good merit of the V2F model is its correct behavior around the stagna-

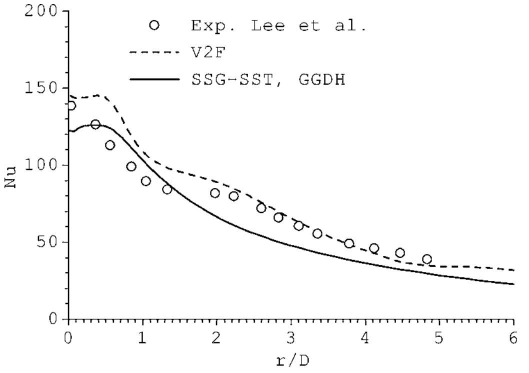

Fig. 13 Predicted Nusselt number in comparison to experiments

tion region, where the normal strain dominates. There is no buildup of turbulence at the stagnation region from either of the implementations. The difference between the results from CALC-MP and FLUENT is negligible.

Figure 9(*b*) shows the predicted Nusselt number. Generally speaking, both of the results are in good agreement with the experiments [13]. The biggest difference between our implementation and that of FLUENT is ~6% at the stagnation region. The reason for the difference might be from some implementation issues, such as the calculation method of Nusselt number, the treatment of boundary conditions.

In general, our implementation of the V2F model in our in-house code is correct, which may indicate that the way we used for implementing turbulence models in our in-house code is correct. In the following paragraphs, evaluation of the proposed new model in predicting the impingement case is carried out.

Figure 10 shows the axial-direction mean velocity contours in comparison to the particle image velocimetry (PIV) data of Ding [14]. The results from the SST, V2F, and SSG-SST models are in good agreement with the PIV experiments. The predicted potential cores (95% of the inlet velocity line in Fig. 10) are in excellent agreement with the experiments.

Figures 11(*a*) and 11(*b*) show the $\overline{u'u'}$ contours. The V2F model, due to the isotropic assumption, overpredicts the $\overline{u'u'}$ at the free jet region because the main flow direction is the V velocity direction. But it provides a reasonably good prediction at the wall jet region, where the U direction is the main flow direction. At this point it is worthwhile to point out that the V2F model is an eddy viscosity model providing an eddy viscosity for the governing equations. Thus, one should not expect it to provide accurate prediction of the normal stress. The SSG-SST model can naturally handle the anisotropy of the turbulence, so that much better prediction of $\overline{u'u'}$ can be observed, as shown in Fig. 11(*b*).

Figures 12(*a*) and 12(*b*) show the plots for $\overline{u'u'}$ and $\overline{v'v'}$ at five lines. For the prediction of $\overline{u'u'}$, the superiority of the SSG-SST model is clearly shown, except very close to the wall region. For $\overline{v'v'}$, the predictions from the three models are very similar. At the inlet region, they all underpredict the peak in the buffer layer. At the regions ($y/D=1$, 2, and 3), the results are reasonably good, but it seems that the V2F model is somewhat better in this region. At the line $y/D=0.2$, the SSG-SST model seems to perform best.

Figure 13 shows the Nusselt number distribution on the impingement wall. In general, both models provide reasonable predictions, but V2F always shows higher values. In the stagnation region, SSG-SST agrees better with experiments while V2F shows better agreement further downstream along the wall. As was mentioned previously, the V2F model provides an overprediction of turbulence, which results in a higher Nusselt number than the SSG-SST model.

4 Conclusions

A new second-closure momentum model, SSG-SST, is proposed. We have the following findings:

1. It resolves the unphysical bulge problem and works very well for predicting the friction coefficient for the backward-facing-step case.
2. The new model works reasonably well for fully developed channel flow.
3. Because anisotropy is naturally predicted for the impingement case, both the mean flow and turbulence field are well predicted. Concerning the heat transfer for the impingement case, the V2F and SSG-SST models perform overall decently well but V2F gives, in this case, higher Nu values. More work should be concentrated on the near-wall region modeling for improved prediction of the stagnation heat transfer.

Acknowledgment

The Swedish Energy Agency (STEM) financially supported this research work.

Nomenclature

C_f = skin friction coefficients based on bulk velocity, $\tau_w/[(1/2)\rho U_b^2]$
D_{ij} = diffusion term
F_1, F_2, F_b = blending functions
h = step height
H = nozzle-to-wall distance or channel height
Nu = Nusselt number $\mathrm{Nu}=hD_h/\lambda$
P = pressure
P_k = turbulent production
Pr = Prandtl number
Pr_τ = turbulent Prandtl number
q_w = wall heat flux
Re = Reynolds number $\mathrm{Re}=U_bD_h/\nu$
Re_τ = Reynolds number based on the friction velocity $\mathrm{Re}_\tau=U_\tau D_h/\nu$
$-R_{ij}$ = specific Reynolds stress tensor, $\equiv -\overline{u_i'u_j'}$
S_{ij} = mean-strain rate
t = time
$\overline{t'u_i'}$ = specific turbulent heat fluxes
T = temperature
u_τ = friction velocity $u_\tau=\sqrt{\tau_w/\rho}$
U_b = bulk velocity
x_i, y = coordinates
y^+ = dimensionless, sublayer-scaled, distance, $y^+ = u_\tau y/\nu$
β^* = coefficient for the k equation
γ = linear temperature increase rate
δ_{ij} = Kronecker δ
ϵ = dissipation rate
λ = thermal conductivity
ν = kinematic viscosity
ν_τ = turbulent kinematic viscosity
ρ = density
τ_w = surface shear stress
Φ_{ij} = pressure strain tensor
ω = specific dissipation rate

References

[1] Speziale, C. G., Sarkar, S., and Gatski, T. B., 1991, "Modeling the Pressure Strain Correlation of Turbulence: An Invariant Dynamical Systems Approach," J. Fluid Mech., **227**, pp. 245–272.

[2] Launder, B. E., Reece, G., and Rodi, W., 1975, "Progress in the Development of a Reynolds-Stress Turbulence Closure," J. Fluid Mech., **68**(3), pp. 537–566.

[3] Wilcox, D. C., 1998, *Turbulence Modelling for CFD*, DCW Industries Inc., La Cañada.

[4] Parneix, S., and Durbin, P., 1996, “A New Methodology for Turbulence Modelers Using DNS Database Analysis,” Center for Turbulence Research, Annual Research Briefs, pp. 17–30.

[5] Menter, F. R., 1994, “Two-Equation Eddy-Viscosity Turbulence Models for Engineering Applications,” AIAA J., **32**(8), pp. 1598–1605.

[6] Durbin, P. A., 1995, “Separated Flow Components With $k-\epsilon-\overline{V^2}$ Model,” AIAA J., **33**(4), pp. 659–664.

[7] Abe, K., Kondoh, T., and Nagano, Y., 1994, “A New Turbulence Model for Predicting Fluid Flow and Heat Transfer in Separating and Reattaching Flows—I. Flow Field Calculations,” Int. J. Heat Mass Transfer, **37**, pp. 139–151.

[8] Jia, R., and Sundén, B., 2003, “Multi-Block Implementation Strategy for a 3D Pressure-Based Flow and Heat Transfer Solver,” Numer. Heat Transfer, Part B, **44**, pp. 457–472.

[9] Rhie, C. M., and Chow, W. L., 1983, “Numerical Study of the Turbulent Flow Past an Airfoil With Trailing Edge Separation,” AIAA J., **21**, pp. 1525–1532.

[10] Le, H., Moin, P., and Kim, J., 1993, “Direct Numerical Simulation of Turbulent Flow Over a Backward-Facing Step,” *Proc. 9th Symp. on Turbulent Shear Flow*, Kyoto, August, 1993, pp. 13.2.1–13.2.6.

[11] Moin, P., and Kim, J., 1982, “Numerical Investigation of Turbulent Channel Flow,” J. Fluid Mech., **118**, pp. 341–377.

[12] Wallin, S., and Johansson, A. V., 2002, “Modelling Streamline Curvature Effects in Explicit Algebraic Reynolds Stress Turbulence Models,” Int. J. Heat Fluid Flow, **23**, pp. 721–730.

[13] Lee, J., and Lee, S., 2000, “The Effect of Nozzle Configuration on Stagnation Region Heat Transfer Enhancement of Axisymmetric Jet Impingement,” Int. J. Heat Mass Transfer, **43**, pp. 3497–3509.

[14] Ding, R., 2004, “Experimental Studies of Turbulent Mixing in Impinging Jets,” Doctoral Thesis, Lund Institute of Technology, Lund, Sweden.

Compressibility and Variable Density Effects in Turbulent Boundary layers

Kunlun Liu[1]
e-mail: liukl@umn.edu

Richard H. Pletcher

Department of Mechanical Engineering,
Iowa State University,
Ames, IA, 50011

Two compressible turbulent boundary layers have been calculated by using direct numerical simulation. One case is a subsonic turbulent boundary layer with constant wall temperature for which the wall temperature is 1.58 times the freestream temperature and the other is a supersonic adiabatic turbulent boundary layer subjected to a supersonic freestream with a Mach number 1.8. The purpose of this study is to test the strong Reynolds analogy (SRA), the Van Driest transformation, and the applicability of Morkovin's hypothesis. For the first case, the influence of the variable density effects will be addressed. For the second case, the role of the density fluctuations, the turbulent Mach number, and dilatation on the compressibility will be investigated. The results show that the Van Driest transformation and the SRA are satisfied for both of the flows. Use of local properties enable the statistical curves to collapse toward the corresponding incompressible curves. These facts reveal that both the compressibility and variable density effects satisfy the similarity laws. A study about the differences between the compressibility effects and the variable density effects associated with heat transfer is performed. In addition, the difference between the Favre average and Reynolds average is measured, and the SGS terms of the Favre-filtered Navier-Stokes equations are calculated and analyzed. [DOI: 10.1115/1.2709971]

Keywords: compressible Navier-Stokes equations, compressibility, variable density effects, turbulent boundary layers

1 Introduction

The compressibility of flows is a measure of the volume change or density change of fluids as a response to a pressure change, $\beta=-(1/V)(\partial V/\partial P)$ or $\beta=(1\rho)(\partial\rho/\partial P)$, under the circumstance that the substantial derivative of the density is nontrivial or the velocity is not divergence free. In this manner, if the pressure gradient or pressure variation is large enough to affect a substantial change in the density of the flow, such a flow is compressible. The effects associated with the volume change of the fluid elements in response to the pressure change are regarded as compressibility effects [1]. For gases, the density is a function of pressure and temperature. Thus, for the gas flows with heat transfer, the major contribution of the density change may be from the temperature change rather than the pressure change. Such flows may be nearly incompressible, but the substantial change in the density is nonzero. In order to distinguish such density changes from the compressibility effects, we call the effects associated with the density change in response to the temperature changes rather than the changes in the pressure the variable density effects. Clearly, for both situations, the governing equations are the compressible Navier-Stokes equations.

In low Mach number turbulent boundary layers, the influence of density fluctuations on the turbulent boundary layer is negligible as long as the mean density remains constant across the boundary layers [2]. Such flows usually are treated as incompressible flows. However, the density varies with the distance from the wall once heat transfer is involved. The density changes that occur with heat transfer can greatly deform the turbulent structures. As a result, the mean velocity profiles will eventually be deformed even though the Mach number is small [3]. The nonzero gradient of the mean density will cause a nontrivial distribution of the substantial derivative of density. Thus, such flows will be incompressible but have large density variations.

Huang et al. [4] and Nicoud and Bradshaw [3] suggested using density-weighted transformations, which are similar to the Van Driest transformation, to modify the velocity profiles. In this manner the similarity law for incompressible flows can be applied to compressible turbulent boundary layers or incompressible turbulent boundary layers with a heated wall [4]. Note that Huang et al. [5] dealt with compressible flows, but Nicoud and Bradshaw [3] dealt with incompressible flows with strong heat transfer. Therefore, it is worthwhile to compare the influence of the compressibility effects and variable density effects on the validation of the Van Driest transformation.

The magnitude of the density fluctuations may be independent of the Mach number. The earlier experiments found that the density fluctuations can be neglected if the freestream pressure gradient is small [2] for a compressible turbulent boundary layer with a Mach number of <5, particularly in the outer part of the turbulent boundary layer, which is fundamental to Morkovin's hypothesis. However, the very recent direct numerical simulation (DNS) results for a supersonic turbulent boundary layer with heat transfer at a Mach number of 2.5 [6] and a thermal turbulent channel flow at the Mach number 1.5 [7] show that $\rho_{\mathrm{rms}}/\bar{\rho}$ is ~0.05 in the buffer zone and logarithmic layer regions. Large eddy simulation (LES) results for a turbulent channel flow at the Mach number 0.01 with the significant heat transfer show that $\rho_{\mathrm{rms}}/\bar{\rho}$ is ~0.08 in these regions [8]. In this sense, the contribution of the density fluctuations to the compressibility effects or variable density effects in the inner part of the wall shear flow is underestimated for the wall shear flows that have a Mach number of <5. Additionally, when the Mach number is <5, such a compressibility is sensitive to the Mach number [9] and weak in the viscous sublayer and outer part of the turbulent boundary layers [6,7,9]. To check $\rho_{\mathrm{rms}}/\bar{\rho}$ quantitatively, we calculate an adiabatic supersonic

---

[1] Present address: Department of Biomedical Engineering, University of Minnesota. Minneapolis, MN 55455.

Contributed by the Heat Transfer Division of ASME for publication in the JOURNAL OF HEAT TRANSFER. Manuscript received April 6, 2006; final manuscript received November 17, 2006. Review conducted by Sumanta Acharya. Paper dedicated to Professor Suhas V. Patankar for his contributions to numerical heat transfer.

turbulent boundary layer with a Mach number of 1.8. Moreover, we consider the effect of heat transfer on density fluctuations for the low Mach number flows.

One influence of the compressibility on the flow is the energy transfer from kinetic energy to internal energy. This process is not reversible. The extra dissipation resulting from the compressibility relates to the turbulent Mach number $M_t=q/c$ (q is a velocity scale characteristic of the turbulence and c is a representative speed of sound), the density variance $\rho_{\mathrm{rms}}/\bar{\rho}$, the mean of the density, and the pressure dilatation [1]. Note that, by the continuity equation, the mean of density is associated with the mean of the dilatation $\theta=\partial u_i/\partial x_i$ and the density fluctuation is associated with the dilatation fluctuation θ' because $D\rho/Dt+\theta=0$. For an adiabatic compressible supersonic turbulent boundary layer (ACSTBL), the order of magnitude of the density fluctuation, turbulent Mach number Ma_t, and the pressure dilatation depends on the temperature difference across the flow. Thus, energy transfer from the kinetic energy to the internal energy is driven by the gradient of the mean density, and the molecular viscosity and the solenoidal part of turbulent viscosity, which are dominated by dissipation and largely independent of compressibility effects. The increasing Ma_t is usually associated with the increasing density fluctuations $\rho_{\mathrm{rms}}/\bar{\rho}$ [1]. When Ma_t is in excess of 0.2–0.3, the compressibility effects become significant [10]. DNS results reported by Guarini et al. [6] show that the local Ma_t exceeds 0.2 in most of the inner part of the supersonic turbulent boundary layer at $\mathrm{Ma}=2.5$. This implies that the compressibility dramatically deforms the near wall turbulent structures even though the Ma_t is <5. Thus, the local distribution of Ma_t must be argued in order to investigate the compressibility effects. To distinguish the compressibility effects from the variable density effects, the turbulent Mach number Ma_t, the density fluctuations $\rho_{\mathrm{rms}}/\bar{\rho}$, and the dilatation fluctuation θ' are calculated for both the compressible and incompressible flows.

An important issue associated with the compressibility and variable density effects is the Favre average [11]. To account for the compressibility and variable density effects, a mass-weighted averaging, Favre average, was suggested. This idea is similar to the Van Driest transformation. Without the compressibility and variable density, the Favre average is equivalent to the Reynolds average. Therefore, the influence of the compressible and variable density effects on the deviation of the Favre average from the Reynolds average should be discussed.

In summary, this paper will focus on testing the strong Reynolds analogy, calculating the density fluctuations for both of the cases, determining the difference between Favre average and Reynolds average for velocities and illustrating the influence of Mach number and heat transfer on additional terms in the Favre-filtered Navier-Stokes equations.

2 Governing Equation and Numerical Method

All of the variables were normalized as follows: $x_i=x_i^*/\delta_d$, $u_i=u_i^*/U_e$, $t=t^*/(\delta_d/U_e)$, $\rho=\rho^*/\rho_e$, $p=p^*/\rho_e U_e^2$, $T=T^*/T_e$, $e=e^*/U_e^2$, $\mu=\mu^*/\mu_e$, $k=k^*/k_e$, $c_v=c_v^*/(U_e^2/T_e)$, $R=R^*/(U_e^2/T_e)$, $c_p=c_p^*/(U_e^2/T_e)$, where the subscript e stands for the freestream properties and δ_d was the displacement thickness of the inlet station. The reference Mach number was $\mathrm{Ma}_e=U_e/\sqrt{\gamma R^* T_e}$. The fluid was assumed to be an ideal gas and the nondimensional equation of state is: $p=\rho RT$. The nondimensional coefficients of viscosity and thermal conductivity were evaluated as: $\mu=T^n$, where n was assumed to be 0.71. The specific heats, c_p and c_v, were treated as constant.

The continuity, momentum and energy equation read:

$$\frac{\partial \rho}{\partial t}+\frac{\partial \rho u_i}{\partial x_i}=0 \tag{1}$$

$$\frac{\partial \rho u_i}{\partial t}+\frac{\partial \rho u_i u_j}{\partial x_i}=-\frac{\partial p}{\partial x_i}+\frac{\partial \sigma_{ij}}{\partial x_i} \tag{2}$$

$$\frac{\partial(\rho E)}{\partial t}+\frac{\partial[(\rho E+p)u_j]}{\partial x_j}=\frac{\partial(u_i\sigma_{ij})}{\partial x_j}-\frac{\partial q_j}{\partial x_j} \tag{3}$$

where E is the total specific energy $(E=c_vT+(1/2)u_iu_i)$, σ_{ij} is the shear stress tensor

$$\sigma_{ij}=\frac{2\mu}{\mathrm{Re}}\left(S_{ij}-\frac{1}{3}S_{kk}\delta_{ij}\right)$$

and q_j is the heat flux $(q_j=-(c_p\mu/\mathrm{RePr})(\partial T/\partial x_j))$.

The numerical method utilized to solve the Navier-Stokes equations, Eqs. (1)–(3), was a quasi-Newton method, according to which the numerical simulation can be reduced to a linear algebraic problem: a Jacobian equation, which follows:

$$J\delta u=\mathrm{RHS} \tag{4}$$

Here, RHS are the residual errors, δu are the variance, and J is the Jacobian matrix. The low Mach number flows are nearly incompressible and the condition number for the Jacobian matrix J is large. This leads to a stiffness problem. In order to achieve a steady convergence of Eq. (4), Liu and Pletcher proposed a new scheme [12], which is a combination of the SIMPLE methods introduced by Patankar and Spalding [13], the fractional step methods developed by Kim and Moin [14] as well as Wall et al. [15], and preconditioning techniques [16].

The main idea of the method is to seek the preconditioning matrix P and factorization matrix M such that the resolved system

$$(PJM)M^{-1}\delta u=P\cdot\mathrm{RHS} \tag{5}$$

has a better distribution of eigenvalues; that is, the eigenvalues of PJM and M^{-1} are positive and cluster around 1. The preconditioning matrix P utilized in this paper was proposed by Pletcher and Chen [17]. The matrix M and M^{-1} were proposed by Liu [12]. Such a factorization matrix M^{-1} taking advantage of the SIMPLE and fractional step methods decomposes the pressure and velocity variances and, thus, accelerates the convergence of the code.

A periodic boundary condition was utilized in the spanwise direction. A characteristic boundary condition [12] was applied at the outlet and a dynamic recycling inlet method [18] was employed to generate the fully developed turbulent boundary layer.

3 Results and Discussion

Four cases were calculated by DNS: Cases 1 and 3 were a turbulent boundary layer with Reynolds number of 2000 based on the inflow displacement thickness at a Mach number $\mathrm{Ma}_e=0.06$ with a constant temperature heated wall, $T_w=1.58T_e$. Cases 2 and 4 were an adiabatic supersonic turbulent boundary layer at a Mach number 1.8, where the Reynolds number is 2000 based on the displacement thickness. Although case 2 was adiabatic, the wall temperature of the turbulent boundary layer was $1.58T_e$ because of the viscous heating effects.

The numerical mesh for cases 1 and 2 was the same, which was uniform in the streamwise and spanwise directions, but was stretched in the normal direction, and $\Delta y^+_{\min}=0.38$, $\Delta y^+_{\max}=65$, $\Delta x^+=18.4$, and $\Delta z^+=5$. The dimensionless time step $\Delta t^+=0.2\delta_d/U_\infty$. The numerical mesh was $240\times 90\times 192$ corresponding to streamwise, normal, and spanwise directions, respectively. To check the validity of the numerical simulations, we calculated cases 3 and 4 by using a finer mesh in which $\Delta y^+_{\min}=0.28$, $\Delta y^+_{\max}=65$, $\Delta x^+=12.0$, and $\Delta z^+=3.6$. Figures 1 and 2 plot the first- and second-order statistics of these cases. Results show that the numerical mesh is fine enough to capture the first- and second-order statistical results.

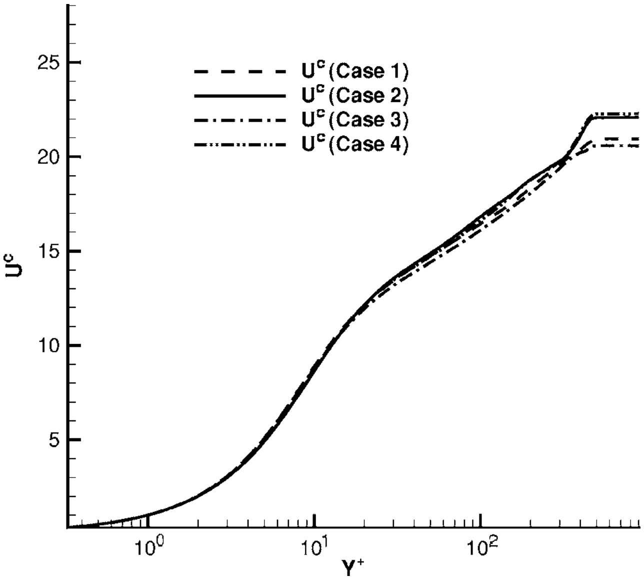

Fig. 1 Comparison of the mean streamwise velocity profiles

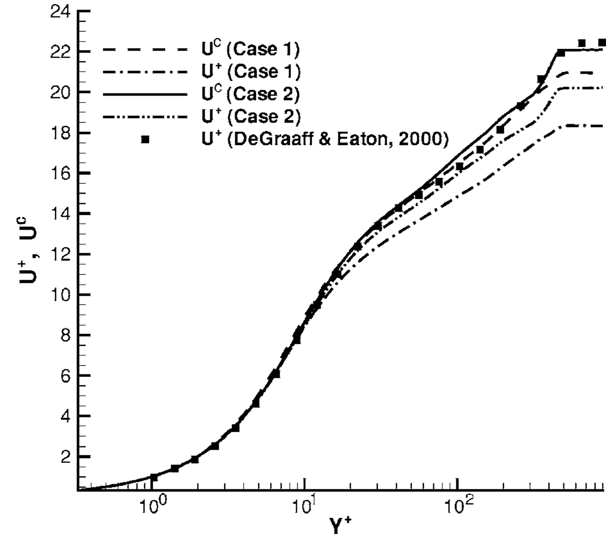

Fig. 3 Comparison of mean streamwise velocity with experimental results reported by [20]

3.1 Compressibility and Variable Density Effects. For purposes of comparison, a density-weighted transformation proposed by Huang et al. [5] was utilized to modify the velocity,

$$U^c = \sqrt{B}\left[\sin^{-1}\left(\frac{A+u}{D}\right) - \sin^{-1}\left(\frac{A}{D}\right)\right] \tag{6}$$

where

$$A = \frac{q_w}{\tau_w}, \quad B = \frac{2C_{p_e}T_w}{\mathrm{Pr}_t}, \quad D = \sqrt{A^2 + B}$$

The subscript w denotes a wall property, and subscript e denotes the freestream property. Figure 3 shows the comparison of modified velocity U^c and u^+ to experimental results of an incompressible turbulent boundary layer. Figure 3 indicates that the velocity profiles are deformed due to the change of the density across the boundary layer. Such a deformation causes u^+ to depart from the law of the wall. However, the modified velocity U^c conforms to the law of the wall. These numerical results match the theoretical and experimental conclusions proposed by Huang et al. [5]. The results confirm that the similarity laws can be approximately satisfied if the density-weighted transformation is applied.

Although the wall temperature was the same for both cases, $u_{\tau_{\mathrm{wall}}}$ was different. Considering that the maximum value of U^+ is $u_e/u_{\tau_{\mathrm{wall}}}$, through Fig. 3, we see that both the heat transfer and higher Mach number will increase $u_{\tau_{\mathrm{wall}}}$, but such a change contributed by heat transfer is larger.

Figure 4 displays the rms profiles of velocities, which were normalized by the local properties as, $U^+_{\mathrm{rms}} = U_{\mathrm{rms}}/U_{\tau,\mathrm{local}}$ and $Y^+ = YU_{\tau,\mathrm{local}}/\nu_{\mathrm{local}}$, where $U_{\tau,\mathrm{local}}$ uses the wall shear stress but local density. More precisely, $U_{\tau,\mathrm{local}} = \sqrt{\rho/\rho_{\mathrm{wall}}}U_{\tau,\mathrm{wall}}$. The magnitude and location of maximum U^+_{rms} agree with Spalart's DNS results [19]. By using the local properties, the U^+_{rms} of the turbulent boundary layer on a heated wall nearly coincides with the distribution for an isothermal incompressible turbulent boundary layer.

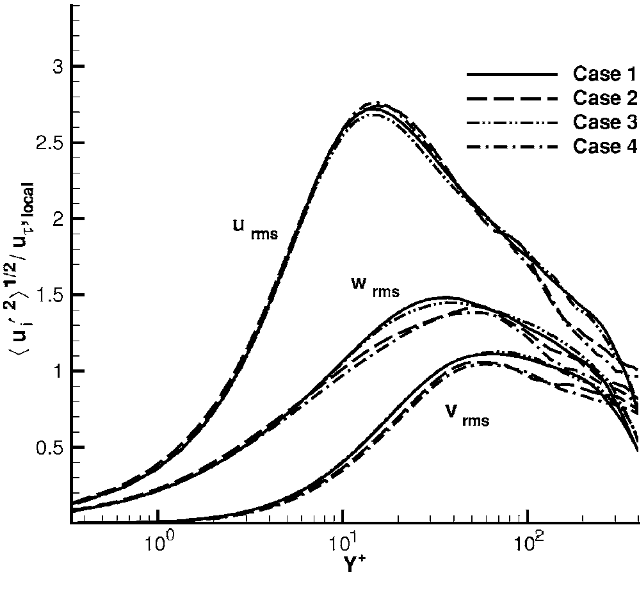

Fig. 2 Comparison of the velocity rms profiles

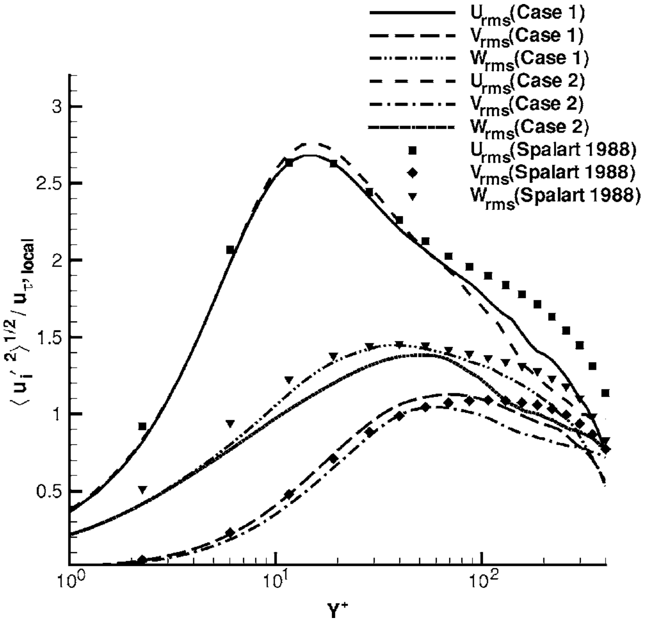

Fig. 4 Comparison of rms profiles normalized using local properties with the DNS results reported by [21]

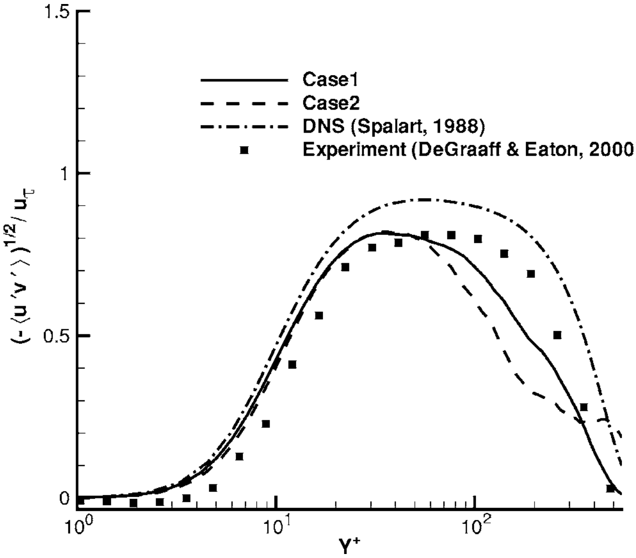

Fig. 5 The plots of $-\sqrt{\overline{u'v'}}/U_{\tau,\mathrm{local}}$ versus Y^+

The DNS and experimental results are both for a Reynolds number of 2000 based on the inlet displacement thickness. The agreement is generally good.

The law of the wall and the defect law for strongly heated subsonic turbulent boundary layers were formulated by Meignen and Berthoud [4] based on the assumption that the $u'v'$ profile was not modified by the heating. The theorem was well established; however, the assumption seems only valid for certain types of flows. For examining the assumption, we calculated $u'v'$ by using the direct numerical simulations. Figure 5 shows $-u'v'/U_{\tau,\mathrm{local}}$ plotted against $Y^+=Y(U_{\tau,\mathrm{local}}/\nu_{\mathrm{local}})$. The distributions agree well with the corresponding incompressible curve in the inner part of the boundary layer. The results shows that $u'v'$ satisfies the Van Driest transformation but is a function of the temperature because the local quantities $U_{\tau,\mathrm{local}}$ and ν_{local} are the functions of the local temperature. This feature does not agree with the assumption made in [4] for the mixing length formula, which said that $u'v'$ does not change with the heat transfer.

When the adiabatic turbulent boundary layer is supersonic, the compressibility effects will have a dramatic influence on the flows. Similarly, for a heated subsonic turbulent boundary layer, the variable density effects will have a significant influence on the flows. Compressibility effects and variable density effects will deform the first- and second-order statistics of velocities and pressure, change the turbulent kinetic energy budget, adjust the anisotropy tensor b_{ij}, and amend the energy transport between the different turbulent components. The compressibility or variable density effects on the turbulent flows are represented by the following components: density fluctuations, gradient of the mean density, pressure dilatation, temperature fluctuations, etc. To sketch the differences between both effects, the density fluctuations and gradient of the mean density were calculated. Figure 6 shows the mean and rms of density for both cases. The results show that the wall density is the same for both cases because the wall temperature is the same. But, over most of the boundary layer, the subsonic flow with strong heat transfer has a larger density compared with the supersonic flow. Since the mean pressure gradient is very small for both cases, the larger density implies a lower temperature and internal energy. Although the wall temperature is the same for both cases, the internal energy is larger for case 2. For both flows, the maximum value of the rms of density is approximately equal. In the near wall region, the rms of density for case 1 is larger than that of case 2, but case 2 has a larger value of the rms of density compared to case 1 in the outer part of boundary layer. For both of the cases, the amplitude of density fluctuations is over 5% of the freestream density. Morinishi et al. [7] found the density fluctuation of the compressible turbulent channel flows at Mach number 1.5 is of this level. Wang and Pletcher [8] reported that the amplitude of the density fluctuation can even be 9% of the freestream density for the very low Mach number turbulent channel flows if the heat transfer is strong enough. These results show the influence of variable density effects on the density fluctuations.

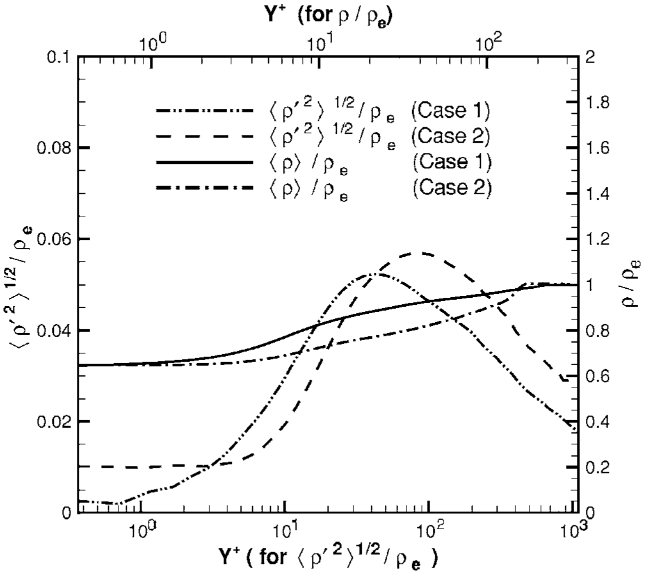

Fig. 6 Plot of the mean density, $\bar{\rho}/\rho_e$, and the rms of density, $\sqrt{\overline{\rho'^2}}/\rho_e$ as functions of Y^+

Dilatation effects have been investigated for a number of flows [1,10,21,22]. However, a comparison of the influence of compressibility and variable density on the dilatation is desired. For this reason, we calculated the mean and the rms of dilatation θ. Figure 7 shows the mean of the dilatation, $\bar{\theta}\delta_d/u_\tau$, and the rms of the dilatation, $\sqrt{\overline{\theta'^2}}\delta_d/u_\tau$, where δ_d is the inlet displacement thick-

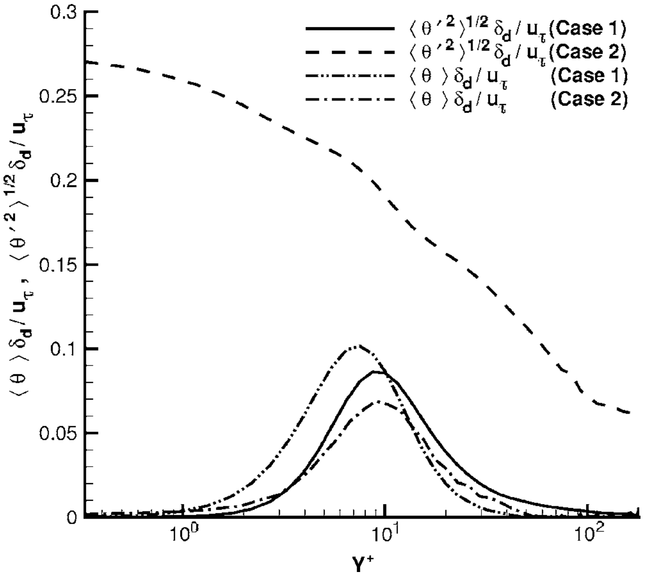

Fig. 7 The mean and rms of dilatation of velocities versus Y^+, i.e., $\bar{\theta}\delta_d/u_\tau$ and $\sqrt{\overline{\theta'^2}}\delta_d/u_\tau$, where δ_d is the displacement thickness

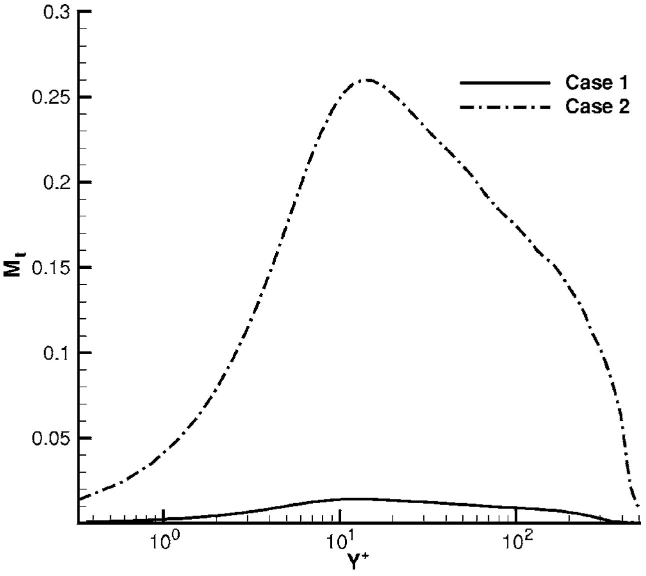

Fig. 8 Turbulent Mach number Ma_t as functions of y^+

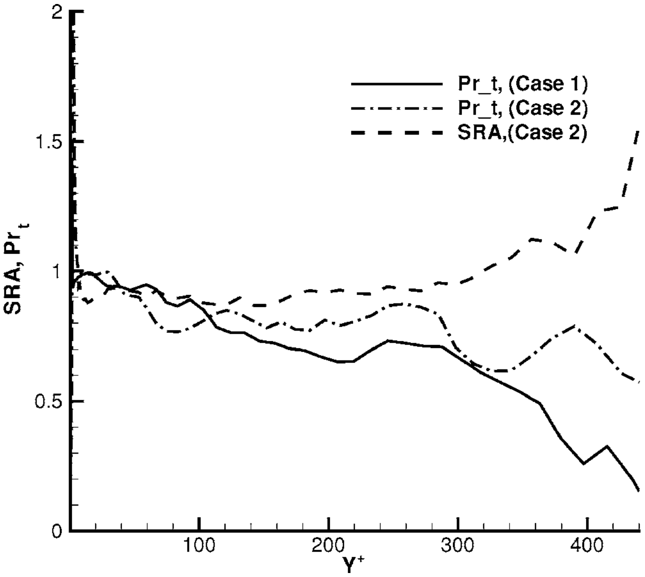

Fig. 9 Turbulent Prandtl number Pr_t as functions of Y^+ and the test of strong Reynolds analogy as express by Eq. (7)

ness, $\bar{\theta}=\overline{\partial u_i}/\partial x_i$ and $\overline{\theta'^2}=\overline{(\partial u_i'/\partial x_i)^2}$. The results show that the value of $\bar{\theta}$ is nontrivial and reaches a peak value in the buffer zone for both the subsonic and supersonic turbulent boundary layers. Moreover, the heat transfer will lead to a nontrivial distribution of θ' even through the Mach number is a factor 16 smaller than the sound speed.

Again, from Fig. 7, we notice that variable density effects make a larger contribution to the density changes in terms of $\bar{\theta}$ compared to compressibility effects even though the flows have the same wall temperature. However, compressibility effects make a larger contribution to the turbulent dilatation. For the subsonic flows, although the heat transfer will cause the variable density effects, the fluctuations of θ or density are still very weak. They achieve the maximum values in the buffer zone. For the supersonic flow, much of the kinetic energy is transferred to internal energy in the near wall region. This feature leads to the strong density fluctuations. Although case 1 is essentially incompressible, its governing equation should be the compressible Navier-Stokes equations because $\bar{\theta}$ and $\overline{\theta'^2}$ are all nontrivial.

Morkovin [23] suggested that the turbulence is weakly affected by compressibility provided the rms fluctuations of the Mach number $\mathrm{Ma}' \leq 0.2$. Guarini et al. [6] reported that when the Mach number is 2.5, the peak values of Ma' and the turbulent Mach number Ma_t of an adiabatic turbulent boundary layer are ~0.3. To illustrate the compressibility of cases 1 and 2, Ma_t is plotted in Fig. 8. The results show that the subsonic flow at a Mach number of 0.06 has a very small Ma_t, although its density and temperature vary as functions of time and space because of the heat transfer. The supersonic adiabatic turbulent boundary layer at Mach number 1.8 still exhibits a fairly strong compressibility in the inner part of the turbulent boundary layer.

The strong Reynolds analogy (SRA) was proposed by Morkovin [23] and suggested that

$$C_pT' + \widetilde{u_1u_1'} \approx 0$$

Based on Morkovin's assumption, Guarini et al. [6] found that

$$\frac{\widetilde{u_1\sqrt{\overline{T'^2}}}}{(\gamma-1)M^2\tilde{T}\sqrt{\overline{u_1'^2}}} \approx 1 \tag{7}$$

The strong Reynolds analogy implies that total temperature fluctuations are negligible compared to static temperature fluctuations [6]. However, this assumption has limited applicability and must be reexamined for the different types of turbulent flows. For the low Mach number turbulent flows with a heated wall, the turbulent heat transfer of the flows relies more on the variable density rather than the compressibility which associates with the Mach number. Since the Mach number is close to zero, the denominator of Eq. (7) approaches zero. The strong Reynolds analogy cannot be obeyed under this circumstance. Indeed, the strong Reynolds analogy terms, $\tilde{u}_1\sqrt{\overline{T'^2}}/[(\gamma-1)M^2\tilde{T}\sqrt{\overline{u_1'^2}}]$ was over 300 for case 1 in the most of the boundary layer. However, Eq. (7) was satisfied by case 2, which was a supersonic turbulent boundary layer. Unlike the strong Reynolds analogy, we found that the turbulent Prandtl number given by

$$\mathrm{Pr}_t = \frac{\widetilde{u_1u_2}(\partial\tilde{T}/\partial y)}{\widetilde{Tu_2}(\partial\widetilde{u_1}/\partial y)}. \tag{8}$$

for both supersonic and subsonic turbulent boundary layers agreed fairly well in the inner wall region. The behavior of the turbulent Prandtl number has been described by a number of studies [24–26]. In this study, we compare the influence of compressibility and variable density on the turbulent Prandtl number. Figure 9 shows the distribution of $\tilde{u}_1\sqrt{\overline{T'^2}}/[(\gamma-1)M^2\tilde{T}\sqrt{\overline{u_1'^2}}]$ and turbulent Prandtl number Pr_t as functions of Y^+. The results indicate that the strong Reynolds analogy was satisfied for case 2. Nevertheless, the turbulent Prandtl numbers Pr_t for both cases are close to each other quantitatively in the inner part of the boundary layer, which ranged from 0.75 to 0.9. As the distance from the wall increases, the deviation between the turbulent Prandtl numbers increases.

3.2 Favre Average. As we described above, the compressible Navier-Stokes equations should be solved if strong heat transfer is involved in wall shear flows even though the Mach number of the flows is low. To account for property changes, a mass-weighted averaging is recommended. Favre average [11] is usually utilized for this purpose. By using the Favre average, the Navier-Stokes equations are modified. Several additional terms are produced. These terms need to be modeled for LES schemes. However, information about the influence of Mach number and heat transfer on these additional terms in the Favre-filtered Navier-Stokes equations is lacking. To provide further information for the LES modeling, we calculate both the compressible and incompressible flows by using DNS and then evaluate these Favre-filtered terms.

Here, we use DNS to evaluate various subgrid scale quantities that appear in the filtered equations used in LES; some of these terms are usually modeled in LES, but some are often neglected. The Favre-filtered compressible Navier-Stokes equations are

$$\frac{\partial\bar{\rho}}{\partial t}+\frac{\partial(\bar{\rho}\tilde{u}_j)}{\partial x_j}=0 \tag{9}$$

$$\frac{\partial(\bar{\rho}\tilde{u}_i)}{\partial t}+\frac{\partial(\bar{\rho}\tilde{u}_i\tilde{u}_j)}{\partial x_j}=-\frac{\partial\bar{p}}{\partial x_i}+\frac{\partial\bar{\sigma}_{ij}}{\partial x_j}-\frac{\partial\tau_{ij}}{\partial x_j} \tag{10}$$

$$\frac{\partial(\bar{\rho}\hat{E})}{\partial t}+\frac{\partial[(\bar{\rho}\hat{E}+\bar{p})\tilde{u}_j]}{\partial x_j}=\frac{\partial(\tilde{u}_i\bar{\sigma}_{ij})}{\partial x_j}-\frac{\partial\bar{q}_j}{\partial x_j}-\frac{\partial Q_j}{\partial x_j}-\gamma-\pi-\varepsilon \tag{11}$$

The effects of the small-scale motions are present in Eqs. (9)–(11) through the subgrid-scale (SGS) stress tensor τ_{ij} in the momentum equation as

$$\tau_{ij}=\bar{\rho}(\widetilde{u_iu_j}-\tilde{u}_i\tilde{u}_j) \tag{12}$$

and the SGS terms that are the last four terms on the right-hand side of Eq. (11) as

$$\begin{gathered}\boldsymbol{Q}_j=\bar{\rho}c_v(\widetilde{Tu_j}-\tilde{T}\tilde{u}_j)\\ \gamma=\tilde{u}_i\frac{\partial\tau_{ij}}{\partial x_j},\quad \pi=\overline{p\frac{\partial u_j}{\partial x_j}}-\bar{p}\frac{\partial\tilde{u}_j}{\partial x_j}\quad\text{and }\varepsilon=\overline{\sigma_{ij}\frac{\partial u_i}{\partial x_j}}-\hat{\sigma}_{ij}\frac{\partial\tilde{u}_j}{\partial x_j}\end{gathered} \tag{13}$$

where $\boldsymbol{Q}_j$ is the SGS heat flux vector. The overtilde and overline stand for the Favre average and Reynolds average, respectively.

By definition, $\tilde{\phi}=\overline{\rho\phi}/\bar{\rho}$. A dynamic model proposed by Moin et al. [27] and recommended by Lilly [28] provides a solution for the SGS stress tensor τ_{ij} and heat flux vector $\bar{\boldsymbol{q}}_j$ in the Favre-filtered equations. The terms γ, π, and ε can be neglected for the low Mach number flows [29]. However, for flows with moderate Mach numbers, the influence of γ, π, and ε on the heat transfer may be significant. Thus, the changes in γ, π, and ε due to the Mach number and heat transfer should be addressed not only for the modeling of the Favre-filtered equations but also for the understanding of turbulent heat and mass transfer. In this section, we are going to illustrate the effect of Mach number and heat transfer on the Favre average, τ_{ij}, γ, and π.

To present the difference between the Favre average and Reynolds average

$$\tilde{u}-\bar{u}=\frac{\overline{\rho u}}{\bar{\rho}}-\bar{u}=\frac{\overline{\rho' u'}}{\bar{\rho}} \tag{14}$$

we plot the difference normalized by u_τ in Fig. 10. The maximum value in Fig. 10 is a factor of 20 smaller than that of Fig. 4 for both of the cases. This implies that the difference between the Favre average and Reynolds average exists but is small. And such a difference can be neglected under the circumstance that 5% errors are acceptable for turbulence modeling. This feature has been found in the experimental study of supersonic jets with a Mach number ranging from 0.8 to 1.8 [30].

The SGS stress tensor can be decomposed as

$$\tau_{ij}=\bar{\rho}(\widetilde{u_iu_j}-\tilde{u}_i\tilde{u}_j)=\bar{\rho}\overline{u_i'u_j'}+\overline{\rho' u_i'u_j'}-\overline{\rho' u'_j}\,\overline{\rho' u'_i}/\bar{\rho}=\tau_{ij_t}+\tau_{ij_c}+\tau_{ij_F} \tag{15}$$

The first term $\tau_{ij_t}=\bar{\rho}\overline{u_i'u_j'}$ is associated with the mean density $\bar{\rho}$ and the Reynolds SGS stress tensor $\overline{u_i'u_j'}$, where $\overline{u_i'u_j'}=\overline{u_iu_j}-\bar{u}_i\bar{u}_j$; the second term $\tau_{ij_c}=\overline{\rho' u_i'u_j'}$ relates to the compressible part of τ_{ij}, and the last term $\tau_{ij_F}=\overline{\rho' u'_j}\,\overline{\rho' u'_i}/\bar{\rho}$ describes the contribution of the difference between Favre and Reynolds averages. Figure 11 gives a comparison of those components. The results show that the major contributions of τ_{11} and τ_{22} are from $\bar{\rho}\overline{u_1'u_1'}$ and $\bar{\rho}\overline{u_2'u_2'}$, respectively. The compressibility and the variable density effects do not have a significant effect on τ_{11} and τ_{22}.

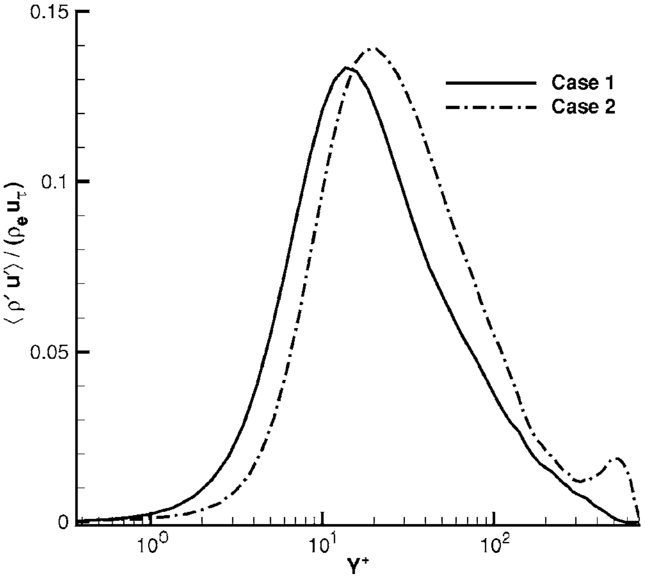

Fig. 10 Comparison of $(\tilde{u}_1-\overline{u_1})/u_\tau$

Figure 12 plots γ and π for both cases, where $\gamma=\tilde{u}_i(\partial\tau_{ij}/\partial x_j)$ and $\pi=\overline{p(\partial u_j/\partial x_j)}-\bar{p}(\partial\tilde{u}_j/\partial x_j)$. By Fig. 12, we found that both γ and π take on larger values for case 1 compared to case 2. This implies that heat transfer has a larger influence on γ and π than the compressibility effects if both flows have the same wall temperature. Clearly, π contains the pressure dilatation $\overline{p'(\partial u_j'/\partial x_j)}$, which is the pressure dilatation relative to the compressibility. The magnitude of γ and π is of the order 10^{-3}, which is much smaller than the amplitude of the heat flux. Thus, γ and π can be neglected even though the Mach number of flow is 1.8 and wall temperature is $T_w=1.58T_e$.

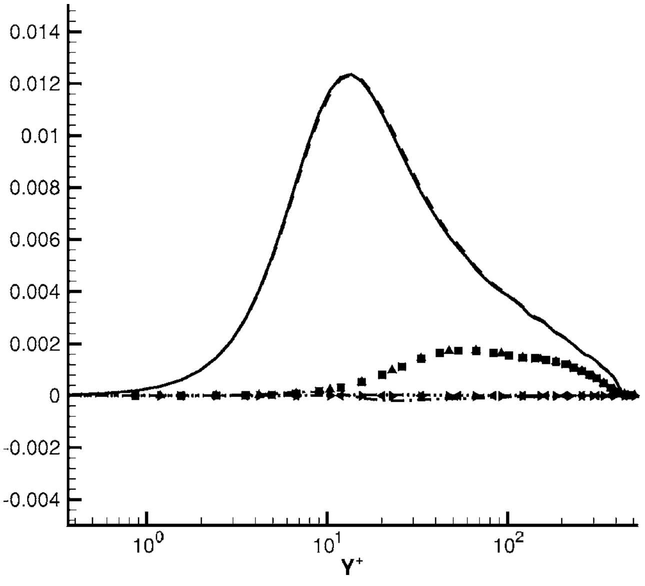

Fig. 11 The components of τ_{11}. The solid line is τ_{11}, the dashed line is the τ_{11_t}, the dashed-dotted line is τ_{11_c}, and the dashed-double-dotted line is τ_{11_F}. The square samples are τ_{22}, the triangle samples are τ_{22_t}, the right triangular samples are τ_{22_c}, and the left triangular samples are τ_{22_F}.

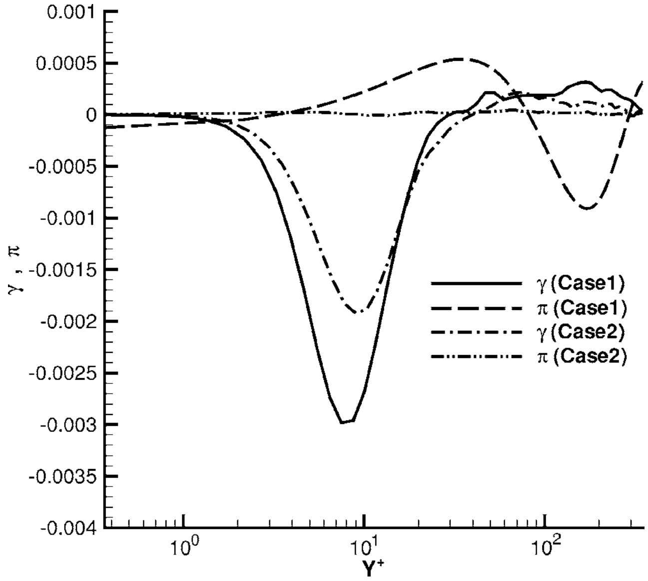

Fig. 12 Comparison of γ and π versus Y^+, where the solid line is γ for the case 1, the dashed-dotted line is γ for the case 2, the dashed line is π for the case 1, the dashed-double-dotted line if π for the case 2

4 Conclusions

Two turbulent flows with a Reynolds number 2000 based on the inflow displacement thickness was calculated by using DNS: Case 1 was an subsonic turbulent boundary layer at Mach number 0.06 over a heated wall and $T_w=1.58T_e$ and case 2 was an adiabatic supersonic turbulent boundary layer at a Mach number of 1.8. The heat transfer driven by the heated wall will cause the variable density effects of the turbulent boundary layer even when the Mach number of flows is as small as 0.06. The results show that the Van Driest transformation can help to collapse the mean profiles of velocity to the corresponding incompressible curves. By using the local properties, the rms of velocities for both of the flows can approach the incompressible curves. These facts reveal that both of the compressibility and variable density effects satisfy the similarity laws. The compressibility effects have a different contribution to the fluctuations of the dilatation compared to the variable density effects. The turbulent dilatation of supersonic flows is stronger than that of the lower Mach flows if the wall temperature is the same. The calculation of Ma_t indicates that the Mach number 1.8 is large enough to produce the compressibility in the inner part of the turbulent boundary layer. The strong Reynolds analogy proposed by Morkovin [23] was tested. The results indicate that the Morkovin's hypothesis is obeyed by the adiabatic supersonic turbulent boundary layer at Mach number 1.8. The variable density effect has a large influence on the density fluctuations. For both cases 1 and 2, the rms of the density fluctuations were 5% of the freestream density although the distributions across the boundary layer were different.

In addition, the Favre average was examined by this paper. The difference between the Favre average and Reynolds average was measured. The results show that such a difference is small compared to the rms of velocities for both cases. The SGS stress tensor τ_{ij} was evaluated; we found that τ_{ij} can be approximated by $\overline{\bar{\rho}u_i'u_j'}$. Furthermore, the calculation shows that γ and π are negligible even when the Mach number is 1.8 as well as for a low-speed case with a heated wall, $T_w=1.58T_e$. These features help to simplify the turbulence modeling of compressible flows.

Acknowledgment

The authors thank the referees for their suggestions and recommendations. This research was partially supported by the Air Force Office of Scientific Research through Grant No. F49620-01-1-0113 and the National Science Foundation though Grant No. CTS-9806989. The Iowa State High Performance Computing Center and the University of Minnesota Supercomputing Institute provided computational resources needed for this research.

Nomenclature

Re_d = Reynolds number based on inflow displacement thickness
δ_d = boundary layer displacement thickness
x = Cartesian coordinates normalized by inflow displacement thickness
u' = fluctuations
U_τ = boundary layer friction velocity, $\sqrt{\tau_w/\rho}$
y^+ = nondimensional normal distance, yU_τ/ν
U^+ = nondimensional velocity, U/U_τ

Subscript

e = freestream property
w = wall property
local = local property
rms = root mean square

References

[1] Lele, S. K., 1994, "Compressible Effects on Turbulence," Annu. Rev. Fluid Mech., **26**, pp. 211–254.
[2] Bradshaw, P., 1977, "Compressible Turbulent Shear Layers," Annu. Rev. Fluid Mech., **9**, pp. 33–54.
[3] Nicoud, N., and Bradshaw, P., 2000, "A Velocity Transformation for Heat and Mass Transfer," Phys. Fluids, **12**(1), pp. 237–238.
[4] Meignen, R., and Berthoud, G., 1998, "A Mixing Length Model for Strongly Heated Subsonic Turbulent Boundary Layers," Int. J. Heat Mass Transfer, **41**, pp. 3373–3385.
[5] Huang, P. G., Bradshaw, P., and Coakley, T. J., 1993, "Skin Friction and Velocity Profile Family for Compressible Turbulent Boundary Layers," AIAA J., **31**(9), pp. 1600–1604.
[6] Guarini, S. E., Moser, R. D., Shariff, K., and Wray, A., 2000, "Direct Numerical Simulation of a Supersonic Turbulent Boundary Layer at Mach 2.5," J. Fluid Mech., **414**, pp. 1–33.
[7] Morinishi, Y., Tamano, S., and Nakabayashi, K., 2004, "Direct Numerical Simulation of Compressible Turbulent Channel Flow Between Adiabatic and Isothermal Walls," J. Fluid Mech., **502**, pp. 273–308.
[8] Wang, W., and Pletcher, P. H., 1996, "On the Large Eddy Simulation of a Turbulent Channel Flow With Significant Heat Transfer," Phys. Fluids, **8**, pp. 3354–3366.
[9] Maise, G., and McDonald, H., 1968, "Mixing Length and Kinematic Eddy Viscosity in a Compressible Boundary Layer," AIAA J., **6**, pp. 73–80.
[10] Bradshaw, P., 1974, "The Effect of Mean Compressible or Dilatation on the Turbulent Structure of Supersonic Boundary Layers," J. Fluid Mech., **63**, pp. 449–464.
[11] Favre, A., 1983, "Turbulence, Space-Time Statistical Properties and Behavior in Supersonic Flows," Phys. Fluids, **26**, pp. 2851–2863.
[12] Liu, K., 2006, "Numerical Simulation of Turbulent Boundary Layers and Film Cooling," Ph.D. thesis, Iowa State University.
[13] Patankar, S. V., and Spalding, D. B., 1972, "A Calculation Procedure for Heat, Mass and Momentum Transfer in Three-Dimensional Parabolic Flows," Int. J. Heat Mass Transfer, **15**, pp. 1787–1806.
[14] Kim, J., and Moin, P., 1985, "Application of a Fractional Step Method to Incompressible Flows," J. Comput. Phys., **59**, pp. 308–323.
[15] Wall, C., Pierce, C. D., and Moin, P., 2002, "A Semi-Implicit Method for Resolution of Acoustic Waves in Low Mach Number Flows," J. Comput. Phys., **181**, pp. 545–563.
[16] Turkel, E., 1999, "Preconditioning Techniques in Computational Fluid Dynamics," Annu. Rev. Fluid Mech., **31**, pp. 385–416.
[17] Pletcher, R. H., and Chen, K.-H., 1993, "On Solving the Compressible Navier-Stokes Equations for Unsteady Flows at Very Low Mach Numbers," AIAA Paper No. 3368.
[18] Liu, K., and Pletcher, R. H., 2006, "Inflow Conditions for the Large Eddy Simulation of Turbulent Boundary Layers, A Dynamic Recycling Procedure," J. Comput. Phys., **219**, pp. 1–6.
[19] Spalart, P. R., 1988, "Direct Simulation of a Turbulent Boundary Layer up to $\mathrm{Re}_\theta=1410$," J. Fluid Mech., **187**, pp. 61–98.
[20] DeGraaff, D. B., and Eaton, J. K., 2000, "Reynolds-Number Scaling of the Flat-Plate Turbulent Boundary Layer," J. Fluid Mech., **422**, pp. 319–346.
[21] Zeman, O., 1990, "Dilatation Dissipation, The Concept and Application in

Modeling Compressible Mixing Layers," Phys. Fluids A, **2**, pp. 178–188.
[22] Sarkar, S., 1992, "The Pressure-Dilatation Correlation in Compressible Flows," Phys. Fluids A, **4**, pp. 2674–2682.
[23] Morkovin, M. V., 1962, "Effects of Compressibility on Turbulent Flows," *Mécannique de la Turbulence*, A. Favre, ed., Centre National de la Recherche Scientifique (CNRS), Paris, France, pp. 367–380.
[24] Antonia, R. A., and Kim, J., 1991, "Turbulent Prandtl Number in the Near-Wall Region of a Turbulent Channel Flow," Int. J. Heat Mass Transfer, **34**, pp. 1905–1908.
[25] Yaglom, A. M., 1979, "Similarity Laws for Constant-Pressure and Pressure-Gradient Turbulent Wall Flows," Annu. Rev. Fluid Mech., **11**, pp. 505–540.
[26] Reynolds, A. J., 1975, "The Prediction of Turbulent Prandtl and Schmidt Numbers," Int. J. Heat Mass Transfer, **18**, pp. 1055–1069.
[27] Moin, P., Squires, K., Cabot, W., and Lee, S., 1991, "A Dynamic Subgrid-Scale Model for Compressible Turbulence and Scalar Transport," Phys. Fluids A, **3**, pp. 2746–2757.
[28] Lilly, D. K., 1992, "A Proposed Modification of the Germano Subgrid-Scale Closure Method," Phys. Fluids A, **4**, pp. 633–635.
[29] Vreman, A. W., Geurts, B. J., and Kuerten, H., 1995, "Subgrid-Modeling in LES of Computational Flow," Appl. Sci. Res., **54**, pp. 191–203.
[30] Panda, J., and Seasholtz, R. J., 1995, "Experimental Investigation of the Differences Between Reynolds' Averaged and Favre Averaged Velocity in Supersonic Jets," AIAA Paper No. 2005-514.

Turbulent Heat Transfer in Ribbed Coolant Passages of Different Aspect Ratios: Parametric Effects

Arun K. Saha

Sumanta Acharya
e-mail: acharya@me.lsu.edu

Turbine Innovation and Energy Research (TIER) Center,
Louisiana State University,
Baton Rouge, LA 70803

Turbulent flow and heat transfer in rotating ribbed ducts of different aspect ratios (AR) are studied numerically using an unsteady Reynolds averaged Navier–Stokes procedure. Results for three ARs (1:1, 1:4, and 4:1) and staggered ribs with constant pitch ($P/e=10$) *in the periodically developed region are presented and compared. To achieve periodic flow behavior in successive inter-rib modules calculations are performed in a computational domain that extends to two or three inter-rib modules. The computations are carried out for an extended parameter set with a Reynolds number range of 25,000–150,000, density ratio range of 0–0.5, and rotation number range of 0–0.50. Under rotational conditions, the highest heat transfer along the leading and side walls are obtained with the 4:1 AR, while the 1:4 AR has the highest trailing wall Nu ratio and the lowest leading wall Nu ratio. The 1:4 AR duct shows flow reversal near the leading wall (leading to low Nu) at high rotation numbers and density ratios. For certain critical parameter values (low Re, high Ro, and/or DR), the leading wall flow is expected to become nearly stagnant, due to the action of centrifugal buoyancy, leading to conduction-limited heat transfer. The 4:1 AR duct shows evidence of multiple rolls in the secondary flow that direct the core flow to both the leading and trailing surfaces which reduces the difference between the leading and trailing wall heat transfer relative to the other two AR ducts.* [DOI: 10.1115/1.2709653]

Introduction

In internal cooling of turbine blades, coolant air is circulated through serpentine ribbed passages and discharged through bleed holes along the trailing edge of the blade. A schematic of the serpentine passages within the blade is illustrated in Fig. 1(*a*). With rotation, the flow is subjected to Coriolis forces and centrifugal-buoyancy effects. Coriolis forces generate secondary flows in the cross-sectional plane, directed from the leading surface to the trailing surface in the radially outward flow passage. It is generally believed that these forces produce two symmetric rolls in the cross-sectional plane, and reduce heat transfer from the leading surface from where the flow lifts off and enhance heat transfer on the trailing surface where the flow impinges. Centrifugal-buoyancy effects also become important at high rotation numbers and density ratios, and for radially outward flow, the primary centrifugally buoyancy forces are directed radially inward producing competing effects of enhanced turbulence (as in counter-shear flows) and reduced inertial forces (as in opposed mixed convection). Since rotation produces the combined effects of Coriolis forces and buoyancy forces, the resulting secondary flows are quite complex, strongly three dimensional, and unsteady. In order to accurately predict the heat transfer, the predictive procedure should be capable of resolving the large-scale unsteadiness in the flow.

The cross section of a turbine blade varies considerably over its axial chord as its thickness changes from the front leading edge to the trailing edges. Near the midchord regions, the coolant passage is almost square in cross section aspect ratio ((AR) of 1:1), and this AR has been extensively studied in the literature. However, the low AR coolant passages which are encountered in the thickest portion of the blade and the high AR's representing passages in the thinnest portion or the trailing edge regions of the blade have received considerably less attention in the literature. Since the strength and the pattern of the secondary flow are expected to be influenced by the AR, the investigation of the effect of the AR on the flow and heat transfer behavior is necessary, particularly for parameter ranges of relevance to engine conditions.

Experimental investigations of flow and heat transfer in smooth and rib-roughened channels have been carried out by a number of different researchers (Han and Park [1], Han et al. [2], Zhou et al. [3], Wagner et al. [4], and Johnson et al. [5]). More recently, Chen et al. [6] have reported detailed mass transfer (naphthalene sublimation) measurements in a stationary duct having a sharp 180 deg bend. Azad et al. [7] have studied the effect of the channel orientation in a two-pass rectangular duct for both smooth and 45 deg ribbed walls. In a recent study, heat transfer in a rib-roughened rectangular channel with aspect ratio 4:1 has been reported by Griffith et al. [8].

Most of the earlier computational studies on internal cooling passage of the blades have been restricted to three-dimensional steady Reynolds averaged Navier–Stokes (RANS) (SRANS) simulations [9–12]. The flow and heat transfer through a two-pass 45 deg rib-roughened rectangular duct having aspect ratio of 2.0 has been conducted by Al-Qahtani et al. [13] using a Reynolds stress turbulence model. They have found reasonable match with experiments, although in certain regions there are significant discrepancies. In Al-Qahtani et al. [13], it is argued that two equation models are unsatisfactory for rotating ribbed duct flows, and that a second moment closure is needed for accurate predictions.

A key deficiency of SRANS is their inability to properly represent the unsteady dynamics of large-scale structures in the turbulence model. Direct numerical simulation (DNS), large Eddy simulation (LES), and Unsteady RANS (URANS) provide alternative and superior approaches to SRANS simulation procedures. In DNS, LES, and URANS all or a portion of the unsteady spectrum is resolved. In DNS all scales are resolved, and no modeling is introduced. In LES, all dynamics of turbulent eddies above a cutoff filter (twice the mesh size) are resolved while only the small-scale fluctuations are modeled. In URANS, all turbulent fluctuations are modeled while the unsteadiness in the large-scale

---

Contributed by the Heat Transfer Division of ASME for publication in Journal of Heat Transfer. Manuscript received January 16, 2005; final manuscript received June 8, 2006. Review conducted by Phillip M. Ligrani.

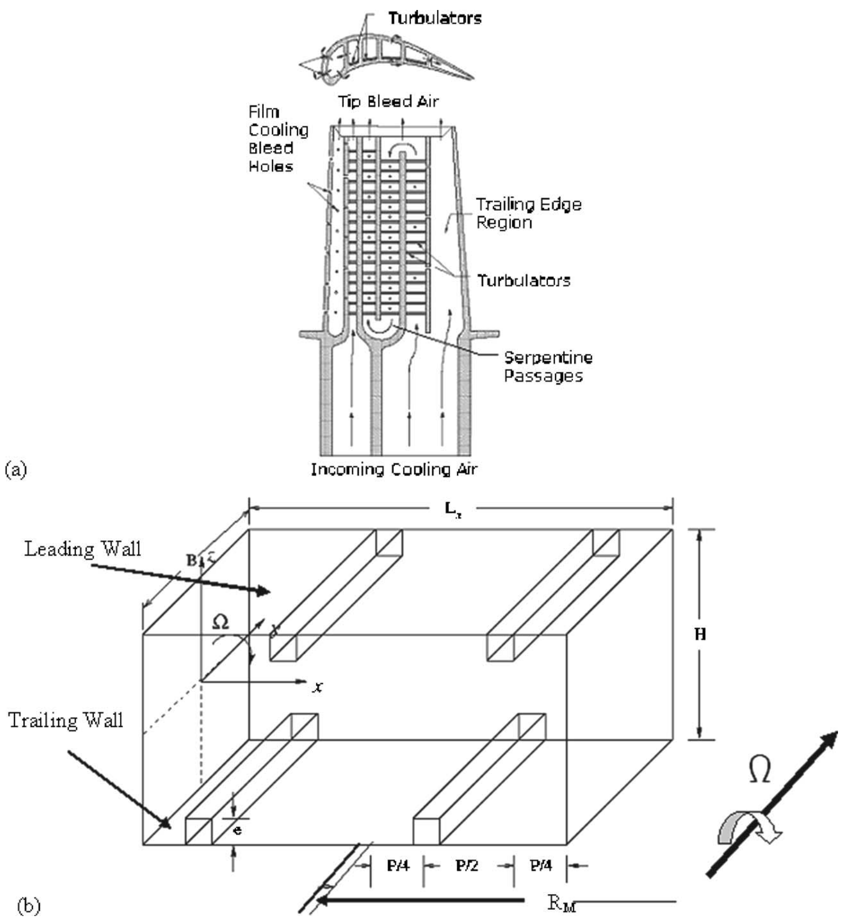

Fig. 1 (*a*) **Schematic of a typical internal cooling strategy [5]; and (*b*) a three-dimensional computational model of a periodic inter-rib module showing two ribs**

bulk motions is resolved. Thus, URANS aims to capture only the first few fundamental frequencies and models the remaining spectrum of fluctuating motions using a standard turbulence closure.

Unsteady flow simulations in rotating coolant passages are very limited. Flow through a rotating square smooth duct has been simulated using LES by Pallares and Davidson [14]. They present turbulent stress budgets in their study. A rotating duct with rib roughened walls has been investigated numerically using LES by Murata and Mochizuki [15]. The effect of centrifugal buoyancy and different rib orientations was investigated in their study. Saha and Acharya [16] reported a comparison of URANS and LES for a rotating 1:1 AR ribbed duct, and concluded that the time-averaged URANS and LES predictions agree well with measurements, and with each other. Murata and Mochizuki [17] carried out an LES study of flow and heat transfer in an orthogonally rotating rectangular duct having AR of 1:1, 1:2, and 1:4 with inline transverse ribs. It was observed that the smaller aspect ratio cases are most affected by the rotation and this effect increases with rotation number. The effect of 60 deg angled ribs in different aspect ratio (4:1, 2:1, 1:1, 1:2, and 1:4) ducts was investigated in a recent study by Murata and Mochizuki [18].

Since there are limited number of studies that explore the role of aspect ratio on the fluid flow and heat transfer in a rotating ribbed duct, the goal of the present paper is to use URANS to study the effect of aspect ratio for a range of Reynolds number, rotation number and density ratio of relevance to gas turbine industry. In the present study, three ARs of 1:1, 4:1, and 1:4 are studied for a Reynolds number (Re) range of 25,000–150,000, density ratio (DR) range of 0–0.5, and for rotation numbers (Ro) in the range of 0–0.50. None of the available studies in the literature provide information over the extended parametric range reported here, and as noted earlier, the majority of the detailed experimental and computational parametric studies are limited to the 1:1 AR case. Furthermore, the present study utilizes an unsteady RANS (URANS) calculation procedure in order to provide a more accurate estimate of the duct heat transfer and fluid flow. In an earlier study, Saha and Acharya [16] demonstrated that for a rotating ribbed duct flow, URANS calculations of the averaged Nusselt number were in close agreement with LES and experimental data [5].

Governing Equations and Boundary Conditions

The geometrical model of the problem to be studied is presented in Fig. 1(*b*). The ribs of dimensions, $e \times e$, form a periodic pattern with streamwise pitch of L_x. For the majority of the calculations, the periodic module in the streamwise direction consists of two ribs. Preliminary studies have shown that a periodic module consisting of one rib suppressed unsteadiness at low Reynolds number and rotation number, while periodic modules containing two or more ribs were able to sustain large-scale unsteadiness. The working fluid chosen in the present study is air whose Prandtl number is 0.7.

The unsteady Navier–Stokes equations along with the incompressibility constraint have been numerically solved in the present study. The equations for continuity, momentum, and energy equations in dimensionless form are expressed as

$$\frac{\partial \langle u \rangle_i}{\partial x_i} = 0 \tag{1}$$

$$\frac{\partial\langle u\rangle_i}{\partial t}+\frac{\partial}{\partial x_j}(\langle u\rangle_j\langle u\rangle_i)=-\frac{\partial\langle p\rangle}{\partial x_i}+\delta_{i1}\beta(t)+\frac{1}{\mathrm{Re}}\frac{\partial^2\langle u\rangle_i}{\partial x_j^2}+\frac{\partial\tau_{ij}}{\partial x_j}$$
$$-2\mathrm{Ro}\varepsilon_{i2k}\langle u\rangle_k-\frac{\mathrm{Bo}}{R_M}(1-\theta)\varepsilon_{i2l}\varepsilon_{l2k}r_k \quad (2)$$

$$\frac{\partial\langle\theta\rangle}{\partial t}+\langle\theta\rangle\Lambda+\frac{\partial}{\partial x_j}(\langle u\rangle_j\langle\theta\rangle)=\frac{1}{\mathrm{Re\,Pr}}\frac{\partial^2\langle\theta\rangle}{\partial x_j^2}+\frac{\partial q_j}{\partial x_j} \quad (3)$$

where $\beta(t)$ is the linear component of the nondimensional pressure that has to be adjusted in each time step to get the desired mass flow rate, $\langle\theta\rangle=(\langle T\rangle-\langle T\rangle_w)/(\langle T\rangle_{m1}-\langle T\rangle_w)$; $\tau_{ij}=\overline{u''_i u''_j}$; and $q_j=-\overline{u''_j\theta''}$. The terms $\langle\tau\rangle_{ij}$ and $\langle q\rangle_j$ in Eqs. (2) and (3) are the turbulent stress contributions that have to be modeled. Here, $\langle T\rangle_w$ is the wall temperature and $\langle T\rangle_{m1}$ is the bulk temperature of the fluid evaluated at the inlet section of the computational domain. The unknown function Λ in the energy equation is given by

$$\Lambda=\frac{1}{\langle T\rangle_{m1}-\langle T\rangle_w}\frac{\partial}{\partial t}(\langle T\rangle_{m1}-\langle T\rangle_w)$$

The coupling between $\langle\theta\rangle$ and Λ can be solved iteratively as described by Wang and Vanka [19]. In the above equations the velocities are nondimensionalized with the average velocity $\langle u_{av}\rangle$, all lengths are scaled with the dimensions of the square cylinder, B, pressure is scaled with $\rho\langle u_{\mathrm{av}}\rangle^2$, and time is scaled by $B/\langle u_{\mathrm{av}}\rangle$.

Unsteady RANS Turbulence Model. The URANS calculations have been carried out using a two-equation ($\langle k\rangle$ and $\langle\varepsilon\rangle$) model. The turbulence closure is based on the gradient transport hypothesis, which correlates $\langle\tau\rangle_{ij}$ to the phase averaged stain-rate tensor

$$\langle\tau\rangle_{ij}=-\overline{u''_i u''_j}=-2\nu_T\langle S\rangle_{ij}+\frac{\delta_{ij}}{3}\langle\tau\rangle_{kk} \quad (4)$$

where δ_{ij} is the Kronecker delta, $\langle\tau\rangle_{kk}=\overline{u''_k u''_k}$, and $\langle S\rangle_{ij}$ is given by

$$\langle S\rangle_{ij}=\frac{1}{2}\left(\frac{\partial\langle u\rangle_i}{\partial x_j}+\frac{\partial\langle u\rangle_j}{\partial x_i}\right)$$

The turbulent eddy viscosity and turbulent thermal diffusivity are given in nondimensional forms as follows

$$\nu_T=C_\mu\mathrm{Re}\frac{\langle k\rangle^2}{\langle\varepsilon\rangle}$$

and

$$\alpha_T=C_\mu\mathrm{Re\,Pr}\frac{\langle k\rangle^2}{\sigma_t\langle\varepsilon\rangle}$$

where σ_T is the turbulent Prandtl or Schmidt number. For k and ε equations, the Kato-Launder model [20] is found to be suitable for bluff body flows since it can handle the stagnation zone properly by reducing the turbulent production in this region. In this model [20], the production of turbulent kinetic energy is written in terms of rotation and shear of fluid elements instead of only shear. The nondimensional transport equations for k and ε are as follows

$$\frac{\partial\langle k\rangle}{\partial t}+\frac{\partial}{\partial x_i}\{\langle k\rangle\langle u\rangle_i\}=\frac{1}{\mathrm{Re}}\frac{\partial}{\partial x_i}\left\{\frac{\nu_t}{\sigma_k}\frac{\partial\langle k\rangle}{\partial x_i}\right\}+P_k-\langle\varepsilon\rangle \quad (5)$$

$$\frac{\partial\langle\varepsilon\rangle}{\partial t}+\frac{\partial}{\partial x_i}\{\langle\varepsilon\rangle\langle u\rangle_i\}=\frac{1}{\mathrm{Re}}\frac{\partial}{\partial x_i}\left\{\frac{\nu_t}{\sigma_\varepsilon}\frac{\partial\langle\varepsilon\rangle}{\partial x_i}\right\}+C_{\varepsilon1}P_k\frac{\langle\varepsilon\rangle}{\langle k\rangle}-C_{\varepsilon2}\frac{\langle\varepsilon\rangle^2}{\langle k\rangle} \quad (6)$$

where

Table 1 Model parameters

C_μ	$C_{\varepsilon1}$	$C_{\varepsilon2}$	σ_k	σ_ε
0.09	1.44	1.92	1.0	1.3

$$P_k=C_\mu\langle\varepsilon\rangle\langle S\rangle\langle\Omega\rangle,\quad\langle\Omega\rangle=\frac{\langle k\rangle}{\langle\varepsilon\rangle}\sqrt{\frac{1}{2}\left\{\frac{\partial\langle u\rangle_i}{\partial x_j}-\frac{\partial\langle u\rangle_j}{\partial x_i}\right\}^2}$$

The parameters for the above equations are given in Table 1.

The periodic boundary conditions for velocities, pressure, and the turbulent kinetic energy and dissipation rate are expressed as

$$\langle\phi\rangle(x+nL_x,y,z,t)=\langle\phi\rangle(x,y,z,t) \quad (7)$$

where $\phi\equiv(u_i,p,k,\varepsilon)$; L_x is the distance between two ribs; and n represents the number of inter-rib module needed for periodicity. The corresponding periodic boundary conditions for the energy equations are

$$\frac{\bar{\theta}(x+nL_x,y,z,t)}{\bar{\theta}_{m2}}=\frac{\bar{\theta}(x,y,z,t)}{\bar{\theta}_{m1}} \quad (8)$$

where $\bar{\theta}_{m1}$ and $\bar{\theta}_{m2}$ are the nondimensional bulk temperatures at the inlet and outlet of the computational domain.

The channel and obstacle surfaces are treated as no-slip boundaries. All the walls are heated ($\langle\theta\rangle_w=0$). The normalized kinetic energy is set to zero at all solid surfaces while zero Neumann boundary conditions are used for the nondimensional dissipation. For near wall modeling, standard wall functions are used and grids are generated such that the Y^+ values of the near-wall grid point lie between 15 and 40.

Solution Method

The differential Eqs. (1)–(3) are solved on a staggered grid by using a modified version of the MAC algorithm of Harlow and Welch [21]. In the present study, convective and diffusion terms are approximated by a third-order upwinding scheme and a second-order central differencing scheme, respectively. An explicit, second-order, Adams–Bashforth differencing scheme is used for the time advancement of the convection and diffusion terms. Once the corrected velocities are obtained using continuity and momentum equations, the energy equation is solved using a second-order temporal (Adams–Bashforth) differencing scheme. The convective and diffusive terms of the energy equation are discretized using the third-order upwinding scheme of Kawamura et al. [22] and a second-order central differencing scheme, respectively. The details of the numerical method are described elsewhere [23].

The present simulations of the square duct are carried out using a grid size of 122×48×50 for the two inter-rib periodic modules. A nonuniform mesh with cells packed toward all the solid boundaries has been used to resolve the near-wall viscous effects. The results were tested for grid independence by comparing the results obtained for a single periodic module square duct with 50×32×42 and 62×48×50 grid cells. The finer grid contains over twice the number of total grid cells as the coarser grid, but the surface-averaged Nusselt number along the side walls show a difference of 2.7% while the leading and trailing walls reveal a discrepancy of 1.6% and 1.7%, respectively. The grid sizes for both one-rib and two-rib periodic module(s) are the same in the vertical and transverse directions, while in the streamwise direction the number of cells is doubled for the two-rib periodic module. Therefore, all the computations for two-rib periodic modules are carried out using a grid size of 122×48×50, and are expected to be grid independent. For a 1:4 AR duct, the grid points in the vertical–height direction are increased and a mesh size of 122×48×78 is

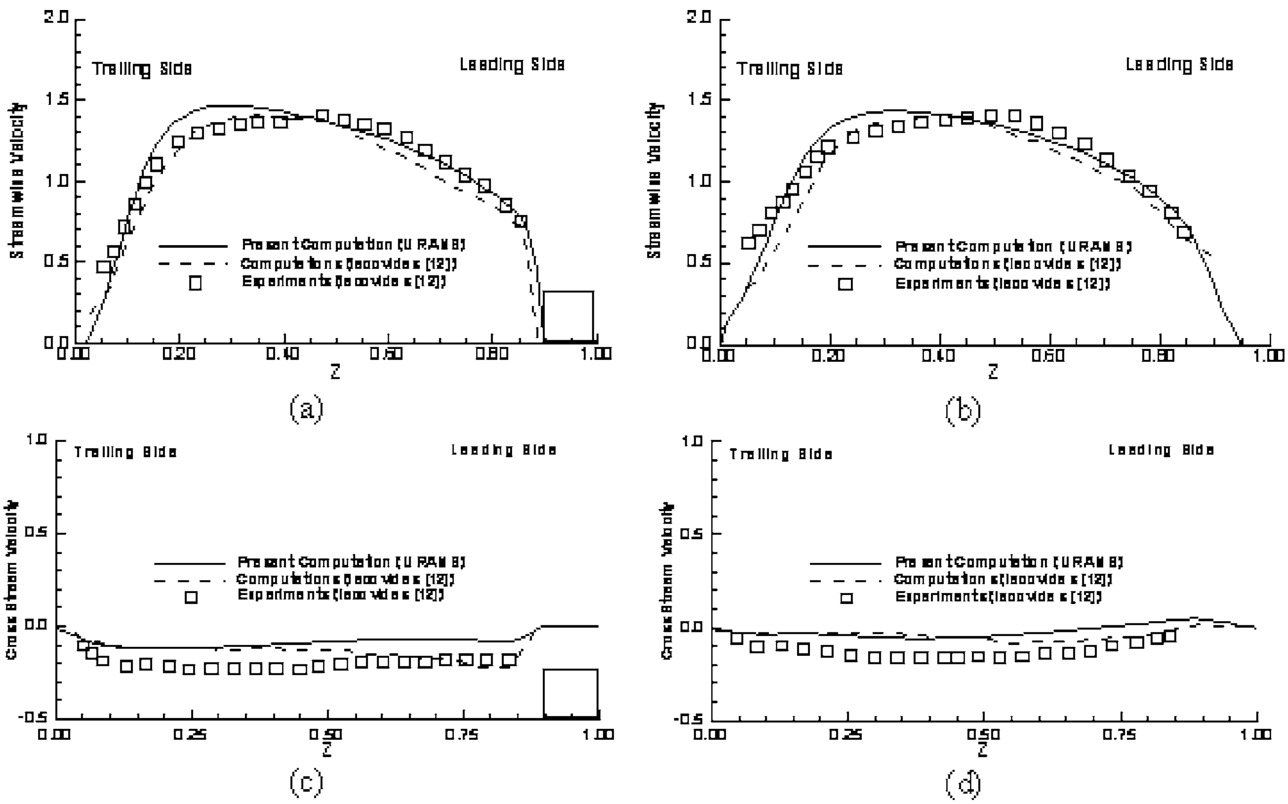

Fig. 2 Comparison of streamwise velocity and cross-stream velocity at (*a*) and (*c*) a streamwise location passing through the rib on the leading wall and (*b*) and (*d*) at a location in between the two consecutive ribs on leading and trailing wall

used, while for the 4:1 AR duct the grid points in the transverse-width directions are increased and computations are carried out using a mesh size of $122\times72\times58$.

Since the present method uses an explicit scheme, the time step is selected using a CFL (Courant-Frederich-Levy) criterion. Therefore, the time step used in the present study is in the range 0.0003–0.0005 depending on the Reynolds number, rotation number, and density ratio. For time-averaged statistics presented here, the averaging is done for at least 15 flow-through time periods which results in a total number of time steps in the range of $6\times10^4-10^5$.

Validation

The present code has been validated thoroughly for both the laminar and turbulent flow in a channel with periodic array of cylinders [23,24]. The code has also been validated against published results for the flow past a square cylinder placed in an infinite medium. The computed drag coefficient and the Strouhal number match the experimental results [25].

For the purposes of the present paper, the present code has been validated by comparing the present URANS predictions with published measurements and SRANS computations for rotating ribbed duct [12]. Figure 2 shows the comparison of the streamwise (Figs. 2(*a*) and 2(*b*)) and cross-stream velocities (Figs. 2(*c*) and 2(*d*)) at two different locations. It is to be noted that in Fig. 2, the origin of the z axis has been shifted to the trailing wall. The streamwise velocity of the present study matches better with experiments than the computations of Iacovides [12] at both locations. The cross-stream velocities are slightly underpredicted relative to the experimental values. However, the cross-stream velocities are relatively low in magnitude, and given the measurement and numerical uncertainties, this level of underprediction in the small v-velocity magnitude is acceptable.

Computations have also been carried out in a square ribbed duct for flow parameters that correspond to the experimental configuration of Johnson et al. [5]. The validation is carried out for 1:1 AR duct at various rotation numbers by comparing the results with experiments. Table 2 lists the Nusselt number ratio on both leading and trailing walls at various rotation numbers for both experiments and computations. At a Ro=0.12, the differences between the predictions and measurements are about 10% on the leading wall and 1.25% on the trailing wall. At Ro=0.25, the agreement with the measurements at Ro=0.22 exhibit a maximum difference of 12%. For stationary conditions, the agreement shows an average (for both ribbed surfaces) deviation of around 10%. This level of match in the measured and predicted Nusselt number is quite satisfactory and provides additional validation and confirmation of the numerical techniques and models utilized. The agreement of the predictions with respect to the measurements to within 12% should be viewed in the context of the experimental uncertainty which is itself on the order of 15% as reported in Ref.

Table 2 Comparison of measured[a] and predicted (present) Nu ratio at various rotation numbers

		Nusselt number, Nu/Nu_0			
		Leading wall		Trailing wall	
Aspect ratio	Rotation number	Present	Johnson et al.[a]	Present	Johnson et al.[a]
1:1	0.00	2.37	2.50	2.37	2.80
	0.12	1.71	1.91	3.17	3.21
	0.22		1.63		3.51
	0.25	1.84		3.54	
	0.32		1.65		3.94
	0.50	2.05		4.27	

[a] See Ref. [5].

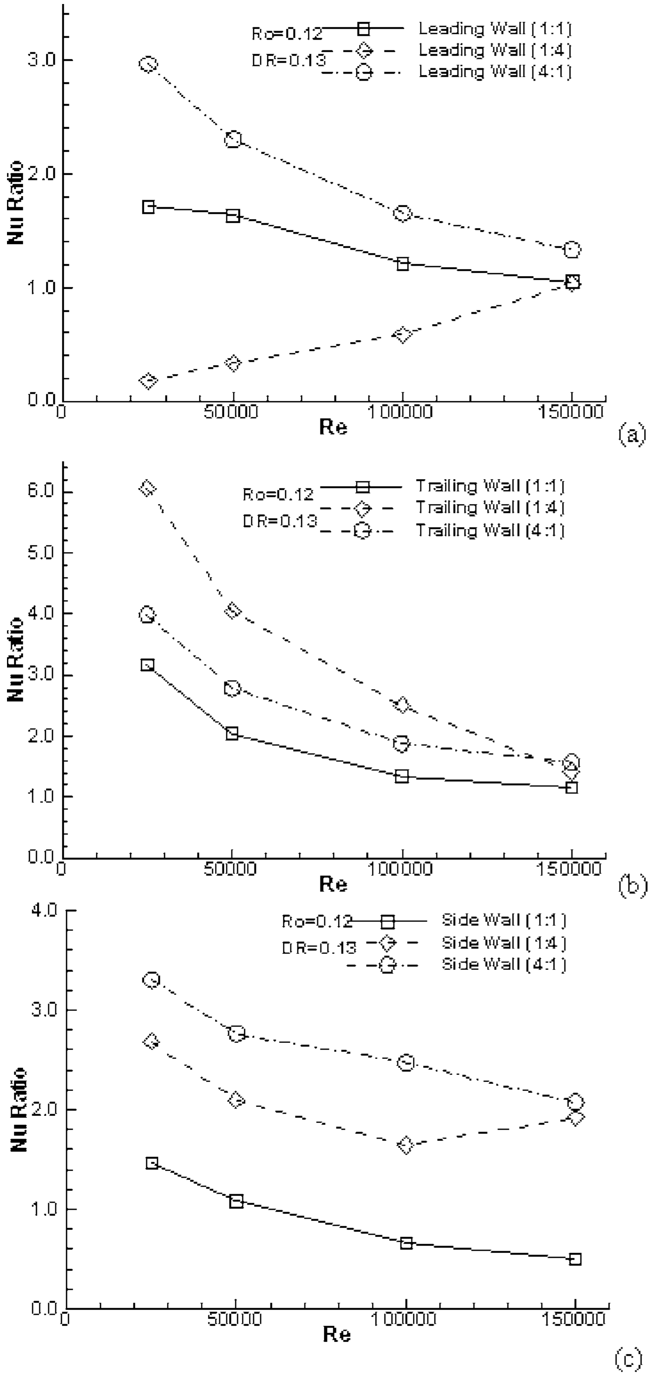

Fig. 3 Effect of Reynolds number on (*a*) leading wall; (*b*) trailing wall; and (*c*) side wall at various AR ducts for Ro=0.12 and DR=0.13

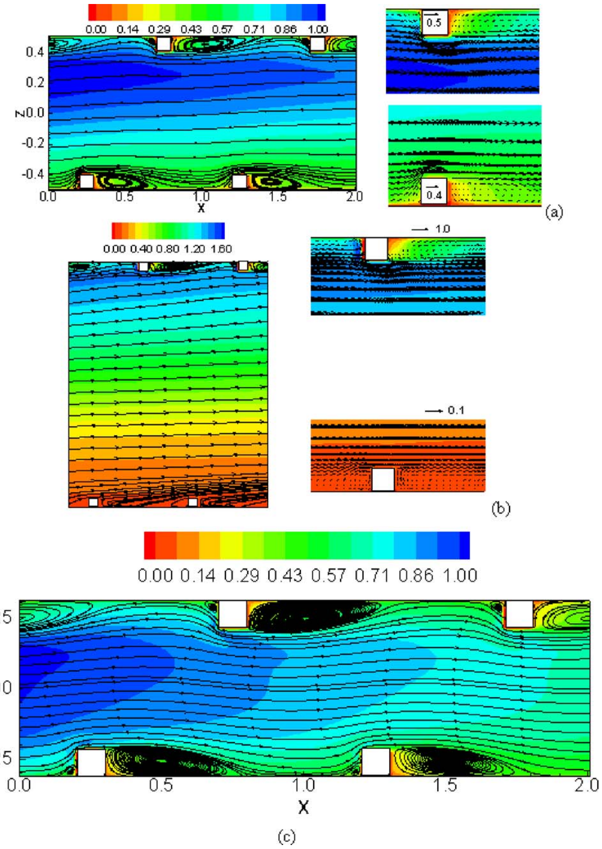

Fig. 4 Streamtraces and temperature contours at midtransverse plane for Re=25,000, Ro=0.12, and DR=0.13: (*a*) AR =1:1; (*b*) AR=1:4; and (*c*) AR=4:1

[5]. Therefore this level of agreement should be considered to be adequate justification for the use of the k-ε turbulence model used in this paper.

Results and Discussion

The time-averaged flow and heat transfer characteristics for the various aspect ratio rotating ribbed ducts is presented in this paper. For every aspect ratio, the effects of Reynolds number, rotation numbers, and density ratio are studied. The Reynolds number, rotation number, and density ratio considered for the present study are in the range of 25,000–100,000, 0–0.5, and 0–0.5, respectively. For comparison at various Reynolds numbers, the rotation number and the density ratio are fixed at 0.12 and 0.13, respectively. Similarly, a Reynolds number of 25,000 and a density ratio of 0.13 are chosen for studying the rotation number effect, while a Reynolds number and a rotation number of 25,000 and 0.12, respectively, are used to compare the flow and heat transfer characteristics at different density ratios.

Effect of Re. The Nusselt number normalized with respect to the smooth duct value, $\mathrm{Nu}/\mathrm{Nu}_0$, ($\mathrm{Nu}_0=0.0176\,\mathrm{Re}^{0.8}$) on the leading wall is presented in Fig. 3(*a*) for the three AR ducts. The Nusselt number ratio decreases with increasing Reynolds number for both the 1:1 and 4:1 AR duct while it increases for the 1:4 AR duct. For 1:4 AR, the heat transfer ratio is very low at the lower Reynolds numbers (about 0.3 at Re=25,000), due to near-stagnant flow or weak flow reversal near the leading wall. An increase in Re increases the flow velocities near the leading wall from the near-stagnant conditions at the lower Reynolds numbers, and therefore leads to substantial increases in the heat transfer. This leads to the observed increase in $\mathrm{Nu}/\mathrm{Nu}_0$ ratio with Re at this AR. At other ARs, the near-stagnant flow conditions and complete flow reversal near the leading wall is not obtained, and therefore increases in Nu with Re are more moderate, and offset by higher increases in Nu_0 with Re, leading to a decrease in $\mathrm{Nu}/\mathrm{Nu}_0$ with Re. The maximum heat transfer ratio for 1:4 AR is about 1.0 (at Re=150,000) while it is the highest for 4:1 (about 3.0 at Re =25,000). The dependence on Reynolds number is the largest for the 1:4 AR (with nearly a fourfold increase in $\mathrm{Nu}/\mathrm{Nu}_0$ over the Re range considered), intermediate for the 4:1 AR duct (with nearly a 50% corresponding decrease in $\mathrm{Nu}/\mathrm{Nu}_0$), and it is the lowest for 1:1 AR duct (with less than a 30% decrease in $\mathrm{Nu}/\mathrm{Nu}_0$ with Re).

The variation of Nusselt number ratio on the trailing wall with Reynolds number is shown in Fig. 3(*b*). For all AR, the Nusselt

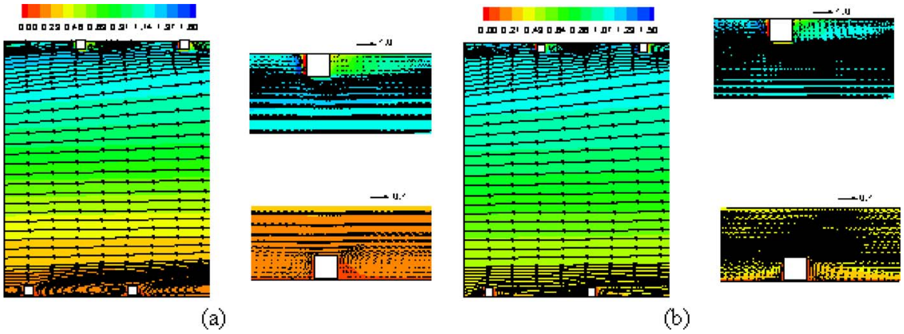

Fig. 5 Streamtraces and temperature contours at mid transverse plane for Ro=0.12 and DR=0.13 and (*a*) Re=50,000 and (*b*) Re=100,000; AR=1:4

number ratio decreases with increasing Reynolds number. Unlike the other two walls (leading and side walls) where the 4:1 AR duct shows the highest heat transfer, the trailing wall reveals the highest heat transfer for the 1:4 AR duct. Thus, the 1:4 AR duct shows the lowest heat transfer on the leading wall, but gives the highest heat transfer on the trailing wall. This observation is related to the magnitude of the velocity, since for the 1:4 AR duct the flow near the leading wall is the lowest and that near the trailing wall is the highest (about 1.8 in nondimensional units compared to the value of 1.3 for 1:1 AR duct). This higher momentum fluid near the trailing wall for 1:4 AR causes the higher heat transfer. The Nusselt number dependence on Re is also the highest for the 1:4 AR duct, but the Nu ratio asymptotes after a Re=100,000 for 1:1 and 4:1, while for 1:4 AR the Nusselt number ratio reveals a strong dependence on the Re for the whole Re regime studied in the present work. At the lowest Reynolds number (Re=25,000), the 1:4 AR duct shows the highest trailing-wall heat transfer, a ratio of

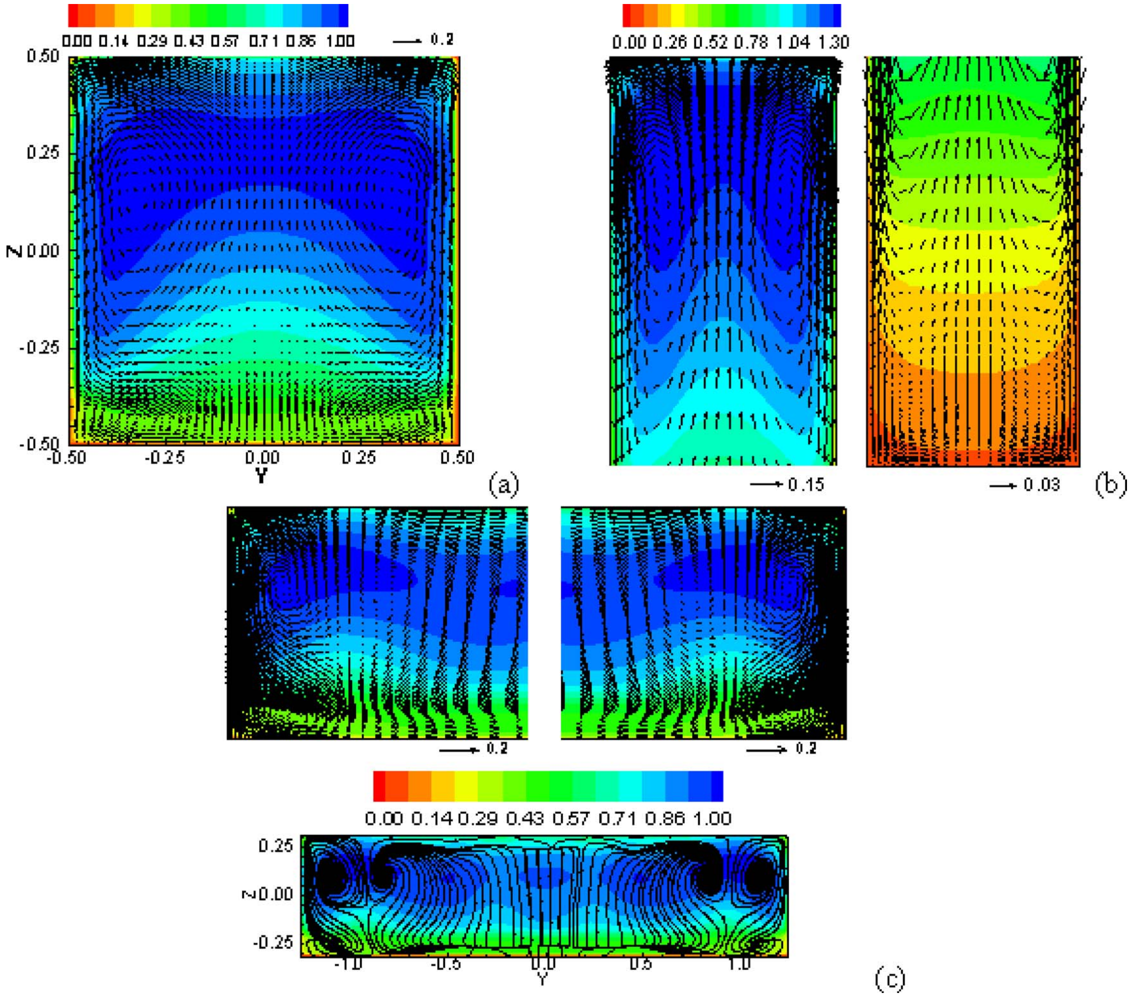

Fig. 6 Secondary flow structures superimposed on temperature contours at $x=0.5$ for Ro=0.12, DR=0.13, Re=25,000 for various aspect ratios: (*a*) AR=1:1; (*b*) AR=1:4; and (*c*) AR=4:1. Bottom surface is the leading wall.

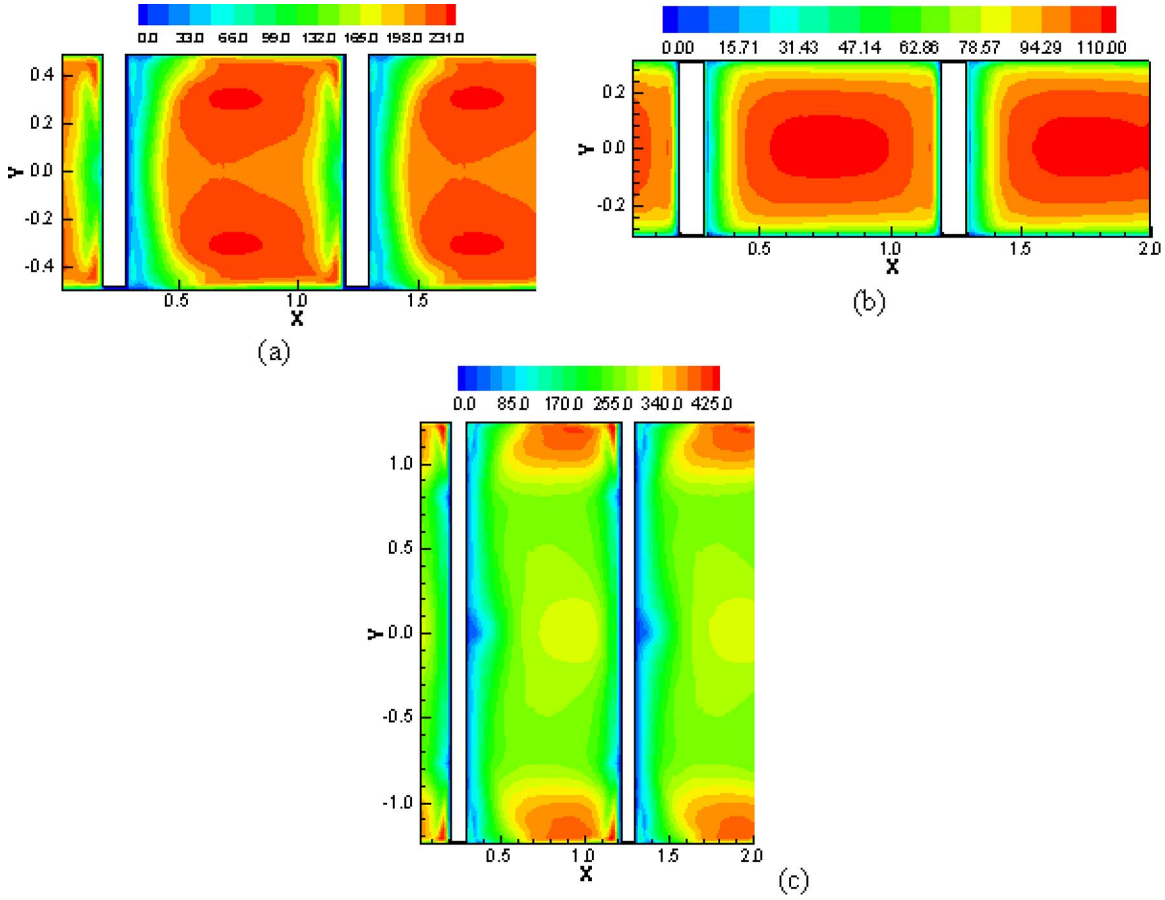

Fig. 7 Distribution of Nusselt number on leading walls at Re=100,000, Ro=0.12, and DR=0.13: (*a*) AR=1:1; (*b*) AR=1:4; and (*c*) AR=4:1

6.05, while the 1:1 AR duct gives the minimum heat transfer ratio of 3.16. However, with increasing Reynolds number the difference in heat transfer on the trailing wall between the different AR ducts decreases and becomes nearly the same (≈1.2–1.6), implying a decrease in the rotational effects.

Figure 3(*c*) presents the Nusselt number ratio as a function of Reynolds number on the sidewall. There is a consistent trend of heat transfer ratio decreasing with Reynolds number for both 1:1 and 4:1 AR ducts. However, for the 1:4 AR duct, the heat transfer ratio decreases up to a Reynolds number of 100,000 and then shows an increase with Re. The 4:1 AR shows the highest heat transfer (Nu ratio: 2.17 to 3.18) on the sidewalls followed by the

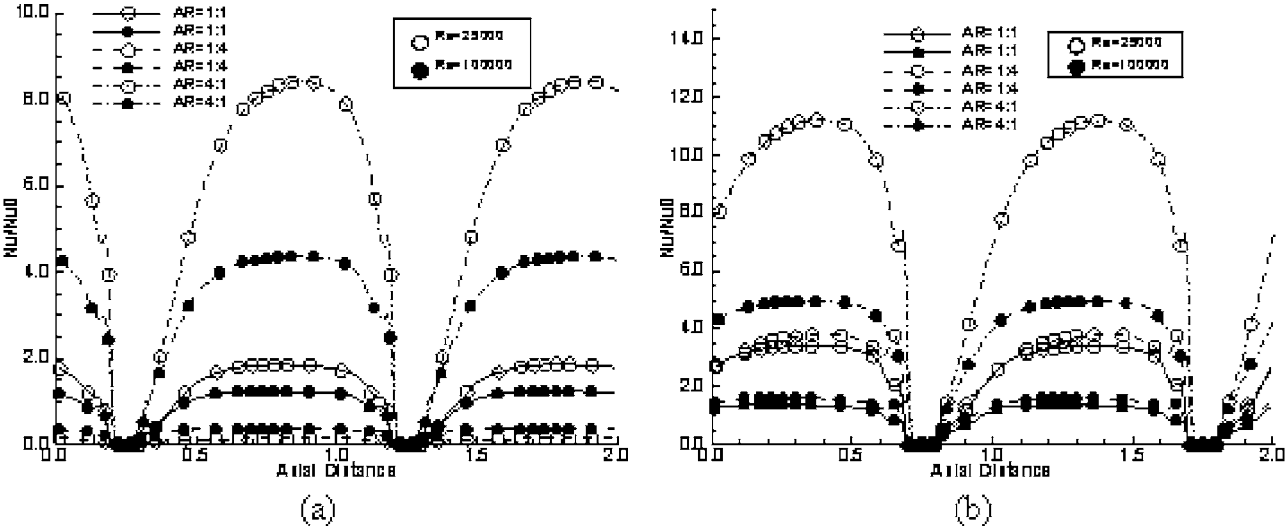

Fig. 8 Axial variation of spanwise averaged Nusselt number on: (*a*) leading wall; and (*b*) trailing wall at various aspect ratios (AR) for Re=25,000 and 100,000 and Ro=0.12 and DR=0.13

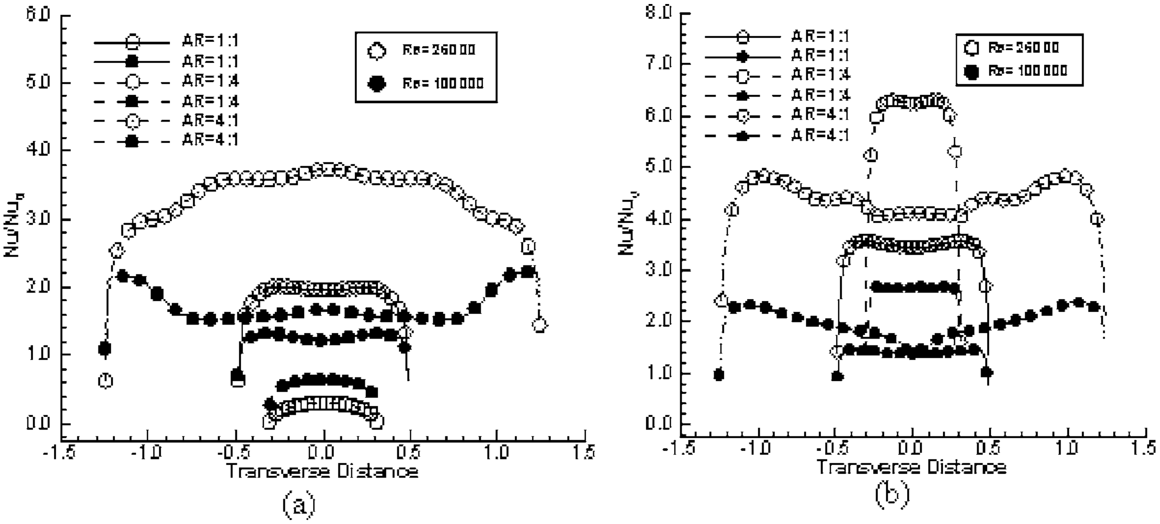

Fig. 9 Transverse variation of local Nusselt number on: (*a*) leading wall; and (*b*) trailing wall at various aspect ratios (AR) and Re=25,000 and 100,000 and Ro=0.12 and DR=0.13

1:4 AR duct (Nu ratio: 1.91 to 2.61) while the 1:1 AR duct reveals the lowest heat transfer ratio in the range of 0.50 to 1.46. At the highest Re, the side wall Nu/Nu$_0$ becomes comparable in value to the ribbed trailing wall for the 4:1 and 1:4 ARs, while for the 1:1 AR the sidewall exhibits lower Nu/Nu$_0$ values relative to the trailing and leading surfaces.

Figure 4 presents the streamtraces superimposed on the temperature contours at the midtransverse plane at Re=25,000, DR=0.13, and Ro=0.12 for various AR ducts. The 1:1 AR (Fig. 4(*a*)) and 4:1 AR (Fig. 4(*c*)) ducts show a similar flow pattern, that of flow separation at the front edges of the ribs and subsequent reattachment on the leading/trailing walls. No significant differences in this flow pattern are seen at higher Re, and therefore are not presented here. However, the 1:4 AR duct does not show reattachment at the leading wall (Fig. 4(*b*)). In the inter-rib region along the leading wall, the flow exhibits a three-dimensional (3D) separation, as evidenced by the saddle point in Fig. 4(*b*), due to the effect of the opposing centrifugal buoyancy and Coriolis forces. The 1:4 AR duct shows the most significant effect of rotation (in terms of the differences along the leading and trailing surfaces) due to its longer transverse length in the direction of rotation. Further, the streamlines near the leading wall show structural changes with increasing Re (due to competition between inertial and buoyancy forces) as opposed to the other two ARs where no structural changes in the flow pattern are observed with increasing Re. This is illustrated in Fig. 5 which shows the streamtraces superimposed on the temperature contours at the midtransverse plane for the 1:4 AR at Re=50,000 and 100,000 (DR=0.13, Ro=0.12). With increasing Reynolds number (Re=100,000), the separated flow bends further toward the leading wall, thus giving a smaller transverse recirculation region between the two ribs. However, the flow is fully separated between the ribs, exhibits characteristics of a cavity flow, and appears more 2D in nature (no saddle points in the mid transverse plane as seen in Fig. 4(*b*)). The comparison of Figs. 4(*b*) and 5 at the three different Reynolds number suggests that the flow near the wall largely depends on the ratio of the inertia and the buoyancy force. If buoyancy force dominates over the inertial force the flow has a tendency to separate within the bulk flow (shown later in Fig. 16 while discussing the effect of density ratio). At low Re, the buoyancy force at high Ro and DR dominates near the leading wall and leads to a situation of near-stagnant flow or flow reversal in the bulk flow. As Reynolds number increases, the increasing inertia force counteracts the buoyancy force and flow reversal is restricted to the inter-rib region. However, even at Re=100,000, the flow near the leading wall of the 1:4 AR does not show any sign of reattachment (unlike the other two AR cases). Instead of reattachment, as in a backstep flow, the flow near the leading wall exhibits characteristics of an open-cavity flow, and Fig. 5 indicates that there is communication in the flow between adjacent cavities.

The secondary flow structures and the temperature contours at $x=0.5$ have been shown in Fig. 6 for the three AR ducts and Re=25,000 (DR=0.13, Ro=0.12). For both 4:1 and 1:1 ARs, at this x location, the flow near the leading wall is separated while that near the trailing wall is attached. For all ARs, the Coriolis force results in the generation of secondary flows directed upward toward the trailing wall and descending along the sidewalls. This causes the migration of the colder core flow toward the trailing surface, leading to higher heat transfer coefficients at this surface. Where the flow is separated near the leading wall, a Coriolis component toward the leading wall is also generated leading to counter-rotating eddies near the leading wall as seen in Fig. 6(*a*). Unlike the 1:1 and 1:4 AR ducts, the 4:1 AR duct shows multiple vortices along its span, which results in the better mixing of fluid between the leading and trailing walls, and causes a smaller variation of heat transfer between the two walls. For the 4:1 AR, the strong secondary vortices seen just adjacent to the two sidewalls cause the sidewall heat transfer to become the highest for this AR as observed earlier in Fig. 3(*c*).

The variation of Nusselt number along the leading walls for the three AR ducts is presented in Fig. 7 for Re=100,000, DR=0.13, and Ro=0.12. The heat transfer is highest in the region where the flow reattaches and is low in the recirculation region behind each rib. The 1:1 AR duct shows two lateral patches of high heat transfer between two consecutive ribs where the flow reattaches (due to the counter-rotating secondary eddy structure near the leading wall in Fig. 6(*a*)) but the 1:4 AR duct shows one single zone of high heat transfer between the ribs. However, the 4:1 AR duct characterized by a multiple-roll secondary flow pattern, shows three lateral zones of high heat transfer with the highest heat transfer zones closer to the sidewalls. The overall leading wall heat transfer (Nu) for 1:1, 1:4, and 4:1 AR ducts are calculated be 70.25, 34.26, and 96.38, respectively. The 1:4 AR duct shows the lowest heat transfer because of the large separation region spanning the entire inter-rib cavity near the leading wall as shown in Fig. 6.

The axial variation of the spanwise-averaged Nusselt number ratio on both leading and trailing walls is shown in Fig. 8 for the different AR ducts and two Reynolds numbers of 25,000 and 100,000 (Ro=0.12 and DR=0.13). The Nu/Nu$_0$ on the rib surface

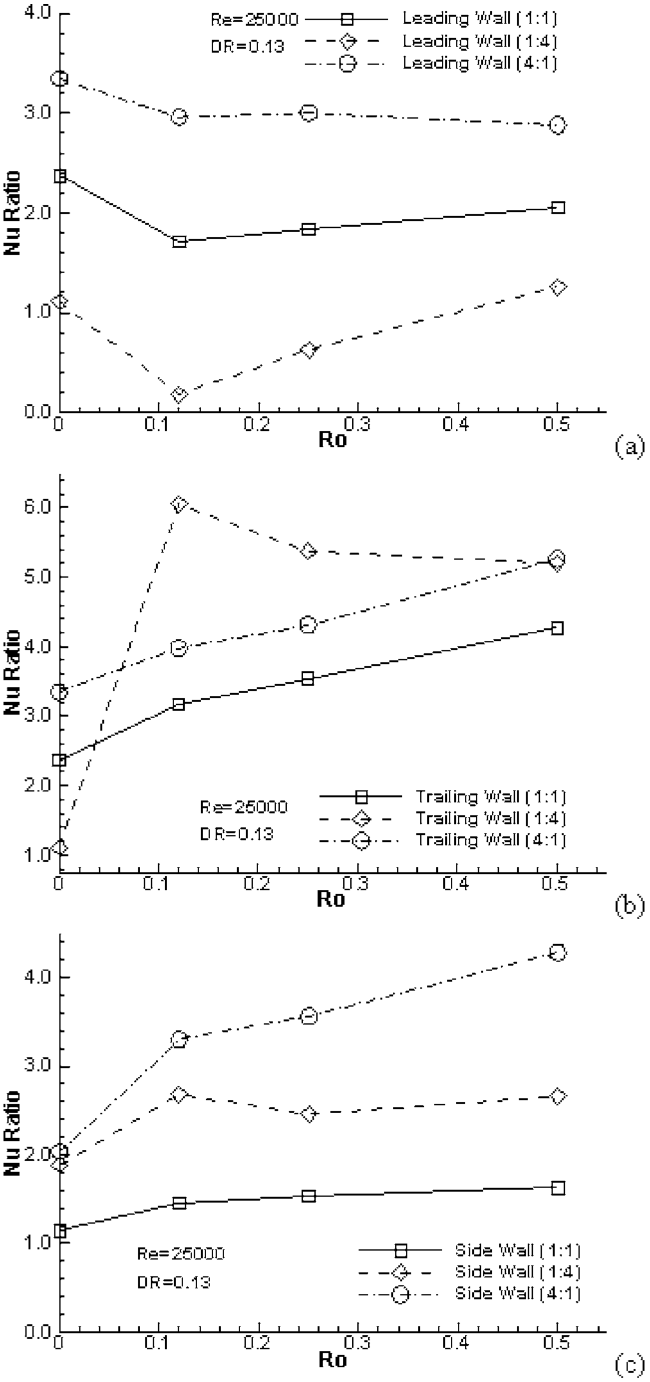

Fig. 10 Effect of rotation number on: (*a*) leading wall; (*b*) trailing wall; and (*c*) sidewall at various AR ducts and Re=25,000 and DR=0.13

is not shown for clarity. The heat transfer on both walls shows similar qualitative distributions. The heat transfer peaks in-between the ribs where the flow reattaches and is low in the separation zones immediately ahead and behind each rib. In general, the Nusselt number decreases with Reynolds number on both the leading and trailing walls. The exception to this observation is the leading wall distribution for the 1:4 AR duct, which shows a lower heat transfer ratio at the lower Reynolds number. For this 1:4 AR case, as noted earlier, due to buoyancy-induced flow separation, the leading wall heat transfer is very low. On the other hand, the 4:1 AR duct gives the highest heat transfer with a significant difference between the two Reynolds number values. The heat transfer on the trailing wall for 1:4 AR duct is less than the 4:1 AR duct but comparable to the 1:1 AR duct.

Figure 9 shows the transverse local Nusselt number ratio distribution on both leading and trailing walls for various AR ducts and two Reynolds numbers. Except at the corners, the distribution does not show significant variation along its span for 1:1 and 1:4 AR ducts. However, moderate variation (20–40%) in the heat transfer along the transverse direction is observed for the 4:1 AR duct. The reason is due to the longer span that accommodates multiple secondary rolls.

Effect of Ro. The effect of rotation number on the leading wall for the three AR ducts is illustrated in Fig. 10(*a*). At no rotation, the leading wall heat transfer ratios for the 1:4, 1:1, and 4:1 AR ducts are 1.10, 2.37, and 3.34 respectively. This trend with the leading wall heat transfer being the highest for the 4:1 AR duct and being the least for the 1:4 AR duct is related, in part, to the blockage ratios (highest for 4:1 and lowest for 1:4) and the secondary-flow structure, and holds at all rotation numbers. For all ARs, the Nusselt number ratio drops initially from the stationary value to a minimum at a Ro near 0.12 due to the Coriolis-generated secondary flows that reduce the flow velocity near the leading wall (Fig. 10(*a*)). For the 1:4 AR duct, with the lowest leading wall heat transfer at no rotation, a further reduction in the flow velocity near the leading wall with rotation leads to very low velocities, and the Nu ratio at Ro=0.12 is as low as 0.18 (below smooth duct value). For this AR, with increasing rotation number, the flow near the leading wall reverts to a radially inward flow (see Fig. 4(*b*) very close to the leading surface and Fig. 16 where bulk-flow separation extends above the ribs) due to the action of the centrifugal buoyancy. Therefore, at some critical Ro (for a given Re and DR), portions of the leading wall can potentially experience stagnant flow and conduction-limited heat transfer. For all ARs, an increase in rotation number to 0.25 and beyond brings about an increase in the leading wall heat transfer. A similar behavior of an initial drop in the leading wall heat transfer with increasing rotation number up to certain rotation number (Ro $\leqslant 0.2$) was reported by Johnson et al. [5] for 1:1 AR smooth and ribbed ducts. Our present computations with the ribbed ducts of different ARs show the decrease in Nu occurs up to a Ro near 0.12 (in the range of 0.12–0.25). At high rotation numbers (>0.25), the combined effects of Coriolis and buoyancy cumulatively produce marginal changes in the Nu value (AR of 1:1 and 4:1) or produce enhancement in the leading wall Nu (AR of 1:4) with increasing Ro. The enhancement in the Nu value for rotation number beyond 0.12 is quite significant for the 1:4 AR duct, and is due to the increased strength of the backflow along the leading wall with the increase in rotation number (or buoyancy parameter). Further, due to the reverse flow along the leading wall for the 1:4 AR duct, the direction of Coriolis force reverses in the region where the axial velocity is negative and is directed toward the leading surface which generates multiple vortices near the leading wall as is seen in Fig. 12. These leading wall secondary vortices intensify with Ro (since Coriolis forces are proportional to both the backflow velocity and the rotational speed), contributing, in part, to the increased heat transfer rates along the leading wall beyond a rotation number of 0.12.

Figure 10(*b*) presents the variation of Nusselt number ratio on the trailing wall for various AR ducts as a function of the rotation number. At no rotation the 1:4 and 4:1 AR ducts show the lowest and the highest heat transfer, respectively, but with rotation the heat transfer for 1:4 AR shoots up significantly and becomes the highest among the three AR ducts. For the 1:1 and 4:1 AR ducts, the trailing surface shows a continuous increase in Nusselt number ratio as the rotation number is increased. This is expected since the rotation-induced secondary flows push the cold core fluid toward the trailing wall and increases the velocities and turbulent fluctuations near the trailing wall. Surprisingly, the Nu ratio for the 1:4 AR duct drops and becomes nearly asymptotic beyond

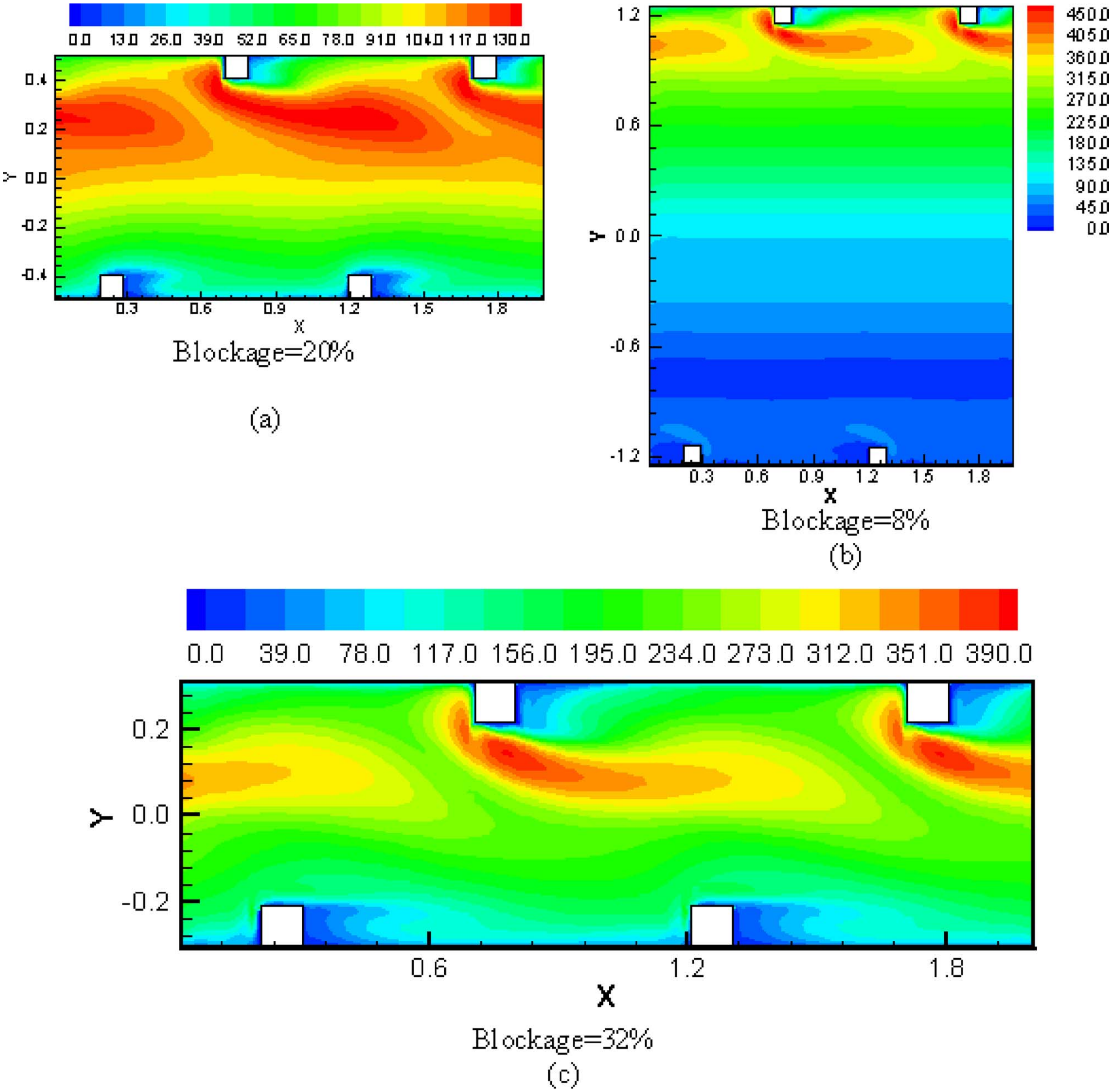

Fig. 11 Distribution of Nusselt number on sidewall at Re=25,000, Ro=0.25, and DR=0.13 at various aspect ratios: (*a*) AR =1:1; (*b*) AR=1:4; and (*c*) AR=4:1

a rotation number of 0.25. Reasons for this are provided later.

The effect of rotation number on the heat transfer along the two sidewalls is shown in Fig. 10(*c*). At no rotation, both the 1:4 and 4:1 AR show almost equal heat transfer ratio (≈1.9) while the 1:1 AR duct shows a lower value of 1.1. At a Ro=0.12, the heat transfer shoots up the most for 4:1 AR duct which shows a relative increase in heat transfer of about 62% relative to no rotation. The corresponding relative increase for the 1:1 AR is 28% while it is 42% for the 1:4 AR duct. Beyond Ro=0.12, the Nusselt number ratio is seen to increase with rotation number for all ARs except for the 1:4 AR duct where, at Ro=0.25, a slight decrease is observed. This decrease in Ro=0.25 is because of the weak (near-stagnant conditions) reversed flow near the leading wall, as a result of which, the regions on sidewalls near the leading wall shows low heat transfer. This observation is supported by the Nusselt number distribution on the sidewalls for the various AR ducts shown in Fig. 11 where, for the 1:4 AR duct (Fig. 11(*b*)), extremely low values of the Nusselt number are observed in the entire lower half region of the duct. In Fig. 11 (Ro=0.25), it can be seen that the shear layers that separate at the front edges of the trailing surface ribs result in high heat transfer rates on the sidewalls. The heat transfer distribution near the leading wall for the 1:1 and 4:1 AR ducts also reveals low values and recirculation zones in the vicinity of the ribs. The 4:1 AR duct gives high heat transfer on the sidewalls (average Nu=206.8) because of the strong secondary flow vortices adjacent to the sidewalls (see Figs. 6 and 12(*c*)). The fact that the 1:4 AR heat transfer ratios along the sidewall are higher (average Nu=142.9) than the corresponding 1:1 AR (average Nu=89.3) values is a consequence of much higher heat transfer ratios for the 1:4 in the upper half of the sidewall (compare peak values in Figs. 11(*a*) and 11(*b*)) resulting partly from the stronger primary flow near the trailing surface which, in turn, is due to the reversed flow near the leading surface (mass flow rate being held constant).

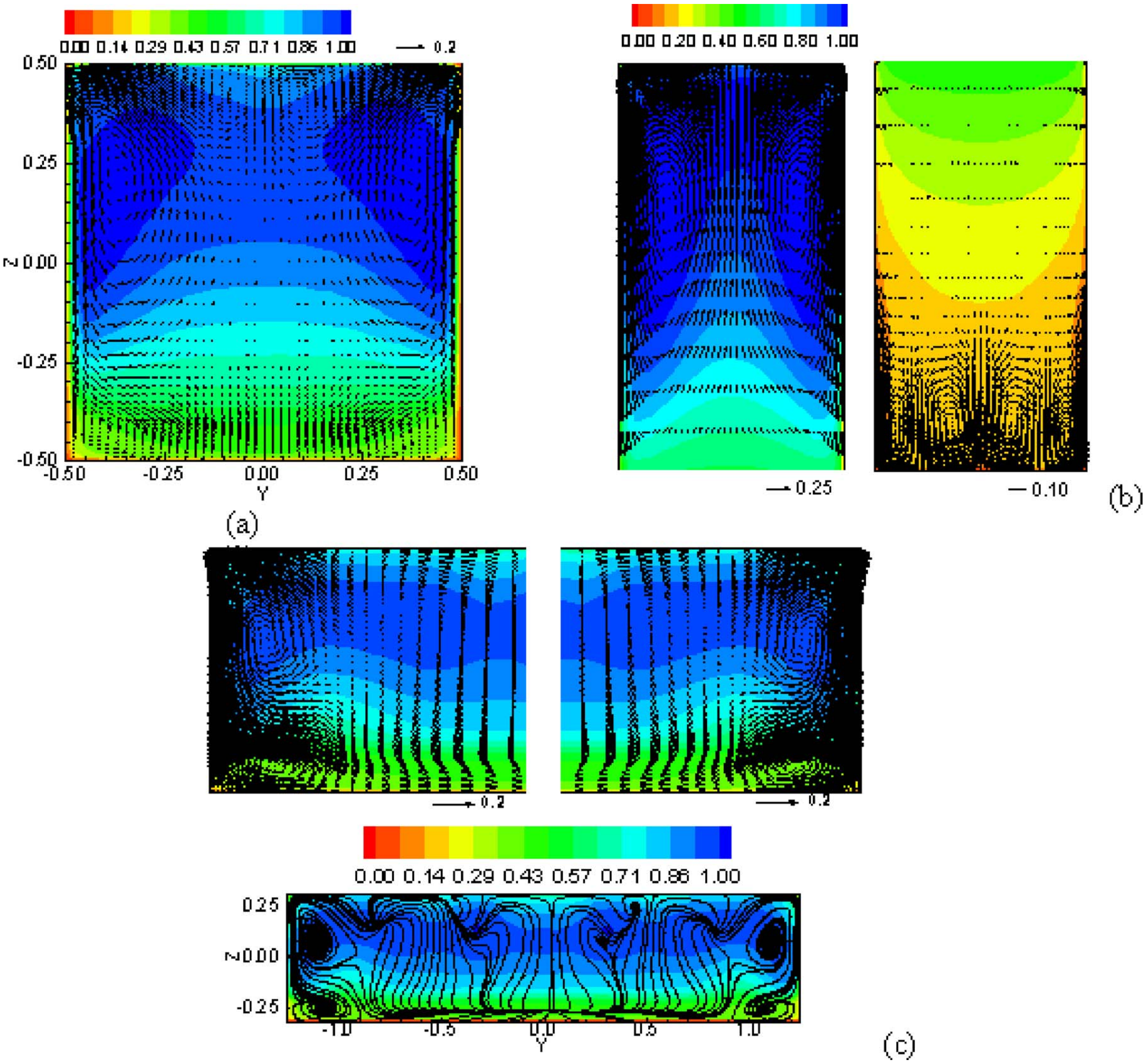

Fig. 12 Secondary flow structures superimposed on temperature contours at $x=0.5$ for Re=25,000, Ro=0.25, and DR=0.13 for various aspect ratios: (*a*) AR=1:1; (*b*) AR=1:4; and (*c*) AR=4:1

Figure 12 presents the cross-stream secondary flow structures along with the temperature contours superimposed for all three ARs. Comparison of secondary flow at two rotation numbers (Fig. 6 for Ro=0.12 and Fig. 12 for Ro=0.25) reveals the significant differences in the flow structures near the leading surface of the 1:4 AR duct. Due to the backflow at high rotation number, the flow near the leading wall sees Coriolis forces directed toward the leading wall. Therefore, the secondary flow near the leading wall shows a strong downwash with the formation of multiple vortices (Fig. 12(*b*)) that increase the heat transfer near the leading wall (Fig. 10(*a*)). For the 1:1 AR duct, the flow structures at the higher rotation number indicates that the center of the counter-rotating vortices moves slightly nearer to the trailing wall and toward the sidewalls leading to the formation of an additional pair of vortices near the midregion of the trailing wall (compare Figs. 12(*a*) and 6(*a*)). Comparison of the secondary structures for the 4:1 AR duct

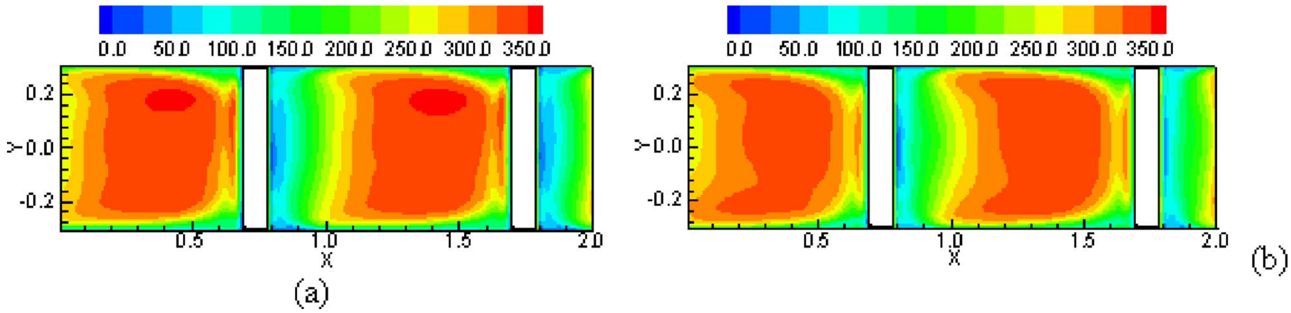

Fig. 13 Contours of time-averaged Nusselt number for 1:4 AR duct on trailing wall at Re=25,000 and DR=0.13 for: (*a*) Ro =0.25; and (*b*) Ro=0.50

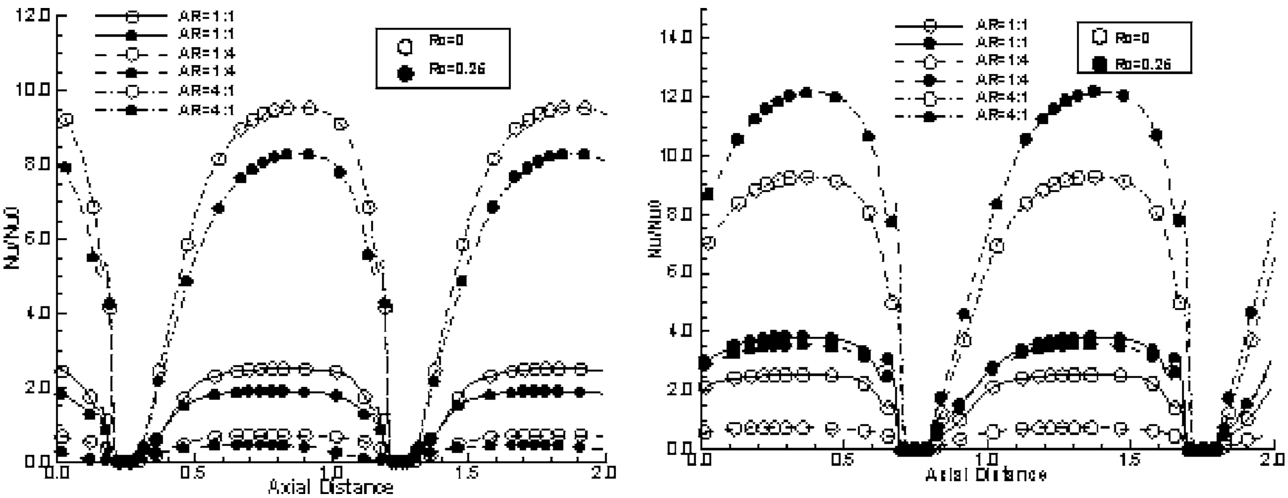

Fig. 14 Axial variation of spanwise averaged Nusselt number on: (*a*) leading wall; and (*b*) trailing wall at various aspect ratios (AR) and Ro=0 and 0.25 (Re=25,000 and DR=0.13)

at the two rotation numbers do not reveal any noticeable topological variation, although the positions and orientation of the rolls are different at the two rotation numbers. The lack of symmetry around the $y=0$ plane is caused due to low-frequency (long time period) unsteadiness associated with the flow, and the inadequate averaging time (the same averaging time as for the AR 1:1 and 1:4 was used).

In Fig. 10(*b*) it was shown that the trailing wall heat transfer rate for the 1:4 AR rapidly asymptotes beyond Ro=0.12, and further increases in Ro do not appear to produce a considerable change in the trailing wall heat transfer. This is further illustrated in Fig. 13 which shows the Nusselt number distribution on the trailing wall at Ro=0.25 and 0.5 for the 1:4 AR duct. The Nusselt number values and distributions appear to be quite similar to each other. With increasing Ro, the backflow (radially inward) flow near the leading wall becomes stronger, and correspondingly, the radially outward flow near the trailing wall has higher velocity magnitude. However, the secondary flow pattern is also influenced by rotation and a slightly larger separated flow region (where Nu values are low) is observed behind the rib as evident in the Nu contours in Fig. 13. The above factors counter each other, and contribute to the observed insensitivity to Ro.

The axial variation of spanwise averaged Nu ratio on both leading and trailing walls for the three AR ducts at two different rotation numbers, namely 0 and 0.25 (Re=25000 and DR=0.13), is shown in Fig. 14. As observed earlier in the surface-averaged Nu ratio, there is a decrease in the Nu ratio along the leading wall with increasing rotation number for all AR ducts. On the other hand, the increase in rotation results in an increase in the trailing wall Nu ratio for all AR ducts, with the percentage increase largest for the 1:4 AR duct and the least for the 4:1 AR duct.

Effect of DR. The effect of buoyancy is presented here by varying the DR at a constant rotation number. Centrifugal-buoyancy effects are often represented by a buoyancy parameter which varies linearly with the density ratio and as the square of the rotation number. However, since in the comparisons shown below, the rotation number is held fixed (Ro=0.12), the variation of density ratio is directly proportional to the variation of the buoyancy parameter.

The effect of density ratio on the heat transfer along the leading wall is depicted in Fig. 15(*a*). The DR effect (at Ro=0.12) does not appear to be significant on the average Nu for the 1:1 and 4:1 ARs. The most noticeable effect appears to be for the 1:4 AR duct which shows a slight decrease in heat transfer up to an intermediate DR (≤ 0.25) and then increases with further increase in DR. Along the trailing wall (Fig. 15(*b*)), the relative increase in the Nusselt number ratio is quite significant for the 1:4 AR duct up to a DR range of 0.13, while for the other two AR ducts the Nu ratio is fairly constant with respect to DR. Figure 15(*c*) shows the variation of Nusselt number ratio on the sidewall with density ratio. The 1:1 AR does not show any observable effect of the density ratio, while the 1:4 and 4:1 AR ducts show a small decrease in the Nusselt number with Ro.

From Fig. 15, it is quite obvious that the 4:1 AR duct has the weakest dependence on density ratio and the DR effect increases with decreasing AR. Since the 1:4 AR shows the greatest dependence on DR, only the 1:4 AR case is discussed in detail here. Figure 16 illustrates the effect of density ratio on the flow structures and heat transfer for the 1:4 AR. Comparison of Figs. 4(*b*) and 16 clearly reveals the significance of the density ratio at this AR. With no density ratio (Fig. 16(*a*)), both the leading and trailing wall regions show radially outward flow (positive axial velocity) without any sign of bulk-flow reversal. As discussed earlier, buoyancy causes the flow near the leading wall for the 1:4 AR duct to separate in the inter-rib region, and at certain values of rotation numbers (in the range of 0.12–0.25 at Re=25,000, DR =0.13), this leads to low heat transfer rates (Fig. 3(*a*), 10(*a*), and 15(*a*)). However, as the rotation number or DR is increased, the heat transfer increases along the leading wall since the reversed bulk flow near the leading wall becomes stronger (compare Fig. 4(*b*) at DR=0.13 with Fig. 16(*b*) at DR=0.25). This is why the heat transfer on the leading wall decreases up to a certain density ratio ($DR \leq 0.12-0.25$) and increases with further increase in the density ratio. Comparing the secondary flow structures in Figs. 16(*a*) and 16(*b*) reveals the weaker secondary vortices (compare the size of the arrow vectors) and streamwise velocities near the leading wall at the higher DR. Due to the reversed flow along the leading wall at the higher DR, the secondary flow near the leading wall exhibits a downwash toward the wall with small corner vortices. With increasing buoyancy parameter, these corner vortices amplify and become stronger, leading to a complex secondary flow pattern near the leading surface with multiple pairs of vortices (see Fig. 12).

The axial distribution of spanwise-averaged Nusselt number on both leading and trailing walls at four DRs, namely 0, 0.13, 0.25, and 0.50 (Re=25000 and Ro=0.12) has been shown only for 1:4 AR ducts in Fig. 17. Since the other AR ducts do not show as significant a variation with density ratio, they are not included in the discussion. At the leading wall (Fig. 17(*a*)), there is an initial drop in the Nu ratio as the DR is increased from 0 to 0.13. This

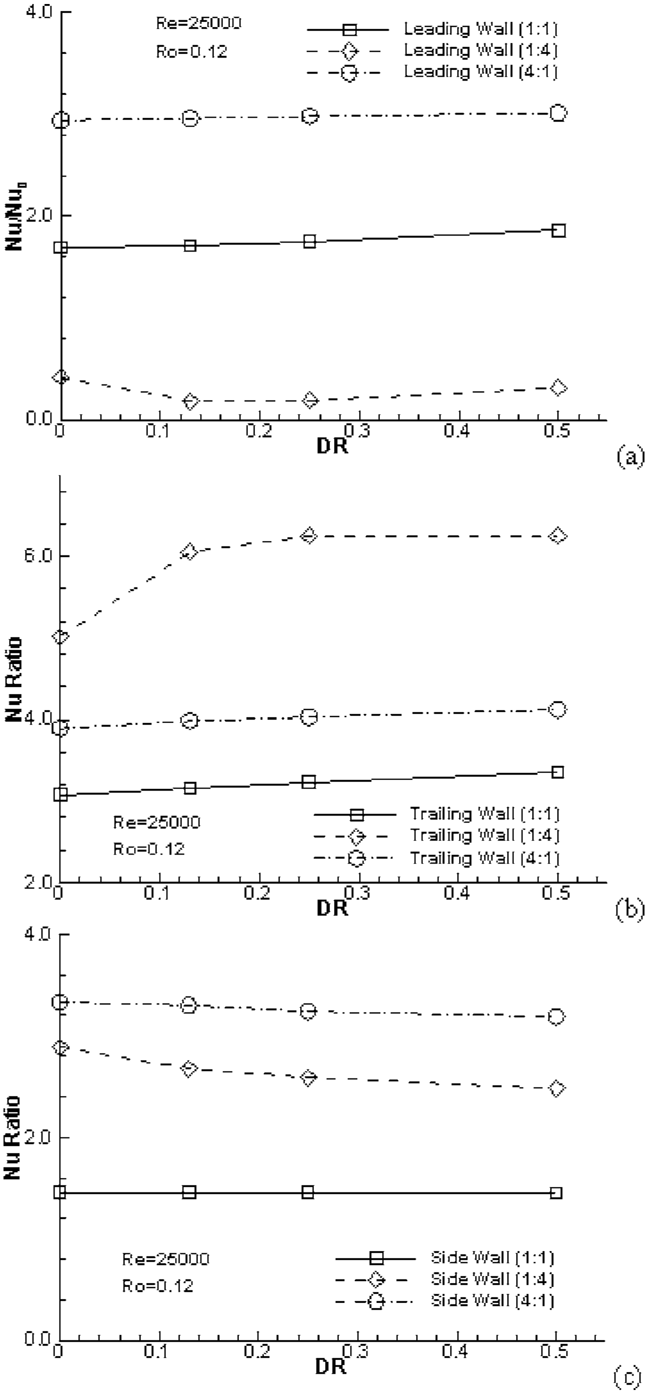

Fig. 15 Effect of density ratio on: (*a*) leading wall; (*b*) trailing wall; and (*c*) sidewall at various AR ducts for Re=25,000 and Ro=0.12

drop is associated with the decrease in the near-leading-wall velocity due to centrifugal buoyancy effects. In the DR =0.13–0.25 range, the Nu ratios are extremely small due to near-stagnant or weakly reversed flow conditions along the leading wall. As mentioned earlier, with a further increase in density ratio, the back flow strengthens, and consequently the leading wall experiences higher momentum fluid leading to increased leading wall Nu values. Therefore, as DR is increased to 0.5, the Nu ratio increases with increasing density ratio. Note that while the percentage increase in the peak Nu ratio along the leading wall is high (over 150%), the Nu ratios themselves are still below 1 due to the flow reversal. The trailing wall shows a more monotonic behavior, with an increase in the Nu ratio with DR. As seen in Fig. 17(*b*), between a DR=0 and 0.25, there is nearly a 25% increase in the peak Nu value. This increase certainly has to do with the upward shift of the core flow toward the trailing wall with increasing DR due to the associated decrease in velocity and flow reversal along the leading wall (since mass flow is a constant). However, this increase in the Nu ratio appears to plateau beyond a DR of 0.25 (implying a balance of competing effects), and the Nu ratio remains almost constant in the DR range of 0.25–0.5.

Conclusions

The flow and heat transfer in a ribbed duct of aspect ratios 1:1, 4:1, and 1:4 are investigated numerically. The Reynolds number, the rotation number, and the density ratio are varied parametrically to observe their effects on the Nusselt number for each AR duct. The following are some key observations made in the present study:

1. Under rotational conditions, the 4:1 AR has the highest Nu ratio along the leading and side walls, while the 1:4 AR has the highest trailing wall Nu ratio. The commonly studied 1:1 AR case has the lowest trailing wall and sidewall Nusselt number ratios. The 1:4 AR has the lowest leading wall Nu ratio due to the effects of the opposed centrifugal-buoyancy force and flow reversal along the leading wall. In general, the average Nu (overall walls) is the highest for the 4:1 AR. Therefore, from a design perspective, higher ARs should be preferred.
2. For all ARs, the heat transfer along the leading and trailing walls shows a strong dependence on Reynolds number. Except for the leading and sidewalls of the 1:4 AR, the Nu ratio decreases with Re. In the vicinity of the leading wall for the 1:4 AR, where flow reversal occurs and Nu ratios are low, increasing Re leads to the strengthening of the near wall flow, and leading wall Nu ratio increases significantly with Re.
3. With rotation, the Nu ratio along the leading wall shows an initial decrease for all ARs up to a Ro of 0.12. This is attributed to the Coriolis-driven secondary flows that direct flow away from the leading surface, and the opposing action of centrifugal buoyancy. However, for Ro=0.25 and beyond, the leading wall Nu ratio for the 1:4 AR shows a significant increase, while the 1:1 and 4:1 AR cases show very small dependence on Ro. Along the trailing and side walls, the 1:1 and 4:1 AR cases exhibit a monotonic increase in the Nu ratio with Ro, while the 1:4 AR shows a sharp increase in the Nu ratio up to a Ro=0.12, followed by a modest decrease with Ro.
4. The effect of centrifugal buoyancy and density ratio is most significant for the 1:4 AR duct where the near-leading-wall flow velocities are reduced to the greatest extent by the Coriolis driven secondary flows. This is detrimental for situations with large load variability (or large changes in rotation number) where the cooling may change significantly with rotational speeds.
5. The 1:4 AR duct shows flow reversal at high rotation number with multiple rolls in the secondary flow structures near the leading wall. The relative difference between the trailing and leading wall heat transfer is the highest in the 1:4 AR duct, indicating the important role of Coriolis driven secondary flows for this case. For certain critical parameter values (low Re, high Ro, and/or DR), the leading wall flow is expected to become nearly stagnant, due to the action of centrifugal buoyancy, leading to conduction-limited heat transfer. Such situations may cause overheating and material failure. Therefore, for tall coolant passages with ARs on the order of 1:4–1:6 particular attention should be paid to enhance the heat transfer along the leading wall.

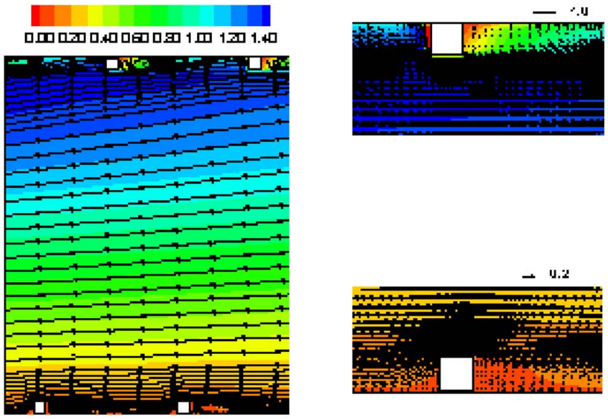

Primary flow and Temperature Contours (a)

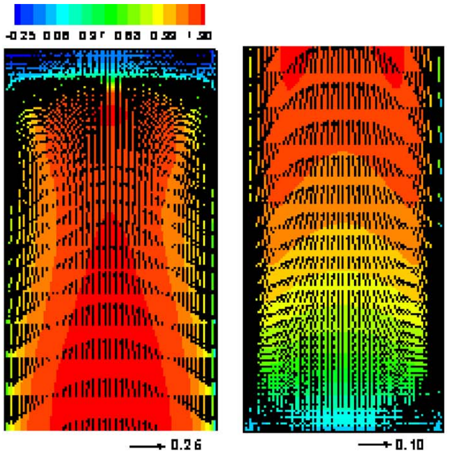

Secondary flow and Axial velocity Contours (a)

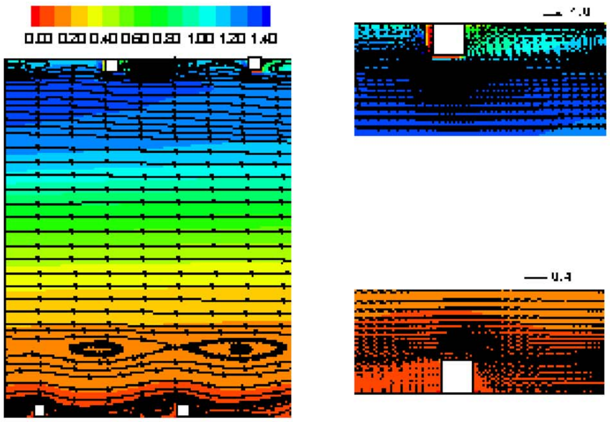

Primary flow and Temperature Contours (b)

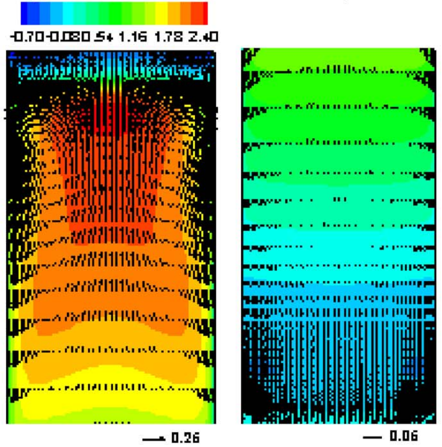

Secondary flow and Axial velocity Contours (b)

Fig. 16 Streamtraces (primary flow) and temperature contours at midtransverse plane and secondary vectors at *x*=1.0: (*a*) DR=0.0; and (*b*) DR=0.25 for AR=1:4 and at Re=25,000 and Ro=0.12

6. The 4:1 AR duct shows evidence of multiple rolls in the secondary flow that direct the core flow to both the leading and trailing surfaces. Therefore the difference between the leading and trailing wall heat transfer in the 4:1 AR duct is not significant, as in the other two AR ducts. Furthermore, the presence of these secondary flows in the vicinity of the sidewalls is responsible for the 4:1 AR sidewalls having the highest Nu ratio for all Re, Ro, and DR.

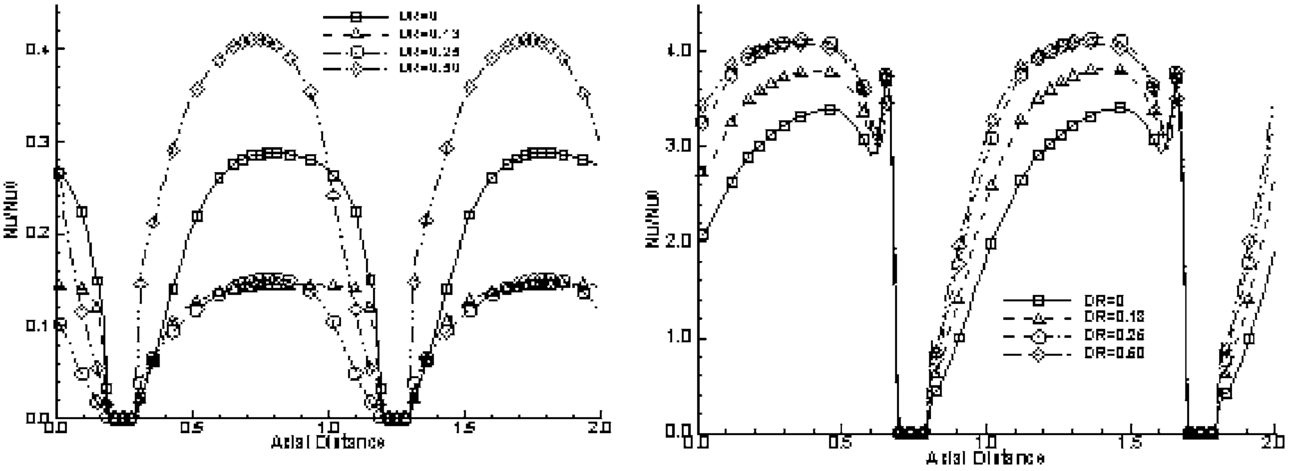

Fig. 17 Axial variation of spanwise averaged Nusselt number on: (*a*) leading wall; and (*b*) trailing wall at various density ratios for 1:4 AR duct (Re=25,000 and Ro=0.12)

Acknowledgment

This work was supported by a grant from South Carolina Institute of Energy Studies (SCIES) under the DOE-University Turbine Systems Research (UTSR) program. Support was also received from the Louisiana Board of Regents through the Clean Power and Energy Research Consortium (CPERC) and from the LSU Center for Computation and Technology.

Nomenclature

B = width of the duct
Bo = buoyancy parameter, $(\Delta\rho/\rho)\mathrm{Ro}^2 R_M$
D_h = hydraulic diameter of the duct, $4HB/(2(H+B))$
e = size of the square ribs
f = friction factor, $[\Delta p_x/(0.5\rho u_{\mathrm{av}}^2)]$
h = local heat transfer coefficient
H = height of the duct
K_f = ratio of thermal conductivity of fluid to that of solid
L_x = streamwise extent of the periodic domain
Nu = Nusselt number, $hB/K_f = -((\partial\theta/\partial n)|_{n=0})/(\theta_w(x,y)-\theta_b(x))$
P = pitch of the ribs
p = periodic component of pressure
Pr = Prandtl number, ν/α
q_j = turbulent thermal subgrid stress
Re = Reynolds number, $u_{\mathrm{av}}B/\nu$
R_M = mean radius of rotation
Ro = rotation number, $\Omega \mathrm{B}/u_{\mathrm{av}}$
t = time
T = temperature
u_τ = frictional velocity, $\sqrt{(\tau_w/\rho)}$
Y^+ = yu_τ/ν
u, v, w = nondimensional velocity in x, y, and z directions (also u_i, u_j)
u_i'', u_j'' = velocity fluctuations
X, Y, Z = nondimensional Cartesian coordinates (also x_i, x_j)

Greek Symbols

α = thermal diffusivity
$\beta(t)$ = mean pressure gradient
ε_{ijk} = alternating tensor
δ_{ij} = Kronecker delta
θ = nondimensional periodic component of temperature, $(T-T_w)/(T_{m1}-T_w)$
ρ = density of the fluid
$\Delta\rho/\rho$ = coolant-to-density ratio, $(T_w-T_b)/T_w$
ν = kinematic viscosity of the fluid
τ_{ij}, τ_w = turbulent stress and wall shear stress, $\mu\,\partial u/\partial n|_{n=0}$, respectively

References

[1] Han, J. C., and Park, J. S., 1988, "Developing Heat Transfer in Rectangular Channel With Rib Turbulators," Int. J. Heat Mass Transfer, **31**(1), pp. 183–195.
[2] Han, J. C., Ou, S., Park, J. S., and Lei, C. K., 1989, "Augmented Heat Transfer in Rectangular Channels of Narrow Aspect Ratios with Rib Turbulators," Int. J. Heat Mass Transfer, **32**(9), pp. 1619–1630.
[3] Zhou, F., Lagrone, J., and Acharya, S., 2004, "Internal Cooling in 4:1 AR Passages at High Rotation Numbers," *Proceedings ASME International Gas Turbine Conference*, Vienna, Austria, June 14–17, Paper No. ASME-GT-2004-53501.
[4] Wagner, J. H., Johnson, B. V., Graziani, R. A., and Yeh, F. C., 1992, "Heat Transfer in Rotating Serpentine Passages With Trips Normal to the Flow," J. Turbomach., **114**, pp. 847–857.
[5] Johnson, B. V., Wagner, J. H., and Steuber, G. D., 1993, "Effect of Rotation on Coolant Passage Heat Transfer," NASA Contractor Report No. 4396, Vol. II, NASA, Washington, D.C.
[6] Chen, Y., Nikitopoulos, D. E., Hibbs, R., Acharya, S., and Myrum, T. A., 2000, "Detailed Mass Transfer Distribution in a Ribbed Coolant Passage with a 180°," Int. J. Heat Mass Transfer, **43**, pp. 1479–1492.
[7] Azad, G. S., Uddin, M. J., Han, J.-C., Moon, H.-K., and Glezer, B., 2002, "Heat Transfer in a Two-Pass Rectangular Rotating Channel with 45° angled rib turbulators," J. Turbomach., **124**, pp. 251–259.
[8] Griffith, T. S., Al-Hadhrami, L., and Han, J. C., 2002, "Heat Transfer in Rotating Rectangular Cooling Channels (AR=4) with Angled Ribs," J. Heat Transfer, **124**, pp. 617–625.
[9] Stephens, M. A., Shih, T. I.-P., and Civinskas, K. C., 1995, "Computation of Flow and Heat Transfer in a Rectangular Channel with Ribs," AIPP Paper No. 95-0180.
[10] Rigby, D. L., Steinthorsson, E., and Ameri, A. A., 1997, "Numerical Prediction of Heat Transfer in a Channel with Ribs and Bleed," ASME Paper No. 97-GT-431.
[11] Bo, T., Iacovides, H., and Launder, B. E., 1995, "Developing Buoyancy-modified Turbulent Flow in Ducts Rotating in Orthogonal Mode," J. Turbomach., **117**, pp. 474–484.
[12] Iacovides, H., 1998, "Computation of Flow and Heat Transfer Through Rotating Ribbed Passage," Int. J. Heat Fluid Flow, **19**, pp. 393–400.
[13] Al-Qahtani, M., Jang, Y.-J., Chen, H.-C., and Han, J. C., 2002, "Prediction of Flow and Heat Transfer in Rotating Two-Pass Rectangular Channels with 45° Rib Turbulators," J. Turbomach., **124**(2), pp. 242–250.
[14] Pallares, J., and Davidson, L., 2000, "Large Eddy Simulations of Turbulent Flow in a Rotating Square Duct," Phys. Fluids, **12**(11), pp. 2878–2894.
[15] Murata, A., and Mochizuki, S., 2001, "Effect of Centrifugal Buoyancy on Turbulent Heat Transfer in an Orthogonally Rotating Square Duct with Transverse or Angled Rib Turbulators," Int. J. Heat Mass Transfer, **44**, pp. 2739–2750.
[16] Saha, A. K., and Acharya, S., 2003, "Flow and Heat Transfer in Internally Ribbed Ducts with Rotation: An Assessment of LES and RANS," GT2003-38619, *Proceedings of the ASME IGTI 2003*, Atlanta, GA, June 16–19.
[17] Murata, A., and Mochizuki, S., 2000, "Large Eddy Simulation with a Dynamic Subgrid-Scale Model of Turbulent Heat Transfer in an Orthogonally Rotating Rectangular Duct with Transverse Rib Turbulators," Int. J. Heat Mass Transfer, **43**(7), pp. 1243–1259.
[18] Murata, A., and Mochizuki, S., 2003, "Effect of Cross-Sectional Aspect Ratio on Turbulent Heat Transfer in an Orthogonally Rotating Rectangular Duct with Angled Rib Turbulators," Int. J. Heat Mass Transfer, **46**(16), pp. 3119–3133.
[19] Wang, G., and Vanka, S. P., 1995, "Convective Heat Transfer in Periodic Wavy Passages," Int. J. Heat Mass Transfer, **38**(17), pp. 3219–3230.
[20] Kato, M., and Launder, B. E., 1993, "The Modelling of Turbulent Flow around Stationery and Vibrating Square Cylinders," *Proceedings 9th Symposium on Turbulent Shear Flows*, Kyoto, Japan, August, Vol. 10-4.
[21] Harlow, F. H., and Welch, J. E., 1965, "Numerical Calculation of Time-Dependent Viscous Incompressible Flow of Fluid with Free Surfaces," Phys. Fluids, **8**, pp. 2182–2188.
[22] Kawamura, T., Takami, H., and Kuwahara, K., 1986, "Computation of High Reynolds Number Flow around a Circular Cylinder with Surface Roughness," Fluid Dyn. Res., **1**, pp. 145–162.
[23] Saha, A. K., and Acharya, S., 2004, "Unsteady Simulation of Turbulent Flow and Heat Transfer in a Channel with Periodic Array of Cubic Pin-Fins," Numer. Heat Transfer, Part A, **46**(6), pp. 510–543.
[24] Saha, A. K., and Acharya, S., 2003, "Parametric Study of Unsteady Flow and Heat Transfer in a Pin-Fin Heat Exchanger," Int. J. Heat Mass Transfer, **46**(20), pp. 3815–3830.
[25] Saha, A. K., Biswas, G., and Muralidhar, K., 2001, "Two-Dimensional Study of the Turbulent Wake Behind a Square Cylinder Subject to Uniform Shear," J. Fluids Eng., **123**, pp. 595–603.

Increasing Adiabatic Film-Cooling Effectiveness by Using an Upstream Ramp

Sangkwon Na

Tom I-P. Shih
e-mail: tomshih@iastate.edu

Department of Aerospace Engineering,
Iowa State University,
Ames, IA 50011-2271

*A new design concept is presented to increase the adiabatic effectiveness of film cooling from a row of film-cooling holes. Instead of shaping the geometry of each hole; placing tabs, struts, or vortex generators in each hole; or creating a trench about a row of holes, this study proposes a geometry modification upstream of the holes to modify the approaching boundary-layer flow and its interaction with the film-cooling jets. Computations, based on the ensemble-averaged Navier–Stokes equations closed by the realizable k-ε turbulence model, were used to examine the usefulness of making the surface just upstream of a row of film-cooling holes into a ramp with a backward-facing step. The effects of the following parameters were investigated: angle of the ramp (*8.5 deg, 10 deg, 14 deg*), distance between the backward-facing step and the row of film-cooling holes (*$0.5D, D$*), blowing ratio (0.36, 0.49, 0.56, 0.98), and "sharpness" of the ramp at the corners. Results obtained show that an upstream ramp with a backward-facing step can greatly increase surface adiabatic effectiveness. The laterally averaged adiabatic effectiveness with a ramp can be two or more times higher than without the ramp by increasing upstream and lateral spreading of the coolant.* [DOI: 10.1115/1.2709965]

Keywords: turbine cooling, film cooling, computational heat transfer

Introduction

To increase thermal efficiency and specific thrust, advanced gas-turbine stages are designed to operate at increasingly higher inlet temperatures [1]. This increase is made possible by advances in materials such as super alloys and thermal-barrier coatings and by advances in cooling technology such as internal, film, and impingement cooling [1–4]. With cooling, inlet temperatures can far exceed allowable material temperatures. Though cooling is an effective way to enable higher inlet temperatures, efficiency considerations demand effective cooling be achieved with minimum cooling flow. This is because turbines operate at very high pressures, and energy is needed to pump the cooling air to those pressures before they can be circulated through the turbine system for cooling.

For advanced gas turbines, the first-stage stator and rotor typically requires film cooling, which strives to form a blanket of cooler air next to the material surface to insulate the material from the hot gas [5]. Many investigators have studied the effects of design and operating parameters on film cooling of a flat plate in which the cooling jets issuing from one or two rows of inclined circular holes. Parameters studied include film-cooling hole inclination, length-to-diameter ratio, spacing between holes, turbulence and embedded vortices in the hot-gas flow, and unsteadiness from rotator–stator interactions (see, e.g., reviews by Han, et al. [6], Goldstein [7], Sundén and Faghri [8], Shih and Sultanian [9], and Bogard and Thole [10]; in addition, see the comprehensive bibliography provided by Kercher [11,12]).

Of the previous studies, Kelso and Lim [13] and Haven et al. [14] showed the important role played by vortices in the evolution of film-cooling jets. One pair, referred to as the counter-rotating vortices (CRVs), was found to lift the jet off the surface that it is intended to protect and to entrain hot gas underneath it. The other pair, referred to an anti-kidney pair, was shown to have a sense of rotation opposite to that of the CRVs, and so can counteract the undesirable effects of the CRVs in entraining hot gas. Thus, it is of interest to develop strategies to control the formation and strength of these vortices in a way that leads to more effective film cooling.

There are many ways to alter the structure of these vortices. Since the vorticity in the cooling jet originates from the flow in the film-cooling hole, the boundary layer upstream of the film-cooling hole, and the boundary-layer/cooling jet interactions, most investigators have focused on the geometry of the film-cooling hole. Shaped-diffusion hole is one approach, which uses the Coanda effect to cause the film-cooling jet to hug the curved surface and an expanding cross-sectional area near the hole exit to decrease cooling-jet speed and to increase lateral spreading. Haven et al. [14] and Hyams et al. [15] investigated the effects of shaped holes on the vorticity dynamics of hot-gas/film-cooling jet interactions. Bunker [16] provides a comprehensive review of the research on shaped holes. Another approach to alter the vortical structures is via vortex generators. Haven and Kurosaka [17] investigated the effects of placing vanes inside film-cooling holes that produce vortices in the same sense as the anti-kidney vortices. Zaman and Foss [18], Zaman [19], and Ekkad et al. [20] investigated the effects of tabs placed at the film-cooling-hole exit. The first two studies showed vortex generators can be quite effective in reducing jet penetration. However, both studies only investigated jets that lifted off the surface once exiting the film-cooling holes. Ekkad et al. [20] showed that placing tabs on the upstream side of the film-cooling-hole exit can improve film-cooling effectiveness. Shih et al. [21] proposed placing a strut or obstruction within each film-cooling hole that do not necessarily generate appreciable vorticity but can cause vortices inside film-cooling holes to be stretched and tilted in a way that would change the magnitude and direction of the vorticity in the CRVs and the anti-kidney pair. Bunker [22] proposed creating a trench about a row of film-cooling holes to modify the boundary-layer/cooling jet interactions. Altorairi [23] showed the trench to be quite useful in improving film-cooling effectiveness.

So far, no one has studied modifying the geometry upstream of a row of film-cooling holes to improve surface effectiveness. In this paper, an "upstream ramp" (Fig. 1) is proposed to modify the hot-gas boundary-layer/cooling jet interaction so that film-cooling effectiveness improves. Since extended surfaces such as a ramp could increase surface heat transfer and this is undesirable on the

---

Contributed by the Heat Transfer Division of ASME for publication in the Journal of Heat Transfer. Manuscript received March 4, 2006; final manuscript received December 14, 2006. Review conducted by Jayathi Murthy.

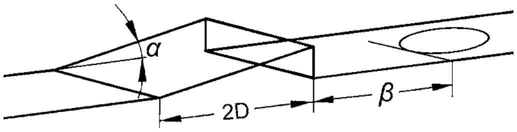

Fig. 1 Schematic of the upstream ramp studied

hot-gas side, it is noted that the ramp can be constructed in the thermal-barrier coating (TBC) system by using the ceramic top coat, which has very low thermal conductivity (private communication with Bunker [24]). The objective of this study is twofold. The first is to examine the nature of the flow induced by an upstream ramp and how that flow can improve film-cooling effectiveness. The second is to perform a parametric study on the effects of design parameters for a generic ramp. This study will be accomplished by using computational fluid dynamics (CFD) analysis that accounts for the three-dimensional nature of the flow and resolves the flow above the surface to be cooled as well as the flow in the plenum and in the film-cooling holes.

Problem Description

To demonstrate the usefulness of an upstream ramp design concept, the problem of film cooling of a flat plate from a row of inclined circular holes is studied. The baseline problem without the upstream ramp is very similar to the experimental study of Kohli and Bogard [25] so that this computational study can be validated by comparing the CFD predictions with experimentally measured values.

Schematic diagrams of the film-cooling problem studied with and without an upstream ramp are shown in Figs. 1–3. For this problem, the cooling jets emerge from a plenum through one row of circular holes. Each hole has a diameter D of 12.7 mm, a length of $3.5D$, and an inclination of 35 deg relative to a plane tangent to the flat plate. The spacing between the centers of the film-cooling holes in the spanwise direction is $3D$. The upstream ramp studied has length $2D$, makes an angle α with respect to the flat plate, and is located β upstream of the film-cooling hole. The following values of α and β were examined: 8.53 deg, 10 deg, and 14 deg for α and $0.5D$ and D for β. Other dimensions that describe the geometry are given in Figs. 1–3. A case was also studied in which the three sharp corners of the ramp are rounded as shown in Fig. 4. The radius of curvature of the rounding is $0.0787D$, which corresponds to 1 mm.

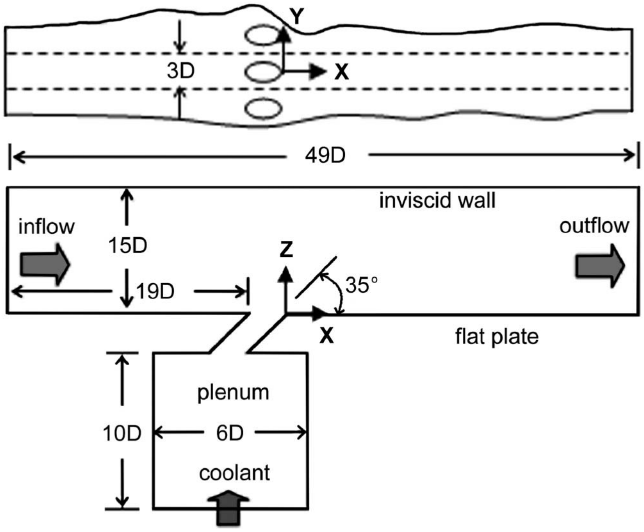

Fig. 2 Schematic of the film-cooling configuration studied (not drawn to scale and ramp not included)

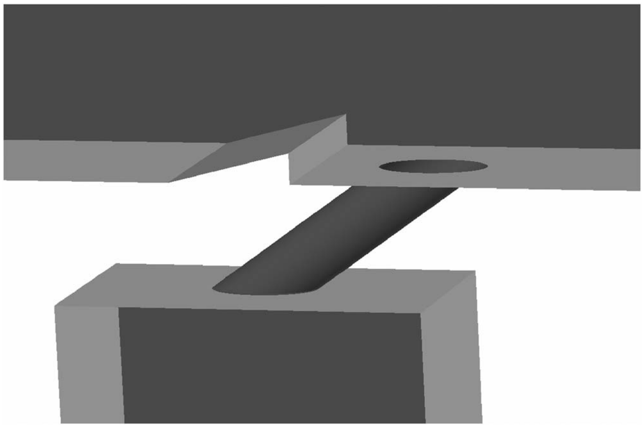

Fig. 3 Schematic of film cooling of a flat plate from a row of inclined circular holes with an upstream ramp

The operating conditions are as follows. The fluid for the main flow (hot gas) and coolant is air. The main flow above the flat plate has a free stream temperature T_∞ of 298 K and a free stream velocity U_∞ of 20 m/s in the X direction. The flow in the boundary layer is assumed to be turbulent from the leading edge of the flat plate. The coolant has a temperature T_c of 188 K in the plenum. This gives a density ratio (DR) of 1.6. When the average velocity at the inlet of the film-cooling holes U_c is 6.25 m/s, the mass flux or blowing ratio M is 0.5. Three other blowing ratios were also studied—0.36, 0.56, and 0.98—by varying the velocity at the plenum inflow.

Two types of boundary conditions were applied on the flat plate for the heat transfer study. When the film-cooling adiabatic effectiveness is sought, the flat plate is made adiabatic. When the surface heat transfer coefficient is sought, the flat plate is maintained at a constant wall temperature T_w of 243 K. All other walls, including the walls of the film-cooling holes and the plenum, are made adiabatic. The back pressure at the outflow boundary above the flat plate is maintained at atmospheric pressure.

For this problem, the computational domain is taken to be the region bounded by the solid and dashed lines shown in Fig. 2, where the dashed lines represent periodic planes. By assuming periodicity in the spanwise direction, only one film-cooling hole needs to be examined. In addition, the "upper channel wall" (i.e., the wall without film-cooling holes) was moved closer to the wall with the film-cooling holes. This was done to reduce the size of the computational domain and hence computational cost. The errors incurred by this are minimized by making the "upper channel wall" sufficiently far away and by making it inviscid (i.e., the velocity there can slip despite the viscous nature of the flow) so

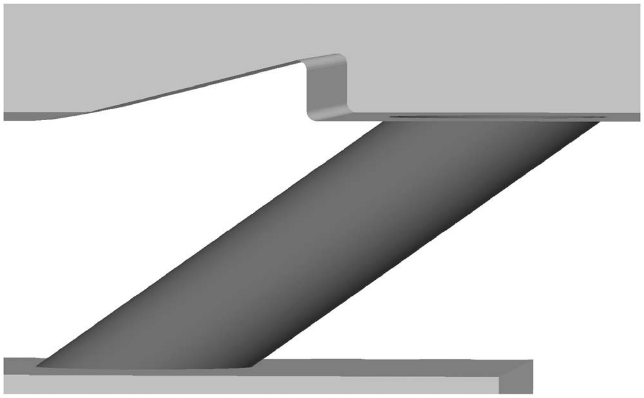

Fig. 4 Schematic of an upstream ramp with rounded corners

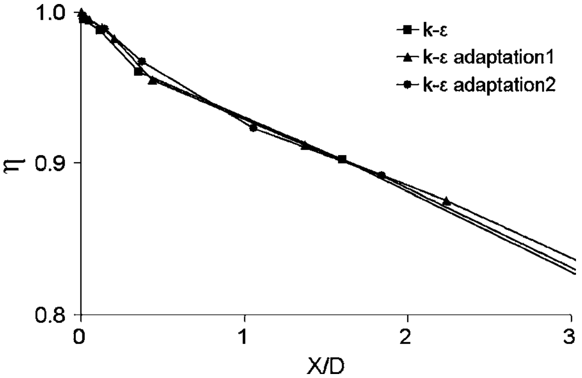

Fig. 5 Grid-independence study: centerline adiabatic effectiveness for three grids at $M=0.5$

that boundary layers will not form there. To ensure that the "upper channel wall" is sufficiently far away, two different channel heights were evaluated, and they are $H=15D$ and $30D$ (see Fig. 2).

Formulation and Numerical Method of Solution

The film-cooling problem described in the previous section was modeled by the ensemble-averaged continuity, full compressible Navier–Stokes, and energy equations that are valid for a thermally and calorically perfect gas. The effects of turbulence were modeled by using the two-equation realizable k-ε model [26]. For all equations, the integration is to the wall (i.e., wall functions were not used).

Solutions to the aforementioned governing equations were obtained by using Version 6.1.18 of the Fluent-UNS code [27]. The following algorithms in Fluent were invoked. Since only steady-state solutions were of interest, the SIMPLE algorithm was used. The fluxes at the cell faces representing advection were interpolated by using second-order upwind differences. The fluxes at the cell faces representing diffusion were interpolated by using second-order central differences. For all computations, iterations were continued until all residuals for all equations plateau to ensure convergence to steady state has been reached. At convergence, the normalized residuals were always less than 10^{-6} for the continuity equation, less than 10^{-6} for the three components of the velocity, less than 10^{-8} for the energy, and less than 10^{-5} for the turbulence quantities.

Grid-Sensitivity and Validation Study

Accuracy of solutions is strongly dependent upon the quality of the grid in minimizing grid-induced errors and in resolving the relevant flow physics. In this study, a grid sensitivity study was performed to determine the appropriate grid. Figure 5 shows the results of this study for the case without the ramp, involving three grids—the baseline grid with 2.291 million cells, a finer grid with 2.716 million cells (adaptation 1), and a still finer grid with 5.252 million cells (adaptation 2). For the two finer grids, the additional cells were all concentrated about the film-cooling hole and the hot-gas/coolant-jet interaction region, where the flow physics is most complicated. From this grid sensitivity study, the baseline grid was found to give essentially the same result for the centerline adiabatic effectiveness as those from adaptation 1 and 2 grids. The relative error in the "average" centerline adiabatic effectiveness is 0.4% when comparing results from the baseline grid with those from the adaptation 2 grid.

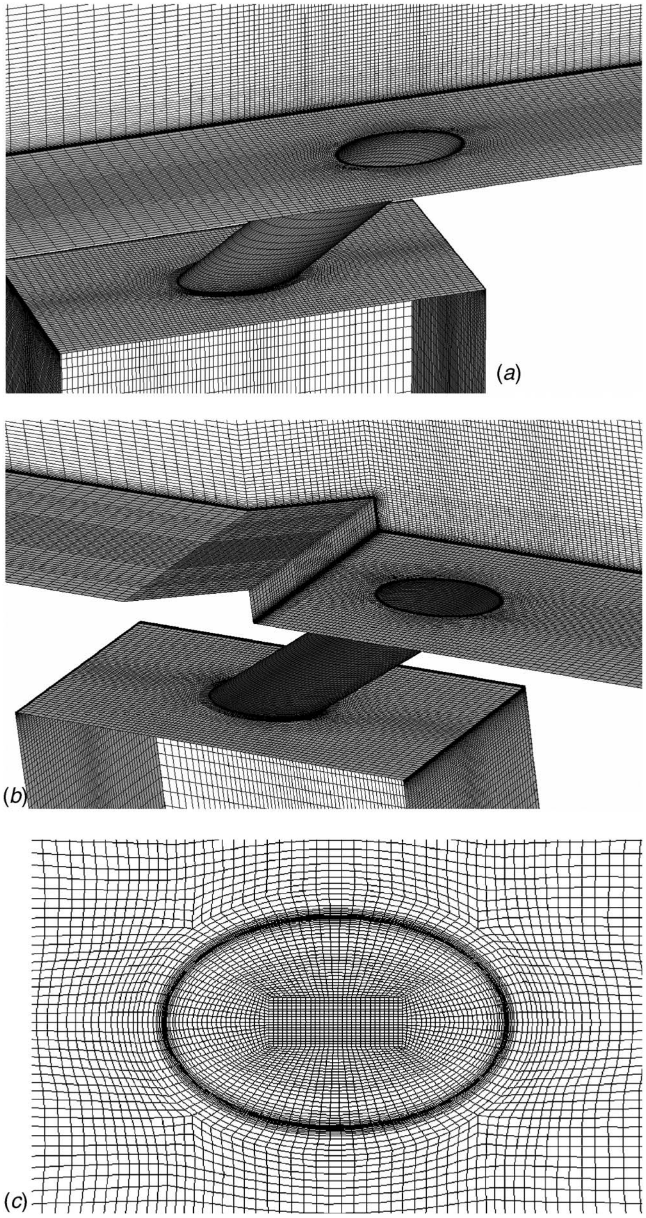

Fig. 6 Grid used: (*a*) no ramp; (*b*) with ramp; and (*c*) grid around film-cooling hole

The grids used for this problem with and without an upstream ramp are shown in Fig. 6. Without the upstream ramp, the grid used has 2.291 million cells. When there is an upstream ramp, the grids used has cells that varied from 2.282 million to 2.367 million, depending upon the angle of the ramp and its distance from the film-cooling hole. For all grids used, the first grid point away from all viscous walls has a y^+ less than unity. Also, the first five grid points have y^+ values within five. Figure 7 shows the distributions of the y^+ values for the first cell away from the flat plate with the ramp for the case with $M=0.98$, $\alpha=14$ deg, and $\beta=0.5D$. From this figure, it can be seen the y^+ values are all less than unity.

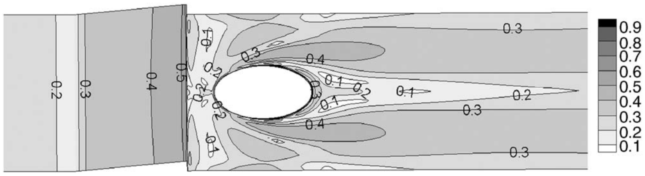

Fig. 7 y^+ values at one cell above the surface of the flat plat with ramp

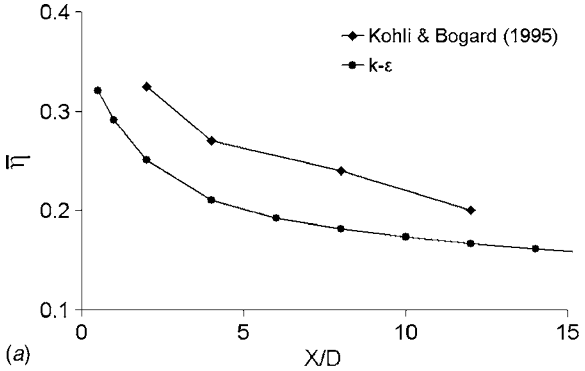

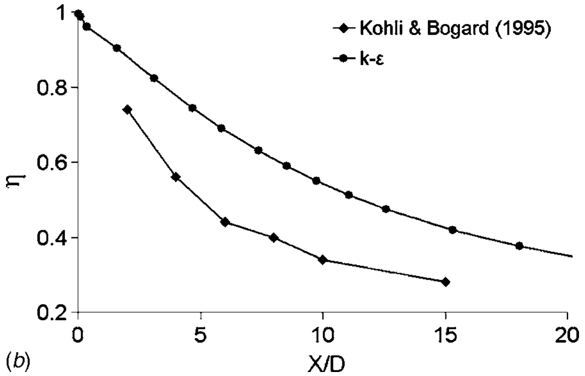

Fig. 8 Validation study: CFD predictions and comparison with experimental data of Kohli and Bogard ($L/D=2.8$ to match experiment): (*a*) laterally averaged; and (*b*) centerline

To assess the meaningfulness of this computational study, the grid-independent solutions generated for the problem of film-cooling over a flat plate were compared with the experimental data provided by Kohli and Bogard [25] for $L/D=2.8$ at a blowing ratio of 0.5. At the leading edge of the film-cooling holes, the computations predicted a boundary-layer thickness of $0.14D$, a shape factor of 1.49, and a Reynolds number based on free stream speed and momentum thickness of 1492. The corresponding measured values are $0.12D$, 1.48, and 1100, respectively. Results for the predicted adiabatic effectiveness are shown in Fig. 8 along with experimentally measured ones. From this figure, it can be seen that the centerline adiabatic effectiveness is overpredicted and the laterally averaged adiabatic effectiveness is underpredicted. This indicates that the realizable k-ε model overpredicts normal spreading and underpredicts lateral spreading of the cooling jet. Despite this, the trends are predicted correctly, and the qualitative features of the flow are captured by the computations. Thus, though the predictions may not be sufficiently accurate quantitatively, they may be good enough to provide insight on the flow and to discern differences in film-cooling designs.

Results

The objective of this study is to understand the usefulness of placing a ramp upstream of a row of film-cooling holes in improving film-cooling adiabatic effectiveness. All configurations simulated to obtain this understanding are summarized in Table 1. In this section, the nature of the flow induced by an upstream ramp is described first. Afterwards, its effects on surface adiabatic effectiveness are presented.

Nature of the Flow Induced by an Upstream Ramp. Figures 9–13 show the interaction of the approaching boundary-layer flow and the film-cooling jets with and without an upstream ramp. In Fig. 9, it can be seen that when there is no ramp, a significant pressure rise occurs just upstream of the film-cooling hole because of approaching boundary-layer/cooling-jet interaction. But, when there is an upstream ramp, the static pressure upstream of each film-cooling hole is reduced significantly. This reduction in pressure gradient on the flat plate just upstream of the film-cooling hole resulted because the boundary-layer flow, being diverted upward by the upstream ramp, now interacts with the film-cooling jets at a distance above the flat plate.

Table 1 Summary of simulations performed

Case no.	α (deg)	β	M	Corner
1	8.53	$0.5D$	0.49	sharp
2	8.53	D	0.49	sharp
3	10.0	D	0.49	sharp
4	14.0	$0.5D$	0.49	sharp
5	14.0	D	0.49	sharp
6	8.53	D	0.36	sharp
7	8.53	D	0.56	sharp
8	8.53	D	0.98	sharp
9	14.0	$0.5D$	0.49	rounded

Figure 10 contrasts the pressure coefficient on the film-cooled plate with and without an upstream ramp for the case with the most protruded ramp, which has a backward-facing step height of $1.0D$. From Fig. 10(*a*), it can be seen that the ramp increases the pressure upstream of the backward-facing step and decreases the pressure downstream of it when compared to the case without the ramp. Thus, having a ramp increases pressure drag. Since pressure drag can be an important issue, the geometry of the ramp needs to be optimized. Another issue about the ramp studied is that sharp corners are hard to manufacture and maintain. Figure 10(*b*) shows that rounding the ramp by 1 mm $(0.0787D)$ does not appreciably change the pressure distribution, which has strong effects on the flow. Figure 10(*c*) shows the pressure coefficient for channel heights of $15D$ and $30D$. Since nearly identical results were obtained, having the inviscid wall at $15D$ away from the film-cooled plate is sufficiently far away.

The flow pattern created by the ramp is shown in Fig. 11. From this figure, it can be seen that there is a separated region that extends from the backward-facing step of the ramp to the upstream end of the film-cooling holes. The recirculating flow in this separated region entrains the cooler fluid from the film-cooling jet and cools the wall bounding the separated region. With the approaching boundary-layer deflected upwards, the cooling jet can flow more easily through the cooling hole as shown in Fig. 12

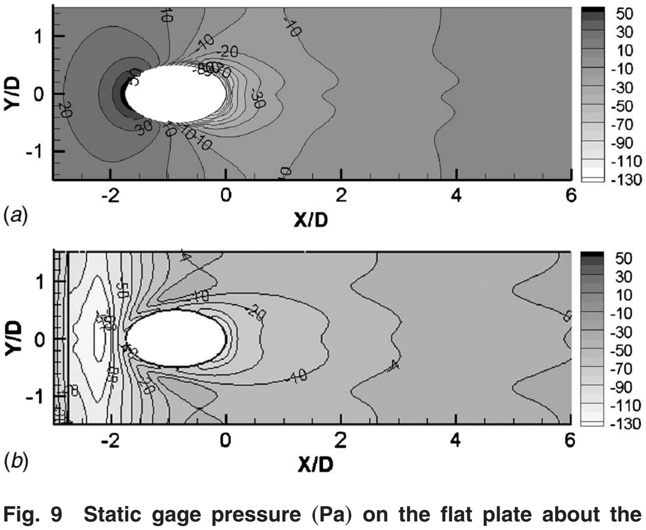

Fig. 9 Static gage pressure (Pa) on the flat plate about the film-cooling hole ($\alpha=8.5$ deg, $\beta=1.0D$, $M=0.49$): (*a*) no ramp; and (*b*) with ramp

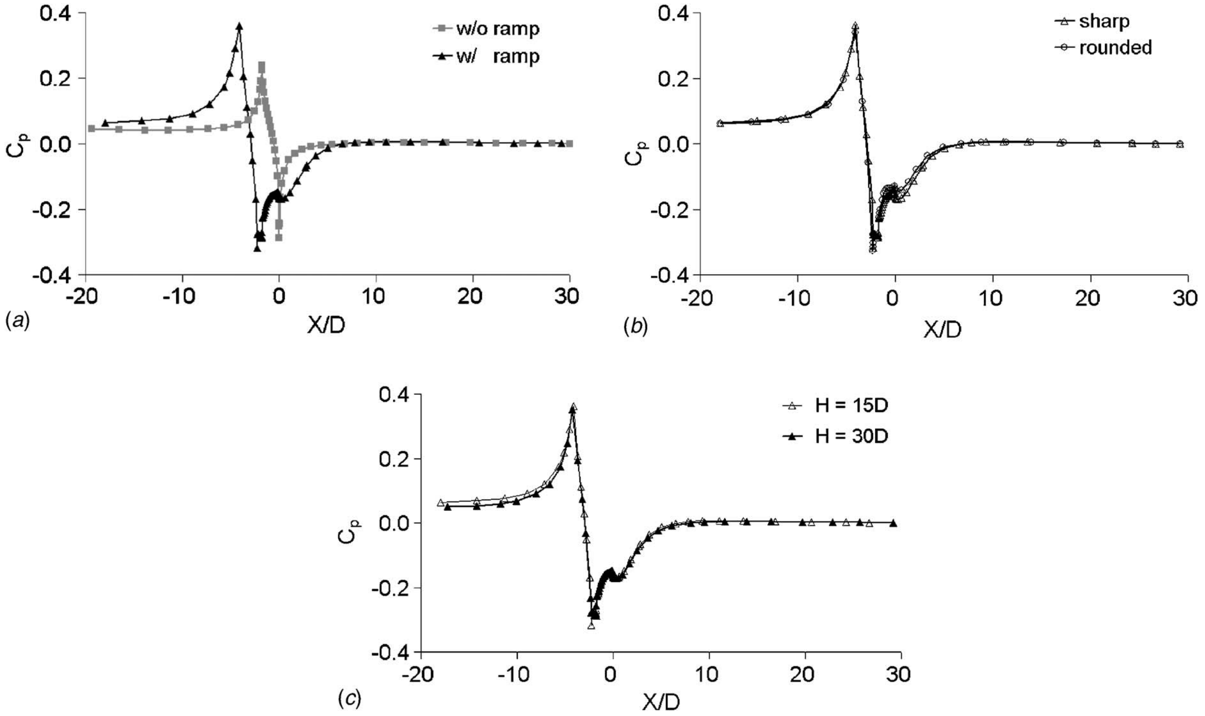

Fig. 10 Pressure coefficient on the plate along center line (α=14.0 deg, β=0.5D, M=0.49): (*a*) with and without ramp; (*b*) with sharp and rounded corners; and (*c*) with ramp in channels of different heights

because the large separated region inside the film-cooling hole for the case without ramp essentially disappears when there is a ramp. Without an upstream ramp, the net pressure force on the cooling jet is high, which causes the jet to bend toward the flat plate, creating a large separated region in the film-cooling hole and thereby reducing the effective flow cross-sectional area. With an upstream ramp, the cooling jet is not deflected by the approaching boundary-layer flow until further above the surface so that the effective cross-sectional area for flow is higher, which reduces the speed of coolant flow and the effective blowing ratio. Also, there is no horseshoe vortex at the base of the cooling jet about the film-cooling-hole exit. Thus, lateral spreading of each cooling jet is increased. In Fig. 13, it can be seen that deflecting the approaching boundary layer (which is made up of hot gas) above the film-cooling hole delays the entrainment of hot gas by the film-cooling jet.

Adiabatic Effectiveness. Figures 14–19 show the results obtained for the film-cooling adiabatic effectiveness. From Fig. 14, it can be seen that with an upstream ramp, the surface adiabatic effectiveness is greatly improved and that a much greater surface about the film-cooling hole is now protected by the cooling jet, including the region upstream of the film-cooling hole. This is consistent with the nature of the fluid flow described earlier (e.g., entrainment of coolant downstream of the ramp's backward facing step by the recirculating flow in the separated region and the in-

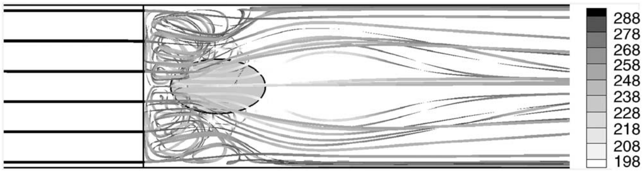

Fig. 11 Streamlines colored by temperature with darker gray being higher and lighter gray being lower (α=8.5 deg, β=0.5D, M=0.49)

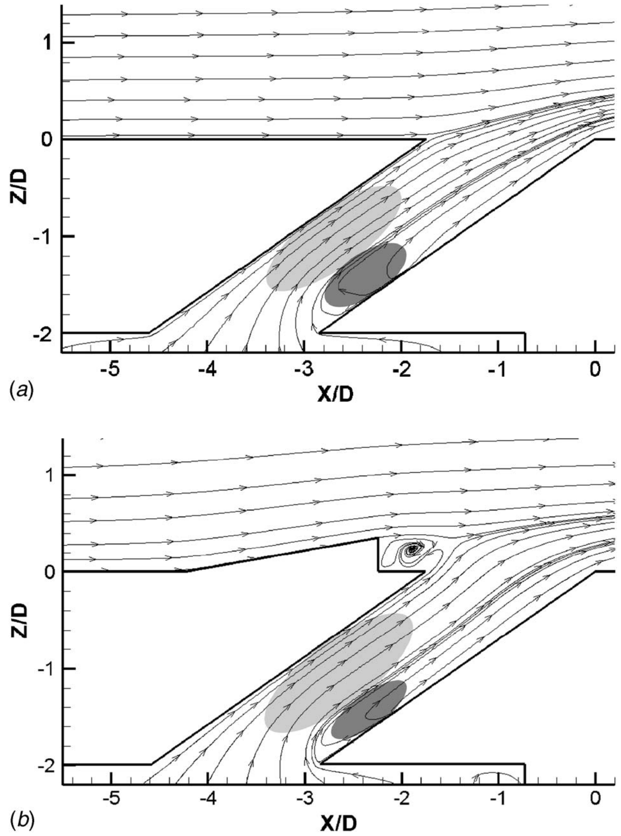

Fig. 12 Velocity vectors and streamlines in an *X-Z* plane that passes through the center of the film-cooling hole (α=8.5 deg, β=0.5D, M=0.49). Lighter gray denotes higher speed region. Darker gray denotes lower speed region with separation.

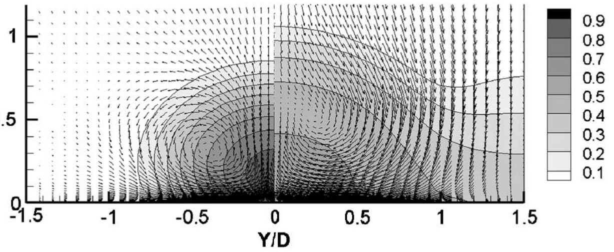

Fig. 13 Normalized temperature $(T_\infty - T)/(T_\infty - T_c)$ at Y-Z plane located at $X/D=3$ ($\alpha=14$ deg, $\beta=0.5D$, $M=0.49$): (left half) no ramp; and (right half) with ramp

creased lateral spreading of the coolant upon exiting the film-cooling hole). Figures 15–17 show the effects of the ramp angle and the distance from the backward-facing step of the ramp to the film-cooling hole. From these figures, the following observations can be made. First, increasing the ramp angle (and hence the height of the backward-facing step), the higher is the laterally averaged adiabatic effectiveness, at least for the two angles studied. Second, placing the ramp $0.5D$ upstream gave higher laterally averaged adiabatic effectiveness than placing it $1.0D$ upstream. The bottom line is that placing a ramp upstream of a row of film-cooling holes increases laterally averaged adiabatic effectiveness significantly. The laterally averaged adiabatic effectiveness with the ramp can be two or more times higher than that without the ramp.

Figure 18 shows the effects of blowing ratio on adiabatic effectiveness. From this figure, it can be seen that laterally averaged adiabatic effectiveness can decrease if the blowing ratio is too high or too low. When it is too high, liftoff can take place. When it is too low, hot gas is entrained behind the backward-facing step. Thus, the optimal angle of the ramp or the height of the backward-facing step depends on the blowing ratio. For a ramp with $\alpha=14.0$ deg that is located at $\beta=0.5D$ upstream of the film-cooling hole, the best results are obtained with a blowing ratio around 0.5. Figure 19 shows rounding the sharp corners of the upstream ramp to have little effect on adiabatic effectiveness (Case 9, Table 1).

Heat Transfer. When the surface heat transfer is of interest, computations were performed for the same configurations and operating conditions except that the flat plate is maintained at a constant wall temperature T_w of 243 K instead of being adiabatic. The average heat transfer rate per unit area for the entire flat plate with and without the ramp (Case 4 in Table 1) is $-916.78\ \mathrm{W/m^2}$ and $-1094.70\ \mathrm{W/m^2}$, respectively. Thus, introducing a ramp can increase adiabatic effectiveness and decrease surface heat transfer.

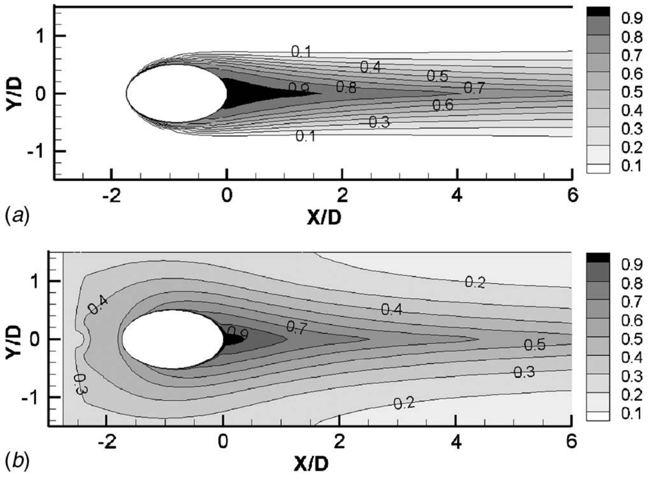

Fig. 14 Adiabatic effectiveness on the flat plate about the film-cooling hole ($\alpha=8.5$ deg, $\beta=1D$, $M=0.49$): (*a*) no ramp; and (*b*) with ramp

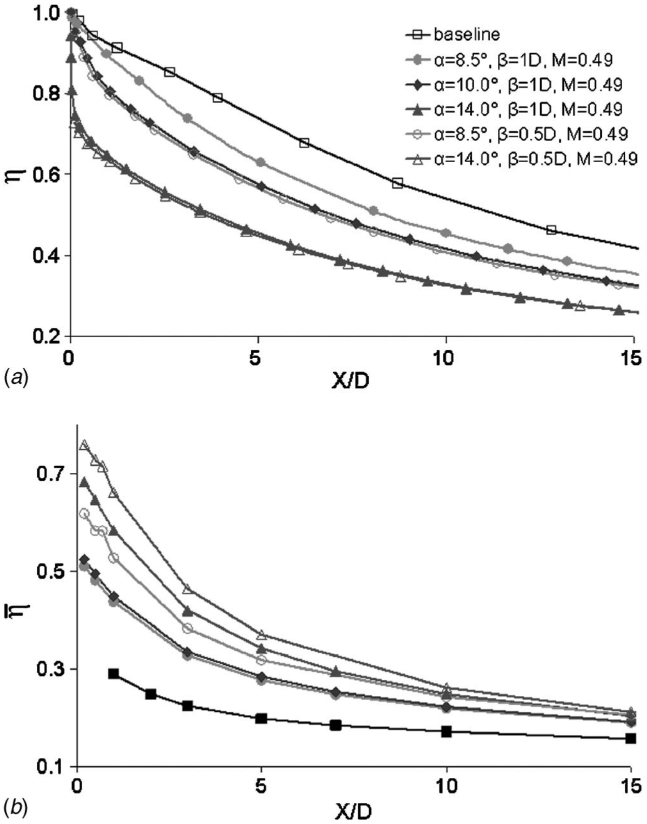

Fig. 15 Adiabatic effectiveness with and without ramp: (*a*) centerline; and (*b*) laterally averaged

Figure 20 shows the predicted normalized surface heat transfer on the flat plate with and without ramp (Case 4 in Table 1). In Fig. 20, a normalized heat transfer flux of unity denotes the surface heat flux at $X/D=10$ upstream of the film-cooling hole without ramp, which equals $-2221.06\ \mathrm{W/m^2}$. From Fig. 20, it can be seen

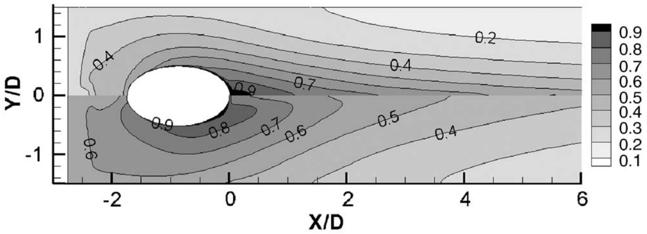

Fig. 16 Adiabatic effectiveness as a function of α ($\beta=D$ and $M=0.49$): (top half) $\alpha=8.5$ deg; and (bottom half) $\alpha=14$ deg

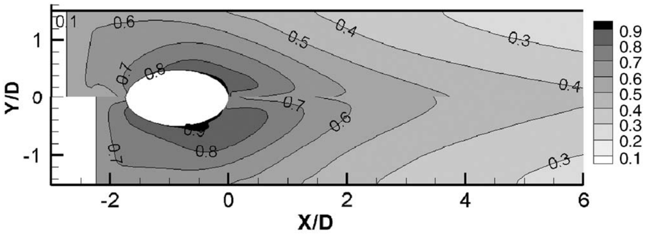

Fig. 17 Adiabatic effectiveness as a function of β ($\alpha=14$ deg and $M=0.49$): (top half) $\beta=1.0D$; and (bottom half) $\beta=0.5D$

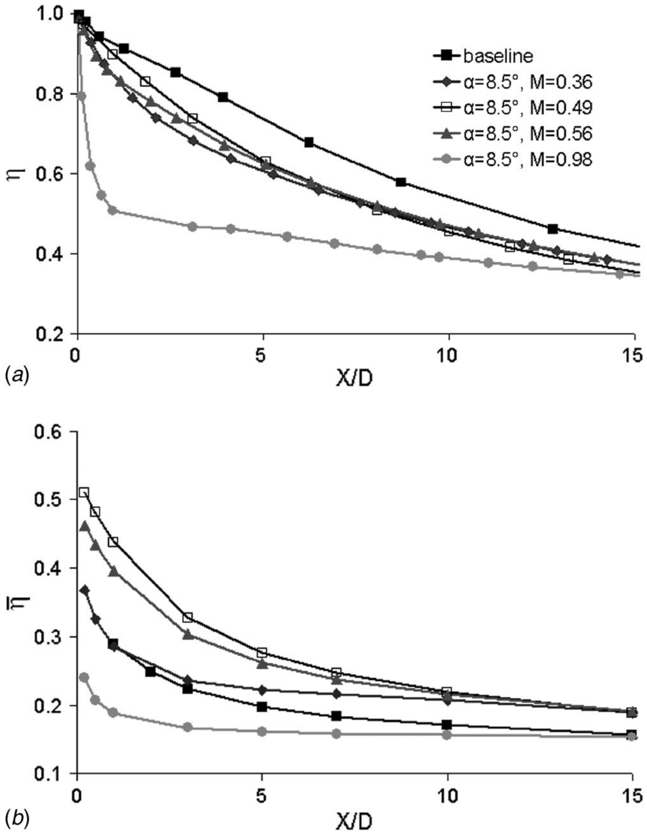

Fig. 18 Adiabatic effectiveness as a function of blowing ratio (α=8.5 deg, β=D): (*a*) centerline adiabatic effectiveness; and (*b*) laterally averaged adiabatic effectiveness

that the ramp changes substantially regions of high and low heat transfer. In particular, though surface heat transfer is reduced overall and is reduced downstream of the ramp, the heat transfer on the ramp itself is slightly increased. Figure 21 shows the normalized surface heat flux along the center line with and without ramp. From this figure, it is clear that ramp greatly reduces surface heat transfer.

Summary

This study proposes to improve the adiabatic effectiveness of film cooling by modifying the geometry upstream of the film-cooling holes. Computations were performed to study the effects of placing a ramp upstream of a row of film-cooling holes. Results obtained showed the ramp to deflect the approaching boundary-layer flow away from the base of the film-cooling jet. This caused the boundary-layer flow/cooling jet interaction to occur further away from the surface, which eliminated the horseshoe vortex at the base of the cooling jet and allowed the film-cooling jet to spread out more laterally. Also, this allowed the coolant from the film-cooling jet to fill the separated region between the backward-facing step of the ramp and the cooling jet and for the cooling jet to entrain cooler fluid. These flow features were found to improve film-cooling adiabatic effectiveness and to decrease surface heat transfer. The laterally averaged adiabatic effectiveness with the ramp can be two or more times higher than that without the ramp. The "optimal" ramp geometry was found to depend on the blowing ratio. There is, however, a penalty in pressure drag, implying a need to optimize the ramp geometry. Also, it should be noted that the ramp geometry studied is for an approaching boundary layer with a thickness of 0.14D, a shape factor of 1.49, and zero free stream turbulence.

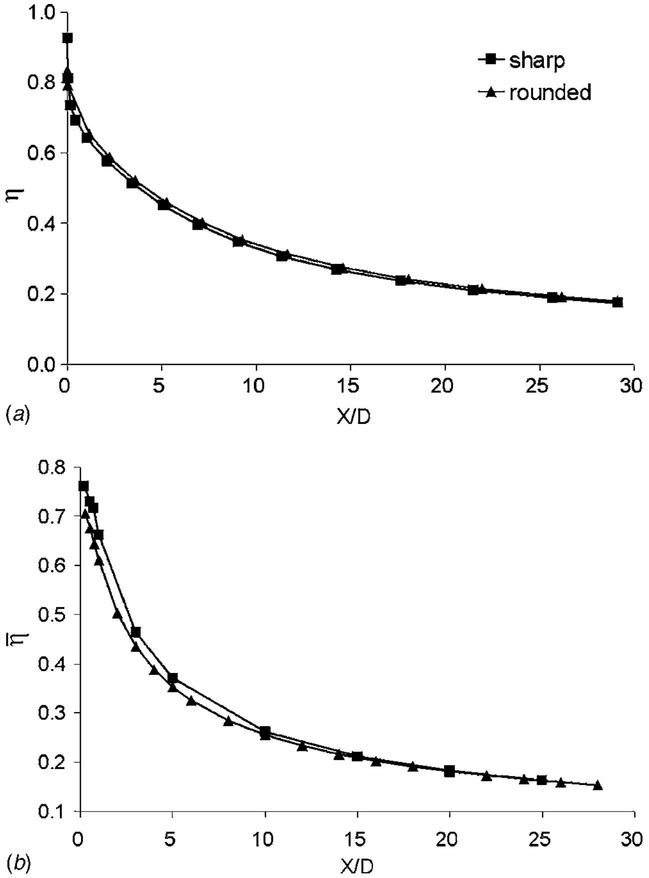

Fig. 19 Effects of rounding the sharp corners of the upstream ramp (α=14.0 deg, β=0.5D): (*a*) centerline adiabatic effectiveness; and (*b*) laterally averaged adiabatic effectiveness

Acknowledgment

This research was supported by the Department of Energy's University Turbine System Research Program with Dr. R. Wenglarz and Dr. L.P. Golan as the Technical Monitors (SCIES Project No. 04-01-SR115). The authors are grateful for this support. The authors are also grateful to Fluent for providing the Fluent-UNS code.

Nomenclature

C_p = pressure coefficient=$(P-P_\infty)/(0.5\rho U^2)_\infty$

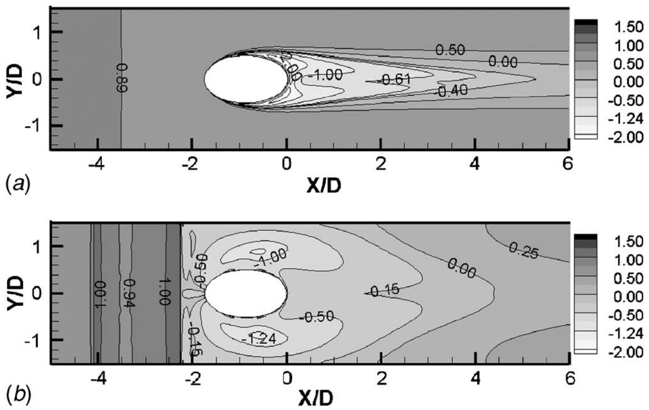

Fig. 20 Normalized surface heat flux (M=0.49, α=14 deg, and β=0.5D): (*a*) no ramp; and (*b*) with ramp

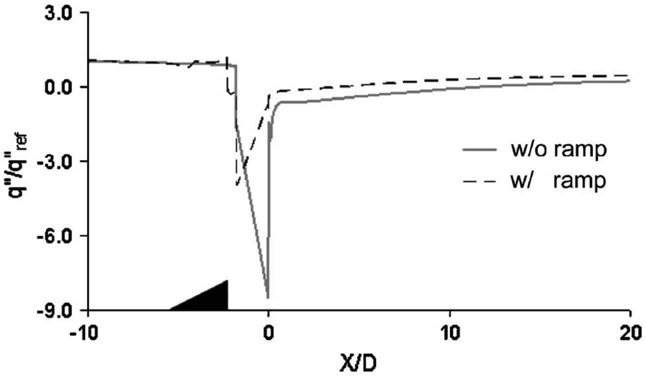

Fig. 21 Normalized surface heat flux along the centerline with and without ramp (α=14 deg, β=0.5D, M=0.49)

D = film-cooling hole diameter
M = blowing ratio$=(\rho U)_c/(\rho U)_\infty$
P = static pressure
q'' = surface heat flux
T, T_c, T_∞ = temperature, coolant temperature in plenum, hot-gas temperature at free stream
T_w, T_{aw} = wall temperature, adiabatic wall temperature
U_c = average speed of coolant flow at the film-cooling-hole inlet
U_∞ = speed of hot gas at free stream
u_τ = friction velocity: $(\tau_w/\rho)^{0.5}$
y^+ = normalized distance from the wall: $\rho u_\tau y/\mu$
y = normal distance from the wall

Greek

η = adiabatic effectiveness/normalized temperature: $(T_\infty - T)/(T_\infty - T_c)$
$\bar{\eta}$ = laterally averaged adiabatic effectiveness (i.e., averaged along the spanwise direction)
μ = dynamic viscosity
ρ = density
τ_w = wall shear stress

References

[1] Suo, M., 1985, *Turbine Cooling, Aerothermodynamics of Aircraft Engine Components*, G. C. Oates, ed., AIAA, New York, pp. 275–328.
[2] Metzger, D. E., 1985, "Cooling Techniques for Gas Turbine Airfoils," AGARD CP 390, pp. 1–12.
[3] Moffat, R. J., 1987, "Turbine Blade Heat Transfer," *Heat Transfer and Fluid Flow in Rotating Machinery*, W. J. Yang, ed., Hemisphere, Washington, D.C., pp. 1–24.
[4] Shih, T. I.-P., and Chyu, M., 2006, Guest eds., "Special Section on Turbine Science and Technology," J. Propul. Power, **22**(2), pp. 225–396.
[5] Goldstein, R. J., 1971, "Film Cooling," *Advances in Heat Transfer*, Academic, New York, Vol. 7, pp. 321–379.
[6] Han, J. C., Dutta, S., and Ekkad, S. V., 2000, *Gas Turbine Heat Transfer and Cooling Technology*, Taylor & Francis, New York.
[7] Goldstein, R., ed., 2001, *Heat Transfer in Gas Turbine Systems*, Annals of the New York Academy of Sciences, Vol. **934**.
[8] Sundén, B., and Faghri, M., 2001, eds., *Heat Transfer in Gas Turbines*, WIT, Ashurst, Southhampton, UK.
[9] Shih, T. I.-P., and Sultanian, B., 2001, "Computations of Internal and Film Cooling," *Heat Transfer in Gas Turbines*, B. Sundén and M. Faghri, eds., WIT, Ashurst, Southhampton, UK, Chap. 5, pp. 175–225.
[10] Bogard, D. G., and Thole, K. A., 2006, "Gas Turbine Film Cooling," J. Propul. Power, **22**(2), pp. 249–270.
[11] Kercher, D. M., 2003, "Film-Cooling Bibliography: 1940–2002," Ipswich, MA, February 28.
[12] Kercher, D. M., 2005, "Film-Cooling Bibliography Addendum: 1999–2004," Ipswich, MA, April 19.
[13] Kelso, R. M., Lim, T. T., and Perry, A. E., 1996, "An Experimental Study of Round Jets in Cross-Flow," J. Fluid Mech., **306**, pp. 111–144.
[14] Haven, B. A., Yamagata, D. K., Kurosaka, M., Yamawaki, S., and Maya, T., 1997, "Anti-Kidney Pair of Vortices in Shaped Holes and Their Influence on Film Cooling Effectiveness," ASME Paper No. 97-GT-45.
[15] Hyams, D. G., McGovern, K. T., and Leylek, J. H., 1997, "Effects of Geometry on Slot-Jet Film Cooling Performance," ASME Paper No. 96-GT-187.
[16] Bunker, R. S., 2005, "A Review of Shaped Hole Turbine Cooling Technology," ASME J. Heat Transfer, **127**, pp. 441–453.
[17] Haven, B. A., and Kurosaka, M., 1996, "Improved Jet Coverage Through Vortex Cancellation," AIAA J., **34**(11), pp. 2443–2444.
[18] Zaman, K. B. M. Q., and Foss, J. K., 1997, "The Effects of Vortex Generators on a Jet in a Cross-Flow," Phys. Fluids, **9**(1), pp. 106–114.
[19] Zaman, K. B. M. Q., 1998, "Reduction of a Jet Penetration in a Cross-Flow by Using Tabs," AIAA Paper No. 98–3276.
[20] Ekkad, S. V., Nasir, H., and Acharya, S. 2003, "Flat Surface Film Cooling from Cylindrical Holes with Discrete Tabs," J. Thermophys. Heat Transfer, **17**(3), pp. 304–312.
[21] Shih, T. I.-P., Lin, Y.-L., Chyu, M. K., and Gogineni, S., 1999, "Computations of Film Cooling from Holes with Struts," ASME Paper No. 99-GT-282.
[22] Bunker, R. S., 2002, "Film Cooling Effectiveness Due to Discrete Holes Within Transverse Surface Slots," Proceedings IGTI Turbo Expo, Amsterdam, The Netherlands, ASME Paper No. GT-2002–30178.
[23] Altorairi, M. S., 2003, "Film Cooling from Cylindrical Holes in Transverse Slots," M.S. thesis, Louisiana State University, Baton Rouge, LA.
[24] Bunker, R. S., 2005, private communication.
[25] Kohli, A., and Bogard, D. G., 1997, "Adiabatic Effectiveness, Thermal Fields, and Velocity Fields for Film Cooling With Large Angle Injections," ASME J. Turbomach., **119**, pp. 352–358.
[26] Shih, T.-H., Liou, W., Shabbir, A., and Zhu, J., 1995, "A New k-ε Eddy-Viscosity Model for High Reynolds Number Turbulent Flows—Model Development and Validation," Comput. Fluids, **24**(3), 1995, pp. 227–238.
[27] http://www.fluent.com/software/fluent/index.htm

Effects of Various Modeling Schemes on Mist Film Cooling Simulation

Xianchang Li
Department of Mechanical Engineering,
Lamar University,
Beaumont, TX 77710
e-mail: xianchang.li@lamar.edu

Ting Wang
Energy Conversion & Conservation Center,
University of New Orleans,
New Orleans, LA 70148-2220
e-mail: twang@uno.edu

Numerical simulation is performed in this study to explore film-cooling enhancement by injecting mist into the cooling air with a focus on investigating the effect of various modeling schemes on simulation results. The effect of turbulence models, dispersed-phase modeling, inclusion of different forces (Saffman, thermophoresis, and Brownian), trajectory tracking, and mist injection scheme is studied. The effect of flow inlet boundary conditions (with/without air supply plenum), inlet turbulence intensity, and the near-wall grid density on simulation results is also included. Simulation of a two-dimensional (2D) slot film cooling with a fixed blowing angle and blowing ratio shows a 2% mist (by mass) injected into the cooling air can increase the cooling effectiveness about 45%. The renormalization group (RNG) k-ε model, Reynolds stress model, and the standard k-ε turbulence model with an enhanced wall treatment produce consistent and reasonable results while the turbulence dispersion has a significant effect on mist film cooling through the stochastic trajectory calculation. The thermophoretic force slightly increases the cooling effectiveness, but the effect of Brownian force and Saffman lift is imperceptible. The cooling performance deteriorates when the plenum is included in the calculation due to the altered velocity profile and turbulence intensity at the jet exit plane. The results of this paper can provide guidance for corresponding experiments and serve as the qualification reference for future more complicated studies with 3D cooling holes, different blowing ratios, various density ratios, and rotational effect.
[DOI: 10.1115/1.2709959]

Keywords: film cooling, gas turbine cooling, mist cooling, two-phase flow simulation

Introduction

For more than half a century [1,2], air film cooling has been commonly applied to cool gas turbine hot components such as combustor liners, combustor transition pieces, turbine vanes (nozzles), and blades (buckets). Numerous studies have been performed to make film cooling more effective by optimizing the injection angles and blowing ratios and designing different injection hole configurations. Open literature shows that the optimal injection angle of forward inclination is about 30–35 deg. Jia et al. [3] verified that the recirculation bubble downstream the jet vanishes when the angle is 30 deg or less. The injection angle in Bell et al. [4] and Brittingham and Leylek [5] is 35 deg. Taslim and Khanicheh [6] conducted experimental and numerical studies with an injection angle of 25 deg. The blowing ratio is another important parameter in film cooling. As found in Ref. [3], it has a large effect on the size of recirculation. Kwak and Han [7] measured heat transfer coefficients and film-cooling effectiveness on a gas turbine blade tip. Their results showed that heat transfer coefficient decreased as the blowing ratio increased, while the film effectiveness increased. Mayhew et al. [8] measured the adiabatic cooling effectiveness of film cooling with compound angle holes using thermochronic liquid crystal. Their photographs show that large blowing ratios lower the cooling performance.

Since the mixing between the coolant and main flow is partially controlled by turbulence diffusion, the inlet turbulence intensity of coolant jet also affects film cooling. As shown in Mayhew et al. [8], low inlet turbulence intensity keeps the coolant close to the wall when the blowing ratio is low; while high inlet turbulence intensity helps bring the coolant back to the wall when the blowing ratio is high. To study the effect of upstream flow conditions on film cooling, an inlet plenum as well as the flow arrangement is considered in numerical studies by Brittingham and Leylek [5], Adami et al. [9], etc. It is concluded that an accurate prediction of coolant discharge and wall coverage of cooling film requires computation of flow field in the cooling air supply plenum and duct.

Many studies have been conducted on shaped holes with various configurations. For example, Bell et al. [4] found laterally diffused compound-angle holes and forward diffused compound-angle holes produce higher effectiveness over much wider ranges of blowing ratio and momentum flux ratio compared to the other three simple-angle configurations tested. Brittingham and Leylek [5] concluded that the compound-angle shaped holes could be designed to eliminate crossflow line-of-sight between adjacent holes, and thus somewhat mimic slot-jet performance. To reduce nonuniform cooling pattern inherent in discrete injection holes, Wang et al. [10] conducted experiments by embedding the discrete injection holes in a slot recessing beneath the surface. Premixing inside the slot makes the film cooling more uniform than discrete injection holes.

Although these technologies can continuously improve the performance of conventional air film cooling, the increased net benefits seem to be approaching their limit. In view of the high contents of H_2 and CO in the synthetic fuels for next generation turbines, the increased flame temperature and flame speed from those of natural gas combustion will make gas turbine cooling more difficult and more important. Therefore, development of new cooling techniques is essential for surpassing current limits. One potential new cooling technique is to inject a small amount of tiny water droplets (mist) into the cooling air to enhance the cooling performance. The key mechanism of mist cooling enhancement is attributed to the heat absorbed by evaporation of droplets when moving along the coolant air. The second cooling enhancement mechanism is contributed by direct contact between water

---

Contributed by the Heat Transfer Division of ASME for publication in the Journal of Heat Transfer. Manuscript received March 1, 2006; final manuscript received January 3, 2007. Review conducted by Jayathi Murthy.

droplet and the wall. Other minor cooling enhancement mechanisms include increased temperature gradient and augmented mixing due to droplet–air interactions. Furthermore, continuous evaporation of droplets can last farther into the downstream region where single-phase air film cooling becomes less effective.

Mist has been used to enhance heat transfer in gas turbine systems in different ways. Gas turbine inlet air fog cooling [11] is a common application where water droplets evaporate to lower the compressor air inlet temperature until the relative humidity reaches 100%. In addition, fog overspray is used in industry to provide evaporative cool inside the compressor. Petr [12] reported the results of thermodynamic analysis of the gas turbine cycle with wet compression based on detailed simulation of a two-phase compression process. In 1998, Nirmalan et al. [13] applied water/air mixture as the impingement coolant to cool gas turbine vanes. To explore an innovative approach to cool future high-temperature gas turbines, the authors' research group has conducted a series of experimental studies of mist/steam cooling by injecting 7 μm (average diameter) water droplets into steam flow, e.g., Refs. [14–17]. For a straight tube [14], the highest local heat transfer enhancement of 200% was achieved with 1–5% (weight) mist, and the average enhancement was 100%. In a 180 deg tube bend [15], the overall cooling enhancement ranged from 40% to 300% with the maximum local cooling enhancement being over 800%, which occurred at about 45 deg downstream of the test section inlet. For jet impingement cooling over a flat surface [16], a 200% cooling enhancement was shown near the stagnation point by adding 1.5% (weight) mist. In jet impingement on a concave surface [17], enhancement of 30–200% was achieved within five-slot distance with 0.5% (weight) mist.

Besides experimental tests, numerical simulation is frequently used to study film cooling. Jia et al. [3] employed a V2F k-ε turbulence model to investigate slot jet film cooling. The standard k-ε model with generalized wall function was used by Brittingham and Leylek [5] to simulate film cooling with compound-angle shaped holes. Taslim and Khanicheh [6] also used the standard k-ε model with generalized wall function in their study. Heidmann et al. [18] employed a k-ω model, which does not require a specified distance to the wall for the near-wall grids. Tyagi and Acharya [19] used the large eddy simulation (LES) to reveal the anisotropic characteristics in the wake region of a cooling jet.

To simulate the flow and heat transfer of a discrete phase, such as droplets in mist film cooling, one approach is to track the particles in a Lagrangian frame of reference, and at the same time compute the heat transfer between the discrete phase and the continuous flow. The effect of discrete phase on flow and heat transfer of the continuous phase is incorporated as a source term to the governing equations. The Lagrangian method has been used in many studies such as dispersion of post-dryout flow [20], evaporating droplets in a swirling jet [21], and evaporating spray in turbulent gas flow [22]. Li and Wang [23] conducted a numerical simulation of mist film cooling using the standard k-ε turbulence model with enhanced wall function. Three different holes are adopted in their study including a two-dimensional (2D) slot, a round hole, and a fan-shaped diffusion hole. A comprehensive study is performed on the effect of main flow temperature, blowing angle, blowing ratio, mist injection rate, and droplet size on the 2D slot cooling effectiveness. Significant cooling enhancement (30–50%) was predicted for all the holes used.

Since the accuracy and validity of simulation depends largely on the accuracy of numerical modeling, this paper focuses on investigating the effect of various modeling schemes on the simulated results of mist film cooling, including effects of turbulence models, different flow–droplet interactions (Saffman force, Brownian lift, and thermophoresis), discrete-phase modeling, mist injection locations, and trajectory tracking. The results of this paper will serve as the qualification reference for more complicated studies including 3D cooling holes, various blowing ratios, various density ratios, and rotational effect. This paper can also serve as guidance for designing and conducting corresponding experiments.

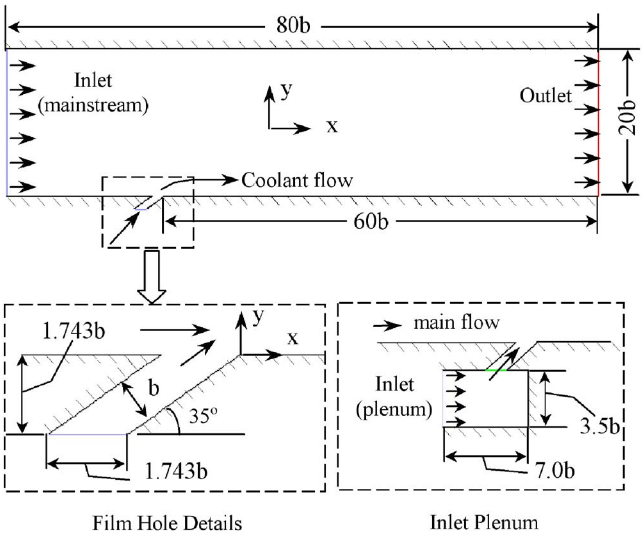

Fig. 1 Computational domain

Numerical Model

Geometrical Configuration. A 2D slot is selected for this study. Its configuration and main dimensions are shown in Fig. 1. The slot width (b) is 4 mm and the slot length is $3b$. The injection angle is 35 deg, which is considered as the optimal value by Refs. [4,5]. The computational domain has a length of $80b$ and a height of $20b$. The slot jet is set to $20b$ from the entrance of the mainstream. To study the effect of upstream conditions of the coolant flow on film cooling performance, a $7.0b \times 3.5b$ extended air supply plenum upstream the film cooling slot is added as a separate case. The cooling air enters the plenum parallel to the main flow.

Governing Equations. The 2D time-averaged steady state Navier–Stokes equations as well as equations for mass, energy, and species transport are solved. The governing equations for conservation of mass, momentum, and energy are given as

$$\frac{\partial}{\partial x_i}(\rho u_i) = S_m \tag{1}$$

$$\frac{\partial}{\partial x_i}(\rho u_i u_j) = \rho \bar{g}_j - \frac{\partial P}{\partial x_j} + \frac{\partial}{\partial x_i}(\tau_{ij} - \rho\overline{u_i' u_j'}) + F_j \tag{2}$$

$$\frac{\partial}{\partial x_i}(\rho c_p u_i T) = \frac{\partial}{\partial x_i}\left(\lambda\frac{\partial T}{\partial x_i} - \rho c_p\overline{u_i' T'}\right) + \mu\Phi + S_h \tag{3}$$

where τ_{ij} is the symmetric stress tensor defined as

$$\tau_{ij} = \mu\left(\frac{\partial u_j}{\partial x_i} + \frac{\partial u_i}{\partial x_j} - \frac{2}{3}\delta_{ij}\frac{\partial u_k}{\partial x_k}\right) \tag{4}$$

The source terms (S_m, F_j, and S_h) are used to include the contribution from the dispersed phase. $\mu\Phi$ is the viscous dissipation and λ is the heat conductivity.

In mist film cooling, water droplets evaporate and the vapor diffuses into its surrounding flow. The flow mixture consists of three main components: water vapor (H_2O), oxygen (O_2), and nitrogen (N_2). The equation for species transport is

$$\frac{\partial}{\partial x_i}(\rho u_i C_j) = \frac{\partial}{\partial x_i}\left(\rho D_j \frac{\partial C_i}{\partial x_i} - \rho \overline{u_i' C_j'}\right) + S_j \tag{5}$$

where C_j is the mass fraction of the species (j) in the mixture, and S_j is the source term for this species. D_j is the diffusion coefficient.

Notice the terms of $\rho\overline{u_i' u_j'}$, $\rho c_p \overline{u_i' T'}$, and $\rho\overline{u_i' C_j'}$ represent the Reynolds stresses, turbulent heat fluxes, and turbulent concentration (or mass) fluxes, which should be modeled properly for a turbulent flow. The Reynolds number of the main flow (based on the duct height and the inlet condition specified later) is about 30,000 in this study. Therefore, turbulence models need to be included.

Turbulence Models

Standard k-ε Model. The standard k-ε model, which, based on the Boussinesq hypothesis, relates the Reynolds stresses to the mean velocity as

$$\rho\overline{u_i' u_j'} = \mu_t\left(\frac{\partial u_i}{\partial x_j} + \frac{\partial u_j}{\partial x_i}\right) - \frac{2}{3}\rho k \delta_{ij} \tag{6}$$

where k is the turbulent kinetic energy, and μ_t is the turbulent viscosity given by

$$\mu_t = \rho C_\mu k^2/\varepsilon \tag{7}$$

where C_μ is a constant and ε is the dissipation rate. The equations for the turbulent kinetic energy (k) and the dissipation rate (ε) are

$$\frac{\partial}{\partial x_i}(\rho u_i k) = \frac{\partial}{\partial x_i}\left[\left(\mu + \frac{\mu_t}{\sigma_k}\right)\frac{\partial k}{\partial x_i}\right] + G_k - \rho\varepsilon \tag{8}$$

$$\frac{\partial}{\partial x_i}(\rho u_i \varepsilon) = \frac{\partial}{\partial x_i}\left[\left(\mu + \frac{\mu_t}{\sigma_\varepsilon}\right)\frac{\partial \varepsilon}{\partial x_i}\right] + C_{1\varepsilon} G_k \frac{\varepsilon}{k} - C_{2\varepsilon}\rho\frac{\varepsilon^2}{k} \tag{9}$$

The term G_k is the generation of turbulent kinetic energy due to the mean velocity gradients.

The turbulent heat flux and mass flux can be modeled with the turbulent heat conductivity (λ_t) and the turbulent diffusion coefficient (D_t), respectively

$$\rho c_p \overline{u_i' T'} = -\lambda_t \frac{\partial T}{\partial x_i} = -c_p \frac{\mu_t}{\mathrm{Pr}_t}\frac{\partial T}{\partial x_i} \tag{10}$$

$$\rho\overline{u_i' C'} = -\rho D_t \frac{\partial C}{\partial x_i} = -\frac{\mu_t}{\mathrm{Sc}_t}\frac{\partial C}{\partial x_i} \tag{11}$$

The constants $C_{1\varepsilon}$, $C_{2\varepsilon}$, C_μ, σ_k, and σ_ε used are: $C_{1\varepsilon}=1.44$, $C_{2\varepsilon}=1.92$, $C_\mu=0.09$, $\sigma_k=1.0$, $\sigma_\varepsilon=1.3$ [24]. The turbulent Prandtl number, Pr_t, is set to 0.85, and the turbulent Schmidt number, Sc_t, is set to 0.7.

Enhanced Wall Function. The above k-ε model is mainly valid for high Reynolds number fully turbulent flow. Special treatment is needed in the region close to the wall. The enhanced wall function is one of several methods that model the near-wall flow. In the enhanced wall treatment, a two-layer model is combined with the wall functions. The whole domain is separated into a viscosity-affected region and a fully turbulent region by defining a turbulent Reynolds number, Re_y

$$\mathrm{Re}_y = y k^{1/2}/\nu \tag{12}$$

where k is the turbulent kinetic energy and y is the distance from the wall. The standard k-ε model is used in the fully turbulent region where $\mathrm{Re}_y > 200$, and the one-equation model of Wolfstein [25] is used in the viscosity-affected region with $\mathrm{Re}_y < 200$. The turbulent viscosities calculated from these two regions are blended with a blending function (θ) to smoothen the transition

$$\mu_{t,\mathrm{enhanced}} = \theta\mu_t + (1-\theta)\mu_{t,1} \tag{13}$$

where μ_t is the viscosity from the k-ε model of high Reynolds number, and $\mu_{t,l}$ is the viscosity from the near-wall one-equation model. The blending function is equal to 0 at the wall and 1 in the fully turbulent region. The linear (laminar) and logarithmic (turbulent) laws of the wall are also blended to make the wall functions applicable throughout the entire near-wall region.

Reynolds Stress Model. In film cooling, the interaction between the injected coolant flow and the approaching main flow could be anisotropic and nonequilibrium with multiscaled integral and dissipation length scales. Therefore, the Reynolds stress model (RSM), a second-moment closure, is considered in this study. The Reynolds stress transport equation can be given as

$$\begin{aligned}\frac{\partial}{\partial x_k}(\rho u_k \overline{u_i' u_j'}) = &-\frac{\partial}{\partial x_k}\left[\rho u_k \overline{u_i' u_j' u_k'} + \overline{P(\delta_{kj}u_i' + \delta_{ik}u_j')}\right.\\ &\left. + \mu\frac{\partial}{\partial x_k}(\overline{u_i' u_j'})\right] - \rho\left(\overline{u_i' u_k'}\frac{\partial u_j}{\partial x_k} + \overline{u_j' u_k'}\frac{\partial u_i}{\partial x_k}\right)\\ &+ \overline{P\left(\frac{\partial u_i'}{\partial x_j} + \frac{\partial u_j'}{\partial x_i}\right)} - 2\mu\overline{\frac{\partial u_i'}{\partial x_k}\frac{\partial u_j'}{\partial x_k}}\end{aligned} \tag{14}$$

The diffusive term on the right-hand side can be modeled as

$$\begin{aligned}-\frac{\partial}{\partial x_k}&\left[\rho u_k \overline{u_i' u_j' u_k'} + \overline{P(\delta_{kj}u_i' + \delta_{ik}u_j')} + \mu\frac{\partial}{\partial x_k}(\overline{u_i' u_j'})\right]\\ &= \frac{\partial}{\partial x_k}\left[\frac{\mu_t}{\sigma_k}\frac{\partial}{\partial x_k}(\overline{u_i' u_j'})\right]\end{aligned} \tag{15}$$

The second term on the right-hand side of Eq. (14) is the production term, and it is notated as G_{ij}

$$G_{ij} = -\rho\left(\overline{u_i' u_k'}\frac{\partial u_j}{\partial x_k} + \overline{u_j' u_k'}\frac{\partial u_i}{\partial x_k}\right) \tag{16}$$

The third term is the pressure–strain term, which can be modeled as

$$\overline{P\left(\frac{\partial u_i'}{\partial x_j} + \frac{\partial u_j'}{\partial x_i}\right)} = C_1\rho\frac{\varepsilon}{k}\left(\overline{u_i' u_j'} - \frac{2}{3}\delta_{ij}k\right) - C_2\left[A_{ij} - \frac{1}{3}\delta_{ij}A_{kk}\right] \tag{17}$$

where $A_{ij}=G_{ij}-\partial(\rho u_k \overline{u_i' u_j'})/\partial x_k$. The constants C_1 and C_2 are 1.8 and 0.6, respectively. By assuming the dissipation is isotropic, the last term in Eq. (14) can be approximated by

$$2\mu\overline{\frac{\partial u_i'}{\partial x_k}\frac{\partial u_j'}{\partial x_k}} = \frac{2}{3}\delta_{ij}\rho\varepsilon \tag{18}$$

Modeling of the turbulent heat flux and mass flux are similar as in the k-ε model. The turbulent kinetic energy and its dissipation rate can be calculated from the Reynolds stresses.

Other Models. Ignoring details here, the turbulence models adopted in this study also include RNG k-ε model, k-ω model, and the shear-stress transport (SST) k-ω model. The RNG k-ε model was derived using renormalization group theory [26]. It has an additional term in the ε equation to improve the accuracy for rapidly strained flows. The effective viscosity is used to account for low-Reynolds-number effect. Theoretically, this model is more accurate and reliable than the standard k-ε model. The standard k-ω model is an empirical model based on transport equations for the turbulent kinetic energy (k) and the specific dissipation rate (ω), which can also be considered as the ratio of ε to k [27]. The low-Reynolds-number effect is accounted for in the k-ω model. The SST model is a mixture of the k-ω model and the k-ε model: close to the wall it becomes the k-ω model while in the far field the k-ε model is applied [28].

Dispersed-Phase Model (Water Droplets)

Droplet Flow and Heat Transfer. Based on Newton's second law, the droplet motion in airflow can be formulated by

$$m_p d\mathbf{v}_p/dt = \sum \mathbf{F} \tag{19}$$

where m_p is the droplet mass, and $\mathbf{v_p}$ is the droplet velocity (vector). The right-hand side is the combined force acting on the droplet, which normally includes the hydrodynamic drag [29], gravity, and other forces such as Saffman's lift force [30], thermophoretic force [31], and Brownian force [32], etc.

Without considering the radiation heat transfer, droplet's heat transfer depends on convection and evaporation as given in the following equation

$$m_p c_p \frac{dT}{dt} = \pi d^2 h (T_\infty - T) + \frac{dm_p}{dt} h_{fg} \tag{20}$$

where h_{fg} is the latent heat. The convective heat transfer coefficient (h) can be obtained with an empirical correlation [33,34]

$$\mathrm{Nu}_d = \frac{hd}{\lambda} = 2.0 + 0.6\mathrm{Re}_d^{0.5}\mathrm{Pr}^{0.33} \tag{21}$$

where Nu is the Nusselt number, and Pr is the Prandtl number.

The mass change rate or vaporization rate in Eq. (20) is governed by concentration difference between droplet surface and the air stream

$$-\frac{dm_p}{dt} = \pi d^2 k_c (C_s - C_\infty) \tag{22}$$

where k_c is the mass transfer coefficient, and C_s is the vapor concentration at the droplet surface, which is evaluated by assuming the flow over the surface is saturated. C_∞ is the vapor concentration of the bulk flow, obtained by solving the transport equations. The value of k_c can be given from a correlation similar to Eq. (21) by [33,34].

$$\mathrm{Sh}_d = \frac{k_c d}{D} = 2.0 + 0.6\mathrm{Re}_d^{0.5}\mathrm{Sc}^{0.33} \tag{23}$$

where Sh is the Sherwood number, Sc is the Schmidt number (defined as ν/D), and D is the diffusion coefficient of vapor in the bulk flow.

When the droplet temperature reaches the boiling point, the following equation can be used to evaluate its evaporation rate [35]

$$-\frac{dm_p}{dt} = \pi d^2 \left(\frac{\lambda}{d}\right)(2.0 + 0.46\mathrm{Re}_d^{0.5})\ln[1 + c_p(T_\infty - T)/h_{fg}]/c_p \tag{24}$$

where λ is the gas/air heat conductivity, and c_p is the specific heat of the bulk flow.

Theoretically, evaporation can occur at two stages: (a) when the temperature is higher than the saturation temperature (based on local water vapor concentration), water evaporates, and the evaporation is controlled by the water vapor partial pressure until 100% relative humidity is achieved; (b) when the boiling temperature (determined by the air-water mixture pressure) is reached, water continues to evaporate. After the droplet evaporates due to either high temperature or low moisture partial pressure, the vapor diffuses into the main flow and is transported away.

Stochastic Particle Tracking. The turbulence models discussed above can only obtain the time-averaged velocity. Using this velocity to trace the droplet will result in an averaged trajectory. In a real flow, the instantaneous velocity fluctuation would make the droplet move around this averaged track. However, the instantaneous velocity is not simulated in the current computation because the turbulence is modeled as time-averaged terms. One way to simulate the instantaneous turbulence effect on droplets dispersion is to "improvise" the random turbulence fluctuation by using the stochastic tracking scheme [36]. Basically, the droplet trajectories are calculated by imposing the instantaneous flow velocity ($\bar{u} + u'$) rather than the average velocity ($\bar{u}$). The velocity fluctuation is then given as

$$u' = \zeta(\overline{u'^2})^{0.5} = \zeta(2k/3)^{0.5} \tag{25}$$

where ζ is a normally distributed random number. This velocity will apply during a characteristic lifetime of the eddy (t_e), a time scale calculated from the turbulent kinetic energy and dissipation rate. After this time period, the instantaneous velocity will be updated with a new ζ value until a full trajectory is obtained. Note when the RSM model is used, the velocity fluctuation is independently decided in each direction. When the stochastic tracking is applied, the basic interaction between droplets and continuous phase keeps the same, accounted by the source terms in the conservation equations. The source terms are not directly but rather indirectly affected by the stochastic method, so formulation of the source terms is not affected by implementing the stochastic tracking method. For example, the drag force between a water droplet and the air flow depends on the slip velocity calculated by the averaged Navier–Stoke equations. When the stochastic tracking method is used, a random velocity fluctuation is imposed at an instant of time, and the drag force will be calculated based on this instantaneous slip velocity. The source term associated with this instantaneous drag force enters into the momentum equation without any additional formulation. For a steady-state calculation, the "instant of time" means "each iteration step."

Boundary Conditions

Continuous Phase. The main flow is assumed to be dry air (zero humidity). Uniform velocity (10 m/s) and temperature (400 K) are assigned to the mainstream inlet. Coolant flow is assigned as saturated air (100% relative humidity). Without the plenum, jet inlet velocity of the coolant slot is 10 m/s, and the temperature is 300 K. For cases with the plenum, the inlet velocity of coolant flow at the plenum inlet is 2.87 m/s, which gives an average jet velocity of 10 m/s. The inlet condition of the turbulence is specified by providing the turbulence intensity and the turbulence length scale (half of the hydraulic diameter times 0.07). The turbulence intensity of both mainstream inlet and coolant flow inlet is 1% for most of the cases, while a turbulence intensity of 10% is assigned to study its effect on cooling performance.

The flow exit (outlet) of main computational domain is assumed to be at a constant pressure. The backflow (reverse flow), if any, is set to 400 K. All the walls in the computational domain are adiabatic and have a nonslip velocity boundary condition.

Note that the above assigned temperature and velocity conditions are referenced in several previous studies of air-film cooling, for example, Refs. [4,5], although they are not corresponding to the real conditions in gas turbine applications. For the convenience of comparing the results of this study to other published work, these values used by the previous published work are adopted in this study. While the current paper serves as a conceptual study on film cooling with mist injection, further research is to be performed with more realistic parameters for gas turbine applications.

Disperse Phase. The droplet size is uniformly given as 10 μm. The mass ratio of mist over cooling airflow is 2%, which is about 7.0×10^{-4} kg/s for the 2D slot with a unit depth of 1 m. Mist is injected at 25 locations uniformly distributed along the jet inlet or the inlet of the air plenum. To examine the effect of the number of mist injection locations, cases with different injection locations are considered. The effect of turbulent dispersion on droplet trajectories is calculated by tracking a number of trajectories with the stochastic method. The trajectory number is chosen to be 50 in most cases. Several test runs are conducted to check the effect of this trajectory number. The boundary condition of droplets at

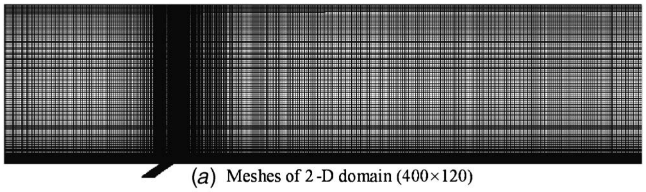

(*a*) Meshes of 2-D domain (400×120)

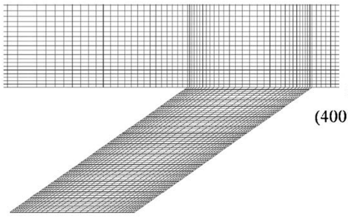

(*b*) Grids close to the 2-D slot (400×120)

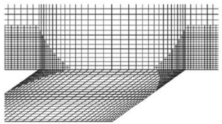

(*c*) Grids close to 2-D slot (400×120 with near-wall adaptation)

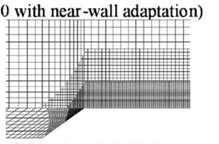

(*d*) Grids close to 2-D slot (400×120 with 2-time near-wall adaptation)

Fig. 2 Meshes

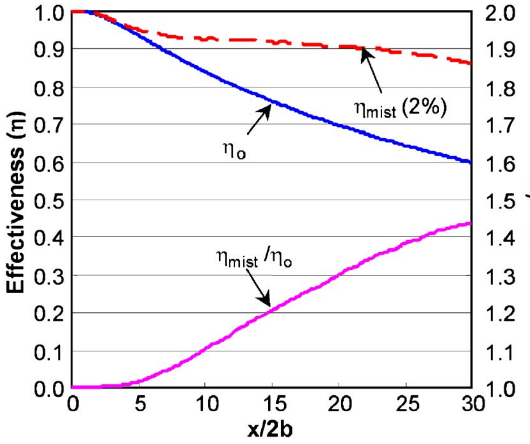

Fig. 3 Baseline cooling effectiveness and enhancement

walls is assigned as "reflect," which means the droplets elastically rebound off once reaching the wall. At the outlet, the droplets just simply flee/escape from the computational domain. A more complex model is needed to determine if the droplets break up, rebound, or are trapped by (or wet) the wall when they hit the wall. However, further analysis shows only a small percentage (approximately 1–2%) of droplets have the chance to contact the wall. In a real gas turbine condition with a wall superheated 700–1000 K above the saturation temperature, the droplets will definitely reflect elastically if they ever touch the wall.

Numerical Method. The commercial software package FLUENT (version 6.2.16) from Fluent, Inc. is adopted in this study. The simulation uses the segregated solver, which employs an implicit pressure–correction scheme [35]. The SIMPLE algorithm is used to couple the pressure and velocity. Second order upwind scheme is selected for spatial discretization of the convective terms and species. Lagrangian trajectory calculations are employed to model the dispersed phase of droplets. The impact of droplets on the continuous phase is considered as source terms to the governing equations. After obtaining an approximate flow field of the continuous phase (airflow in this study), droplets are injected and their trajectories are calculated. At the same time, drag, heat, and mass transfer between the droplets and the airflow is calculated. The simulation is conducted as a steady-state problem.

As shown in Fig. 2, structured but nonuniform grids are constructed in this study. The grids near the jet wall and the bottom wall of the main domain are denser than the other area. The grid number is 400 in the x direction and 120 in the y direction. Different meshes are tested for grid dependence. Furthermore, the near-wall grid is adapted twice to test its effect on calculated results for both single-phase and mist film cooling cases.

Iteration proceeds alternatively between the continuous and discrete phases. Ten iterations in the continuous phase are conducted between two iterations in the discrete phase. Converged results are obtained after the specified residuals are met. A converged result renders mass residual of 10^{-4}, energy residual of 10^{-6}, and momentum and turbulence kinetic energy residuals of 10^{-5}. These residuals are the summation of the imbalance for each cell, scaled by a representative of the flow rate. Typically, 1000–2000 iterations are needed to obtain a converged result, which takes about 1–2 h on a 2.8 GHz Pentium 4 personal computer. The simulation precision is estimated to be 10%; and the accuracy of the results is estimated to be 15%.

Results and Discussion

Baseline Case. The baseline case is run with the basic mesh (400×120) shown in Fig. 2(*a*). The inlet velocity is 10 m/s for both the mainstream and jet flow. The temperatures are 400 K and 300 K for the mainstream and jet flow, respectively. Considering the density difference, the blowing ratio, defined as $M = (\rho u)_c/(\rho u)_g$, is 1.3 in this case, while the ratio of velocity is 1. Here the subscript "c" represents the coolant flow, and "g" represents the main flow. The standard k-ε turbulence model with enhanced wall treatment is used with an inlet turbulence intensity of 1%. Mist mass ratio is 2%, and the droplet size is 10 μm. The mist is injected into the jet flow uniformly at 25 locations of the inlet. Stochastic tracking is used with a trajectory number of 50. Therefore, the total number of trajectories is 1250 (50×25).

The adiabatic cooling effectiveness (η) is used to examine the performance of mist film cooling. The definition of η is

$$\eta = (T_g - T_{\mathrm{aw}})/(T_g - T_c) \tag{26}$$

where T_g is the mainstream hot gas inlet temperature, which is a fixed value for calculating the adiabatic cooling effectiveness of any location. T_c is the temperature of the coolant (jet), which is assigned as a constant of 300 K in this study. T_{aw} is the adiabatic wall temperature, which is calculated for each location by assigning a zero wall heat flux as the boundary condition to simulate a perfectly insulated wall. η ranges from 0 (no cooling) to 1 (ideal case). Figure 3 shows the effectiveness along the cooling surface. Note that the hydraulic diameter of the slot $(2b)$ is used to scale the distance downstream. It can be seen that film cooling is significantly enhanced by mist injection, especially in the downstream region, where the evaporation of droplets becomes stronger because of deterioration of air film cooling and the resulted higher flow temperature. Due to continuous mixing between the main flow and coolant, film cooling inevitably becomes less effective downstream. It has been a serious challenge to enhance cooling downstream of $x/2b=15$. The injection of water droplets works very well to meet this challenge. Also shown in Fig. 3 is the cooling enhancement ratio with and without mist $(\eta_{\mathrm{mist}}/\eta_0)$. The cooling enhancement can be defined as $(\eta_{\mathrm{mist}}/\eta_0 - 1)$. It is seen that the maximum enhancement can reach 42% further downstream $(x/2b=30)$ with an average cooling enhancement of 15.5%.

Effect of Near-Wall Grid. To apply the enhanced wall treatment in resolving the viscosity-affected near-wall region, the near-wall mesh should be constructed to have y^+ at the order of 1. It is also reported that a higher y^+ is acceptable as long as it is well inside the viscous sublayer $(y^+ < 4-5)$. Figure 4 shows the y^+

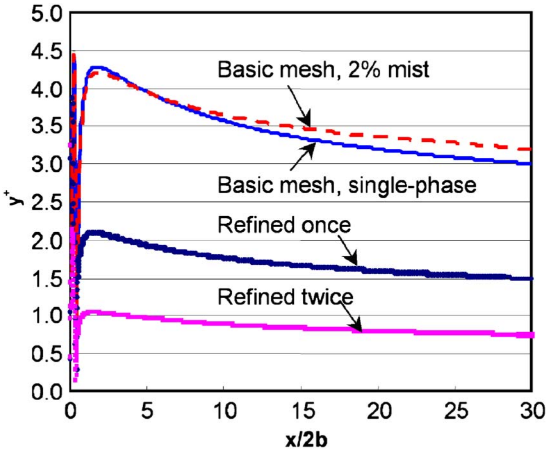

Fig. 4 y^+ **along the wall with different grid systems**

value along the wall in the current study. It can be seen that y^+ ranges from 3 to 4.5 for the basic grid. The y^+ value of film cooling with mist is almost the same as the case without mist. To examine the effect of near-wall grid on mist film cooling simulation, the near-wall grid is refined twice—each time the density of ten grids close to the wall are doubled in both directions: The first doubling brings the y^+ value to 1.5–2, and the second doubling makes the y^+ value lower than 1 at most of the locations.

The effect of near-wall grids on film cooling is shown in Fig. 5. All three single-phase film cooling cases show identical values. This indicates that the first near-wall grid could be placed at $y^+ = 5$ and does not affect the results for the air–film cases. As to mist film cooling, there is a 3–5 percentage points increase of the cooling effectiveness when the finer grids are adopted. A possible reason is that the source terms contributed by droplet evaporation become more important to smaller control volumes near the wall. The low velocity close to the wall keeps the droplets in the viscous layer longer. Evaporative cooling is more effective near the wall because the droplets are physically present near the wall when finer near-wall grids are present in the computational domain. However, the wall function treatment could represent the velocity profile adequately but does not include the discrete phase if no grids are present near the wall.

Due to the low velocity close to the wall, more time steps are needed to calculate the droplets' trajectories and the CPU time increases significantly (3–5 times).

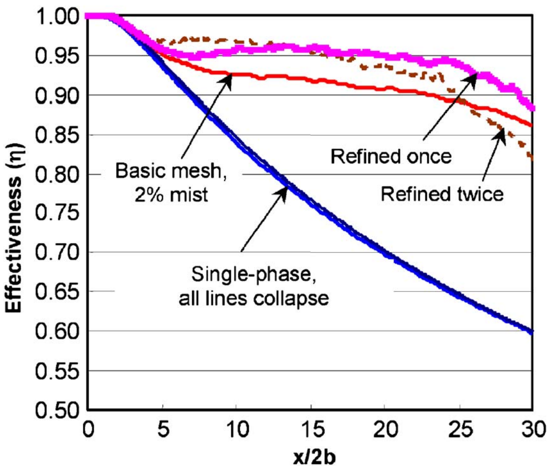

Fig. 5 Cooling effectiveness with different grid systems

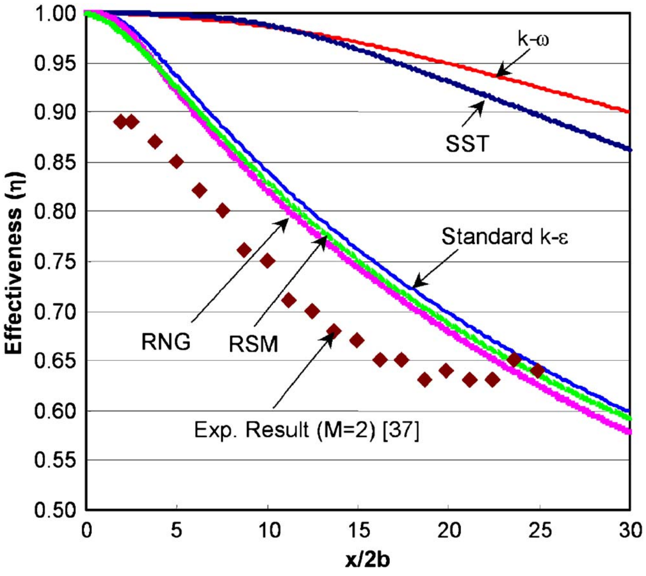

Fig. 6 Effect of turbulence models on single-phase film cooling performance

Effect of Turbulence Models. To study the effect of turbulence models on film cooling simulation, different turbulence models, including the RNG k-ε, k-ω, and Reynolds stress model, are employed. It is noted that the constants in turbulence equations may not be the most appropriate values for mist film cooling flow. Usually these constants need to be "tuned" for different flow physics such as accelerated flow, decelerated flow, separated flow, low-Reynolds number flow, curved flow, and rotating flow, etc. Since a better knowledge is needed on what values these turbulence constants should be for a mist film cooling flow, the current approach is conservative and appropriate by not tuning the values of these constants. Furthermore, the main purpose of this study is to investigate the effect of adding mist to the air flow on film cooling effectiveness, rather than study how turbulence models should be modified to predict mist film cooling flow more accurately. Therefore, using the same values of these turbulence constants for both the air-only flow and the air/mist flow provides a controlled condition for a meaningful comparison of the results.

Figure 6 shows the cooling effectiveness from different models. Basically, the standard k-ε, RNG, and RSM models give very similar results: The cooling effectiveness differs only by 0.02, which is slightly higher than the test data in Ref. [37]. The possible reasons that may cause the difference between the experimental data and simulation are (a) edge effect—the slot is not truly two-dimensional in the test. The data in Ref. [37] represent averaged values in the spanwise direction. (b) The test surface is not truly adiabatic in experiments, so the coolant flow could be preheated by the test section wall and lead to a lower film cooling effectiveness. (c) The boundary layer approaching the injection holes is different between simulation and experimental cases. The boundary layer in the experiment of Ref. [37] was tripped by a wire, which was not simulated in this study. (d) The inherited errors contributed from numerical formulating, calculation, and modeling. However, the k-ω and SST give results significantly deviating from the former group; the difference of cooling effectiveness can be as large as 0.2. Further analysis shows that the flow structure near the jet exit also varies with the turbulence model used. It is speculated that the different flow patterns predicated by various turbulence models could shed some light on explaining the different cooling performance. Figure 7 shows that the standard k-ε model predicts a small recirculation region induced by flow separation downstream the jet, while all the other models, including both the SST model and RSM model, predict a

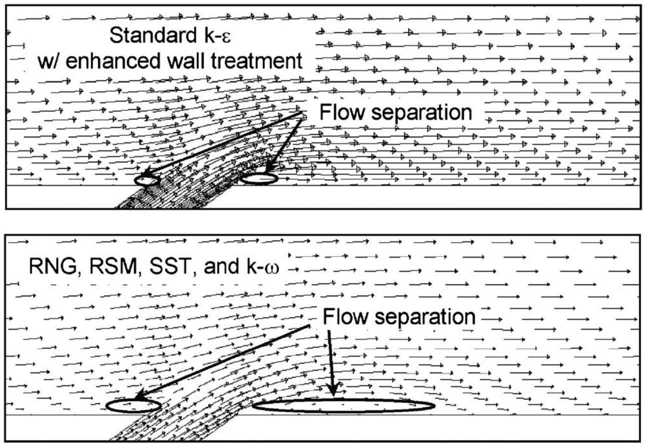

Fig. 7 Flow field close to the jet exit predicted by different turbulence models

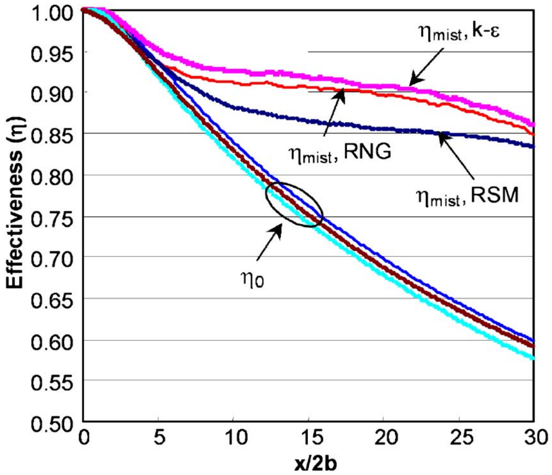

Fig. 8 Effect of turbulence models on mist film cooling performance

larger flow separation. Since both RNG and RSM predict similar cooling performance as the standard *k*-*ε* model, the effect of the different sizes of separation region does not seem to be predominant on cooling effectiveness in this study. An even smaller vortex located immediately upstream of the jet exit is predicted. Its effect on cooling effectiveness could be ignored. The downstream separation is expected to exert a negative impact on aerodynamic efficiency.

The characteristics of the approaching boundary layer predicted by different turbulence models are documented in Table 1. The location is at 60 mm downstream of the mainstream inlet and 20 mm upstream of the coolant jet. *k*-*ω* and SST models result in a thinner boundary layer thickness, which is consistent with the higher cooling effectiveness. Note that the boundary layer close to the coolant jet hole is disturbed by the jet flow, so it is not appropriate to document the approaching boundary layer characteristics too close to the jet hole.

Figure 8 shows the effect of turbulence models on mist film cooling. Since single-phase experimental results support that *k*-*ω* and SST models (without fine tuning of the turbulence constants) are poorer for the current problem, these two models are not applied for mist cooling cases. The RNG model gives a similar result as the standard *k*-*ε* model does. The cooling effectiveness from RSM model is consistently lower than the other two turbulence models by 0.05. The explanation can be sought by looking into the prediction of turbulence characteristics in Figs. 9 and 10.

Figure 9 shows the distribution of the Reynolds stresses in contour plots, and Fig. 10 presents the Reynolds stress values at $y/2b=0.125$. As expected, the turbulence is anisotropic near the jet exit and the adiabatic wall. The Reynolds stress of $\overline{u'u'}$ is larger than $\overline{v'v'}$ in most cases, and even far downstream the anisotropy index (ratio of $\overline{u'u'}$ and $\overline{v'v'}$) can be as high as 5. Compared to other models, RSM predicts smaller turbulence fluctuations in the *y* direction, and that makes the droplets move at a lower speed towards the wall. Therefore, the droplet effect predicted by the RSM model becomes relatively weaker. The Reynolds stresses become very small in the field far away from the wall (not shown in the figure), and the ratio of Reynolds stresses ($\overline{u'u'}/\overline{v'v'}$) is close to 1, which means the flow is close to isotropic in the far field. Rigorous turbulence transport, represented by the value of $\overline{u'v'}$, seems to be present in the region of $x/2b<5$ as shown in Fig. 10.

Table 1 Characteristics of approaching boundary layers with different turbulence models, located at 60 mm downstream the mainstream inlet and 20 mm before the coolant jet hole

	k-*ε*	RNG	*k*-*ω*	SST	RSM
Boundary layer thickness, δ (mm)	2.8	2.8	2.1	2.1	2.5
Displacement thickness, δ_1 (mm)	0.68	0.68	0.72	0.72	0.76
Momentum thickness, δ_2 (mm)	0.31	0.31	0.28	0.27	0.31
Shape factor, $H_{12}=\delta_1/\delta_2$	2.19	2.19	2.57	2.67	2.45

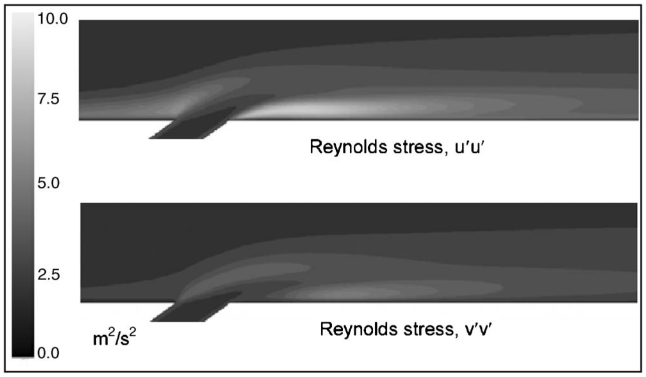

Fig. 9 Distribution of Reynolds stresses close to the jet exit predicted by the RSM model

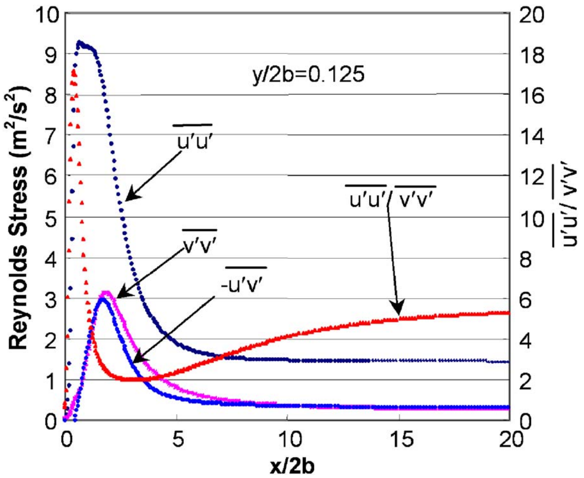

Fig. 10 Reynolds stresses predicted by the RSM model

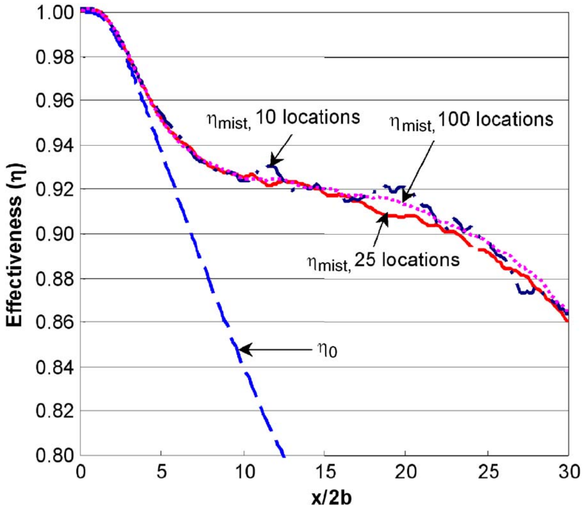

Fig. 11 Effect of the number of injection locations

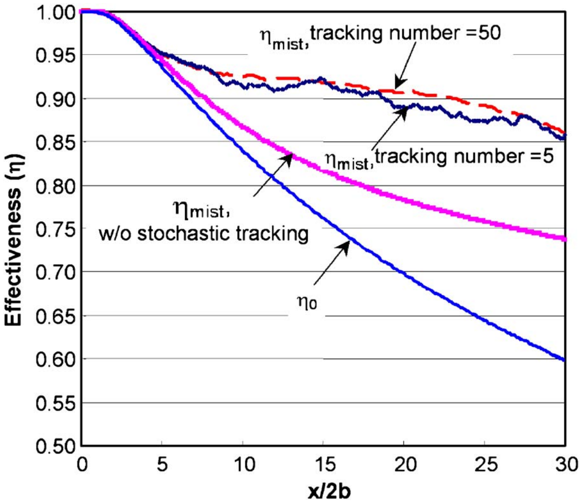

Fig. 12 Effect of number of stochastic tracking

Effect of the Number of Injection Locations. In a real application, the droplets are expected to be premixed uniformly in the coolant before entering the plenum. In simulation, the droplets are uniformly injected into the flow from a limited number of locations with a specified flow rate. It is understandable that the simulation results will be more accurate when more injection locations are applied in simulation. However, more injection locations will require more computational time. To examine how the injection number affects the numerical results, Fig. 11 shows the cooling effectiveness with three different injection numbers while the overall mist concentration keeps the same. The results show that the average cooling effectiveness is similar for all three injection numbers. The smaller injection number at 10 has caused unrealistic numerical jiggles. The highest injection number at 100 locations gives the smoothest cooling effectiveness distribution. To save computational time, the injection number is selected to be 25 for all cases because the overall results are sufficiently comparable within one percentage point to that predicted by employing 100 injection locations.

Effect of the Number of Stochastic Tracking. To take into account the effect of turbulence on the dispersion of droplets by using stochastic tracking scheme, trajectories are calculated and traced multiple times for each droplet injection and the averaged effect is applied to the main flow. It is desirable to know how many times the trajectories should be tracked and how important the turbulence dispersion is on mist film cooling. Figure 12 shows the results with different tracking numbers. Without random tracking, the effectiveness of mist film cooling is about ten percentage points lower because all the droplets follow the streamline closely and theoretically never have a chance to move closer or touch the wall. The instantaneous, unsteady droplet dynamics induced by instantaneous turbulence fluctuations is not included in the Reynolds average equation. Random tracking scheme creates a distributed random number to simulate the instantaneous random turbulence fluctuations and applies the random fluctuations to droplets only (see Eq. (25)). The turbulence calculation is not affected. Although the droplets' trajectory is not the same as the streamline, they are very close when the droplet size is small. By considering the turbulence dispersion, the droplets deviate from the streamline and some of them move towards the surface, leading to a significantly increased effectiveness downstream of $x/2b=5$. The random effect of the turbulence on the droplets can be reasonably predicted only if a sufficient number of trajectories are calculated. Fewer trajectories will show a nonsmooth distribution of the effectiveness, which does not correctly reflect the actual effect from numerous droplets. In this study, the trajectory number for the baseline case is chosen to be 50 at each injection location. The total trajectory number is $50\times25=1250$, which gives a reasonable smooth curve.

It should be noted that the iteration convergence becomes difficult after introducing the stochastic tracking, especially with a small number of trajectories. As seen in Fig. 13, after activating the mist injection, the residuals drop first, followed by fluctuation at a certain level. The fluctuation does not exist in the case of mist film cooling without stochastic tracking. This is because with stochastic tracking, the trajectories change each time the discrete phase information is updated and the source terms contributed by the droplets change accordingly, even though the flow field of continuous phase keeps the same. Therefore, the residuals increase each time the droplets are retracked. Tracking more trajectories from a large number of injections reduces the level of residuals fluctuations.

Effect of Inlet Turbulence Intensity. Four cases have been considered: 1% for both main flow and jet flow; 1% for main flow, and 10% for jet flow; 10% for main flow and 1% for jet flow; and 10% for both main and jet flow. Figure 14 presents the results of two cases to show the effect of inlet turbulence intensity; the other two cases are bound by the two cases shown in Fig. 14. Higher turbulence intensity reduces the cooling effectiveness due to a higher mixing rate between the main flow and coolant. The maximum reduction of cooling effectiveness is about 0.05 under the conditions of this study. It is found that the coolant inlet turbu-

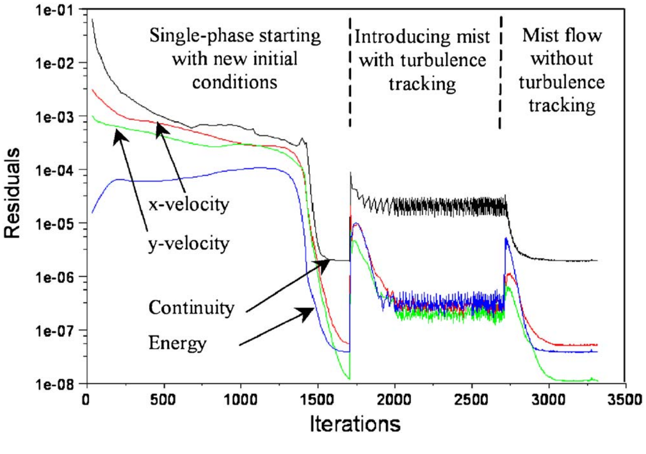

Fig. 13 Residual histories

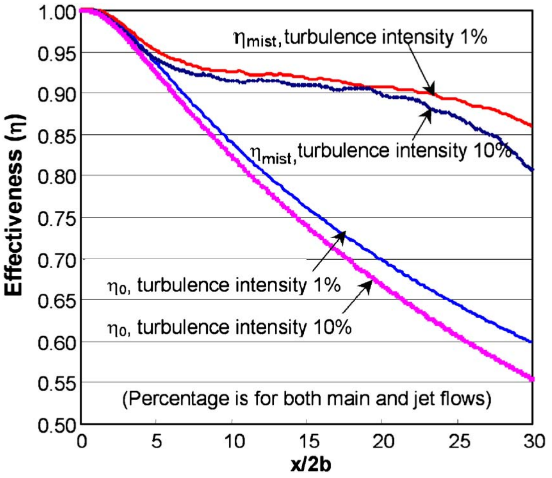

Fig. 14 Effect of inlet turbulence intensity

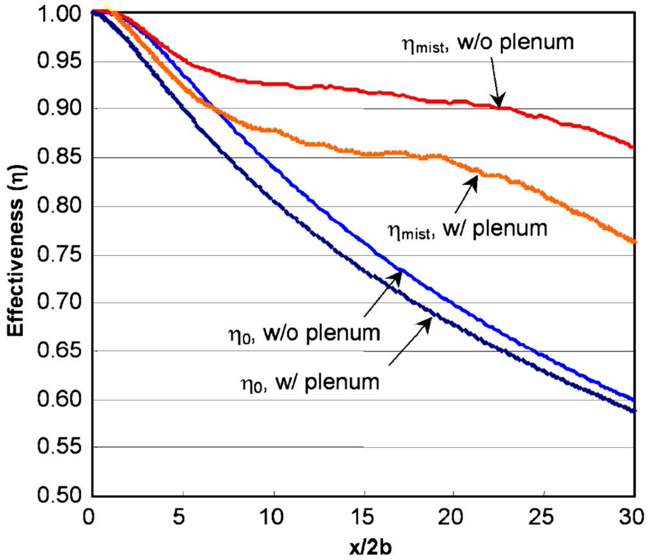

Fig. 15 Effect of inlet plenum on film cooling performance

lence intensity mainly affects the cooling performance close to the jet exit and the main flow inlet turbulence intensity affects the result far downstream. As to the mist film cooling, the higher inlet turbulence intensity enhances the mixing of the coolant and main flow, but at the same time it can augment the droplet turbulence dispersion towards the wall. The combined effect produces a little bit lower cooling effectiveness (0.01–0.02) in this study, which is also shown in Fig. 14.

Mayhew et al. [9] reported that higher jet inlet turbulence intensity produces a lower cooling effectiveness when the blowing ratio is low (0.5). However, at high blowing ratio (1.5), higher jet inlet turbulence intensity helps bring the coolant toward the wall and improves the cooling performance. The cases in Ref [9] are for three-dimensional holes, and the 3D effect can contribute to this difference.

Effect of Inlet Plenum. Several numerical studies, for example, Refs. [5,9], included a plenum with different flow arrangements to account for the effect of flow entering the jet hole on film cooling. They reported that the plenum geometry could largely affect film cooling flow pattern and cooling performance. The effect of plenum is also examined for mist film cooling in this study. The plenum has a size of $7.0b \times 3.5b$, and its inlet velocity is parallel to the main flow.

As shown in Fig. 15, under the parameters of the current study, the plenum does play an important role for both the single-phase and mist film cooling. With the plenum considered, the effectiveness decreases by 0.03–0.04 for single-phase and 0.07–0.1 for mist film cooling, respectively. Figure 16 gives the details of flow fields close to the injection slot. It can be seen that the flow separates inside the coolant supply passage. The turbulence intensity of the coolant flow increases significantly due to flow separation inside the film slot. The high turbulence results in reduced cooling effectiveness due to a rapid mixing between the coolant and main flow. As seen in Fig. 16, the droplet trajectories significantly deviate from the case without the plenum. When the turbulent dispersion is not considered by applying stochastic tracking, all the droplets tend to merge into a finite string after leaving the plenum, which is the typical “roping” phenomenon. The turbulent fluctuation can cause the droplets “string” to loosen. However, compared to the case without plenum, the average trajectory of the droplets moves away from the cooling wall, which degrades the cooling performance. The effect of plenum on mist film cooling performance is more than on single-phase film cooling performance. More studies are needed to determine optimizing plenum geometries for mist film cooling applications.

Effect of Gravity. Film cooling orientation can be in any direction. In this study, the effect of gravity is examined by setting the gravity normal to the cooling surface. As expected, if the gravity makes the droplets move towards the wall, the cooling enhancement will be 2–5% higher (no figure is shown here). This effect is also related to the droplet size and jet velocity. In a real application at high pressure and velocity conditions, the effect of gravity could be neglected.

Effect of Saffman Lift, Thermophoretic, and Brownian Forces. Recognizing that the motion of droplets in film cooling is subject to additional forces such as thermophoretic force, Saffman lift, and Brownian force, cases are run to investigate the importance of these forces with one force exclusively activated each time. Saffman force [30] concerns a sphere moving in a shear

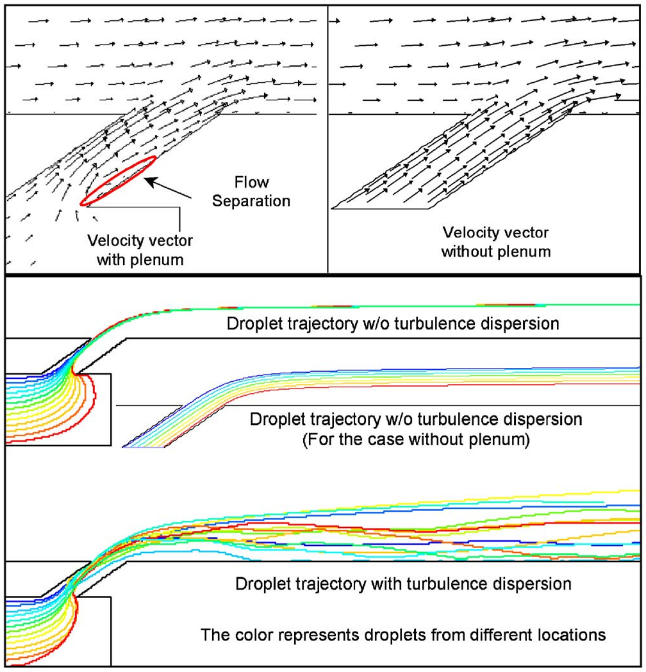

Fig. 16 Velocity vector and droplet trajectories near the jet slot with inlet plenum for mist film cooling

field. It is perpendicular to the direction of flow, originating from the inertia effects in the viscous flow around the particle. It can be given as

$$F_{\text{saff}} = 1.615\rho\nu^{0.5}(u_g - u_p)(du/dn)^{0.5} \tag{27}$$

where du/dn is the gradient of the tangential velocity. It is valid only when $\text{Re}_p \ll 1$.

The thermophoretic force is arisen from asymmetrical interactions between a particle and the surrounding fluid molecules due to a temperature gradient. This force tends to repel particles or droplets from a high temperature region to a low-temperature region. The following equation can be used to model this force

$$F_n = -K\frac{1}{m_p T}\frac{\partial T}{\partial n} \tag{28}$$

where K is a thermophoretic coefficient, and more details can be found in Talbot et al. [31]

Brownian force involves random motion of a small particle suspended in a fluid, which resulted from the instantaneous impact of fluid molecules. It can be modeled as a Gaussian white noise process with spectral intensity given by Ref. [32].

Results indicate that the effect of Saffman lift and Brownian force is imperceptible. The thermophoretic force, which tends to move the droplets toward the cold wall, increases the cooling effectiveness by 0.01 on average. Since all the curves collapse into the baseline case, no figure is given here.

Concerns and Future Research

The main objective of this study is to explore the concept of mist film cooling and disparity induced by applying various models and schemes on mist film cooling simulation. Although numerical simulation shows promising results by employing mist film cooling, experimental studies are needed to verify these simulated results. For example, the interaction of droplet with heated wall could be more complicated than the simple reflection applied in this study. The importance of droplet collision and coalescence could be evaluated in future studies. There is a concern on the potential erosion and corrosion introduced by the water droplets on the gas turbine airfoils. This concern needs to be investigated before implementing the mist film cooling scheme.

Conclusions

By injecting a small amount of droplets (mist) into the cooling air, the performance of film cooling could be improved significantly. This paper conducts numerical simulation to explore this new concept, focusing on the effect of turbulence models and numerical modeling schemes of the dispersed phase. The effects of inlet turbulence intensity as well as the grid density on numerical results are also studied. The conclusions are as follows:

1. Injecting 2% mist by mass into the coolant can increase the cooling effectiveness downstream ~45%;
2. Near-wall grids within a y^+ of 5 show little effect on the single-phase film cooling result. Refined grids close to the wall are needed to provide more accurate predictions for mist film cooling;
3. Results given by the RNG k-ε model, RSM, and the standard k-ε model with enhanced wall treatment are consistent. Both the k-ω and SST models show much higher cooling effectiveness. Simulation with RSM model indicates that the lower normal Reynolds stress $(\overline{v'v'})$ in the y direction results in a lower cooling effectiveness than other turbulence models;
4. The turbulence dispersion shows a significant effect on mist film cooling by using the stochastic tracking scheme. Approximately ten percentage points cooling effectiveness enhancement result in addition to the enhancement from the mist film cooling without considering turbulence dispersion. Random tracking makes the calculation convergence difficult. Adequate cooling effectiveness distribution can be obtained with calculation of 50 or more trajectories at each injection location;
5. 25 injection locations of droplets are enough to catch the effect of the mist on film cooling in this study. Numerical jiggles on the cooling effectiveness curve appear when fewer injection locations are employed;
6. Increasing the inlet turbulence intensity from 1% to 10% gives a five percentage point decrease of cooling effectiveness in this study. The effect of inlet turbulence intensity on single-phase and mist film cooling is similar;
7. The plenum changes the coolant velocity profile and turbulence intensity at the injection slot exit. The cooling performance is adversely affected when the plenum is included in this study due to a flow separation in the coolant slot and roping phenomenon of droplets; and
8. The cooling effectiveness increases by one percentage point on average when the thermophoretic force is included, which tends to move the droplets toward the wall. The effect of Brownian force and Saffman lift is imperceptible.

Acknowledgment

This study is supported by the Louisiana Governor's Energy Initiative via the Clean Power and Energy Research Consortium (CPERC) and administered by the Louisiana Board of Regents.

Nomenclature

b = slot width (m)
C = concentration (kg/m^3)
c_p = specific heat (J/kg K)
D = mass diffusion coefficient (m^2/s)
d = droplet diameter (m)
F = force (N)
k = turbulent kinetic energy (m^2/s^2)
k_c = mass transfer coefficient (m/s)
h = convective heat transfer coefficient (W/m^2 K)
h_{fg} = latent heat (J/kg)
M = blowing ratio, $(\rho u)_c/(\rho u)_g$
m = mass (kg)
Nu = Nusselt number, hd/λ
P = pressure (N/m^2)
Pr = Prandtl number, ν/α
Re = Reynolds number, ud/ν
Sc = Schmidt number (ν/D)
Sh = Sherwood number $(k_c d/D)$
T = temperature (K, °F)
t = time (s)
u = streamwise velocity component (m/s)
u', T', C' = turbulence fluctuation terms
v = spanwise velocity component (m/s)
x, y = coordinates

Greek

α = thermal diffusivity (m^2/s)
ε = turbulent dissipation rate (m^2/s^3)
η = film cooling effectiveness, $(T_g\text{-}T_{\text{aw}})/(T_g\text{-}T_c)$
λ = heat conductivity (W/m K)
μ = dynamic viscosity (kg/m s)
ν = kinematic viscosity (m^2/s)
ρ = density (kg/m^3)
τ = stress tensor (kg/ ms^2)

Subscripts

aw = adiabatic wall
c = coolant or jet flow
g = hot gas/air
p = particle or droplet

t = turbulent
0 = air film cooling without mist
∞ = far away from droplets

References

[1] Eriksen, V. L., and Goldstein, R. J., 1974, "Heat Transfer and Film Cooling Following Injection Through Inclined Tubes," ASME J. Heat Transfer, **96**, pp. 239–245.

[2] Goldstein, R. J., Eckert, E. R. G., and Burggraf, F., 1974, "Effects of Hole Geometry and Density on Three-Dimensional Film Cooling," Int. J. Heat Mass Transfer, **17**, pp. 595–607.

[3] Jia, R., Sunden, B., Miron, P., and Leger, B., 2003, "Numerical and Experimental Study of the Slot Film Cooling Jet With Various Angles," *Proceedings of the ASME Summer Heat Transfer Conference*, Las Vegas, NV, July 21–23, pp. 845–856.

[4] Bell, C. M., Hamakawa1, H., and Ligrani, P. M., 2000, "Film Cooling From Shaped Holes," ASME J. Heat Transfer, **122**, pp. 224–232.

[5] Brittingham, R. A., and Leylek, J. H., 2002, "A Detailed Analysis of Film Cooling Physics: Part IV—Compound-Angle Injection With Shaped Holes," ASME J. Turbomach., **122**, pp. 133–145.

[6] Taslim, M. E., and Khanicheh, A., 2005, "Film Effectiveness Downstream of a Row of Compound Angle Film Holes," ASME J. Heat Transfer, **127**, pp. 434–439.

[7] Kwak, J. S., and Han, J. C., 2003, "Heat Transfer Coefficients and Film-Cooling Effectiveness on a Gas Turbine Blade Tip," ASME J. Heat Transfer, **125**, pp. 494–502.

[8] Mayhew, J. E., Baughn, J. W., and Byerley, A. R., 2004, "Adiabatic Effectiveness of Film Cooling With Compound Angle Holes—The Effect of Blowing Ratio and Freestream Turbulence," ASME J. Heat Transfer, **126**, pp. 501–502.

[9] Adami, P., Martelli, F., Montomoli, F., and Saumweber, C., 2002, "Numerical Investigation of Internal Crossflow Film Cooling," *Proceedings ASME Turbo Expo 02*, Amsterdam, Netherlands, June 3–6, 3A, pp. 51–63.

[10] Wang, T., Chintalapati, S., Bunker, R. S., and Lee, C. P., 2000, "Jet Mixing in a Slot," Exp. Therm. Fluid Sci., **22**, pp. 1–17.

[11] Chaker, M., Meher-Homji, C. B., and Mee, M., 2002, "Inlet Fogging of Gas Turbine Engines—Part A: Fog Droplet Thermodynamics, Heat Transfer and Practical Considerations," *ASME Proceedings of Turbo Expo 2002*, Amsterdam, Netherlands, June 3–6, 4, pp. 413–428.

[12] Petr, V., 2003, "Analysis of Wet Compression in GT's," *Energy and the Environment—Proceedings of the International Conference on Energy and the Environment*, Atlanta, GA, June 16–19, 1, pp. 489–494.

[13] Nirmalan, N. V., Weaver, J. A., and Hylton, L. D., 1998, "An Experimental Study of Turbine Vane Heat Transfer With Water-Air Cooling," ASME J. Turbomach., **120**, pp. 50–62.

[14] Guo, T., Wang, T., and Gaddis, J. L., 2000, "Mist/Steam Cooling in a Heated Horizontal Tube, Part 1: Experimental System, Part 2: Results and Modeling," ASME J. Turbomach., **122**, pp. 360–374.

[15] Guo, T., Wang, T., and Gaddis, J. L., 2001, "Mist/Steam Cooling in a 180° Tube Bend," ASME J. Heat Transfer, **122**, pp. 749–756.

[16] Li, X., Gaddis, J. L., and Wang, T., 2003, "Mist/Steam Cooling by a Row of Impinging Jets," Int. J. Heat Mass Transfer, **46**, pp. 2279–2290.

[17] Li, X., Gaddis, J. L., and Wang, T., 2003, "Mist/Steam Heat Transfer With Jet Impingement onto a Concave Surface," ASME J. Heat Transfer, **125**, pp. 438–446.

[18] Heidmann, J. D., Rigby, D. L., and Ameri, A. A., 2000, "A Three-Dimensional Coupled Internal/External Simulation of a Film-Cooled Turbine Vane," ASME J. Turbomach., **122**, pp. 348–359.

[19] Tyagi, M., and Acharya, S., 2003, "Large Eddy Simulation of Film Cooling Flow From an Inclined Cylindrical Jet," ASME J. Turbomach., **125**, pp. 734–742.

[20] Wang, M. J., and Mayinger, F., 1995, "Post-Dryout Dispersed Flow in Circular Bends," Int. J. Multiphase Flow, **21**, pp. 437–454.

[21] Aggarwal, S. K., and Park, T. W., 1999, "Dispersion of Evaporating Droplets in a Swirling Axisymmetric Jet," AIAA J., **37**, pp. 1578–1587.

[22] Chen, X.-Q., and Pereira, J. C. F., 1995, "Prediction of Evaporating Spray in Anisotropically Turbulent Gas Flow," Numer. Heat Transfer, Part A, **27**, pp. 143–162.

[23] Li, X., and Wang, T., 2005, "Simulation of Film Cooling Enhancement With Mist Injection," *Proceedings ASME Turbo Expo 2005*, Reno-Tahoe, NV, June 6–9.

[24] Launder, B. E., and Spalding, D. B., 1972, *Lectures in Mathematical Models of Turbulence*, Academic Press, London, UK.

[25] Wolfstein, M., 1969, "The Velocity and Temperature Distribution of One-Dimensional Flow With Turbulence Augmentation and Pressure Gradient," Int. J. Heat Mass Transfer, **12**, pp. 301–318.

[26] Choudhury, D., 1993, "Introduction to the Renormalization Group Method and Turbulence Modeling," Technical Memorandum, TM-107, Fluent Inc., Lebanon, NH.

[27] Wilcox, D. C., 1998, *Turbulence Modeling for CFD*, DCW Industries, Inc., La Canada, CA.

[28] Menter, F., 1993, "Zonal Two Equation Model for Aerodynamic Flows," AIAA Paper No. 93–2906.

[29] Munson, B., Young, D., and Okiishi, T., 2006, *Fundamentals of Fluid Mechanics*, 5th ed., Wiley, New York.

[30] Saffman, P. G., 1965, "The Lift on a Small Sphere in a Slow Shear Flow," J. Fluid Mech., **22**, pp. 385–400.

[31] Talbot, L., Cheng, R. K., Schefer, R. W., and Willis, D. R., 1980, "Thermophoresis of Particles in a Heated Boundary Layer," J. Fluid Mech., **101**, pp. 737–758.

[32] Li, A., and Ahmadi, G., 1992, "Dispersion and Deposition of Spherical Particles From Point Sources in a Turbulent Channel Flow," Aerosol Sci. Technol., **16**, pp. 209–226.

[33] Ranz, W. E., and Marshall, W. R., Jr., 1952, "Evaporation From Drops, Part I," Chem. Eng. Prog., **48**, pp. 141–146.

[34] Ranz, W. E., and Marshall, W. R., Jr., 1952, "Evaporation From Drops, Part II," Chem. Eng. Prog., **48**, pp. 173–180.

[35] Kuo, K. Y., 1986, *Principles of Combustion*, Wiley, New York.

[36] Fluent, Inc., 2005, *Fluent Manual*, Version 6.2.12, Fluent, Inc., Lebanon, NH.

[37] Rhee, D. H., Lee, Y. S., and Cho, H. H., 2002, "Film Cooling Effectiveness and Heat Transfer of Rectangular-Shaped Film Cooling Holes," *Proceedings ASME Turbo Expo 2002*, Amsterdam, Netherlands, June 3–6, 3, pp. 21–32.

W. Zhang

T. S. Fisher
e-mail: tsfisher@purdue.edu

School of Mechanical Engineering,
Birck Nanotechnology Center,
Purdue University,
West Lafayette, IN 47907

N. Mingo
NASA-Ames Center for Nanotechnology,
229-1,
Moffett Field, CA 94035

Simulation of Interfacial Phonon Transport in Si–Ge Heterostructures Using an Atomistic Green's Function Method

An atomistic Green's function method is developed to simulate phonon transport across a strained germanium (or silicon) thin film between two semi-infinite silicon (or germanium) contacts. A plane-wave formulation is employed to handle the translational symmetry in directions parallel to the interfaces. The phonon transmission function and thermal conductance across the thin film are evaluated for various atomic configurations. The contributions from lattice straining and material heterogeneity are evaluated separately, and their relative magnitudes are characterized. The dependence of thermal conductance on film thickness is also calculated, verifying that the thermal conductance reaches an asymptotic value for very thick films. The thermal boundary resistance of a single Si/Ge *interface is computed and agrees well with analytical model predictions. Multiple-interface effects on thermal resistance are investigated, and the results indicate that the first few interfaces have the most significant effect on the overall thermal resistance.* [DOI: 10.1115/1.2709656]

Introduction

The characteristic feature sizes of modern electronic devices are rapidly approaching nanometer scales, and nanoengineered materials such as superlattices and quantum wires have been shown to possess excellent thermoelectric properties [1]. Heat transport in these systems, particularly across embedded interfaces, is critical to their performance and can exhibit significant differences as compared to conventional Fourier heat conduction. In this paper, an atomistic Green's function method is developed to study cross-plane heat conductance through a strained thin film between two semi-infinite contacts and the thermal boundary resistance between two dissimilar diamond-structure crystals.

The atomistic Green's function method is an effective tool to simulate ballistic transport in nanoscale devices and has been widely used in the simulation of electron transport [2]. The primary advantage of this approach is its efficiency in handling interfacial and boundary scattering, two important mechanisms in nanoscale devices. The dominant phonon mean free path (MFP) in silicon at room temperature is approximately 300 nm [3]. When the device characteristic length is much smaller than the MFP, ballistic transport dominates, and the major resistance to heat flow is imposed by interfaces and boundaries.

Several theoretical models exist to estimate thermal boundary resistance (TBR). The acoustic mismatch model (AMM) by [4] accounts for long-wavelength phonons and relates the transmission coefficient to acoustic impedances of the two adjacent materials; therefore it is strictly valid only at low temperatures. The diffuse mismatch model (DMM) by [5] assumes complete diffuse scattering of phonons at interfaces and ascribes the thermal interface resistance to mismatches of phonon density of states. In order to estimate thermal boundary resistance with the DMM, the phonon density of states must be supplied, either from a priori calculations or experiments. Neither the AMM nor DMM includes the details of interfacial microstructure, i.e., in both models, thermal boundary resistance is determined solely by the two joining materials without regard to how they are joined. This approximation limits the application of these two models [6].

Several numerical tools have been employed to simulate subcontinuum heat conduction. One of them is based on the phonon Boltzmann transport equation (BTE), which describes phonon transport by a statistical distribution function. The BTE can be solved by making an analogy to the equation of radiative transport (ERT) [7], using finite volume methods [8] or with Monte Carlo methods [9], with various assumptions and simplifications. Yazdani and Asheghi [10] used the acoustic mismatch model to predict interface resistance between strained Si/SiGe and solved the BTE for phonons with a single mode relaxation time assumption in a strained silicon transistor. Prasher and Phelan [7] developed a scattering-mediated AMM with the BTE to investigate bulk scattering effects on thermal boundary resistance. In both studies, the phonon density of states and group velocity were supplied as assumed quantities, and different polarization branches needed to be considered separately. Further, the nature of phonon interfacial transport was simplified through AMM, DMM, or other models.

Another relevant computational tool is molecular dynamics (MD), which is computationally expensive and treats atomic vibrational modes classically. Thus, strictly speaking, it is not applicable at temperatures much lower than the Debye temperature. Picu et al. [11] employed equilibrium molecular dynamics to study strain and size effects in solid Ar nanostructures and concluded that lattice thermal conductivity in strained nanostructures under plane stress is controlled by boundary scattering. Abramson et al. [12] used nonequilibrium molecular dynamics to study interface and strain effects in Kr and Ar heterostructures and observed that an imposed tensile strain resulted in a significant decrease in thermal conductivity. Schelling et al. [13] used MD to simulate phonon wave-packet dynamics through perfectly coher-

---

Contributed by the Heat Transfer Division of ASME for publication in Journal of Heat Transfer. Manuscript received December 15, 2005; final manuscript received May 30, 2006. Review conducted by Yogendra Joshi. Paper presented at the 2005 ASME International Mechanical Engineering Congress (IMECE2005), Orlando, FL, USA, November 5–11, 2005.

ent interfaces between two materials with different masses and obtained energy transmission coefficients that were similar to those of Young and Maris [14].

The atomistic Green's function method is based on a quantum mechanical description of the phonon energy distribution, rather than the classical description employed in MD. Therefore, the atomistic Green's function method has significant advantages over MD at low temperatures. As long as the harmonic assumption is satisfied, the atomistic Green's function (AGF) method retains these advantages over MD. Practical examples include nanostructures with characteristic lengths that are much smaller than phonon mean free paths (typically 100–300 nm at room temperature) and transport across interfaces. Computationally, the calculation of interfacial phonon transmission using Green's functions is much faster than that by MD. Many numerical challenges such as finite-size effects in MD are also mitigated.

Unlike the BTE with a boundary scattering model or a continuous acoustic wave model [15], atomistic numerical methods (including MD, lattice dynamics, and the atomistic Green's function method) provide sound solutions without excessively complicated appreciation of phonon transport fundamentals [16]. To date, atom-based simulations of phonon interfacial transport have not been widely investigated and documented. Young and Maris [14] investigated phonon transmission between two identical semi-infinite (face centered cubic) (FCC) lattices with different masses and spring constants using lattice dynamics, and the spectral dependence of the phonon transmission coefficient was calculated. Their method was later extended by Pettersson and Mahan [17] to handle dissimilar lattices. However, this method requires two lattices fully connected at the interface, whereas the atomistic Green's function method can be used in cases where the two materials are connected by a nonperiodic junction, such as a point contact or a nanowire. Sui Herman [18] used a modified Keating/valence-force-field model to study the effect of strain on phonon dispersion and elastic constants of Group IV semiconductors, but thermal transport calculations were not reported.

The atomistic Green's function method, as shown in this paper, provides an accurate and versatile approach to perform nanoscale heat transport simulations. The atomistic Green's function method is based on a dynamical equation and the quantum mechanical phonon energy distribution. The method incorporates the phonon density of states into transmission function calculations. Therefore no a priori knowledge of phonon density of states is required. The inputs are equilibrium locations of atoms and interatomic potentials, and experimentally fitted phonon dispersion curves are not needed. Under harmonic transport, the transmission function and thermal conductance given by the atomistic Green's function method are exact. The wave nature of phonon transport is also captured, and a method to introduce the effect of anharmonicity has recently been developed [19]. The atomistic Green's function method also holds the promise to provide boundary conditions for mesoscale simulation tools, such as BTE solvers.

Strained silicon technology provides a means to increase carrier mobility in the channel region of a metal–oxide–semiconductor field effect transistor (MOSFET) by altering electron energy bands to reduce effective mass and intervalley scattering rates. MOSFETs based on this technology exhibit 10–25% improvements in device performance metrics as compared to conventional unstrained silicon transistors [20]. Pop et al. [21] used a Monte Carlo method to simulate electron–phonon interactions in order to determine the phonon generation rate and associated Joule heating effects in bulk and strained silicon. They found that generated phonon distributions are different in bulk and strained silicon at low fields. Phonon transport simulations with the atomistic Green's function method in this emerging technology can provide not only insights into heat transport through the strained silicon layer, but also a potentially common framework to simulate electron–phonon scattering and related local heat generation and dissipation processes when combined with electron transport solvers.

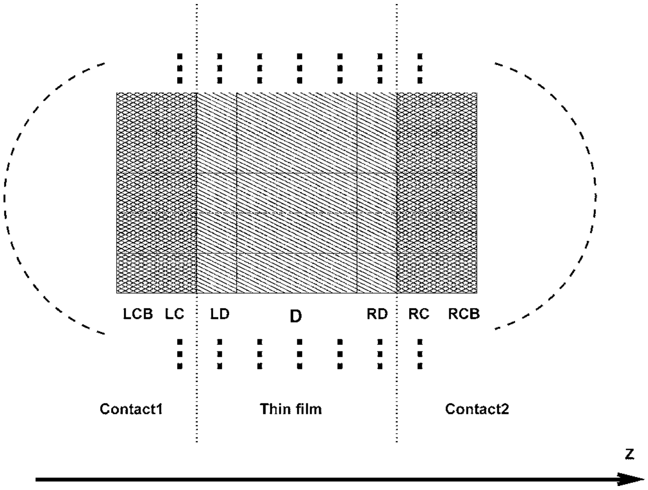

Fig. 1 Schematic diagram of a five-unit-cell thin film between two semi-infinite contacts. The definitions of different groups of atoms are shown. In this case, Region D includes three unit-cell layers.

The theoretical framework of the atomistic Green's function method in phonon transport simulations has been described previously and implemented for a nanowire system in Refs. [22,23]. The theory is extended in this paper to handle a thin-film system. The transmission function and thermal conductance (resistance) for strained thin films are evaluated, and their dependencies on thickness, temperature, and other factors are discussed. A special case is also considered in which the thermal boundary resistance between two dissimilar materials is predicted. The general AGF method presented in this paper can be readily extended to more complicated nanostructures (such as nanowires or nanocrystals with defects) between two bulk contacts.

Problem Definition

Actual atomic configurations at heterogeneous interfaces are very complicated and vary significantly with deposition conditions [24]. To define atomic locations in a reasonably simple way, an idealized geometry has been chosen and is shown in Fig. 1. The atomic lattice is based on an undistorted diamond lattice and is later modified using Poisson's ratio to reflect changes due to strain.

In Fig. 1, each square represents a unit cell in a crystal lattice. "Contact1" (including atom Groups LCB and LC) and "Contact2" (including atom Groups RCB and RC) are two semi-infinite thermal reservoirs at constant temperatures T_1 and T_2, respectively. Atom Group LC includes atoms in "Contact1" that bond with the thin-film atoms. Atoms in Group LCB do not have any bonds with the thin-film atoms. Therefore, the dynamical properties of these two regions (LCB and LC) are different. Similar definitions apply to atom groups RC and RCB. A thin film (including atom groups LD, D, and RD) of infinite extent in the x and y directions is placed between the two contacts. Atom Groups LD and RD include thin-film atoms that bond with "Contact1" and "Contact2" atoms, respectively. Atoms in Group D have no bond with either contact. In the cases discussed later, the contact and thin-film material can be either germanium or silicon, and their (100) directions are oriented along the z axis.

The size mismatch between silicon and germanium lattices creates either tensile or compressive strains on the thin film. The semi-infinite contacts are assumed to remain unstrained due to their bulk volumes. In this paper, we assume that the lattice mis-

Table 1 Computational parameters used in the construction of Si and Ge harmonic matrices. The first number in C_0 is the unstrained value and the second number is the strained value.

	Silicon	Germanium
Atomic mass m (kg)	4.664×10^{-26}	1.206×10^{-25}
Lattice constant (Å)	5.43	5.65
C_0 in Harrison's potential (eV)	49.1/44.8	47.2/51.2
C_1 in Harrison's potential (eV)	1.07	0.845
Poisson's ratio	0.28	0.26

match creates a pure-strained thin film without inducing dislocations. Such lattices typically occur in extremely thin films, while thicker films usually include buffer zones and relaxed lattices [25]. In the Ge/Si/Ge case (Ge contacts, Si thin film), germanium contacts stretch the silicon thin film by 4% in the in-plane direction (xy plane), creating biaxial strains of 0.04 in both x and y directions. The silicon thin-film lattice tends to maintain its volume, and consequently, it contracts in the z direction. We assume that the z strain can be calculated using the bulk Poisson's ratio (0.28 for silicon (100) and 0.26 for germanium (100) [26]). Thus, the z distance between any two atoms is reduced by a factor of approximately 0.01 (biaxial strain multiplied by Poisson's ratio). Similar lattice adjustments have been applied to the Si/Ge/Si case.

Theory

Harmonic Matrix and Interatomic Potential. The atomistic Green's function method starts by building harmonic matrices. Prior work [22] has shown that anharmonic scattering in Si at room temperature can be neglected if the device's characteristic length is less than 20 nm, and even at the 45 nm semiconductor technology node, many film structures possess cross-plane thicknesses less than 20 nm. In such cases, a harmonic potential can be used to build the harmonic matrix **H**, which represents interactions among different degrees of freedom (d.o.f). The mathematical definition of the harmonic matrix is [22]

$$\mathbf{H} = \{H_{ij}\} = \frac{1}{\sqrt{M_i M_j}} \begin{cases} -\dfrac{\partial^2 U}{\partial u_i \partial u_j}, & \text{if } i \neq j \\ -\displaystyle\sum_{r \neq j} \dfrac{\partial^2 U}{\partial u_i \partial u_j}, & \text{if } i = j \end{cases} \tag{1}$$

where u_i and u_j refer to any two atomic displacement degrees of freedom respectively; and U represents the total bonding energy. M_i and M_j are atomic masses associated with degrees of freedom u_i and u_j, respectively. The dynamical equation of the entire lattice can be written as

$$(\omega^2 \mathbf{I} - \mathbf{H})\tilde{u} = 0 \tag{2}$$

where $\tilde{u}$ is a column vector of degrees of freedom. We use Harrison's interatomic potintial [27] to evaluate the harmonic matrix **H**

$$\Delta U_i = \frac{1}{2} C_0 \frac{(d_i - d_{i,e})^2}{d_{i,e}^2} + \frac{1}{2} C_1 (\Delta\theta_i)^2 \tag{3}$$

where d_i represents the bond length; and $d_{i,e}$ represents the equilibrium bond length. $\Delta\theta_i$ is the change to the equilibrium tetrahedral angle θ_i (1.9106 rad). Although this simple potential model has only two independent parameters, C_0 and C_1 (see potential parameters in Table 1), it includes bond-stretching/bending potentials and reproduces bulk phonon dispersion curves reasonably well [27]. This potential model was used to predict the thermal conductivity of silicon nanowires, and the numerical results agree well with experimental data [28]. Because of the harmonic assumption, potential variations in the vicinity of the equilibrium atomic positions are the only information needed to evaluate harmonic matrices. Near the equilibrium locations, more complicated inter-atomic potentials can be simplified parabolically to a form that is consistent with Harrison's potential. However, we also note that the bond-stretching and bond-bending parts of the potential are actually correlated, and other advanced potentials have been developed to address this problem [29].

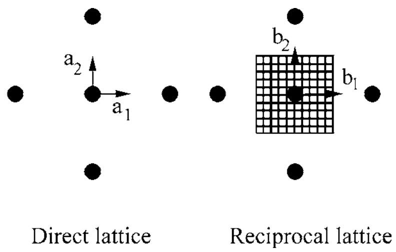

Fig. 2 The 2D direct lattice (left) and reciprocal lattice (right) in a fcc structure. A 10×10 mesh is placed on the first Brillouin zone in the right subfigure.

Plane-Wave Formulation in Thin Films. The system of interest in this work is infinitely large in the x and y directions and contains infinite degrees of freedom. Therefore the harmonic matrix defined in Eq. (1) is infinitely large. For these directions we use the wave vector representation, in terms of $\vec{\mathbf{k}}_{\parallel}$, to build harmonic matrices ($\tilde{\mathbf{H}}$) with the assumption of ideal translational invariance in x and y directions. The thin film and contacts are divided into unit-cell layers along the z axis. One unit cell in each layer is sufficient to represent the whole layer. A 6×6 harmonic matrix $\tilde{\mathbf{H}}_p$ is defined to represent the intralayer interaction in layer p, while another 6×6 harmonic matrix $\tilde{\mathbf{T}}_{p,q}$ is defined to represent the interlayer interaction between layer p and the layer to its right (q)

$$\tilde{\mathbf{H}}_p(\vec{\mathbf{k}}_{\parallel}) = \sum_{n=0}^{4} \mathbf{H}_{t,n} e^{-i\vec{\mathbf{k}}_{\parallel}\vec{\mathbf{R}}_n} \tag{4}$$

$$\tilde{\mathbf{T}}_{p,q}(\vec{\mathbf{k}}_{\parallel}) = \sum_{m=1}^{4} \mathbf{H}_{t,m} e^{-i\vec{\mathbf{k}}_{\parallel}\cdot\vec{\mathbf{R}}_m} \tag{5}$$

where t is an arbitrary unit cell on layer p. The index n loops through the neighboring unit cells of unit cell t that are in the same layer (p), including itself (n ranges from 0 to 4 for a (100) diamond lattice), and the index m loops through the neighboring cells in the next layer q (m ranges from 1 to 4 for a (100) diamond lattice). $\mathbf{H}_{t,n}$ (or $\mathbf{H}_{t,m}$) is the regular harmonic matrix that links unit cells t and n (or m). With these two types of matrices ($\tilde{\mathbf{H}}_p$ and $\tilde{\mathbf{T}}_{p,q}$), the complete harmonic matrix for any system can be assembled. For example, the matrix to represent an l-layer thin film is

$$\tilde{\mathbf{H}}_{\mathrm{tf}}(\vec{\mathbf{k}}_{\parallel}) = \begin{bmatrix} \tilde{\mathbf{H}}_1 & \tilde{\mathbf{T}}_{1,2} & 0 & \cdots & 0 \\ \tilde{\mathbf{T}}_{2,1} & \tilde{\mathbf{H}}_2 & \tilde{\mathbf{T}}_{2,3} & \cdots & 0 \\ \vdots & \vdots & \vdots & \vdots & \vdots \\ 0 & \cdots & 0 & \tilde{\mathbf{T}}_{l,l-1} & \tilde{\mathbf{H}}_l \end{bmatrix} \tag{6}$$

where $\tilde{\mathbf{T}}_{p,q} = \tilde{\mathbf{T}}_{q,p}^{\dagger}$ (conjugate transpose). $\vec{\mathbf{k}}_{\parallel}$ in Eqs. (4)–(6) is an arbitrary two-dimensional (2D) lattice wave vector. Each wavevector ($\vec{\mathbf{k}}_{\parallel} = k_x \vec{b}_1 + k_y \vec{b}_2$) represents phonons traveling in one distinct x-y direction. The 2D lattice perpendicular to the (100) direction is a square lattice, and its first Brillouin zone is a square ($k_x \in [-\sqrt{2}\pi/a, \sqrt{2}\pi/a), k_y \in [-\sqrt{2}\pi/a, \sqrt{2}\pi/a)$), as shown in Fig. 2. Because of translational invariance in the x and y directions, the transmission function for each $\vec{\mathbf{k}}_\parallel$ can be solved independently, and the total heat flux can be expressed as an integral of the independent heat fluxes for each $\vec{\mathbf{k}}_\parallel$. We emphasize that this simplification would not be valid if the x and y translational symmetries were broken, such as in the case of a point contact. The total heat flux calculation must account for phonons traveling in all directions. Thus, it is expressed as an integral over $\vec{\mathbf{k}}_\parallel$ as shown in the next section.

Green's Function Matrices. The response of a dynamic system (defined by Eq. (2)) to an infinitesimal perturbation can be described by a Green's function. In the present work, the Green's functions $\mathbf{g}_{\mathrm{LCB}}$ and $\mathbf{g}_{\mathrm{RCB}}$ represent the responses of the two semi-infinite contacts, respectively

$$\mathbf{g}_{\mathrm{LCB}}(\omega,\vec{\mathbf{k}}_\parallel) \equiv \lim_{\delta\to 0}[(\omega^2+\delta i)\mathbf{I} - \tilde{\mathbf{H}}_{\mathrm{LCB}}(\vec{\mathbf{k}}_\parallel)]^{-1} \tag{7}$$

$$\mathbf{g}_{\mathrm{RCB}}(\omega,\vec{\mathbf{k}}_\parallel) \equiv \lim_{\delta\to 0}[(\omega^2+\delta i)\mathbf{I} - \tilde{\mathbf{H}}_{\mathrm{RCB}}(\vec{\mathbf{k}}_\parallel)]^{-1} \tag{8}$$

where $\mathbf{H}_{\mathrm{LCB}}$ and $\mathbf{H}_{\mathrm{RCB}}$ are the dynamical matrices of the left and right contacts. $\mathbf{g}_{\mathrm{LCB}}$ and $\mathbf{g}_{\mathrm{RCB}}$ are determined by decimation techniques [30,31], and their imaginary parts are directly associated with phonon density of states [32]. In Eqs. (7) and (8), δ is a small number corresponding to phonon energy dissipation in contacts whose role is elaborated in Ref. [33]. The choice of δ affects the energy resolution of the uncoupled Green's function and subsequent calculations. A smaller δ value gives better energy resolution but requires longer computational times. A method to choose an appropriate value of the perturbation δ is documented in Ref. [22].

Referring again to Fig. 1, atoms in LC (or RC) are different than other atoms in "Contact1" (or "Contact2") because they are bonded to atoms in the thin film. Therefore, $\mathbf{g}_{\mathrm{LC}}$ ($\mathbf{g}_{\mathrm{RC}}$) must be defined separately and differs from $\mathbf{g}_{\mathrm{LCB}}$ ($\mathbf{g}_{\mathrm{RCB}}$) in a general heterogeneous system. Green's function matrices $\mathbf{g}_{\mathrm{LC}}$ and $\mathbf{g}_{\mathrm{RC}}$ are defined as

$$\mathbf{g}_{\mathrm{LC}}(\omega,\vec{\mathbf{k}}_\parallel) \equiv [\omega^2\mathbf{I} - \tilde{\mathbf{H}}_{\mathrm{LC}}(\vec{\mathbf{k}}_\parallel) - \tilde{\mathbf{T}}_{\mathrm{LC,LCB}}\mathbf{g}_{\mathrm{LCB}}\tilde{\mathbf{T}}_{\mathrm{LCB,LC}}]^{-1} \tag{9}$$

$$\mathbf{g}_{\mathrm{RC}}(\omega,\vec{\mathbf{k}}_\parallel) \equiv [\omega^2\mathbf{I} - \tilde{\mathbf{H}}_{\mathrm{RC}}(\vec{\mathbf{k}}_\parallel) - \tilde{\mathbf{T}}_{\mathrm{RC,RCB}}\mathbf{g}_{\mathrm{RCB}}\tilde{\mathbf{T}}_{\mathrm{RCB,RC}}]^{-1} \tag{10}$$

where $\tilde{\mathbf{H}}_{\mathrm{LC}}$ and $\tilde{\mathbf{H}}_{\mathrm{RC}}$ are intralayer matrices (see Eq. (4)) for regions LC and RC, respectively.

The Green's function of the device is defined as

$$\mathbf{G}(\omega,\vec{\mathbf{k}}_\parallel) \equiv [\omega^2\mathbf{I} - \tilde{\mathbf{H}}_{\mathrm{tf}} - \mathbf{\Sigma}_L - \mathbf{\Sigma}_R]^{-1} = \begin{bmatrix} \mathbf{G}_{\mathrm{LD,LD}} & \mathbf{G}_{\mathrm{LD,D}} & \mathbf{G}_{\mathrm{LD,RD}} \\ \mathbf{G}_{\mathrm{D,LD}} & \mathbf{G}_{\mathrm{D,D}} & \mathbf{G}_{\mathrm{D,RD}} \\ \mathbf{G}_{\mathrm{RD,LD}} & \mathbf{G}_{\mathrm{RD,D}} & \mathbf{G}_{\mathrm{RD,RD}} \end{bmatrix} \tag{11}$$

where $\tilde{\mathbf{H}}_{\mathrm{tf}}$ is the harmonic matrix of the thin film (see Eq. (6)). $\mathbf{\Sigma}_L$ and $\mathbf{\Sigma}_R$ are self-energy matrices that physically represent changes to the thin film's dynamical behavior caused by contacts

$$\mathbf{\Sigma}_L(\omega,\vec{\mathbf{k}}_\parallel) \equiv \begin{bmatrix} \tau_L & 0 & 0 \\ 0 & 0 & 0 \\ 0 & 0 & 0 \end{bmatrix} \tag{12}$$

$$\mathbf{\Sigma}_R(\omega,\vec{\mathbf{k}}_\parallel) \equiv \begin{bmatrix} 0 & 0 & 0 \\ 0 & 0 & 0 \\ 0 & 0 & \tau_R \end{bmatrix} \tag{13}$$

τ_L and τ_R are defined as

$$\tau_L(\omega,\vec{\mathbf{k}}_\parallel) \equiv \tilde{\mathbf{T}}_{\mathrm{LD,LC}}\mathbf{g}_{\mathrm{LC}}\tilde{\mathbf{T}}_{\mathrm{LC,LD}} \tag{14}$$

$$\tau_R(\omega,\vec{\mathbf{k}}_\parallel) \equiv \tilde{\mathbf{T}}_{\mathrm{RD,RC}}\mathbf{g}_{\mathrm{RC}}\tilde{\mathbf{T}}_{\mathrm{RC,RD}} \tag{15}$$

where $\tilde{\mathbf{T}}_{\mathrm{LD,LC}}$, $\tilde{\mathbf{T}}_{\mathrm{LC,LD}}$, $\tilde{\mathbf{T}}_{\mathrm{RD,RC}}$, and $\tilde{\mathbf{T}}_{\mathrm{RC,RD}}$ are matrices that link contact and thin-film atom groups (see Eq. (5)). Matrices $\mathbf{\Gamma}_L$ and $\mathbf{\Gamma}_R$, later used in the expression of the transmission function, are defined as

$$\mathbf{\Gamma}_L(\omega,\vec{\mathbf{k}}_\parallel) \equiv i(\tau_L - \tau_L^\dagger) \tag{16}$$

$$\mathbf{\Gamma}_R(\omega,\vec{\mathbf{k}}_\parallel) \equiv i(\tau_R - \tau_R^\dagger) \tag{17}$$

and i is the unitary imaginary number.

Transmission and Heat Flux. Our ultimate goal is to calculate the heat flum and thermal conductance across thin films. The propagation of phonons between two contacts is determined by the transmission function $\Xi\ (\omega,\vec{\mathbf{k}}_\parallel)$ [34]

$$\Xi(\omega,\vec{\mathbf{k}}_\parallel) = \mathrm{Trace}[\mathbf{\Gamma}_L\mathbf{G}_{\mathrm{LD,RD}}\mathbf{\Gamma}_R\mathbf{G}_{\mathrm{LD,RD}}^\dagger] \tag{18}$$

$\mathbf{G}_{\mathrm{LD,RD}}$ in Eq. (18) is the top right block matrix in the device Green's function matrix (see Eq. (11)). The total heat flux is defined as an integral over frequency and $\vec{\mathbf{k}}_\parallel$

$$J = \int_0^\infty \int_{\vec{\mathbf{k}}_\parallel} \frac{\hbar\omega}{2\pi}\Delta\tilde{N}(\omega)\Xi(\omega,\vec{\mathbf{k}}_\parallel)\frac{d\vec{\mathbf{k}}_\parallel}{(2\pi)^2}d\omega \tag{19}$$

The integral over $\vec{\mathbf{k}}_\parallel$ in Eq. (19) can be converted to a summation over a finite number of $\vec{\mathbf{k}}_\parallel$ upon discretizing the first Brillouin zone (see Fig. 2) with an $N\times N$ uniform mesh

$$J = \frac{1}{s}\int_0^\infty \frac{\hbar\omega}{2\pi}\Delta\tilde{N}\left[\frac{1}{N^2}\sum_{\vec{\mathbf{k}}_\parallel}\Xi(\omega,\vec{\mathbf{k}}_\parallel)\right]d\omega \tag{20}$$

where s is the cross-sectional area of one unit cell. If the temperature difference between the two bulk contacts is sufficiently small, the phonon occupation difference $\Delta\tilde{N}(\omega)$ in Eq. (19) becomes

$$\Delta\tilde{N}(\omega) = \frac{\hbar\omega}{k_B T^2}\frac{e^{\hbar\omega/k_B T}}{(e^{\hbar\omega/k_B T}-1)^2}\Delta T \tag{21}$$

Otherwise, actual occupation numbers can be used to calculate the phonon occupation difference ($\Delta\tilde{N}=\tilde{N}_{\mathrm{contact1}}-\tilde{N}_{\mathrm{contact2}}$). The thermal conductance across a thin film is then defined as the ratio of heat flux to temperature difference

$$\sigma = \frac{J}{\Delta T}\left(\frac{\mathrm{W}}{\mathrm{m}^2\,\mathrm{K}}\right) \tag{22}$$

Thermal resistance (R) is the inverse of conductance and has units of [$\mathrm{m}^2\,\mathrm{K/W}$].

Results and Discussion

The atomistic Green's function method described above has been used to simulate ballistic phonon transport in a thin-film system. Several numerical benchmarks, such as the known parabolic frequency dependence of a pure material's transmission function at low frequencies [28], were conducted before the following numerical investigations. The thermal conductance of a pure material has also been verified to exhibit a T^3 dependence at low temperatures. Upon testing for grid independence, a Brillouin-zone mesh of 100 × 100 was needed to achieve thermal conductances that converged to within 1%. The computational time varies from several minutes to several hours on a common workstation in the following cases.

The Effects of Heterogeneous Materials and Strains. In the Si/Ge/Si and Ge/Si/Ge heterogeneous thin-film cases, thermal resistance occurs due to two factors. One factor is the heterogeneous-material effect, which causes mismatches of phonon density of states and group velocity. Another factor is lattice

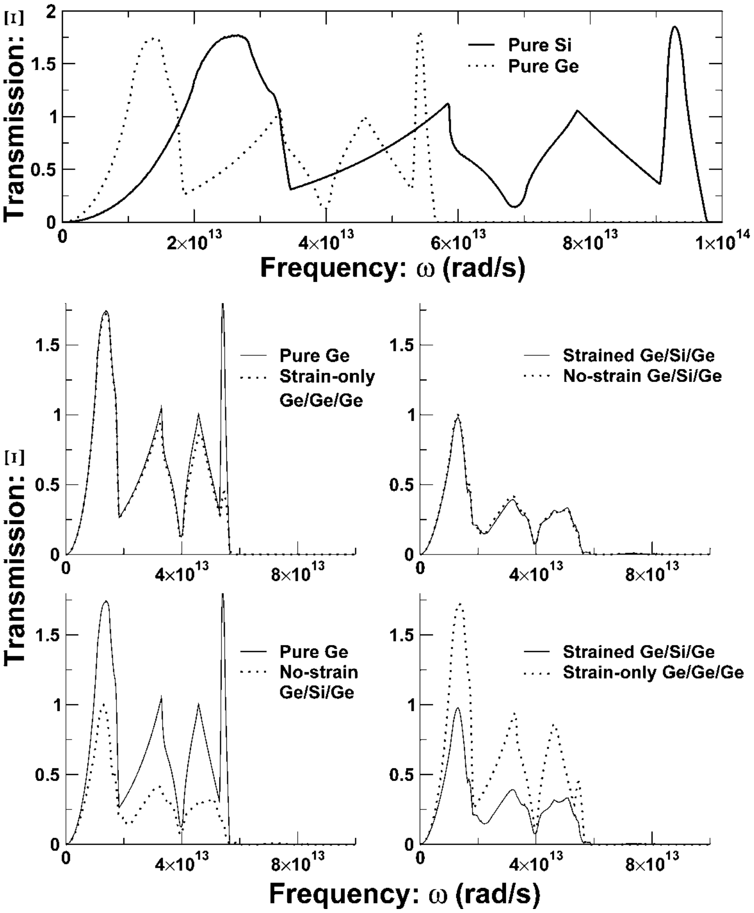

Fig. 3 Comparisons of full-spectrum transmission functions

strain, which displaces atoms and alters bond strength. Several computational examples are constructed here to demonstrate the relative significance of these two effects.

Transmission functions of these different atomic configurations are compared in Figs. 3 and 4. A strained heterogeneous case in which a stretched silicon thin film is placed between two germanium contacts (represented by "Strained Ge/Si/Ge") and another strained heterogeneous case in which a compressed germanium thin film is placed between two silicon contacts (represented by "Strained Si/Ge/Si") are included. Strains displace atoms away from their equilibrium positions. Therefore, both the geometric configuration of atoms (bond length and bond angles) and the force constants between atoms need to be modified. Based on Grüneisen's rule, we estimate that the change in the primary force constant (C_0 in Table 1) is four times that of the bond length.

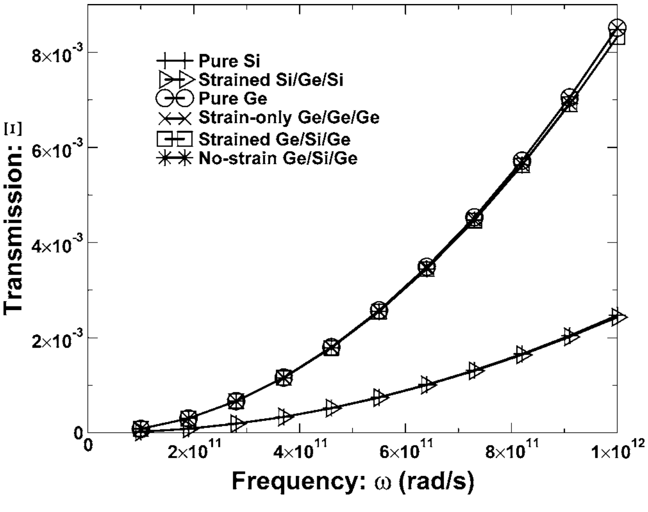

Fig. 4 Comparison of the straining effect with the heterogeneous-material effect on phonon transmission functions across a one-unit-cell thin film at low frequencies

The "No-strain Ge/Si/Ge" and "Strain-only Ge/Ge/Ge" cases shown in Figs. 3 and 4 are not physical but are included as informative thought experiments. The "No-strain Ge/Si/Ge" case is derived from the pure germanium case, in which germanium atoms in the thin-film region are replaced by silicon atoms while the lattice in the thin-film region remains a germanium lattice. In this case, only the heterogeneous effect exists because strain has been artificially removed. The "Strain-only Ge/Ge/Ge" case is derived from the "Strained Ge/Si/Ge" case such that silicon atoms in the thin-film region are replaced with germanium atoms, but the thin-film lattice remains stretched as in the "Strained Ge/Si/Ge" case. In this case, only lattice-straining effects exist because all atoms are germanium. In all cases discussed in this subsection, the film thickness equals the thickness of one unit cell in the (100) direction.

In pure materials, the phonon transmission function at one frequency depends only on the number of available phonon modes at that frequency. Pure germanium is known to have a higher density of states at low frequency than pure silicon [35]. Therefore, its transmission is higher than that of pure silicon at low frequencies. This trend is confirmed by predictions from the atomistic Green's function method, as shown by the pure Si and pure Ge results in Fig. 3(*a*). Pure silicon also has a more extensive spectrum than

Table 2 Zero-frequency group velocities of longitudinal acoustic (LA) phonons and transverse acoustic (TA) phonons calculated by Harrison's potential (the first number), compared with the zero-frequency group velocities estimated from elastic constants by Holland[a] (the second number). Harrison's potential is known to underestimate the zero-frequency group velocities. Densities of Si and Ge are shown as well. These values obtained from Harrison's potential are used in the acoustic mismatch model to predict the thermal boundary resistance across a Si/Ge interface.

	Silicon	Germanium
LA group velocity (m/s)	6877/8480	4114/4920
TA group velocity (m/s)	3535/5860	1978/3550
Density (kg/m^3)	2330	5323

[a] See Ref. [42].

pure germanium. The maximum phonon frequency is approximately 98×10^{12} rad/s in silicon and approximately 58×10^{12} rad/s in germanium.

The results of these calculations indicate that the straining effect is small in the ballistic transport regime in comparison to the heterogeneous-material effect. As shown in Fig. 3(*b*), no significant difference exists between the pure Ge and the strain-only Ge/Ge/Ge cases. If we compare the strained Ge/Si/Ge case to the no-strain Ge/Si/Ge case, the difference is also negligible. However, the difference between the pure Ge case and the no-strain Ge/Si/Ge case is large, as is the difference between the strained Ge/Si/Ge case and the strain-only Ge/Ge/Ge case (see Fig. 3(*b*)). The Si–Ge lattice mismatch is only 4%. The difference between silicon and germanium atomic masses is more than 50%, and the difference between their group velocities is approximately 40% (see Tables 1 and 2). This large difference in group velocities causes heterogeneous effects to be more prominent.

The transmission functions at low frequencies converge to two curves, corresponding to pure Si and pure Ge (see Fig. 4). We note that for the ultralow frequencies considered in Fig. 4 (for which the transmission function goes to zero), a much finer Brillouin zone mesh (3000×3000) was employed to produce the parabolic frequency dependence. The straining and heterogeneous-material effects both vanish because the lattice vibrates very slowly at low frequencies, and the whole solid resembles a rigid body, with neighboring atoms vibrating nearly in phase. Therefore, heterogeneous-material and straining effects are minor at low frequencies. This phenomenon also causes the low-temperature conductances to collapse to those of two pure materials, because low-frequency phonons dominate thermal transport at low temperatures. However, at room temperature, the heterogeneous interface effect is significant. The conductance of Ge/Si/Ge is approximately half that of pure Ge at room temperature, and the room-temperature conductance of Si/Ge/Si is 30% that of pure Si. At room temperature and higher, the conductance of Ge/Si/Ge is close to the conductance of Si/Ge/Si (see Fig. 5). This result is related to the fact that the areas under the Si/Ge/Si and Ge/Si/Ge transmission curves are comparable around the dominant phonon frequency at room temperature.

In the ballistic transport regime, scattering is only caused by interfaces and boundaries, and the scattering rate is roughly a constant that is independent of temperature. Therefore, thermal conductance is governed by the average phonon energy and has the same temperature dependence as thermal capacitance. Consequently, as shown in Fig. 5, thermal conductance increases with temperature and reaches a plateau at temperatures significantly higher than the Debye temperature.

Film Thickness Dependence. Figure 6 shows the thermal conductance through a Ge/Si/Ge system as a function of film thickness at different temperatures. The thickness of the thin film is expressed in terms of the number of unit cells. For a strained silicon thin film, one unit cell has a thickness of 2.69 Å. In the ballistic transport regime, the film thickness dependence of conductance is mainly attributed to the coupling and decoupling of phonon wave functions. If the two interfaces are extremely close, phonons can easily propagate from one side to another; thus the conductance in the one-unit-cell case is the largest. As the film thickness increases, thermal conductance decreases. Finally the conductance converges to the value corresponding to an infinitely thick, scattering-free film.

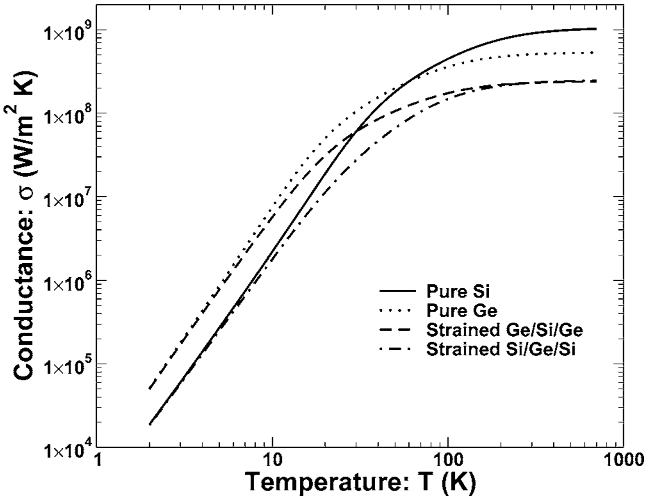

Fig. 5 Comparison of the thermal conductances of heterogeneous materials and those of homogeneous materials across a one-unit-cell thin film

Thermal Boundary Resistance Across a Single Si/Ge Interface. TBR is present across interfaces between any dissimilar materials, and it results from differences in lattice vibration properties. If the material in the thin-film region is selected to be the same as that of one contact region, a single interface between the thin film and the other contact is created. Consequently, the atomistic Green's function method described above can be used to calculate TBR. However, the straining effect cannot be easily included in this structure because the three-dimensional layout of the interfacial atoms is complicated and difficult to predict. Thus, we choose to simulate the TBR between Si and Ge, assuming that

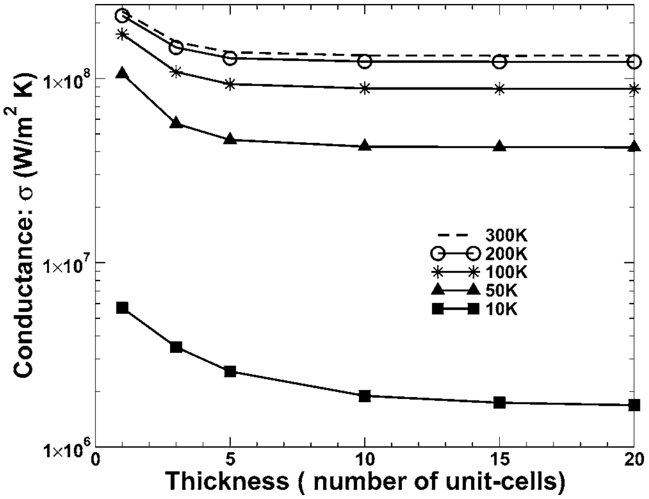

Fig. 6 Thickness dependence of thermal conductance in the Ge/Si/Ge configuration. Each unit cell is 2.69 Å.

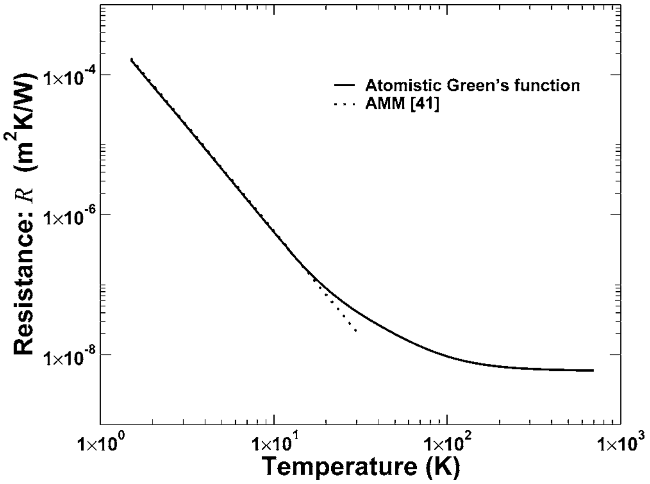

Fig. 7 Comparison of the thermal boundary resistance across a Si/Ge interface calculated by atomistic Green's function method to that by the acoustic mismatch model [41]

they both have germanium lattice distances.

Direct TBR measurements of Si/Ge interfaces are not readily available because most prior work [36,37], has reported only the thermal conductivity of Si/Ge superlattices. It remains unclear how to convert the thermal conductivity of a nanometer-size periodic structure to the thermal conductance of a single interface. In one attempt [38], the converted thermal interface conductance was reported to be ten times larger than the largest thermal interface conductance ever measured. Direct measurements of thermal resistance for other heterogeneous materials have been conducted by several groups. Stoner and Maris [39] used a picosecond optical technique to measure the thermal boundary resistances between metals and dielectrics. Costescu et al. [40] measured the TBR between epitaxial TiN and single crystal oxide with the time-domain thermoreflectance (TDTR) method.

The acoustic mismatch model (AMM) has been used to estimate the thermal conductance of a single interface. This model assumes that phonon interfacial transport is governed by continuum acoustics, and the interface is treated as an ideal plane. Therefore, it produces similar results at low temperatures to the atomistic Green's function method. We use the AMM thermal boundary resistance equation and associated tables published by Cheeke et al. [41] to estimate TBR at low temperatures ($T < 30$ K). Harrison's potential is used again to calculate bulk dispersion curves and group velocities in the (100) direction. The calculated zero-frequency group velocities, the zero-frequency group velocities estimated from elastic constants by Holland [42], and densities used in the AMM are listed in Table 2. Harrison's potential is known to predict lower group velocities [27].

A comparison between the atomistic Green's function results and the TBR predicted by the AMM is shown in Fig. 7. The AMM and the atomistic Green's function method both predict an expected cubic temperature dependence of TBR at low temperatures and agree very well at temperatures less than 20 K. This result is expected because the dominant phonons at low temperatures exhibit linear dispersion and the AMM works reasonably well. The Si/Ge interface produces a thermal boundary resistance of 6.2×10^{-9} m^2 K/W at room temperature according to the present results. The calculated interface thermal resistances can be used as boundary conditions in large-scale BTE simulations. In a rigorous BTE simulation that distinguishes phonon branch, phonon wave vector, and phonon frequency, the AGF method also must be (and can be) decomposed in terms of these variables.

Thermal Resistance Across Multiple Si/Ge Interfaces. Multiple-interface structures are of great importance in engineering applications. The overall thermal resistance of a multiple-interface structure is generally considered to increase with additional interfaces, because more phonons are reflected or scattered at interfaces. To evaluate the dependence of thermal resistance on the number of interfaces, the device region shown in Fig. 1 was made to include a multiple-interface structure. As an example, a six-interface structure is shown in Fig. 8(*a*). Mathematically, the matrix $\tilde{\mathbf{H}}_{\mathrm{tf}}$ in Eq. (6) now is more complicated and contains contributions from each layer. Every layer in the multiple-interface structure is one-unit-cell thick. The effects of strain are excluded from the calculation because they were shown to be negligible in the foregoing analysis. Resistances at different temperatures as functions of the number of interfaces are shown in Fig. 8(*b*). The trend in the figure confirms that as the number of interfaces increases, thermal resistance increases. However, the change from two interfaces to four interfaces is much larger than changes caused by additional interfaces. The thermal resistance curve eventually levels out and approaches an asymptotic value. This observation agrees with a previous study [12], with the conclusion that the effect of the first few interfaces is much more significant than subsequently added interfaces.

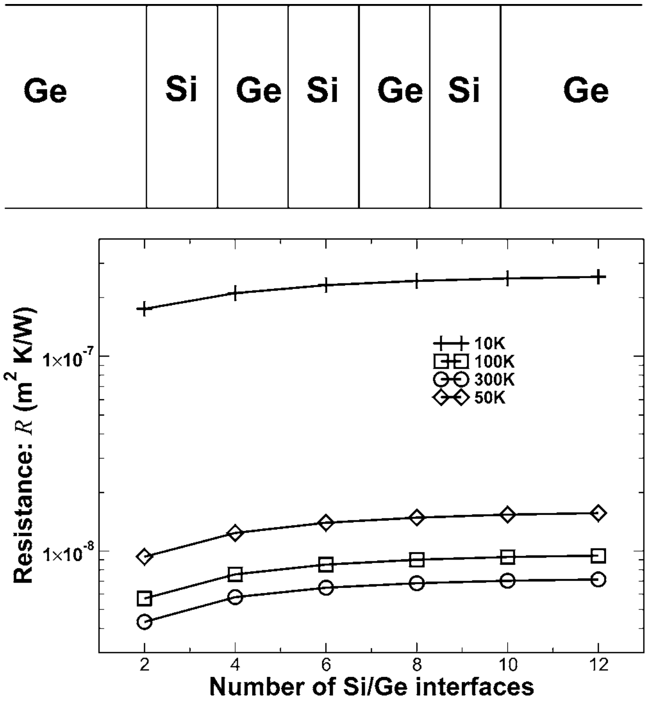

Fig. 8 The effect of multiple interfaces on thermal resistance

To make a quantitative comparison between the AGF method and prior experimental data, we have simulated the superlattice sample with the shortest period (3 nm) considered in the experimental study of Lee et al. [38], and the results are shown in Fig. 9. The thermal conductance is plotted as a function of the total superlattice sample thickness for a temperature of 200 K. Because of the higher computational expense in simulating the full thickness (900 nm) due to the fine $\vec{\mathbf{k}}_{\parallel}$ discretization, we have calculated several cases of shorter samples. A clear conductance asymptote of 9.5×10^7 W/m^2 K is reached beyond 20 nm and agrees with the trend shown in Fig. 8(*b*). The extrapolated thermal conductance at 900 nm is approximately one order of magnitude larger than the experimental thermal conductance. The difference can be ascribed to anharmonic effects in the experiment and to possible imperfections in the superlattice sample.

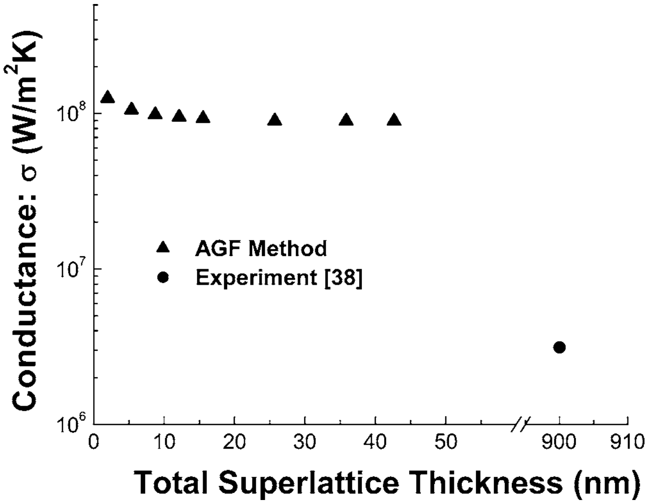

Fig. 9 Comparison of the thermal conductance of Si–Ge superlattice samples with 3 nm period at 200 K. The experimental result is from Lee et al. [38].

Conclusions

We have developed and described an atomistic Green's function method to study phonon transmission and thermal conductance (resistance) of atomistically defined Ge/Si/Ge and Si/Ge/Si strained thin films. The straining effect on thermal transport is found to be negligible as compared to the heterogeneous-material effect. At low frequencies, the transmission functions of the heterogeneous cases converge to those of the homogeneous cases because long phonon wavelengths result in rigid-body-like atomic motions. Room-temperature thermal conductances are reduced significantly by heterogeneous interfaces. The ballistic thermal conductance decreases as the thickness of the thin-film increases and reaches an asymptotic value, corresponding to the value of an infinitely thick film. We have also computed the thermal boundary resistance of a single Si/Ge interface and verified that it agrees with AMM results at low temperatures. A multiple interface case was also investigated, showing that the first few heterogeneous interfaces affect the thermal resistance to a much larger extent than subsequent interfaces.

Nomenclature

J = heat flux, W/m^2
M = atomic mass, kg
$\tilde{N}$ = phonon occupation number
N = mesh size, see Eq. (20)
R = thermal resistance, m^2 K/W
T = temperature, K
U = interatomic potential, J
$\vec{\mathbf{k}}$ = wave vector, 1/m
a = lattice constant, m
i = unit of imaginary number
k_B = Boltzmann constant, m^2 kg/s^2 K
s = cross-sectional area, m^2
u = displacement degree of freedom, m
d = bond length, m

Greek Symbols

δ = A small number corresponding to phonon energy dissipation in contacts
$\hbar$ = Planck constant, m^2 kg/s
ω = angular frequency, rad/s
σ = thermal conductance, W/m^2 K
Ξ = Transmission function

Vector and Matrix

$\mathbf{\Gamma}$ = matrix defined in Eqs. (16) and (17)
$\mathbf{\Sigma}$ = self-energy matrix defined in Eqs. (12) and (13)
τ = matrix defined in Eqs. (14) and (15)
$\mathbf{G}$ = Green's function matrix defined in Eq. (11)
$\mathbf{g}$ = uncoupled Green's function matrix defined in Eqs. (9) and (10)
$\mathbf{H}$ = harmonic matrix, defined in Eq. (1)
$\mathbf{I}$ = unity matrix
$\tilde{\mathbf{H}}$ = matrix representing intralayer interaction, defined in Eq. (4)
$\tilde{\mathbf{T}}$ = matrix representing interlayer interaction, defined in Eq. (5)
$\tilde{u}$ = column vector consisting of vibrational degrees of freedom
$\vec{\mathbf{R}}$ = lattice vector

Subscripts and Superscripts

D = device region
LC = left contact region
LCB = left contact bulk region
LD = left device region
RC = right contact region
RCB = right contact bulk region
RD = right device region
tf = thin film
i = matrix row index, also the index of degree of freedom
j = matrix column index, also the index of degree of freedom
m = unit cell running index
n = unit cell running index
p = layer index
q = layer index
r = degree of freedom running index
t = unit cell index
$\dagger$ = conjugate transpose of a matrix
$\parallel$ = parallel direction to the thin film

References

[1] Chen, G., Dresselhaus, M., Dresselhaus, G., Fleurial, J., and Caillat, T., 2003, "Recent Developments in Thermoelectric Materials," Int. Mater. Rev., **48**(1), pp. 45–66.
[2] Datta, S., 2000, "Nanoscale Device Modeling: The Green's Function Method," Superlattices Microstruct., **28**, pp. 253–278.
[3] Ju, Y., and Goodson, K., 1999, "Phonon Scattering in Silicon Films With Thickness of Order 100 nm," Appl. Phys. Lett., **74**(20), pp. 3005–3007.
[4] Little, W., 1959, "The Transport of Heat Between Dissimilar Solids at Low Temperature," Can. J. Phys., **37**, pp. 334–349.
[5] Swartz, E., and Pohl, R., 1989, "Thermal Boundary Resistance," Rev. Mod. Phys., **61**, pp. 605–668.
[6] Stevens, R., Smith, A., and Norris, P., 2005, "Measurement of Thermal Boundary Conductance of a Series of Metal-Dielectric Interfaces by the Transient Thermoreflectance Technique," ASME J. Heat Transfer, **127**, pp. 315–322.
[7] Prasher, R., and Phelan, P., 2001, "A Scattering-Mediated Acoustic Mismatch Model for the Prediction of Thermal Boundary Resistance," ASME J. Heat Transfer, **123**, pp. 105–112.
[8] Narumanchi, S., Murthy, J., and Amon, C., 2004, "Submicron Heat Transport model in Silicon Accounting for Phonon Dispersion and Polarization," ASME J. Heat Transfer, **126**, pp. 946–955.
[9] Mazumdar, S., and Majumdar, A., 2001, "Monte Carlo Study of Phonon Transport in Solid Thin Films including Dispersion and Polarization," ASME J. Heat Transfer, **123**, pp. 749–759.
[10] Yazdani, K., and Asheghi, M., 2004, "Ballistic Phonon Transport in Strained Si/SiGe Nanostructures With an Application to Strained-silicon Transistors," *Proceedings of the 9th Intersociety Conference on Thermal and Thermomechanical Phenomena In Electronic Systems*, Las Vegas, NV, June 1–4, Paper No. 04CH37543.
[11] Picu, R., Borca-Tasciuc, T., and Pavel, M., 2003, "Strain and Size Effects on Heat Transport in Nanostructure," J. Appl. Phys., **93**(6), pp. 3535–3539.
[12] Abramson, A., Tien, C., and Majumdar, A., 2002, "Interface and Strain Effects on the Thermal Conductivity of Heterostructures: A Molecular Dynamics Study," ASME J. Heat Transfer, **124**(5), pp. 963–970.

[13] Schelling, P., Phillpot, S., and Keblinski, P., 2002, "Phonon Wave-Packet Dynamics at Semiconductor Interfaces by Molecular-Dynamics Simulation," Appl. Phys. Lett., **80**, pp. 2484–2486.
[14] Young, D., and Maris, H., 1989, "Lattice-dynamical Calculation of the Kapitza Resistance Between FCC Lattices," Phys. Rev. B, **40**(6), pp. 3685–3693.
[15] Nishiguchi, N., Tamura, S., and Nori, F., 1993, "Phonon-transmission Rate, Fluctuations, and Localization in Random Semiconductor Superlattices: Green's-Function Approach," Phys. Rev. B, **48**, pp. 2515–2528.
[16] Cahill, D., Ford, W., Goodson, K., Mahan, G., Majumdar, A., Maris, H., Merlin, R., and Phillpot, S., 2003, "Nanoscale Thermal Transport," J. Appl. Phys., **93**(2), pp. 793–818.
[17] Pettersson, S., and Mahan, G., 1990, "Theory of the Thermal Boundary Resistance Between Dissimilar Lattices," Phys. Rev. B, **42**, pp. 7386–7390.
[18] Sui, Z., and Herman, I., 1993, "Effect of Strain on Phonons in Si, Ge, and Si/Ge Heterostructures," Phys. Rev. B, **48**, pp. 17938–17953.
[19] Mingo, N., 2006, "Anharmonic Phonon Flow Through Molecular Sized Junctions," Phys. Rev. B, **74**, p. 125402.
[20] Thompson, S., Armstrong, M., Auth, C., Alavi, M., Buehler, M., Chau, R., Cea, S., Ghani, T., Glass, G., Hoffman, T., Jan, C., Kenyon, C., Klaus, J., Kuhn, K., Ma, Z., Mcintyre, B., Mistry, K., Murthy, A., Obradovic, B., Nagisetty, R., Nguyen, P., Sivakumar, S., Shaheed, R., Shifren, L., Tufts, B., Tyagi, S., Bohr, M., and El-Mansy, Y., 2004, "A 90-nm Logic Technology Featuring Strained-Silicon," IEEE Trans. Electron Devices, **51**(11), pp. 1790–1797.
[21] Pop, E., Dutton, R., and Goodson, K., 2005, "Monte Carlo Simulation of Joule Heating in Bulk and Strained Silicon," Appl. Phys. Lett., **86**, p. 082101.
[22] Mingo, N., and Yang, L., 2003, "Phonon Transport in Nanowires Coated With an Amorphous Material: An Atomistic Green's Function Approach," Phys. Rev. B, **68**, p. 245406.
[23] Mingo, N., and Yang, L., 2004, "Erratum: Phonon Transport in Nanowires Coated With an Amorphous Material: An Atomistic Green's Function Approach [Phys. Rev. B 68, 245406 (2003)]," Phys. Rev. B, **70**, p. 249901.
[24] Shilkrot, L., Srolovitz, D., and Tersoff, J., 2000, "Morphology Evolution During the Growth of Strained-Layer Superlattices," Phys. Rev. B, **62**(12), pp. 8397–8409.
[25] Ohring, M., 2001, *Materials Science of Thin Films*, Academic Press, New York, pp. 417–492.
[26] Wortman, J., and Evans, R., 1965, "Young's Modulus, Shear Modulus, and Poisson's Ratio in Silicon and Germanium," J. Appl. Phys., **36**, pp. 153–156.
[27] Harrison, W. A., 1989, *Electronic Structure and the Properties of Solids*, Dover, New York, pp. 181–208.
[28] Mingo, N., 2003, "Calculation of Si Nanowire Thermal Conductivity Using Complete Phonon Dispersion Relations," Phys. Rev. B, **68**, p. 113308.
[29] Keating, P. N., 1966, "Effect of Invariance Requirements on the Elastic Strain Energy of Crystals With Application to the Diamond Structure," Phys. Rev., **145**, pp. 637–645.
[30] Lannoo, M., and Friedel, P., 1991, *Atomic and Electronic Structure of Surfaces*, Springer, New York, pp. 42–48.
[31] Guinea, F., Tejedor, C., Flores, F., and Louis, E., 1983, "Effective Two-Dimensional Hamiltonian at Surfaces," Phys. Rev. B, **28**(8), pp. 4397–4402.
[32] Zhang, W., and Fisher, T., 2005, "Simulation of Phonon Interfacial Transport in Strained Silicon-Germanium Heterostructures," ASME Paper No. 80053.
[33] Datta, S., 2005, *Quantum Transport: Atom to Transistor*, 1st ed., Cambridge University Press, Cambridge, UK, pp. 223–233.
[34] Venugopal, R., Ren, Z., Datta, S., and Lundstrom, M., 2002, "Simulating Quantum Transport in Nanoscale Transistors: Real Versus Mode-Space Approaches," J. Appl. Phys., **92**, pp. 3730–3739.
[35] Kittel, C., 2005, *Introduction to Solid State Physics*, 8th ed., Wiley, New York, p. 108.
[36] Tascius, T., Liu, W., Liu, J., Zeng, T., Song, D., Moore, C., Chen, G., Wang, K., Goorsky, M., Radetic, T., Gronsky, R., Koga, T., and Dresselhaus, M., 2000, "Thermal Conductivity of Symmetrically Strained Si/Ge Superlattices," Superlattices Microstruct., **28**, pp. 199–206.
[37] Chakraborty, S., Kleint, C., Heinrich, A., Schneider, C., and Schumann, J., 2003, "Thermal Conductivity in Strain Symmetrized Si/Ge Superlattices on Si(111)," Appl. Phys. Lett., **83**, pp. 4184–4186.
[38] Lee, S.-M., Cahill, D., and Venkatasubramanian, R., 1997, "Thermal Conductivity of Si-Ge Superlattices," Appl. Phys. Lett., **70**, pp. 2957-2959.
[39] Stoner, R., and Maris, H., 1993, "Kapitza Conductance and Heat Flow Between Solids at Temperature From 50 to 300 K," Phys. Rev. B, **48**, pp. 16373–16387.
[40] Costescu, R., Wall, M., and Cahill, D., 2003, "Thermal Conductance of Epitaxial Interfaces," Phys. Rev. B, **67**, p. 054302.
[41] Cheeke, J., Ettinger, H., and Herbal, B., 1976, "Analysis of Heat Transfer Between Solids at Low Temperatures," Can. J. Phys., **54**, pp. 1749–1763.
[42] Holland, M., 1963, "Analysis of Lattice Thermal Conductivity," Phys. Rev., **132**, pp. 2461–2471.

Modeling of Thermoelectric Properties of Semi-Conductor Thin Films With Quantum and Scattering Effects

A. Bulusu
Interdisciplinary Program in Materials Science,
Vanderbilt University,
Nashville, TN 37235

D. G. Walker[1]
Department of Mechanical Engineering,
Vanderbilt University,
Nashville, TN 37235
e-mail: greg.walker@vanderbilt.edu

Several new reduced-scale structures have been proposed to improve thermoelectric properties of materials. In particular, superlattice thin films and wires should decrease the thermal conductivity, due to increased phonon boundary scattering, while increasing the local electron density of states for improved thermopower. The net effect should be increased ZT, the performance metric for thermoelectric structures. Modeling these structures is challenging because quantum effects often have to be combined with noncontinuum effects and because electronic and thermal systems are tightly coupled. The nonequilibrium Green's function (NEGF) approach, which provides a platform to address both of these difficulties, is used to predict the thermoelectric properties of thin-film structures based on a limited number of fundamental parameters. The model includes quantum effects and electron-phonon scattering. Results indicate a 26–90 % decrease in channel current for the case of near-elastic, phase-breaking, electron-phonon scattering for single phonon energies ranging from 0.2 meV to 60 meV. In addition, the NEGF model is used to assess the effect of temperature on device characteristics of thin-film heterojunctions whose applications include thermoelectric cooling of electronic and optoelectronic systems. Results show the predicted Seebeck coefficient to be similar to measured trends. Although superlattices have been known to show reduced thermal conductivity, results show that the inclusion of scattering effects reduces the electrical conductivity leading to a significant reduction in the power factor ($S^2\sigma$).

[DOI: 10.1115/1.2709962]

Keywords: quantum simulation, thermoelectric, electron-phonon scattering

1 Introduction

Quantum-well superlattices have been proposed as a nanoscale structure that could potentially lead to dramatic increases in the performance of thermoelectric devices [1,2]. The use of quantum-well structures as thermoelectric materials is believed to enhance the thermoelectric figure of merit ($ZT=S^2\sigma T/\kappa$, where S is the Seebeck coefficient, σ is the electrical conductivity, and κ is the thermal conductivity) for several reasons: (i) The reduced dimensionality of a two-dimensional (2D) quantum well increases the local electron density of states per unit volume near the Fermi energy leading to an increase in the Seebeck coefficient [3]. (ii) The introduction of material interfaces promotes phonon scattering, which theoretically reduces the effective thermal conductivity. (iii) Phonon interference effects caused by phonon-interface scattering give rise to phonon band gaps at the interface of the thin films in a superlattice, which further reduces phonon transport [4]. The net result of these effects is a structure with a theoretically higher ZT than its bulk counterparts. Consequently, several researchers have experimentally investigated the role of quantum well, wire, and dot [5–9] superlattice layers on thermal transport. For example, Chen [10,11] has studied the phonon transport in Si/Ge superlattices using the Boltzmann transport equation for phonons. Phonon interface scattering was included through a combination of diffuse and specular scattering. They found that the greatest temperature drop occurred at the interfaces rather than within the layers due to a combination of diffuse and inelastic scattering processes thus developing the concept of phonon engineering to build structures having low thermal conductivity. Based on these findings alone, superlattices should improve the performance of thermoelectric devices compared to bulk materials.

Unfortunately, observations especially in the case of Si/Ge superlattices have not been able to recognize the presumed benefits of superlattice thermoelectric devices despite a theoretically predicted and experimentally observed reduction in the thermal conductivity of a superlattice compared to its bulk counterpart [3,5]. If we assume the thermal conductivity can be reduced by introducing phonon scattering sites, then the lack of performance must be attributed to a corresponding reduction in electrical properties (both σ and S). Normally, the electrical properties are not expected to be affected by the lattice structure because of the disparity between electron and phonon wavelengths and mean free paths [12]. Nevertheless, this presumption does not consider confinement, interface scattering of electrons, and electron-phonon scattering in the lattice. Therefore, to understand the effects of a lattice structure on thermoelectric performance, the Seebeck coefficient and electrical conductivity of a heterojunction are investigated using a nonequilibrium Green's function (NEGF) technique. The approach incorporates quantum as well as scattering effects, both of which are important in describing the physical behavior of confined structures.

The physical features that differentiate nanoscale device modeling from bulk modeling are quantum confinement and noncontinuum effects. Quantum effects usually dominate when the device length scales are of the order of the deBroglie wavelength. Quantum effects can have a detrimental impact in the form of leakage currents in very small transistors [13] or can be very

---

[1] Corresponding author.

Contributed by the Heat Transfer Division of ASME for publication in the JOURNAL OF HEAT TRANSFER. Manuscript received March 3, 2006; final manuscript received July 29, 2006. Review conducted by Jayathi Murthy.

useful as a high-performance alternative to very large-scale integration (VLSI) [14] in the form of resonant tunneling diodes. Noncontinuum effects can significantly influence charge as well as thermal transport in devices when characteristic lengths are of the order of the mean free path of energy carriers (~10–100 nm) [15]. For example, films as large as 0.5 μm have exhibited a reduction in thermal conductivity by as much as 30% [16] compared to bulk quantities at room temperature. Similarly, wires of decreasing diameter (150–25 nm) show dramatically reduced thermal conductivity as well as strong temperature dependence [17]. In terms of electrons, noncontinuum effects, particularly "hot electron" effects, have been studied for their impact on device performance [18].

The most common approach for thermal modeling at reduced scales is based on the Boltzmann transport equation (BTE). Tractable solutions of the BTE include limited carrier scattering through a relaxation-time approximation, where the system is considered to be only slightly perturbed from equilibrium. Numerical solutions to the BTE are possible using Monte Carlo techniques [19] in which particle distributions are solved using stochastic processes. Mazumder and Majumdar [20] describes such an approach that includes phonon dispersion and various phonon modes independently. For coupled solutions, an electrothermal model based on moments of the BTE for phonons and electrons was developed to simulate electron-phonon interactions [21]. This nonequilibrium approach has shown that the energy distributions for optical and acoustic phonons differ significantly, suggesting that nonequilibrium behavior is very different from continuum behavior. Using a similar model, Raman et al. [22] showed that nonequilibrium significantly affects the location and generation of the hot spot in microelectronic power devices. To remove the gray assumption in moment-based solutions, an unstructured finite-volume discrete ordinates scheme has been used to solve the BTE with spectral information [23]. Isotropic scattering in the form of impurity and Umklapp scattering was considered, and a favorable match with exact solutions was found. However, in spite of all the progress made in small-scale device modeling, the fact remains that rigorous scattering cannot be fully included in most models and coupling scattering models to quantum models continues to remain extremely challenging.

Efforts to include quantum effects in essentially particle-based models usually involve correction terms. Common methods of incorporating quantum effects are the density gradient formalism and the effective potential method [24]. The density gradient formalism is derived from the equation of motion for the one-particle Wigner function where quantum corrections are introduced by expressing the mean potential energy as a power series in Planck's constant h. The transport equation for the Wigner distribution function can now be written in the form of a modified BTE. In the effective potential method, a spatially localized wave packet is used as a representation of the electron where the size of the wave packet is defined roughly by the thermal deBroglie wavelength. The nonlocal form of the charge distribution introduces an effective potential when the inhomogeneous potential is introduced in the Hamiltonian. The generation of the effective potential determines the onset of quantization in the system due to the nonlocal nature of the potential. The quantum correction methods have been found to give an excellent match with the Poisson-Schrödinger solver for the case of carrier confinement and tunneling. More recently, attempts have been made to combine quantum corrections with the Monte Carlo technique [25], which is a numerical solution to the BTE. The results have been found to match well with the Schrödinger solution in the case of carrier confinement while a reasonably close match was observed for the case of tunneling. However, extension of this model to two and three dimensions remains, computationally tedious and difficult. Furthermore, the corrections are often heuristic and not based solely on first principles.

Quantum transport models often involve the solution to the Schrödinger equation and can be used to study current flow where the transport either is ballistic or includes limited scattering. Common models used to predict near-ballistic transport are quantum transmitting boundary model (QTBM) [26] and the quantum device analysis by mode evaluation (QDAME) [27]. QTBM involves formulating the boundary conditions for a given problem by calculating the transmission and reflection coefficients for a known boundary potential. These boundary conditions are then used in a discretized solution to obtain the wave function over the entire problem domain. Although this method is suitable for solving the Schrödinger equation for various boundary potentials, inclusion of dissipation due to scattering becomes very difficult. QDAME involves discretely sampling a device's density of states using standing wave boundary conditions. The standing waves are decomposed into traveling waves and injected from the contacts from which their occupancies are assigned.

Some of the contributing factors for problems associated with coupling quantum effects and scattering effects in device simulation are (i) time involved in converting new electronic device models including quantum effects into functioning simulation software and (ii) the immense computational resource requirement for accurate simulations of commercially important electronic devices. With device dimensions continuing to shrink, there is an increasing need for a simple model that can effectively couple quantum and scattering effects. The nonequilibrium Green's function formalism provides a framework for natural coupling of quantum and scattering effects. The source and drain contacts are coupled to the device through self-energy terms. The introduction of the Green's function for these terms eliminates the huge matrices that would normally be required to model the wave functions in an infinite reservoir. Instead matrices that are the size of the device Hamiltonian only are needed. In addition, the NEGF formalism allows for the rigorous incorporation of both elastic and inelastic scattering effects using the concept of Buttiker probes where scattering is treated as another contact, allowing it to be coupled to the device using the self-energy terms [28,29]. Unlike many other Schrödinger-based solver, the Green's function allows us to eliminate periodic boundary conditions leading to solutions for a device under bias. We present a brief synopsis of the formalism in Sec. 2 while a more thorough and detailed development can be found in [30] and [31].

Using the Green's function approach the performance of a silicon film and a Si/Ge heterostructure as thermoelectric materials are numerically investigated. Both structures are infinite in two directions and confined in the direction of transport. Therefore, the computational domain is one-dimensional. We are interested in calculating the electron transport due to a bias as a function of the confinement and scattering. Specifically, the IV characteristics can lead to direct calculation of the Seebeck coefficient and electrical conductance, which are desired for thermoelectric performance. By holding the two sides of the device at different temperatures a thermally induced electrical current is generated. A voltage is applied to bring the current to zero. This condition yields the Seebeck coefficient for the device. The electrical conductance is found from IV characteristics as the inverse of the slope of the linear region. We consider these performance characteristics in the presence of incoherent electron-phonon scattering, where the electrons interact inelastically with the surroundings. The energy lost or gained during this interaction with the lattice manifests itself in the form of phonons. The change in channel potential due to single electron charging effects is solved self consistently with the scattering model.

Effects believed to be important, but not addressed here, include energy-dependent scattering, inelastic electron-phonon scattering, crystal orientation, and full lattice structures. Although these effects are expected to affect the magnitude of transport, the trends of the predictions are not expected to change significantly. Furthermore, the application of NEGF to thermoelectric device is new and immature. Therefore, these simple models were chosen to study the gross effects of reduced scale on thermoelectric material properties. The present study, therefore, will identify the important physical mechanisms responsible for determining the electrical properties of thermoelectric materials. We would also like to point out that coupled thermal-electrical solutions are rare, particularly those with quantum and scattering effects. Therefore, this approach represents an emerging technology to study multiphysics device performance. Some results involving the IV characteristics and the formalism used in the present study have previously been used in a conference proceedings [32]. Some results are repeated here where indicated for archival purposes and because of their importance in the prediction of the power factor $S^2\sigma$, which is the focus of the present work.

2 NEGF Formalism

2.1 Ballistic Development. In general, an isolated device and its energy levels are described using a Hamiltonian matrix H, where U is the Hartree potential and α is the energy eigenstate of the electron,

$$(H+U)\psi_\alpha(\vec{r}) = \varepsilon_\alpha \psi_\alpha(\vec{r}) \tag{1}$$

The electron density matrix in real space is given by [31]

$$\rho(\vec{r},\vec{r}\,') = \int_{-\infty}^{\infty} f_0(E-\mu)\delta(EI-H)dE \tag{2}$$

where f_0 is the Fermi function, and $\delta(EI-H)$ identifies the energies associated with the device Hamiltonian. Using an expansion of the δ function, we obtain

$$\delta(EI-H) = \frac{i}{2\pi}\{[(E-i0^+)I-H]^{-1} - [(E+i0^+)I-H]^{-1}\} \tag{3}$$

The two terms on the right-hand side can be reduced to

$$\delta(EI-H) = \frac{i}{2\pi}[G(E) - G^+(E)] \tag{4}$$

where the retarded Green's function is defined as

$$G(E) = [(E-i0^+)I-H]^{-1} \tag{5}$$

In general, the Green's function can be interpreted as the response of the Schrödinger equation to an impulse. In the present scenario, the impulse is essentially an electron density at a particular energy. In the energy domain, the Green's function gives the energy eigenvalues for the eigenstates that are occupied in response to the applied impulse. The density of states in real space is represented by the spectral function,

$$A(\vec{r},\vec{r}\,',E) = 2\pi i[G(E) - G^+(E)] \tag{6}$$

The diagonal elements of the spectral function represent the local electron density of states. Thus, the electron density matrix for an isolated device can also be written in the form

$$\rho(\vec{r},\vec{r}\,') = \frac{1}{2\pi}\int_{-\infty}^{\infty} f_0(E-\mu)A(E)dE \tag{7}$$

The density solution is solved self-consistently with Poisson's equation,

$$\nabla^2 U = -\frac{q}{\epsilon_s}(N_d - n) \tag{8}$$

where n is the real diagonal of the density matrix ρ and represents the real-space electron density along the device. N_d is the donor level, and ϵ_s is the permittivity.

Consider a simple nanotransistor consisting of source and drain contacts as in Fig. 1. Let μ_1 and μ_2 be the chemical potentials of the source and the drain where subsequent numerical subscripts will denote the source and drain, respectively. The energy distribution of electrons in the source and drain follows the Fermi-Dirac distribution where f_1 and f_2 are the corresponding Fermi functions. The difference in the chemical potentials of the source and drain, which results from the applied bias, causes electrons to flow between the contacts through the channel. When no scattering is included in the channel, the transport is ballistic in nature and the channel is expected to have zero resistance to current flow (infinite conductance). However, experimental measurements [33] have shown that the maximum measured conductance of a one-energy level channel approaches a limiting value $G_0 = 2q^2/\hbar = 51.6\ \mathrm{k}\Omega^{-1}$. The reason for this limit to conductance arises from the fact that current in a contact is carried by infinite transverse modes while the number of available modes in the channel is limited. Therefore, the density of states in the contact is spread over a large energy range while the channel density of states lies specifically between μ_1 and μ_2. Upon coupling the contact and the channel, some of the density of states from the contact spread into the channel while the channel loses some of its density of states to the contact. As a result, the coupling causes the density of states in the channel to spread out over a wider range of energy levels resulting in a reduction in the number of states lying between μ_1 and μ_2.This reduction limits the amount of current in the device.

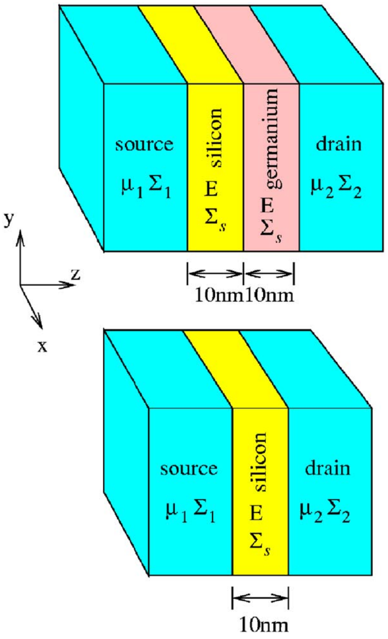

Fig. 1 Schematic representation of the nanodevice modeled in the simulation. *E* is the electron energy in the device while Σ_s is the scattering self-energy.

In the NEGF formalism, the coupling of the device to the source and drain contacts is described using self-energy matrices Σ_1 and Σ_2. The self-energy term can be viewed as a modification to the channel Hamiltonian to incorporate the boundary conditions. Accordingly, Eqs. (1) and (5) can be rewritten as

$$[H+U+\Sigma_1+\Sigma_2]\psi_\alpha(\vec{r}) = \varepsilon_\alpha\psi_\alpha(\vec{r}) \tag{9}$$

$$G(E) = [(E-i0^+)I-H-\Sigma_1-\Sigma_2]^{-1} \tag{10}$$

The self-energy term originates from the solution of the contact Hamiltonian. In this semi-infinite system, which is connected to the channel, there will be an incident wave from the channel as well as a reflected wave from the contact. The wave function at the interface is matched to conserve energy giving the boundary condition

$$\Sigma_i = -t\exp(ika) \tag{11}$$

where t is a result of the discretization and will be discussed later.

The broadening of the energy levels introduced by connecting the device to the source and drain contacts is incorporated through the functions Γ_1 and Γ_2 given by

$$\Gamma_1 = i(\Sigma_1 - \Sigma_1^+) \tag{12}$$

and

$$\Gamma_2 = i(\Sigma_2 - \Sigma_2^+) \tag{13}$$

The self-energy terms affect the Hamiltonian in two ways. The real part of the self-energy term shifts the device eigenstates or energy level while the imaginary part of Σ causes the density of states to broaden while giving the eigenstates a finite lifetime. The spectral function is defined as before in Eq. (6).

The electron density for the open system is now given as

$$\rho = \frac{1}{2\pi}\int_{-\infty}^{\infty} G^n(E)dE \tag{14}$$

where $G^n(E) \equiv G[\Gamma_1 f_1 + \Gamma_2 f_2]G^+$ for convenience and represents the electron density per unit energy. For plane wave basis functions, the current through the channel is calculated as the difference between the inflow and the outflow at any given contact

$$I_i = \frac{-q}{\hbar}\int_{-\infty}^{\infty} \mathrm{Tr}[\Gamma_i A]f_i - \mathrm{Tr}[\Gamma_i G^n]dE \tag{15}$$

where the i subscript indexes the contacts. For a two terminal device $I_1 = -I_2$.

2.2 Electron-Phonon Coupling. An electron in a device can interact with its surroundings elastically or inelastically, depending on the nature of surroundings. Elastic interactions occur when the surroundings are rigid leading to energy and momentum conservation. Such interactions are coherent in nature. Inelastic interactions occur when energy is dissipated through the emission or absorption of phonons, photons, etc. Such types of interactions are known as incoherent or phase-breaking processes. Inelastic scattering is, in general, difficult to model exactly. In this paper, we treat the phase-breaking scattering to be nearly elastic, i.e., $E \approx E + \hbar\omega \approx E - \hbar\omega$. The effect of scattering is incorporated into the coherent model discussed previously by treating it as another contact where electrons enter and leave the contact leading to no net current at that contact [31]. However, because the scattering terminal does not have a defined Fermi level, the scattering terms Σ_s and Γ_s have to be determined through other means. As such,

$$\Sigma_s^{\mathrm{in}}(\vec{r},\vec{r}',E) = D_0 G^n(\vec{r},\vec{r}',E) \tag{16}$$

$$\Gamma_s(E) = D_0 A(E), \quad \text{and} \quad \Sigma_s(E) = D_0 G(E) \tag{17}$$

D_0 is defined as the phonon correlation function and is calculated using the phonon deformation potential and the phonon wave vector β [31]

$$D_0(\vec{r},\vec{r}',\hbar\omega) = \sum_p \delta[E - \hbar\omega(\beta)]U_\beta(\vec{r})U_\beta^*(\vec{r}') \tag{18}$$

$$U_\beta(\vec{r}) = D_{\mathrm{adp}}\beta\sqrt{\frac{2\hbar}{\rho\omega\Omega}}\exp(i\beta\vec{r}) \tag{19}$$

D_{adp} is the acoustic deformation potential, ρ is the mass density, and Ω is the normalization volume. The values of D_0 represent the energy of the phonon with which the electrons scatter. Depending on the system temperature, there is a wide range of phonons with which electrons scatter. However in our model, we use a simplified case of the electrons interacting with phonons of a single frequency in an attempt to illustrate the effect of scattering on electron transport in devices. For example, $D_0 = 0.1\ \mathrm{eV}^2$ corresponds to a phonon energy of 20 meV [31]. This phonon energy is not related to the temperature of the device. In fact, the NEGF model does not include temperature within the system as temperature can be expressed only for a system that is in equilibrium. The only place where temperature is included in the model is in the source and drain Fermi functions. Instead, the phonon energy represents the dominant phonon frequency available for scattering [34]. In the present model, we assume D_{adp} is independent of the electron energy in the channel and corresponds to optical phonon scattering only, which is expected to be the dominant electron scatterer [35].

2.3 Numerical Scheme. The foregoing model is discretized on a uniform one-dimensional grid with a lattice spacing of a. Transport occurs parallel to the grid, which is also the confined direction. The Hamiltonian in Eq. (10) is an effective mass Hamiltonian, which averages the effects of the underlying periodic potential, and is given as the Laplacian operator. The discretized linear version is an $N \times N$ tridiagonal matrix given as

$$t\nabla^2 = [H] = \begin{bmatrix} Ec + 2t & -t & \\ -t & Ec + 2t & -t \\ & -t & Ec + 2t \end{bmatrix} \tag{20}$$

where t is the coupling energy between adjacent nodes and is given in terms of the discretized spacing a and the effective mass m^* as

$$t = \frac{\hbar^2}{2m^* a^2} \tag{21}$$

The grid spacing a and grid size N is chosen such that the channel thickness $L = a(N-1)$. The grid spacing a must be chosen such that the coupling energy t is larger than the energy range of integration above the conduction band edge. In order to ensure current conservation, the energy eigenvalues of the Hamiltonian must be real. In order to meet this criterion, the Hamiltonian must be Hermitian. In the case where we are modeling a heterojunction, such as Si/Ge, there will be a spatially varying effective mass as well as conduction band edges. The spatial variation of the conduction band edges in the Hamiltonian allows for the automatic inclusion of boundary effects across interfaces. We employ the standard nonlinear control-volume approach [36] and require that the material interface lies at a node to ensure that the Hamiltonian remains Hermitian.

$$\nabla(t\nabla) = [H] = \begin{bmatrix} Ec_A + 2t_A & -t_A & \\ -t_A & Ec_J + t_A + t_B & -t_B \\ & -t_B & Ec_B + 2t_B \end{bmatrix} \tag{22}$$

To initiate the solution, only the self-energy matrices for the source and drain contacts, which we can calculate directly, are used to obtain the values of $G(E)$. The self-energy term for the scattering contact is then calculated self-consistently from Eqs. (16) and (17) using the recently calculated values of $G(E)$. The source, drain and scattering self-energy terms are then used to obtain the final Green's function from which the net channel current is calculated as a difference in the inflow and outflow currents using Eq. (15) [29]. For the doping levels considered in this paper, the contacts are generally ohmic in nature, thus eliminating the need to model any barrier effects at the source and drain electrodes. The entire calculation is carried out self-consistently with Poisson's equation to account for the dependence of the channel potential on the electron density. This process is depicted in Fig. 2.

The computational requirements to solve for the current at a particular voltage depends on a number of factors. The grid size used in the present model consisted of 101 nodes. The resulting size of the Hamiltonian was a 101×101 matrix. For an energy range of 0–0.5 eV, we used 300 uniform integration steps. In the case of degenerate doping, however, the maximum contribution to current comes from energy values concentrated near the conduc-

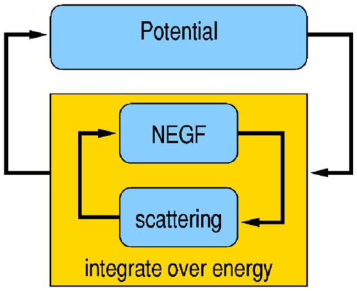

Fig. 2 Self-consistent iterations between the Green's function, scattering, and the potential. The inner process is integrated over energy.

tion band edge. In this case, care must be taken to choose an energy range close to the conduction band edge to ensure that the contribution from those energy steps is properly included. The matrix inversion in Eq. (10) was performed for each integration step, and the integration was performed self-consistently with the potential. This process was repeated for each voltage in the calculated IV characteristics.

To ensure numerical accuracy, first the number of integration steps was selected to ensure a suitable error. Next convergence of the potential calculation was set to an acceptable error. A relaxation of 0.2–0.5 on the density usually allowed convergence in about 20 iterations. The self-consistent approach can be used as long as the value of $U_o=q^2/\epsilon_0\epsilon_r$ as well as the value of the broadening Γ is comparable to k_BT. If U_o exceeds k_BT, the channel goes into the Coulomb blockade regime where the self-consistent method cannot be used anymore to solve for potential. The coupling energy t also has a similar effect as broadening and ensuring that $t \geq U_o$ will keep the channel in the self-consistent field regime. A large t implies that the grid spacing a is small, leading to more delocalization of the electron wave function, which, in turn, improves the accuracy of the self-consistent field calculation.

2.4 Physical Model. The silicon thin films modeled in our simulations were 10 nm thick as shown in Fig. 1. In the case of the Si/Ge heterostructure, each of the individual thin films were modeled as 10 nm thick layers each, leading to a combined thickness of 20 nm for the heterostructure. The bias applied on the devices ranged from 0–0.1 V on the drain.

3 Results and Discussion

3.1 Effects of Phase-Breaking Near Elastic Scattering. The channel current-voltage characteristics with incoherent, near-elastic scattering are shown in Fig. 3 for various scattering energies. Initially at zero bias, the source and drain Fermi levels are separated by a voltage V. The application of bias causes the energy levels of the drain to shift until the source and drain Fermi levels are equal. The channel current increases linearly during this time. Once the two Fermi levels align there are no additional energy states for the electron coming from the channel to occupy in the drain, causing the current to saturate. As mentioned in the Introduction, we have considered electron energy-independent near-elastic phonon scattering in this analysis. For this study, the free parameter D_0 was varied from a very low phonon energy of 0.2 meV to 60 meV, which is the optical phonon energy limit in the case of silicon, and the IV characteristics were collected. While $D_0=0.001\ \mathrm{eV}^2$ corresponding to phonon energy of 0.2 meV causes a reduction of 26% in the channel current, the current for $D_0=0.01\ \mathrm{eV}^2$ is found to decrease by 60% of the ballistic value. When D_0 is increased to $0.05\ \mathrm{eV}^2$ corresponding to a phonon energy of 10 meV the current decreases further by 80%, demonstrating the importance of scattering effects on electron transport in small-scale devices. Further increase in phonon energy to 20 meV and 40 meV results in an additional decrease of only 5–10% in the current, indicating saturation in the amount of electron interaction with higher energy phonons. There is no additional decrease in the current for the 60 meV case.

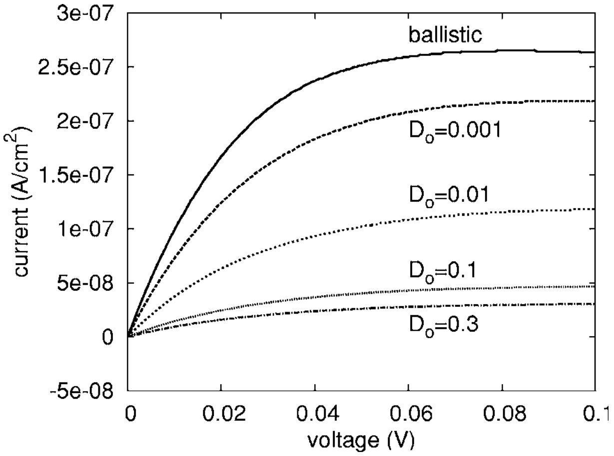

Fig. 3 Current versus voltage characteristics for incoherent, near-elastic scattering in a silicon thin film for $n=5\times10^{18}\ \mathrm{cm}^{-3}$

3.2 Thermoelectric Effects in Silicon Thin Films. The Seebeck coefficient for silicon thin films were studied for various temperature ranges of the source and drain contacts while varying the doping in silicon. The source temperature was maintained constant at 300 K, whereas the drain contact was maintained a higher temperature relative to the source. The film thickness was 10 nm, and the applied bias ranged from 0 to 0.1 V. Figure 4 shows the current-voltage characteristics for a silicon thin film doped to electron concentration of $5\times10^{18}\ \mathrm{cm}^{-3}$ without scattering (ballistic case). The source-drain temperature difference ranged from 0 K to a maximum of 30 K. For low-bias conditions, the number of high-energy electrons generated in the drain contact is higher than the number of electrons arriving at the drain through the channel leading to negative current values. As the bias is increased gradually, more electrons from the source are drawn toward the drain due to the applied bias leading to higher inflow at the drain and positive current values. To estimate the Seebeck coefficient S, the applied bias is adjusted to obtain zero current.

For the case of near-elastic scattering, the value of the Seebeck coefficient was found to be independent of the scattering strength

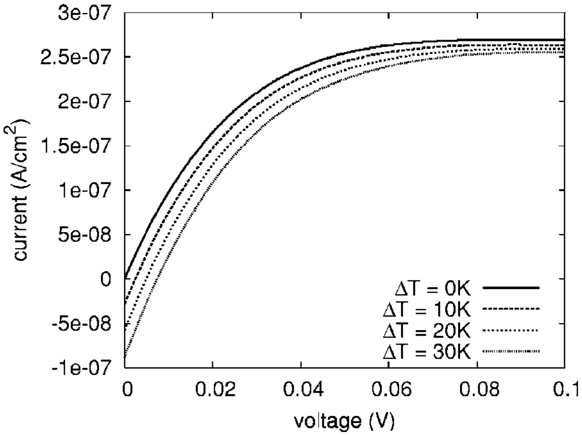

Fig. 4 Temperature-dependent current-voltage characteristics of a silicon thin film for a channel temperature difference of 0–30 K without scattering: $n=5\times10^{18}\ \mathrm{cm}^{-3}$

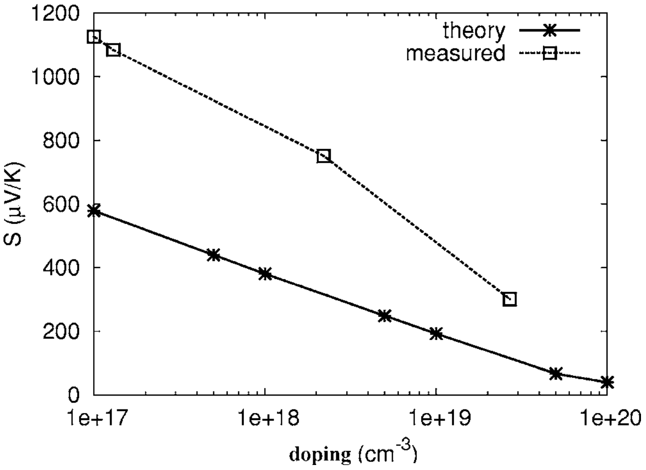

Fig. 5 Predicted versus measured [39] values of Seebeck coefficient for silicon at 300 K as a function of doping levels

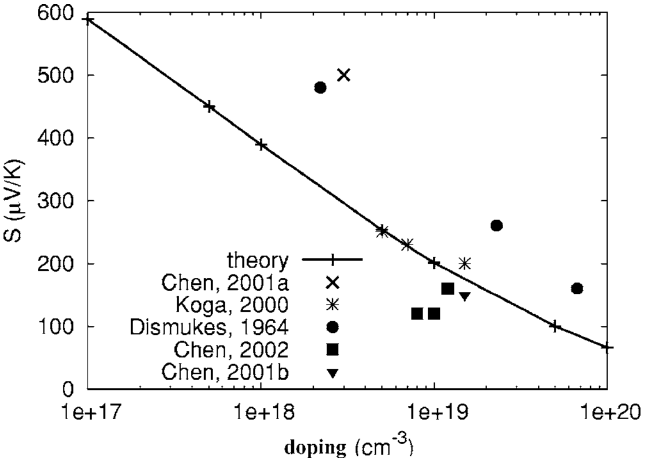

Fig. 6 Predicted versus measured Seebeck [5,6,41–43] coefficient for ballistic Si(10 nm)/Ge(10 nm) superlattice with doping

D_0. However, S is a function of doping. The conduction band edge and Fermi level are related to the doping level in the semiconductors by the carrier density

$$n = N_c \exp\left(-\frac{E_c - E_f}{k_B T}\right) \tag{23}$$

Here, N_c is the effective density of states at the conduction band edge and E_c and E_f the conduction band edge and Fermi level, respectively [37]. Varying the relative values of the conduction band edge and the Fermi level allows us to vary the doping level in the semiconductors. For all doping levels, the Seebeck coefficient was found to change almost linearly as a function of the temperature difference for small temperature changes. However, this does not hold true as the temperature difference across the device is increased. Yang et al. [38] studied the anisotropic thermoelectric properties of superlattices. They reported that although the Seebeck coefficient does not exhibit very high anisotropy between the in-plane and cross-plane directions, the cross-plane Seebeck coefficient rises rapidly with device temperature. The value of Seebeck coefficient in our calculations changes by ~4–5 μV/K for a temperature range of 0–30 K. This small change in S allows us to report an average value rather than the slope of the Seebeck voltage versus ΔT plot (Fig. 4).

Figure 5 shows the averaged predicted and measured Seebeck coefficient values for silicon for various doping levels in all temperature ranges considered. The predicted values of S differ from the experimentally measured values [39] approximately by a factor of 2. Although there is limited experimental data for the Seebeck coefficient for silicon thin films, it must be noted that the trends predicted by our model match the trends of the experimental data for bulk silicon.

3.3 Thermoelectric Effects in Si/Ge Thin Films. The thermoelectric properties of Si/Ge heterostructures were studied in a manner similar to silicon by maintaining the drain at higher temperatures than the source. Quantum confinement effects can be found in [40] and in a forthcoming paper derived from [40]. Each of the semiconductor thin films was modeled as 10 nm thick, leading to a combined thickness of 20 nm for the heterojunction. Similar to silicon, the doping in silicon and germanium was varied by changing the relative values of E_c and μ. The amount of doping was modeled to be constant throughout the two materials. The predicted values of the Seebeck coefficients with doping is shown in Fig. 6. Although there is a large spread in the experimentally measured results for various doping levels in the superlattices, the results from our model show fair agreement with the measured values. We do not expect our results to match the experimental data exactly for a number of reasons: (i) although our model incorporates quantum effects in the form of discrete energy states in the channel, it does not include the additional effect of electron confinement induced by the quantum well Si-Ge-Si superlattice. (ii) The superlattices used in the experiments consist of 300–1200 alternating layers of silicon and germanium films whose thicknesses are of the order of a few angstroms while our model consists of a single heterojunction where each film is 10 nm thick. (iii) The values used for the effective mass for silicon and germanium correspond to bulk values while the experiments were performed on single crystalline epitaxial layers. It was seen in our simulations that the value of the effective mass used in the calculations significantly affects the current-voltage characteristics. For film thicknesses of the order of few nanometers as used in our calculations, both silicon and germanium can be considered to be single crystals, allowing us to use the effective mass for that particular orientation. (iv) We have used the Fermi-Dirac function to model the inflow of electrons supplied by the source and drain contacts. This means that the contacts will supply electrons having a continuum energy distribution in all directions while entering the channel. However, for film thicknesses used in our simulations, additional electron confinement due to the reduced dimensionality of the 2D film is expected causing the electrons entering the channel to have discrete energy levels in the direction of transport. This effect of reduced dimensionality can be modeled by using a 2D Fermi function that will treat the electrons entering from the contacts as having infinite boundary conditions in the bulk directions and discrete energy states in the direction of confinement. It is expected that incorporating this effect of reduced dimensionality in our model will increase the local density of states per unit volume at the Fermi level leading to an increase in the predicted Seebeck coefficient.

Conductivity values for each value of D_0 were calculated from the slope of the linear portion of the IV characteristics.

$$\sigma = \frac{dI}{dV} L \tag{24}$$

where L is the channel thickness. It was seen that inclusion of electron-phonon scattering caused a significant drop in the current conducted through the channel indicating increased resistance to current flow with scattering. The $S^2\sigma$ value was calculated using the conductivity values predicted for each level of scattering along with the Seebeck coefficient obtained for each doping level considered. The decrease in conductivity led to an overall decrease in the power factor as demonstrated from the reduction in $S^2\sigma$ values with increasing scattering seen in Fig. 7. However, the $S^2\sigma$ values

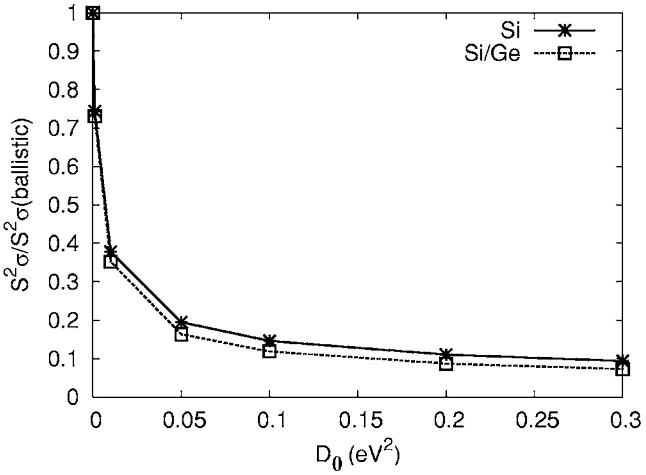

Fig. 7 Change in $S^2\sigma$ with incoherent electron-phonon scattering for silicon thin films and Si/Ge heterojunctions: $N_{d,\mathrm{Si}}=5\times10^{18}$ cm^{-3}, $N_{d,\mathrm{SiGe}}=5\times10^{18}$ cm^{-3}

of Si/Ge were found to be two times greater than the silicon thin films for the same doping level.

4 Conclusions

The nonequilibrium Green's function formalism was used to couple quantum effects and scattering effects in a 10 nm thick silicon film. The model was used to demonstrate near-elastic, phase-breaking electron-phonon scattering effects in very small-scale devices. A 26–90% decrease in current was noted when phonon scattering was included. The NEGF formalism was used to study thermoelectric behavior of electrons in silicon thin films and Si/Ge heterojunction. The predicted Seebeck coefficient values for silicon and Si/Ge heterojunctions matched well with the experimentally measured values. Inclusion of electron-phonon scattering in the model increased the electrical resistance causing the value of $S^2\sigma$ for silicon thin film and the heterojunction to decrease by 26–90% of their ballistic values. However, the $S^2\sigma$ values for the Si/Ge heterojunction was found to be enhanced compared to the $S^2\sigma$ values for silicon thin films. Current research efforts are focused toward incorporating electron energy-dependent inelastic electron-phonon scattering as well as phonon transport through devices to study all coupled effects present in the prediction of *ZT* for devices and materials.

Acknowledgment

We are grateful to Prof. Supriyo Datta, Department of Electrical and Computer Engineering, Purdue University, for providing us with a preprint of his book [31] on which much of this work is based. This research was funded through a Vanderbilt Discovery Grant and a Vanderbilt Institute of Nanoscale Science and Engineering (VINSE) fellowship.

References

[1] Hicks, L. D., and Dresselhaus, M. S., 1993, "Effect of Quantum-Well Structures on the Thermoelectric Figure of Merit," Phys. Rev. B, **47**(19), pp. 12727–12731.

[2] Hicks, L. D., Harman, T. C., and Dresselhaus, M. S., 1993, "Use of Quantum-Well Superlattices to Obtain a High Figure of Merit From Nonconventional Thermoelectric Materials," Appl. Phys. Lett., **63**(23), pp. 3230–3232.

[3] Tritt, T. M., 2001, *Recent Trends in Thermoelectric Materials Research III: Semiconductors and Semimetals*, Academic Press, New York, Vol. 3.

[4] Simkin, M. V., and Mahan, G. D., 2000, "Minimum Thermal Conductivity of Superlattices," Phys. Rev. Lett., **84**(5), pp. 927–930.

[5] Koga, T., Cronin, S. B., Dresselhaus, M. S., Liu, J. L., and Wang, K. L., 2000, "Experimental Proof-of-Principle Investigation of Enhanced $Z_{3D}T$ in 001 Oriented Si/Ge Superlattices," Appl. Phys. Lett., **77**(10), pp. 1490–1492.

[6] Yang, B., Liu, J., Wang, K., and Chen, G., 2001, "Characterization of Cross-Plane Thermo-Electric Properties of Si/Ge Superlattices," *Proc. of 20th International Conference on Thermoelectrics (ICT)*, Beijing, China, June, pp. 344–347.

[7] Yang, B., Liu, J. L., Wang, K. L., and Chen, G., 2002, "Simultaneous Measurements of Seebeck Coefficient and Thermal Conductivity Across Superlattice," Appl. Phys. Lett., **80**(10), pp. 1758–1760.

[8] Harman, T. C., Taylor, P. J., Walsh, M. P., and La Forge, B. E., 2002, "Quantum Dot Superlattice Thermoelectric Materials and Devices," Science, **297**(27), pp. 2229–2232.

[9] Venkatasubramanian, R., Siivola, E., Colpitts, T., and O'Quinn, B., 2001, "Thin-Film Thermoelectric Devices With High Room-Temperature Figures of Merit," Nature (London), **413**(11), pp. 597–602.

[10] Chen, G., 1998, "Thermal Conductivity and Ballistic-Phonon Transport in the Cross-Plane Direction of Superlattices," Phys. Rev. B, **57**(23), pp. 14958–14973.

[11] Chen, G., 1999, "Phonon Wave Heat Conduction in Thin Films and Superlattices," ASME J. Heat Transfer, **121**, pp. 945–953.

[12] Dresselhaus, M. S., 2003, "Nanostructures and Energy Conversion Devices," *Proc. of 2003 Rohsenow Symposium on Future Trends of Heat Transfer*, Cambridge, MA, May, pp. 1–3.

[13] Rahman, A., Ghosh, A., and Lundstrom, M., "Assessment of Ge n-MOSFETs by Quantum Simulation," IEEE International Electron Devices Meeting (IEDM) Technical Digest, pp. 19.4.1–19.4.4, December 2003.

[14] Mazumder, P., Kulkarni, S., Bhattacharya, M., Sun, J. P., and Haddad, G. I., 1998, "Digital Circuit Applications of Resonant Tunneling Devices," Proc. IEEE, **86**(4), pp. 664–686.

[15] Cahill, D. G., Ford, W. K., Goodson, K. E., Mahan, G. D., Majumdar, A., Maris, H. J., Merlin, R., and Phillpot, S. R., 2003, "Nanoscale Thermal Transport," J. Appl. Phys., **93**(2), pp. 793–818.

[16] Asheghi, M., Leung, Y. K., Wong, S. S., and Goodson, K. E., 1997, "Phonon-Boundary Scattering in Thin Silicon Layers," Appl. Phys. Lett., **71**(13), pp. 1798–1800.

[17] Zhou, J. H., Jin, C. G., Li, X. G., and Shi, L., 2005, "Thermoelectric Properties of Individual Electrodeposited Bismuth Telluride Nanowires," Appl. Phys. Lett., **87**(13), p. 133109.

[18] Blotekjaer, K., 1970, "Transport Equations for Electrons in Two-Valley Semiconductors," IEEE Trans. Electron Devices, **17**(1), pp. 38–47.

[19] Lugli, P., 1990, "The Monte Carlo Method for Semiconductor Device and Process Modeling," IEEE Trans. Comput.-Aided Des., **9**(11), pp. 1164–1176.

[20] Mazumder, S., and Majumdar, A., 2001, "Monte Carlo Study of Phonon Transport in Solid Thin Films Including Dispersion and Polarization," ASME J. Heat Transfer, **123**(4), pp. 749–759.

[21] Lai, J., and Majumdar, A., 1996, "Concurrent Thermal and Electrical Modeling of Sub-Micrometer Silicon Devices," J. Appl. Phys., **79**(9), pp. 7353–7361.

[22] Raman, A., Walker, D. G., and Fisher, T. S., 2003, "Simulation of Nonequilibrium Thermal Effects in Power LDMOS Transistors," Solid-State Electron., **47**(8), pp. 1265–1273.

[23] Murthy, J. Y., and Mathur, S. R., 2002, "Computation of Sub-Micron Thermal Transport Using an Unstructured Finite Volume Method," ASME J. Heat Transfer, **124**(6), pp. 1176–1181.

[24] Asenov, A., Watling, J. R., Brown, A. R., and Ferry, D. K., 2002, "The Use of Quantum Potentials for Confinement and Tunnelling in Semiconductor Devices," J. Comput. Electron., **1**(4), pp. 503–513.

[25] Tang, T., and Wu, B., 2004, "Quantum Correction for the Monte Carlo Simulation Via the Effective Conduction-Band Edge Equation," Semicond. Sci. Technol., **19**(1), pp. 54–60.

[26] Lent, C. S., and Kirkner, D. J., 1990, "The Quantum Transmitting Boundary Method," J. Appl. Phys., **67**(10), pp. 6353–6359.

[27] Laux, S. E., Kumar, A., and Fischetti, M. V., 2002, "Ballistic Fet Modeling Using QDAME: Quantum Device Analysis by Modal Evaluation," IEEE Trans. Nanotechnol., **1**(4), pp. 255–259.

[28] Datta, S., 1989, "Steady-State Quantum Kinetic Equation," Phys. Rev. B, **40**(8), pp. 5830–5833.

[29] Datta, S., 1990, "A Simple Kinetic Equation for Steady-State Quantum Transport," J. Phys.: Condens. Matter, **2**(40), pp. 8023–8052.

[30] Datta, S., 2000, "Nanoscale Device Modeling: The Green's Function Method," Superlattices Microstruct., **28**(4), pp. 253–278.

[31] Datta, S., 2005, *Quantum Transport: Atom to Transistor*, Cambridge University Press, Cambridge, MA.

[32] Bulusu, A., and Walker, D. G., 2005, "Modeling of Electron Transport in Thin Films With Quantum and Scattering Effects," ASME/Pacific Rim Technical Conference and Exhibition on Integration and Packaging of MEMS, NEMS and Electronic Systems, San Francisco, July, ASME Paper No. IPACK2005–73212.

[33] Szafer, A., and Stone, A. D., 1989, "Theory of Quantum Conduction Through a Constriction," Phys. Rev. Lett., **62**(3), pp. 300–303.

[34] Lundstrom, M., and Ren, Z., 2002, "Essential Physics of Carrier Transport in Nanoscale MOSFETs," IEEE Trans. Electron Devices, **49**(1), pp. 133–141.

[35] Tien, C.-L., Majumdar, A., and Gerner, F. M., eds. 1998, *Microscale Energy Transport*, Taylor & Francis, New York, pp. 3–94.

[36] Patankar, S. V., 1980, *Numerical Heat Transfer*, Taylor and Francis, New York.

[37] Muller, R., and Kamins, T., 1986, *Device Electronics for Integrated Circuits*, Wiley, New York.

[38] Yang, B., Liu, W. L., Liu, J. L., Wang, K. L., and Chen, G., 2002, "Measurements of Anisotropic Thermoelectric Properties in Superlattices," Appl. Phys.

Lett., **81**(19), pp. 3588–3590.

[39] Geballe, T. H., and Hull, G. W., 1955, “Seebeck Effect in Silicon,” Phys. Rev., **98**(4), pp. 940–948.

[40] Bulusu, A., and Walker, D. G., 2006, “Effect of Quantum Confinement on Thermoelectric Properties of 2D and 1D Semiconductor Thin Films,” *Proc. of ITherm*, San Diego, July.

[41] Dismukes, J. P., Ekstrom, L., Steigmeier, E. F., Kudman, I., and Beers, D. S., 1964, “Thermal and Electrical Properties of Heavily Doped Ge-Si Alloys up to 1300 k,” J. Appl. Phys., **35**(10), pp. 2899–2907.

[42] Liu, W. L., Tasciuc, T. B., Liu, J. L., Taka, K., Wang, K. L., Dresselhaus, M. S., and Chen, G., 2001, “In-Plane Thermoelectric Properties of Si/Ge Superlattices,” *Proc. of 20th International Conference on Thermoelectrics (ICT)*, Beijing, China, July, pp. 340–343.

[43] Liu, W. L., Chen, G., Liu, J. L., and Wang, K. L., 2002, “Quantum and Classical Size Effects on Thermoelectric Transport in Si/Ge Superlattices,” *Proc. of 21st International Conference on Thermoelectrics (ICT)*, pp. 130–134.

Computational Model for Transport in Nanotube-Based Composites With Applications to Flexible Electronics

Satish Kumar
School of Mechanical Engineering,
Purdue University,
West Lafayette, IN 47907

Muhammad A. Alam
School of Electrical and Computer Engineering,
Purdue University,
West Lafayette, IN 47907

Jayathi Y. Murthy[1]
Schoo of Mechanical Engineering,
Purdue University,
585 Purdue Mall,
West Lafayette, IN 47907
e-mail: jmurthy@ecn.purdue.edu

Thermal and electrical transport in a new class of nanocomposites composed of random isotropic two-dimensional ensembles of nanotubes or nanowires in a substrate (host matrix) is considered for use in the channel region of thin-film transistors (TFTs). The random ensemble of nanotubes is generated numerically and each nanotube is discretized using a finite volume scheme. To simulate transport in composites, the network is embedded in a background substrate mesh, which is also discretized using a finite volume scheme. Energy and charge exchange between nanotubes at the points of contact and between the network and the substrate are accounted for. A variety of test problems are computed for both network transport in the absence of a substrate, as well as for determination of lateral thermal and electrical conductivity in composites. For nanotube networks in the absence of a substrate, the conductance exponent relating the network conductance to the channel length is computed and found to match experimental electrical measurements. The effective thermal conductivity of a nanotube network embedded in a thin substrate is computed for a range of substrate-to-tube conductivity ratios. It is observed that the effective thermal conductivity of the composite saturates to a size-independent value for large enough samples, establishing the limits beyond which bulk behavior obtains. The effective electrical conductivity of carbon nanotube-organic thin films used in organic TFTs is computed and is observed to be in good agreement with the experimental results.

[DOI: 10.1115/1.2709969]

Keywords: nanotube, thin film transistor, nanocomposite, percolation

Introduction

In recent years, there has been growing interest in low-cost large-area manufacture of thin-film transistors (TFTs) on flexible substrates for use in applications such as displays, *e*-paper, *e*-clothing, biological and chemical sensing, conformal radar, and others. TFTs based on amorphous silicon (*a*-Si) now dominate the market for large-area flat-panel displays [1,2]. When transistor performance is not critical, low-cost organic TFTs on flexible, lightweight, plastic substrates [3–7] are emerging as an alternative in many nondisplay applications. For high-performance applications, however, the choices are limited: single crystal silicon or poly-silicon based TFTs [8,9] cannot be manufactured at low temperature ($<200^\circ C$) and are therefore not suitable for plastic substrates. As a result, researchers are exploring a new class of nanocomposite TFTs based on networks of silicon nanowires (Si-NWs) or carbon nanotubes (CNTs) [10–12]. Here, high-quality, nearly crystalline NWs and CNTs are grown at high temperature on a temporary substrate and released into a carrier fluid, which is then spin coated onto arbitrary (flexible) substrates at room temperature to form a thin film of randomly oriented NWs or CNTs. Once the source and drain contacts are defined, this thin film of nearly crystalline nanowires or nanotubes constitutes the high performance channel of a TFT (see Fig. 1). In other applications, the performance of organic TFTs is improved by dispersing nanotubes at low densities in organic substrates [13]. Since the thermal conductivity of both plastic and organic substrates is very low ($\sim 0.1-1$ W/mK), and since cooling options are limited if the electronics are to be kept flexible, self-heating is expected to emerge as a significant bottleneck to performance in this new class of electronics. At the same time, the electrical performance of these network composite transistors is poorly understood, and it has been difficult to interpret seemingly disparate experimental data [11,12,14].

An important property determining device performance is the lateral thermal and electrical conductivity of the composite film. The thermal and electrical conductivity of the network composite depends on the percolation properties of the network. In the absence of the substrate, the network conductivity is zero if the tube density is below the percolation threshold [15]. The presence of the substrate allows conduction to occur below the percolation threshold, and the degree to which percolation matters depends in large part on the coherence length of transport in the tubes [16], i.e., the length over which the temperatures of the two media remain unequilibrated. In the limit of low coherence length, leakage of either heat or charge from the tubes to the substrate predominates, and percolation effects are unimportant. On the other hand, if the coherence length is competitive with the sample size, network percolation would be important. The thermal and electrical behavior of TFTs spans these limits. In general, both substrate and network play important roles in determining the thermal performance of typical nanotube–plastic composites. An analogous problem occurs in electrical transport in nanotube–organic composites whereby charge transport in the organic substrate is enhanced by the presence of subpercolating nanotubes [13]. On the

---

[1] Corresponding author.

Contributed by the Heat Transfer Division of ASME for publication in the JOURNAL OF HEAT TRANSFER. Manuscript received March 28, 2006; final manuscript received August 25, 2006. Review conducted by Sumanta Acharya.

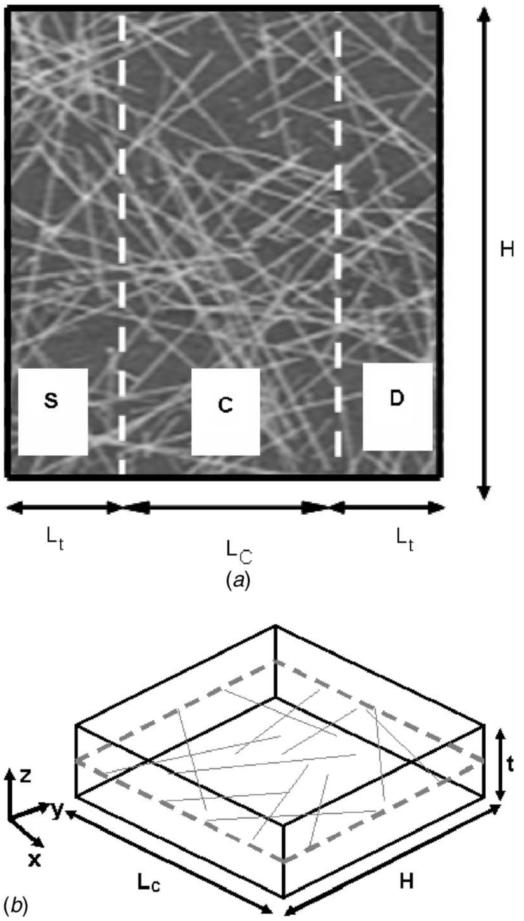

Fig. 1 (*a*) Schematic of thin-film transistor showing source (*S*), drain (*D*), and channel (*C*). The channel region is composed of a network of CNTs; (*b*) geometric parameters.

other hand, the electrical conductivity of carbon nanotubes and silicon nanowires in plastic is entirely network dominated due to the nearly insulating substrate.

Though there is much literature on composite thermal and electrical properties [17–19], as well as on the percolation behavior of tubes and wires [14,16,20], two important features distinguish TFT composites. First, our interest is in *finite* nanocomposites, where the length scale of the composite, i.e., the distance between the transistor's source and drain, may be competitive with the length of the nanotubes in the composite, making standard periodic-domain percolation analyses invalid [15]. Second, the composite is a thin film with a thickness of no more than a few microns at the maximum. There are few experimental results or theoretical and computational models which predict the conductivity of finite two-dimensional (2D) nanotube composites. Nearly all experiments have concentrated on bulk 3D samples. Biercuk et al. reported 125% increase in thermal conductivity of epoxy–single wall nanotube (SWNT) composites for 1 wt % SWNT loading at room temperature [21]. Liu et al. used a silicon elastomer as the matrix and CNT as the filler in their experiments and reported 65% enhancement in thermal conductivity with 3.8 wt % CNT loading [22]. Theoretical analyses of bulk composites have, for the most part, addressed low volume fractions using effective medium theories [19], most recently accounting for interfacial resistance [17,23]. However, these studies assume tube densities well below the percolation threshold. Lusti and Gusev predicted the thermoelastic properties of nanotube-reinforced polymers using the finite element method [24]. Using their numerical model, they explored the enhancement in Young's modulus and the decrease in thermal expansion coefficient for different orientations of CNTs inside the polymer. Yang and Chen used the phonon Boltzmann equation to study the phonon thermal conductivity of Si–Ge composites using a periodic two-dimensional model [18] and found phonon ballistic effects to be important. However, their findings are appropriate only for aligned rods, with the primary direction for transport being *normal* to the rod axis. To our knowledge, there have been no published analyses of either thermal or electrical transport in nanocomposites composed of random nanotube networks.

The objective of the present work is to develop a framework for the simulation of thermal and electrical transport for finite-length two-dimensional network composites and to validate the model with experimental data where possible. Though our ultimate goal is to simulate the concurrent electro-thermal performance of network TFTs, this paper focuses on the determination of lateral composite conductivity. Thermal transport in the Fourier conduction limit and charge transport in the low bias voltage limit are analogous and can be described by similar governing equations. A random two-dimensional network of tubes is generated numerically and embedded in a substrate. A finite volume method is developed for the coupled solution of the network and the substrate and shown to work satisfactorily by comparison to analytical solutions. The method is then applied to the problem of lateral conductivity determination in 2D networks and composites and shown to match experimental data satisfactorily.

Governing Equations

Thermal Transport. The computational domain is shown in Fig. 1, and is of height H and width L_C. It consists of the channel region of the transistor and is composed of a random network of nanotubes or nanowires embedded in the midplane of a substrate represented by a three-dimensional box of size $L_C \times H \times t$. Diffusive transport in the tube or wire is obtained when there are a sufficient number of scattering events during the residence time of the phonon in the domain. The phonon residence time τ_f scales as L_t/v_g, where v_g is the phonon group velocity. The main scattering events of importance at room temperature in pure samples are either three-phonon processes, occurring on a time scale $\tau_{3\text{ph}}$, or boundary scattering events, occurring on a time scale τ_b. For nanowires, $\tau_b \sim d/v_g$, so that $\tau_f/\tau_b \sim L_t/d$; since $L_t/d \gg 1$, diffusive transport due to boundary scattering is expected to prevail. For nanotubes embedded in a substrate, boundary scattering and three-phonon time scales are difficult to estimate and would depend on the nature of the nanotube–substrate interface as well as the modulation of phonon velocities due to the presence of the substrate. However, for sufficiently long tubes, three-phonon processes are expected to lead to diffusive behavior in their own right. For freestanding CNTs, acoustic phonon velocities of 9–20 km/s have been reported in Ref. [25]. Assuming axial thermal conductivities in the 1000 W/mK range, $L/(\tau_{3\text{ph}}v_g) \gg 1$ would be achieved for tubes of about 1 μm or longer; the presence of interface scattering is expected to further reduce this value. Thus, Fourier conduction in both nanotubes and nanowires may be assumed, albeit with a thermal conductivity that may differ significantly from bulk or freestanding values. Assuming one-dimensional diffusive transport along the length s of the tube and three-dimensional conduction in the substrate, the governing energy equations in the tube and substrate may be written, respectively, as

$$k_t A \frac{d^2 T_i}{ds^2} + \sum_{\text{intersecting tubes } j} h_c P_c (T_j - T_i) + h_s P_s (T_s - T_i) = 0 \tag{1a}$$

$$k_s\nabla^2 T_s + \sum_{i=1}^{N_{\text{tubes}}} h_s\alpha_v(T_i - T_s) = 0 \qquad (1b)$$

Here, $T_i(s)$ is the temperature of the ith tube at a location s along its length; A is the area of cross section of the tube or wire; and k_t is the corresponding thermal conductivity. The term h_c is the heat transfer coefficient governing the transfer of heat to other tubes j making contact with tube i through a contact perimeter P_c, and the heat transfer coefficient h_s governs the transfer of heat between the tube and the substrate through a contact perimeter P_s. $T_s(x,y,z)$ is the substrate temperature and k_s is the substrate thermal conductivity; the second term in Eq. (1b) contains the heat exchange with tubes traversing the substrate, which are N_{tubes} in number, through a contact area per unit volume, α_v. Using the dimensionless variable $\theta=(T-T_{\text{drain}})/(T_{\text{source}}-T_{\text{drain}})$ and nondimensionalizing all lengths by the tube diameter d, the dimensionless governing equations in the tubes and substrate may be written as

$$\frac{d^2\theta_i}{ds^{*2}} + \sum_{\text{intersecting tubes } j} Bi_c(\theta_j - \theta_i) + Bi_s(\theta_s - \theta_i) = 0 \qquad (2a)$$

$$\nabla^{*2}\theta_s + \sum_{i=1}^{N_{\text{tubes}}} Bi_s\beta_v\frac{k_t}{k_s}(\theta_i - \theta_s) = 0 \qquad (2b)$$

For thermal conductivity calculations, the thermal boundary conditions for all tubes originating at the source and terminating in the drain are given by

$$\theta_i = 1 \text{ at } s^* = 0; \quad \theta_i = 0 \text{ at } s^* = \frac{L_t}{d} \qquad (3)$$

and the boundary conditions for the substrate are given by

$$\theta_s = 1 \text{ at } x^* = 0; \quad \theta_s = 0 \text{ at } x^* = \frac{L_C}{d}$$

$$\frac{\partial\theta_s}{\partial z^*} = 0 \text{ and at } z^* = 0\text{at } z^* = \frac{t}{d} \qquad (4)$$

All the tube tips terminating inside the substrate are assumed adiabatic. The boundaries $y^*=0$ and $y^*=H/d$ are assumed as periodic boundaries for both substrate and tubes. The dimensionless parameters are defined as

$$Bi_c = \frac{h_c P_c d^2}{k_t A}; \quad Bi_s = \frac{h_s P_s d^2}{k_t A}; \quad \frac{k_s}{k_t}$$

$$\beta_v = \alpha_v\left(\frac{A}{P_s}\right); \quad \frac{L_C}{L_t}; \quad \frac{H}{L_t}; \quad \frac{L_t}{d}; \quad \frac{t}{d}$$

Bi_c represents the dimensionless contact conductance for tube-to-tube contact; and Bi_s represents the dimensionless interfacial (Kapitza) resistance between the tube and substrate [17]. The geometric parameter β_v may be determined from the tube density per unit area ρ; the corresponding dimensionless parameter is ρ^*, which is obtained by normalizing with the percolation threshold ρ_{th}. The percolation threshold for the network is estimated as the density at which the average distance between the nanotubes equals the average length of the tubes, so that $\rho_{\text{th}}=1/\langle L_t\rangle^2$.

Electrical Transport. The dimensionless potential equation in the linear regime is analogous to the thermal transport equation in the Fourier conduction limit, with the potential being analogous to temperature and the current being analogous to the heat transfer rate. For charge transport in CNTs in plastic, the substrate is considered insulating and only transport in the tube network is considered. For organic transistors with dispersed CNTs [13], the substrate is not insulating and charge leaks from the CNTs to the organic matrix, analogous to thermal transport in a composite, and charge exchange with the substrate must be considered. Since $L_C \gg \lambda$, the mean free path of electrons, a drift-diffusion model based on Kirchoff's law for carrier transport may be employed [26]. In this linear regime, which occurs for low source–drain voltage V_{DS}, the current density along the tube is given by

$$J = \sigma\, d\Phi/ds \qquad (5)$$

where σ is the electrical conductivity and Φ is the potential, and is only a function of the source–drain voltage V_{DS}. Using the current continuity equation $dJ/ds=0$ and accounting for charge transfer to intersecting tubes as well as to the substrate [26], the dimensionless potential distribution ϕ_i along tube i, as well the three-dimensional potential field in the substrate are given by:

$$\frac{d^2\phi_i}{ds^{*2}} + \sum_{\text{intersecting tubes } j} c_{ij}(\phi_j - \phi_i) + d_{is}(\phi_s - \phi_i) = 0 \qquad (6a)$$

$$\nabla^{*2}\phi_s + \sum_{i=1}^{N_{\text{tubes}}} d_{is}\beta_v\frac{\sigma_t}{\sigma_s}(\phi_i - \phi_s) = 0 \qquad (6b)$$

Here c_{ij} is the dimensionless charge-transfer coefficient between tubes i and j at their intersection point, analogous to Bi_c in Eq. (2a), and is specified *a priori*; it is nonzero only at the point of intersection. The term d_{is} is analogous to Bi_s term in Eq. (2a) and is active only for nanotubes in organic substrates. The electrical conductivity ratio is σ_t/σ_s. For computing the voltage distribution, boundary conditions $\phi_i=1.0$ and $\phi_i=0$ are applied to tube tips embedded in the source and drain regions, respectively. For the organic substrate, $\phi_s=1.0$ and $\phi_s=0$ are applied at $x^*=0$ and $x^*=L_C/d$, respectively; for the other boundaries, a treatment similar to that for the substrate temperature is applied. This computation of voltage distribution is only valid for low V_{DS}. For higher V_{DS}, the complete drift-diffusion equations for electron (n) and hole (p) transport in the network, coupled to a 3D Poisson equation for the potential, would need to be solved [27] and the direct analogy with thermal transport would no longer be valid.

Numerical Method

Network Generation Procedure. We consider a percolating random network of nanotubes or nanowires of length L_t and diameter d randomly dispersed in the midplane of a substrate of thickness t. Thus the nanotube network is essentially 2D, while the substrate containing it is 3D, as shown in Fig. 1(b); the geometry in the midplane is shown in Fig. 1(a). The boundaries at $y^*=0$ and $y^*=H/d$ are assumed periodic.

The source, drain, and channel regions in Fig. 1 are divided into finite rectangular control volumes. A fixed probability p of a control volume originating a nanotube is chosen a priori. A random number is picked from a uniform distribution and compared with p. If it is less than p, a nanotube is originated from the control volume. The length of source and drain for tube generation is L_t, which ensures that any tube that can penetrate the channel region from either the left or the right is included in the simulations. The orientation of the tube is also chosen from a uniform random number generator. Since the tube length is fixed at L_t, all tubes may not span the channel region even for shorter channel lengths L_C, depending on orientation. Tubes crossing the $y^*=0$ and $y^*=H/d$ boundaries are treated assuming translational periodicity; that part of the tube crossing one of these boundaries reappears on the other side. Tube–tube intersections are computed from this numerically generated random network and stored for future use. The analysis is conducted only on the tubes that lie in the channel region.

Finite Volume Discretization. We now describe the finite volume discretization procedure [28] used to obtain the temperature distribution in the tubes and the substrate. A similar procedure is adopted for solving the potential equation (Eq. (6)). Each tube is

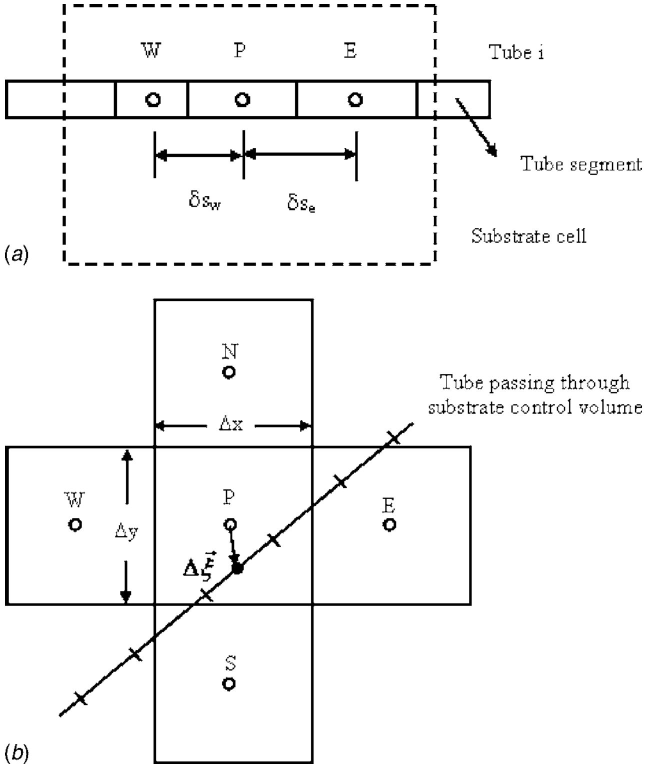

Fig. 2 **(*a*) Tube segment nomenclature, and (*b*) substrate control volume nomenclature. The displacement vector $\Delta\vec{\xi}$ from substrate cell centroid to tube segment centroid is shown.**

divided into 1D segments, as shown in Fig. 2(*a*) and a control volume balance is performed on each tube segment. Using second-order accurate linear profile assumptions, this yields the following equation for the tube segment *i*

$$k_t A\frac{T_{E,i}-T_{P,i}}{\delta s_e} - k_t A\frac{T_{P,i}-T_{W,i}}{\delta s_w} + \sum_{\text{intersecting tubes } j} h_c A_c (T_{P,j}-T_{P,i}) + h_s A_s (T_s' - T_{P,i}) = 0 \qquad (7)$$

Here, δs_e and δs_w are the distances shown in Fig. 2(*a*); A_c is the contact area between tubes *i* and *j*; $T_{P,i}$ is the temperature at the control volume *P* for tube *i*; and $T_{P,j}$ is the temperature of intersecting tube *j* at the same location. Similar conservation equations are written for all the tubes in the domain. Energy lost by tube *i* to tube *j* is gained by tube *j* and vice versa, guaranteeing perfect energy conservation. A_s is the surface area of contact between the tube segment and the substrate, and T_s' is the temperature of the substrate at the location of the cell centroid of tube segment *P*.

The substrate is discretized into rectangular control volumes of extent $\Delta x\Delta y\Delta z$. Figure 2(*b*) shows the geometry in 2D for clarity. Writing a control volume balance over each substrate control volume and discretizing using linear profile assumptions, we obtain

$$\sum_{f=1}^{6} k_s A_f \frac{T_{\text{nb},s}-T_{P,s}}{\Delta x_f} - \sum_{\text{segments}} h_s A'_{si}(T'_s - T_{P,i}) = 0 \qquad (8)$$

Here, $T_{P,s}$ is the substrate temperature at the centroid of the substrate cell *P*; *f* refers to the six faces of cell *P*; and A_f to the corresponding face areas. The length Δx_f is distance between the two cell centroids on either side of the face *f* (between *P* and *E*, for example) and $T_{\text{nb},s}$ is the substrate temperature at the neighbor cell centroid (*E* or *W*, for example). The summation term represents the heat exchange with all tube segments intersecting the substrate control volume, and A'_{si} is that portion of the tube segment surface area that is ascribed to substrate cell *P*. In this way, energy lost by the tube is gained by the substrate and vice versa, and perfect conservation is guaranteed.

Since the substrate discretization is coarser than the tube discretization, it is important to account for gradients in the substrate temperature in determining the term T_s' in the tube–substrate heat exchange in Eqs. (7) and (8). Otherwise, significant errors were found in the calculation, including an inability to reproduce linear temperature profiles exactly in 1D conduction problems with identical tube and substrate thermal conductivities. Therefore, the substrate temperature gradient in the plane of the nanotube network is computed and is used to interpolate the substrate temperature to the tube centroid location

$$T_s' = \nabla T_{P,s}\cdot \Delta\vec{\xi} + T_{P,s} \qquad (9)$$

Here $\Delta\vec{\xi}$ is the position vector of tube segment centroid relative to the cell centroid of the substrate, as shown in Fig. 2(*b*). The substrate temperature gradient in cell *P*, $\nabla T_{P,s}$, is computed using second-order central difference operators.

Equations (7) and (8) constitute a coupled equation set for the tube segment temperatures T_i and the substrate temperatures T_s at the substrate cell centroids. Though these equations may be solved for each tube and the substrate sequentially and iteratively [28], such a loosely coupled procedure fails when the coupling terms Bi_c and Bi_s become large. Similar problems occur for long channel lengths and high tube densities; here the equations become strongly coupled to each other due to a large number of tube–tube contacts and a large tube-substrate contact area. Consequently, a direct sparse solver developed by Kundert [29] is used to solve the resulting system of equations. To account for randomness in the sample, most of the results reported here are computed by taking an average over 100 random realizations of the network. More realizations are used for low densities and short channel lengths where statistical invariance is more difficult to obtain due to the small number of tubes in the domain.

Computation of Effective Lateral Thermal Conductivity. The lateral thermal conductivity of the composite is computed using the expression

$$k_{\text{eff}} = \frac{\displaystyle\sum_{\text{tubes}} k_t A \left.\frac{dT_i}{ds}\right|_{x=0} + \sum_{\text{substrate}} k_s \Delta y \Delta z \left.\frac{dT_s}{dx}\right|_{x=0}}{Ht\left(\dfrac{T_{\text{drain}}-T_{\text{source}}}{L_C}\right)} \qquad (10)$$

where the first term in the numerator is the heat flow through the tubes in the lateral direction, while the second term represents the lateral heat flow in the substrate. The heat flow in both tubes and substrate is computed at the source–channel junction, $x=0$.

Results

In this section, we apply the method described in previous sections to five problems. The first two problems compare numerical results with analytical solutions. The last three problems address lateral conductivity calculations in finite-length nanotube networks and composites both above and below the percolation threshold.

Comparison With Analytical Solution. For the simple case of a CNT composite in which a single CNT is located along the axis of a cylindrically shaped substrate, the temperature distribution in both CNT and substrate can be obtained analytically in the presence of the heat source term inside the CNT. The two ends of the CNT as well as the two planar ends of the substrate cylinder are held at a temperature T_{inf}; the outer cylindrical surface of the substrate is insulated; and q''' is the average power dissipated per unit volume in the CNT (see inset in Fig. 3). An extra term for Joule heating is added in the Fourier conduction equation for the

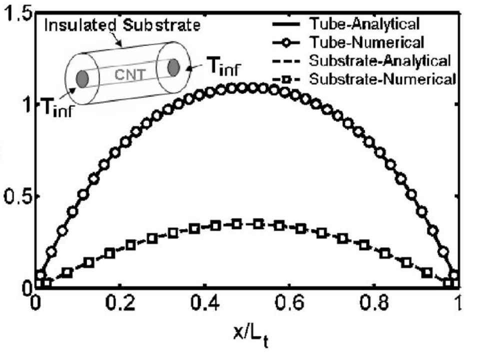

Fig. 3 Comparison of numerically computed dimensionless temperature distribution in tube and substrate with analytical results (*θ* definition corresponds to that in Eq. (11)). The schematic of the tube embedded in the substrate and the boundary conditions are shown in the inset.

tube [Eq. (2*a*)]. The temperature distribution inside the tube, T_t, and the substrate, T_s, can be obtained analytically as

$$\theta_t = (T_t - T_{\text{inf}})/(q''' L_t^2/k_t) = ae^{\sqrt{c}x} + be^{-\sqrt{c}x} + d(x - x^2) + g \tag{11a}$$

$$\theta_s = (T_s - T_{\text{inf}})/(q''' L_t^2/k_t) = [0.5(x - x^2) - \theta_t]/m \tag{11b}$$

where

$$a = \frac{g(e^{-\sqrt{c}} - 1)}{(e^{\sqrt{c}} - e^{-\sqrt{c}})}; \quad b = \frac{g(1 - e^{\sqrt{c}})}{(e^{\sqrt{c}} - e^{-\sqrt{c}})}; \quad d = \frac{f}{c}; \quad g = \frac{1 - 2f/c}{c}$$

$$f = \frac{h_s L_t}{2k_t m}; \quad c = \frac{h_s L_t(1 + m)}{k_t m}; \quad m = \frac{k_s}{k_t}$$

The model developed here is used to compute the temperature distribution inside the tube and the substrate and compared against the analytical results. Figure 3 shows a comparison of the computed tube and substrate temperatures for a mesh of 80 tube segments and 20 substrate cells. The numerical results are in excellent agreement with analytical results.

Transport In the Limit of Zero Contact. In the limit when there is no contact between tubes ($Bi_c=0$, $c_{ij}=0$) and between tube and substrate ($Bi_s=0$, $d_{is}=0$) a simple analytical solution for the heat transfer rate through the domain (and correspondingly the drain current I_D for electron transport) may be derived. Only the tubes are considered in this 2D planar calculation, and the substrate contribution is neglected. In this limit, the in-plane heat transfer rate through the composite, q, is directly proportional to the number of bridging tubes N_S (tubes directly bridging source and drain) but inversely proportional to the tube length contained in the channel. By computing the number of bridging tubes from geometric considerations, it may be shown that [26]

$$q \propto I_D \propto \frac{N_S}{W} = \left(\frac{2}{\pi}\right)\rho H L_t \left[\cos^{-1}\left(\frac{L_C}{L_t}\right) - \left(\frac{L_C}{L_t}\right)\sqrt{1 - \left(\frac{L_C}{L_t}\right)^2}\right] \tag{12}$$

where W is

$$\left(\sum_{i=1}^{N_S} \frac{1}{L_i}\right)^{-1}$$

The constant of proportionality in Eq. (12) depends on the conductivity of the tubes. Figure 4 shows a comparison of the analytical result obtained using Eq. (12) with that computed numerically. The ratio q/q_{ref} is plotted, where q_{ref} is the reference heat transfer rate at $L_C/L_t=0.1$. One hundred random realizations of the network for the case $L_C=3$ μm, $H=4$ μm, and $\rho=5.0$ μm^{-2} are used. The analytical and numerical results are in good agreement with each other, confirming the validity of our approach. When the channel length becomes comparable to or longer than the tube length, q/q_{ref} is seen to go to zero; in the absence of tube–tube and tube–substrate contact, heat, or current can flow through the tubes only if the tubes bridge source and drain. As a practical matter, the result in Fig. 4 is applicable to electrical transport in short-channel CNT/plastic TFTs where the short-channel lengths imply few tube–tube interactions.

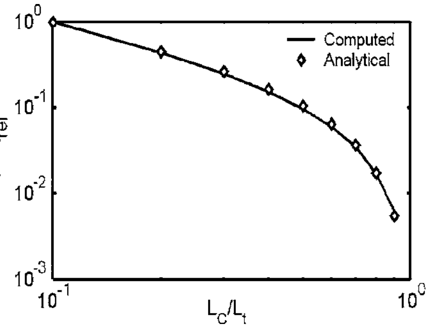

Fig. 4 Comparison of heat transfer rate in a nanotube network with analytical results for the case of zero tube–tube contact

Network Conductance Exponent Calculation. Thin film lateral thermal conductivity measurements are generally difficult to perform. Here we compare the network conductance predicted using our model with electrical conductance measurements by Snow et al. [11]. A pure planar tube network is considered, assuming that the substrate is entirely nonconducting. This is typical of electrical transport in CNT/plastic composites. The average length of the tubes in Ref. [11] ranges from 1 to 3 μm. The exact length distribution of nanotubes has not been reported in Ref. [11]. For the numerical model, random networks with a tube length of 2 μm are generated, and an average of over 200 random realizations is taken. The percolation threshold for the network is estimated using $\rho_{\text{th}}=1/\langle L_t\rangle^2$ to be 0.25 μm^{-2}. Simulations are performed for densities in the range $1-10$ μm^{-2} for channel lengths varying from 1 to 25 μm^{-2}, and with a width H of 90 μm, corresponding to the dimensionless parameters $L_C/L_t \sim 0.5-12.5$ and $H/L_t=45$. The device dimensions and tube lengths are chosen to match those in Ref. [11].

In Fig. 5(*a*), the normalized network conductance G/G_0 is shown as a function of L_C/L_t for several tube densities above the percolation threshold for nearly perfect tube–tube contact (i.e., $c_{ij}=50$). For long channels ($L_C>L_t$) there are no tubes directly bridging the source and drain, and current (heat) can flow only because of the presence of the network. If the tube density is greater than the percolation threshold, a continuous path for carrier transport exists from source to drain, and G is seen to be nonzero even for $L_C/L_t>1$. Figure 5(*a*) shows that the conductance exponent, n, is close to -1.0 for the high densities ($\rho=10$ μm^{-2}; $\rho^*=40$), indicating ohmic conduction, in good agreement with Ref. [11]. The exponent increases to -1.80 at lower densities (1.35 μm^{-2}; $\rho^*=5$), indicating a nonlinear dependence of conductance on channel length. The asymptotic limit of the conductance exponent for infinite samples with perfect tube/tube contact has been found to be -1.97 in Refs. [30,31]. The observed nonlinear behavior for low density is expected because the density value is close to the percolation threshold. Snow et al. reported a conductance-exponent of -1.80 for a density of 1.0 μm^{-2} and channel length >5 μm. For the same device dimensions, this value of the exponent is close to that obtained from our simulations for a density of 1.35 μm^{-2}. At densities close to the percolation threshold, computations are very sensitive to variations in

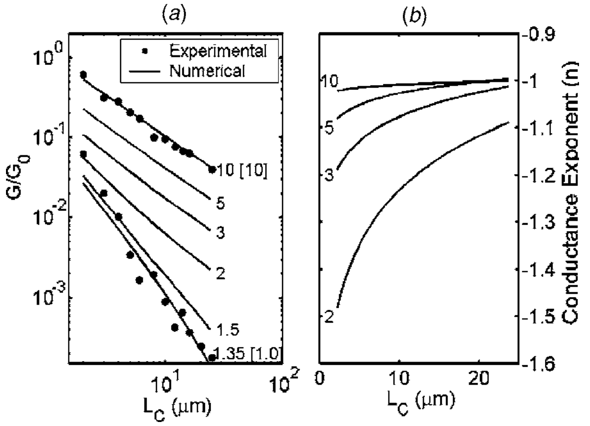

Fig. 5 **(*a*) Computed conductance dependence on channel length for different densities (ρ) in the strong coupling limit (c_{ij}=50) compared with experimental results from Ref. [11]. For ρ=10.0 μm^{-2}, G_o=1.0 (simulation), and G_o=1.0 (experiment). For ρ=1.35 μm^{-2}, G_o=1.0 (simulation) and G_o=2.50 (experiment). The number after each curve corresponds to the value of ρ used in the simulation. The number in [] corresponds to ρ in experiments from Ref. [11]; (*b*) dependence of conductance exponent (*n*) on channel length for different densities (ρ) based on (*a*).**

computational parameters. Small variations in experimental parameters such as tube diameter, nanotube contact strength, tube electronic properties, as well as the presence of a distribution of tube lengths (1–3 μm), which is not included in the simulation, may explain the difference. The contact resistance between the nanotubes and the source and drain electrodes as well as insufficiently large samples for ensemble averaging in the experimental setup may also be responsible. Some evidence of this is visible in the scatter in the experimental data at low densities.

The dependence of conductance exponent on channel length is explored in Fig. 5(*b*) for c_{ij}=50 and for densities in the range of 2.0–10 μm^{-2}, corresponding to ρ^* values of 8–40. For densities >3.0 μm^{-2} (ρ^*>12), the exponent approaches the ohmic limit, −1.0, with increasing channel length. Larger exponents, corresponding to nonohmic transport are observed for the shorter channel lengths. This is consistent with experimental observations, where conductance is seen to scale more rapidly with channel length for small L_C [11].

Effective Thermal Conductivity of Nanotube Composites. In this problem, we compute the effective lateral thermal conductivity of a nanotube or nanowire composite. These composites may span a wide range of values of k_s/k_t, Bi_c, and Bi_s. The thermal conductivity of free-standing multiwalled CNTs has been measured at 3000–6000 W/m K [32], though the corresponding values when embedded in a composite are expected to be far smaller due to interface scattering. Though bulk silicon has a thermal conductivity of approximately 150 W/m K at room temperature, the thermal conductivity of Si nanowires in the 22–115-nm-diameter range is one to two orders of magnitude smaller due to phonon boundary scattering and confinement effects [33]. The thermal conductivity of the substrate is generally low, ranging from 0.1 to 1.0 W/m K, leading to a wide range in k_s/k_t. For the present case, we consider values in the 10^{-1}–10^{-3} range. The values of the tube–tube contact conductance Bi_c and the tube–substrate contact conductance Bi_s are not known. However, our calculations show that Bi_c>5 is tantamount to perfect tube–tube contact. For Bi_s, an estimate of the total thermal resistance between silicon nanowires and a planar interface has been found in Ref. [34] by combining the constriction resistance, gap resistance, and thermal interfacial resistance; however, the model requires the interfacial phonon transmissivity, which must be obtained through experiments or atomistic level simulations. Recent experiments [35] indicate that for CNTs in organic liquids, contact conductance may be extremely low. Yu et al. measured the thermal contact resistance between a carbon fiber and a planar substrate [36]; however, no experimental data are presently available for CNTs or Si NWs embedded in plastic substrates. For the purposes of this simulation, a value of $Bi_s=10^{-5}$ is chosen, consistent with interface resistance values cited in Ref. [35].

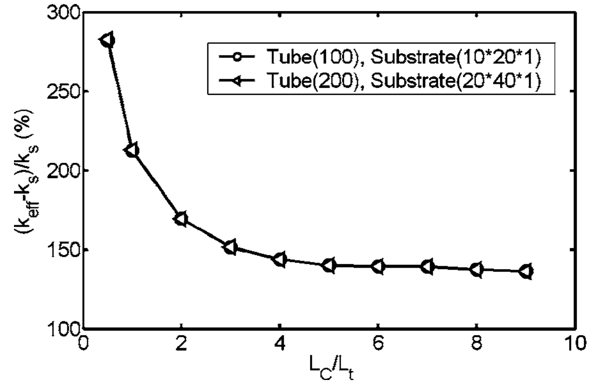

Fig. 6 **Increase in composite effective thermal conductivity (k_{eff}) over the substrate value for two different grid sizes: L_C/L_t=2.0; H/L_t= 2, Bi_c=10.0, $Bi_s=10^{-5}$, k_s/k_t= 0.001, and ρ^* =10.0**

Grid independence tests were conducted for the case of L_C/L_t =2.0, H/L_t=2, Bi_c=10.0, $Bi_s=10^{-5}$, k_s/k_t=0.001, and ρ^*=10.0, corresponding to L_C=4 μm, H=4 μm, and ρ=2.5 μm^{-2} for nondimensional channel length L_C/L_t varying from 0.5 to 9 (L_C =1–18 μm). Figure 6 shows the percentage change in the composite thermal conductivity over the substrate value for two different grid sizes. For the first case there are 100 segments per unit tube length, and mesh of 10×20×1 cells is used in the substrate in the *x*, *y*, and *z* directions, respectively. The second case corresponds to 200 segments per tube, with a mesh of 20×40×1 cells in the substrate. The results are seen to differ by less than 0.5% between the two cases. The simulations presented in this problem were therefore performed using a mesh of size 100 segments per tube and a mesh of 10×20×1 cells in the substrate. An average over 200 random realizations is used.

A typical temperature distribution in the tube network and the substrate is shown in Figs. 7(*a*) and 7(*b*). For this case, L_C/L_t =2.0, H/L_t=2, Bi_c=10.0, $Bi_s=10^{-5}$, k_s/k_t=0.001, and ρ^*=14.0, corresponding to L_C=4 μm, L_t=2 μm, H=4 μm, and ρ =3.5 μm^{-2}. Contours of constant temperature in the substrate would be one dimensional in *x* for Bi_s=0, but due to the interaction with the tubes, distortion in the contours is observed, consistent with the temperature plots in the tube in Fig. 7(*b*). The departure from one dimensionality in the substrate temperature profile is related to local variations in tube density; regions of high tube density convey the boundary temperature further into the interior.

The effect of thermal conductivity ratio is explored by varying k_s/k_t from 10^{-1} to 10^{-3} keeping other parameters constant at L_C/L_t=0.25–7.0, H/L_t=2, Bi_s=10.0, $Bi_s=10^{-5}$, and ρ^*=10.0 (L_C=0.5–14 μm, H=4 μm, ρ=2.5 μm^{-2}). The lower limit would correspond approximately to Si NWs in plastic, accounting for reduced thermal conductivity due to scattering and confinement; the upper limit would correspond approximately to CNTs in plastic. The percentage increase in composite thermal conductivity over that of the substrate is presented in Fig. 8. In general, bulk behavior, whereby the effective thermal conductivity becomes invariant with domain size, is obtained for L_C/L_t>5 or so. Below this, the composite displays finite length effects and is dominated by source–drain bridging for L_C/L_t<1. In general, for bulk

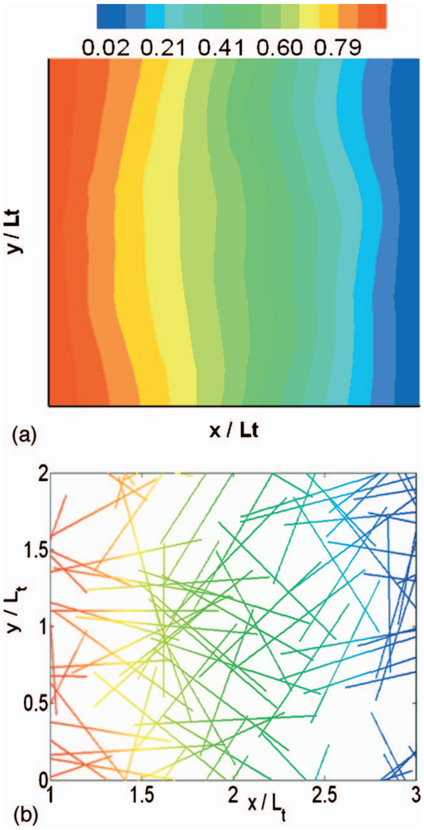

Fig. 7 Nondimensional temperature distribution in (*a*) substrate (*b*) tube network: L_C/L_t=2.0, H/L_t=2, Bi_c=10.0, Bi_s=10^{-5}, k_s/k_t=0.001, and ρ^*=14.0

samples, the effective thermal conductivity of the composite may be as much as 125% above k_s for $k_s/k_t=10^{-3}$. However, this only implies a value of k_{eff} in the 0.25–2.5 W/m K, which is still very low, signaling incipient thermal problems in nanocomposite TFTs. As k_s/k_t is increased, some evidence of finite-length effects may still be detected for $k_s/k_t < 5\times10^{-3}$. For higher values, though, network conductance ceases to be a dominant contributor and the increase in k_{eff} over k_s drops to zero, signifying that the substrate now dominates conduction through the composite. These computations point to the necessity of accurately characterizing the thermal conductivity of CNTs and Si NWs embedded in substrates. If the presence of the substrate substantially reduces k_t, it is possible that k_s/k_t would be relatively high and the network would no longer provide a significant pathway for heat transfer even if effective tube–tube contact could be maintained. In this limit, in the presence of self-heating, the large surface area of contact between the tubes and the substrate would allow heat to leak from the network to the substrate, and the primary mechanism for heat removal would be the substrate. However, since both substrate and network conductance would be low in this limit, high channel temperatures and degradation of electrical performance may be expected.

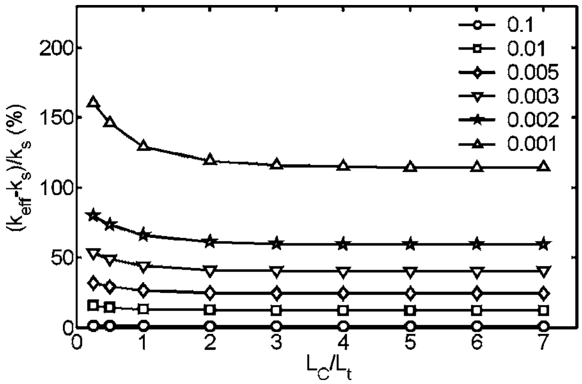

Fig. 8 Effect of substrate–tube conductivity ratio on k_{eff} for varying channel length: L_C/L_t=0.25–7.0, Bi_c=10.0, Bi_s=10^{-5}, and ρ^*=10.0

Electrical Conductivity of CNT-Organic Composites. The focus of this problem is the prediction of the effective electrical conductivity of CNT–organic composites. Recently, a 60-fold increase in mobility in organic TFTs has been obtained by dispersing high-conducting CNTs in an organic substrate [13]. The carriers flowing from source to drain take advantage of the highly conducting CNT pathways within the semi-conducting organic substrate, flowing partially within the semiconductor and partially through the CNTs. The potential drop across the CNTs is nearly negligible compared to that in the organic substrate, resulting in an overall reduction in the potential drop in the channel for a given drive current. This is equivalent to an effective channel length reduction, or an effective increase in the mobility or electrical conductivity.

The electrical performance of the organic TFT is characterized by the relationship between the drain current I_D and the gate voltage V_G for a given source–drain voltage V_{DS}. The I_D-V_G characteristics of organic TFTs for different volume percent of CNTs has been reported in Ref. [13]. Approximately a third of the CNTs are reported to be metallic, while the rest are semiconducting [13]. Each type has a different electrical conductivity and this heterogeneity must be accounted for in the network model. To reproduce the I_D-V_G curves for this type of device, it is necessary to solve the complete drift-diffusion equations for electrons and holes, in addition to Eq. (6). However, in the linear regime (low V_{DS}) and with $V_G=0$, electrical transport in the organic–CNT composite can be analyzed using Eq. (6). For zero gate voltage, the electrical conductivity of the organic–CNT composite is directly proportional to the current flowing through the TFT. Thus the data in Ref. [13] for $V_G=0$ and low V_{DS} may be used to deduce the effective conductivity of the composite and provide an experimental benchmark against which to test our model.

In order to conduct the computation, it is necessary to determine the density ρ of tubes in the matrix. The CNT fraction in the organic substrate has been reported in terms of volume percent in Ref. [13], while the present model uses a 2D area density ρ to characterize the fraction of CNTs in the substrate. The conversion between the two different representations of the CNT fraction is performed in the following way. It has been reported in Ref. [13] that transistors get shorted at 1% volume fraction of CNT or greater implying that metallic CNTs begin to percolate at this volume fraction. From Ref. [14], the percolation threshold for the CNT network is given by $\rho_{\text{th}}=4.236^2/\pi L_S^2=5.7\ \mu\text{m}^{-2}$ using an average tube length of 1 μm [13]. Accounting for the fact that one-third of the CNTs are metallic, the total density ρ of the CNTs at 1% volume fraction may be computed as $\rho=3\times5.7=17.1\ \mu\text{m}^{-2}$. Using this conversion, the volume fraction data in Ref. [13] may be converted into the area density ρ needed for our computation.

Device dimensions reported in Ref. [13] are used in the simulation, and correspond to $L_C/L_t=20.0$, $H/L_t=4$, $c_{ij}=10^{-4}$, and $d_{is}=10^{-4}$. The electrical conductivity ratio, σ_t/σ_s, for metallic CNTs is taken as 5.0×10^6, while that for semiconducting CNTs is 5.0×10^4 [37]. The density ρ is varied in the range 1–17 μm^{-2}, below the percolation threshold. The computed electrical conductivity is presented as a function of dimensionless density ρ^* in Fig. 9. The error bars represent the variability in the prediction for all the realizations computed. The effective electrical conductivity σ_{eff} for both experiments [13] and computations is normalized by

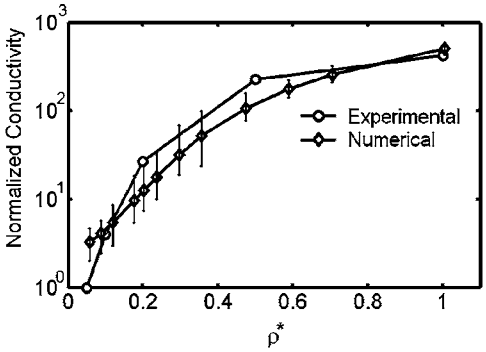

Fig. 9 Comparison of computed conductivity (normalized by the conductivity at $\rho^*=0.05$) of organic transistor against the experimental conductivity [13]

the experimental σ_{eff} at 0.05% volume fraction ($\rho^*=0.05$). Numerical results are found to be in good agreement with the experimental observations over the range of tube densities considered.

Conclusions

In this paper, a computational model for thermal and electrical transport in nanotube composites has been developed and applied to the determination of lateral electrical and thermal conductivity of finite thin films. The model has been verified against analytical solutions, and validated against experimental data for tube densities above and below the percolation threshold, both for nanotube networks in the absence of a substrate, as well as for nanotube–plastic and nanotube–organic composites. Reasonable matches with experimental data have established the general validity of the model.

Nevertheless, a number of important issues remain to be addressed. The model employs thermal contact parameters Bi_c, Bi_s, and electrical contact parameters c_{ij} and d_{is}, which are at present unknown. These must be determined either from careful experiments or from atomistic simulations of tube–tube and tube–substrate contact. Furthermore, while the thermal conductivities of individual freestanding nanotubes and nanowires has been measured and modeled, the modification of these values for tubes and wires encased in plastic or organic substrates is not well understood. Ultimately, our interest is not only in the simulation of conductivity but also in the coupled electro-thermal analysis and design of flexible large-area electronics. Research in these directions is underway and results will be reported in due course.

Acknowledgment

Support of J. Murthy and S. Kumar under NSF Grant Nos. CTS-0312420, CTS-0219098, EE-0228390, the Purdue Research Foundation, and Purdue's Network for Computational Nanotechnology (NCN), is gratefully acknowledged.

Nomenclature

A = tube cross-sectional area, m^2
A_c = contact area between tubes, m^2
A_s = contact area between tube and substrate, m^2
Bi_c = contact conductance parameter between tubes
Bi_s = contact conductance parameter between tube and substrate
c_{ij} = dimensionless charge-transfer coefficient between tubes
d = diameter of tube, m
d_{is} = dimensionless contact parameter for charge transfer between tube and substrate
G = conductance, Ω^{-1}
h_c = heat transfer coefficient characterizing tube–tube contact, W/m^2 K
h_s = heat transfer coefficient characterizing tube–substrate contact, W/m^2 K
H = height of the channel, m
I_D = drain current, A/m^2
k_{eff} = effective lateral thermal conductivity, W/m K
k_t = thermal conductivity of tube, W/m K
k_s = thermal conductivity of substrate, W/m K
L_C = channel length, m
L_t = tube length, m
m = substrate–tube conductivity ratio
n = electron concentration, m^{-3}
P_c = contact perimeter for tube–tube contact, m
P_s = contact perimeter for tube–substrate contact, m
s = length along tube, m
t = substrate thickness, m
T = temperature, K
T_i = temperature of ith tube, K
T_s = substrate temperature, K
T_{drain} = drain temperature, K
T_{source} = source temperature, K
v_g = phonon group velocity, m/s
V_G = gate voltage, V
V_{DS} = drain–source voltage, V

Greek Symbols

θ = nondimensional temperature
ϕ_i = dimensionless potential distribution along tube
ϕ_s = dimensionless potential distribution in substrate
$\Delta\vec{\xi}$ = displacement vector from tube segment centroid to substrate cell centroid
σ = electrical conductivity, S/m
ρ = tube density, m^{-3}
ρ_{th} = tube density at percolation threshold, m^{-2}
ρ^* = dimensionless tube density ρ/ρ_{th}
β_v = parameter characterizing contact geometry between substrate and tube
λ = mean free path, m
τ_r = phonon residence time in the tube, s
τ_b = time scale for phonon boundary scattering, s
$\tau_{3\text{ph}}$ = time scale for three-phonon scattering processes, s

Subscripts

c = tube–tube contact
s = substrate
t = tube
th = threshold

Superscript

$*$ = nondimensional

References

[1] Kagan, C. R., and Andry, P., 2003, *Thin Film Transistors*, Marcel–Dekker, New York.
[2] Madelung, O., ed., 2000, *Technology and Applications of Amorphous Silicon*, Springer, Berlin.
[3] Dimitrakopoulos, C., and Mascaro, D., 2001, "Organic Thin-film Transistors: A Review of Recent Advances," IBM J. Res. Dev., **45**, pp. 11–27.
[4] Curioni, A., and Andreoni, W., 2001, "Computer Simulations for Organic Light-Emitting Diodes," IBM J. Res. Dev., **45**, pp. 101–113.
[5] Wisnieff, R., 1998, "Printing Screens," Nature (London), **394**, pp. 225.
[6] Pope, M., and Swenberg, C. E., 1999, *Electronic Processes in Organic Crystals and Polymers*, 2nd ed., Oxford University Press, New York, pp. 337–340.
[7] Peumans, P., 2003, "Small Molecular Weight Organic Thin-Film Photodetectors and Solar Cells," J. Appl. Phys., **93**, pp. 3693–3723.
[8] Tamura, T., Ogata, K., Takahashi, M., Suzuki, K., Yamaguchi, H., and Todoroki, S., 2000, "Crystal Growth of Laser Annealed Polycrystalline Silicon as a Function of Hydrogen Content of Precursors," Mater. Res. Soc. Symp. Proc., **621**, pp. Q9.5.1-Q9.5.6.
[9] Ucjikoga, S., 2002, "Low-Temperature Polycrystalline Silicon Thin-Film Tran-

sistor Technologies for System-on-Glass Displays," MRS Bull., **27**, pp. 881–886.

[10] Duan, X., Niu, C., Sahi, V., Chen, J., Parce, J. W., Empedocles, S., and Goldman, J. L., 2003, "High-Performance Thin-Film Transistors Using Semiconductor Nanowires and Nanoribbons," Nature (London), **425**, pp. 274–278.

[11] Snow, E. S., Novak, J. P., Campbell, P. M., and Park, D., 2003, "Random Networks of Carbon Nanotubes as an Electronic Material," Appl. Phys. Lett., **82**(13), pp. 2145–2147.

[12] Menard, E., Lee, K. J., Khang, D. Y., Nuzzo, R. G., and Rogers, J. A., 2004, "A Printable Form of Silicone for High-Performance Thin-Film Transistors on Plastic Substrates," Appl. Phys. Lett., **84**(26), pp. 5398–5400.

[13] Bo, X. Z., Lee, C. Y., Strano, M. S., Goldfinger, M., Nuckolls, C., and Blanchet, G. B., 2005, "Carbon Nanotubes-Semiconductor Networks for Organic Electronics: The Pickup Stick Transistor," Appl. Phys. Lett., **86**, p. 182102.

[14] Hu, L., Hecht, D. S., and Gruner, G., 2004, "Percolation in Conducting and Transparent Carbon Nanotube Networks," Nano Lett., **4**(12), pp. 2513–2517.

[15] Stauffer, D., and Aharony, A., 1992, *Introduction to Percolation Theory*, 2nd ed., Taylor and Francis, Philadelphia, PA.

[16] Shenogina, N., Shenogin, S., Xue, L., and Keblinski, P., 2005, "On the Lack of Thermal Percolation in Carbon Nanotube Composites," Appl. Phys. Lett., **87**, p. 133106.

[17] Nan, C. W., Liu, G., Lin, Y., and Li, M., 2004, "Interface Effect on Thermal Conductivity of Carbon Nanotube Composites," Appl. Phys. Lett., **85**(16), pp. 3549–3551.

[18] Yang, R., and Chen, G., 2004, "Thermal Conductivity Modeling of Periodic Two-Dimensional Nanocomposites," Phys. Rev. B, **69**, p. 195316.

[19] Milton, G. W., 2002, *The Theory of Composites*, Cambridge University Press, New York.

[20] Foygel, M., Morris, R. D., Anez, D., Frencs, S., and Sobolev, V. L., 2005, "Theoretical and Computational Studies of Carbon Nanotube Composites and Suspensions: Electrical and Thermal Conductivity," Phys. Rev. B, **71**(10), p. 104201.

[21] Bieurck, M. J., Liaguno, M. C., Radosavljevic, M., Hyun, J. K., and Johnson, A. T., 2002, "Carbon Nanotubes for Thermal Management," Appl. Phys. Lett., **80**(15), pp. 2767–2770.

[22] Liu, C. H., Hunag, H., Wu, Y., and Fan, S. S., 2004, "Thermal Conductivity Improvement of Silicone Elastomer With Carbon Nanotube Loading," Appl. Phys. Lett., **84**(21), pp. 4248–4250.

[23] Hasselman, D. P. H., and Johnson, L. F., 1987, "Effective Thermal Conductivity of Composites With Interfacial Barrier Resistance," J. Compos. Mater., **21**, pp. 508–515.

[24] Lusti, H. R., and Gusev, A. A., 2004, "Finite Element Predictions for the Thermoelastic Properties of Nanotube Reinforced Polymers," Modell. Simul. Mater. Sci. Eng., **12**, pp. 107–119.

[25] Dresselhaus, M. S., and Eklund, P. C., 2000, "Phonons in Carbon Nanotubes," Adv. Phys., **49**(6), pp. 705–814.

[26] Kumar, S., Murthy, J. Y., and Alam, M. A., 2005, "Percolating Conduction in Finite Nanotube Networks," Phys. Rev. Lett., **95**, p. 066802.

[27] Pierret, R. F., 1996, *Semiconductor Device Fundamentals*, Addison–Wesley, New York.

[28] Patankar, S. V., 1980, *Numerical Heat Transfer and Fluid Flow*, Hemisphere, New York.

[29] Kundert, K. S., 1988, *Sparse User's Guide*, University of California Press, Berkeley, CA.

[30] Lobb, C. J., and Frank, D. J., 1984, "Percolative Conduction and the Alexander-Orbach Conjecture in Two Dimensions," Phys. Rev. B, **30**(7), pp. 4090–4092.

[31] Frank, D. J., and Lobb, C. J., 1988, "Highly Efficient Algorithm for Percolative Transport Studies in Two Dimensions," Phys. Rev. B, **37**(1), pp. 302–306.

[32] Kim, P., Shi, L., Majumdar, A., and McEuen, P. L., 2001, "Thermal Transport Measurements of Individual Multiwalled Nanotubes," Phys. Rev. Lett., **87**(21), p. 215502.

[33] Li, D., Wu, Y., Kim, P., Shi, L., Yang, P., and Majumdar, A., 2003, "Thermal Conductivity of Individual Silicon Nanowires," Appl. Phys. Lett., **83**(14), pp. 2934–2936.

[34] Prasher, R., 2005, "Predicting the Thermal Resistance of Nanosized Constrictions," Nano Lett., **5**(11), pp. 2155–2159.

[35] Huxtable, S. T., Cahill, D. G., Shenogin, S., Xue, L., Oziski, R., Barone, P., Usrey, M., Strano, M. S., Siddons, G., Shim, M., and Keblinski, P., 2003, "Interfacial Heat Flow in Carbon Nanotube Suspensions," Nat. Mater., **2**, pp. 731–734.

[36] Yu, C., Saha, S., Zhou, J., Shi, L., Cassell, A. M., Cruden, B. A., Ngo, Q., and Li, J., 2006, "Thermal Contact Resistance and Thermal Conductivity of a Carbon Nanofiber," J. Heat Transfer, **128**, pp. 234–239.

[37] Seidel, R. V., Graham, A. P., Rajasekharan, B., Unger, E., Liebau, M., Duesberg, G. S., Kreupl, F., and Hoenlein, W., 2004 "Bias Dependence and Electrical Breakdown of Small Diameter Single-Walled Carbon Nanotubes," J. Appl. Phys., **96**(11), pp. 6694–6699.

P. Rath
Department of Mechanical Engineering,
National Institute of Technology,
Rourkela, India 769008

J. C. Chai[1]
ASME Fellow
e-mail: mckchai@ntu.edu.sg

Y. C. Lam

V. M. Murukeshan

School of Mechanical and Aerospace Engineering,
Nanyang Technological University,
50 Nanyang Avenue,
Singapore 639798, Singapore

H. Zheng
Singapore Institute of Manufacturing Technology,
Singapore 638075, Singapore

A Total Concentration Fixed-Grid Method for Two-Dimensional Wet Chemical Etching

A total concentration fixed-grid method is presented in this paper to model the two-dimensional wet chemical etching. Two limiting cases are discussed, namely—the diffusion-controlled etching and the reaction-controlled etching. A total concentration, which is the sum of the unreacted and the reacted etchant concentrations, is defined. Using this newly defined total concentration, the governing equation also contains the interface condition. A new update procedure for the reacted concentration is formulated. For demonstration, the finite-volume method is used to solve the governing equation with prescribed initial and boundary conditions. The effects of reaction rate at the etchant–substrate interface are examined. The results obtained using the total concentration method, are compared with available results from the literature.

[DOI: 10.1115/1.2709654]

Keywords: wet chemical etching, fixed-grid method, numerical methods, finite-volume method

Introduction

Wet chemical etching (WCE) is a technique by which materials can be removed selectively from the surface of a substrate (the solid). When the reactive fluid called as etchant comes in contact with the substrate, it erodes the substrate surface and gives a specific desired pattern on it. This technique has potential application in the manufacturing of shadow mask for color-television tubes [1], integrated circuit (IC) devices in microelectronics industries [2], microelectro mechanical systems (MEMS) devices such as hinges [3], pressure sensors [4], etc.

Theoretically, the WCE process can be described as a moving boundary problem as the etchant–substrate interface moves because of erosion of the substrate surface by the etchant. For the theoretical analysis of the WCE process, different researchers proposed various mathematical models. These include analytical models such as the asymptotic solution [5,6] and numerical models such as the variational inequality approach [7,8], the moving-grid (MG) approach [7,9–15], the level-set method [16–18], and the fixed-grid (FG) method [19,20]. Depending on the reaction rate at the etchant-substrate interface, two possible cases namely—the diffusion-controlled [5–9,21,10–12,15,19,20] and the reaction-controlled [7,10–15,20] etching are examined using the above mentioned mathematical models. These two cases are studied in the modeling of one-dimensional [9,13,19,20], two-dimensional [5–9,21,10–12,14–16,22], and three-dimensional [17] WCE. The effect of flowing etchant in the etching process is studied by Shin and Economou [10,11], Driesen [12], Kaneko et al. [14], and Sudirham et al. [15].

The analytical model based on the asymptotic solution is presented by Kuiken [5,6] to model the two-dimensional WCE. The asymptotic solution is valid for diffusion-controlled etching using a dilute etchant. Kuiken et al. [9] presented the exact solution for the one-dimensional diffusion-controlled WCE. The analytical treatment is then extended to a two-dimensional diffusion-controlled WCE based on perturbation principle. The substrate is partly protected by a semi-infinite mask (infinitely thin) making it a two-dimensional etching problem. The analytical asymptotic solution is verified with experiments [21].

The most widely used numerical models for WCE are based on the MG method. In the MG method, the computational domain is limited to the space occupied by the etchant. Because of the moving etchant–substrate interface, the computational domain expands with time. The etchant concentration is solved using appropriate boundary conditions and a specified initial condition. Using the interface condition at the etchant–substrate interface, the etch-front velocities are calculated to find the new position of the interface. The process is repeated until the desired etch depth has been achieved or when the specified etching time has been reached. Due to the changing computational domain, the computation mesh has to be regenerated at every time step. As a result, the computation mesh also moves with respect to time, which makes the diffusion problem to a convection–diffusion problem. This is because of the extra convection term associated with the mesh velocities [7,14]. Further, an unstructured mesh system or a body-fitted grid system is needed to model the multidimensional WCE.

Vuik and Cuvelier [7] presented a numerical model for WCE. The finite-element method (FEM) is used for discretization of the problem in the space variables and a finite difference method is used for discretizing the time variable. The MG method and the variational inequality approach are used to track the etchant–substrate interface. The mesh velocities in the MG method due to the movements of the computational grids are taken into account in the model. Bruch et al. [8] developed a highly efficient parallel algorithm based on the variational inequality approach for the same etching problem. Shin and Economou [10] studied the effect of etchant flow field (forced convection) on the shape evolution of etching cavities. The FEM was used to solve for the etchant velocity distribution and the etchant concentration distribution in the etched cavities. The MG method was used to track the etchant–substrate interface. The extra convection term due to grid velocities was neglected as the interface moves very slowly. The FEM model is extended to compare the effects of forced and natural convection on the shape evolution of etching cavities [11]. Li et al. [13] presented a one-dimensional moving boundary numerical

---

[1] Corresponding author.

Contributed by the Heat Transfer Division of ASME for publication in the JOURNAL OF HEAT TRANSFER. Manuscript received June 15, 2005; final manuscript received October 21, 2006. Review conducted by Sumanta Acharya.

scheme to predict the motion of the etchant-substrate interface while etching the phosphosilicate-glass (PSG) with hydrofluoric acid (HF). The one-dimensional model solves a radial diffusion equation. The fully implicit scheme was used to solve the radial diffusion equation. Kaneko et al. [14] used a MG approach to model a two-dimensional reaction-controlled WCE of an aluminium substrate using the FEM under etchant flow condition. A first-order reaction kinetic was assumed. The extra convection term due to grid velocities was also taken into account. Sudirham et al. [15] discussed the application of a space-time discontinuous Galerkin finite-element method for convection–diffusion problems while simulating the WCE of microstructures. Adalsteinsson and Sethian [16,17] developed a level-set formulation to simulate deposition, etching, and lithography in integrated circuit fabrication using two-dimensional and three-dimensional models. La Magna et al. [18] used a level-set method for a moving front to simulate two-dimensional profile evolution in the WCE process.

Chai and co-workers [19,20,22] presented a fixed-grid approach based on the total concentration of etchant to model the WCE process. This method is analogous to the enthalpy method used in the modeling of melting/solidification processes [23–26]. A total concentration, which is the sum of the unreacted etchant concentration and the reacted etchant concentrations, is defined. The modified governing equation includes the interface condition. In this formulation, the reacted concentration of the etchant is a measure of the etchfront position when etching progresses. Unlike the MG method, the etchfront is found implicitly using the total concentration method. Since the grids are fixed, there is no grid velocity. Hence a diffusion problem always remains a diffusion problem. Simple Cartesian grid is used to capture the complicated etchfront evolution in multidimensional etching. The model has been tested for one-dimensional diffusion-controlled [19] and reaction-controlled [20] WCE. The method further extended to model the two-dimensional diffusion-controlled etching [22].

In this paper, the FG method is extended to model the two-dimensional reaction-controlled WCE. The conventional update procedure of the reacted concentration assumed the concentration along the etchant–substrate interface as constant. However, in reaction-controlled WCE, the etchant concentration can vary along the interface. Therefore, the conventional update procedure is not applicable in reaction-controlled situations. Hence, a new procedure is presented to update the reacted concentration when etching progresses. The new update procedure is applicable to both diffusion- as well as reaction-controlled WCE. The effect of the reaction rate at the etchant–substrate interface on the etching process is examined.

The remainder of this paper is divided into six sections. In the next section, a two-dimensional WCE problem, the governing equation, the interface condition and the boundary conditions are described. The new update procedure of the reacted concentration is then discussed. A brief description of the numerical method used in this article is given. The overall solution procedure is then summarized. Discussion of the results obtained using the proposed FG method is presented. Some concluding remarks are then given.

Problem Description and Governing Equation

The schematic and computational domain for the two-dimensional problem considered is shown in Fig. 1. A gap of half width a is to be etched in a substrate. For demonstration purposes, the width of the mask is assumed to be large enough so that the concentration of etchant far away from the gap will remain unaltered at the initial concentration. The initial concentration of the etchant at $t=0$ is c_0. The etchant solution is assumed relatively dilute, i.e., the dimensionless etching parameter (defined in "Results and Discussion" section), $\beta \geq 1$. At $t>0$, the reaction between the etchant and the substrate at the etchant–substrate interface results in the reduction of the concentration of etchant adjacent to the etchant–substrate interface and the depletion of the substrate. The concentration of etchant on the boundaries far away from the gap is kept at the initial concentration, i.e., $c=c_0$. The origin of the coordinate system is set to the etchant–substrate interface at the center of the gap. Since the problem is symmetrical about the origin, only half of the domain is considered as shown in Fig. 1. The governing equation, the interface condition and the boundary conditions are presented next.

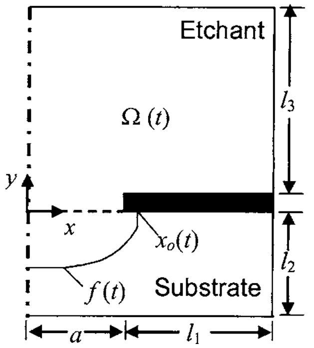

Fig. 1 Schematic of the two-dimensional wet chemical etching problem

Governing Equation. In the absence of convection, the etchant concentration within the etchant domain is governed by the mass diffusion equation given by

$$\frac{\partial c}{\partial t} = \frac{\partial}{\partial x}\left(D\frac{\partial c}{\partial x}\right) + \frac{\partial}{\partial y}\left(D\frac{\partial c}{\partial y}\right) \quad \text{in } \Omega(t) \tag{1a}$$

The initial and boundary conditions are

Initial Condition at $t=0$.

$$c = c_0 \quad \text{in } \Omega(t) \tag{1b}$$

Boundary Conditions for $t>0$.

$$\frac{\partial c}{\partial x} = 0 \quad x = 0 \tag{1c}$$

$$c = c_0 \quad y = h + l_3 \tag{1d}$$

$$c = c_0 \quad x = a + l_1, \quad h \leq y \leq h + l_3$$

$$J_y = -D\frac{\partial c}{\partial y} = 0 \quad y = h, \quad a \leq x \leq a + l_1 \tag{1e}$$

and

$$y = 0, \quad a \leq x \leq a + x_0(t) \tag{1f}$$

$$J_x = -D\frac{\partial c}{\partial x} = 0 \quad x = a, \quad 0 \leq y \leq h \tag{1g}$$

$$-D(\hat{n} \cdot \nabla c) = kc \quad \text{on } f(t) \tag{1h}$$

In Eq. (1h), $\hat{n}$ is the unit normal vector to the interface which points towards the substrate region. The negative sign on the left side of Eq. (1h) is because of the negative concentration gradient at the interface as the concentration of etchant at the interface is always less than the concentration in the bulk. To make the concentration gradient positive, a negative sign is multiplied.

Interface Condition for $t>0$ on $f(t)$.

$$\vec{v} = -\frac{DM_{\text{Sub}}}{m\rho_{\text{Sub}}} \nabla c \tag{1i}$$

where $\vec{v}$ is the velocity of the etchant–substrate interface; D is the diffusion coefficient of etchant; M_{Sub} is the molecular weight of the substrate; ρ_{Sub} is the density of the substrate; and m is the stoichiometric reaction parameter of the etchant–substrate reaction. The normal speed of the etchant–substrate interface v_n is obtained by dotting both sides of Eq. (1i) with the unit vector $\hat{n}$ normal to the interface which points towards the substrate region. This can be written as

$$\vec{v}\cdot\hat{n} = -\frac{DM_{\text{Sub}}}{m\rho_{\text{Sub}}}\nabla c\cdot\hat{n} \Rightarrow v_n = -\sigma_e\frac{\partial c}{\partial n} \tag{1j}$$

where $\sigma_e = DM_{\text{Sub}}/m\rho_{\text{Sub}}$ is the etching parameter.

The Total Concentration Method

In this paper the concept of *total concentration* is introduced which is defined as

$$c_T \equiv c + c_R \tag{2}$$

where c_T is the total concentration; c is the unreacted etchant concentration; and c_R is the reacted etchant concentration, respectively. Physically, c_R is the etchant concentration *consumed* in the reaction process. As such it is constant except at the etchant–substrate interface. This is used to capture the etchfront implicitly. The value of c_R changes from 0 to its maximum possible value of $c_{R,\max}$ in a control volume where etching is taking place. The maximum possible value of the reacted concentration termed $c_{R,\max}$, is the amount of etchant required per unit volume of substrate to dissolve the substrate during reaction. In a unit volume, there are $\rho_{\text{Sub}}/M_{\text{Sub}}$ moles of substrate. The reaction between the etchant and the substrate is given as

$$S + mE \rightarrow qP \tag{3}$$

where S is the substrate; E is the etchant; and P is the product, respectively. From Eq. (3) it is seen that the amount of etchant needed to dissolve a unit volume of substrate is $m\rho_{\text{Sub}}/M_{\text{Sub}}$. As $c_{R,\max}$ is the amount of etchant required per unit volume of substrate to dissolve the substrate during reaction, it can be written as

$$c_{R,\max} = \frac{m\rho_{\text{Sub}}}{M_{\text{Sub}}} \tag{4}$$

The governing equation based on the total concentration is given as

$$\frac{\partial c_T}{\partial t} = \frac{\partial}{\partial x}\left(D\frac{\partial c}{\partial x}\right) + \frac{\partial}{\partial y}\left(D\frac{\partial c}{\partial y}\right) \tag{5}$$

Combining Eqs. (2) and (5), results in

$$\frac{\partial c}{\partial t} = \frac{\partial}{\partial x}\left(D\frac{\partial c}{\partial x}\right) + \frac{\partial}{\partial y}\left(D\frac{\partial c}{\partial y}\right) - \frac{\partial c_R}{\partial t} \tag{6}$$

Procedure to Update C_R. The conventional c_R update procedure [20–22] is applicable as long as the unreacted etchant concentration along the interface is constant. However, in two-dimensional reaction-controlled etching, the unreacted etchant concentration along the interface is not constant as evident from the boundary condition at the interface (Eq. (1h)). Hence a new procedure to update c_R in the etching-control volume (ECV) is presented in this section. The ECVs are the substrate control volumes with adjacent etchant control volumes. The new update procedure is applicable to diffusion- as well as reaction-controlled etching. Results will show that the current c_R update procedure converges to conventional c_R update procedure in diffusion-controlled etching, where the etchant concentration along the etchant-substrate interface is closes to zero.

In the proposed update procedure, the interface condition (Eq. (1j)) is used to update c_R. As discussed earlier, the reacted concentration c_R is a measure of the interface displacement. Note that the normal displacement of the interface can be decomposed into horizontal and vertical components. Both the horizontal and the vertical displacements lead to changes in the c_R value of a control volume. In the proposed procedure the change in the c_R value of a control volume is the maximum of the changes in c_R due to the horizontal and the vertical displacements. For a two-dimensional problem, this can be written as

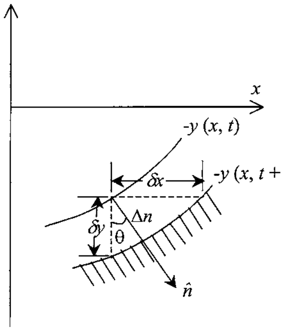

Fig. 2 Sketch for evaluation of normal concentration gradient at the interface

$$\Delta c_R = \max(\Delta c_{R,E}, \Delta c_{R,W}, \Delta c_{R,N}, \Delta c_{R,S}) \tag{7}$$

In Eq. (7), $\Delta c_{R,E}$ and $\Delta c_{R,W}$ are the changes in the reacted concentrations due to the horizontal displacements δx_E and δx_W, respectively. The remaining two terms in Eq. (7) are the changes in the reacted concentrations due to the vertical displacements. The relation between $\Delta c_{R,N}$ and the vertical displacement δy_N can be written as

$$\delta y_N(x,t) = \frac{\Delta c_{R,N}}{c_{R,\max}}\Delta y_P \tag{8}$$

where δy_N, $\Delta c_{R,N}$, and Δy_P are the vertical displacement due to etching by the etchant adjacent to the north interface, the resulting change in the reacted etchant concentration, and the height of the control volume P, respectively. A procedure to calculate the displacement and the resulting reacted concentrations is described next.

Figure 2 shows the locations of the etchfront at two consecutive times namely, t and $t+\Delta t$. At a given x location, the vertical displacement δy is related to the speed normal to the etchfront by

$$v_n = \frac{\Delta n}{\Delta t} = \frac{\delta y\cos\theta}{\Delta t} \tag{9}$$

In Eq. (9), Δn is the displacement *normal* to the etchfront and θ is the angle subtends by the normal with the vertical. The term δy can be approximated as

$$\delta y = y(x,t+\Delta t) - y(x,t) \approx \frac{\partial y}{\partial t}\Delta t \tag{10}$$

Combining Eq. (9) and (10), gives

$$v_n \approx \frac{\partial y}{\partial t}\cos\theta \tag{11}$$

From the interface condition, the same speed can be obtained from the normal concentration gradient and the reaction rate via

$$v_n = -\sigma_e\left(\sin\theta\frac{\partial c}{\partial x} - \cos\theta\frac{\partial c}{\partial y}\right) \tag{12}$$

Combining Eq. (11) and (12), results in

$$\frac{\partial y}{\partial t} = \sigma_e\left(\frac{\partial c}{\partial y} - \frac{\partial c}{\partial x}\tan\theta\right) = \sigma_e\left(\frac{\partial c}{\partial y} + \frac{\partial c}{\partial x}\frac{\partial y}{\partial x}\right) \tag{13}$$

The proposed c_R update procedure is obtained by combining Eqs. (8) and (13). This can be written as

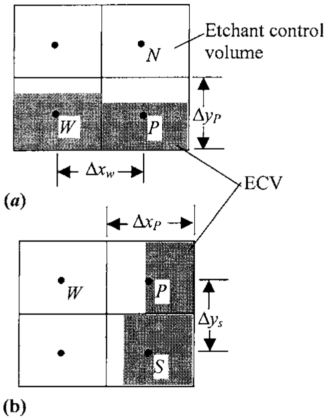

Fig. 3 Etching control volumes undergoing etching

$$c_{R,N} = \frac{c^0_{R,P} + \frac{\Delta t D}{\Delta y_P}\frac{\partial c}{\partial y} - \frac{\Delta t}{\Delta x_w}\frac{D}{c_{R,\max}}\frac{\partial c}{\partial x}c_{R,W}}{1 - \frac{\Delta t}{\Delta x_w}\frac{D}{c_{R,\max}}\frac{\partial c}{\partial x}} \tag{14}$$

Equation (14) is the recursive equation for the c_R value due to the vertical displacement of the interface in contact with an etchant at the north interface of the ECV. The concentration gradient terms in Eq. (14) can be evaluated in each ECVs (as shown in Fig. 3(*a*)) as

$$\frac{\partial c}{\partial y} = \frac{c_N - c_{P,I}}{\Delta y_n} \tag{15a}$$

$$\frac{\partial c}{\partial x} = \frac{c_{P,I} - c_W}{\Delta x_w} \tag{15b}$$

where $c_{P,I}$ is the interface unreacted etchant concentration in the ECV evaluated by using the boundary condition at the interface (Eq. (1*h*)); c_W and c_N are the unreacted etchant concentrations in the neighboring control volumes at west and north of ECV, respectively; $\Delta x_w = x_P - x_W$; and $\Delta y_n = y_N - y_P$. Following the same procedure as discussed above, a recursive equation for $c_{R,S}$ can be obtained, when the vertical displacement of the interface is due to the etchant at the south interface of ECV.

With a similar approach, it can be shown that the horizontal motion of the interface is given by

$$\frac{\partial x}{\partial t} = -\sigma_e\left(\frac{\partial c}{\partial x} - \frac{\partial c}{\partial y}\frac{\partial x}{\partial y}\right) \tag{16}$$

The horizontal displacement δx_W is related to change in the reacted concentration $\Delta c_{R,W}$ as

$$\delta x_W(y,t) = \frac{\Delta c_{R,W}}{c_{R,\max}}\Delta x_P \tag{17}$$

where δx_W, $\Delta c_{R,W}$, and Δx_P are the horizontal displacement of the interface due to etching by the etchant adjacent to the west interface, the resulting change in the reacted etchant concentration, and the width of the control volume *P*, respectively. Combining Eqs. (16) and (17), gives c_R due to the horizontal motion of the interface as

$$c_{R,W} = \frac{c^0_{R,P} - \frac{\Delta t D}{\Delta x_P}\frac{\partial c}{\partial x} - \frac{\Delta t}{\Delta y_s}\frac{D}{c_{R,\max}}\frac{\partial c}{\partial y}c_{R,S}}{1 - \frac{\Delta t}{\Delta y_s}\frac{D}{c_{R,\max}}\frac{\partial c}{\partial y}} \tag{18}$$

The above equation represents the recursive equation for the c_R value due to the horizontal displacement of the interface in contact with an etchant at the west of the ECV. The concentration gradient $\partial c/\partial x$ in Eq. (18) can be obtained by using Eq. (15*b*) and $\partial c/\partial y$ can be evaluated in each ECV (as shown in Fig. 3(*b*)) as

$$\frac{\partial c}{\partial y} = \frac{c_{P,I} - c_S}{\Delta y_s} \tag{19}$$

where c_S is the unreacted etchant concentration in the neighboring control volume at south of ECV and $y_s = y_P - y_S$. Following a similar procedure a recursive equation for $c_{R,E}$ can be obtained, when the horizontal displacement of the interface is due to the etchant at the east of ECV. The final c_R value for an ECV is taken as the maximum of the c_R values due to the horizontal and the vertical displacement of the interface as given in Eq. (7). The other two c_R updates in Eq. (7) can be derived without any new concept and are left for explorations by the interested readers.

Initial Unreacted Etchant Concentration in the ECV. When etching starts in an ECV in the current time step, the initial unreacted etchant concentration (from the previous time step) of the ECV is approximated using the boundary condition of the interface as given in Eq. (1*h*). The initial unreacted etchant concentration is the maximum of the interface concentrations due to the chemical reaction from all possible directions. This can be written as

$$c^0_P = \max(c^0_{P,E}, c^0_{P,W}, c^0_{P,N}, c^0_{P,S}) \tag{20a}$$

$$c^0_{P,E} = \frac{c^m_E}{1 + \frac{k_P \Delta x_e}{D_P}} \tag{20b}$$

$$c^0_{P,W} = \frac{c^m_W}{1 + \frac{k_P \Delta x_w}{D_P}} \tag{20c}$$

$$c^0_{P,N} = \frac{c^m_N}{1 + \frac{k_P \Delta y_n}{D_P}} \tag{20d}$$

$$c^0_{P,S} = \frac{c^m_S}{1 + \frac{k_P \Delta y_s}{D_P}} \tag{20e}$$

where $c^0_{P,E}$, $c^0_{P,W}$, $c^0_{P,N}$, and $c^0_{P,S}$ are the initial unreacted etchant concentration due to the chemical reaction from east, west, north, and south interfaces of the ECV, respectively. The superscript *m* is the *m*th iteration of the current time step.

Numerical Method

In this paper, the finite-volume method (FVM) of Patankar [27] is used to solve the governing mass-diffusion equation (Eq. (6)). A brief description of the major features of the FVM used is given here. A detailed discussion of the FVM is available in Patankar [27]. In the FVM, the domain is divided into a number of control volumes such that there is one control volume surrounding each grid point. The grid point is located at the center of a control volume. The governing equation is integrated over each control volume to derive an algebraic equation containing the grid point values of the dependent variable. The discretized algebraic equation for each control volume *P* is

$$a_P\phi_P = a^0_P\phi^0_P + a_W\phi_W + a_E\phi_E + a_N\phi_N + a_S\phi_S + S_C\Delta V_P \tag{21a}$$

where the coefficient a_P is given as

$$a_P = a_P^0 + a_W + a_E + a_N + a_S + S_P \Delta V_P \qquad (21b)$$

In Eqs. (21*a*) and (21*b*), ϕ is the variable to be evaluated in each control volumes; a is the coefficient of the discretization equation; ΔV is the volume of the control volume; and the terms S_C and S_P represents the source terms of the discretization equation. The subscripts W, E, N, and S in Eqs. (21*a*) and (21*b*) represent the neighboring control volumes at west, east, north, and south of the control volume P, respectively. The discretization equation then expresses the conservation principle for a finite control volume just as the partial differential equation expresses it for an infinitesimal control volume. The resulting solution implies that the integral conservation of mass is exactly satisfied for any control volume and of course, for the whole domain. The resulting algebraic equations are solved using a line-by-line tri-diagonal matrix algorithm. In the present study, a solution is deemed converged when the maximum change in the concentration and the maximum change in the reacted concentration between two successive iterations are less than 10^{-11}.

Overall Solution Procedure

The overall solution procedure for the proposed total concentration method can be summarized as follows:

1. Specify the etchant domain, the substrate domain, and the mask region. Ensure that the etchant–substrate interface lies on the interface between two control volumes;
2. Set the initial etchant concentration as c_0 in the etchant domain and zero in the substrate domain including the mask region;
3. Initially set c_R to 0 in the substrate domain including the mask region and to $c_{R,\max}$ in the etchant domain, respectively;
4. Advance the time step to $t+\Delta t$;
5. Identify the ECVs. These are the substrate control volumes with adjacent etchant control volumes;
6. Set the initial etchant concentration using Eq. (20*a*) in the ECVs if etching starts in those ECVs;
7. Set the unreacted etchant concentration to zero in the mask and substrate regions (except the ECVs). One possible way to do this is by adding a big number in the denominator term while evaluating the concentration at a given node point (e.g., by setting S_P to a big number in Eq. (21*b*) to make ϕ_P to zero in Eq. (21*a*));
8. Calculate c_P^0 in the ECVs to ensure that the interface condition is satisfied with a finite time step size;
9. Set c_P to c_P^0 as the initial guess;
10. Solve Eq. (6) for the unreacted concentration;
11. Update the reacted concentration (c_R) in the ECVs using Eq. (7); and
12. Check for convergence
    (a) If the solution has converged, then check if the required number of time steps has been reached. If yes, stop. If not, repeat 4–12; and
    (b) If the solution has not converged, then check the calculated reacted concentration

- If $c_R < c_{R,\max}$, repeat 10–12; and
- If, $c_R \geq c_{R,\max}$ then set $c_R = c_{R,\max}$ and repeat 5–12.

Results and Discussion

The two-dimensional problem shown in Fig. 1 is modeled using the proposed total concentration approach. Due to the symmetry of the problem about the y axis, only half of the domain is used for computation as shown in Fig. 1. For ease of presentation, the following dimensionless variables are defined

$$X \equiv x/a \qquad (22a)$$

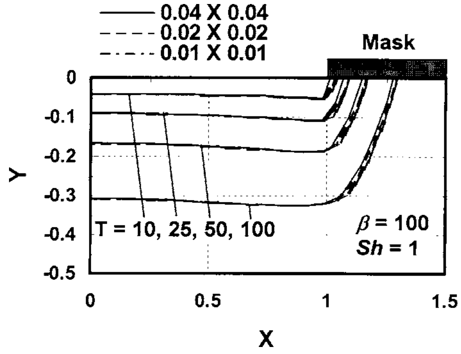

Fig. 4 Grid-independent test for nondimensional etching parameter β=100 and Sh=1

$$Y \equiv y/a \qquad (22b)$$

$$C \equiv c/c_0 \qquad (22c)$$

$$t^* \equiv tD/a^2 \qquad (22d)$$

$$\beta \equiv \frac{m\rho_{\mathrm{Sub}}}{c_0 M_{\mathrm{Sub}}} \qquad (22e)$$

$$\mathrm{Sh} \equiv \frac{ka}{D} \qquad (22f)$$

The nondimensional width of the mask is taken as $L_1 = l_1/a = 6.5$ and the dimensionless height of etchant is taken as $L_3 = l_3/a = 6.5$. The width and thickness of the substrate are taken as $L_{\mathrm{Sub}} = 1 + L_1 = 7.5$ and $L_2 = l_2/a = 1.0$, respectively. The mask thickness is taken as infinitely thin. This is done by setting $H = h/a = 0.005$ in this paper. Further decrease in the mask thickness does not alter the solution.

A grid refinement study was performed to ensure the solutions to be grid independent. Figure 4 shows the evolution of etch profiles at four different nondimensional times for the dimensionless etching parameter; β=100 and the dimensionless reaction parameter (known as Sherwood number); Sh=1. Three dimensionless grid sizes namely, – 0.04, 0.02, and 0.01 are chosen for this study. The dimensionless time step size is Δt^*=0.01. It is found that by decreasing the grid size beyond 0.02 does not alter the etchfront. The dimensionless time step, Δt^*=0.01, also produces the time independent solution. Hence, 0.02×0.02 grid size is used in this paper.

Figure 5 shows the etch profiles obtained from the present FG method compared with the existing MG method [10,15] and the analytical asymptotic solution [6] (valid for infinite reaction rate with dilute etchant). Figure 5(*a*) shows the comparison for reaction-controlled etching with the finite element based MG method proposed by Sudirham et al. [15]. Figure 5(*b*) shows a comparison for diffusion-controlled etching with the finite element based MG method proposed by Shin and Economou [10] and the analytical asymptotic solution proposed by Kuiken [6]. A nondimensional number Sh (defined in Eq. (22*f*)) called as *Sherwood number* determines the reaction rate at the etchant–substrate interface. Based on the reaction rate at the interface, two cases are examined, namely the reaction-controlled (Fig. 5(*a*)) and the diffusion-controlled (Fig. 5(*b*)) etching. The diffusion-controlled etching is associated with the infinitely fast reaction at the etchant–substrate interface, which corresponds to large values of Sh (of the order of 10^3). It is found that with Sh≥1000, the diffusion-controlled condition is achieved, as further increase in Sh beyond 1000 does not alter the etchfront. For a reaction-controlled case the Sh is taken as 1.0, which accounts for finite reaction rate at the interface. It is seen that the FG method is

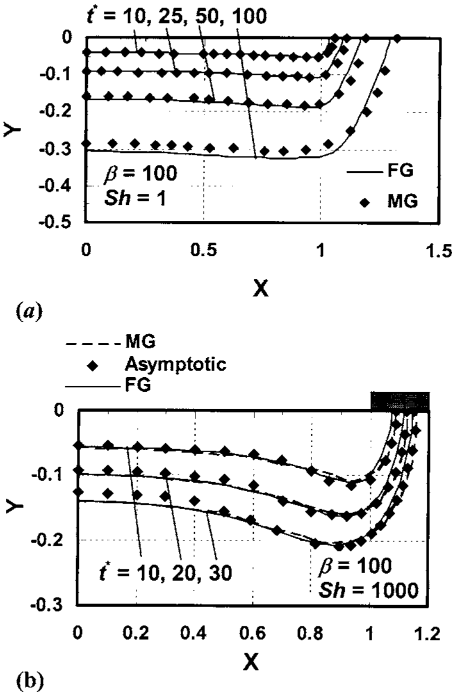

Fig. 5 Comparison of etch profiles for: (*a*) reaction-controlled etching (Sh=1); and (*b*) diffusion-controlled etching (Sh =1000) with $\beta=100$

predicting the etch profiles accurately. The bulging effect near the mask region is more pronounced with large values of Sh. It is because of the high rate of diffusion of etchant near the mask region. Since the diffusion-controlled etching is associated with infinitely fast reaction at the interface, hence the etchant diffusion rate controls the etching process. The fresh etchant is more readily available near the mask corner due to the high rate of diffusion, thereby increasing the etch rate near the mask. As a result, bulging is seen near the mask corner in diffusion-controlled etching.

Figure 6 shows the concentration contours near the etchant–substrate interface for two limiting etching conditions: the reaction-controlled etching and the diffusion-controlled etching based on the magnitude of Sh. The dimensionless etching parameter is $\beta=100$. Figure 6(*a*) shows the dimensionless etchant concentration contours near the etchfront at times $t^*=25$ in reaction-controlled etching for which the magnitude of Sh is 1. It is seen that the concentration is finite ($C=0.34$) just adjacent to the etchfront. However, when the magnitude of Sh is large, the etchant concentration just adjacent the etchfront closes to zero as shown in Fig. 6(*b*) for Sh=1000. It is also seen that the gap between the two adjacent contours for diffusion-controlled etching is smaller than the corresponding gap in reaction-controlled etching near the mask corner. This gives a higher concentration gradient near the mask corner when the etching is diffusion limited compared to the reaction-controlled limit. As a result, the etch rate is higher which produces a significant bulging of etch profiles near the mask corner.

A comparison of two update procedures, namely the current update procedure and the conventional update procedure [19,20,22] of the reacted concentration (c_R) for diffusion-controlled etching (Sh=1000) is shown in Fig. 7. The dimensionless etching parameter β is 10. It is seen that the new c_R update procedure produces the same etchfront as obtained with the conventional update procedure. Hence the current update procedure of c_R reduces to the conventional update procedure in diffusion-controlled etching.

Figure 8 shows the evolution of the etchfront at different times

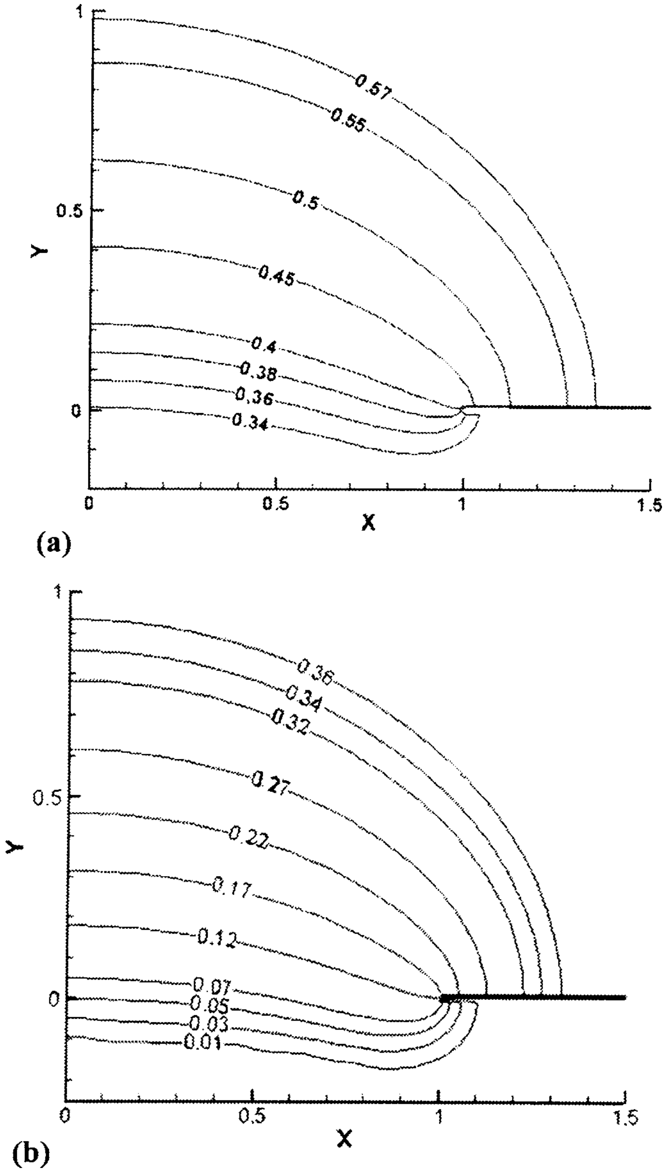

Fig. 6 Etchant concentration contours near the etchfront for $\beta=100$: (*a*) reaction-controlled etching (Sh=1); and (*b*) diffusion-controlled etching (Sh=1000)

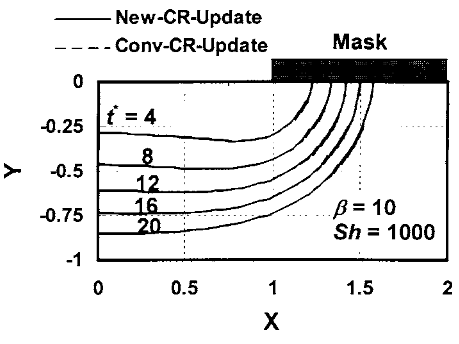

Fig. 7 Comparison of two update procedures of reacted concentration (c_R) for diffusion-controlled etching (Sh=1000) with $\beta=10$

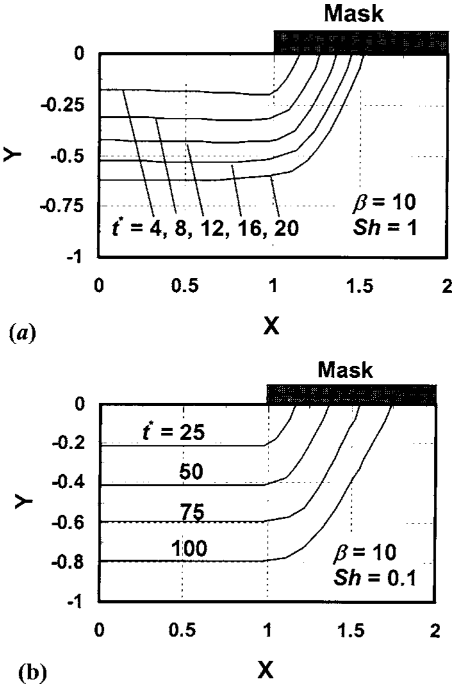

Fig. 8 Evolution of etch profiles at different time levels for finite reaction at the interface with $\beta=10$

when the interface reaction rate is finite. The effect of finite reaction on the etching process is studied using two values of Sh, namely 1 and 0.1. It is seen that the bulging effect is less pronounced near the mask region. This is unlike the case with the large values of Sh where significantly noticeable bulging is seen near the mask region. This is because the etching process in reaction-controlled etching is governed by the rate of reaction at the interface. Due to the slow rate of reaction at the interface, etch rate is slower near the mask region as compared to the diffusion-controlled case. As a result, the bulging is not significantly pronounced. It is seen from Fig. 8(*b*) that for Sh=0.1, the etch profiles at equal interval times are nearly equidistant. This is due to the nearly constant concentration gradient at the etchant–substrate interface. When the reaction rate at the interface is very slow, the decrease in the etchant concentration at the interface due to reaction has negligible effect on the bulk etchant concentration. Hence, the concentration gradient is nearly constant. Since the velocity of the interface is directly proportional to the concentration gradient (Eq. (1*i*)), the etchfront velocity is also constant. As a result the etch profiles are nearly equidistant.

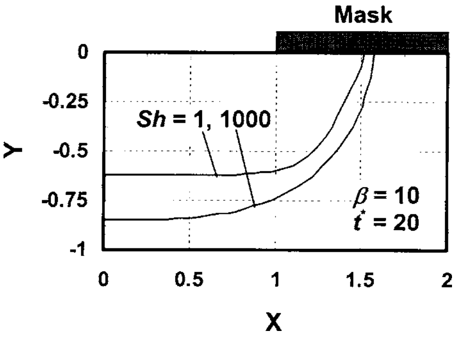

Fig. 9 Effect of reaction rate on etch profile shape

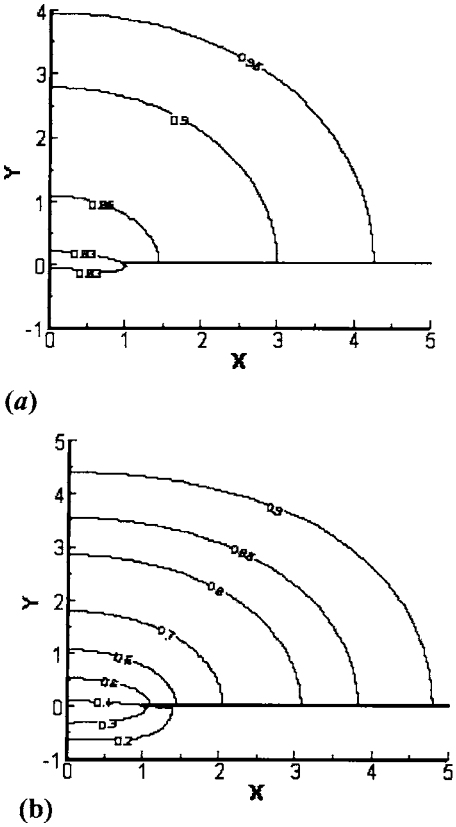

Fig. 10 Concentration contours at $t^*=20$ for $\beta=10$: (*a*) contours for Sh=0.1; and (*b*) contours for Sh=1.0

The effect of the reaction rate on the etch profile evolution is shown in Fig. 9. The dimensionless etching parameter is taken as $\beta=10$. The etch profiles are studied at nondimensional time $t^*=20$. It is seen that the tangent to the etch profile with Sh=1.0 subtends an angle with the mask layer which is less than the corresponding angle subtended by the tangent with Sh=1000. This can be explained by considering the horizontal motion of the interface below the mask for the above two values of Sh. The horizontal motion of the interface is governed by Eq. (16). When the value of Sh is large, the etchant concentration at the interface closes to zero. Hence, the concentration gradient along the y direction is negligibly small. As a result, the second term on the right hand side of Eq. (16) is negligible. But with the smaller value of Sh, due to finite concentration gradient along y direction, that term has significant effect, which gives an additional horizontal displacement of the interface below the mask, thus resulting in a smaller angle.

Figure 10(*a*) shows the concentration contours for Sh=0.1 and Fig. 10(*b*) shows the concentration contours for Sh=1.0. It is seen that as Sh increases from 0.1 to 1.0, the concentration of etchant near the interface decreases. This is because of the increase in the reaction rate at the etchant–substrate interface with the increase in Sh. As the reaction rate increases, the consumption of etchant at the reaction interface increases which results in decreased etchant concentration near the interface.

Concluding Remarks

A fixed-grid method based on the total concentration of etchant has been presented for two-dimensional WCE. In the proposed approach the governing equation includes the interface condition. The etchfront position can be found implicitly using the proposed method. A new procedure to update the reacted concentration is presented. The method has been applied to model the two-dimensional diffusion- and reaction-controlled etching. For demonstration purposes, the finite-volume method is used to discretize the governing equation. The results from the present approach are compared with the results from other existing methods from the literature. The results show that the etchfront profile can be predicted accurately using the proposed method.

Nomenclature

a = coefficient of the discretization equation
c = unreacted etchant concentration
c_R = reacted etchant concentration
$c_{R,\max}$ = maximum possible value of the reacted concentration
c_T = total concentration
D = diffusion coefficient of etchant
M_{Sub} = molecular weight of the substrate
m = stoichiometric reaction parameter
t = time
t^* = nondimensional time
Sh = Sherwood number
v_n = normal speed of the etchant–substrate interface
x, y = coordinate directions
X, Y = nondimensional coordinate directions

Greek Symbols

α = under-relaxation factor
β = nondimensional etching parameter
∇ = vector differential operator
Δt = time step
ρ_{Sub} = density of the substrate

Subscripts

Et = the etchant
o = initial
P = control volume P
Sub = the substrate
T = total

Superscripts

m = iteration number
o = previous time step

References

[1] Hoffman, K. H., and Sprekels, J., 1990, “*Free Boundary Problems: Theory and Applications*,” Longman Scientific and Technical, Harlow, Essex, England, Vol. 1, pp. 89.

[2] Madou, M. J., 2002, *Fundamentals of Microfabrication* 2nd Ed., CRC, New York.

[3] Pister, K. S. J., Judy, M. W., Burgett, S. R., and Fearing, R. S., 1992, “Microfabricated Hinges,” Sens. Actuators, A, **33**, pp. 249–256.

[4] Mastrangelo, C. H., Zhang, X., and Tang, W. C., 1995, “Surface Micromachined Capacitive Differential Pressure Sensor with Lithographically-Defined Silicon Diaphragm,” *Proceedings 8th International Conference on Solid-State Sensors and Actuators*, Eurosensor IX, Stockholm, June 25–29, pp. 612–615.

[5] Kuiken, H. K., 1984, “Etching: A Two-Dimensional Mathematical Approach,” Proc. R. Soc. London, Ser. A, **392**, pp. 199–225.

[6] Kuiken, H. K., 1984, “Etching Through a Slit,” Proc. R. Soc. London, Ser. A, **396**, pp. 95–117.

[7] Vuik, C., and Cuvelier, C., 1985, “Numerical Solution of an Etching Problem,” J. Comput. Phys., **59**, pp. 247–263.

[8] Bruch, J. C. Jr., Papadopoulos, C. A., and Sloss, J. M., 1993, “Parallel Computing Used in Solving Wet Chemical Etching Semiconductor Fabrication Problems,” GAKUTO International Series, Mathematical Sciences and Applications, **1**, pp. 281–292.

[9] Kuiken, H. K., Kelly, J. J., and Notten, P. H. L., 1986, “Etching Profiles at Resist Edges—I. Mathematical Models for Diffusion-Controlled Cases,” J. Electrochem. Soc., **133**, pp. 1217–1226.

[10] Shin, C. B., and Economou, D. J., 1989, “Effect of Transport and Reaction on the Shape Evolution of Cavities During Wet Chemical Etching,” J. Electrochem. Soc., **136**, pp. 1997–2004.

[11] Shin, C. B., and Economou, D. J., 1991, “Forced and Natural Convection Effects on the Shape Evolution of Cavities During Wet Chemical Etching,” J. Electrochem. Soc., **138**, pp. 527–538.

[12] Driesen, C. H., 1999, “Simulation of Convection-Driven Wet-Chemical Etching,” Ph.D. Thesis, University of Twente, Twente, The Netherlands.

[13] Li, W. J., Shih, J. C., Mai, J. D., Ho, C-M., Liu, J., and Tai, Y-C., 1998, “Numerical Simulation for the Sacrificial Release of MEMS Square Diaphragms,” *Proceedings 1st International Conference on MSMSSA*, San Jose, CA, April.

[14] Kaneko, K., Noda, T., Sakata, M., and Uchiyama, T., 2003, “Observation and Numerical Simulation for Wet Chemical Etching Process of Semiconductor,” *Proceedings of 4th ASME-JSME Joint Fluids Engineering Conference*, Honolulu, HA, July 6–10.

[15] Sudirham, J. J., Van Damme, R. M. J., and Van Der Vegt, J. J. W., 2004, “Space-Time Discontinuous Galerkin Method for Wet Chemical Etching of Microstructures,” Annual Report, Memorandum No. 1720, University of Twente, Twente, The Netherlands.

[16] Adalsteinsson, D., and Sethian, J. A., 1995, “A Level Set Approach to a Unified Model for Etching, Deposition and Lithography I: Alogorithms and Two-Dimensional Simulations,” J. Comput. Phys., **120**, pp. 128–144.

[17] Adalsteinsson, D., and Sethian, J. A., 1995, “A Level Set Approach to a Unified Model for Etching, Deposition, and Lithography II: Three-Dimensional Simulations,” J. Comput. Phys., **122**, pp. 348–366.

[18] La Magna, A., D’Arrigo, G., Garozzo, G., and Spinella, C., 2003, “Computational Analysis of Etched Profile Evolution for the Derivation of 2D Dopant Density Maps in Silicon,” Mater. Sci. Eng., B, **102**(1–3), pp. 43–48.

[19] Lam, Y. C., Chai, J. C., Rath, P., Zheng, H., and Murukeshan, V. M., 2004, “A Fixed Grid Method for Chemical Etching,” Int. Commun. Heat Mass Transfer, **31**(8), pp. 1123–1131.

[20] Rath, P., Chai, J. C., Zheng, H., Lam, Y. C., Murukeshan, V. M., and Zhu, H., 2005, “A Fixed-Grid Approach for Diffusion- and Reaction-Controlled Wet Chemical Etching,” Int. J. Heat Mass Transfer, **48**(11), pp. 2140–2149.

[21] Notten, P. H. L., Kelly, J. J., and Kuiken, H. K., 1986, “Etching Profiles at Resist Edges—II. Experimental Confirmation of Models Using GaAs,” J. Electrochem. Soc., **133**, pp. 1226–1232.

[22] Rath, P., Chai, J. C., Zheng, H. Y., Lam, Y. C., and Murukeshan, V. M., 2005, “A Total-Concentration Fixed-Grid Method for Two-Dimensional Diffusion-Controlled Wet Chemical Etching,” *Proceedings ASME Summer Heat Transfer Conference*, San Francisco, CA, July 17–22, Paper No. HT2005-72186.

[23] Shamsundar, N., and Sparrow, E. M., 1975, “Analysis of Multidimensional Conduction Phase Change via the Enthalpy Method,” J. Heat Transfer, **97**, pp. 333–340.

[24] Brent, A. D., Voller, V. R., and Reid, K. J., 1988, “Enthalpy-Porosity Technique for Modeling Convection-Diffusion Phase Change: Application to the Melting of a Pure Metal,” Numer. Heat Transfer, **13**, pp. 297–318.

[25] Kaenton, J., Semma, E., Timchenko, V., Ganaoui, M. El., Leonardi, E., and de Vahl Davis, G., 2004, “Effects of Anisotropy and Solid/Liquid Thermal Conductivity Ratio on Flow Instabilities During Inverted Bridgman Growth,” Int. J. Heat Mass Transfer, **47**(14–16), pp. 3403–3413.

[26] Kaenton, J., de Vahl Davis, G., Leonardi, E., and Leong, S. S., 2002, “A Numerical Study of Anisotropy and Convection During Solidification,” Numer. Heat Transfer, Part B, **41**(3–4), pp. 309–323.

[27] Patankar, S. V., 1980, *Numerical Heat Transfer and Fluid Flow*, 1st ed., Hemisphere, New York.

Balaji Jayaraman[1]
e-mail: jbalaji@ufl.edu

Siddharth Thakur

Department of Mechanical and Aerospace Engineering,
University of Florida,
Gainesville, FL 32611

Wei Shyy
Department of Aerospace Engineering,
University of Michigan,
Ann Arbor, MI 48109

Modeling of Fluid Dynamics and Heat Transfer Induced by Dielectric Barrier Plasma Actuator

Glow discharge at atmospheric pressure using a dielectric barrier discharge can induce fluid flow, and can be used for active control of aerodynamics and heat transfer. In the present work, a modeling framework is presented to study the evolution and interaction of such athermal nonequilibrium plasma discharges in conjunction with low Mach number fluid dynamics and heat transfer. The model is self-consistent, coupling the first-principles-based discharge dynamics with the fluid dynamics and heat transfer equations. Under atmospheric pressure, the discharge can be simulated using a plasma–fluid instead of a kinetic model. The plasma and fluid species are treated as a two-fluid system coupled through force and pressure interactions, over decades of length and time scales. The multiple-scale processes such as convection, diffusion, and reaction/ionization mechanisms make the transport equations of the plasma dynamics stiff. To handle the stiffness, a finite-volume operator-split algorithm capable of conserving space charge is employed. A body force treatment is devised to link the plasma dynamics and thermo-fluid dynamics. The potential of the actuator for flow control and thermal management is illustrated using case studies. [DOI: 10.1115/1.2709659]

Keywords: aerodynamics, heat transfer, plasma, actuator, flow control, dielectric, discharge

1 Introduction

Recent research [1–4] on the efficient generation of ionized fluid in a glow discharge at atmospheric pressure using a dielectric barrier discharge (DBD) technique has attracted interest from the thermo-fluid dynamics and control communities. The largely athermal surface plasma generation investigated in the above studies can be used for achieving flow control by modifying the flow structure through electrohydrodynamic (EHD) effects [1]. A typical flow control application is illustrated in Fig. 1 where an insulator separates the electrodes powered by a radio frequency (1–50 kHz) alternating voltage (1–20 kV) for actuation at atmospheric pressure. The collisional plasma under such pressures can result in a significant momentum exchange with the neutral species. The effect of the plasma generated EHD flow on a surface manifests as a wall jet-type flow. This can be used to inject momentum in regions of adverse pressure gradients, boundary layers, and high heat flux. Compared to mechanical devices such as synthetic jets [5], the glow discharge actuator involves no moving parts, and can offer control capabilities in complementary fashion.

The detailed mechanism of EHD flow generation induced by the DBD is still being investigated although the concept behind the force generation is believed to be from collision-dominated effects [1,4,6]. The coupled plasma–fluid problem is inherently nonlinear and exhibits wide ranges of time and length scales. Experimental and analytical studies of atmospheric pressure glow discharge plasma-based flow were conducted by Roth et al. [2]; EHD body force was modeled as an electrostatic force acting on the charged particles which impacts the neutral gas. Enloe et al. [4] studied the plasma morphology and operating mechanism using optical measurements using a photomultiplier tube (PMT) which revealed the characteristic temporal and spatial structure. Parametric studies for improving actuator design [6] for separation control were studied by means of experiments in [3,4,7,8]. The plasma operation significantly reduces the size of the separation bubble. Chan [9] applied plasma-based EHD flow control in the study of acoustic effects in subsonic cavity flows. There have also been efforts to use plasma-based actuators in the context of turbulent boundary layer flow control [10].

The effect of the plasma on the fluid can be modeled as a localized body force [1] on the neutral particles. Most of the investigations so far have been based on experimental observations and phenomenological arguments using simplified models [1–3]. Shyy et al. [1] proposed that the asymmetries introduced through the electrode arrangement and consequently the discharge structure has a significant role to play in the generation of glow-discharge-induced flow. This model employs prior knowledge garnered from the discharge visualization studies [11] such as the discharge duty cycle, assumed species-density distributions, and a linearized electric field distribution. The objective of such a body force formulation is to develop modeling concepts to account for the plasma-induced momentum imparted to the fluid. The above mentioned analytical–empirical model represents a time-averaged body force component acting on the fluid given as

$$\bar{F}_{\text{tave}} = \rho_c e_c \bar{E} \delta \frac{\Delta t}{T} \tag{1}$$

where $\vec{E}$ is a linearized electric field; $\rho_c e_c$ is the charge density (assumed uniform); $\Delta t/T$ is the discharge duty cycle; and δ is a binary valued multiplier which is zero outside the region of discharge operation and one otherwise. The discharge region is actually determined from experimental visualization for this case and is modeled as shown in Refs. [1,2]. This modeling is based on the observation that the discharge operation time scale is much larger than that for the fluid flow. The above linearized body force model was also adopted by Gaitonde et al. [12] for modeling plasma-

---

[1] Corresponding author.

Contributed by the Heat Transfer Division of ASME for publication in JOURNAL OF HEAT TRANSFER. Manuscript received April 5, 2006; final manuscript received January 2, 2007. Review conducted by Jayathi Murthy.

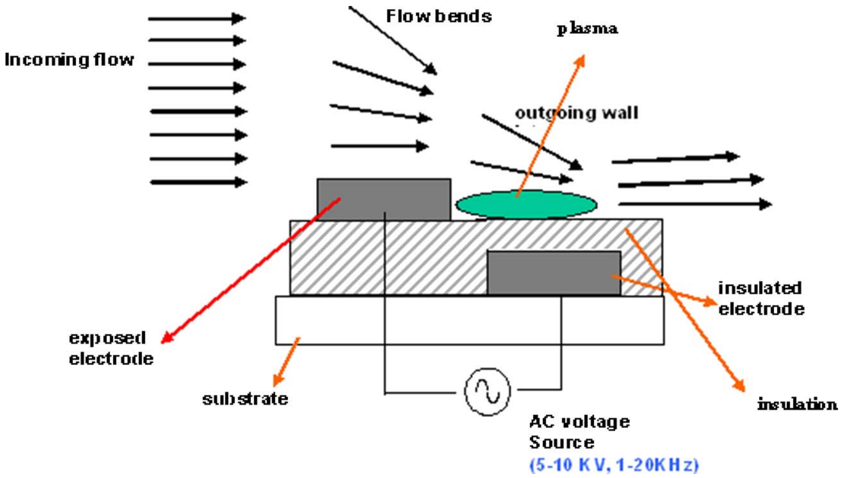

Fig. 1 Illustration of glow discharge induced fluid flow

based separation control in a NACA 0015 wing section.

The limitations imposed by the above analytical–empirical models include dependence on parameters which need to be experimentally measured and preclude predicting the resulting flow field. An improvement to the above is the self-consistent force field model developed from fundamental plasma dynamics principles [13]. Computational modeling of discharge plasmas can be classified into three types, namely, fluid models, kinetic/particle models and hybrid approaches [13], as shown in Fig. 2. Kinetic models involve the solution of the Boltzmann equation [14] for the species velocity or energy distribution function in both space and time or particle simulations, often using Monte Carlo methods, and are generally computationally more expensive than the fluid models. The fluid models consist of a few moments of the Boltzmann equation. However, the choice of the model is also dependent on the regime of modeling interest. Particle techniques such as Monte Carlo methods are used to model the collision term. Particle-in-cell (PIC) techniques have been used for discharge modeling in Refs. [14–16]. However, for the simulation of higher pressure discharges (~100 Torr or higher), the velocity probability distribution function can be assumed to be close to equilibrium and, therefore, fluid models can adequately capture the relevant physics [14] and will be the focus of the present study.

Fluid models have been used to model both high- [17,18] and low-pressure [19–21] discharges. Colella et al. [20,21] employed a space-charge conserving finite difference method for low-pressure discharge modeling using local grid refinement in two dimensions. Multidimensional studies [22–24] at atmospheric pressures have

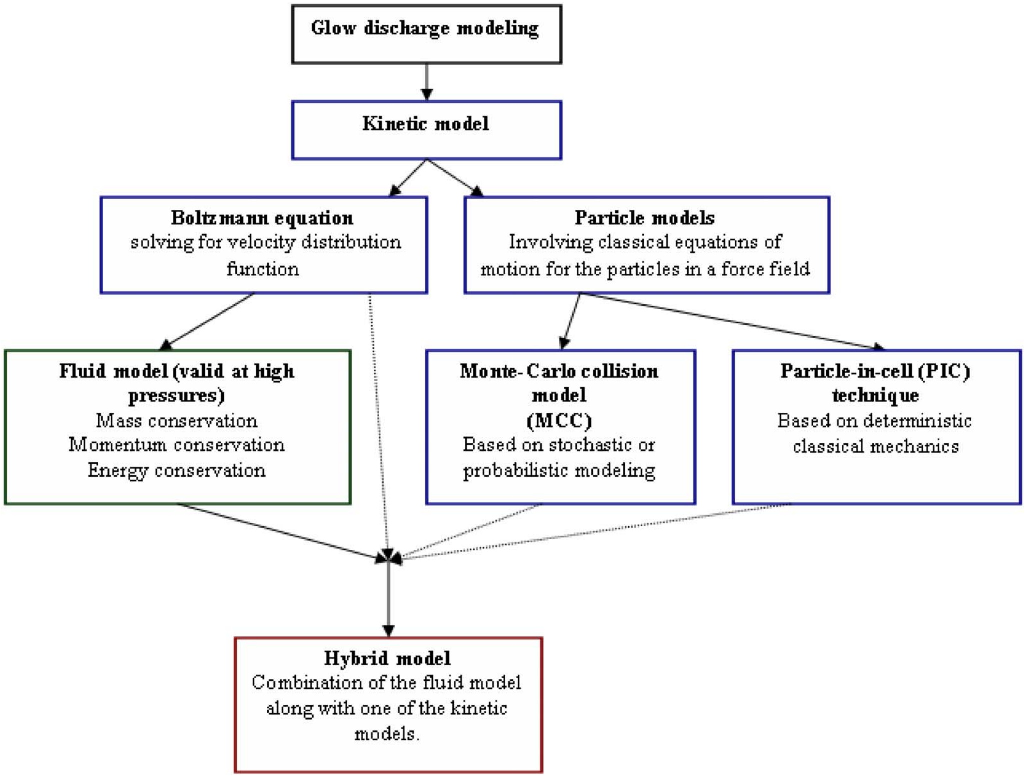

Fig. 2 Plasma modeling hierarchy

been attempted only recently in the context of modeling DBD plasma-induced flow effects. Roy et al. [22,23] proposed a self-consistent two-dimensional DBD fluid model for helium gas with application to separation control using the finite-element techniques. Singh et al. [24], in a related paper, present a parametric study of the different conditions in an asymmetric discharge configuration. The present and the above-mentioned modeling studies employ similar two-fluid systems to model the plasma species and the neutral fluid, coupled through dynamic forces and pressure interactions. However, the numerical framework and the modeling details are different.

Computationally, the combined discharge physics and thermofluid transport is a challenging problem due to multiple nonlinear partial equations with strong source terms, and widely distributed length and time scales. The disparate length and time scales make the system computationally stiff, often requiring that computational simulations be conducted with very small time-step sizes. Roy et al. [22,23] used a globally implicit finite element procedure where the system of species continuity and momentum equations are assembled as part of a global matrix to solve for the solution vector. Globally implicit integration methods are attractive because, for linear problems, they are unconditionally stable but are computationally expensive in highly nonlinear situations. Alternatively, a sequential solution approach has been employed by Hammond et al. [19] and Colella et al. [20,21].

In the present study, we have employed an operator-split sequential solution algorithm which can handle the plasma fluid model. In using timesplit algorithms for processes operating in a wide range of time scales, the choice of time-step size is typically determined by the smallest time scale, but need not necessarily be chosen as such. To speed up the solution procedure, an intermediate time scale is chosen to advance the overall system in time, while the faster processes are advanced by subcycling within the time step. Also, a predictor–corrector approach is used to ensure sufficient coupling between the solution variables. The method is employed to model the plasma dynamics in an asymmetric electrode configuration similar to that shown in Fig. 1. We also investigate the effect on the flow field using the resulting body force field in a low Reynolds number flow regime. The present study is part of an ongoing effort to develop a capability to study fully coupled multidimensional plasma dynamics with the fluid flow.

The rest of the paper is organized as follows. Section 2 presents the plasma fluid model along with the techniques employed to handle multiscale discharge dynamics and the Navier–Stokes equations for fluid flow. In Sec. 3, we present some representative results for the two modeling approaches discussed above. A two-dimensional (2D) helium discharge in an asymmetric electrode arrangement is modeled using the self-consistent force model along with the resulting flow field. This is followed by a study to assess the fidelity of the body force model [1] with experimental data reported by van Dyken et al. [6]. In order to illustrate the potential of the discharge actuator, representative fluid flow and heat transfer applications are presented.

2 Numerical Model

2.1 Fluid Model for Discharge Equations. The fluid model used consists of the first few moments of the Boltzmann equation for the various species with a near-Maxwellian distribution function. The plasma is considered as a multicomponent fluid comprised of two types of primary species, namely, ions and electrons (represented by subscripts "*i*" and "*e*", respectively).

2.1.1 Continuity Equation.

Electrons

$$\frac{\partial n_e}{\partial t} + \nabla \cdot (n_e v_e) = n_e S_{ie} - r n_i n_e \tag{2}$$

Table 1 Representative time scales in the problem

Time scale		Order
Operating frequency timescale, τ_ω	$\tau = \tau_w = \frac{1}{f} = T$	T
Ion drift $\tau_{\mathrm{dr,ion}}$	$\tau_{\mathrm{dr,ion}} = \frac{L}{V_{\mathrm{ion}}}$	$O(10^{-4})T$
Electron drift $\tau_{\mathrm{dr},e}$	$\tau_{\mathrm{dr},e} = \frac{L}{V_e}$	$O(10^{-6})T$
Dielectric relaxation τ_{diel}	$\tau_{\mathrm{diel}} = \frac{\varepsilon_0 E}{eNV_e}$	$O(10^{-7})T$
Ionization timescale τ_c	$\tau_c = \frac{1}{\nu_c}$	$O(10^{-6})T$

Ions

$$\frac{\partial n_i}{\partial t} + \nabla \cdot (n_i v_i) = n_e S_{ie} - r n_i n_e \tag{3}$$

Here, the source terms on the right hand side represent the reaction/ionization processes which result in the creation (S) or destruction (r) of the species, as applicable.

2.1.2 Momentum Equation. The momentum equation for the species at high pressures can be reduced to the drift-diffusion form which neglects the inertial and unsteady terms and balances the thermodynamic pressure gradient with the drift force and collision terms.

Electrons

$$n_e \mu_e E - \nabla(n_e D_e) = n_e v_e \tag{4}$$

Ions

$$n_i \mu_i E - \nabla(n_i D_i) = n_i v_i \quad \text{(for high-pressure discharges)} \tag{5}$$

As long as the thermal velocity is comparable to the drift velocity and we are in the continuum regime $(\gamma/L = \ll 1)$, the inertial components in the momentum equation can be neglected. What is realized is a balance between the collision/ionization effects and the drift-diffusion components.

2.1.3 The Electric Field Equation. The electric field E is obtained using the solution of the Poisson equation, given by

$$\nabla \cdot (\varepsilon_d E) = \frac{e(n_i - n_e)}{\varepsilon_0} \tag{6}$$

Defining a source/ionization frequency to simplify the source term, we can write

$$v_c = S_{ie} - r n_i \tag{7}$$

We denote the reference number density, species velocity, length, time, electric field by N, $V_{i/e}$, L, τ and E, respectively. To give an idea of the characteristic time scales in the system, their representative orders of magnitude based on a rf discharge operating at a few kHz based on helium gas [11] are given in Table 1.

2.2 Solution Algorithm. The operator-split algorithm capable of efficiently handling the different time scales arising from the various processes such as ionization, convection, and diffusion is embedded as part of a projection method to enhance coupling between the various species equations being solved.

The split solution algorithm consists of the following steps:

1. Predictor step;
2. Solution of the electric field equation; and
3. Corrector step.

2.2.1 Predictor Step. Here the species continuity Eqs. (2) and (3), along with the drift-diffusion momentum Eqs. (4)–(6) are integrated using lagged values for the various coefficients (as they are a function of the electric field E). The source term is integrated using a higher-order (fifth-order) backward difference formula (BDF) using the CVODE solver [25]. The convection and diffusion operators can be treated either implicitly or explicitly. In this case, we employ a second-order upwind for the convection term and second-order central difference for the diffusion term. The continuity equation can be written as

$$\frac{\partial n_k}{\partial t} + \nabla \cdot (n_k v_k) = v_{c,k} n_k \tag{8}$$

Three types of splitting are popular, namely (1) the standard first-order splitting, (2) Strang splitting, and (3) source splitting. In the following, we offer a brief description of these splitting techniques. The technique adopted in the present approach is source splitting.

1. First-order splitting. The first-order splitting was employed by Colella et al. [21] and can be written symbolically as

   $$\bar{n}_k = T^{M_k}(\Delta t') S(\Delta t) n_k^n \tag{9}$$

   where S is the reaction operator integrated using the ordinary differential equation (ODE) solver [25] and T is the transport operator. M_k is the number of substeps used for the transport term integration to march to the global timestep Δt and $\Delta t' = \Delta t / M_k$ is the substep size.
2. Strang splitting. Here, the transport term integration is usually split into two halves to achieve the symmetry since the ODE solver used in the reaction part is more computationally burdensome.

   $$\bar{n}_k = T^{M_k/2}(\Delta t') S(\Delta t) T^{M_k/2}(\Delta t') n_k^n \tag{10}$$
3. Source splitting. Source splitting [26] has certain advantages over the standard first-order splitting and the higher-order Strang splitting methods. The Strang splitting is formally second order which is achieved by splitting the operators symmetrically. It is worth noting that, in both the first-order and Strang splitting procedures, the initial guess for the reaction part is not directly from the previous time step, but after a half or full time step of the transport term integration. This results in the introduction of stiff transients in the solution which are nothing but an artifact of the splitting errors. These can be highly significant in the presence of strong nonlinearities. To overcome the solution discontinuities which give rise to stiff transients in the above two splitting methods, the source splitting treats the transport as a piecewise constant source. For example, we can write

   $$\tilde{n}_k = S(\Delta t) n_k^n$$

   and

   $$\dot{n}_k = \frac{\tilde{n}_k - n_k^n}{\Delta t} \tag{11}$$

   Therefore, we have

   $$\bar{n}_k = [T(\Delta t') + n_k(\Delta t)]^{M_k} n_k^n \tag{12}$$

   where S is the reaction operator integrated using the ODE solver CVODE [25] and T is the transport operator. M_k is the number of substeps used for the transport term integration to march to the global time step Δt. The ODE solver employs a fifth-order BDF for time integration with Newton iteration for nonlinearity.

2.2.2 Solving the Electric Field Equation. Now that we have the predicted values of the species densities, $\bar{n}_k$, we can use it to update the electric field by solving the following Poisson equation

$$\nabla \cdot (\varepsilon_d E^{n+1}) = \frac{\sum_k \bar{n}_k q_k}{\varepsilon_o} \tag{13}$$

where q_k is the signed charge content of each species. The elliptic solver employed in the present study is either the Gauss–Seidel method with successive over-relaxation or the algebraic multigrid method.

2.2.3 Corrector Step. At the end of the previous step, the predicted species densities $\bar{n}_k$ and the electric field at the new time level E^{n+1} are available and the corrected densities are obtained using the updated coefficients.

One of the important aspects is to determine the proper choice of the global time step Δt and the number of substeps M_k which would require balancing computing efficiency with stability. Choosing Δt too small will make the computation inefficient and a reasonable choice in this case is the slower species convection time scale. Also, issues such as dynamic equilibrium and nonlinearity can affect the solution procedure and the size of the global time step. While subcycling is an important technique for improving accuracy and stability, its ability to increase the global time step is limited. It is important to gauge the overall accuracy with the global time step size.

It is noted that for the low speed, i.e., incompressible fluid flow applications, which is the current focus, the fluid characteristic time scales are much larger than that of the operating plasma dynamics. Hence, we can safely treat the coupling between the fluid and plasma physics as one way, i.e., from the plasma to the fluid by means of the body force model. A more detailed discussion has been presented in Ref. [13]. To extend further, if the fluid dynamic time scales become comparable, then the two-way coupling will need to be handled and the fluid solution advancement should be performed using the global time-step size.

2.3 Navier–Stokes Equations. The neutral fluid is modeled using the Navier–Stokes equations and the energy transport equation for a steady, incompressible flow. The body force terms, which are added to the momentum equations, couple the discharge effects to the fluid flow. As discussed earlier, the disparity in the time scales between the low-speed flow and the high-frequency actuator operation enables the treatment of the plasma body force in a quasi-steady manner. The fluid is assumed to be incompressible in view of the plasma being essentially isothermal. In the following, governing equations in the two-dimensional form are presented

$$\frac{\partial \bar{A}}{\partial t} + \frac{\partial \bar{B}}{\partial x} + \frac{\partial \bar{C}}{\partial y} = \bar{D} \tag{14}$$

where

$$\bar{A} = \begin{bmatrix} \rho \\ \rho u \\ \rho v \\ e \end{bmatrix}, \quad \bar{B} = \begin{bmatrix} \rho u \\ \rho u^2 + p - \tau_{xx} \\ \rho u v - \tau_{xy} \\ u(e-p) - \tau_{xx} u - \tau_{xy} v - k \partial_x T \end{bmatrix},$$

$$\bar{C} = \begin{bmatrix} \rho v \\ \rho u v - \tau_{xy} \\ \rho v^2 - \tau_{yy} + p \\ u(e+p) - \tau_{xy} u - \tau_{yy} v - k \partial_y T \end{bmatrix}$$

and

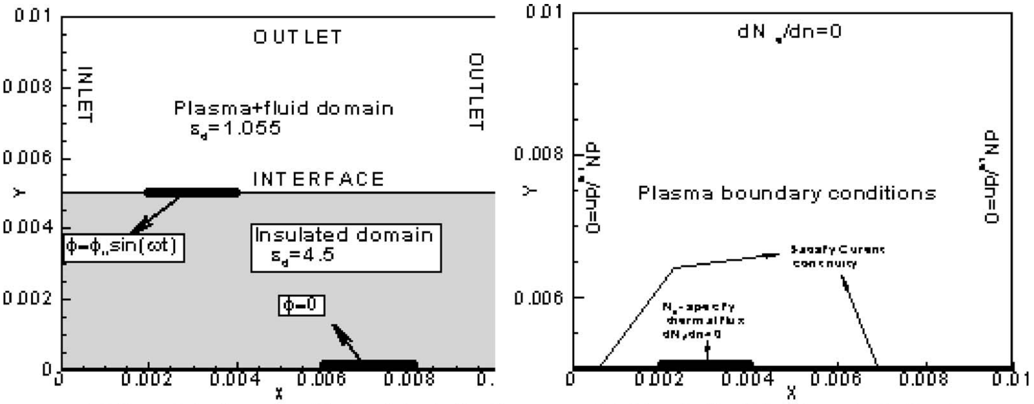

(a) Complete domain with insulator indicating boundary conditions for fluid flow

(b) Top half of the domain indicating boundary conditions for plasma species

Fig. 3 2D computational domain with boundary conditions

$$\bar{D} = \begin{bmatrix} 0 \\ F_x \\ F_y \\ 0 \end{bmatrix}$$

The F_x and F_y are the body force terms calculated from the solution of the plasma dynamics, as

$$F_x = E_x \sum_k q_k n_k, \quad F_y = E_y \sum_k q_k n_k \tag{15}$$

The Navier–Stokes equations are solved using a pressure-based algorithm with a second-order upwind scheme as discussed in Refs. [27,28].

3 Results and Discussion

3.1 Plasma Model. A schematic of the computational domain is shown in Fig. 3. The electrodes are 2 mm in length and the insulated bottom electrode is shifted downstream by 2 mm. A similar case has been studied by Roy et al. [22]. The helium discharge is modeled at a pressure of 300 Torr, and a temperature of 300 K and is driven by an ac voltage of 1.5 kV (peak voltage) operating at 5 kHz. The thickness of the electrodes is negligible and the dielectric thickness is 5 mm. The electron temperature is assumed to be 1 eV (~11,600 K), while the ions and the neutrals are essentially in thermal equilibrium at 300 K. The various transport properties and property relationships are available in the literature and we have employed the ones used by Roy et al. [22] for the present study. These are summarized in Table 2.

The computational domain employed is a square region of size 1 cm × 1 cm. The grid consists of 127 × 61 points for the 2D case. This computational grid was selected based on the outcome of testing several grid sizes to ensure that the plasma sheath near the wall–gas interface can be adequately resolved while balancing the consideration of the computational costs. The dielectric constant in the fluid/discharge domain is 1.0055; the permittivity of vacuum and that of the insulator is 4.5. For investigation purposes two different frequencies are considered, namely, 5 kHz and

Table 2 Summary of property models employed for the He discharge simulation[a]

Transport/reaction properties	Models/values employed
μ_i (ion mobility)	$=\dfrac{8\times10^3}{p}(1-8\times10^{-3}\,E/p)$ cm^2 V^{-1} s^{-1} for $E/p \leqslant 25$ V cm^{-1} Torr^{-1} $=\dfrac{4.1\times10^4}{p\sqrt{E/p}}\left(1-\dfrac{27.44}{(E/p)^{1.5}}\right)$ cm^2 V^{-1} s^{-1} for $E/p > 25$ V cm^{-1} Torr^{-1}
μ_e (electron mobility)	$=\dfrac{e}{m_e \nu_{en}}$cm^2 V^{-1} s^{-1} where $\nu_{en}=10^{12}$/s
S_{ie} (species ionization model)	$=4.4\exp\left(\dfrac{-14}{(E/p)^{0.4}}\right)p\mu_e E$ s^{-1}
r (recombination coefficient)	$=1.09\times10^{-20}T^{-9/2}n_e$ m^3/s
D_i (ion diffusivity)	$=500$ cm^2/s
D_e (electron diffusivity)	$=\dfrac{kT_e}{e}\mu_e$ cm^2/s
μ (viscosity of He gas)	$=2.0\times10^{-5}$ N s/m^2

[a] See Ref. [22].

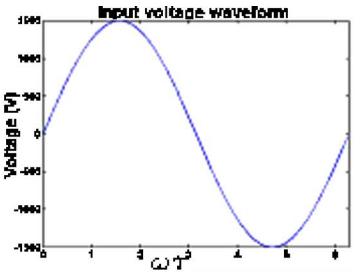

(a) Sinusoidal input voltage waveform

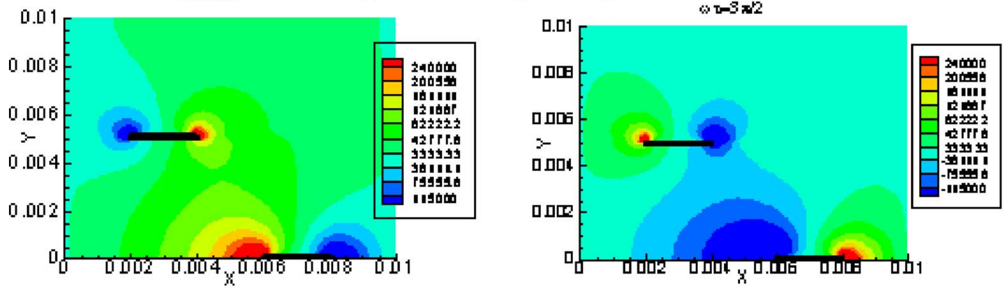

(b) Axial Electric field (E_x) contours (V/m) at 5KHz, $\omega t = \frac{\pi}{2}$ (c) E_x contours (V/m) at 5KHz, $\omega t = \frac{3\pi}{2}$

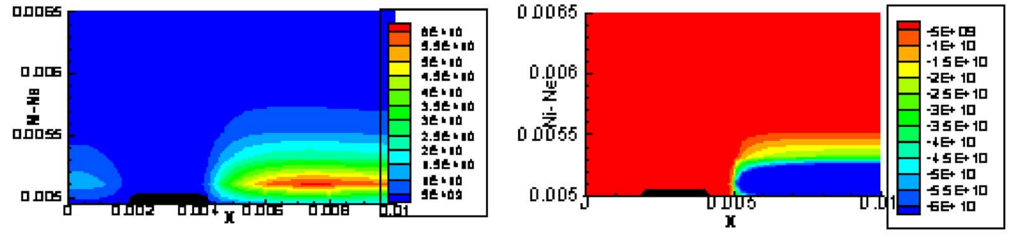

(d) Net charge density contours at 5KHz, $\omega t = \frac{\pi}{2}$ (e) Net charge density contours at 5KHz, $\omega t = \frac{3\pi}{2}$

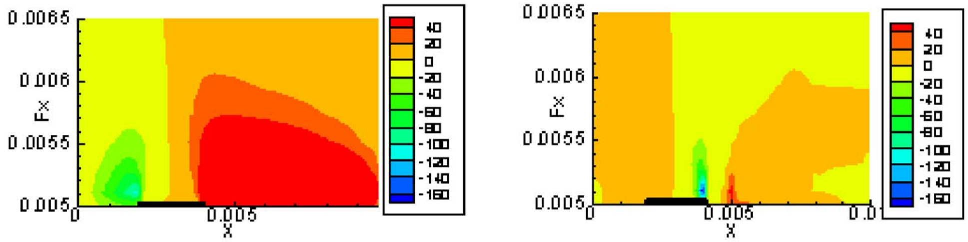

(f) Axial force contours (N/m^3) at 5KHz, $\omega t = \frac{\pi}{2}$ (g) Axial force contours (N/m^3) at 5KHz, $\omega t = \frac{3\pi}{2}$

Fig. 4 Plasma dynamics based force calculation using the electric field and number density distributions are illustrated here. Results are compared at two different time instants belonging to the opposite half-cycles. The positive force values correspond to the positive x,y axes.

10 kHz, respectively, with all other conditions remaining constant. A global time step of 10^{-8} s is used for the computations. The initial number density in the plasma is $10^{15}/\mathrm{m}^3$ for all the different species.

The homogeneous Neumann boundary condition is applied for the electrostatic potential at the open boundaries while the Dirichlet boundary condition is used at the electrode:

- At the exposed electrode: $\phi=\phi_0 \sin(2\pi f t)$, $\phi_0=1.5$ kV (Fig. 4(*a*)); and
- At the submerged electrode: $\phi=0$.

For the plasma species modeling (see Fig. 3(*b*)), the domain boundaries away from the insulator/electrode surface are assigned a zero gradient condition considering insignificant impact far away from the fluid–actuator interface. At the dielectric surface, the current continuity is enforced. This equates the transport current and the displacement current in the fluid domain to the displacement current in the insulator and can be written as

$$\frac{\partial(\varepsilon_{\mathrm{fl}}E_{\mathrm{fl}})}{\partial t} + e(n_i v_i - n_e v_e)_{\mathrm{fl}} = \frac{\partial(\varepsilon_{\mathrm{insulator}}E_{\mathrm{insulator}})}{\partial t} \tag{16}$$

The electrons are assumed to be isothermal (at 11,600 K or 1 eV) at boundaries. At the exposed electrode, the thermal flux toward the wall is considered when the drift is toward the wall and zero flux otherwise. For the ions, a zero gradient is assumed for the velocity when the drift is toward the wall and zero flux otherwise. Also, a weak secondary emission coefficient of 0.02 is used at the electrode. For the ions or the heavier species, the drift effects are significant and hence a zero gradient condition ($\partial n_i/\partial n=0$) is applied. For the neutral fluid, the insulator/electrode interface is as-

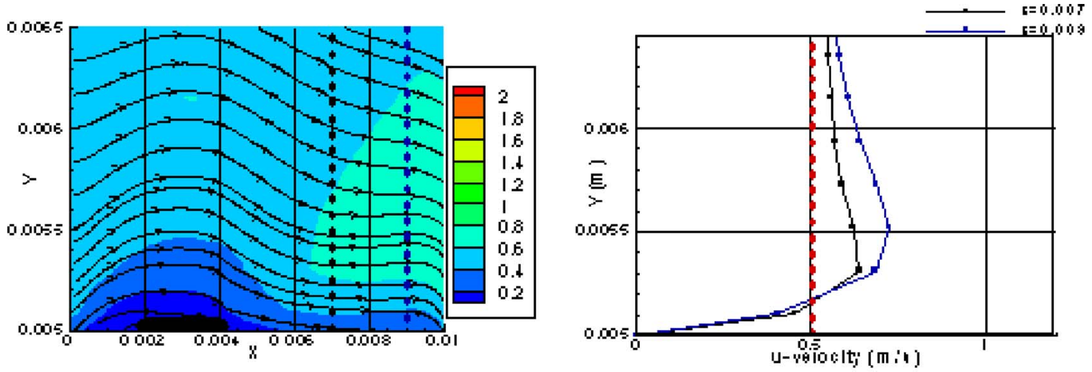

(a) Streamlines modified by the computed force field at $\omega t = \frac{\pi}{2}$ 5KHz, Re=45

(b) Velocity profiles show a distinct wall-jet type flow at the two different stations downstream of the electrode.

Fig. 5 Resulting flow field obtained from detailed plasma dynamics computed from the plasma–fluid model at the instant $\omega t=\pi/2$

signed a no-slip condition for the momentum equation. A small mass flux is specified at the left edge of the domain to simulate a low Reynolds number flow, while at the other open boundaries, a zero velocity gradient condition is imposed considering negligible impact away from the wall. The Reynolds number is chosen to be small so that the effect of the discharge-induced flow field can be sufficiently observed. The time-dependent plasma–fluid transport was solved using the solution algorithm presented above. The results exhibit qualitative similarity to those reported in Ref. [13].

In Fig. 4, we present the plasma physics by comparing the solution at two instants in time corresponding to the peak positive ($\omega t=\pi/2$) and negative ($\omega t=3\pi/2$) voltages. The resulting force described in Eq. (15) is computed based on the full field plasma simulation. The electric field (Fig. 4(*b*)) at the instant of peak positive voltage is characterized by a large positive field in the region near the inner edge of the two electrodes and a large negative field near the outer edges. The electrode–dielectric interface exhibits a discontinuity in the potential and hence the field strength on the edges is expected to be strong there. The region of strong electric field coincides with the region of strong ionization. In Fig. 4(*c*) the electric field contours at the instant of peak negative voltage ($\omega t=3\pi/2$) display the reversal of polarity, but the magnitudes are not comparable to that during the positive half-cycle. The instantaneous charge distribution is determined by the electric field dynamics. The region of substantial charge accumulation is expected to be near the electrodes and the dielectric surfaces where the field lines originate and end. In Figs. 4(*d*) and Fig. 4(*e*), the net charge species number density (i.e., n_i-n_e) is presented at the two time instants. It is clear that the bulk of the positive charge has accumulated near the dielectric surface which acts as the negative electrode for the positive half-cycle. However for the negative voltage peak, the strong negative charge accumulation is observed slightly downstream of the exposed electrode, dictated by possible residual voltage effects.

The force distribution (Eq. (15)) in the domain is a product of the net charge and the local field strength. The instantaneous electric field and charge (number density) data obtained can be used to calculate the net force field in the computational region. The axial force fields at the two time instants are calculated for 5 kHz frequency and are shown in Figs. 4(*f*) and 4(*g*). As can be seen, the region of strong force coincides with the region of peak charge density. The horizontal force for a higher frequency has been shown to result in a larger force lobe and a stronger core as compared to a low-frequency case in Ref. [13]. This is to be expected since the driving voltage fluctuations are faster in time and hence, there is a much stronger momentum transfer effect. The strong force field at the positive voltage peak is in stark contrast to the negative voltage peak where the force is relatively weak over the whole domain. This disparity in the strength of the forces between the two half-cycles when averaged over time results in a unidirectional flow effect. Now that the force field has been obtained, we can solve for the fluid flow by representing the plasma as a body force effect in the Navier–Stokes equations. In order to model this, we consider a very low Reynolds number flow ($\mathrm{Re}_L=45$) of helium gas in the domain such that the plasma induced flow is pronounced. The Reynolds number, Re_L, is calculated based on the inlet flux and the edge length of the domain (0.5 cm) as $\mathrm{Re}_L=\rho_{\mathrm{He}}V_{\mathrm{in}}L/\mu_{\mathrm{He}}$. The computed force field obtained for a frequency of 5 kHz at the instant $\omega t=\pi/2$ is used as a body force in the fluid flow momentum equations to obtain a steady-state solution of the flow field. Figure 5(*a*) shows the bending of the streamlines and the wall jet generated by the force field. The velocity profiles (Fig. 5(*b*)) indicate the large suction taking place at the top boundary in trying to correct the mass imbalance caused by the generated wall jet. This fluid dynamics effect can be used in flow control and heat transfer applications.

3.2 Assessment of Body Force Model. In order to assess the fidelity of the plasma force model [1], we compare the thrust produced with the experimental studies. A particular issue pertaining to the model is the need for using the experimental data to fix up certain empirical parameters such as the duty cycle. A detailed discussion of this study was offered in Ref. [29] and will not be reproduced here. Here, we use the force data under the quiescent

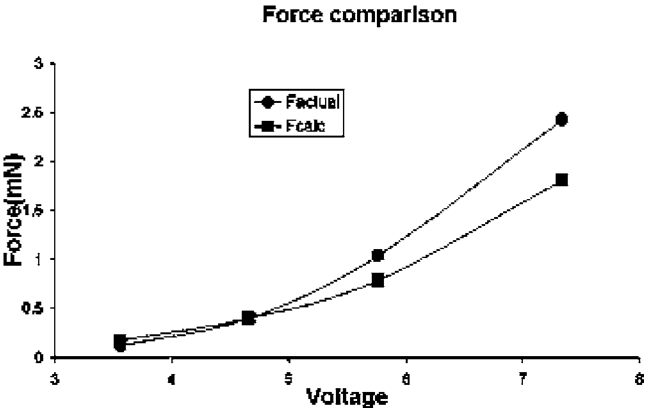

Fig. 6 Assessement of the plasma force model using experimental data

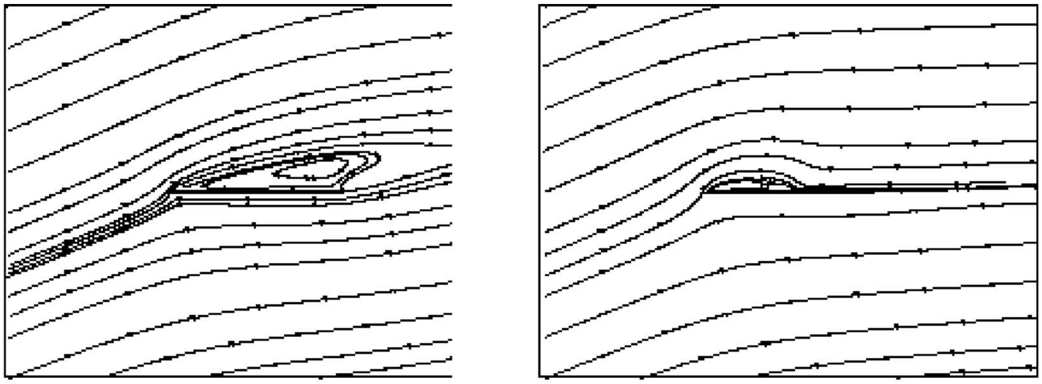

(a) Streamlines indicate flow separation over a flat plate at Re=333 and a 20° angle of attack

(b) Streamlines show separation control using a plasma actuator placed at the middle of the plate.

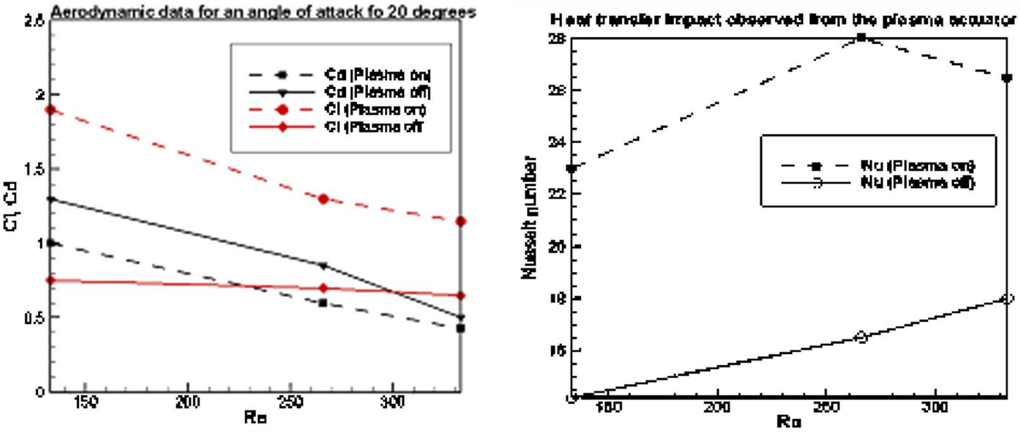

(c)Effect of the plasma actuator on the lift and drag characteristics for various Re and a 20° angle of attack.

(d)Effect of the plasma actuator on heat transfer for various Re and a 20° angle of attack.

Fig. 7 Aerodynamics and heat transfer potential of a representative plasma actuator

condition, in accordance with the experiment conducted by Van Dyken et al. [6]. In these experiments, the force measured is the shear caused by the induced flow on the contact surface in a quiescent environment. The experimental results [6] present the force generated for various voltages with an electrode 0.625 mm wide and Teflon dielectric. The comparison is shown in Fig. 6. Here the F_{actual} represents experimentally measured force while the $F_{\text{calculated}}$ represents the predicted values. Overall, the trends between the experiment and model prediction are consistent. The difference in the results is likely caused by linearization of the electric field as well as other simplifications made as shown in Sec. 1 and also in Ref. [29].

3.3 Thermo-Fluid Applications. In order to illustrate the thermo-fluid applications of the dielectric barrier plasma actuator, we will consider the effect of the plasma actuator on a low Reynolds number flow and associated heat transfer. The computational model consists of a flat plate placed in a free stream of fluid with the plasma electrode arrangement serving as an actuator being placed at the middle of the plate. The plate is 1 cm long, and the electrode is 0.5 mm long and 0.25 mm thick. The number of grid points used for the overall thermofluid dynamics simulation is 161×112. It is noted that, wherever not mentioned, the values for the voltage, frequency, and Re are 4 kV (rms), 3 kHz, and 333, respectively. For heat transfer computations, the plate was assumed to be maintained at twice the ambient flow temperature. The values of the various parameters used are

$$L = 0.01\ \text{m}; \quad \rho = 1.2\ \text{kg/m}^3; \quad U_\infty = 2{,}4 \text{ and } 5\ \text{m/s};$$

$$\text{Re}_l = 133{,}266 \text{ and } 333; \quad \mu = 1.8 \times 10^{-4}\ \text{kg/ms}$$

Figures 7(*a*) and 7(*b*) show the potential for separation control for an angle of attack of 20 deg and Re=333. The actuator is placed in the middle of the flat plate leading to a partial reduction of the separation bubble. An actuator placed at the leading edge was observed to remove separation more effectively in our previous work [2]. Figure 7(*c*) shows the lift and drag characteristics of the flat plate for various Re and a 20 deg angle of attack. There is substantial improvement in the drag for the plasma-on case. This can be attributed to significant shear drag from the wall jet as compared to the form drag for such a small flat plate. It is evident that the effectiveness of the actuator wears down with increasing inertial effects in the mean flow. In the present modeling the heat transfer is studied for various Reynolds numbers and a 20 deg angle of attack. Figure 7(*d*) presents the Nusselt number variation with angle of attack for various Reynolds numbers. In the cases considered, the heat transfer is enhanced significantly (almost doubled) when there is flow separation since the recirculation zone prevents the heat from convecting out.

4 Conclusions

A combined hydrodynamics and plasma dynamics model in the context of a discharge-induced thermofluid transport is presented. This provides a way of self-consistent modeling of the discharge effects as opposed to an analytical–empirical model previously presented [1]. The two-dimensional helium dielectric barrier discharge in an asymmetric geometry has been modeled using a finite volume operator-split sequential approach to efficiently solve the multiscale problem. The time-dependent results obtained from the plasma equation were used to calculate the body force. The resulting body force distribution displays overall qualitative agreement with the physics and observed effects. The force comparison at similar time instants in the two half-cycles exhibited dissimilar behavior, hence generating a unidirectional wall jet type fluid flow over time. The potential of the actuator in aerodynamics and surface cooling effects is illustrated. The effect of the discharge-induced wall jet reduces the separation region by half for the above discussed actuator placement. The lift coefficient showed improvement with the discharge actuation, while the drag increase was due to dominant wall shear effects. The surface heat transfer showed close to 100% increment due to the actuator.

Acknowledgment

The present effort was supported by NASA. We are delighted to have a chance to contribute to this special issue as a tribute to Professor Patankar for his pioneering contributions.

Nomenclature

n_i, n_e, ρ_c = species number density
N = abient gas number density
v_i, v_e = species velocity
ϕ = electrostatic potential
E = electric field
D = species diffusivity
M = species mass
e, q_i = species charge
ϵ_0 = permittivity of free space
K = Boltzmann constant
S_{ie} = species collision rates
ϵ_k = internal energy density
μ = species mobility
T = time period of applied voltage
F_{tave} = time averaged plasma body force

References

[1] Shyy, W., Jayaraman, B., and Anderson, A., 2002, "Modeling of Glow-Discharge Induced Flow Dynamics," J. Appl. Phys., **92**(11), pp 6434–6443.

[2] Roth, J. R., Sherman, D. M., and Wilkinson, S. P., 1998, "Boundary Layer Flow Control with a One Atmosphere Uniform Glow Discharge," *Proceedings 36th AIAA Aeropsace Sciences Meeting and Exhibit*, Reno NV, January 12–15 AIAA Paper No. 98-0328.

[3] Corke, T. C., Jumper, E. J., Post, M. L., Orlov, D., and Mclaughlin, T. E., 2003, "Application of Weakly-Ionized Plasmas as Wing Flow-Control Devices," *Proceedings 41st Aerospace Sciences Meeting & Exhibit*, Reno, NV, Jan 6–9, AIAA Paper No. 2002-0350.

[4] Enloe, C. L., Mclaughlin, T. E., Van Dyken, R., and Kachner, K. D., 2004, "Mechanisms and Responses of a Single Dielectric Barrier Plasma Actuator: Plasma Morphology," AIAA J., **42**(3), pp. 589–594.

[5] Smith, B. L., and Glezer, A., 1998, "The Formation and Evolution of Synthetic Jets," Phys. Fluids, **10**(9), pp. 2281–2297.

[6] Van Dyken, R., Mclaughlin, T. E., and Enloe, C. L., 2004, "Parametric Investigations of a Single Dielectric Barrier Plasma Actuator," *Proceedings 42nd Aerospace Sciences Meet & Exhibit*, Reno, NV, Jan 5–8, AIAA Paper No. 2004-846.

[7] Corke, T. C., and Matlis, E., 2000, "Phased Plasma Arrays for Unstaeady Flow Control," *Proceedings Fluids 2000*, Denver, CO, June 19–22, AIAA Paper No. 2000-2323.

[8] Post, M. L., and Corke, T. C., 2003, "Separation Control on High Angle of Attack Airfoil Using Plasma Actuators," *Proceedings 41st Aerospace Sciences Meeting & Exhibit*, Reno, NV, Jan 6–9, AIAA Paper No. 2003-1024.

[9] Chan, S., 2004 "The Application of Plasma and Electrohydrodynamic Control to Subsonic Cavity Flows," personal communication.

[10] Soldati, A., and Banerjee, S., 1998 "Turbulence Modification by Large-scale Organized Electro-hydrodynamic flows," Phys. Fluids, **10**(7), pp 1742-1756.

[11] Segur, P., and Massines, F., 2000, "The Role of Numerical Modeling to Understand the Behavior and to Predict the Existence of an Atmospheric Pressure Glow Discharge Controlled by a Dielectric Barrier," *Proceedings of the 13th International Conference of Gas Discharges and Their Applications*, Glasgow, Sept. 3–8, pp. 15–24.

[12] Gaitonde, D. V., Visbal, M. R., and Roy, S., 2005, "Control of Flow Past a Wing Section With Plasma-Based Body Forces," *Proceedings 36th Plasma Dynamics and Lasers Conference*, Toronto, Canada, June 6–9, AIAA Paper No. 2005-5302.

[13] Jayaraman, B., Thakur, S., and Shyy, W., 2006, "Modeling of Dielectric Barrier Discharge and Resulting Fluid Dynamics," *Proceedings 44th Aerospace Sciences Meeting* Reno, NV, January 9–12, AIAA Paper No. 2006-0686.

[14] Riley, M. E., Greenberg, K. E., Hebner, G. A., and Drallos, P., 1994 "Theoretical and Experimental Study of Low-Temperature, Capacitiviley Coupled, Radio-Frequency Helium Plasmas," J. Appl. Phys., **75**(6), pp. 2789–2798.

[15] Nitschke, T. E., and Graves, D. B., 1994, "A Comparison of Particle in Cell and Fluid Model Simulations of Low-Pressure Radio Frequency Discharges," J. Appl. Phys., **76**(10), pp. 5646–5660.

[16] Kushner, M. J., 1985, "Mechanisms for Power Deposition in $\mathrm{Ar/SiH_4}$ Capacitively Coupled RF Discharges," IEEE Trans. Plasma Sci., **14**(4), pp. 188–195.

[17] Massines, F., Ben Gadri, R., Rabehi, A., Decomps, Ph., Segur, P., and Mayoux, Ch., 1998, "Experimental and Theoretical Study of a Glow Discharge at Atmospheric Pressure Controlled by Dielectric Barrier," J. Appl. Phys., **83**(6), pp. 2950–2957.

[18] Ben Gadri, R., 1999, "One Atmospheric Glow Discharge Structure Revealed by Computer Modeling," IEEE Trans. Plasma Sci., **27**(1), pp. 36–37.

[19] Hammond, E. P., Mahesh, K., and Moin, P., 2002, "A Numerical Method to Simulate Radio-Frequency Plasma Discharges," J. Comput. Phys., **176**, pp. 402–429.

[20] Colella, P., Dorr, M. R., and Wake, D. D., 1999, "Numerical Solution of Plasma Fluid Equations Using Locally Refined Grids," J. Comput. Phys., **152**, pp. 550–583.

[21] Colella, P., Dorr, M. R., and Wake, D. D., 1999, "A Conservative Finite Difference Method for the Numerical Solution of Plasma Fluid Equations," J. Comput. Phys., **149**, pp. 168–193.

[22] Roy, S., and Gaitonde, D. V., 2005, "Modeling Surface Discharge Effects of Atmospheric rf on Gas Flow Control," *Proceedings 43rd AIAA Aeropsace Sciences Meeting*, Reno NV, Jan 10–13, AIAA Paper No. 2005-0160.

[23] Roy, S., and Gaitonde, D. V., 2005, "Multidimensional Collisional Dielectric Barrier Discharge for Flow Separation Control at Atmospheric Pressures," *Proceedings 35th AIAA Fluid Dynamics Conference*, Toronto, Canada, June 6–9, AIAA Paper No. 2005-4631.

[24] Singh, K. P., and Roy, S., 2005, "Simulation of an Asymmetric Single Dielectric Barrier Plasma Actuator," J. Appl. Phys., **98**, p. 083303.

[25] Cohen, S. D., and Hindmarsh, A. C., 1996, "CVODE, a Stiff/Nonstiff ODE Solver in C," Comput. Phys., **10**(2), pp. 138–143.

[26] Verwer, J. G., 1996, "Explicit Runge-Kutta Methods for Parabolic Partial Differential Equations," Appl. Numer. Math., **22**, pp. 359–379.

[27] Shyy, W., Thakur, S., Ouyang, H., Liu, J., and Blosch, E., 1997, *Computaional Techniques for Complex Transport Phenomena*, Cambridge University Press, Cambridge, UK.

[28] Thakur, S., Wright, J., and Shyy, W., 2002, *STREAM: A Computational Fluid Dynamics and Heat Transfer Navier-Stokes Solver: Theory and Applications*, Streamline Numerics, Inc., Gainesville, FL.

[29] Jayaraman, B., and Shyy, W., 2003, "Flow Control and Thermal Management using Dielectric Glow Discharge Concepts," *Proceedings 33rd AIAA Fluid Dynamics Conference and Exhibit*, Orlando, FL, June 23–26, AIAA Paper No. 2003-3712.

Modeling Full-Scale Monolithic Catalytic Converters: Challenges and Possible Solutions

Sandip Mazumder
Mem. ASME
Department of Mechanical Engineering,
The Ohio State University,
Columbus, OH 43210
e-mail: mazumder.2@osu.edu

Modeling full-scale monolithic catalytic converters using state-of-the-art computational fluid dynamics algorithms and techniques encounters a classical multiscale problem: the channels within the monolith have length scales that are ~1–2 mm, while the converter itself has a length scale that is ~5–10 cm. This necessitates very fine grids to resolve all the length scales, resulting in few million computational cells. When complex heterogeneous chemistry is included, the computational problem becomes all but intractable unless massively parallel computation is employed. Two approaches to address this difficulty are reviewed, and their effectiveness demonstrated for the computation of full-scale catalytic converters with complex chemistry. The first approach is one where only the larger scales are resolved by a grid, while the physics at the smallest scale (channel scale) are modeled using subgrid scale models whose development entails detailed flux balances at the "imaginary" fluid–solid interfaces within each computational cell. The second approach makes use of the in situ adaptive tabulation algorithm, after significant reformulation of the underlying mathematics, to accelerate computation of the surface reaction boundary conditions. Preliminary results shown here for a catalytic combustion application involving 19 species and 24 reactions indicate that both methods have the potential of improving computational efficiency by several orders of magnitude.

[DOI: 10.1115/1.2709655]

Keywords: CFD modeling, catalytic converter, multi-scale, subgrid model, ISAT, catalytic combustion

1 Introduction

Despite tremendous progress in computer technology over the past 2 decades, simulation of full-scale catalytic converters remains elusive. With existing computational fluid dynamics (CFD) techniques, such simulations require extreme computational resources. A thorough review of the literature failed to reveal a single instance where a three-dimensional industrial-scale catalytic converter with realistic chemistry has been modeled using conventional CFD techniques. On the other hand, numerous publications on CFD modeling of a single channel of the monolith exist (Ref. [1] and the references cited therein). Currently, due to lack of better alternatives, the knowledge gained from the simulation of a single channel is extrapolated to the entire catalytic converter. Since the channels are coupled to each other through heat transfer, and individual channels may encounter different flow rates, extrapolation of the results of a single channel to the entire converter is dangerous and may lead to flawed designs [2]. In recent years, in realization of the need to address variations of flow and temperature from channel to channel, attempts have been made to model a "representative" number of channels rather than a single one, and the results have been coupled through network-type models [2]. While such an approach is an improvement over modeling a single channel, the robustness and accuracy of such an approach remains questionable.

The core of a simple cylindrical catalytic converter is shown in Fig. 1. It is comprised of a honeycomb monolithic ceramic structure whose inner surfaces are coated with a catalyst. Reactants flow through the small channels and undergo catalytic conversion. Modeling of catalytic converters is made complicated by the fact that the channels within the monolith have a characteristic width of ~1–2 mm, while the full converter has a diameter of ~5–10 cm. Surface reactions occur at the surfaces of the monolith channels. With conventional CFD techniques, each channel must be resolved by a grid if the physics within the boundary layer next to the reacting surface is to be captured. If a coarse 10×10 mesh is used to resolve the cross section of each channel, a converter with 5 cm diameter will require ~50,000 cells in each cross-sectional plane. A moderately coarse mesh with ~100 points along the direction of flow will result in ~5 million grid cells. This simple estimate reveals that flow calculations alone will require significant computational effort for such geometries, and is clearly beyond the capability of a single-processor computer.

The inclusion of surface chemistry in such simulations complicates matters exponentially. The treatment of surface chemistry requires solution of a set of stiff nonlinear differential algebraic equations (DAE), representative of the balance between reaction and diffusion, at each boundary face and at each iteration/time step. If a catalytic converter has a diameter of 5 cm, and channel cross-sectional dimensions of 2 mm × 2 mm, there will be roughly 500 channels in the converter. If each channel has a grid density of 10×10 (across cross section) $\times 100$ (along length), the total number of boundary faces on which surface reactions have to be computed is $4\times 10\times 100\times 500=2\times 10^6$ faces. These calculations will have to be performed at each iteration, and experience shows that a three-dimensional steady state calculation of this type reqires ~1000 global iterations for all conservation equations to converge adequately. This implies that the reaction–diffusion balance equation for computing fluxes due to surface reaction need to be solved $2\times 10^6\times 1000=2\times 10^9$ times. Based on the author's own calculations, if simplistic chemistry with just five species and five reaction steps is considered, the CPU time taken for a single solution of the reaction–diffusion balance equation is approximately 0.4 ms on a 3 GHz Intel Pentium processor, which

---

Contributed by the Heat Transfer Division of ASME for publication in the Journal of Heat Transfer. Manuscript received March 27, 2006; final manuscript received July 24, 2006. Review conducted by Jayathi Murphy.

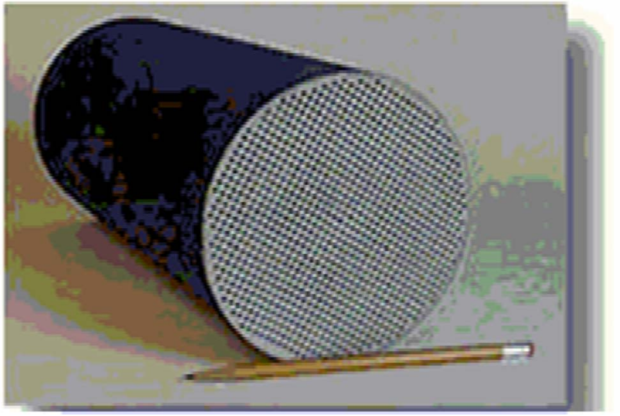

Fig. 1 Monolithic core of a catalytic converter

implies that the surface chemistry calculations alone for this particular problem will require approximately 200 h. With realistic chemistry described by approximately 10–20 species and 10–20 reaction steps, such calculations can be performed within reasonable time frame (1 week or less) only if massively parallel computations are employed.

The preceding estimate clearly points to the fact that simulation of full-scale catalytic converters using conventional CFD techniques will require impractically large computational resources and time. In this paper, two approaches that make simulation of full-scale catalytic converters with complex chemistry feasible are discussed and demonstrated. The first approach, subgrid scale modeling, has witnessed tremendous success in other disciplines such as large eddy simulation of turbulence, and modeling of porous media. The second approach, strictly mathematical in nature, employs the idea of storing results of chemistry calculations in a binary look-up table in situ and adaptively, and reusing that information later when deemed appropriate. The in situ adaptive tabulation (ISAT) algorithm [3] has witnessed tremendous success in the treatment of homogeneous reactions, especially in the context of probability density function (PDF) methods for reacting turbulent flows. Here, the basic ISAT algorithm, after significant modifications of the underlying mathematical formulations to adapt it to heterogeneous reactions, is being used. The results presented here are only preliminary proof-of-concept results, meant to show that both methods hold considerable promise. It is hoped that these results will trigger sufficient interest and curiosity among active researchers in this area so that further research is continued along the directions outlined in this paper, and the ultimate objective is met with within a relatively short period of time.

2 Mathematical Model for Direct Simulation

Prior to discussion of algorithms and models to enhance efficiency, it is necessary to discuss the governing equations (and accompanying boundary conditions) that one would need to solve in the context of a full-fledged CFD calculation in which all length scales are resolved by a grid. These equations will lay the foundation for development of the subgrid scale models, to be discussed in later sections. Another motivation for detailed discussion of the governing equations is that in catalytic conversion applications, diffusive transport of mass is critical. Reacting flow formulations outlined in various textbooks and published articles pay little or no attention to diffusive (molecular) transport of species since turbulent transport dominates in the vast majority of applications of such flows. Thus, there is a need to critically assess commonly used formulations for the treatment of mass transport in low Péclet number multicomponent systems, as prevalent in catalytic conversion applications.

2.1 Governing Equations.

The governing equations are the equations of conservation of mass (both overall and individual species), momentum and energy, and are written as [4–6]

Overall mass

$$\frac{\partial}{\partial t}(\rho) + \nabla \circ (\rho \mathbf{U}) = 0 \tag{1}$$

Momentum

$$\frac{\partial}{\partial t}(\rho \mathbf{U}) + \nabla \circ (\rho \mathbf{U}\mathbf{U}) = -\nabla p + \nabla \circ \boldsymbol{\tau} + \rho \mathbf{B} \tag{2}$$

Energy

$$\frac{\partial}{\partial t}(\rho h) + \nabla \circ (\rho \mathbf{U} h) = -\nabla \circ \mathbf{q} + \dot{S}_h \tag{3}$$

Species mass

$$\frac{\partial}{\partial t}(\rho Y_k) + \nabla \circ (\rho \mathbf{U} Y_k) = -\nabla \circ \mathbf{J}_k + \dot{S}_k \quad \forall\, k = 1,2,\ldots,N \tag{4}$$

where ρ is the mixture density; p is the pressure; $\boldsymbol{\tau}$ is the shear stress tensor; and $\mathbf{B}$ is the body force vector. Equations (1) and (2) are the well known Navier–Stokes equations, and need no further discussion. In Eq. (4), Y_k is the mass fraction of the kth species, $\mathbf{J}_k$ is the mass diffusion flux of the kth species, and $\dot{S}_k$ is the production rate of the kth species due to homogeneous chemical reactions. The total number of gas-phase species in the system is denoted by N. In Eq. (3), $\dot{S}_h$ represents the net source due to viscous dissipation and other work and heat interactions, and $\mathbf{q}$ denotes the net heat flux due to molecular conduction, radiation, and interspecies diffusion, and is written as [4]

$$\mathbf{q} = \mathbf{q}_C + \mathbf{q}_R + \mathbf{q}_D = -k_c \nabla T + \mathbf{q}_R + \sum_{k=1}^{N} \mathbf{J}_k h_k \tag{5}$$

where h_k is the enthalpy of the kth species; k_c is the thermal conductivity of the mixture; and h is the enthalpy of the mixture $(=\sum_{k=1}^{N} h_k Y_k)$. The heat flux due to interdiffusion of species, $\mathbf{q}_D$, is often neglected in reacting flow formulations without any justification. In many practical applications of multispecies flows, this term can be comparable or larger than the Fourier conduction flux $\mathbf{q}_C$, and can result in net heat flux that is opposite in direction to the imposed temperature gradient [7]. In the above formulation, the enthalpy of the kth species, h_k, includes the enthalpy of formation and the sensible enthalpy, and is written as

$$h_k(T) = h_{f,k}^0 + \int_{T_0}^{T} c_{p,k}(T)\,dT \tag{6}$$

where $h_{f,k}^0$ is the enthalpy of formation of species k at the standard state; and $c_{p,k}$ is the specific heat capacity of species k. The species enthalpy is generally computed using standard thermodynamic databases, such as the JANNAF database.

Equation (1) can be derived from Eq. (4) if and only if the following two constraints are satisfied: at any point in space

$$\sum_{k=1}^{N} Y_k = 1 \tag{7}$$

at any arbitrary cutting plane

$$\sum_{k=1}^{N} \mathbf{J}_k \circ \hat{\mathbf{n}} = 0 \tag{8}$$

where $\hat{\mathbf{n}}$ is the surface normal to the cutting plane in question. Equation (7) is generally enforced either by solving only N-1 equations from the set in Eq. (4), and then using Eq. (7) directly to determine the mass fraction of the last species, or by normalizing the calculated mass fractions by their sum, resulting in an indirect correction strategy. In diffusion dominated (i.e., low mass transport Peclet number) systems, nonsatisfaction of the constraint given by Eq. (8) results in a serious inconsistency. The inconsistency is a result of the fact that the sum of the species conservation equations over all species does not result in the continuity equation [Eq. (1)]. Rather, it results in a continuity equation with a spurious mass source.

In general, the mass diffusion flux, $\mathbf{J}_k$, includes diffusion due to concentration gradients, temperature gradients (Soret diffusion), and pressure gradients (pressure diffusion) [4]. Here, only mass transport due to concentration gradients is considered for the sake of simplicity. The most common approach for modeling diffusive transport of species due to concentration gradients is to use the Fick's law of diffusion. In a binary system, consisting of Species A and B, the diffusion flux is accurately described by the Fick's law of diffusion [4]

$$\mathbf{J}_A = -\rho \mathcal{D}_{AB} \nabla Y_A, \quad \mathbf{J}_B = -\rho \mathcal{D}_{BA} \nabla Y_B \tag{9}$$

where $\mathcal{D}_{AB}$ is the binary diffusion coefficient of Species A into B; and is equal to $\mathcal{D}_{BA}$, which is the binary diffusion coefficient of Species B into A. Using the mass fraction summation constraint [Eq. (7)], it can be readily shown that $\mathbf{J}_A = -\mathbf{J}_B$, i.e., Eq. (8) is automatically obeyed. The same law, when used for multicomponent systems with more than two species, leads to violation of mass conservation due to nonsatisfaction of the constraint given by Eq. (8).

In a multicomponent system, diffusion is best described by the Stefan–Maxwell equation [4], which implicitly relates molar fluxes of species to mole fraction gradients

$$\nabla X_i = \frac{M}{\rho} \sum_{\substack{j=1 \\ j \neq i}}^{N} \left(\frac{X_i \mathbf{J}_j}{M_j D_{ij}} - \frac{X_j \mathbf{J}_i}{M_i D_{ij}} \right) \tag{10}$$

where M is the mixture molecular weight; M_k is the molecular weight of the kth species; and X_k is the mole fraction of the kth species. The Stefan–Maxwell equation has been formulated in such a manner that Eq. (8) is satisfied for an arbitrary multicomponent system. Unfortunately, it can only be used for pure diffusion problems, and is not amenable for use in a CFD framework since it is not an equation of the generalized advection–diffusion form. Upon significant manipulation, Eq. (10) can be rewritten as [8,9]

$$\mathbf{J}_k = -\rho \frac{M_k}{M^2} \sum_{n=1}^{N} M_n D_{\text{kn}} \nabla X_n \tag{11}$$

where D_{kn} is the ordinary multi-component diffusion coefficient [4,10], and is different from the binary diffusion coefficient $\mathcal{D}_{kn}$. Specifically, while the binary diffusion coefficients are independent of the mole fractions, the ordinary multicomponent diffusion coefficients are strong nonlinear functions of the mole fractions. Also, it is worth noting that while $D_{kk}=0$, $D_{kn} \neq D_{nk}$. The ordinary multicomponent diffusion coefficients can be computed using well-known relationships [4,10,11]. Equation (11) essentially states that in a multicomponent system, diffusion of a certain species is governed not only by its own concentration gradient, but also the concentration gradient of the other species in the system.

In a reacting flow, mass is always conserved while moles are not. Thus, it is advantageous to rewrite Eq. (11) in terms of mass fractions rather than mole fractions. Using the conversion relation $Y_k = X_k M_k / M$, Eq. (11) may be written as [8,9]

$$\mathbf{J}_k = -\rho \sum_{n=1}^{N} \Gamma_{\text{kn}} \nabla Y_n \tag{12}$$

where Γ_{kn} is a new tensor, written as [8,9]

$$[\Gamma] = -\frac{1}{M^2}[M][D][M][C] \tag{13}$$

In Eq. (13), $[M]=\text{diag}[M_1, M_2, \ldots, M_N]$; $[D]$ is the matrix notation for the ordinary multicomponent diffusion tensor D_{kn}; and $[C]$ the Jacobian of the transformation between mass and mole fraction, and is written as

$$C_{\text{kn}} = \left(\delta_{\text{kn}} - Y_k \frac{M}{M_k} \right) \frac{M}{M_n} \tag{14}$$

where δ_{kn} is the Kronecker delta. Substitution of Eq. (12) in Eq. (4) yields

$$\frac{\partial}{\partial t}(\rho Y_k) + \nabla \circ (\rho \mathbf{U} Y_k) = \nabla \circ \left(\rho \sum_{n=1}^{N} \Gamma_{\text{kn}} \nabla Y_n \right) + \dot{S}_k \quad \forall\, k = 1, 2, \ldots, N \tag{15}$$

Equation (15) represents the governing equation for species transport in a multicomponent system. It satisfies the constraint posed by Eq. (8) automatically. It is important to note at this point that even in the absence of any homogeneous chemical reactions (i.e., $\dot{S}_k=0$), the mass fractions of the individual species are tightly coupled through the diffusion operator. Thus, the segregated solution (i.e., one species at a time) of the equations represented by Eq. (15) has inherent instabilities associated with it. Details pertaining to these numerical issues may be obtained from Ref. [9] and are not discussed here for the sake of brevity.

2.2 Boundary Conditions.

The boundary conditions for the mass and momentum conservation equations are the no-slip conditions at walls, and appropriate mass flux or pressure boundary conditions at inflow and outflow boundaries. These boundary conditions and their numerical implementation are well known and need no further discussion. The focus of this subsection is the boundary conditions for species and energy associated with heterogeneous chemical reactions at fluid–solid interfaces.

At a reacting surface, the diffusion flux of species is balanced by the reaction flux since the surface cannot store any mass. At the heart of surface reaction processes is adsorption and desorption of species at the surface, the treatment of which requires inclusion of so-called surface-adsorbed species [12]. At steady state, the net production rate of the surface-adsorbed species is zero. In the absence of etching or deposition of material from the surface (i.e., zero Stefan flux), the reaction–diffusion balance equation at the surface may be written as [12,13]

$$\mathbf{J}_k \circ \hat{\mathbf{n}} = M_k \dot{R}_k \quad \forall\, k \in \text{ gas-phase species} \tag{16a}$$

$$\dot{R}_k = \begin{cases} d\Lambda_k/dt & \text{for unsteady} \\ 0 & \text{for steady} \end{cases} \quad \forall\, k \in \text{ surface-adsorbed species} \tag{16b}$$

where $\dot{R}_k$ is the molar production rate of species k due to heterogeneous chemical reactions; Λ_k is the molar concentration of species k at the fluid–solid interface; and $\hat{\mathbf{n}}$ is the outward unit surface normal. Since $\dot{R}_k$ is an extremely nonlinear function of the molar concentrations (or mass fractions) [12,13], Eq. (16) represents a nonlinear set of DAEs. The solution of this stiff set of nonlinear DAE is generally obtained using the Newton method, but requires special preconditioning to address stiffness and ill-posedness in the case of steady-state solutions. Details pertaining to these numerical issues may be found elsewhere [13]. The solution of Eq. (16) provides the near-wall mass fractions and mass fluxes (represented by the left-hand side of Eq. (16*a*)) of all gas-phase species, which appear as sources/sinks for control volumes adjacent to the surface in a finite-volume formulation [13].

The balance of energy at the surface yields the following equation

$$\left(-k\nabla T+\mathbf{q}_R+\sum_{k=1}^{N}\mathbf{J}_k h_k\right)_F\circ\hat{\mathbf{n}}=(-k\nabla T+\mathbf{q}_R)_S\circ\hat{\mathbf{n}} \tag{17}$$

where the subscript "F" denotes quantities on the fluid–side of the fluid-solid interface, while the subscript "S" denotes quantities on the solid side of the same interface. The solution of Eq. (17), which is also a nonlinear equation, yields the temperature at the fluid–solid interface, and subsequently provides the flux of energy at the interface, which can then be used as a source/sink for the cells adjacent to the interface after appropriate linearization. In this enthalpy formulation, the heat of surface reaction actually manifests itself through the $\Sigma\mathbf{J}_k h_k$ term—another reason why the energy carried by species interdiffusion should never be neglected for such applications.

Equations (1)–(3) and (15), when solved along with the appropriate boundary conditions described in the preceding subsection, will produce flow, temperature, and mass fraction distributions of all species within the entire catalytic converter. A prerequisite to the use of these equations is that the computational grid must be fine enough to resolve the individual channels within the monolith. Otherwise, the boundary conditions to describe heterogeneous reactions at the fluid–solid interface cannot be applied. If the grid is sufficiently fine, no other models are necessary to obtain a solution. As discussed earlier, sufficient resolution demands use of several million computational cells making such direct calculations prohibitively expensive. In the section to follow, two different approaches to make such calculations feasible are described.

3 Algorithms for Efficiency Enhancement

Estimates provided earlier clearly indicate that simulation of full-scale catalytic converters with realistic chemistry will require orders of magnitude improvement over the state-of-the-art. Two different approaches are employed to achieve this goal. The first approach, subgrid scale modeling, is employed to address difficulties associated with modeling transport phenomena and heterogeneous reactions at multiple scales. The second approach, ISAT, is used to accelerate calculation of the surface reactions. Although not demonstrated here, these two algorithms can be used in tandem to derive greatest computational gains. This section presents these two approaches.

3.1 The Subgrid Scale Modeling Approach. The fundamental premise behind this approach is that the computational grid will only resolve the largest length scales, and the physics at the smallest (channel or pore) scale will be modeled using subgrid scale (i.e., scale smaller than the grid size) models. The first step in the development of the mathematical model using this approach is to perform a volume average of the governing conservation equations at the pore scale over a representative elemental volume (REV). This REV must be smaller than the grid scale but significantly larger than the smallest length scale of the problem—that being the width of the monolith channels in this particular case (Fig. 2). Upon volume averaging, the governing equations of conservation of mass, momentum, energy, and species are as follows [14–16]

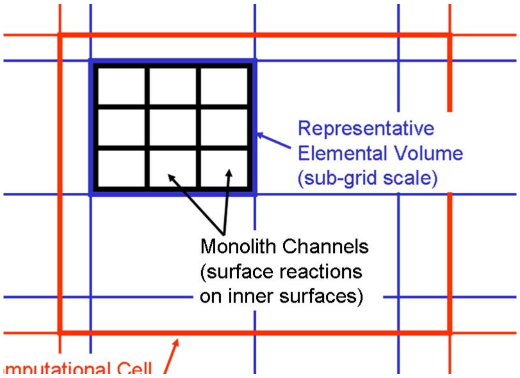

Fig. 2 The various length scales within a monolithic catalytic converter (cross-sectional view shown in figure), their relationship, and the idea behind the subgrid scale modeling approach

Mass

$$\frac{\partial}{\partial t}(\varepsilon\rho)+\nabla\circ(\varepsilon\rho\mathbf{U})=\mathbf{0} \tag{18}$$

Momentum

$$\frac{\partial}{\partial t}(\rho\varepsilon\mathbf{U})+\nabla\circ(\rho\varepsilon\mathbf{U}\mathbf{U})=-\varepsilon\nabla p+\nabla\circ(\mu_{\mathrm{eff}}\nabla\mathbf{U})-\mu\varepsilon[\mathbf{K}]^{-1}\mathbf{U} \tag{19}$$

Energy

$$\frac{\partial}{\partial t}[\rho_s(1-\varepsilon)h_s+\rho\varepsilon h]+\nabla\circ(\rho\varepsilon\mathbf{U}h)=-\nabla\circ\left(-k_{\mathrm{eff}}\nabla T+\sum_{i=1}^{N}\mathbf{J}_{i,\mathrm{eff}}h_i+\langle\mathbf{q}_R\rangle\right)+\langle\dot{S}_h\rangle+\langle\dot{R}_h\rangle \tag{20}$$

Species

$$\frac{\partial}{\partial t}(\rho\varepsilon Y_k)+\nabla\circ(\rho\varepsilon\mathbf{U}Y_k)=-\nabla\circ\mathbf{J}_{k,\mathrm{eff}}+\langle\dot{S}_k\rangle+\langle\dot{R}_k\rangle \quad \forall\, k=1,2,\ldots,N \tag{21}$$

where ε is the porosity, and is defined as the volume of pores to the total volume. Volume averaging of the pore-scale governing equations results in additional terms that arise out of the physics at the smallest scales. For example, volume averaging of the Navier–Stokes equation results in the so-called Darcy–Forchheimer–Brinkman equation [14,15], in which, additional terms arise out of modeling the frictional drag at the smallest scales. Equation (19) shows a simplified version of this equation, in which the nonlinear Forchheimer term has been neglected, and the last term is the linear Darcy term written in generalized tensor form. Dispersion is neglected here since the geometry under consideration here is comprised of straight parallel channels. Dispersion results from the interaction between microvortices (smaller in scale than the REV) shed by various parts of the random porous structure. Such effects are absent in this particular case since the channels walls are impermeable to flow and mass diffusion, and the fluid within each channel does not communicate. The last term in the energy equation, $\langle\dot{R}_h\rangle$, is the net volumetric production rate of heat due to surface reactions, averaged over an REV. The last term in the species transport equation, $\langle\dot{R}_k\rangle$, represents the average production rate of species k within an REV due to heterogeneous reactions. Once again, it is an artifact of the volume averaging process, and would be absent if the computational grid resolved the smallest scales, as evident from the equations presented in Sec. 2. In deriving Eq. (20) local thermal equilibrium between the fluid and solid phase has been assumed, and the mixed phase is assumed to have a single temperature T. In addition to the birth of additional terms in the governing equations, all transport properties to be used are effective volume-averaged properties, denoted by the subscript "eff."

Accuracy of the subgrid scale modeling approach depends, in large part, on how well these unclosed terms in the volume-averaged governing equations are modeled, and how closely these subgrid scale models mimic the actual physical phenomena occurring at the smallest scales. Specific details, pertaining to the development of the subgrid scale models for momentum, energy, and species are discussed next.

3.1.1 Closure of the Momentum Equation. Volume averaging of the momentum equation results in an additional Darcy term, represented by the last term in Eq. (19). It represents the drag force acting on the fluid due to viscous effects at the smallest (subgrid) scales. In this case, volume averaging results in two unknown parameters, namely the porosity, ε, and the permeability, $\mathbf{K}$ [14]. The porosity is the ratio of the volume of pores to the total volume, and can directly be obtained from the geometry of the monolith. The permeability, $\mathbf{K}$, is proportional to the square of the volume to surface ratio. Since it is tensor, the drag force acting at the subgrid scale may be different in different directions. For the case of straight-channel monoliths, the drag (or resistance to flow) in the cross-flow direction will be infinite since no mass transfer can occur from channel to channel due to advection. Thus, the permeability is zero in the cross-flow direction, and only one component of the permeability tensor (assuming that the off-diagonal components are also zero) in the direction of the flow has to be determined to attain closure of the volume-averaged momentum equation. For one-dimensional flow, Darcy's law states that the pressure drop per unit length, is inversely proportional to the permeability [14]: $\Delta p/L = \mu U/K$. In general, for a porous medium, if experimental data for pressure drop is available, the permeability can be calibrated for various flow velocities to fit the pressure drop data. In the case of straight-channel monoliths experimental data is not necessary and the permeability can be obtained by matching data generated using direct numerical simulation using the following procedure:

1. First a CFD simulation of a single channel of the monolith is performed, in which the channel and its walls is completely resolved by a mesh, i.e., direct numerical simulation;
2. From this simulation, the pressure drops along the length, including exit and entrance losses is computed for various flow velocities;
3. The single channel will then be replaced by a porous medium, and a set of simulations with various permeability values is performed with the goal to match the pressure drops obtained using the direct numerical simulations; and
4. The permeability data fitted using the least squares approach since a single value that best fits the data for several different flow velocities is desired.

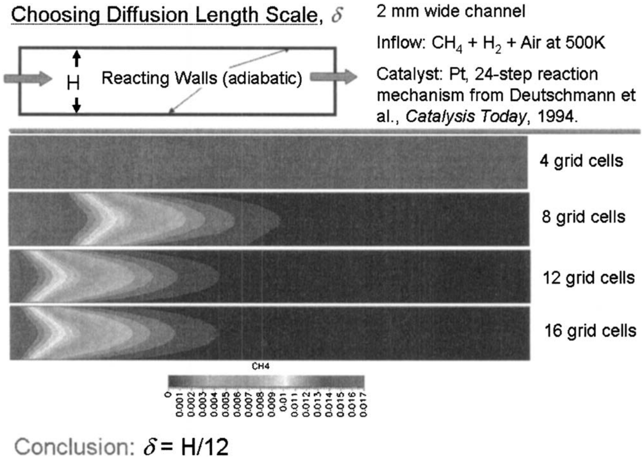

Fig. 3 Procedure for determining the diffusion length scale, δ

3.1.2 Closure of Species and Energy Transport Equations. Closure of the volume-averaged energy and species transport equations is attained by considering detailed flux balance of energy and species at the pore scale, and subsequently, by performing a summation over an REV (Fig. 2). Balance of mass flux for gas-phase species at the reacting surface is represented by Eq. (16*a*). Substitution of Eq. (12) into Eq. (16*a*) followed by discretization yields

$$\left[-\rho\sum_{n=1}^{N}\Gamma_{\mathrm{kn}}\left(\frac{Y_{n,C}-Y_{n,I}}{\delta}\right)\right] = M_k\dot{R}_k(\underline{Y}) \quad \forall\, k \in \text{ gas-phase species} \tag{22}$$

where $Y_{n,I}$ is the mass fraction of species n at the fluid–solid interface, and $Y_{n,C}$ is the mass fraction of species n at a normal distance δ away from the interface. δ represents a characteristic diffusion length scale. If the computational mesh resolves the channels, $Y_{n,C}$ represents the mass fraction of species n at the cell center adjacent to the interface, and δ the normal distance between the interface and the cell center adjacent to it (using a first-order approximation). In the context of subgrid scale models, the channel is not resolved by a computational mesh, and therefore, δ has to be estimated. The most rigorous procedure for determining δ is to perform a separate pore-scale calculation with increasing number of grid points across the channel until the solution becomes grid independent. The grid spacing between the wall and the adjacent cell is then an appropriate measure of δ, and ascertains that the value used within the subgrid model exactly recovers the results of direct calculations. The idea is depicted in Fig. 3. While it is perfectly justifiable (i.e., answers will remain unaltered) to use an arbitrarily small value for δ, in lieu of the procedure just described, such a choice would make the system of equations unnecessarily stiff. Once δ has been estimated, Eqs. (22) and (16*b*) can be solved to determine the mass fractions or molar concentrations of all species at the "imaginary" fluid–solid interfaces. The local flux of each species due to surface reaction can then be determined, and the average volumetric production rate of each species due to heterogeneous reactions, $\langle\dot{R}_k\rangle$, can be obtained using

$$\langle\dot{R}_k\rangle = \left[-\rho\sum_{n=1}^{N}\Gamma_{\mathrm{kn}}\left(\frac{Y_{n,C}-Y_{n,I}}{\delta}\right)\right]\left(\frac{S}{V}\right)_{\mathrm{eff}} \tag{23}$$

where $(S/V)_{\mathrm{eff}}$ is the effective surface area on which the catalytic reactions occur per unit volume of the catalyst monolith. The effective surface to volume ratio is a true representation of catalyst loading [16]. The maximum effective surface to volume ratio is the geometrically available surface to volume ratio and represents 100% catalyst loading. If only part of the geometrically available surface is coated with the catalyst, the effective surface to volume ratio will be much smaller. In the particular case of straight-channel monoliths, the geometric surface to volume ratio can be computed directly using the available geometric dimensions. In order to estimate the effective surface to volume ratio, additional information pertaining to the catalyst loading is necessary, and certain approximations need to be made concerning the composition of the catalyst washcoat. An example is shown in Fig. 4. A similar procedure is also implemented to solve Eq. (17) at the subgrid scale and determine the net heat source $\langle\dot{R}_h\rangle$.

From the preceding discussion it is clear that the development of the subgrid scale models and the fitting of unknown parameters involve some assumptions and approximations. Thus, results obtained using subgrid scale models will not exactly match results of direct numerical simulation. On the positive side, in addition to being computationally very efficient, subgrid scale models offer the advantage that additional small-scale physical phenomena can

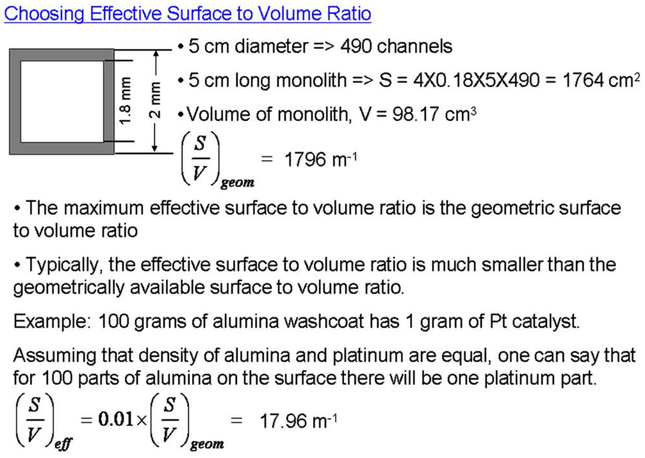

Choosing Effective Surface to Volume Ratio

- 5 cm diameter => 490 channels
- 5 cm long monolith => S = 4X0.18X5X490 = 1764 cm^2
- Volume of monolith, V = 98.17 cm^3

$$\left(\frac{S}{V}\right)_{geom} = 1796 \text{ m}^{-1}$$

- The maximum effective surface to volume ratio is the geometric surface to volume ratio
- Typically, the effective surface to volume ratio is much smaller than the geometrically available surface to volume ratio.

Example: 100 grams of alumina washcoat has 1 gram of Pt catalyst.

Assuming that density of alumina and platinum are equal, one can say that for 100 parts of alumina on the surface there will be one platinum part.

$$\left(\frac{S}{V}\right)_{eff} = 0.01\times\left(\frac{S}{V}\right)_{geom} = 17.96 \text{ m}^{-1}$$

Fig. 4 Procedure for determining the effective surface to volume ratio $(S/V)_{\mathrm{eff}}$

be included with relative ease in comparison to direct simulations. For example, phenomenon such as diffusion through the washcoat is easily implemented by adding a diffusion resistance to the existing diffusion formulation.

3.2 Acceleration of Surface Chemistry Calculations.

Profiling of the code during direct numerical simulation of catalytic converters revealed that more than 50% of the overall CPU time is spent in solving the reaction–diffusion flux balance equation [Eq. (16)] at the surface if the surface reaction mechanism involves more than ten species. Many applications of catalytic conversion, such as NOx removal using three-way catalysts, involve extremely complex surface chemistry. In such cases, the reaction mechanism may involve several tens of reactions and several tens of species (see for example Ref. [17]), and the surface reaction calculations may consume more than 90% of the overall CPU time. Thus, computation of the surface reaction boundary condition is a major bottleneck in the overall computational algorithm if sufficiently realistic reaction mechanisms are used. Consequently, it is logical to devote attention to develop algorithms that will significantly enhance the efficiency of these calculations.

Difficulties, similar to the ones just described, arise in the treatment of homogeneous reactions, as well. Over the past two decades, several approaches have been developed to address this issue in the context of homogeneous reactions. Notable amongst these approaches are: (1) genetic algorithms (GAs) [18–23]; (2) artificial neural networks (ANNs) [24,25]; (3) high dimensional model representation (HDMR) [26–28]; (4) intrinsic low-dimensional manifolds (ILDMs) [29–33]; and (5) in ISAT [3,34–44]. A detailed discussion of these methods and their pros and cons is beyond the scope of this paper. It should suffice to say here that of the five methods, the first four require generation of an initial dataset or population to generate low-dimensional models that are ultimately employed to accelerate the chemistry calculations. In other words, the first four methods require preprocessing, and therefore, lack portability. For example, if an additional reaction step is added or an existing step is altered, the initial dataset generation and the "training" of the reduced model has to be performed from groundup. In contrast, the in situ adaptive tabulation method does not require any preprocessing. The algorithm works in situ, rendering it portable and extremely flexible in terms of its capabilities.

The ISAT algorithm was developed by Pope [3] to enable inclusion of detailed chemistry in turbulent combustion calculations using the PDF transport method [45]. In the PDF method, the governing PDF transport equation is solved using a Monte Carlo technique in which the state of a stochastic particle is marched forward in time using a set of ordinary differential equations in time. The composition of the stochastic particles changes due to homogeneous reactions and turbulent transport (or mixing) and these two processes are treated sequentially. The initial conditions encountered by these stochastic particles, of which several hundred thousand need to be traced, are often similar. This led to the ISAT algorithm, in which instead of computing the reaction sources for each particle, the results are stored in situ, and reused later if another particle encounters a similar set of initial conditions. The data are stored in a hyperdimensional binary table, in which errors due to interpolation are adaptively controlled.

While the ISAT algorithm was originally developed to avoid repetitive solution of the initial value problem, just described, it is equally applicable to other types of mathematical models, such as ones that involve repetitive solution of nonlinear algebraic equations, ordinary differential equations, or a combination thereof. The ISAT algorithm was recently adapted for heterogeneous chemistry [46] by developing a new formulation for the treatment of DAE systems rather than the initial value problem for which ISAT was originally developed. This algorithm will henceforth be referred to as ISAT-S, briefly described below. Extensive details on this algorithm may be obtained from Ref. [46]. In what follows, only a brief description of the algorithm is provided for the sake of completeness.

The solution of Eq. (16) ultimately reduces to finding the roots of a set of nonlinear algebraic equations of the general form $f_i(\bar{\phi})=0$, where $\bar{\phi}$ is the vector of outputs in the problem. The number of outputs must be equal to the number of equations, and is denoted by n. The solution of the equation $f_i(\bar{\phi})=0$ will depend on the specific value(s) of the parameter(s) in the equation. For example, in this particular case, the solution of Eq. (16) will depend on the wall temperature, which is treated as an input parameter. Let the parameters (or inputs) be denoted by the vector $\bar{\psi}$, of length m, such that the number of independent inputs is m. If the set of outputs $\bar{\phi}_0$ are known for a certain set of inputs $\bar{\psi}_0$ through a direct calculation, then we can seek the change in the outputs caused by changes in the inputs using a Taylor series expansion [46]

$$\begin{aligned} f_i(\bar{\psi}_0+\Delta\bar{\psi},\bar{\phi}_0+\Delta\bar{\phi}) &= f(\bar{\psi}_0,\bar{\phi}_0) + \left.\frac{\partial f_i}{\partial \psi_j}\right|_{\psi_{j0}} \Delta\psi_j + \left.\frac{\partial f_i}{\partial \phi_j}\right|_{\phi_{j0}} \Delta\phi_j \\ &\quad + \frac{1}{2}\left.\frac{\partial^2 f_i}{\partial \psi_j^2}\right|_{\psi_{j0}} \Delta\psi_j^2 + \frac{1}{2}\left.\frac{\partial^2 f_i}{\partial \phi_j^2}\right|_{\phi_{j0}} \Delta\phi_j^2 \\ &\quad + \cdots \quad \forall\, i=1,2,\cdots,n \end{aligned} \tag{24}$$

where tensor notation has been used for all the derivative terms. If the higher order terms in the expansion are dropped (i.e., within the bounds of the linear approximation), and $f_i(\bar{\psi}_0+\Delta\bar{\psi},\bar{\phi}_0+\Delta\bar{\phi})$ and $f_i(\bar{\psi}_0,\bar{\phi}_0)$ are set to zero, a linear expression relating the changes in the output to the changes in the input is obtained. In matrix form, this expression may be written as

$$[J_\psi][\Delta\bar{\psi}]+[J_\phi][\Delta\bar{\phi}] \approx 0 \tag{25}$$

where $[J_\psi]$ is the Jacobian matrix of the inputs and is of size $n\times m$, $[J_\phi]$ is the Jacobian matrix of the outputs and is of size $n\times n$. Equation (25) may be rearranged in the following form to obtain the change in the outputs from a change in the output

$$[\Delta\bar{\phi}] \approx [J_\phi]^{-1}[J_\psi][\Delta\bar{\psi}] = [A][\Delta\bar{\psi}] \tag{26}$$

where the matrix $[J_\phi]^{-1}[J_\psi]$ has been denoted by $[A]$, the so-called mapping or sensitivity matrix [3].

In the ISAT algorithm, data are stored in a binary table. Each point of the table has a so-called ellipsoid of accuracy (EOA), which represents a hyperdimensional convex region around each point within which the linear approximation is valid to a user-prescribed tolerance. If a query is found to be within the EOA,

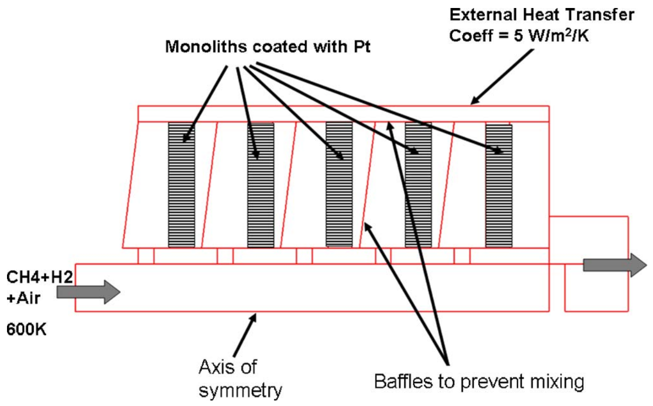

Fig. 5 Geometry and boundary conditions for the full-scale catalytic converter modeled using the subgrid scale approach.

data is retrieved from the table directly. Otherwise, a direct calculation of Eq. (16) is performed and the results are either added to the table as a new entry, or are used to grow the EOA. The size of the EOA is calculated from the criterion $[\Delta\bar{\psi}]^T[Q]^T[\Sigma][Q][\Delta\bar{\psi}] \leqslant 1$, where $[Q]^T[\Sigma][Q]$ represents a singular value decomposition (SVD) of the matrix $[A]^T[A]$ after appropriate scaling and normalization [3]. The matrix $[\Sigma]$ is a diagonal matrix consisting of singular values $[\sigma_1 \geqslant \sigma_2 \geqslant \cdots \geqslant \sigma_M \geqslant 0]$. The half-axis lengths of the EOA in the various input directions are given by $1/\sqrt{\sigma_i}$. The matrix $[Q]$ is a result of the SVD, and represents rotation of the ellipsoid of accuracy about the principal input directions. As more queries are processed, the ISAT table grows in size, and the EOA around each point also grows, thereby increasing the probability of retrieval. The retrieval rate becomes almost 100% (i.e., the algorithm is asymptotically optimal) if a large number of queries are processed, which is ideal for the problem at hand, in which Eq. (16) may have to be solved more than 1 billion times based on estimates provided earlier. In Sec. 4.2, preliminary results demonstrating the efficacy of ISAT-S for the computation of complex heterogeneous chemistry will be provided.

4 Results and Discussion

In this section, preliminary results are presented to demonstrate the effectiveness of the two approaches, just described, to enable modeling of full-scale catalytic converters.

4.1 Subgrid Scale Modeling Results. Validation studies that highlight the accuracy as well as the deficiencies of the subgrid scale models have been presented elsewhere [16]. In this paper, results that demonstrate the effectiveness of this model for large-scale catalytic converters are presented.

The case considered is a catalytic combustion of a methane–air mixture on platinum in a converter with multiple monolithic plugs. The geometry and boundary conditions for the case under study are illustrated in Fig. 5. A single manifold is sealed off at the right end thereby forcing the flow to pass through the five monolithic plugs. The converter was modeled as an axisymmetric geometry. It is worth pointing out here that this is another advantage of using a subgrid scale model. Since square channels are embedded in a cylindrical monolith, full-fledged CFD calculations would force one to perform fully three-dimensional calculations. In the subgrid scale approach, since the square channels are at the subgrid scale, their exact shape can easily be accounted for within the subgrid description, as discussed earlier, while still allowing axisymmetric calculations for the large-scale geometry. Thin baffles separate the outgoing streams from the incoming fuel, and were modeled using thin-wall or contact resistance models. A finite-volume unstructured grid formulation [47,48] was used to discretize and solve the governing equations. A total of only 55,000 colocated cells were used. Pressure–velocity coupling was resolved using the SIMPLEC algorithm [49,50] and a pressure-weighted interpolation technique [51,52] was used to damp out pressure oscillations. The fluid was assumed to obey the ideal gas law, and all its transport properties were computed using the Chapman–Enskog equations of kinetic theory [10] with Lennard-Jones potentials obtained from the CHEMKIN transport property database. The thermodynamic properties of the species were computed using data obtained from the JANNAF database. Radiative heat transfer was also considered, and was modeled assuming that the fluid is optically thin, and that all solids are opaque, i.e., only surface-to-surface radiation exchange was considered. The absorption coefficient of the monolithic plugs was set to a value of 100 m^{-1} to simulate optically thick behavior. Gas-phase reactions were neglected, and the surface reaction mechanism chosen for the study was adopted from the literature [53]. It consisted of eight gas-phase species and 11 surface-adsorbed species undergoing 24 reactions.

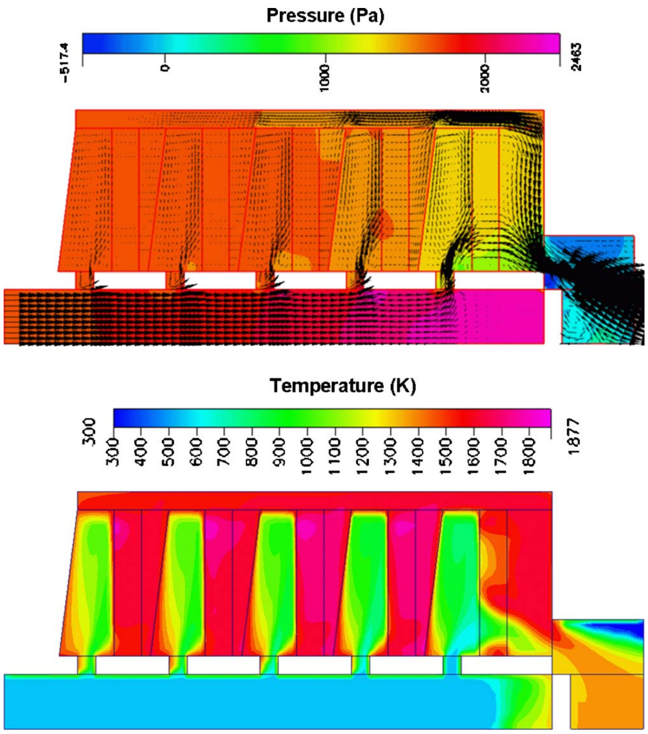

Fig. 6 Flow and temperature distributions in a full-scale catalytic converter modeled using the subgrid scale approach

The flow (velocity vectors and pressure) and temperature distributions within the full converter are shown in Fig. 6. An observation of interest is the fact that the last monolith encounters the highest flow rate because the flow essentially gets "squeezed" into it due to the main supply manifold being sealed at the right end. Consequently, some of the fuel leaks through the last monolith without being fully converted, as shown in Fig. 7. The site fraction of platinum is about 95% when the reactions are fast and is much lower in the regions where full conversion did not occur. Parametric studies were conducted, and showed that at inlet flow velocities of 10 m/s or less, 100% conversion can be achieved. At a velocity of 25 m/s, 99% conversion can be achieved, and at a velocity of 50 m/s (for which results have been shown here), only 71% conversion can be achieved. A single simulation required about 1500 iterations for all residuals to decrease by four orders of magnitude, and took about 25 h of CPU time on a 3 GHz Intel Pentium processor. Based on the results shown, and the computational effort and resources needed to obtain them, it is clear that

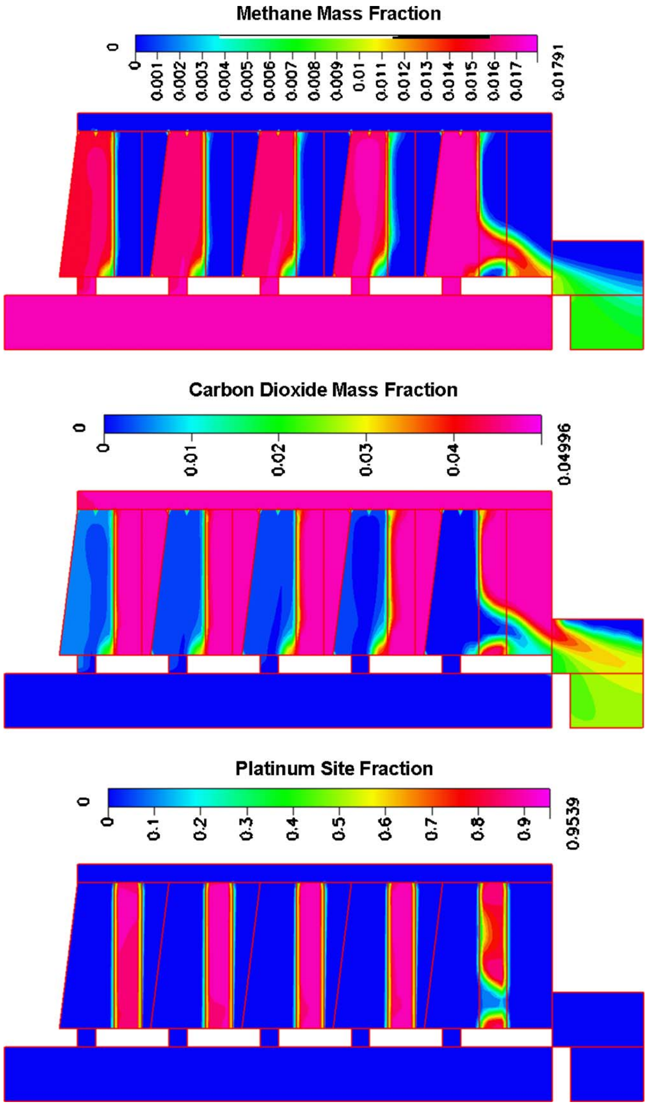
Methane Mass Fraction

Carbon Dioxide Mass Fraction

Platinum Site Fraction

Fig. 7 Mass fractions of one of the reactants (CH_4) and products (CO_2) and the site fraction of platinum

the subgrid scale approach is a feasible modeling strategy for practical catalytic conversion applications with realistic chemistry.

4.2 ISAT-S Results. Instead of coupling ISAT-S to a full-fledged CFD code, for preliminary feasibility studies, the inputs to the surface reaction solver were randomly perturbed, with the maximum and minimum perturbations set to physically realizable values. The inputs to the surface reaction solver [Eq. (16)] were the species diffusion coefficients, the surface temperature, and the cell center mass fractions of the species. The surface temperature was varied randomly between 1080 K and 1320 K, the species diffusion coefficients were varied randomly by 20% from a baseline value, and the cell center mass fractions of the fuel and oxidizer species were varied randomly between 0 and 0.1. The same reaction mechanism, described in the preceding subsection, was used. This resulted in a total of 17 inputs ($=n$) and 19 outputs ($=m$). The outputs, in this particular case, are the near-wall mass (or mole in the case of surface-adsorbed species) fractions of the various species, and a tolerance of 10^{-3} was set on them, implying that each retrieved mass (or mole) fraction value must be within 10^{-3} of the exact value for the retrieved result to be deemed usable. About 5.4% of the retrieved values violated the tolerance criterion.

Table 1 shows the enhancement of efficiency that can be achieved by using ISAT-S for such applications. SUF is the speedup factor, defined as the ratio of CPU times without and with ISAT-S in place, and Q is the number of queries (or number of times Eq. (16) is solved). The table shows that for this particular test case, SUF of 89 is achieved using ISAT-S if sufficiently large number of queries is processed, and a reasonably large sized table is used. The fact that the SUF increases with the number of queries is also indicative of the fact that the algorithm is asymptotically optimal. As the problem size increases, its effectiveness also increases. While these preliminary results (without actual coupling to a CFD code) do not conclusively prove the effectiveness of the ISAT-S algorithm for catalytic conversion applications, they certainly establish ISAT-S as a method that has strong potential in enhancing computational efficiency by several orders of magnitude for problems with reasonably complex chemistry.

5 Summary and Conclusions

Modeling full-scale catalytic converters using conventional CFD techniques is prohibitively expensive because of the need to treat transport phenomena at multiple length scales and the need to treat heterogeneous chemical reactions at the smallest length scale. Two different approaches, namely subgrid scale modeling and in situ adaptive tabulation, which break away from conventional direct CFD approaches, were discussed briefly and preliminary results were presented to indicate their efficiency. Both approaches are capable of enhancing the computational efficiency by several orders of magnitude, as demonstrated here. In principle, the two approaches can be used in tandem for maximum benefit. In other words, the ISAT-S algorithm can be used for acceleration of chemistry calculations at the subgrid scale. Future work needs to be directed in two specific areas. First, the two approaches need to be refined further. In the case of the subgrid scale approach, issues that particularly need attention are nonequilibrium thermal transport (i.e., thermal transport in the solid and fluid phases need to be treated separately [54]) and anisotropic diffusion at the subgrid scale to eliminate diffusion between channels of the monolith. For the ISAT approach, research needs to be directed toward improving the accuracy of the retrieved results through better strategies for error control [46,55]. Following these refinements, research needs to be directed toward integrating the various pieces for which preliminary results have been shown in this paper into a single simulation environment. It is hoped that in due course, the

Table 1 Effect of size of ISAT-S binary table on performance. All CPU times, shown in minutes, are for a 3 GHz Intel Pentium processor: SUF=actual speed-up factor.

		80 k points		40 k points		20 k points		10 k points	
Q	Direct CPU	CPU	SUF	CPU	SUF	CPU	SUF	CPU	SUF
10^6	107.9	19.6	5.5	15.3	7.1	13.3	8.1	12.3	8.7
10^7	1078	44.6	24.2	40.5	26.6	38.3	28.1	40.9	26.4
10^8	10,780	121.1	89	125	86.2	131.2	82.1	166.6	64.7

research directions laid out here will lead to computationally cheap and accurate simulation tools for the study of full-scale catalytic converters with realistic chemistry.

Nomenclature

$\mathbf{B}$ = body force vector (m s^{-2})
$c_{p,k}$ = specific heat capacity of species k (J kg^{-1} K^{-1})
$\mathcal{D}_{kn}$ = binary diffusion coefficient of species k into n (m^2/s)
D_{kn} = ordinary multicomponent diffusion coefficient (m^2/s)
h = enthalpy of mixture (J/kg)
h_k = enthalpy of the kth species (J/kg)
$h^0_{f,k}$ = enthalpy of formation of species k at standard state (J/kg)
$\mathbf{J}_k$ = diffusion mass flux of the kth species
$\mathbf{K}$ = permeability tensor (m^2)
k_c = thermal conductivity of mixture (W m^{-1} K^{-1})
m = number of outputs in ISAT table
M = molecular weight of the mixture (kg/kmol)
M_k = molecular weight of k-th species (kg/kmol)
$\hat{\mathbf{n}}$ = unit surface normal vector
n = number of inputs in ISAT table
N = total number of gas-phase species
p = pressure (Pa)
$\mathbf{q}$ = heat flux (W m^{-2})
$\mathbf{q}_C$ = heat flux due to conduction (W m^{-2})
$\mathbf{q}_D$ = heat flux due to interdiffusion of species (W m^{-2})
$\mathbf{q}_R$ = heat flux due to radiation (W m^{-2})
$\dot{R}_k$ = production rate of species due to heterogeneous reactions (kmol m^{-3} s^{-1})
$\dot{S}_k$ = production rate of kth species due to homogeneous reactions (kg m^{-3} s^{-1})
$\dot{S}_h$ = volumetric heat generation rate (W m^{-3})
T = temperature (K)
$\mathbf{U}$ = mass averaged velocity (m/s)
X_k = mole fraction of kth species
Y_k = mass fraction of kth species

Greek

δ = diffusion length scale (m)
δ_{kn} = Kronecker delta
ε = porosity
Γ_{kn} = transformed diffusion coefficient tensor (m^2/s)
Λ_k = molar concentration of species k at fluid–solid interface (kmol m^{-3})
ρ = mixture density (kg m^{-3})
$\boldsymbol{\tau}$ = shear stress (N m^{-2})

Subscripts

C = at cell center
I = at fluid–solid interface

Other

$\langle\,\rangle$ = volume average over representative elemental volume

References

[1] Raja, L. L., Kee, R. J., Deutschmann, O., Warnatz, J., and Schmidt, L. D., 2000, "A Critical Evaluation of Navier-Stokes, Boundary-Layer, and Plug-Flow Models of the Flow and Chemistry in a Catalytic-Combustion Monolith," Catal. Today, **59**, pp. 47–60.
[2] Tischer, S., Correa, C., and Deutschmann, O., 2001, "Transient Three-Dimensional Simulations of a Catalytic Combustion Monolith Using Detailed Models for Heterogeneous and Homogeneous Reactions and Transport Phenomena," Catal. Today, **69**, pp. 57–62.
[3] Pope, S. B., 1997, "Computationally Efficient Implementation of Combustion Chemistry Using In Situ Adaptive Tabulation," Combust. Theory Modell., **1**, pp. 41–63.
[4] Bird, R. B., Stewart, W. E., and Lightfoot, E. N., 2001, *Transport Phenomena*, 2nd ed., Wiley, New York.
[5] Kuo, K. K., 1986, *Principles of Combustion*, Wiley, New York.
[6] Whitaker, S., 1983, *Fundamental Principles of Heat Transfer*, Krieger, Melbourne, FL.
[7] Kumar, A., and Mazumder, S., 2007, "Assessment of the Dilute Approximation for the Prediction of Combined Heat and Mass Transfer Rates in Multi-Component Systems," *Heat and Mass Transfer*, published online, doi: 10 1007/s00231-006-0223-6
[8] Wangard, W., Dandy, D. S., and Miller, B. J., 2001, "A Numerically Stable Method for Integration of the Multi-Component Species Diffusion Equations," J. Comput. Phys., **174**, pp. 460–472.
[9] Mazumder, S., 2006, "Critical Assessment of the Stability and Convergence of the Equations of Multi-Component Diffusion," J. Comput. Phys., **212**(2), pp. 383–392.
[10] Hirschfelder, J. O., Curtiss, C. F., and Bird, R. B., 1954, *Molecular Theory of Gases and Liquids*, Wiley, New York.
[11] Sutton, K., and Gnoffo, P. A., 1998, "Multicomponent Diffusion With Application to Computational Aerothermodynamics," AIAA Paper No. 98-2575.
[12] Coltrin, M., Kee, R., and Rupley, F., 1991, "Surface Chemkin: A General Formalism and Software for Analyzing Heterogeneous Chemical Kinetics at Gas-Solid Interfaces," Int. J. Chem. Kinet., **23**, pp. 1111–1128.
[13] Mazumder, S., and Lowry, S. A., 2001, "The Treatment of Reacting Surfaces for Finite-Volume Schemes on Unstructured Meshes," J. Comput. Phys., **173**(2), pp. 512–526.
[14] Kaviany, M., 1991, *Principles of Heat Transfer in Porous Media*, Springer, New York.
[15] Whitaker, S., 1996, "The Forchheimer Equation: A Theoretical Development," Transp. Porous Media, **25**, pp. 27–61.
[16] Mazumder, S., and Sengupta, D., 2002, "Subgrid Scale Modeling of Heterogeneous Chemical Reactions and Transport in Full-Scale Catalytic Converters," Combust. Flame, **131**(1–2), pp. 85–97.
[17] Chatterjee, D., Deutschmann, O., and Warnatz, J., 2001, "Detailed Surface Reaction Mechanism in a Three-Way Catalyst," Faraday Discuss., **119**, pp. 371–384.
[18] Holland, J., 1975, *Adaptation in Natural and Artificial Systems*, University of Michigan Press, Ann Arbor, MI.
[19] Homma, R., and Chen, J., 2001, "Combustion Process Optimization by Genetic Algorithms: Reduction of NO_2 Emission via Optimal Post-Flame Process," Proc. Combust. Inst., **28**, pp. 2483–2489.
[20] Elliott, L., Ingham, D., Kyne, A., Mera, N., Pourkashanian, M., and Wilson, C., 2003, "Incorporation of Physical Bounds on Rate Parameters for Reaction Mechanism Optimisation Using Genetic Algorithms," Combust. Sci. Technol., **175**(4), pp. 619–648.
[21] Elliott, L., Ingham, D., Kyne, A., Mera, N., Pourkashanian, M., and Wilson, C., 2004, "Genetic Algorithms for Optimisation of Chemical Kinetics Reaction Mechanisms," Prog. Energy Combust. Sci., **30**(3), pp. 297–328.
[22] Takahashi, T., Funatsu, K., and Ema, Y., 2005, "Automatic Modeling of Reaction Systems Using Genetic Algorithms and its Application to Chemical Vapor Deposition Processes: Advanced Utilizations of Simulators for Chemical Systems," Meas. Sci. Technol., **16**, pp. 278–284.
[23] Majumdar, S., and Mitra, K., 2004, "Modeling of Reaction Network and its Optimization by Genetic Algorithms," Chem. Eng. J., **100**, pp. 109–118.
[24] Chen, J., Blasco, J., Fueyo, N., and Dopazo, C., 2001, "An Economical Strategy for Storage of Chemical Kinetics: Fitting In Situ Adaptive Tabulation With Artificial Neural Networks," Proc. Combust. Inst., **28**, pp. 115–121.
[25] Kapoor, R., and Menon, S., 2002, "Computational Issues for Simulating Finite-rate Kinetics in LES," *Proceedings of the ASME Turbo-Expo, IGTI*, June 3–6, Amsterdam, Netherlands, Vol. 1, pp. 781–789.
[26] Li, G., Rosenthal, C., and Rabitz, H., 2001, "High Dimensional Model Representations," TASK Q., **105**(33), pp. 7765–7777.
[27] Shorter, J., Ip, P., and Rabitz, H., 1999, "An Efficient Chemical Kinetics Solver Using High Dimensional Model Representation," TASK Q., **103**, pp. 7192–7198.
[28] Wang, S., Levy, H., Li, G., and Rabitz, H., 1999, "Fully Equivalent Operational Models for Atmospheric Chemical Kinetics Within Global Chemistry-Transport Models," J. Geophys. Res., **104**(D23), pp. 30417–30426.
[29] Maas, U., and Pope, S. B., 1992, "Simplifying Chemical Kinetics: Intrinsic Low-Dimensional Manifolds in Composition Space," Combust. Flame, **88**, pp. 239–264.
[30] Nafe, J., and Mass, U., 2003, "Hierarchical Generation of IDLMs of Higher Hydrocarbons," Combust. Flame, **135**, pp. 17–26.
[31] Bender, R., Blasenbrey, T., and Maas, U., 2000, "Coupling of Detailed and IDLM-reduced chemistry With turbulent mixing," Proc. Combust. Inst., **28**(1), pp. 101–106
[32] Blasenbrey, T., and Maas, U., 2000, "IDLMs of Higher Hydrocarbons and the Hierarchy of Chemical Kinetics," Proc. Combust. Inst., **28**(2), pp. 1623–1630
[33] Yan, X., and Maas, U., 2000, "Intrinsic Low-Dimensional Manifolds of Heterogeneous Combustion Processes," Proc. Combust. Inst., **28**(2), pp. 1615–1621.
[34] Raman, V., Fox, R., Harvey, A., and West, D., 2001, "CFD Analysis of Premixed Methane Chlorination Reactors With Detailed Chemistry," Ind. Eng. Chem. Res., **40**(23), pp. 5170–5176.
[35] Raman, V., Fox, R., and Harvey, A., 2004, "Hybrid Finite-Volume/ Transported PDF Simulations of a Partially Premixed Methane-Air Flame," Com-

bust. Flame, **136**(3), pp. 327–350.

[36] Xu, J., and Pope, S. B., 2000, "PDF Calculations of Turbulent Nonpremixed Flames With Local Extinction," Combust. Flame, **123**(3), pp. 281–307.

[37] Saxena, V., and Pope, S. B., 1998, "PDF Calculations of Major and Minor Species in a Turbulent Piloted Jet Flame," Sym. (Int.) Combust., [Proc.], **1**, pp. 1081–1086.

[38] Saxena, V., and Pope, S. B., 1999, "PDF Simulations of Turbulent Combustion Incorporating Detailed Chemistry," Combust. Flame, **117**(1–2), pp. 340–350.

[39] Chen, J.-Y., 2004, "Analysis of In Situ Adapative Tabulation Performane for Combustion Chemistry and Improvement With a Modified Search Algorithm," Combust. Sci. Technol., **176**(7), pp. 1153–1169.

[40] Goldin, G., Madsen, J., Straub, D., Rogers, W., and Castleton, K., 2003, "Detailed Chemistry Simulations of a Trapped Vortex Generator," *Proceedings of the ASME Turbo-Expo, IGTI*, Atlanta, GA, June 16–19, Vol. 1, pp. 121–128.

[41] Tang, Q., and Pope, S. B., 2002, "Implementation of Combustion Chemistry by In Situ Adaptive Tabulation of Rate-Controlled Constrained Equilibrium Manifolds," Proc. Combust. Inst., **29**(1), pp. 1411–1417.

[42] Sankaran, V., and Menon, S., 2000, "Structure of Premixed Turbulent Flames in the Thin-Reaction-Zones Regime," Proc. Combust. Inst., **28**(1), pp. 203–209.

[43] Shah, J., and Fox, R., 1999, "Computational Fluid Dynamics Simulation of Chemical Reactors: Application of In Situ Adaptive Tabulation to Methane Thermochlorination Chemistry," Ind. Eng. Chem. Res., **38**(11), pp. 4200–4212.

[44] Zhao, W., Montgomery, C., Cremer, M., Adams, B., Eklund, D., and Chen, J., 2003, "Implementation of Reduced Mechanisms With ISAT into CFD Simulations of Full-Scale Combustion Systems," *Proceedings Energy Conversion and Resources—2003*, Washington, D.C., Nov. 15–29, pp. 27–32.

[45] Pope, S. B., 1985, "PDF Methods for Turbulent Reactive Flows," Prog. Energy Combust. Sci., **11**, pp. 119–192.

[46] Mazumder, S., 2005, "Adaptation of the In Situ Adaptive Tabulation (ISAT) Procedure for Efficient Computation of Surface Reactions," Comput. Chem. Eng., **30**(1), pp. 115–124.

[47] Mathur, S., and Murthy, J. Y., 1997, "A Pressure Based Method for Unstructured Meshes," Numer. Heat Transfer, Part B, **31**(2), pp. 195–216.

[48] Ferziger, J., and Peric, M., 1999, *Computational Methods for Fluid Dynamics*, 2nd ed, Springer, New York.

[49] Patankar, S. V., 1980, *Numerical Heat Transfer and Fluid Flow*, Hemisphere, Washington, D.C.

[50] Van Doormal, J., and Raithby, G., 1984, "Enhancement of the SIMPLE Method for Predicting Incompressible Fluid Flows," Numer. Heat Transfer, **7**, pp. 147–163.

[51] Rhie, C. M., and Chow, W. L., 1983, "A Numerical Study of the Turbulent Flow Past an Isolated Airfoil With Trailing Edge Separation," AIAA J., **21**, pp. 1525–1532.

[52] Miller, T. F., and Schmidt, F. W., 1988, "Use of a Pressure Weighted Interpolation Method for the Solution of Incompressible Navier-Stokes Equations With Non-Staggered Grid System," Numer. Heat Transfer, **14**, pp. 213–233.

[53] Deutschmann, O., Behrendt, F., and Warnatz, J., 1994, "Modeling and Simulation of Heterogeneous Oxidation of Methane on a Platinum Foil," Catal. Today, **21**, pp. 461–471.

[54] Oliveira, A. A. M, and Kaviany, M., 2001, "Nonequilibrium in the Transport of Heat and Reactants in Combustion in Porous Media," Prog. Energy Combust. Sci., **27**, pp. 523–545.

[55] Liu, B. J. D., and Pope, S. B., 2005, "The Performance of In Situ Adaptive Tabulation in Computations of Turbulent Flames," Combust. Theory Modell., **9**(4), pp. 549–568.

Heat and Mass Transfer Evaluation in the Channels of an Automotive Catalytic Converter by Detailed Fluid-Dynamic and Chemical Simulation

Cinzio Arrighetti
Dipartimento di Meccanica e Aeronautica,
Università di Roma "La Sapienza,"
via Eudossiana 18,
00184 Roma, Italy

Stefano Cordiner

Vincenzo Mulone[1]
e-mail: mulone@ing.uniroma2.it

Dipartimento di Ingegneria Meccanica,
Università di Roma "Tor Vergata,"
via del Politecnico 1,
00133 Roma, Italy

The role of numerical simulation to drive the catalytic converter development becomes more important as more efficient spark ignition engines after-treatment devices are required. The use of simplified approaches using rather simple correlations for heat and mass transfer in a channel has been widely used to obtain computational simplicity and sufficient accuracy. However, these approaches always require specific experimental tuning so reducing their predictive capabilities. The feasibility of a computational fluid dynamics three-dimensional (3D) model coupled to a surface chemistry solver is evaluated in this paper as a tool to increase model predictivity then allowing the detailed study of the performance of a catalytic converter under widely varying operating conditions. The model is based on FLUENT to solve the steady-state 3D transport of mass, momentum and energy for a gas mixture channel flow, and it is coupled to a powerful surface chemistry tool (CANTERA). Checked with respect to literature available experimental data, this approach has proved its predictive capabilities not requiring an ad hoc tuning of the parameter set. Heat and mass transfer characteristics of channels with different section shapes (sinusoidal, hexagonal, and squared) have then been analyzed. Results mainly indicate that a significant influence of operating temperature can be observed on Nusselt and Sherwood profiles and that traditional correlations, as well as the use of heat/mass transfer analogy, may give remarkable errors (up to 30% along one-third of the whole channel during light-off conditions) in the evaluation of the converter performance. The proposed approach represents an appropriate tool to generate local heat and mass transfer correlations for less accurate, but more comprehensive, 1D models, either directly during the calculation or off-line, to build a proper data base.

[DOI: 10.1115/1.2709657]

Keywords: computational fluid dynamics, automotive catalytic converters, heat transfer, mass transfer, detailed chemistry

1 Introduction

As automotive emission regulations become tighter and tighter, more efficient exhaust after-treatment devices are required to reduce engine tailpipe emissions under all operating conditions [1,2]. To this aim, monolith catalytic converters for spark ignition engines need to be improved in terms of performance which depends on processes taking act on different time and space scales. In fact, while the interaction with the engine exhaust system (e.g., inlet temperature or velocity profile) determines the overall thermal-fluid-dynamic behavior, pollutant conversion depends on surface heat and mass transfer occurring at the scale of a single monolith channel. Proper efforts to increase catalyst performances should then proceed towards the improvement of efficiency of the processes acting on the small scales as well as to the study of a closer integration between the engine and the whole exhaust system.

Numerical modeling represents a powerful tool to drive the catalytic converter development, and then, the availability of suitable models related to each scale (referred as modeling levels) is required. This usually leads to hybrid three-dimensional–one-dimensional (3D–1D) numerical approaches by which the behavior of the whole exhaust system [3,4] may be represented. Under this scheme, the converter is described as an equivalent porous medium with fluid-dynamic and chemical behavior similar to the monolith. Local information are provided by coupling this equivalent porous medium description to a detailed model of selected channels located in representative regions of the converter. Either plug flow (1D) or boundary layer (2D) approaches can be used to describe the channel flow, where surface phenomena are taken into account by mass and heat transfer correlations which may however require ad hoc experimental tuning so reducing the model predictive capabilities [5,6].

Since both local geometry effects and surface reaction may strongly influence mass and heat transfer, the choice of a proper correlation becomes a crucial issue. Moreover, as far as recent design solutions for monoliths are concerned, the channel shape is also modified, exploiting the material characteristics (ceramic or metal) to enhance transport phenomena [7] (e.g., helicoidal profiles for ceramic and guiding shovels for metal). These effects have also been recently pursued for other kinds of applications such as air conditioning, electronics cooling, or biomedical devices, by means of cross-corrugated arrangements [8] or dimples [9]. For these new geometries neither standard correlations nor analytic closures may be found to describe the transport process.

---

[1] Corresponding author.

Contributed by the Heat Transfer Division of ASME for publication in the JOURNAL OF HEAT TRANSFER. Manuscript received January 26, 2006; final manuscript received July 12, 2006. Review conducted by Sumanta Acharya.

The use of computational techniques could then be a valid approach to analyze the flow occurring into a given geometry [8,10], and to characterize the channel behavior, namely heat/mass transfer performance and pressure losses.

In the present paper heat and mass transfer processes in the channel of an automotive catalytic converter have been analyzed by means of a 3D computational fluid dynamics (CFD) approach coupled to a tool describing detailed surface chemistry. The commercial code FLUENT [11] has been coupled to a catalytic surface reaction mechanism for the conversion of nitric oxides (NO_x), unburned hydrocarbons (HC), and carbon monoxide (CO). Surface chemistry has been solved by a specialized tool based on the open access solver CANTERA, characterized by excellent performance in terms of computational cost [12]. The coupling of CFD and chemistry solvers allowed us to describe in detail the interaction between boundary layer development and surface chemistry. The whole numerical tool has been used to provide detailed channel-level information on thermal and pollutant species profiles as functions of the most influencing parameters, such as temperature and air/fuel ratio, without any preliminary tuning. Moreover, the influence of channel geometry on the converter performance has been analyzed proving the model capabilities to evaluate innovative solutions in terms of geometry, materials, and technology [13,14].

2 Numerical Modeling

Numerical simulation tools are more and more utilized to design automotive catalytic converters and many efforts have been spent so far to develop proper methods. Koltsakis et al. [3] and, more recently Pontikakis [4], reported rather complete analysis of the models available in literature identifying different approaches. The performances of after-treatment systems are evaluated with respect to reference driving cycles (e.g., the new European driving cycle with an overall length of 10 km and a 1200 s duration). Hybrid models (i.e., characterized by different levels of description and taking into account the real engine behavior) are the most diffused ones to study these processes as they are able to manage long transient simulations together with rather detailed descriptions of local phenomena. Such models are typically built as modular frameworks [15], where the singular modules are usually characterized as follows:

1. A transient, 1D model of the solid phase of the entire catalytic converter (reactor level modeling);
2. A quasi-steady 1D model of temperature and gas distributions into a representative channel (channel level modeling);
3. A local 0D chemical scheme featuring a given set of reactions (wash-coat level modeling).

Despite their simplicity, the previous models are rather effective once properly tuned for given geometry, substrate characteristics, and catalyst composition.

At channel level, heat and mass transfer (of a generic species, i) occurring between gas and wash-coat are taken into account by means of heat and mass transfer coefficients k and $k_{m,j}$, respectively, by the following equations

$$\rho_g u_z \frac{\partial Y_i(z)}{\partial z} = \rho_g k_{m,i} GSA[Y_i(z) - Y_{w,i}(z)] \quad (1)$$

$$\rho_g c_p u_z \frac{\partial T_g(z)}{\partial z} = kGSA[T_s(z) - T_w(z)] \quad (2)$$

k and $k_{m,j}$ depend on Nusselt and Sherwood number, which are defined as $\mathrm{Nu}=kD_h/\lambda$; and $\mathrm{Sh}_i=k_{m,i}D_h/D_i$. Usually, these parameters are evaluated by general expressions, valid for simple geometries and standard boundary conditions (e.g., constant wall temperature/concentration or heat/mass flux) [16]

$$\mathrm{Nu} = 3.66\left(1 + 0.095\frac{D_h}{L}\mathrm{Pe}_H\right)^{0.45} \quad (3)$$

$$\mathrm{Sh} = 3.66\left(1 + 0.095\frac{D_h}{L}\mathrm{Pe}_M\right)^{0.45} \quad (4)$$

The above equations are valid for circular sections and constant temperature/concentration boundary conditions. However, this simple description does not take into account important phenomena occurring in the real channel flow, such as the entry effect or the influence of surface reactions on mass and energy transfer processes [5]. Specific experimental data, such as light-off behavior of the converter [17], are then needed in advance, so reducing the potential of numerical simulation.

On the contrary, a complete analysis of 3D flow into the channel coupled to a detailed description of the surface reaction allows to evaluate the local behavior starting from the actually occurring phenomena. Reliable correlations of mass and energy transfer leading parameters may then be evaluated starting from detailed channel analysis. This represents a viable solution to obtain a more physical description which includes heat and mass transfer and chemical kinetics. Parametric functions in the form $\mathrm{Nu}=\mathrm{Nu}(x,y,z,t)$ and $\mathrm{Sh}_i=\mathrm{Sh}_i(x,y,z,t)$ may be derived from this detailed analysis and could be used in a hierarchical numerical framework. Moreover, by in this way, the model would also be capable of directly taking into account the section shape influence on the converter performance and the presence of the porous wash-coat which affects species diffusion [18].

The presented 3D model is based on two main modules, one describing the surface processes (e.g., absorption of reacting species on the active sites in the wash-coat; their reaction and back diffusion in the bulk gas) and the other taking into account thermal-fluid dynamics of the exhaust in the monolith channel. The two modules are separately described in the following subsections.

2.1 The General Fluid Dynamic Problem. Steady-state flow equations for a 3D single channel are solved for a perfect-gas mixture representing the main composition of internal combustion engine exhaust: the mixture includes eight species (O_2, N_2, CO_2, CO, NO, C_3H_6, H_2, and H_2O):

Mass

$$\nabla \cdot \rho u = 0 \quad (5)$$

Species

$$\nabla \cdot \rho Y_i u - \nabla \cdot (\rho D_i \nabla Y_i) = 0 \quad (i = 1, \ldots, N_g) \quad (6)$$

Momentum

$$\nabla \cdot (\rho u \otimes u - \mu \nabla u) = -\nabla\left(p + \frac{2}{3}\mu \nabla \cdot u\right) \quad (7)$$

Enthalpy

$$\nabla \cdot (\rho u h - \lambda \nabla T) = 0 \quad (8)$$

Only surface reactions are implemented into the model, whereas bulk reactions are not expected due to the limited concentration of reacting species. Accordingly, chemical source terms are taken into account via channel surface boundary conditions. Standard boundary conditions are imposed at the channel inlet (velocity, temperature, and species mass fraction array) and at the channel outlet (developed flow, atmospheric static pressure). A schematic of the flow domain is provided in Fig. 1 to further clarify boundary conditions assignment.

The equations have been solved by means of the commercial finite volume CFD code FLUENT 6.2, which allows to easily manage the fluid dynamic equations for ideal gas mixtures and the related thermodynamic and transport properties as functions of composition and temperature.

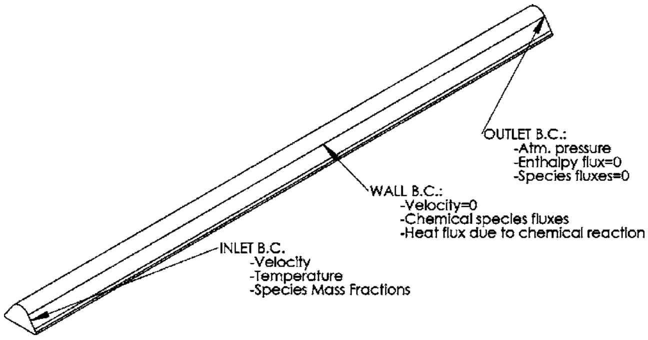

Fig. 1 Schematic of channel boundary conditions

2.2 Surface Chemical Reactions.

The overall reactions occurring into three way converter may be summarized by the following global mechanism

$$CO + 1/2O_2 \rightarrow CO_2$$

$$C_aH_b + (a + b/4)O_2 \rightarrow bCO_2 + a/2H_2O$$

$$CO + NO \rightarrow CO_2 + 1/2N_2 \tag{9}$$

Unfortunately, no reliable simplified rate laws for such a mechanism exist [19]. In this work, the detailed chemistry approach has been instead adopted to overcome this lack of accuracy. Following this approach, each reaction of the global mechanism has been replaced by a number of elementary steps to the aim of better describing the actual reaction paths.

The detailed mechanism has been derived by Ref. [20], and it is composed by 61 elementary reactions involving 31 species (eight in the gas mixture, 23 in the surface adsorbed phase). Surface species are furthermore divided into platinum-adsorbed and rhodium-adsorbed ones. Further details on the mechanism and kinetic parameters may be found in Refs. [20,21].

Some simplification hypothesis are taken into account not to make the chemical computational effort more difficult. In particular:

1. OH adsorption and desorption are not taken into account. OH therefore appears only as a surface species, neglecting the contribution of OH into the exhaust gas;
2. N_2O production is not taken into account in the mechanism as typical operating temperatures are relatively high. N_2O in fact plays a role at lower temperatures [22];
3. NO_2 is not considered in the exhaust. This hypothesis is certainly confirmed for rich and stoichiometric mixtures; it is retained acceptable also for lean mixtures;
4. C_3H_6 is considered as representative of the THC. C_3H_6 in fact should only represent the easily oxidizing HC ("fast" HC), which however includes the major part of the total amount of HC [15].

The local status of the catalytic surface is described by temperature, gas species molar fractions on the wall, and surface coverage θ_i of each adsorbed species. θ_i is defined as the ratio of occupied sites by species i to the totally available sites per surface area Γ. Surface coverages follow the fundamental property

$$\sum_{i=1}^{N_s} \vartheta_i = 1 \tag{10}$$

where N_s represents the total number of surface adsorbed species, and are independently defined for Pt and Rh sites.

Elementary steps reaction rates per unit volume (gas phase) and per unit area (surface adsorbed phase) $\dot{s}_i$ are modeled by Arrhenius laws. Kinetic data for the specific set of reactions are taken from literature, and include competitive adsorption and desorption on platinum and rhodium catalytic sites [23]

$$\dot{s}_i = \sum_{k=1}^{K_s} \nu_{ik} k_k^{(s)} \prod_{j=1}^{N_g+N_s} c_{sj}^{\nu'_{ik}} \quad i = 1, \ldots, N_g + N_s \tag{11}$$

In Eq. (11) the rate coefficient $k_k^{(s)}$ is modeled by an extension of the classical Arrhenius law to take into account the additional dependence on surface coverages

$$k_k^{(s)} = A_k T^{\beta_k} \exp\left(-\frac{E_{a,k}}{RT}\right) \prod_{i=1}^{N_s} \vartheta_i^{\mu_{i,k}} \exp\left(\frac{\varepsilon_{i,k}\vartheta_i}{RT}\right) \tag{12}$$

The rate coefficient of adsorption reactions is defined in the sticking form [24]

$$k_k^{(s)} = S_i^{(0)} \frac{1}{\Gamma^{\tau}} \sqrt{\frac{RT}{2\pi M_i}} \tag{13}$$

CANTERA has been selected as chemical solver to evaluate reaction rates of gas species and the associated heat release in any position of the channel wall, once the local thermodynamic state (temperature and molar fractions) is defined. The chemical solver therefore iterates until the steady-state condition is reached for each surface species coverage

$$\frac{\partial \vartheta_i}{\partial t} = 0; \quad i = N_g + 1, \ldots, N_g + N_s \tag{14}$$

The corresponding gas species molar sources per unit volume $\dot{s}_i$ are evaluated and constitute the flux boundary conditions for species 3D transport equations, by means of the following equation

$$\eta_i F_{\mathrm{cat/geo}} \dot{s}_i M_i = j_i \quad i = 1, \ldots N_g \tag{15}$$

Stefan velocity contribution in Eq. (15) is neglected as the problem is solved under steady-state hypothesis. The effectiveness factor allows to take into account diffusion into the wash-coat, and it is defined as $\eta_i = \bar{\dot{s}}_i / \dot{s}_i$, where $\bar{\dot{s}}_i$ is the mean surface reaction rate into the porous structure. It can be analytically calculated in terms of $\eta_i = \tanh(\Phi)/\Phi$, Φ being the Thiele module which depends on the wash-coat parameters [24]. Although thicker wash-coats may not be suitable [24], the effectiveness factor approach has been preferred instead of the solution of the complete diffusion problem. The examined wash-coats are 100 μm (4 mil) thick and less, so the proposed mean surface reaction rate expressions may be retained to be valid since homogeneous wash-coat coverage and temperature fields are assumed to occur over the thickness under that hypothesis.

Heat released by heterogeneous chemistry is added to the gas phase by imposing an equivalent heat flux as boundary condition at the gas–solid interface using the following relation

$$S^{\mathrm{het}} = \sum_{i}^{Ng} h_i^{\mathrm{FORM}} R_i^{\mathrm{het}} \tag{16}$$

where S^{het} represents the heat flux of enthalpy on the boundary.

2.3 Computational Details.

As already mentioned, chemical source terms are calculated by using the specialized open source solver CANTERA. A procedure able to couple the CFD solver FLUENT to the surface chemistry solver has then been developed. CANTERA, an efficient stiff-equation chemical solver, allows to easily manage species reaction rates and remarkably reduce computational effort with respect to traditional chemical solvers. Moreover, the use of CANTERA allowed us to parallelize the chemical computation.

In fact, since the local chemical problem solving requires a large computational effort in terms of time, the computational grid, constituted by a number of approximately 15,000 wedge cells with an average grid spacing of 0.13 mm, has been split into

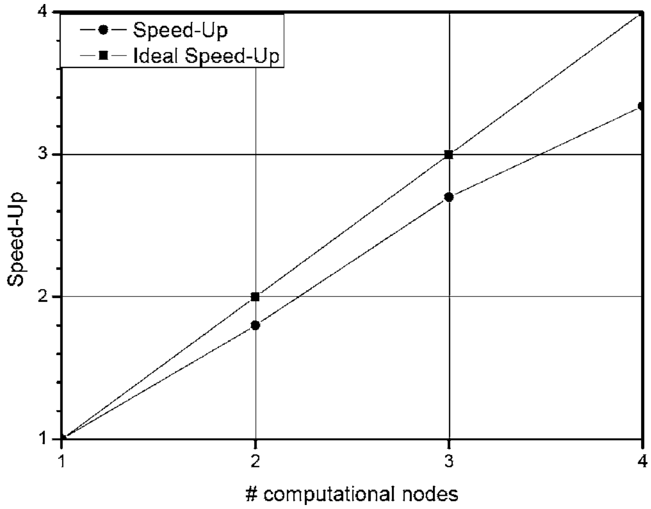

Fig. 2 Computational time speed-up as a function of the number of employed nodes

several partitions to minimize the overall computational time. The independence of local chemical problem on the neighbor information, and the different computational time required to solve chemistry and fluid dynamics, allowed to get to obtain a great advantage from such a procedure by means of a chemical parallelization. Results in terms of speedup are presented in Fig. 2 which refers to a four node Pentium IV 3.0 GHz linux cluster.

A channel computation takes about 7 s CPU time per iteration. A rather high number of iterations (around 2000) is required to reach the steady-state solution as the appearance of significant source terms requires the use of an under-relaxing factor on the order of 0.5 for species and energy transport equations.

The chemistry related computational effort is around ten times the fluid-dynamics characteristic one. This may be interpreted as the extra cost to increase the model predictivity.

Grid independence has been evaluated by halving the grid spacing until a variation of less than 4% in Nu and Sh numbers prediction has been found.

3 Discussion of Results

The model has been first tested with respect to literature available experimental data. Once predictive capabilities have been assessed, the model has been used to analyze the influence of channel section shape on mass and heat transfer processes.

3.1 Numerical Model Validation. Experimental data reported in Ref. [25] refer to a Pt/Rh three-way catalyst impregnated on γ-Al_2O_3 and supported by a common square section cordierite monolith. The converter has a channel density of 400 CPSI, and it is put into an isothermal laboratory-scale tube reactor (diameter of 22 mm and length of 29 mm). Further parameters are provided in Table 1.

Table 1 Experimental/numerical validation operating conditions

Property	Value
Pt/Rh composition	5:1
Noble metal loading	50 g/ft^3
Active catalytic surface	28 m^2/g
$F_{\mathrm{cat/geom}}$	70
Site density Γ	2.72×10^{-9} mol/cm^2
Single channel diameter	1 mm
Single channel length	29 mm
Inlet velocity at 25°C, 1 atm	1.35 S m/s
Inlet Λ	0.5; 0.9; 1.8
Washcoat thickness	4 mil
Washcoat tortuosity	3
Washcoat porosity	27.9%
Pore mean diameter	12.29 nm
Washcoat surface/volume ratio	$7.77\times10-5$ m^{-1}

Operating conditions have been largely varied in terms of air/fuel ratio λ_{ox}, defined as

$$\lambda_{\mathrm{ox}}=\frac{X_{\mathrm{NO}}+2X_{\mathrm{O}_2}}{X_{\mathrm{CO}}+9X_{\mathrm{C}_3\mathrm{H}_6}} \tag{17}$$

This parameter has been set equal to 0.5, 0.9, and 1.8 referring, respectively, to rich, near-to-stoichiometric, and lean conditions. A rather large inlet temperature variation ranging from 100°C to 600°C has been simulated, allowing a complete test of the model performance under kinetic limited (low temperature), mass limited (high temperature), and intermediate regimes. Poor conversion is expected at low temperatures in the kinetic limited regime and vice versa at high temperature where mass transfer limited conditions are reached.

The species conversion efficiency (η_{CONV}) is used as reference parameter for comparison with experiments. Results are reported in Figs. 3(*a*)–3(*c*) for the $\lambda_{\mathrm{ox}}=0.9$ condition. High-temperature efficiencies are very well predicted by the model, since error lies under 5%. At intermediate temperatures, however, both CO and NO conversion efficiencies are underestimated, whereas C_3H_6 is overestimated. The model performance may nevertheless be considered good as the temperature range is rather wide and no preliminary tuning has been performed.

For lean conditions ($\lambda_{\mathrm{ox}}=1.8$) a rather different behavior can be observed in Fig. 3(*d*). The excess of available O_2 gives a maximum efficiency at 630 K. Despite the more complex physical behavior, the model still proves to be able to capture the main characteristics of the involved phenomena.

Similar results can be observed for rich mixtures ($\lambda_{\mathrm{ox}}=0.5$) as far as CO and NO are concerned. In those conditions, the model instead gives poor prediction of C_3H_6 conversion (Fig. 3(*e*)); the proposed mechanism fails under the rich regime as C_3H_6 probably follows a different reaction path, involving a wider variety of adsorbed chemical species which should be included.

According to the previous discussion, the model can be considered reliable as an analysis tool for heat and mass transfer processes under surface reacting conditions.

3.2 Analysis of Different Channel Sections. The performance of different channel sections, namely sinusoidal, squared, and hexagonal, have then been analyzed using the model. Different section shapes basically reflect the use of different support materials (sinusoidal for metallic, squared and hexagonal for ceramic). Accordingly, several wall thicknesses (2 mil for metallic and 4 mil for ceramic) have also been chosen as representative of common applications. The operating conditions refer to engine-realistic values (200 kg/h flow rate) with regard to 400 cells per square inch (CPSI) cell density 63 mm long three-way catalyst channels.

A detailed description of the section parameters and operating conditions are provided in Tables 2 and 3. To further increase the significance of the test, the influence of wash-coat on the section shape also has been considered [26]. All other parameters assume the same values as reported in Table 1 except for air/fuel ratio, which has been kept constant and equal to 0.9.

Section-averaged Nusselt number trends have been investigated as representative of heat transfer nondimensional behavior for all the sections, as reported in Fig. 4. The influencing effect of surface reaction on heat and mass transfer has been initially evaluated with respect to the solutions of the Graetz–Nusselt problem (i.e., constant wall temperature and heat flux as boundary conditions for energy equation). The overall profiles show the charac-

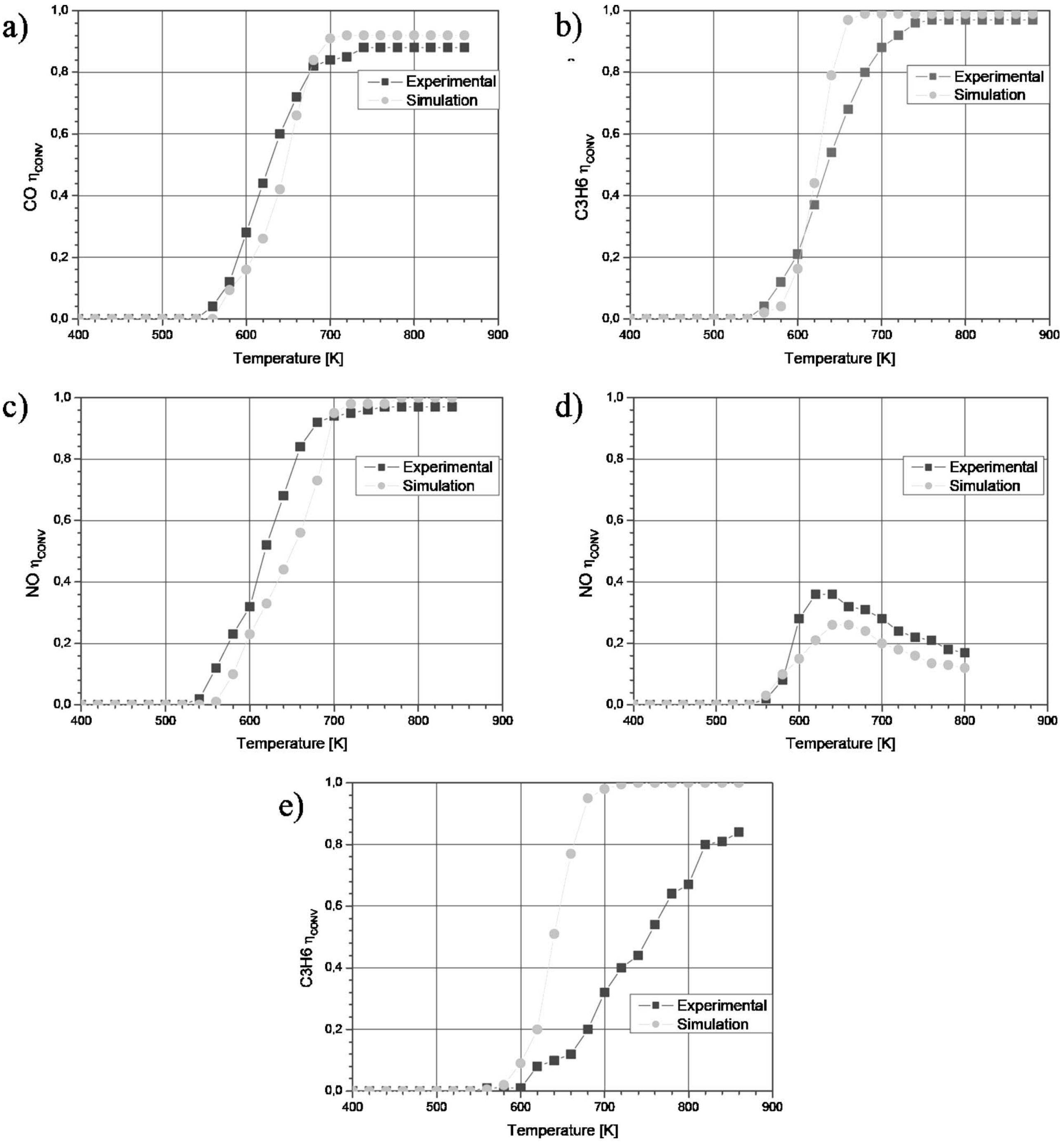

Fig. 3 Comparison between experimental and computed conversion: (*a*)–(*c*) $\lambda_{ox}=0.9$; (*d*) $\lambda_{ox}=1.8$, NO; (*e*) $\lambda_{ox}=0.5$, C_3H_6

teristic behavior with a significant entry effect (1 cm long about for all sections, which agrees with an entry length z_e evaluated by $(z_e/D_h)/(\mathrm{Re}_D/\mathrm{Pr})\approx 0.05$ [27]), and then an asymptotic value. However, it can be observed that surface chemistry radically changes the wall heat transfer mechanism. In fact, for moderate temperatures (600 K), the constant-heat-flux behavior is approximately followed, whereas a constant temperature can be observed for higher temperatures (800 K) [28]. Intermediate temperatures, corresponding to light-off conditions, give intermediate results as far as the asymptotic value is concerned, and also a marked change of heat transfer mechanism near the entrance region [29]. This phenomenon is particularly relevant for squared and hexagonal sections and leads to a deviation of up to 30% with respect to

Table 2 Operating conditions for different sections analysis

Property	Value (common to all sections)
Pt/Rh composition	5:1
Noble metal loading	50 g/ft^3
Active catalytic surface	28 m^2/g
$F_{\mathrm{cat/geom}}$	70
Site density Γ	2.72×10^{-9} mol/cm^2
Single channel length	63 mm
Inlet Λ	0.9
Washcoat tortuosity	3
Washcoat porosity	27.9%
Pore mean diameter	12.29 nm
Washcoat surface/volume ratio	$7.77\times10-5$ m^{-1}

Table 3 Main parameters for different sections analysis

Section parameters	Sinusoidal	Squared	Hexagonal
CPSI	400	400	400
Support thickness (mil)	2	4	4
Washcoat thickness (mil)	1	1	1
Open frontal area	0.8	0.725	0.763
Inlet velocity (m/s)	9.53	10.5	10

standard correlations along one-third of the whole channel.

This behavior can be explained observing the section-averaged bulk-temperature trends for the different sections (Fig. 5). For 600 K inlet temperature, the occurrence of an approximately linear temperature trend can be observed, that can be related to a constant heat-flux boundary condition as far as the mixture specific heat does not remarkably vary; at 650 K, instead, a sudden temperature rise in the central region of the channel may be observed, which is more evident for hexagonal and squared sections; this occurrence gives rather large wall-bulk gradients which in turn mean high Nusselt numbers. As far as higher temperatures are approached (800 K), reaction rates become higher and therefore a sudden temperature increase may be observed in the entrance region. In this case, higher reaction rates are also expected which in turn determine higher species consumption rates. Temperature trends towards the end of the channel have then the tendency to flatten for lack of reactants: this can explain the reason why Nu distribution is closer to constant wall temperature conditions for higher inlet temperatures.

The local heat transfer capabilities can be evaluated, by the 3D model, by defining the local surface Nusselt number

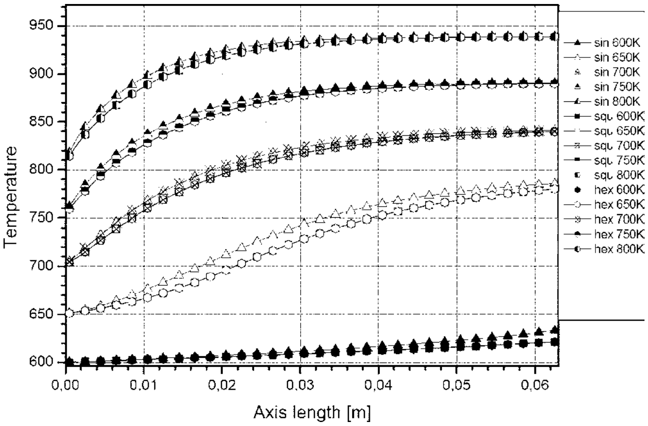

Fig. 5 Bulk temperature axial profiles for all sections and operating conditions

$$\mathrm{Nu}(x,y,z)|_w = \frac{\left.\dfrac{\partial T}{\partial n}\right|_w D_h}{T(x,y,z)|_w - T_{\mathrm{bulk}}(z)} \tag{18}$$

where T_{bulk} represents the section bulk temperature; its analysis is important to optimize the section shape and get the best performance in terms of heat and mass transfer.

Nusselt number distributions in the outlet region (corresponding to developed conditions) are reported in Fig. 6 for 650 K inlet temperature and all the sections: it can be observed that, in any

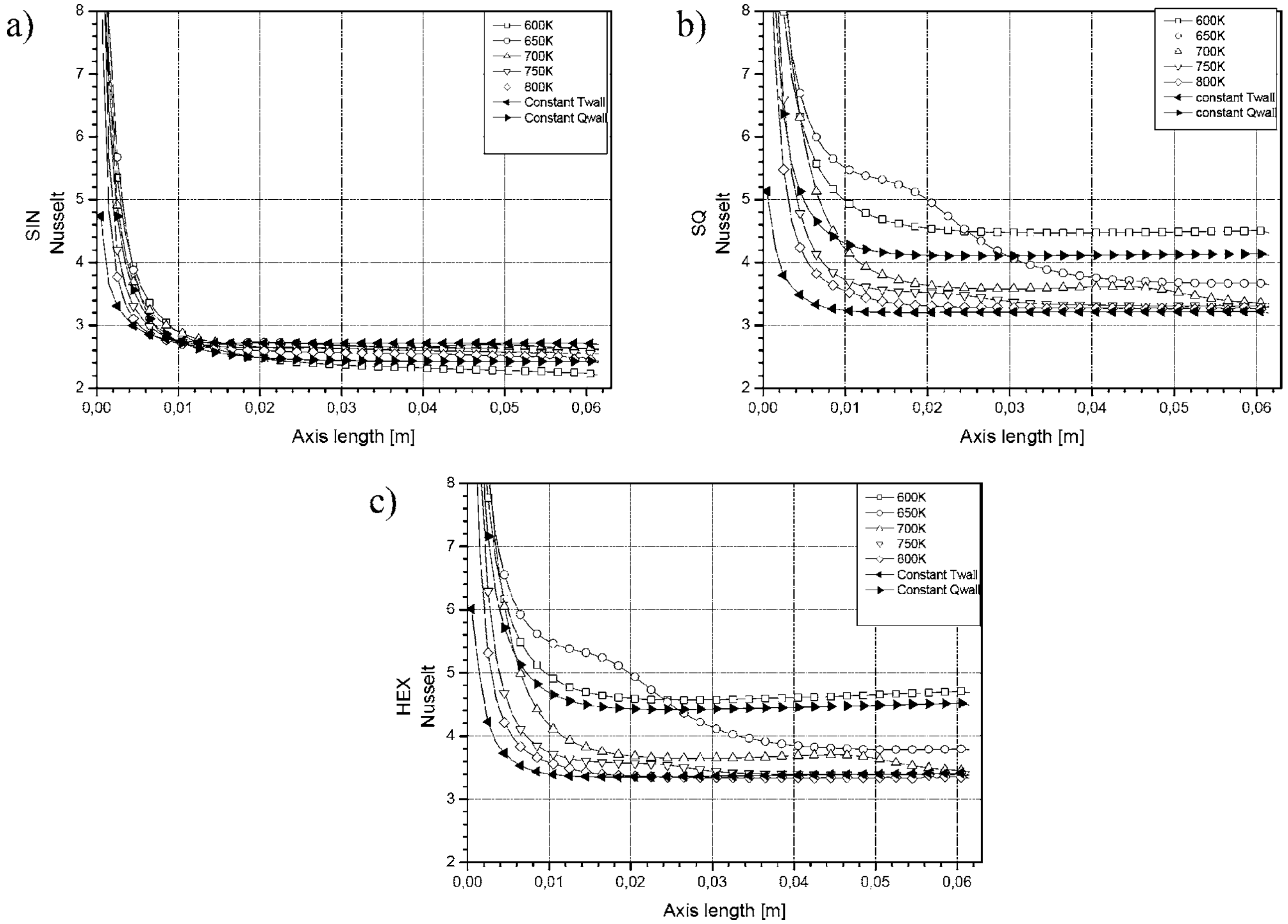

Fig. 4 (*a*) Sinusoidal; (*b*) squared; and (*c*) hexagonal section Nusselt number trends

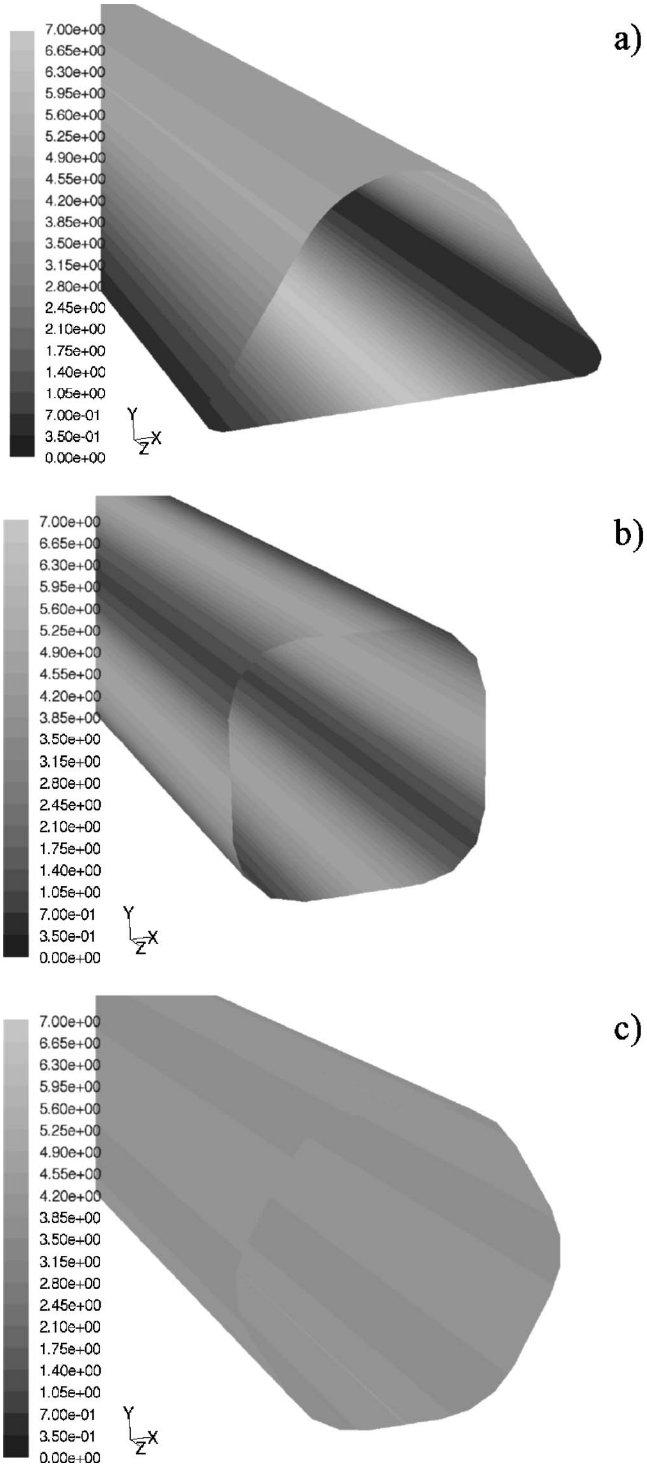

Fig. 6 Wall Nusselt distribution: (*a*) sinusoidal; (*b*) squared; and (*c*) hexagonal section, 650 K

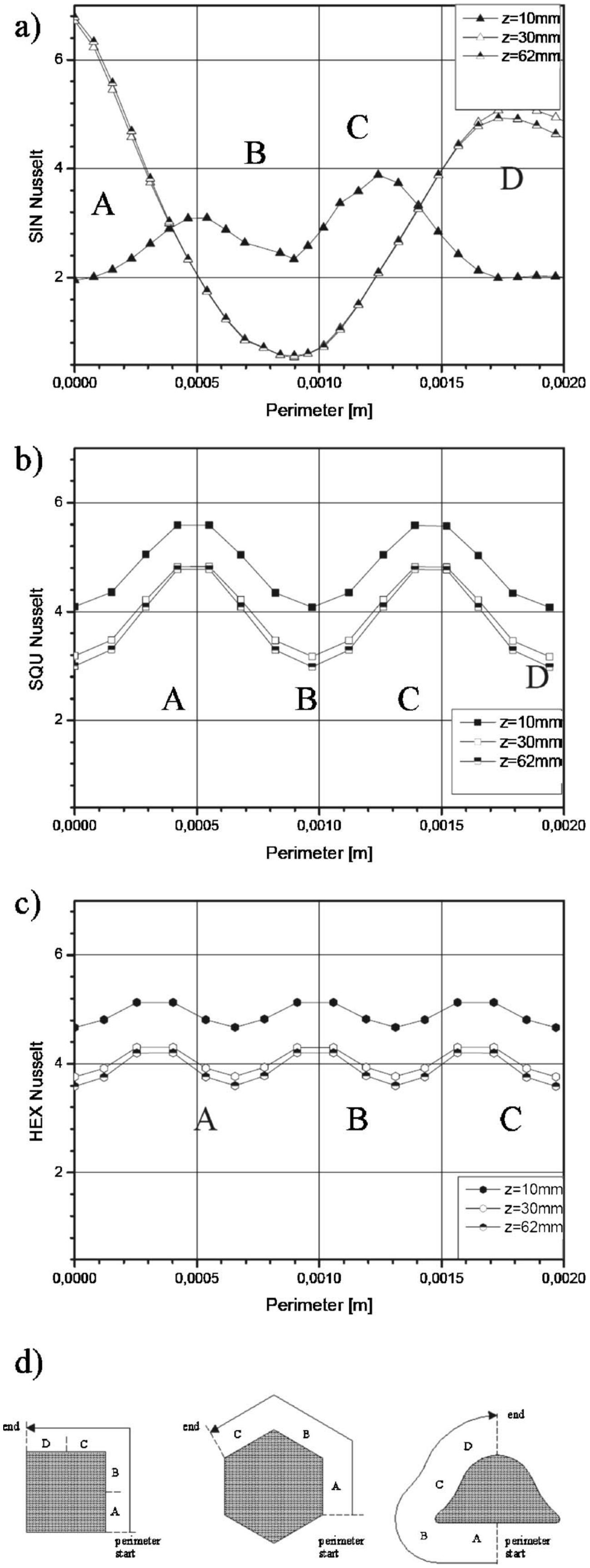

Fig. 7 Wall Nusselt number profiles for (*a*) sinusoidal; (*b*) squared; and (*c*) hexagonal sections, 650 K; (*d*) perimeter definition

case, the section heat transfer characteristics are rather inhomogeneous, whereas efficiency (related to the local Nusselt number) heavily depends on local surface curvature. The sinusoidal section exhibits the highest deviation from the mean value, while the hexagonal, whose wash-coated section appears similar to the circular one, presents the most regular one.

The local Nusselt number distribution along the section perimeter is reported in Fig. 7(*a*)–7(*c*), whose reference frame is sketched in Fig. 7(*d*). It may be observed that Nu is unevenly

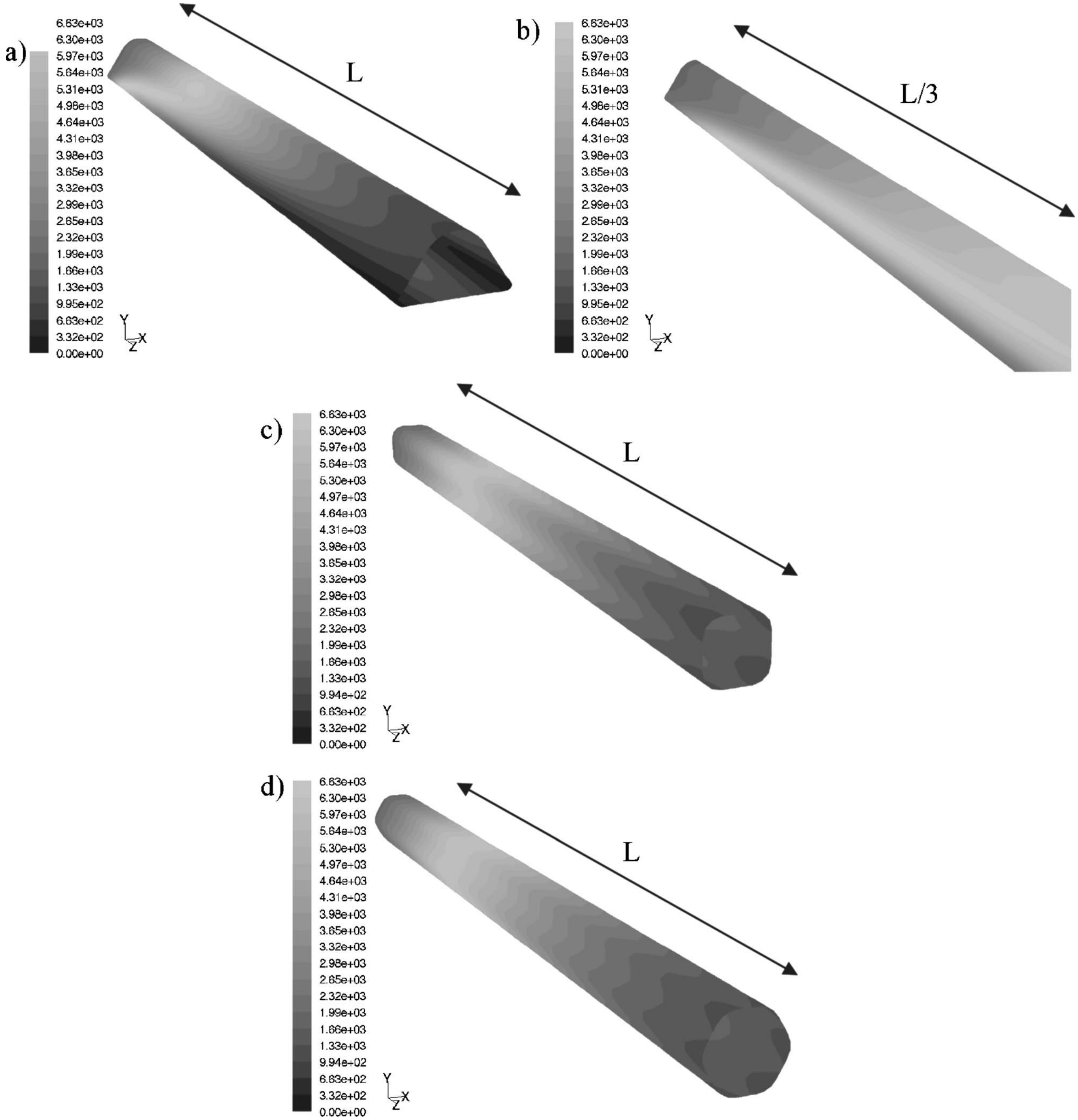

Fig. 8 Wall heat flux: (*a*) sinusoidal; (*c*) squared; (*d*) hexagonal sections, 650 K; (*b*) entrance detail of sinusoidal section

distributed along the perimeter. This information may be useful to identify the key section design parameters which influence its heat and mass transfer characteristics. The role of section corners can also be highlighted in these pictures, as Nu profiles get minimum values in those regions. With respect to this general trend, the sinusoidal section shows a different behavior near the channel inlet. Within the development length, in fact, Nu profile shows a more homogeneous behavior which results in a higher average Nu. The previous observations may be better understood if the actual heat flux distributions (Figs. 8(*a*)–8(*d*)) are analyzed. In fact, a very effective heat exchange can be observed for the sinusoidal section at the inlet (Fig. 8(*b*)), whereas only downstream of the entry length the more inhomogeneous Nu distribution influences heat flux in the corners. However, the latter effect takes act where temperature and mass fraction gradients between the wall and the bulk are already diminished and, consequently, plays a minor role. The above mentioned phenomenon allows the sinusoidal section to obtain the fastest bulk temperature trend, as reported in Fig. 9 where the practically coincident behavior of the hexagonal and square can also be observed. Similar conclusions could be drawn for other operating conditions.

Another important consideration on the influence of surface chemistry can be finally observed. Following the heat/mass transfer analogy [27], these processes are governed by dimensionless equations of the same form as far as constant heat (mass) flux or temperature (concentration) boundary conditions can be assumed on the wall. While at low temperatures heat/mass transfer analogy is almost confirmed, showing that Nu and Sh_i numbers can be related by an equation of the following form

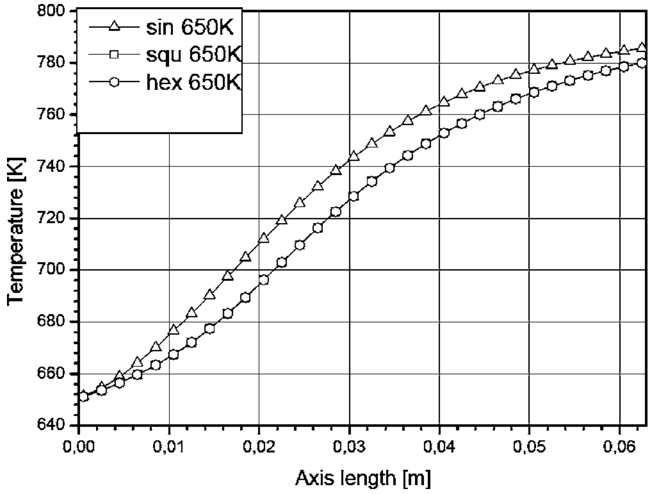

Fig. 9 Bulk temperature trend for all sections, 650 K

$$\frac{\mathrm{Nu}}{\mathrm{Sh}_i}=\left(\frac{\mathrm{Pr}}{\mathrm{Sc}_i}\right)^m \tag{19}$$

where m is a positive exponent less than 1 [27], at higher temperatures, boundary conditions must take into account the surface chemistry and cannot then be described by a simple constant flux/concentration hypothesis. In Fig. 10(*a*), as an example, squared section Sh profiles with respect to CO, C_3H_6, and NO are reported and compared to Nu number for 600 K inlet operating conditions. The similarity of the profiles is evident here, which means that the analogy is satisfied for this operating condition; the shift between Sh and Nu depends on the examined species Lewis number ($\mathrm{Le}_i = \mathrm{Sc}_i/\mathrm{Pr}$) which assumes an approximately 1 value for CO and NO and 1.6 value for C_3H_6.

At higher temperatures, Nu and Sh deviate from Eq. (19): squared section Nu and Sh numbers are again plotted in Fig. 10(*b*) for 650 K operating conditions, where a lack of similarity is evident. That lack of similarity is further put into evidence in Figs. 10(*c*)–10(*f*) where profiles of bulk temperatures and pollutant species mass fractions are reported for the same operating condition.

Results in terms of pollutant outlet fractions (defined as $1\text{-}\eta_{\mathrm{CONV}}$) are finally summarized in Fig. 11. Almost coincident asymptotic values can be observed as temperature goes up: under these conditions flow residence time is definitely higher than chemical conversion time. Conversely, at intermediate temperatures, where characteristic times are comparable, the more efficient heat and mass transfer characteristics of sinusoidal section allow to get better performance under the overall temperature range.

On the basis of the previous results it can be concluded that standard correlations, where available, are not always reliable for predicting heat and mass transfer parameters for intermediate temperature operating conditions under reacting conditions. The use of a detailed numerical tool has proved to allow the evaluation of the characteristics of given sections, and directly determine their performances in terms of species conversion efficiency.

Conclusions

A numerical analysis has been conducted to study heat and mass transfer processes in the channels of a three-way catalytic converter. The main purpose of the analysis has been the evaluation of the influence of surface reactions on these processes with respect to different channel geometries. To this aim, a 3D description of the flow field into the channel has been coupled to a detailed surface chemistry reaction mechanism describing the conversion of gaseous pollutants (HC, NO_x, and CO) on a Pt/Rh catalyst. The model has proved to be sufficiently predictive with regard to lean to stoichiometric operating conditions in the whole temperature range and it has been used as a basic design tool to evaluate different channel designs.

Sinusoidal, squared, and hexagonal shapes have been selected to represent different support materials and technologies: they have been analyzed to compare their performances in terms of heat and mass transfer capabilities, measured by Nu and Sh distributions.

Results mainly indicate that:

1. Heat and mass transfer characteristics are remarkably different for the different sections, and mostly depend on wall temperature and gaseous species concentration distribution;
2. Section averaged Nu and Sh profiles for reacting flows assume approximately intermediate trends between constant heat flux and constant temperature. By increasing operating temperature, the wall constant temperature conditions are reached although some differences can still be observed in terms of entrance length;
3. Nu (Sh) along the section perimeter has a rather inhomogeneous profile. The sinusoidal section is particularly prone to this effect. The sections corners constitute, especially for that section, low-efficiency heat transfer zones as far as the asymptotic behavior is concerned; conversely, in the entrance region the corners remarkably contribute to the sudden temperature increase;
4. Despite the nonuniform Nu (Sh) local distribution, the sinusoidal section showed the best performance in terms of heat exchange and pollutant conversion in all conditions;
5. Sh can be computed following heat and mass transfer analogy as far as constant flux and mass fraction boundary conditions may be taken as representative; on the contrary, mass transfer behavior deviates from the Nu trend since a nonlinear relation exists between energy and mass equation boundary conditions.

On the basis of these results, the proposed approach may represent an effective way to study heat and mass transfer processes in the channels of a catalytic converter and can also be used to generate basic correlations for Nu and Sh numbers with no requirements of experimental data needed for the parameter set estimation.

Nomenclature

A = transversal channel section, m^2
A_k = reaction k Arrhenius pre-exponential coefficient, mol cm s
c = concentration, $\mathrm{mol/m^3}$, $\mathrm{mol/m^2}$
c_p = constant pressure specific heat, kJ/kg K
CFD = computational fluid dynamics
CPSI = cells per square inch
D_h = hydraulic diameter $(4A/P)$, m
D_i = species i mass diffusivity, $\mathrm{m^2/s}$
E_a = activation energy, kJ/mol
$F_{\mathrm{cat/geo}}$ = catalytic versus geometrical surface ratio
GSA = geometric surface area per unit reactor volume, $\mathrm{m^2/m^3}$
h = enthalpy, kJ/kg
HC = hydrocarbons
j = diffusive flux, $\mathrm{kg/m^2\,s}$
k_k = reaction k Arrhenius coefficient, mol cm s
k = convection coefficient, $\mathrm{W/m^2\,K}$
$k_{m,i}$ = species i convection mass transfer coefficient, m/s
L = channel length, m
Le_i = Species i Lewis number $(\mathrm{Sc}_i/\mathrm{Pr})$
m = constant
mil = one thousandth of an inch, 2.54E-5 m

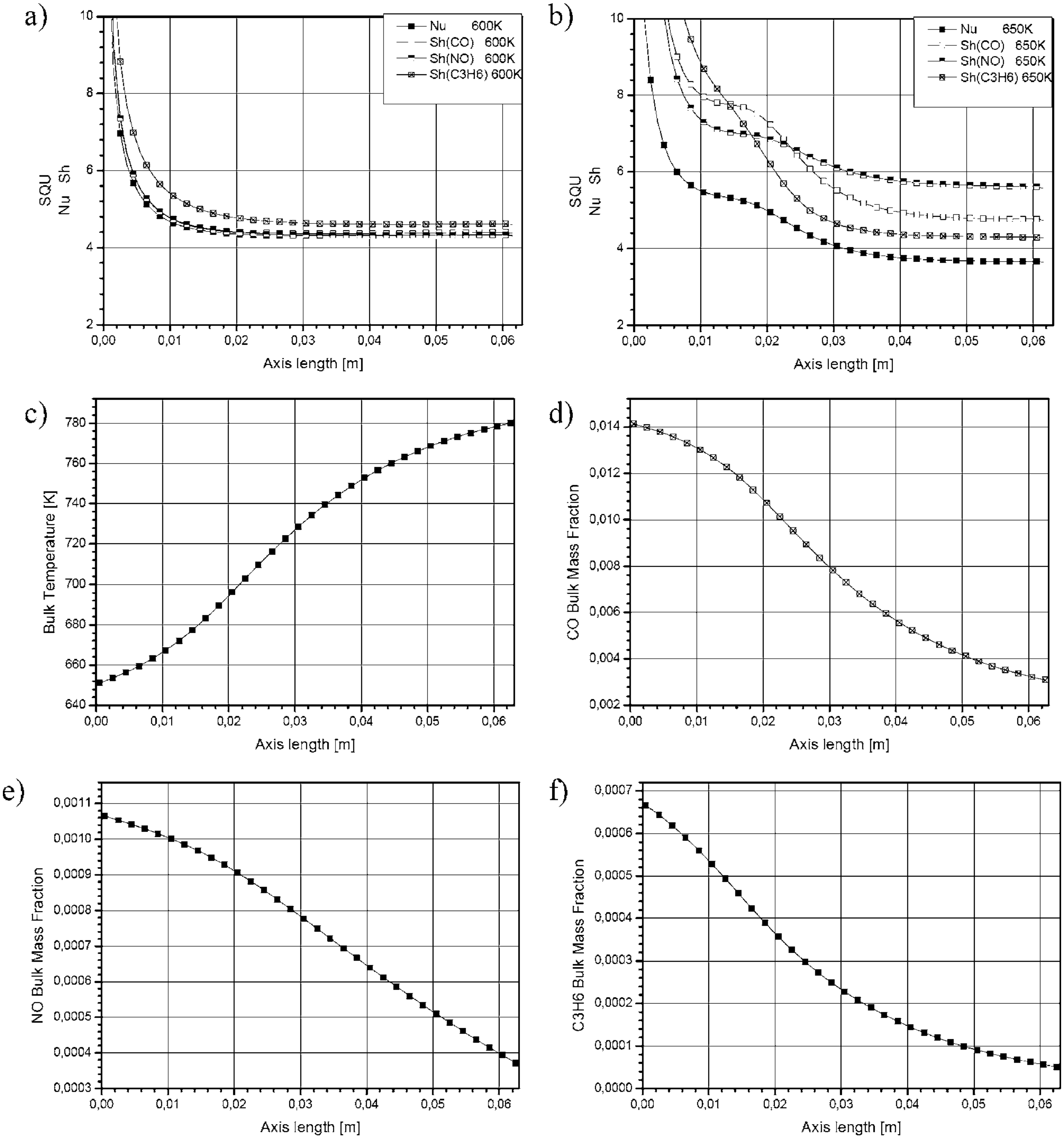

Fig. 10 Squared section Nusselt and Sherwood numbers ((*a*) 600 K and (*b*) 650 K); bulk temperature and pollutant species mass fractions, 650 K (*c*)–(*f*)

N = total number (species, reactions)
M = molecular weight
n = outward surface normal
NEDC = New European driving cycle
Nu = Nusselt number, kD_h/λ
p = pressure, Pa
P = section perimeter, m
Pe_H = heat Péclet number, $\mu L/\alpha$
Pe_M = mass Péclet number, $\mu L/D$
Pr = Prandtl number, $\mu c_p/k$
R_i^{het} = species i reaction rate per unit surface, kg/m^2 s
R = universal gas constant, J/kmol K
$\dot{s}$ = molar reaction rate per unit surface, kmol/m^2 s
S = adsorption/desorption sticking coefficient
S^{het} = enthalpy surface heat flux, W/m^2
Re_D = Reynolds number $(\rho u D_h/\mu)$
Sc_i = species i Schmidt number (ν/D_i)
Sh_i = species i Sherwood number $(k_{m,i}D_h/D)$
t = time, s
T = Temperature, K
THC = total hydrocarbons
u = velocity, m/s
X = molar fraction
Y = mass fraction
z = axial coordinate, m
z_e = entry length, m

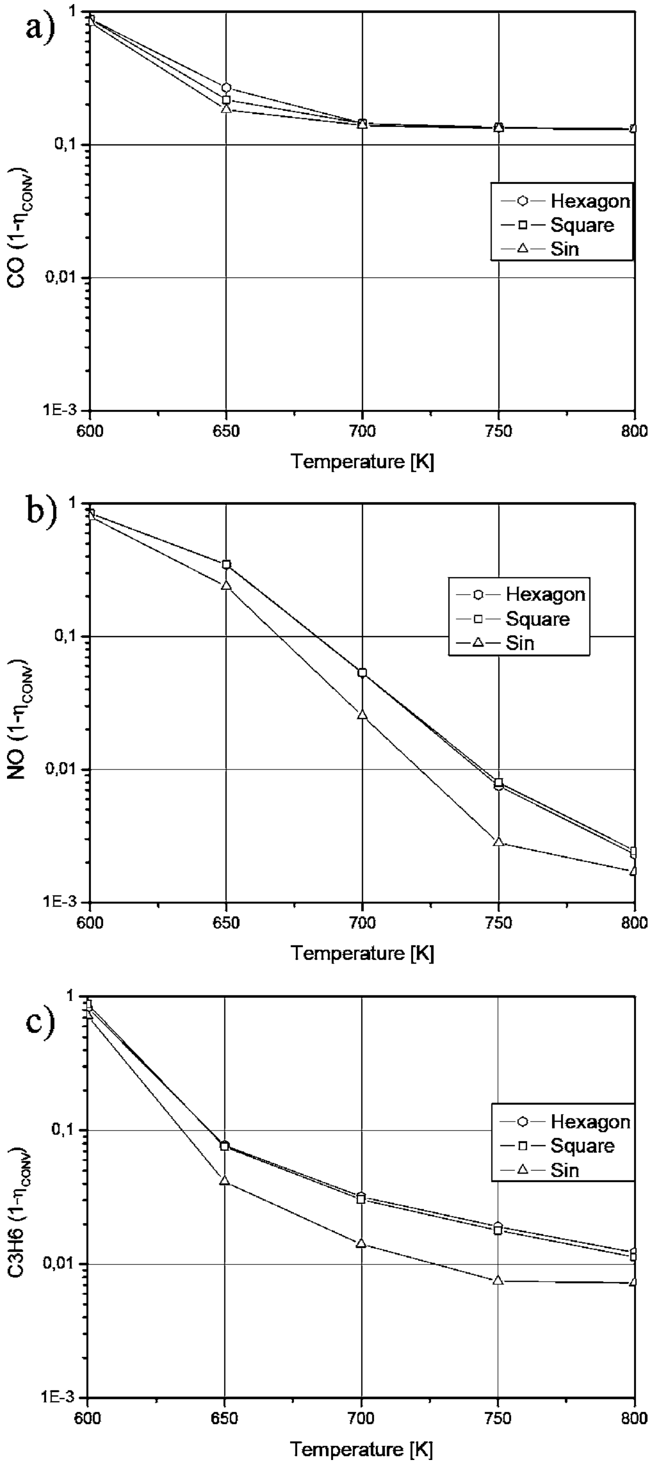

Fig. 11 (*a*) **CO,** (*b*) **NO, and** (*c*) **C_3H_6 conversion efficiencies for all sections and operating conditions**

Greek Symbols

β, μ = kinetic coefficients
ε_i = kinetic coefficient, kJ/mol
η = effectiveness factor
η_{CONV} = species conversion efficiency
θ_i = species i surface coverage
λ = thermal conductivity, W/m K
λ_{ox} = air fuel ratio
μ = dynamic viscosity, kg/ms
ν = stoichiometric coefficient
ν' = order coefficient
ρ = gas density, kg/m^3
τ = number of occupied adsorption sites of species i
Γ = site density, mol/m^2
Φ = washcoat Thiele module

Subscripts and superscripts

FORM = formation
i = ith chemical species
k = kth chemical reaction
g = gas phase
s = solid-gas interface
w = wall
z = z component

References

[1] Dembski, N., Guezennec, Y., and Soliman, A., 2002, "Analysis and Experimental Refinement of Real-World Driving Cycles," SAE Paper No. 2002-01-0069.
[2] Presti, M., and Pace, L., 2005, "Optimisation Development of Advanced Exhaust Gas Aftertreatment Systems for Automotive Applications," SAE Paper No. 2005-01-2157.
[3] Koltsakis, G. C., and Stamatelos, A. M., 1997, "Catalytic Automotive Exhaust Aftertreatment," Prog. Energy Combust. Sci., **23**, pp. 1–39.
[4] Pontikakis, G. N., 2003, "Modeling, Reaction Schemes and Kinetic Parameter Estimation in Automotive Catalytic Converters and Diesel Particulate Filters," Ph.D. thesis, University of Thessaly.
[5] Hayes, R. E., and Kolaczowski, S. T., 1999, "A Study of Nusselt and Sherwood Numbers in a Monolith Reactor," Catal. Today, **47**, pp. 295–303.
[6] Holmgren, A., and Andersson, B., 1998, "Mass Transfer in Monolith Catalysts-CO Oxidation Experiments and Simulations," Chem. Eng. Sci., **53**, pp. 2285–2298.
[7] Bollig, M., Liebl, J., Zimmer, R., Kraum, M., Seel, O., Siemund, S., Brück, R., Diringer, J., and Maus, W., 2004, "Next Generation Catalysts are Turbulent: Development of Support and Coating," SAE Paper No. 2004-01-1488.
[8] Zhang, L. Z., 2005, "Turbulent Three-Dimensional Air Flow and Heat Transfer in a Cross-Corrugated Triangular Duct," ASME J. Heat Transfer, **127**, pp. 1151–1158.
[9] Burgess, N. K., and Ligrani, P. M., 2005, "Effects of Dimple Depth on Channel Nusselt Numbers and Friction Factors," ASME J. Heat Transfer, **127**, pp. 839–847.
[10] Egner, M. W., and Burmeister, L. C., 2005, "Heat Transfer for Laminar Flow in Spiral Ducts of Rectangular Cross Section," ASME J. Heat Transfer, **127**, pp. 352–356.
[11] *FLUENT 6.2, User Guide*, 2004, Fluent, Inc., Lebanon, NH.
[12] Goodwin, D. G., 2003, "An Open-Source, Extensible Software Suite for CVD Process Simulation, Chemical Vapor Deposition," Proceedings 16th and EUROCVD, 14, ECS, Volume 2003-08, M. Allendorf, F. Maury, and F. Teyssandier, ed., The Electrochemical Society, pp. 155–162.
[13] Miyairi, Y., Aoki, T., Hirose, S., Makino, M., Miwa, S., Abe, and F., 2003, "Effect of Cell Shape on Transfer of Mass and Pressure Loss," SAE Paper No. 2003-01-0659.
[14] Groppi, G., and Tronconi, E., 1997, "Theoretical Analysis of Mass and Heat Transfer in Monolith Catalysts With Triangular Channels," Chem. Eng. Sci., **52**, pp. 3521–3526.
[15] Pontikakis, G. N., Konstantas, G. N., and Stamatelos, A. M., 2004, "Three-Way Catalytic Converter Modelling as a Modern Engineering Design Tool," ASME J. Eng. Gas Turbines Power, **126**, pp. 906–923.
[16] Hawthorn, R. D., 1974, Afterburner Catalysts: "Effect of Heat and Mass Transfer Between Gas and Catalyst Surface," AIChE Symp. Ser., **70**, pp. 428–438.
[17] Matthess, N., Schweich, D., Martin, B., and Castagna, F., 2001, "From Light-off Curves to Kinetic Rate Expressions for Three-Way Catalysts," Top. Catal., **16/17**, pp 119–124.
[18] Keil, F. J., 1999, "Diffusion and Reaction in Porous Networks," Catal. Today, **53**, pp. 245–258.
[19] Voltz, S. E., Morgan, C. R., Liederman, D., and Jacob, S. M., 1973, "Kinetic Study of Carbon Monoxide and Propylene Oxidation on Platinum Catalysts," Ind. Eng. Chem. Prod. Res. Dev., **12**, pp. 294–301.
[20] Chatterje, D., Deutschmann, O., and Warnatz, J., 2001, "Detailed Surface Reaction Mechanism in a Three-Way Catalyst," Faraday Discuss., **119**, pp. 371–384.
[21] Arrighetti, C., Cordiner, S., and Mulone, V., 2005, "Simulazione Termo-Fluidodinamica 3D di un Canale di Marmitta Catalitica a Tre Vie per MCI a Mezzo di Schemi Chimici Dettagliati," 60° Congresso Nazionale ATI.
[22] Granger, P., Dujardin, C., Paul, J.-F., and Leclercq, G., 2005, "An Overview of Kinetic and Spectroscopic Investigations on Three-Way Catalysts: Mechanistic Aspects of the CO+NO and CO+N2O Reactions," J. Mol. Catal. A: Chem., **228**, pp. 241–253.
[23] Kissel-Osterrieder, R., Behrendt, F., Warnatz, J., Metka, U., Volpp, H.-R., and Wolfrum, J., 2000, "Experimental and Theoretical Investigation of Co Oxidation on Platinum: Bridging the Pressure and Materials Gap," Proc. Combust.

Inst., **28**, pp. 1341–1348.
[24] Deutschmann, O., 2001, “Interactions Between Transport and Chemistry in Catalytic Reactors,” Habilitation thesis, Ruprecht-Karls-Universität, Heidelberg, Germany.
[25] Braun, J., Hauber, T., Tobben, H., Zacke, P., Chatterje, D., and Deutschmann, O., 2000, “Influence of Physical and Chemical Parameters on the Conversion Rates of a Catalytic Converter: A Numerical Simulation Study,” SAE Paper No. 2000-01-0211.
[26] Andreassi, L., Cordiner, S., and Mulone, V., 2004, “Cell Shape Influence on Mass Transfer and Backpressure Losses in an Automotive Catalytic Converter,” SAE Paper No. 2004-01-1837.
[27] Incropera, F. P., and De Witt, D. P., 2001, *Fundamentals of Heat and Mass Transfer*, Wiley, New York.
[28] Groppi, G., Belloli, A., Tronconi, E., and Forzatti, P., 1995, “A Comparison of Lumped and Distributed Models of Monolith Catalytic Combustors,” Chem. Eng. Sci., **50**, pp. 2705–2715.
[29] Renksizbulut, M., and Niazmand, H., 2006, “Laminar Flow and Heat Transfer in the Entrance Region of Trapezoidal Channels With Constant Wall Temperature,” ASME J. Heat Transfer, **128**, pp. 63–74.

Numerical Studies on Channel Formation and Growth During Solidification: Effect of Process Parameters

Jayesh Jain

Arvind Kumar

Pradip Dutta[1]
e-mail: pradip@mecheng.iisc.ernet.in

Department of Mechanical Engineering,
Indian Institute of Science,
Bangalore 560012, India

In the present work, solidification of a hyper-eutectic ammonium chloride solution in a bottom-cooled cavity (i.e. with stable thermal gradient) is numerically studied. A Rayleigh number based criterion is developed, which determines the conditions favorable for freckles formation. This criterion, when expressed in terms of physical properties and process parameters, yields the condition for plume formation as a function of concentration, liquid fraction, permeability, growth rate of a mushy layer, and thermophysical properties. Subsequently, numerical simulations are performed for cases with initial and boundary conditions favoring freckle formation. The effects of parameters, such as cooling rate and initial concentration, on the formation and growth of freckles are investigated. It was found that a high cooling rate produced larger and more defined channels which are retained for a longer durations. Similarly, a lower initial concentration of solute resulted in fewer but more pronounced channels. The number and size of channels are also found to be related to the mushy zone thickness. The trends predicted with regard to the variation of number of channels with time under different process conditions are in accordance with the experimental observations reported in the literature.
[DOI: 10.1115/1.2709660]

Keywords: solidification, channels, process parameters, numerical simulation

1 Introduction

During solidification of a binary substance, the melt interacts with the mush and its diffusion layer both solutally and thermally, resulting in a situation where both temperature and solute concentration gradients play significant roles. These gradients lead to convection due to thermal and solutal buoyancy in both mushy and liquid regions, resulting in double-diffusive convection.

The physical issues pertaining to any solidification process generally depend on the externally imposed boundary conditions and the initial concentration of the binary substance. In the case of a melt cooled from below, the fluid layer is always thermally stable, and hence a thermal-buoyancy driven flow does not occur. However, if the thermally stable system rejects a lighter residual upon solidification, the situation leads to density inversion. Such inversions are generally unstable and can give rise to finger type, solutally driven convection which leads to the formation of channels in localized regions of the mushy layer, known as freckles. The formation of channels within a casting represents a severe form of macrosegregation [1], since the composition and crystalline structure of solid, which ultimately forms within the channels, differs significantly from those of the surrounding solid regions.

The defects caused by freckles in alloy castings, along with the interesting fluid mechanical phenomenon associated with their formation [2], have attracted the attention of various researchers in the past. Many experimental studies have been made to better understand the conditions of freckles initiation and characteristics [3–10]. The experimental work cited above mainly focused on the measurement of liquid fraction [3], temperature [4], concentration [6], and flow field [7]. All the above investigations report observations and explain the phenomena associated with freckles formation. Means to offset the naturally induced fluid motion have also been investigated [8–11]. Tan et al. [10] and Tan [11] studied experimentally the effect of base plate temperature, initial concentration, inclination angle of the cavity, and vibration on freckle formation. The complex convection phenomena occurring during freckle formation represent a formidable challenge for numerical simulation. Neilson and Incropera [12] numerically simulated solidification in a bottom-chilled cavity under conditions for which large-scale convection results from a compositionally induced density inversion in the mushy region. It was observed that channel growth is predicted to begin at the liquidus front and, due to localized freezing point depression, propagated downward toward the chill plate. Since then, numerous studies have been performed to simulate and predict freckling in upward directional solidification [13–19]. Felicelli et al. [13] simulated channel formation in directional solidification of Pb–Sn alloys in two dimensions. Neilson and Incropera [14] performed three-dimensional simulations of channel formation. Three-dimensional simulations have also been performed by Felicelli et al. [15] for binary alloys. Some numerical studies were carried out to model the macrosegregation and freckle channel segregates formation during the directional solidification of super alloy casting by Schneider et al. [16]. In their work, a model for the fragment movement and remelting was developed that pertains to realistic conditions involving a multicomponent Ni-based superalloy. Sarazin and Hellawell [17] studied channel formation in Pb–Sn, Pb–Sb and Pb–Sn–Sb alloy ingots and compared the results with the NH_4Cl-H_2O system. A Rayleigh number based criterion was developed for predicting the formation of freckles in Pb–Sn alloys by Bergman et al. [18] and more recently by Beckermann et al. [19] for Ni-base superalloy castings. Detailed mesh spacing sensitivity studies have been performed by Sung et al. [20] for two-dimensional simulations of freckle formation in upward directional solidification.

Although there are numerous numerical studies on freckle formation reported in the literature, systematic studies on the effects

---

[1] Corresponding author.

Contributed by the Heat Transfer Division of ASME for publication in the JOURNAL OF HEAT TRANSFER. Manuscript received February 11, 2006; final manuscript received October 13, 2006. Review conducted by Jayathi Murthy.

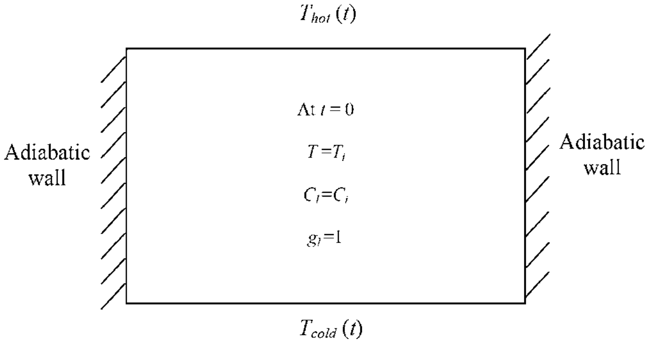

Fig. 1 Problem domain with initial and boundary condition

of various parameters on the mechanism of plume formation and the conditions leading to freckle formation are relatively few. Most of the literature on freckles formation [13–20] focused mainly on predication of freckles formation in the mushy zone. However, few studies have been is reported with regard to parameters (such as cooling rate, growth rate of the mushy zone, and initial concentration of the system) affecting the mechanism of plume growth, leading to formation of freckles, their evolution, and the variation of number of channels with time. In this context, there have been some recent experimental studies by Tan et al. [10] and Tan [11] on the effect of base plate temperature, initial concentration, inclination angle of the cavity, and vibration on freckle formation. These studies attempt to relate the time evolution of channels and their thickness and depth to the parameters mentioned above. However, there is a need for a comprehensive and systematic numerical study on the effect of various parameters on the freckles formation mechanism which can also support the experimental observations reported in Tan et al. [10,11]. The present numerical study is based on the establishment of a Rayleigh number based criterion to determine the conditions favorable for freckles formation, leading to the identification of some relevant physical parameters. Numerical studies are performed with regard to the general trend of freckle formation, and its sensitivity to various process parameters. The findings from the present numerical studies are in accordance with those of experimental results [10,11]. The numerical studies also provide insight into the physics involved in the formation, growth and destruction of channels.

2 The Model System and Physical Issues

The model system for the present study consists of a rectangular cavity of height H and width H/A (where A is aspect ratio), filled with a hyper-eutectic binary solution of aqueous NH_4Cl. A schematic diagram of the model is shown in Fig. 1. At the start of the solidification experiment, a temperature gradient, G, is imposed across the height of the cavity, such that the temperature increases linearly from the bottom wall to the top wall. The side walls of the cavity are insulated. Cooling is achieved by lowering the temperatures of the top and bottom walls of the cavity at a constant rate, r, such that the overall temperature gradient is maintained across the height of the cavity.

The configuration described above will lead to directional solidification from the bottom, once the bottom wall temperature falls below the liquidus temperature. From a heat transfer point of view, the bottom cooled fluid layer is thermally stable. However, upon solidification from the bottom surface, the hyper-eutectic solution will reject water at the interface due to partitioning. The lighter solute (i.e., water) released at the interface will cause a density inversion, leading to the possibility of solutally driven plume convection.

Since plumes are a prerequisite for channel formation, we would first like to determine a criterion for their formation. The condition for the onset of plumes is generally based on the classical Fleming's criterion [21] which states that for plumes to form, the interdendritic fluid velocity, V, should be greater than the isotherm velocity, R (which refers to the growth rate of the mush). In other words, the criterion is

$$\frac{V}{R} > 1 \tag{1}$$

If we assume that the velocity in the mushy region follows Darcy's law, the magnitude of V can be expressed as

$$V = \frac{\Delta\rho g K}{\nu f_l} \tag{2}$$

where K is the permeability, f_l is the liquid fraction, and $\Delta\rho$ is the net density gradient which can be expressed as

$$\Delta\rho = \frac{(\rho - \rho_0)}{\rho_0} = \beta^1 (C - C_0) \tag{3}$$

In Eq. (3), C is the liquid concentration, C_0 is a reference concentration, and β^1 is the effective expansion coefficient which can be expressed as

$$\beta^1 = \beta_s - \beta_T / m \tag{4}$$

where $m = dC/dT$ is the slope of liquidus line in the phase diagram. Substituting the expression for velocity in Eq. (2) and choosing a length scale, l, as D/R, where D is the species mass diffusivity in the liquid and R is the growth rate, Eq. (1) takes the following form

$$\frac{\Delta\rho g K}{\nu f_l D} l > 1 \tag{5}$$

The left hand side of Eq. (5) is a nondimensional expression resembling a Rayleigh number, which can be defined in the present context as

$$\mathrm{Ra} = \frac{\Delta\rho g K}{\nu f_l D} l \tag{6}$$

The Rayleigh number in this case is a function of concentration, liquid fraction, permeability, growth rate of mushy layer, and thermophysical properties. Accordingly, using Eq. (5), we can define a critical Rayleigh number, $\mathrm{Ra}_{\mathrm{cr}} = 1$, for onset of plumes.

The Rayleigh number, defined above, measures the ratio of the driving buoyancy force to the retarding frictional force associated with the permeability of the mush. It is a function of several parameters as given in Eq. (6). This kind of criterion includes all factors governing channel formation, i.e., permeability, physical system, alloy properties, and processing parameters. However, one of the ambiguities in this kind of criterion, as discussed in the literature [17–19], lies in the definition of the length scale in Rayleigh number. In the present definition of Ra number, the length scale (l) involves mass diffusivity instead of thermal diffusivity. The reason for selecting solutal diffusivity is obvious, as the solutal gradient is the driving force for the channels in the thermally stable vertical solidification system.

2.1 Key Parameters Affecting Freckle Formation. The Rayleigh number definition includes density gradient as a driving force for the plumes which, in turn, depends on the local concentration gradient in the direction of plume growth $(C - C_0)$. Now, the role of local concentration gradient in determining the plume growth depends on the initial condition (concentration and temperature) of the system. Further initiation of plumes depends upon the growth rate of the mush (R), which, in turn, depends on the cooling temperature and the applied heat extraction rate ($r = GR$), where r and G are cooling rate and temperature gradient, respectively. After plumes are initiated, their growth depends on the resistance offered by the mush, i.e., permeability of the mush (K). Permeability is a complex parameter, which depends on the local

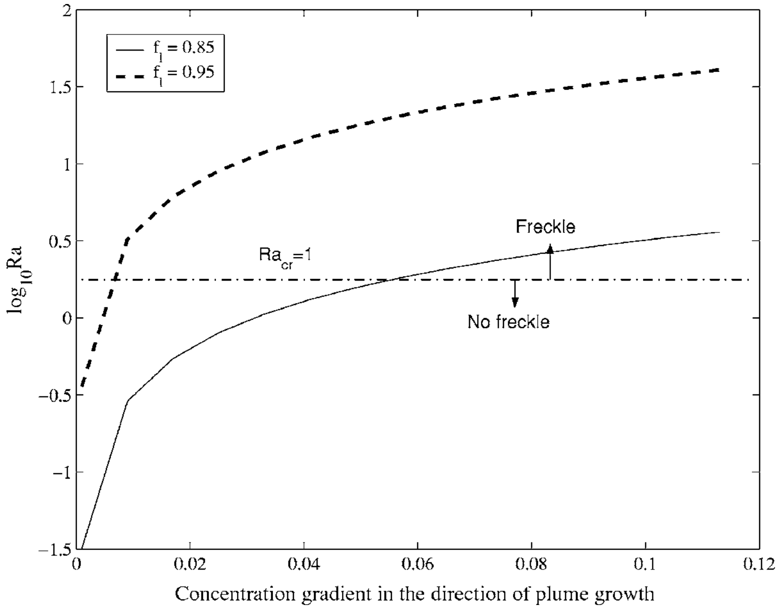

Fig. 2 Variation of Ra number with concentration gradient in the direction of plume growth for $R=6\times10^{-6}$ m/s, $G=7.7$ K/mm, $r=0.046$ K/s

liquid fraction (f_l) and the dendritic arm spacing (d_1) [22].

From the preceding discussion, it is apparent that the plume formation and their growth are dependent on several interlinked parameters which finally affect the formation of channels in the mushy zone. The Rayleigh number, defined in Eq. (6) in terms of process parameters and thermophysical properties, can hence be used to arrive at the conditions favoring freckle formation. To appreciate this methodology, we have plotted the Ra number versus each parameter (used in Ra number definition), by keeping other parameters constant, for an aqueous ammonium chloride solution. Each plot will give us the range of parameters determining freckle formation, based on the critical Ra number criterion (Eq. (6)) of plume formation.

Figure 2 shows a plot between Ra number and concentration gradient in the direction of plume growth, for different values of liquid fraction. The maximum value of concentration gradient to be used, (C_e-C_0), comes from the chosen initial condition of the system ($C_i=0.68$) and the reference concentration ($C_0=C_e=0.793$). Figure 2 shows that for lower liquid fraction, a higher concentration gradient is required for freckling to take place. The same conclusion can be drawn from Fig. 3, which shows a plot between Ra number and liquid fraction for different concentration gradients.

Figure 4 depicts a plot between Rayleigh number and concentration gradient for different growth rates, R. Here, growth rate is controlled by the cooling rate ($r=GR$) applied. This plot shows that higher growth rates will require more concentration gradients

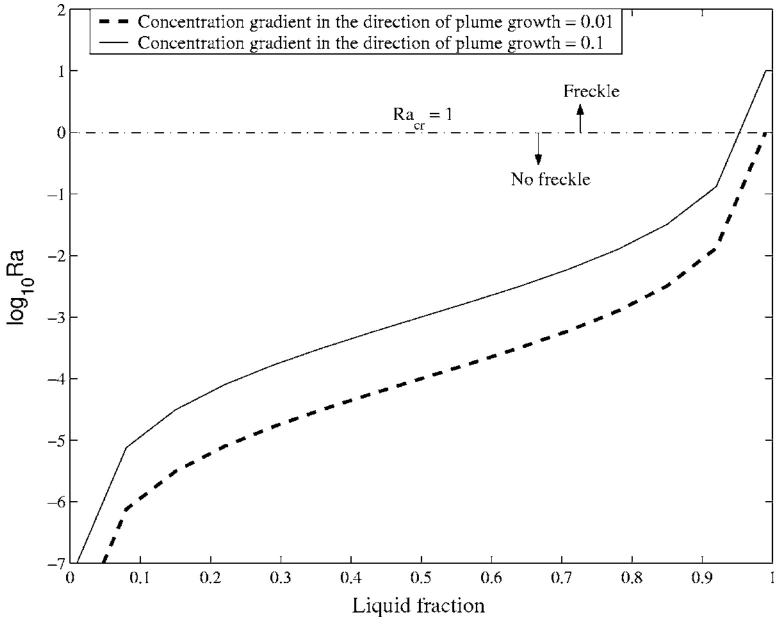

Fig. 3 Variation of Ra number with liquid fraction for $R=6\times10^{-6}$ m/s, $G=7.7$ K/mm, $r=0.046$ K/s

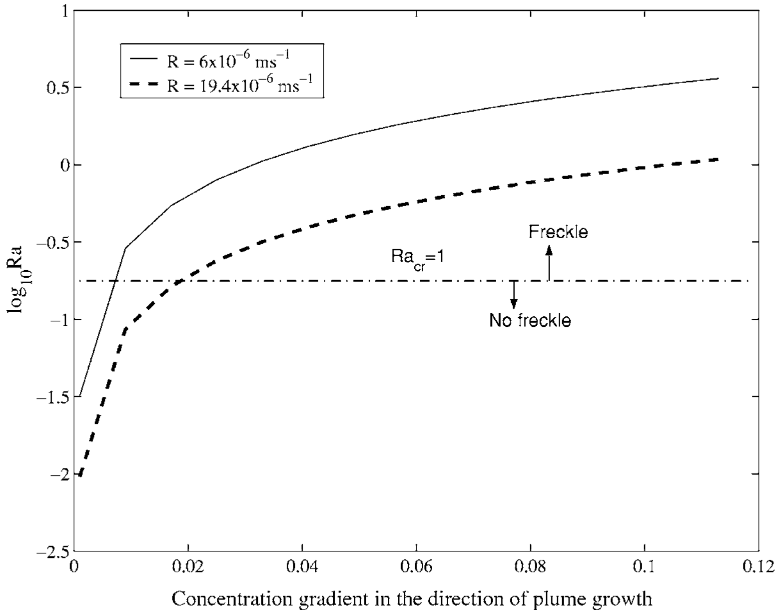

Fig. 4 Variation of Ra number with concentration gradient in the direction of plume growth for different growth rates (R=6×10^{-6} m/s, G=7.7, K/mm, f_l=0.85, r=0.046 K/s)

for plume initiation. In other words, high growth rates makes channeling less probable, the same conclusion as stated in Fleming's criterion [21].

Figure 5 shows a plot between Rayleigh number and concentration gradient, for different values of Schmidt number, Sc. This variation of Sc refers to different alloy systems. Figure 5 shows that for high Schmidt number alloys, plumes are more likely to form, and hence they are more prone to freckling. It can be observed from the plot that the NH_4Cl-H_2O system, with Sc=250, will require less concentration gradient for driving the plumes, compared to the Pb–Sn system (with Sc=62.5).

Based on the Rayleigh number criterion established above and its dependence on various parameters, it is possible to choose initial and boundary conditions favoring freckle formation. Parametric studies, described subsequently in Sec 4, are performed accordingly.

3 Mathematical and Numerical Modeling

3.1 Governing Equations. For solidification modeling, a fixed-grid single domain formulation is adopted, based on the classical mixture theory [23]. For the purpose of mathematical modeling, we invoke assumptions consistent with the continuum model described in Ref. [23]. In the fixed grid single domain

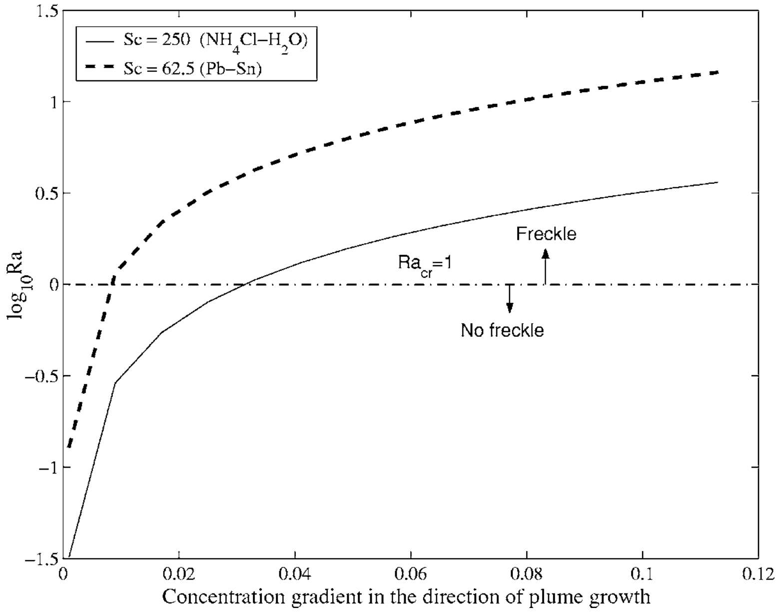

Fig. 5 Variation of Ra number with concentration gradient in the direction of plume growth for different Sc number (R=6×10^{-6} m/s, G=7.7 K/mm, f_l =0.85, r=0.046 K/s)

formulation [23–28], conservation equations are employed for the entire domain, such that they are equally valid in the fully solid, mushy (solid plus liquid), and fully liquid regions. In this approach, the interface is captured (i.e., it is a part of the solution) and does not need to be tracked separately. The details of the continuum formulation are given in Refs. [23,24,29]. The equations governing conservation of mass, momentum, energy, and species concentration appropriate to the present study can be stated as [23–28]

$$\frac{\partial}{\partial t}(\rho) + \nabla \cdot (\rho \vec{u}) = 0 \tag{7}$$

$$\frac{\partial}{\partial t}(\rho \vec{u}) + \rho \vec{u} \cdot (\nabla \vec{u}) = \nabla \cdot \left(\mu_l \frac{\rho}{\rho_l} \nabla \vec{u}\right) - \nabla p + S_b - S\vec{u} \tag{8a}$$

where

$$S_b = \rho \vec{g}[\beta_T(T - T_0) + \beta_C(C_l - C_0)] \tag{8b}$$

The last term on the right-hand side of Eq. (8*a*) originates from the assumption that the mushy zone is a saturated porous medium that offers frictional resistance toward fluid flow in that region. However, since the framework of the present model is fairly general, any appropriate porous-medium model can be chosen to describe the flow in the mushy region, in accordance with the morphology of the phase-changing domain. Here, this term is modeled as

$$S\vec{u} = \frac{\mu_l \rho \vec{u}}{K\rho_l} \tag{9}$$

where K is the permeability. The permeability, K, in the principal directions is calculated using the liquid fraction and primary dendritic arm spacing, as reported in Heinrich and Poirier [22]. This term resembles the resistance term for flow through porous media [29]. In the fully solid region, this source term provides a large flow resistance, making the velocities effectively zero. In the fully liquid region, this term offers no resistance. In the mushy region, where the liquid fraction ranges from zero to one, the porous medium resistance varies smoothly from zero in the liquid region to a high value in the solid region, thus making the velocities vary accordingly.

The energy conservation equation can be written as

$$\frac{\partial}{\partial t}(\rho c T) + \nabla \cdot (\rho c \vec{u} T) = \nabla \cdot [(\ g_s k_s + g_l k_l) \nabla T)] + S_h \tag{10a}$$

where source term, S_h, is expressed as

$$S_h = -\left[\frac{\partial}{\partial t}(\rho \Delta H) + \nabla \cdot (\rho \vec{u} \Delta H)\right] \tag{10b}$$

In Eq. (10*b*), ΔH is the latent enthalpy of the cell. Since a cell in a mushy region consists of both solid and liquid, ΔH can be defined as

$$\Delta H = f_l L, \quad \text{for } T \geqslant T_{\text{solidus}}$$

$$0, \quad \text{for } T < T_{\text{solidus}} \tag{11}$$

where f_l is liquid fraction and L is the latent heat of fusion.

In implementing the preceding equations, we make an extended Boussinesq approximation by neglecting solidification shrinkage and making a conventional assumption that the important density changes are those associated with the buoyancy in the liquid. The terms f_l and f_s denote mass fraction of the liquid and solid phases, respectively. Since shrinkage is neglected, the mass fraction, f_l, and the volume fraction, g_l, of liquid are equivalent and can be used interchangeably in the subsequent analysis. The continuum density and velocity are, respectively, defined as

$$\rho = (1 - g_l)\rho_s + g_l \rho_l \tag{12}$$

where g_l is the volume fraction of liquid

$$\vec{u} = f_s \vec{u}_s + f_l \vec{u}_l \tag{13}$$

The single-phase solute transport equation is derived directly on considering a macroscopic solute balance in an arbitrary fixed control volume within the mushy region. From such a balance the following equation can be derived [25–28]

$$\frac{\partial}{\partial t}(\rho C_{\text{mix}}) + \nabla \cdot (\rho \vec{u} C_l) = \nabla \cdot (\rho_s g_s D_s \nabla C_s + \rho_l g_l D_l \nabla C_l) \tag{14}$$

where C$_{\text{mix}}$ is a representative value of concentration obtained by averaging over a volume defined on the microscopic scale. Representing this microscopic volume as $V = V_s$ (i.e., volume of the solid fraction) $+V_l$ (i.e., volume of the liquid fraction), the general form of C_{mix} can be written as

$$C_{\text{mix}} = \frac{\int \rho_l C_l dV_l + \int \rho_s C_s dV_s}{\rho V} \tag{15}$$

With Scheil's assumption [25,27], Eq. (15) for C_{mix} becomes

$$\rho C_{\text{mix}} = \rho_l f_l C_l + \rho_s \int_0^{g_s} C_s d\alpha \tag{16}$$

where α is a dummy variable for carrying out the integration [24]. The concentration of solute in the liquid and solid phases will be related via $C_s = k_p C_l$. With $C_s = k_p C_l$ at the solid-liquid interface and using the definition of C_{mix} from Eq. (16) the single-phase solute conservation equation (Eq. (14)) can be written as

$$\frac{\partial}{\partial t}(\rho C_l) + \nabla \cdot (\rho \vec{u} C_l) = \nabla \cdot (D^+ \nabla C_l) + S_c \tag{17a}$$

where D^+ is the mass diffusion coefficient and S_c is the species source term. With Scheil's model, the above terms can be written as [25–28]

$$D^+ = \rho f_l D_l \tag{17b}$$

$$S_c = \frac{\partial}{\partial t}(\rho f_s C_l) - k_p C_l \frac{\partial}{\partial t}(\rho f_s) \tag{17c}$$

The initial conditions appropriate to the model system are

At $t = 0$

$$T_i = T_b + Gy, \quad C = C_i, \quad f_l = 1, \quad u = v = 0$$

The boundary conditions, pertaining to the domain shown in Fig. 1, can be summarized as

At $x = 0$, H/A

$$u = v = \frac{\partial T}{\partial x} = \frac{\partial C_l}{\partial x} = 0$$

At $y = 0$, H

$$u = v = \frac{\partial C_l}{\partial x} = 0, \quad T = T_b + Gy - rt$$

where H is the height of the cavity. A is the aspect ratio. and T_b is the bottom wall temperature at $t = 0$.

3.2 Numerical Procedure. In the fixed grid continuum formulation [23–28], conservation equations are employed for the entire domain, such that they are equally valid in the fully solid, mushy, and fully liquid regions. Using a fixed grid, single domain approach, the interface is part of the solution and does not need to be tracked separately. The governing equations of conservation are discretized using a pressure-based finite volume method according to the SIMPLER algorithm [30]. The porous medium source terms in momentum Eq. (8*a*) are calculated for each control volume using the value of liquid fraction. The value of liquid fraction, f_l, of a control volume is calculated from the latent heat content of a cell, as given by

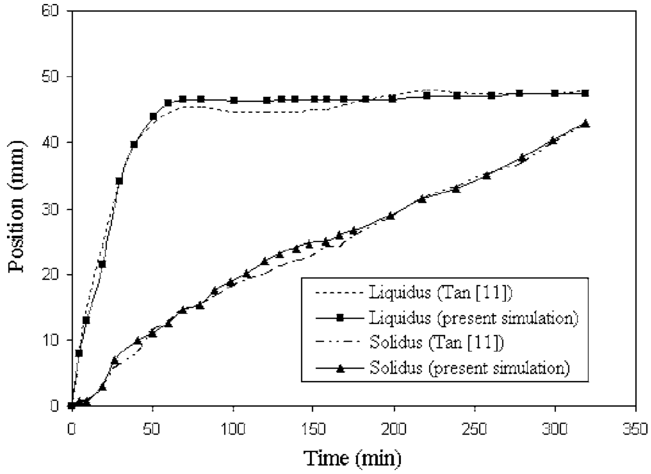

Fig. 6 Comparison of predicted Liquidus and solidus position with time from experimental results of Tan [11]

$$f_l=\frac{\Delta H}{L} \tag{18}$$

For an accurate prediction of the liquid fraction, the latent heat content of each computational cell needs to be updated according to the temperature and/or species concentration values predicted by the macroscopic conservation equations, in each iteration within a time step. In the present context, an iterative updating scheme is chosen, which is of the form [25–27,29]

$$[\Delta H_P]_{n+1}=[\Delta H_P]_n+\frac{a_P}{a_P^0}\lambda(\{h_P\}_n-F^{-1}\{\Delta H_P\}_n) \tag{19}$$

In Eq. (19), $a_P^0=\rho\Delta V/\Delta t$; a_P is the coefficient of T_P in the discretization equation of the governing energy equation; λ is a relaxation factor; F^{-1} is inverse of suitable latent heat function depending on the phase change morphology; ΔV is the volume of a computational cell centered around the grid pint P; Δt is the time step chosen; and h_P is the sensible enthalpy appropriate to the nodal point P. A detailed outline of algebraic steps for construction of physically consistent latent heat function is described by Chakraborty and Dutta [31].

In order to resolve the formation of freckle defects the computational domain should be discretized with elements that are smaller than d_1 and D/V in the horizontal and vertical directions, respectively [20]. The number of grids chosen in the present case (400×30) ensures sufficient resolution to resolve the channel formation. However, it is observed that the exact locations and number of channels formation is still sensitive to grid size, as also reported in the literature. The grid size chosen here allows us to observe the general trend of freckle formation, and its sensitivity to various process parameters, which is the focus of the present study. It is also found that the time step has a profound effect on the convergence of the solution for predicting the freckles. In this study, the time step for computation is varied from 0.1 s during the conduction dominated regime to 0.0005 s during plume convection.

4 Results and Discussion

As a validation exercise, the variation of solidus and liquidus positions with time predicted by the present model are compared with the experimental results reported in Tan [11]. This validation was performed for aqueous ammonium chloride solution in a cylindrical cavity with an initial concentration of ammonium chloride as 32 wt %. Other initial and boundary conditions are the same as those used in Tan [11]. In the plot shown in Fig. 6 the solidus and liquidus positions are predicted at the midwidth of the

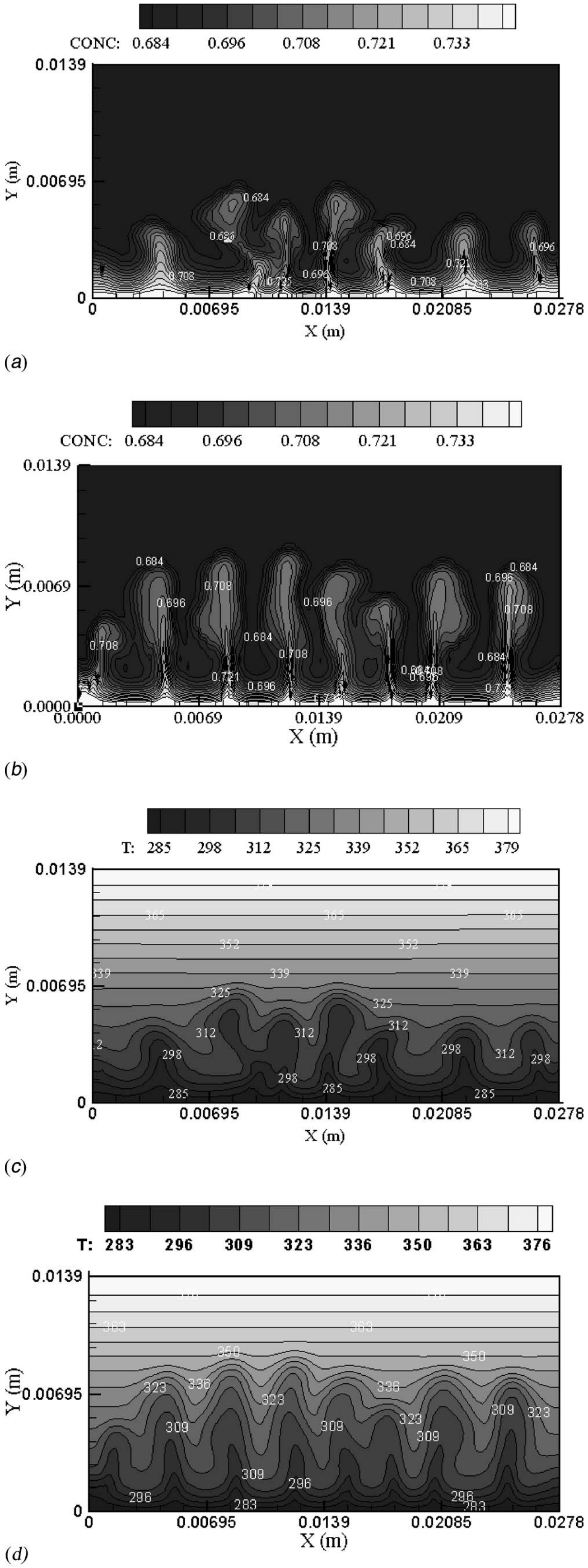

Fig. 7 Predicted liquid concentration plots: (*a*) $r=0.046$ K/s, (*b*) $r=0.15$ K/s and temperature distribution in K, (*c*) $r=0.046$ K/s; and (*d*) $r=0.15$ K/s at $t=15$ s for different cooling rates ($C_i=68\%$, $T_b=279$ K, $G=7.7$ K/mm)

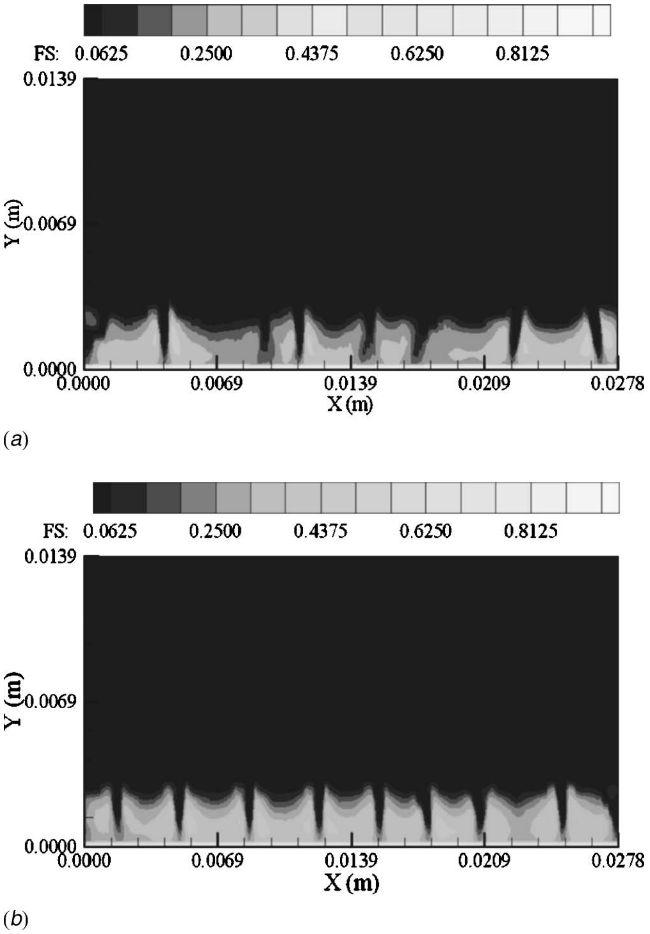

Fig. 8 Predicted solid fraction plot at $t=50$ s for different cooling rates: (*a*) $r=0.046$ K/s; and (*b*) $r=0.15$ K/s ($C_i=68\%$, $T_b=279$ K, $G=7.7$ K/mm)

cavity, as also done in the experiments of Tan [11]. The solidus position increases at a nearly constant rate with time, while the liquidus position increases rapidly at the initial stage and then reaches a nearly stable position. Thus, the mushy zone grows rapidly at the beginning, reaches a maximum, and then starts shrinking. From Fig. 6, it is found that the prediction of liquidus and solidus positions with the present model agrees well with experimental results.

Based on the Rayleigh number criterion discussed earlier, we performed a systematic study with respect to parameters such as cooling rate and initial concentration for the case of solidification of aqueous ammonium chloride solution in a rectangular cavity (Fig. 1). The cavity height is chosen such that it meets the requirement for minimum liquid layer height for freckle formation, which is twice the height of the mushy zone [32]. The thermophysical properties of aqueous ammonium chloride solution used in the present numerical simulation are taken from Ref. [24]. For aqueous ammonium chloride the eutectic temperature, T_e, is 15.4°C and the eutectic concentration, C_e, is 19.7 wt % NH_4Cl.

4.1 Effect of Cooling Rate. In order to understand the effect of cooling rate on the formation of freckles, we have considered two different cooling rates: 0.046 K/s and 0.15 K/s, keeping other parameters constant. The other parameters, which are based on the Rayleigh number criterion and chosen so as to make the conditions favorable for freckle formation, correspond to $A=0.5$, $H=0.0139$ m, $C_i=68$ wt % of water (water as solute), $T_b=279$ K, and $G=7.7$ K/mm.

Figure 7 shows liquid concentration plot and temperature distribution in which finger type structures are visible. The protuberances correspond to fingers rising from the mushy layer as a result of density inversion. In these cases, the magnitude of the maximum velocity is on the order of 10^{-4} m/s, which is greater than the isotherm velocity/growth rate ($R \sim 10^{-6}$ m/s), a condition necessary for finger formation. This onset of convection depends strongly on the mush structure, and hence on the value of mush permeability. Hence, the choice of anisotropic variation of permeability in the present study is appropriate [22]. In Fig. 7(*a*), we can see seven such fingers, and their height ranges from 3 mm to 5 mm, indicating different initiation time at different locations.

As the mass diffusivity of the liquid is much lower than its heat diffusivity (the ratio of the latter to the former is almost 100 times for the present case), the segregated melt retains its composition as it flows upward through the mush into regions of higher temperature. The rising colder fluid has a higher concentration of water than the descending warm fluid. Corresponding to this high concentration, the liquidus temperature is lower, thus causing remelting of the solute-rich mush. There, the melt causes delayed growth and localized remelting of solid/mush, resulting in patches

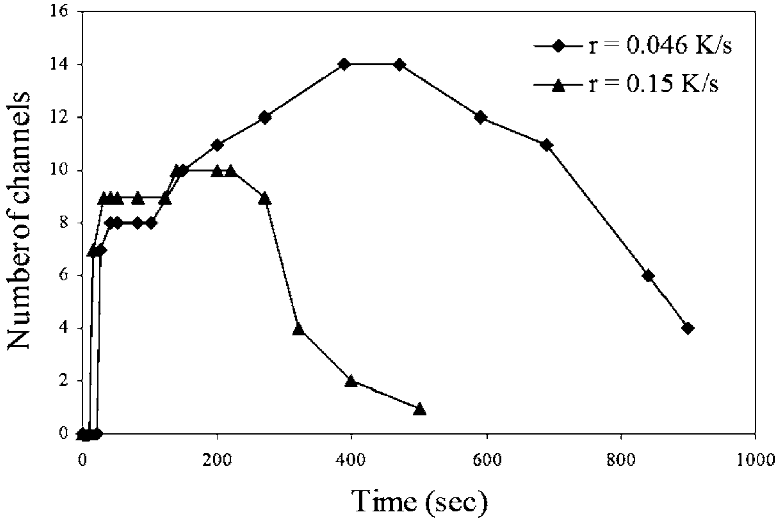

Fig. 9 Number of channels versus time for different cooling rates ($C_i=68\%$, $T_b=279$ K, $G=7.7$ K/mm)

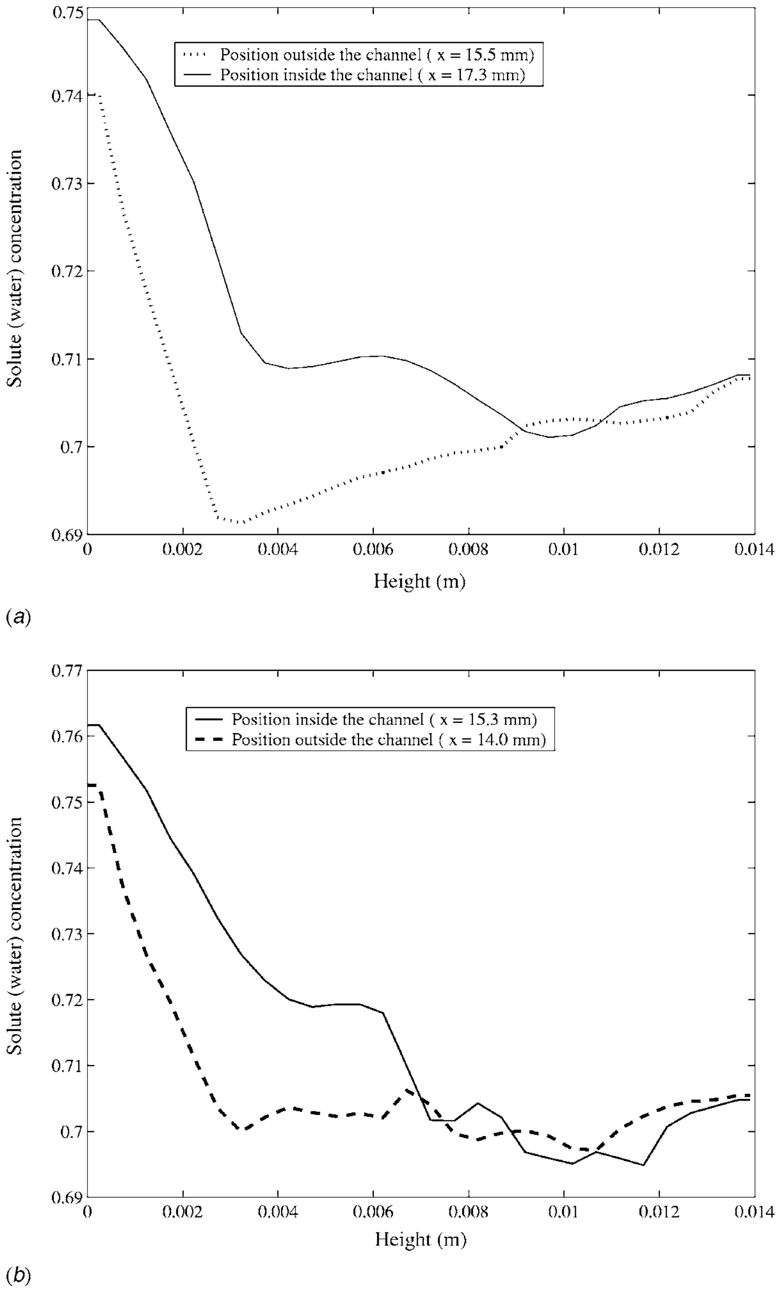

Fig. 10 Variation of solute (water) concentration and in the channel and in a location where there is no channel at $t=70$ s: (*a*) for $r=0.046$ K/s; and (*b*) $r=0.15$ K/s

of thin structure having more liquid fraction than in the surrounding regions. In this manner channels are formed in the mushy zone. Corresponding to fingers locations as shown in Fig. 7 we can observe channel type structure penetrating the mushy layer as shown in Fig. 8.

4.1.1 Variation of Number of Channels With Time. Figure 9 shows the variation of number of channels with time for the two cooling rates. Although it shows that the number of channels has an almost similar trend for both cooling rates, there are differences in the number of channels and the duration over which they are sustained. A similar trend with regard to the variation of number of channels was also observed by Tan [11].

For both cooling rates, there is an initial stage during which no channel is observed in the mushy region, corresponding to the period before the onset of convection. From Fig. 9, we can observe the difference in the time of initiation of the plumes (and hence formation of channels) for the two cases. The phenomenon can be understood from the liquid concentration plot in Figs. 7(*a*) and 7(*b*), which shows that after 15 s of solidification the plume penetration is more extensive in the bulk liquid for the case of high cooling rate, suggesting strong plume convection. The enhanced solidification rate with higher cooling rate increases the rate of rejection of the solute, thus increasing the concentration gradient. This makes the interdendritic fluid velocity high enough for crossing the barrier of critical Rayleigh number at an early stage of solidification, thus resulting in faster growth of plumes. Hence, with higher cooling rate, the initiation of channel takes place earlier. It is also observed from Fig. 9 that for a higher cooling rate, the channels are more pronounced (i.e., more permeable) and also higher in number. This can be explained from Figs.

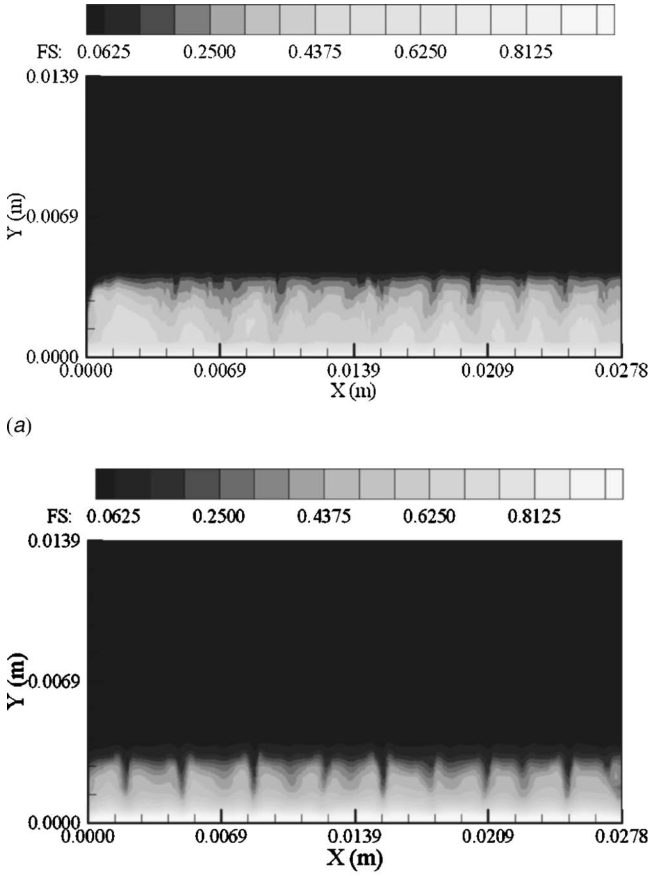

(*a*)

(*b*)

Fig. 11 Predicted solid fraction plot (*a*) at $t=590$ s and $r=0.046$ K/s; (*b*) at $t=270$ s and $r=0.15$ K/s ($C_i=68\%$, $T_b=279$ K, $G=7.7$ K/mm)

10(*a*) and 10(*b*), which show the variation of solute concentration with cavity height, inside and outside the channel, at $t=70$ s. Comparing Figs. 10(*a*) and 10(*b*), it can be observed that with high cooling rate, the plumes are more extensive and strong, and mixing is more pronounced in the bulk liquid, resulting in straight and deep channels.

It is also observed from Fig. 9 that the number of channels rises to a peak value and then decreases. The cause of formation of these new channels can be explained as follows. The plumes, after reaching the top of the cavity, begin to spread laterally along the top wall. As a result, they mix with neighboring plumes, making liquid concentration more uniform at that location. At the same time, the bottom and middle portions of the cavity do not experience this mixing, and hence concentration gradient still acts between bulk fluid and mush. This gives rise to initiation of new fingers at the mush–liquid interface, which are smaller (of depth less than 1 mm, typically) and weaker in convection strength, resulting in the formation of smaller channels.

With higher cooling rate, the initially formed channels are more permeable (as observed in Fig. 8), thus offering less resistance to fluid flow. Hence, there is a tendency for the solute-rich fluid to feed the existing channels more than the newly formed ones. This phenomenon restricts the initiation of new fingers (and hence new channels) with high cooling rate, as observed in Fig. 9. In addition, for lower cooling rate, the number of channels at around the peak number is sustained for a longer duration. For this case, the existing as well as newly formed channels have comparable permeability to allow solute rich fluid to feed them continuously. This leads to prolonged existence of a high number of weak and narrow channels lying only at the top of the mushy zone (Fig. 11(*a*)). After reaching a peak, some of the channels begin to close (Fig. 9) as a result of decrease in concentration gradient and increase of flow resistance in the mush.

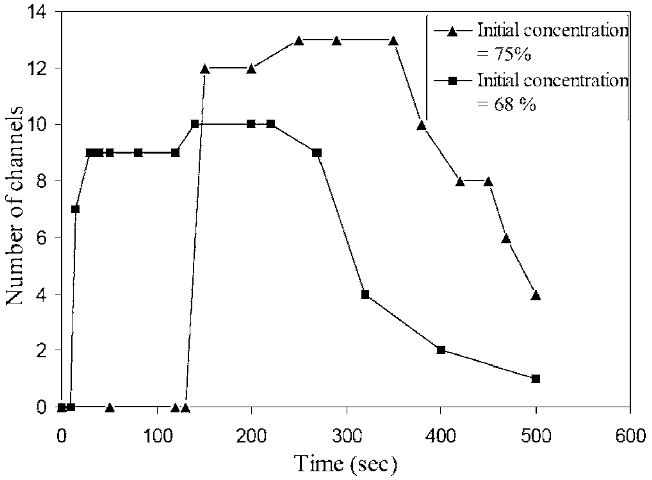

Fig. 12 Number of channels versus time for different initial concentration of solute ($T_b=279$ K, $r=0.15$ K/s)

4.2 Effect of Initial Concentration. Freckles formation is simulated for two different initial concentrations of 75 wt % and 68 wt % of water, respectively. The other parameters remain the same as in the high cooling rate case in the previous parametric study. In this study, too, the variation of number of channels with time is almost similar for both cases (Fig. 12), and similar explanations for channel evolution can be provided as in the parametric study with different cooling rates. There is, however, a difference in the time of initiation of the channels (Fig. 12). The initial bottom plate temperature of 279 K is equal to the liquidus temperature corresponding to the higher (75%) initial concentration case, and is correspondingly lower than the case with initial concentration of 68%, which corresponds to a liquidus temperature of 312 K. Hence, with higher concentration, there is a corresponding delay in initiation of finger convection.

Further, one can observe in Fig. 12 that the peak number of channels is more for the case with higher initial concentration, even if the onset of plume convection is delayed. A higher initial concentration also results in a thinner mushy zone, as indicated in Fig. 13. Hence, there seems to be a correlation between the mushy zone thickness and the number of channels formed. A thicker mushy zone implies more availability of high-solute-content liquid which sustains the initially formed plumes for a longer period of time, thus reducing the possibility of new plumes and hence new channels. It is also observed from the solid fraction plot in Fig. 14 that channels are more pronounced for the case of a thicker mushy zone. These observations have good qualitative agreement with the experimental results reported in Tan et al. [10].

5 Conclusions

A Rayleigh number criterion was developed for characterizing freckle formation during solidification of a hyper-eutectic solution cooled from the bottom. The effects of process parameters, namely cooling rate and initial concentration, were investigated with respect to the formation and evolution of freckles. It was found that the number of channels reduces with increase in cooling rate. However, a high cooling rate produced larger and more defined channels which are retained for longer durations. Similarly, a lower initial concentration of solute resulted in fewer but more pronounced channels. The number and size of channels are

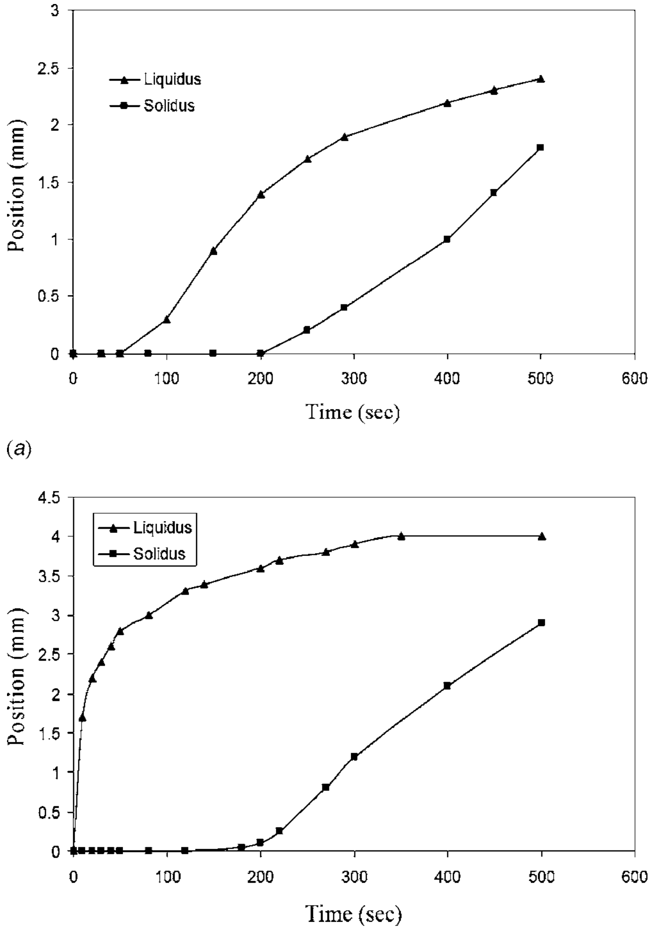

(*a*)

(*b*)

Fig. 13 Solidus and liquidus position with time for different initial concentration: (*a*) 75%; and (*b*) 68% (T_b=279 K, r =0.15 K/s)

also found to be related to the mushy zone thickness. These numerical studies provide the insight into the physics involved in the formation, growth, and destruction of channels.

Nomenclature

a_P, a_P^0 = coefficient in discretization equation
A = aspect ratio
C = species concentration (kg/kg)
c = specific heat (J/kg K)
D = mass diffusion coefficient of the species (m^2/s)
d_1 = dendritic arm spacing (m)
f = weight fraction
F^{-1} = inverse of latent heat function (J/kg)
G = temperature gradient (K/m)
g = acceleration due to gravity (m^2/s)
g_s = volume fraction of solid
g_l = volume fraction of liquid
H = height of the cavity (m)
ΔH = latent enthalpy (J/kg)
l = length scale for the definition of Rayleigh number (m)
K = permeability (m^2)
k = thermal conductivity (W/m K)
k_p = partition coefficient
L = latent heat of fusion (J/kg)

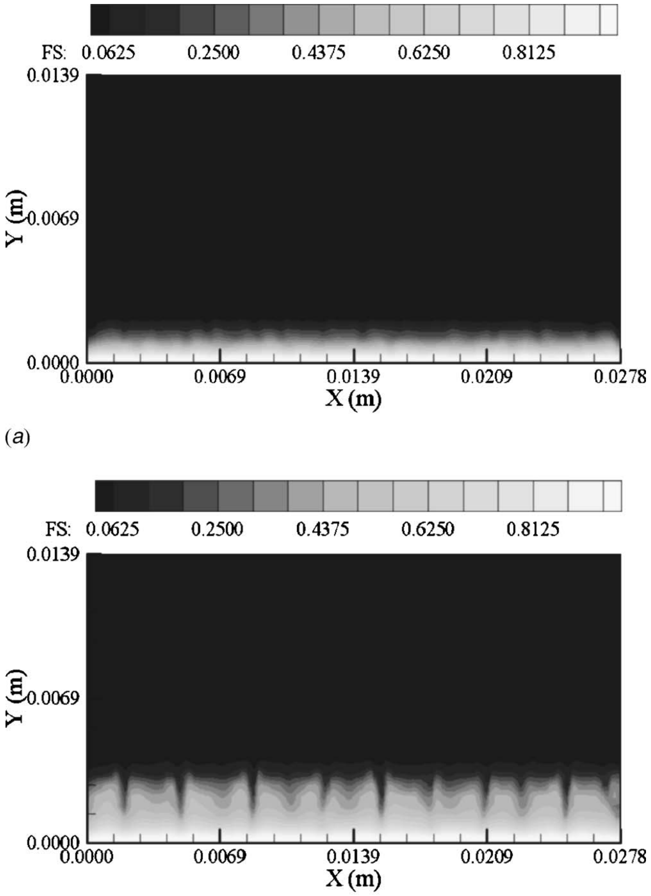

(*a*)

(*b*)

Fig. 14 Predicted solid fraction plot at t=270 s: (*a*) C_i=75%; and (*b*) C_i=68% (T_b=279 K, G=7.7 K/mm, r=0.15 K/s)

m = slope of liquidus (L/K)
P = pressure ($\mathrm{N/m}^2$)
r = heat extraction rate or cooling rate (K/s)
R = growth rate of crystal or isotherm velocity (m/s)
Ra = Rayleigh number
S = source term
Sc = Schmidt number
t = time (s)
T = temperature (K)
u, v = velocities in x, and y directions (m/s)
$\vec{u}$ = continuum velocity vector (m/s)
V = interdendritic fluid velocity (m/s)

Greek Symbols

α = thermal diffusivity (m^2/s)
β_T = thermal expansion coefficient(L/K)
β_S = solutal expansion coefficient
μ = dynamic viscosity (kg/s m)
ν = kinematic viscosity (m^2/s)
ρ = density ($\mathrm{kg/m}^3$)

Subscripts

b = bottom wall
e = eutectic
i = initial
l = liquid phase
s = solid phase
cr = critical

References

[1] Copeley, S. M., Giamei, A. F., and Hornbecker, M. F., 1970, "The Origin of Freckles in Unidirectionally Solidified Castings," Metall. Trans., **1**, pp. 2193–2204.

[2] Worster, M. G., 1997, "Convection in Mushy Layers," Annu. Rev. Fluid Mech., **29**, pp. 91–122.

[3] Chen, F., Lu, J. W., and Yang, T. L., 1994, "Convection Instability in Ammonium Chloride Solution Directionally Solidified From Below," J. Fluid Mech., **276**, pp. 163–188.

[4] Chen, F., 1995, "Experimental Study of Convection in a Mushy Layer During Directional Solidification," J. Fluid Mech., **293**, pp. 277–286.

[5] Solomon, T. H., and Hartley, R. R., 1998, "Measurements of the Temperature Field of Mushy and Liquid Regions During Solidification of Aqueous Ammonium Chloride," J. Fluid Mech., **358**, pp. 87–106.

[6] Nishimura, T., and Wakamatsu, M., 2000, "Natural Convection Suppression and Crystal Growth During Unidirectional Solidification of a Binary System," Heat Transfer Asian Res., **29**, pp. 120–131.

[7] Nishimura, T., Sasaki, J., and Htoo, T. T., 2003, "The Structure of Plumes Generated in the Unidirectional Solidification Process for a Binary System," Int. J. Heat Mass Transfer, **46**, pp. 4489–4497.

[8] Sampel, A., and Hellawell, A., 1982, "The Effect of Mold Precession on Channel and Macro-Segregation in Ammonium Chloride Water Analog Castings," Metall. Trans. B, **13B**, pp. 495–501.

[9] Sampel, A., and Hellawell, A., 1984, "The Mechanisms of Formation and Prevention of Channel Segregation During Alloy Solidification," Metall. Trans. A, **15A**, pp. 2163–2173.

[10] Tan, F. L., Tso, C. P., and Pek, P. K., 2003, "An Experimental Investigation on Freckles Formation During Solidification of Aqueous Ammonium Chloride," Int. Commun. Heat Mass Transfer, **30**(8), pp. 1101–1114.

[11] Tan, F. L., 2005, "An Experimental Study on Channels Formation During Solidification of Aqueous Ammonium Chloride," Appl. Therm. Eng., **25**(14–15), pp. 2169–2192.

[12] Neilson, D. G., and Incropera, F. P., 1993, "Unidirectional Solidification of a Binary Alloy and the Effects of Induced Fluid Motion," Int. J. Heat Mass Transfer, **34**, pp. 1717–1732.

[13] Felicelli, S. D., Heinrich, J. C., and Poirier, D. R., 1991, "Simulation of Freckles During Vertical Solidification of Binary Alloys," Metall. Trans. B, **22B**, pp. 847–859.

[14] Neilson, D. G., and Incropera, F. P., 1993, "Three-Dimensional Considerations of Unidirectional Solidification in a Binary Liquid," Numer. Heat Transfer, Part A, **23**, pp. 1–20.

[15] Felicelli, S. D., Heinrich, J. C., and Poirier, D. R., 1998, "Three-Dimensional Simulations of Freckles in Binary Alloys," J. Cryst. Growth, **191**, pp. 879–888.

[16] Schneider, M. C., Gu, J. P., Beckermann, C., Boettinger, W. J., and Kattner, U. R., 1997, "Modeling of Micro- and Macrosegregation and Freckle Formation in Single-Crystal Nickel-Base Superalloy Directional Solidification," Metall. Mater. Trans. A, **28A**, pp. 1517–1531.

[17] Sarazin, J. R., and Hellawell, A., 1988, "Channel Formation in Pb–Sn, Pb–Sb and Pb–Sn–Sb Alloy Ingots and Comparison With the System NH_4Cl-H_2O," Metall. Trans. A, **19A**, pp. 1861–1871.

[18] Bergman, M. I., Fearn, D. R., Bloxhan, J., and Shannon, M. C., 1997, "Convection and Channel Formation in Solidifying Pb–Sn Alloys," Metall. Mater. Trans. A, **28A**, pp. 859–866.

[19] Beckermann, C., Gu, J. P., and Boettinger, W. J., 2000, "Development of a Freckle Predictor via Rayleigh Number Method for Single-Crystal Nickel-Base Superalloy," Metall. Mater. Trans. A, **31A**, pp. 2545–2557.

[20] Sung, P. K., Poirier, D. R., and Felicelli, S. D., 2001, "Simulating the Iinitiation of a Channel During Directional Solidification of a Superalloy," Metall. Mater. Trans. A, **32A**, pp. 202–207.

[21] Mehrabian, R., Keane, M., and Flemings, M. C., 1970, "Interdendritic Fluid Flow and Macrosegregation: Influence of Gravity," Metall. Trans., **1**, pp. 1209–1220.

[22] Heinrich, J. C., and Poirier, D. R., 2004, "Convection Modeling in Directional Solidification," C. R. Mec., **332**, pp. 429–445.

[23] Bennon, W. D., and Incropera, F. P., 1987, "A Continuum Model for Momentum, Heat, and Species Transport in Binary Solid-Liquid Phase Change Systems—I Model Formulation," Int. J. Heat Mass Transfer, **30**(16), 2161–2170.

[24] Voller, V. R., Brent, A. D., and Prakash, C., 1989, "The Modeling of Heat, Mass and Solute Transport in Solidification Systems," Int. J. Heat Mass Transfer, **32**(9), pp. 1719–1731.

[25] Chakraborty, S., and Dutta, P., 2003, "Three Dimensional Double-Diffusive Convection and Macrosegregation During Non-Equilibrium Solidification of Binary Mixtures," Int. J. Heat Mass Transfer, **46**(12),) pp. 2115–2134.

[26] Kumar, P., Chakraborty, S., Srinivasan, K., and Dutta, P., 2003, "Studies on Transport Phenomena During Directional Solidification of a Non-Eutectic Binary Solution Cooled From the Top," Metall. Mater. Trans. B, **34**(6), pp. 899–909.

[27] Kumar, P., Chakraborty, S., Srinivasan, K., and Dutta, P., 2002, "Rayleigh-Benard Convection During Solidification of a Binary Alloy Cooled From the Top: Experiments and Numerical Simulation," Metall. Mater. Trans. B, **33**, pp. 605–612.

[28] Kumar, A., and Dutta, P., 2005, "Modeling of Transport Phenomena in Continuous Casting of Non-Dendritic Billets," Int. J. Heat Mass Transfer, **48**, pp. 3674–3688.

[29] Brent, A. D., Voller, V. R., and Reid, K. J., 1988, "The Enthalpy Porosity Technique for Modeling Convection-Diffusion Phase Change: Application to the Melting of a Pure Metal," Numer. Heat Transfer, **13**, pp. 297–318.

[30] Patankar, S. V., 1980, *Numerical Heat Transfer and Fluid Flow*, Hemisphere, Washington, D.C., pp. 113–134.

[31] Chakraborty, S., and Dutta, P., 2001, "A Generalized Formulation for Evaluation of Latent Heat Functions in Enthalpy-Based Macroscopic Models for Convection-Diffusion Phase Change Processes," Metall. Mater. Trans. B, **32B**, pp. 562–564.

[32] Frueh, C., Poirier, D. R., and Felicelli, S. D., 2000, "Effect of Computational Domain Size on the Mathematical Modeling of Transport Processes and Segregation During Directional Solidification," Metall. Mater. Trans. A, **31A**, pp. 3129–3135.

Numerical Simulation of Transport in Optical Fiber Drawing with Core–Cladding Structure

Chunming Chen

Yogesh Jaluria
e-mail: jaluria@jove.rutgers.edu

Department of Mechanical and Aerospace Engineering,
Rutgers, The State University of New Jersey,
New Brunswick, NJ 08903

Optical fibers are typically drawn from silica preforms, which usually consist of two concentric cylinders called the core and the cladding, heated in a high-temperature furnace. For optical communication purposes, the core always has a higher refractive index than the cladding to obtain total internal reflection. In order to investigate the effect of this core–cladding structure on optical fiber drawing, a numerical model has been developed in this work. Axisymmetric flows of a double-layer glass and aiding purge gas in a concentric cylindrical furnace are considered. The thermal and momentum transport in both glass layers and gas are coupled at the interface boundaries. The neck-down profile is generated using an iterative numerical scheme. The zonal method is applied to model the radiation transfer in the glass preform. The gas is taken as nonparticipating. Coordinate transformations are used to convert the resulting complex domains into cylindrical regions. The stream function, vorticity, and energy equations for the core, the cladding, and the purge gas are solved by finite difference methods, using a false transient approach coupled with the alternating direction implicit method. A second-order differencing scheme is used for discretization. The numerical results are validated by comparing with results available in the literature. The effects of changes in the refractive index and absorption coefficient due to doping on fiber drawing are investigated. This problem has received very little attention in the literature, particularly with respect to modeling, and this paper presents an initial study of the underlying transport.

[DOI: 10.1115/1.2709968]

Keywords: optical fiber drawing, core-cladding structure, zonal method, glass radiation

1 Introduction

The manufacture of optical fibers typically begins with silica preforms, which usually consist of two concentric cylinders called the core and the cladding and which are doped with various chemicals to enhance optical properties. In a draw tower, the preform is traversed through a high-temperature cylindrical furnace. When the glass is heated beyond its softening point of about 1900 K for silica, it is drawn into a fiber of diameter around 125 μm by applying an axial tension. Studies on pure, single-layer, silica optical fiber drawing have been carried out by a number of researchers. Paek and Runk [1] studied the neck-down profile and temperature distribution within the neck-down region using a one-dimensional analysis. Myers [2] developed a one-dimensional model for unsteady glass flow. More comprehensive models have been developed by Lee et al. [3–9]. They investigated the flow and the thermal transport in detail, including the convective and radiative heat transfer in an axisymmetric configuration of the glass preform and the inert gas. Based on radial lumping of axial velocity for iteration, a combined analytical and numerical method was developed to generate the neck-down profile. The effects of fiber draw speed, inert gas velocity, gas properties, furnace dimensions, and furnace temperature distribution on the flow and temperature distribution were obtained and discussed. In these studies, the preform was assumed to be optically thick, which is not valid in the lower neck-down region.

Instead of the optically thick and Rosseland approximation, several advanced radiation models have also been proposed. The $P1$ method was used by Kaminski [10] to compute the radiation transfer in the upper neck-down region and Yin and Jaluria [11] applied the zonal method to simulate the radiative transport in the whole neck-down region. Yin and Jaluria also investigated high-speed optical fiber drawing, up to 20 m/s, with preform diameters of around 5.0 cm [12]. Recently, Wei et al. [13] presented an axisymmetric model for the neck-down region and used the discrete ordinate method to solve the radiative transfer equation. Numerical results for higher speed (25 m/s) drawing with a larger preform diameter of 9.0 cm were obtained.

For telecommunication purposes, the optical fiber usually consists of two layers of glass: the core and the cladding. In this structure, a dielectric layer (called "cladding") surrounds the light-guiding central portion (called "core"), which always has a refractive index higher than that of the cladding to obtain total internal reflection in the core [14]. In general, core sizes in the fiber vary from 8.3 μm to 62.5 μm in industry. The standard telecommunications core sizes in use today are 8.3 μm, 50 μm, and 62.5 μm. The diameter of the cladding surrounding each of these cores is around 125 μm [15]. In order to change the refractive index in the core or the cladding, chemicals called dopants are added to the preform [16,17]. The dopants increase the refractive index in the core and decrease that in the cladding. Some of the dopants also result in a significant increase in the absorption coefficient and in a decrease in the viscosity of the silica preform. Since radiation heat transfer is the dominant mode of transport in the heating process, a nonuniform distribution of radiation properties in the preform due to doping will significantly affect the generation of the neck-down profile. The viscosity of the preform is directly

---

Contributed by the Heat Transfer Division of ASME for publication in the JOURNAL OF HEAT TRANSFER. Manuscript received March 28, 2006; final manuscript received September 24, 2006. Review conducted by Sumanta Acharya. Paper presented at the 2004 ASME Heat Transfer/Fluids Engineering Summer Conference (HT-FED2004), Charlotte, NC, USA, July 11–15, 2004.

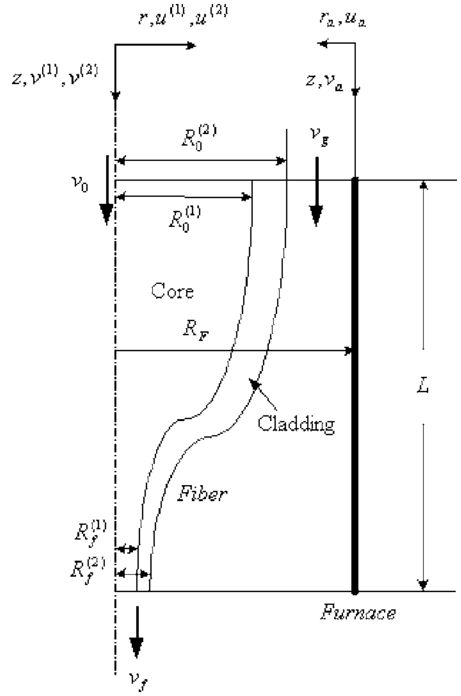

Fig. 1 Schematic diagram of the process for double-layer optical fiber drawing

related to the draw tension, which is one of the most important parameters in optical fiber drawing. High draw tension may affect the transmission properties in the fiber and also result in strength degradation [18]. A numerical simulation of optical fiber drawing, including the effect of doping, will provide more detailed and useful information for the manufacture of optical fibers.

Yin [19] investigated the effect of nonuniform refractive index and absorption coefficient in double-layer cylinder on the temperature distribution, using the zonal method. However, optical fiber drawing with the more important core–cladding structure has not been investigated in any detail. In the present study, the core and the cladding are treated as two different fluids with different properties. Separate body-fitted grids are applied to the core, the cladding and the inert gas respectively. The interface between the cladding and the inert gas and that between the core and the cladding are iteratively generated by using a radial lumping of the axial velocity distribution. The zonal method is applied to calculate the radiative transfer. Each of the two separate layers in the glass preform is assumed to have a uniform refractive index, bounded by diffuse surfaces. The conjugate problem including momentum and energy transport in the core, the cladding and the gas, within the neck-down region, has been solved. The numerical results are validated by comparing with the few results available in the literature. The effects of changes in the refractive index and in the absorption coefficient due to doping on optical fiber drawing are also investigated.

2 Governing Equations

Axisymmetric flows of the double-layer glass preform and aiding purge gas in a cylindrical furnace are considered. A schematic diagram of the double-layer optical fiber drawing process is shown in Fig. 1. The governing equations for the glass layers and the gas are given as

$$\frac{\partial v}{\partial z} + \frac{1}{r}\frac{\partial (ru)}{\partial r} = 0 \tag{1}$$

$$\frac{\partial v}{\partial t} + u\frac{\partial v}{\partial r} + v\frac{\partial v}{\partial z} = -\frac{1}{\rho}\frac{\partial p}{\partial z} + \frac{1}{r}\frac{\partial}{\partial r}\left[r\nu\left(\frac{\partial v}{\partial r} + \frac{\partial u}{\partial z}\right)\right] + 2\frac{\partial}{\partial z}\left(\nu\frac{\partial v}{\partial z}\right) \tag{2}$$

$$\frac{\partial u}{\partial t} + u\frac{\partial u}{\partial r} + v\frac{\partial u}{\partial z} = -\frac{1}{\rho}\frac{\partial p}{\partial r} + \frac{2}{r}\frac{\partial}{\partial r}\left(r\nu\frac{\partial u}{\partial r}\right) + \frac{\partial}{\partial z}\left[\nu\left(\frac{\partial v}{\partial r} + \frac{\partial u}{\partial z}\right)\right] - \frac{2\nu u}{r^2} \tag{3}$$

$$\rho C_p\left(\frac{\partial T}{\partial t} + u\frac{\partial T}{\partial r} + v\frac{\partial T}{\partial z}\right) = \frac{1}{r}\frac{\partial}{\partial r}\left(rK\frac{\partial T}{\partial r}\right) + \frac{\partial}{\partial z}\left(K\frac{\partial T}{\partial z}\right) + \Phi + S_r \tag{4}$$

where Φ is the viscous dissipation term; and S_r is the radiation source term. The other variables are defined in the nomenclature.

For computational purposes, all the three regions, the core, the cladding, and the gas, with complex boundaries, are converted into cylindrical regions. Using Landau's transformation [20], the first region, consisting of the core of the preform, bounded by the centerline, the inner interface, inlet and exit, is transformed to a cylinder in η and β by the equations

$$\eta^{(1)} = \frac{r^{(1)}}{R^{(1)}(z)}, \quad \beta = \frac{z}{L} \tag{5}$$

For the second region, consisting of the cladding of the preform, bounded by two interfaces, inlet and exit, the same coordinate system is employed as the first region. The transformed system is defined as

$$\eta^{(2)} = \frac{r^{(2)} - R^{(1)}(z)}{R^{(2)}(z) - R^{(1)}(z)}, \quad \beta = \frac{z}{L} \tag{6}$$

For the region of the purge gas, bounded by the outer interface, furnace surface, inlet and exit, a different coordinate system is used, with the same axial coordinate as the z axis and a radial direction opposite to the r axis, the origin being at the furnace wall. The transformed system for purge gas is given as [7]

$$\eta_a = \frac{r_a}{R_F - R^{(2)}(z)}, \quad \beta = \frac{z}{L} \tag{7}$$

Using these coordinate transformations, the computational domains are simplified. The stream function and vorticity equations are solved instead of the primitive variables to avoid solving for the pressure and thus eliminate one equation [21].

The zonal method is applied to calculate the radiation transfer inside the three enclosures, as developed by Chen and Jaluria [22]. The two-band model presented by Myers [2] for the absorption coefficient of pure silica is used here. This is given by the equations

$$a = 0, \quad \text{for } \lambda < 3.0\ \mu\text{m} \tag{8}$$

$$a = 400.0\ \text{m}^{-1}, \quad \text{for } 3.0\ \mu\text{m} \leqslant \lambda < 4.8\ \mu\text{m} \tag{9}$$

$$a = 15{,}000\ \text{m}^{-1}, \quad \text{for } 4.8\ \mu\text{m} \leqslant \lambda < 8.0\ \mu\text{m} \tag{10}$$

Both the external surface and the internal interface of the preform are assumed to be diffuse. From the enclosure theory, the outgoing and incoming heat fluxes at every surface can be obtained for each absorbing band, as shown in Fig. 2. The incoming heat fluxes are given as

$$G_{i,\lambda}^{(l)} = \frac{1}{A_i^{(l)}}\left[\sum_{j=1}^{N_s^{(l)}} (\overline{S_jS_i})_\lambda^{(l)} J_{j,\lambda}^{(l)} + \sum_{j=1}^{N_g^{(l)}} (\overline{G_jS_i})_\lambda^{(l)} n^{(l)^2} \sigma T_j^{(l)4} f_{j,\lambda}\right] (l = 1,2) \tag{11}$$

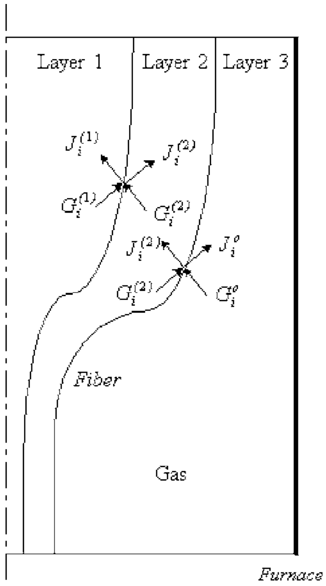

Fig. 2 Radiosities and irradiations at the interfaces

$$G_{i,\lambda}^{(3)} = \sum_{j=1}^{N_s} F_{i-j} J_{j,\lambda}^{(3)} \tag{12}$$

In the enclosure of the inert gas, the outgoing heat fluxes at the openings and furnace surface are

$$J_{i,\lambda}^{(3)} = \varepsilon_i \sigma T_i^4 f_{i,\lambda} + (1-\varepsilon_i) G_{i,\lambda}^{(3)} \tag{13}$$

The outgoing heat fluxes at the external surface of the preform are

$$J_{i,\lambda}^{(3)} = \rho^{(3)} G_{i,\lambda}^{(3)} + \tau^{(2)} G_{i,\lambda}^{(2)} \tag{14}$$

In the enclosure of the core, the outgoing heat fluxes at the internal interface of the preform are given as

$$J_{i,\lambda}^{(1)} = \tau^{(2)} G_{i,\lambda}^{(2)} + \rho^{(1)} G_{i,\lambda}^{(1)} \tag{15}$$

In the enclosure of the cladding, the outgoing heat fluxes at the internal interface of the preform are

$$J_{i,\lambda}^{(2)} = \tau^{(1)} G_{i,\lambda}^{(1)} + \rho^{(2)} G_{i,\lambda}^{(2)} \tag{16}$$

The outgoing heat fluxes at the external surface of the preform are

$$J_{i,\lambda}^{(2)} = \tau^{(3)} G_{i,\lambda}^{(3)} + \rho^{(2)} G_{i,\lambda}^{(2)} \tag{17}$$

The radiative source term can be obtained as

$$S_{rk}^{(l)} = \frac{1}{V_k^{(l)}} \sum_{\lambda=1}^{2} \left[\sum_i (\overline{S_i G_k})_\lambda^{(l)} \left(J_{i,\lambda}^{(l)} - n^{(l)^2} \sigma T_k^{(l)^4} f_{k,\lambda}\right) + \sum_{j \neq k} (\overline{G_j G})_\lambda^{(l)} n^{(l)^2} \sigma \left(T_j^{(l)^4} f_{j,\lambda} - T_k^{(l)^4} f_{k,\lambda}\right) \right] \quad (l=1,2) \tag{18}$$

where the direct exchange areas $(\overline{S_i S_j})_\lambda^{(l)}, (\overline{S_i G_j})_\lambda^{(l)}, (\overline{G_i G_j})_\lambda^{(l)}$, and view factor $F_{i,j}$ are defined by Modest [23]. The view factors are computed using the approach from Lee and Jaluria [3]. The direct exchange areas for each absorption band are computed using Gaussian quadrature and the limits of the azimuthal angles between two axisymmetric rings are obtained using the results derived by Modest [24].

For a typical optical fiber drawing, the variation of the axial velocity in the radial direction is fairly small. Thus, radial lumping of axial velocity and mass conservation were used by Roy Choudhury and Jaluria [9] to develop an iteratively neck-down profile generation scheme, as given by

$$R^{(2)}(z) = \sqrt{\frac{R_0^{(2)^2} v_0}{\bar{v}}} \tag{19}$$

The average axial velocity in the glass is given as

$$\begin{aligned}\bar{v} = {} & C_1 \int_0^z \frac{dz}{\mu R^{(2)^2}} - \int_0^z \frac{\rho g}{C_2 \mu R^{(2)^2}} \left(\int_0^z R^{(2)^2} dz \right) dz \\ & - \int_0^z \frac{1}{C_2 \mu R^{(2)^2}} \left(\frac{R^{(2)} \zeta}{\sqrt{1 + R^{(2)'^2}}} + \frac{\zeta}{R_1} \right) dz \\ & - 2\rho R_0^{(2)^4} v_0^2 \int_0^z \frac{1}{C_2 \mu R^{(2)^2}} \left(\int_0^z \frac{R^{(2)'}}{R^{(2)^3}} dz \right) dz + v_0 \end{aligned} \tag{20}$$

where

$$\begin{aligned} C_1 = {} & \left[(v_f - v_0) + \int_0^{L_f} \frac{\rho g}{C_2 \mu R^{(2)^2}} \left(\int_0^z R^{(2)^2} dz \right) dz \right. \\ & + \int_0^{L_f} \frac{1}{C_2 \mu R^{(2)^2}} \left(\frac{R^{(2)} \zeta}{\sqrt{1 + R^{(2)'^2}}} + \frac{\zeta}{R_1} \right) dz \\ & \left. + 2\rho R_0^{(2)^4} v_0^2 \int_0^{L_f} \frac{1}{C_2 \mu R^{(2)^2}} \left(\int_0^z \frac{R^{(2)'}}{R^{(2)^3}} dz \right) dz \right] \left(\int_0^{L_f} \frac{dz}{\mu R^{(2)^2}} \right)^{-1} \end{aligned} \tag{21}$$

$$C_2 = 2 + \frac{1 - 2R^{(2)'^2} + 2R^{(2)'} - R^{(2)} R^{(2)''}}{1 + R^{(2)'^2}} \tag{22}$$

$$R_1 = R^{(2)''} \left(1 + R^{(2)'^2}\right)^{-1.5} \tag{23}$$

A comparison between the neck-down profile generated from the axial velocity lumping assumption and that from the two-dimensional scheme employed by Wei et al. [13] showed that the difference was quite small even for high-speed drawing (at 25 m/s). Because of its robustness and efficiency, this one-dimensional neck-down profile correction scheme is used for the current study. The location of the interface, between the core and cladding, is also determined using the radial lumping of the axial velocity as

$$R^{(1)}(z) = \frac{R_0^{(1)}}{R_0^{(2)}} R^{(2)}(z) \tag{24}$$

3 Boundary Conditions

At the axis of the fiber, the boundary conditions are given by symmetry. At the inlet, the temperature and the axial velocity are assumed to be uniform, and the radial velocity is assumed to be zero. At the outlet, the second derivatives of all the variables are taken as zero in the flow direction, indicating negligible axial diffusion. At the furnace surface, the no-slip conditions are applied and specified wall temperature distributions are given. For the two interfaces among the core, the cladding, and the inner gas, a zero penetration condition is applied. The thermal condition at the interface is determined by the heat flux continuity in the normal direction to the interface.

4 Numerical Scheme

Body-fitted grid systems are generated for the domains of the core, the cladding and the inert gas based on the method proposed by Lee and Jaluria [5] and Yin and Jaluria [11]. Two grid sets are applied here. Both of these are nonuniform. A fine grid system is used to discretize the stream function, vorticity, and temperature equations. The coarse grid system is applied to the radiation analysis. After optimization, the grids are obtained as 369×21, in axial and radial directions respectively, for the core, 369×21 for

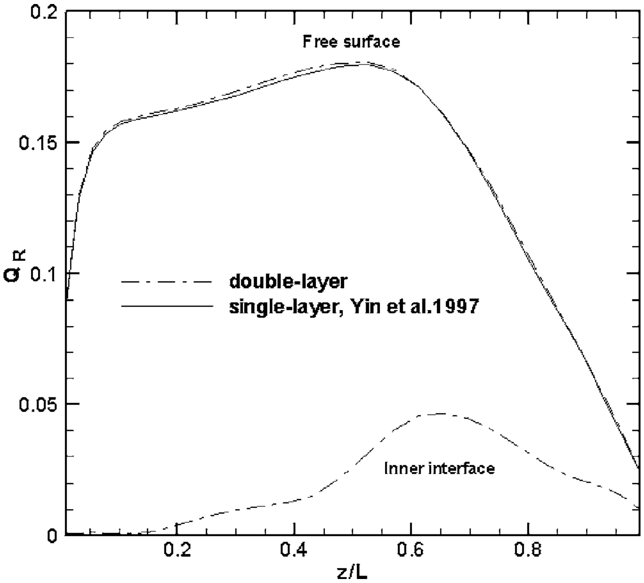

Fig. 3 Radiative heat flux for uniform temperature distribution in the preform

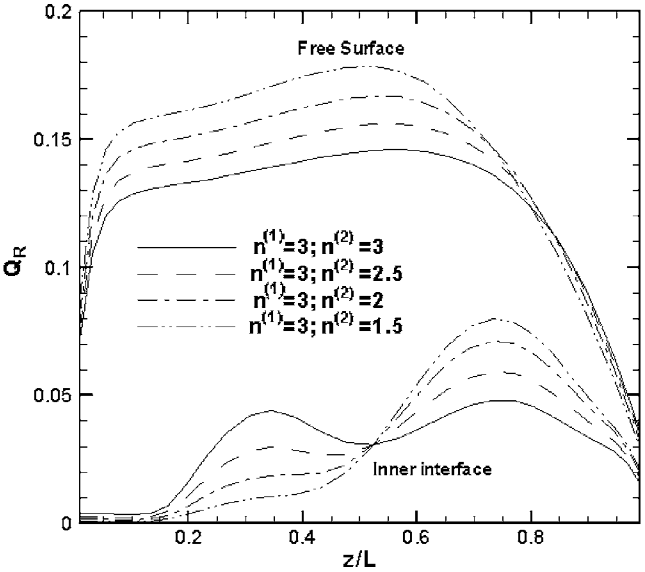

Fig. 4 Effect of change in the refractive index on radiative heat flux

the cladding and 369×61 for the gas. Coarser grids are obtained for radiation, 30×8 for the core and 30×10 for the cladding. The radiative heat fluxes absorbed by axisymmetric volume ring elements within the preform are first calculated by the zonal method using the coarse grid system and then interpolated to obtain the radiative source terms at the fine grid for the energy equation. Since the computation of the direct exchange areas for the zonal method is very time consuming, a parallelization for this computation is developed with the message-passing interface (MPI).

The stream function, vorticity, and energy equations are approximated by second-order differencing schemes. The final discretization equations are solved using an alternating direction implicit (ADI) approach and the successive under-relaxation (SUR) method [21]. The overall iterative process begins with the solution of the stream function, vorticity, and energy equations for a given neck-down profile. Then the neck-down profiles are corrected using the force imbalance. After that, the grids are modified. The view factors and the direct exchange areas are updated, corresponding to the new neck-down profile. This procedure is repeated until steady state conditions are obtained, as indicated by convergence of the iterative scheme. The convergence criteria were obtained as 10^{-5} for the stream function, vorticity, and temperature, and as 10^{-4} for the neck-down profile after varying these over wide ranges. A typical run was about 8 h on the MPHASE cluster at Rutgers University, which has 44 dual CPU rack-mount AMD MP 1.6 GHZ, from Aspen Systems.

5 Results and Discussion

A prescribed neck-down profile is employed for the validation of the model. The errors in the sum of view factors and in the area average of the sum of direct exchange areas are found to be within 0.5%, except at the inlet for $a=15{,}000\ \mathrm{m}^{-1}$ ($<5\%$). Yin and Jaluria [11] applied the zonal method to the radiation transport in a single-layer optical fiber drawing. A simple case is used to verify the radiation model. The temperature of the furnace and the preform is set at 2000 K and 1000 K, respectively. The normalized radiative heat flux is given as $Q_R=q_R/\sigma(T_F^4-T_f^4)$. For the case of uniform refractive index distribution $n^{(1)}=n^{(2)}=1.42$, Fig. 3 shows that the radiative heat flux at the external surface is in excellent agreement with the results from Yin and Jaluria. [11]. The effects of nonuniform refractive index on the radiative heat flux distribution are presented in Fig. 4, where the refractive index of the core is 3, and that of the cladding varies from 3 to 1.5. Larger radiative heat flux is absorbed by the preform with lower refractive index for the cladding because the transmittivity of the external surface is increased. For $n^{(1)}=n^{(2)}=3$, there are no reflections at the interface between the core and the cladding. The increased reflections are transferred to the lower neck-down region as the refractive index of the cladding becomes smaller.

Since experimental results on double-layer fiber drawing are not available in the literature, validation of the double-layer model is done by comparing with the results from a single-layer model developed by Roy Choudhury and Jaluria [7–9]. The operating conditions are given in Table 1. The furnace temperature profile is taken as parabolic, with a maximum of 2500 K in the middle and a minimum of 2000 K at both ends. Argon enters the furnace as aiding flow at 0.1 m/s. The inlet temperature of the preform and the gas are assumed to be 300 K. The radiation properties and the viscosity are assumed to be uniform for the core and the cladding. Figure 5 shows that a lower temperature at the external surface of the preform is obtained by the double-layer model using the zonal method for radiation analysis. Since the optically thick assumption is only valid in the upper neck-down region, the temperature distribution is overestimated by the optically thick approximation. The neck-down profile of the fiber is also compared with the numerical results of the single-layer model [9]. Optically thick assumption is used for the radiation analysis in this comparison. Figure 6 shows that the obtained neck-down profile is in excellent agreement with the results for single-layer fiber drawing.

When the core and the cladding are doped with various dopants, the change in refractive index and absorption coefficients could be very different. Assumed magnitudes of change in the refractive index and absorption coefficients are used in this paper to capture the generic effects of variation in these two properties. It would provide some useful insight into the effect of core–cladding structure and further proof for the validity of the double-layer model.

Table 1 Typical operating conditions

$D_0^{(2)}$	$D_f^{(2)}$	$D_0^{(1)}/D_0^{(2)}$	$D_f^{(1)}/D_f^{(2)}$	D_F	L	v_f	v_a
5 cm	125 μm	0.5	0.5	7 cm	30 cm	10 m/s	0.1 m/s

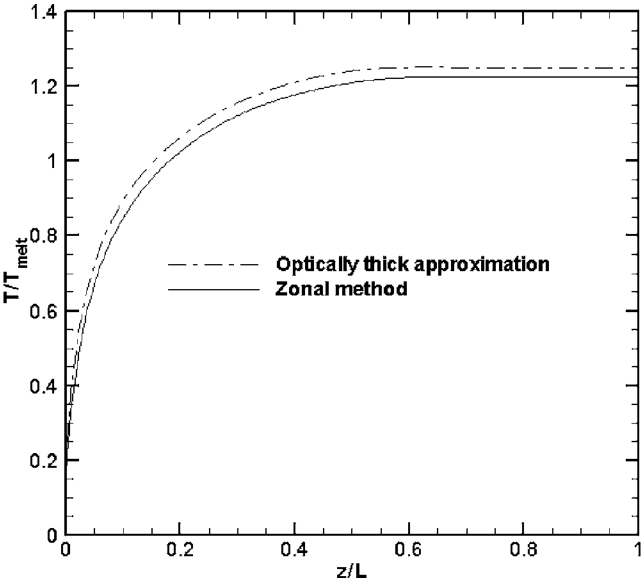

Fig. 5 Validation of the numerical model by comparing the temperature distribution at the free surface with single-layer fiber drawing

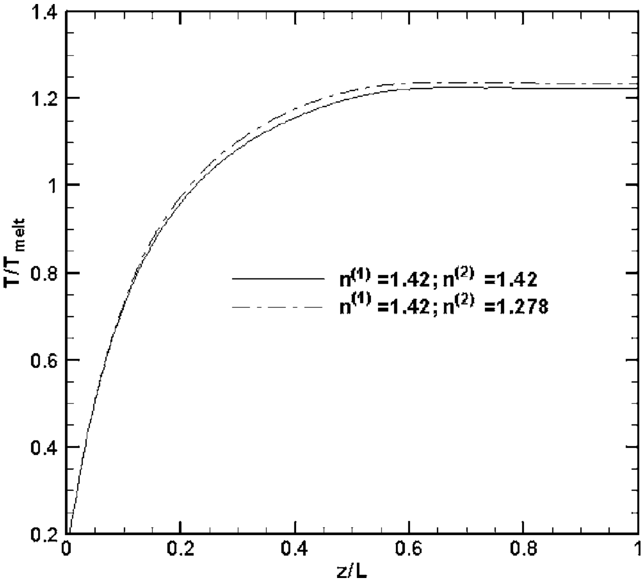

Fig. 7 Effect of change in the refractive index on the temperature distribution at the centerline

In order to investigate the effects of refractive index and absorption coefficient on the double-layer fiber drawing, two typical cases for double-layer fiber drawing are studied. The core is taken as pure fused silica and the cladding is doped. Due to doping, the refractive index and absorption coefficient of the cladding are changed. The other properties, including the viscosity, are assumed to be the same in this study. In the first case, the refractive index of the cladding is assumed to be 10% lower than that of the core. The absorption coefficient and absorption bands of both the glass layers remain the same as those for pure fused silica. The temperature distribution along the centerline is shown in Fig. 7 for double-layer and single-layer preforms. It is seen that the centerline temperature in the double-layer preform is higher than that in the single-layer preform. The reason for this is that the core absorbs larger radiation energy because of reflection and a higher transmissivity of the cladding. The radial temperature lag $T_{\text{lag}} = (T-T_c)/T_c$ in the double-layer preform becomes slightly larger than that in the single-layer preform, as expected and as shown in Fig. 8. The internal reflections in the core and the cladding, due to the difference in the refractive index, increase the variation of the radial temperature in a double-layer preform. Figure 8 also shows that the magnitude of the temperature gradient becomes smaller near the free surface because of the radiative heat flux from the furnace. Figure 9 depicts the neck-down profiles for both the preforms. Since the double-layer preform reaches the softening point closer to the entrance, the diameter of the double-layer preform is smaller than that of the single-layer preform during neck-down.

The E' defect is a point defect, which is generated at high temperature during the drawing process and which causes transmission loss and mechanical strength degration in the fiber [25].

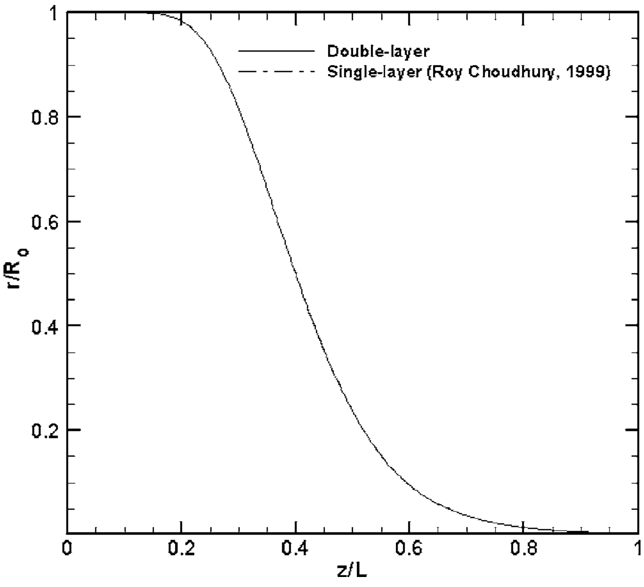

Fig. 6 Validation of the numerical model by comparing the neck-down profile

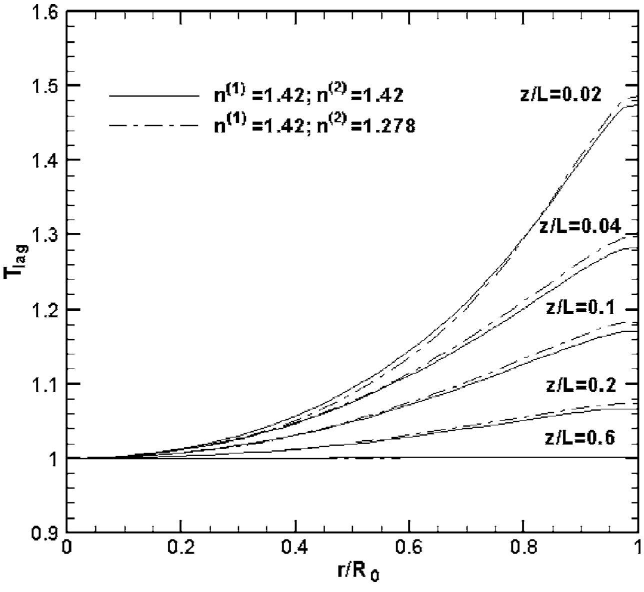

Fig. 8 Effect of change in the refractive index on the radial temperature lag

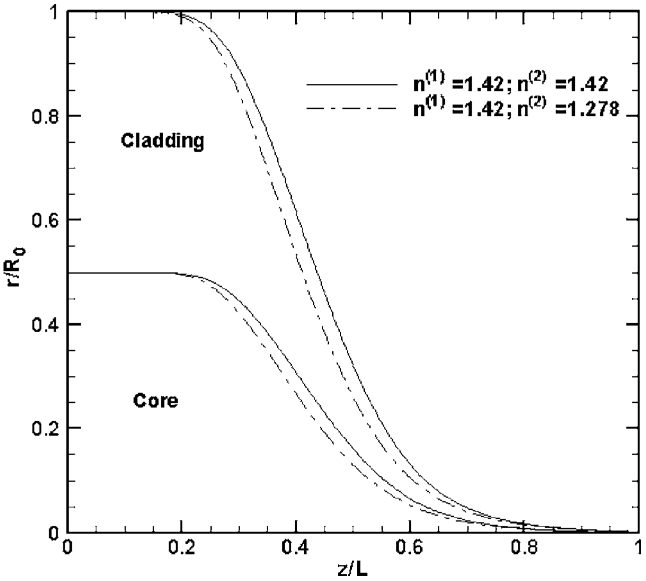

Fig. 9 Influence of the refractive index on the neck-down profile

Using the equation for E' defect concentration derived by Hanafusa et al. [26], the defect concentration along the streamline can be calculated with the following expression:

$$v\frac{dn_d}{dz}=n_p(0)v\exp\left(-\frac{E_p}{KT}\right)-n_d v\left[\exp\left(-\frac{E_p}{KT}\right)+\exp\left(-\frac{E_d}{KT}\right)\right] \tag{25}$$

where n_d and E_d represent the concentration and activation energy of the E' defect; and n_p and E_p represent those of the precursors. The initial values and constants are defined as [26]: $n_d(0)=0$, $n_p(0)=7\times10^{22}\ \mathrm{g}^{-1}$, $E_p=6.4087\times10^{-19}$ J, $E_d=0.3204\times10^{-19}$ J, $v=8\times10^{-3}\ \mathrm{s}^{-1}$, and $K=1.380658\times10^{-23}$ J/K. As expected, the concentration of E' defects is found to be larger in the double-layer preform due to higher preform temperature, as shown in Fig. 10. It is indicated that the fiber quality is degraded with an increase in refractive index difference between the core and the cladding in terms of E' defects.

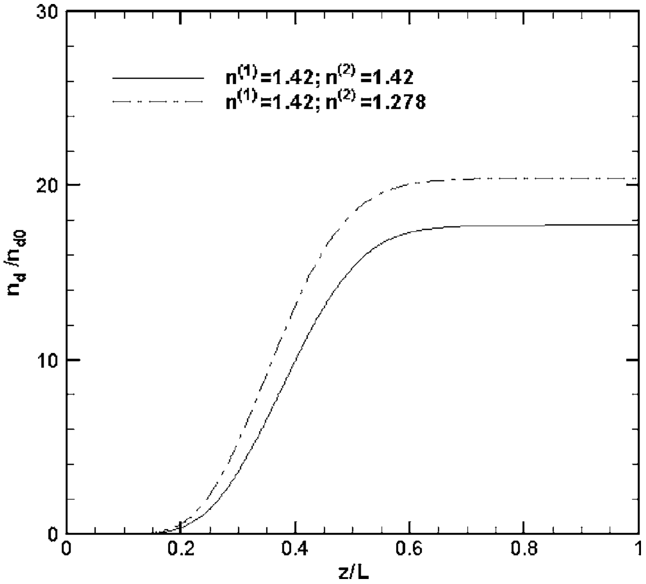

Fig. 10 Influence of the refractive index on normalized defect distribution at the free surface

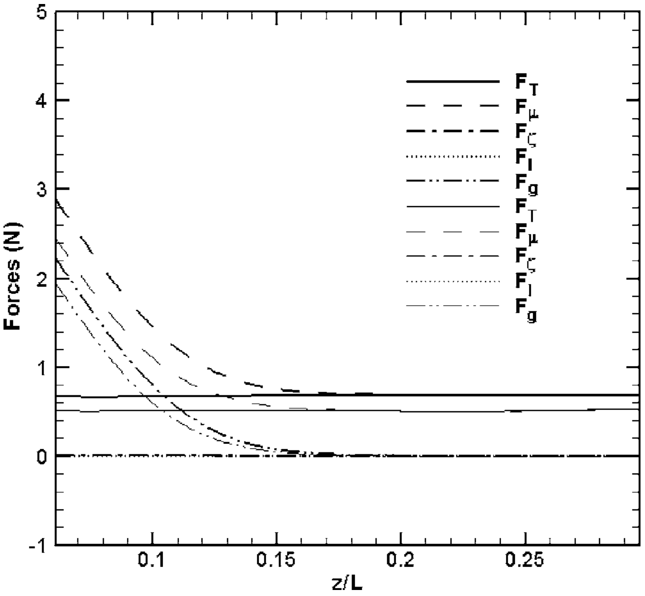

Fig. 11 Influence of the refractive index on draw tension: (thick lines) $n^{(1)}=n^{(2)}=1.42$; and (thin lines) $n^{(1)}=1.42$; $n^{(2)}=1.278$

Neglecting the shear force exerted by the gas, the draw tension can be obtained from the following equation [8,27]

$$F_T=3\pi\mu R^{(2)^2}\frac{\partial v}{\partial z}+\pi R^{(2)^2}\zeta H+\pi\rho\int_z^{L_f}R^{(2)^2}v\frac{\partial v}{\partial z}dz-\pi\rho g\int_z^{L_f}R^{(2)^2}dz \tag{26}$$

The calculated forces including draw tension F_T, and forces due to viscous stress F_μ, surface tension F_ζ, inertia F_I, and gravity F_g, are shown in Fig. 11. It is seen that a smaller draw tension is obtained for the double-layer preform drawing. It is because the force due to viscous stress is much smaller since viscosity of silica decreases drastically with increasing temperature, although the magnitude of the force due to gravity decreases as well.

We now study the effect of variation in the absorption coefficient. The absorption coefficient of doped silica cladding is assumed to be 100% larger than that for pure silica cladding. The refractive index is taken as uniform in the double-layer preform. Figure 12 indicates the temperature distributions along the centerline for both the double-layer and the single-layer preforms. It is interesting to note that when the absorption coefficient in the cladding gets larger, the centerline temperature drops due to the lower transmissivity of the cladding. The effect of change in the absorption coefficient on the temperature lag is shown in Fig. 13. It is seen that the difference between the surface temperature and centerline temperature becomes larger near the entrance. This is because the cladding is heated up faster near the entrance with larger absorption coefficient and the centerline temperature becomes lower as shown in Fig. 12. Since the temperature of preform decreases with an increase in absorption coefficient of the cladding, the neck-down region of double-layer preform starts farther from the entrance than that for the single-layer preform, as shown in Fig. 14. Figure 15 shows that the concentration of E' defects along the free surface in the double-layer preform is lower than that in the single-layer preform, as expected. The draw tension for double-layer preform drawing is also obtained, as shown in Fig. 16. It is found that a larger absorption coefficient in the cladding

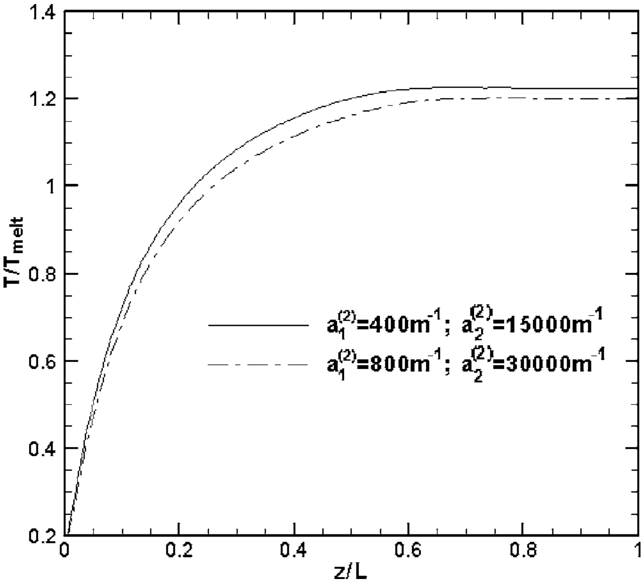

Fig. 12 Effect of change in the absorption coefficient on the temperature distribution at the centerline

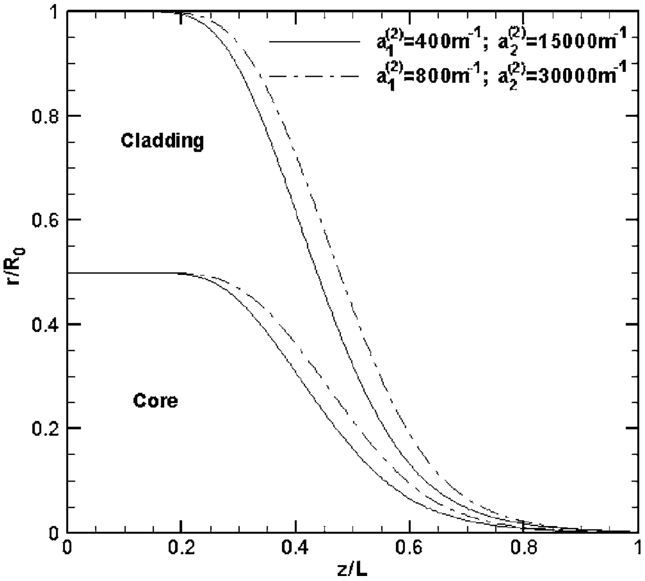

Fig. 14 Effect of change in the absorption coefficient on the neck-down profile

has a stronger effect on forces due to viscous stress F_μ than forces due to gravity F_g. This results in larger draw tension with larger absorption coefficient in the cladding.

6 Conclusions

A numerical model has been developed for the flow and thermal transport in optical fiber drawing with core–cladding structure, within the neck-down region. The zonal method is employed to simulate the radiation transport in the core and the cladding at various uniform refractive indices in the two regions. The model is validated by comparing it with numerical results for single-layer fiber drawing. In this study, the effects of changes in the refractive index and in the absorption coefficient of the cladding due to doping on the fiber drawing are investigated. The results indicate that when the cladding has a lower refractive index than the core, the centerline temperature rises, reflecting higher transmissivity at the free surface and larger internal reflection in the core. Higher temperature lag and concentration of E' defects are also found, while the draw tension becomes smaller. On the other hand, a higher absorption coefficient in the cladding has the opposite effect on the fiber drawing. The doped silica cladding decreases the transmissivity and increases the difference between the temperatures of the core and the cladding. This lowers the centerline temperature, decreases the concentration of E' defects, but increases the draw tension. It is clear that changes in the refractive index and in the absorption coefficient have significant effects on the optical fiber drawing process. Therefore, the effect of a core–cladding structure should be included in the numerical simulation of the optical fiber drawing process. In the future, a thorough study including more accurate physical properties for doped silica needs to be carried out to determine the resulting effects of dopants.

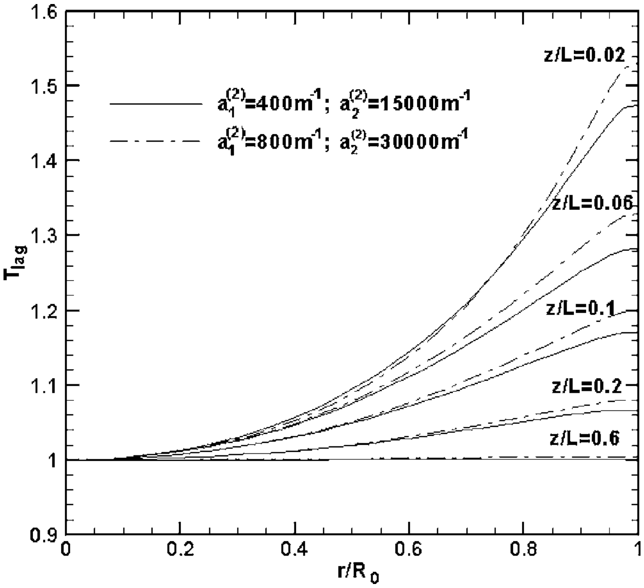

Fig. 13 Effect of change in the absorption coefficient on temperature lag

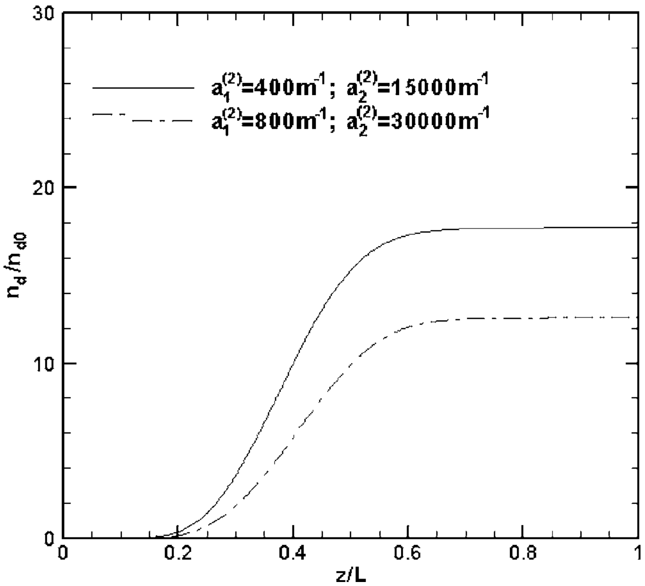

Fig. 15 Influence of the absorption coefficient on normalized defect distribution at free surface

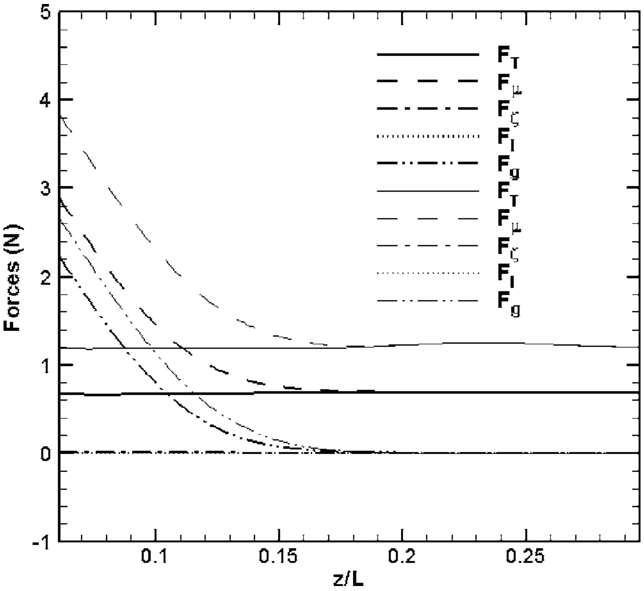

Fig. 16 Influence of the absorption coefficient on draw tension: (thick lines) $a_1^{(2)}=400\ \mathrm{m}^{-1}$, $a_2^{(2)}=15{,}000\ \mathrm{m}^{-1}$; (thin lines) $a_1^{(2)}=800\ \mathrm{m}^{-1}$, $a_2^{(2)}=30{,}000\ \mathrm{m}^{-1}$

Nomenclature

a = absorption coefficient
C_p = specific heat at constant pressure
D = diameter
F_{i-j} = view factor between surface ring element i and j
f = fraction of black body emissive power
G = irradiation
$\overline{G_jG_i}$ = direct exchange area between volume ring element i and volume ring element j
$\overline{G_jS_i}$ = direct exchange area between surface ring element i and volume ring element j
g = acceleration due to gravity
J = radiosity
K = thermal conductivity
L = preform length
n = refractive index
N_s = number of discretized surface zones
N_g = number of discretized volume zones
p = pressure
r = radial coordinate
$R^{(1)}$ = radius of the core
$R^{(2)}$ = radius of the cladding
S_r = radiation source term
$\overline{S_jS_i}$ = direct exchange area between surface ring element i and j
T = temperature
t = time
u = radial velocity component
v = axial velocity component
z = axial coordinate

Greek Symbols

β = dimensionless axial coordinate
ε = emissivity
ζ = surface tension
η = dimensionless radial coordinate
λ = wavelength
μ = dynamic viscosity
ν = kinematic viscosity
τ = transmissivity
ρ = reflectivity; density
σ = Stefan–Boltzmann constant $(=5.67051\times10^{-8}\ \mathrm{W/(m^2\,K^4)})$
Φ = viscous dissipation term

Subscripts

0 = preform inlet
c = centerline
F = furnace
f = fiber
i = surface or volume ring element i
j = surface or volume ring element j
k = volume ring element k
λ = absorbing band

Superscripts

(1) = core
(2) = cladding
(3) = gas
$'$ = first derivative with respect to z
$''$ = second derivative with respect to z

References

[1] Paek, U. C., and Runk, R. B., 1978, "Physical Behavior of the Neck-down Region during Furnace Drawing of Silica Fibers," J. Appl. Phys., **49**, pp. 4417–4422.
[2] Myers, M. R., 1989, "A Model for Unsteady Analysis of Preform Drawing," AIChE J., **35**, pp. 592–602.
[3] Lee, S. H.-K., and Jaluria, Y., 1995, "The Effects of Geometry and Temperature Variations on the Radiative Transport during Optical Fiber Drawing," J. Mater. Process. Manuf. Sci., **3**, pp. 317–331.
[4] Lee, S. H.-K., and Jaluria, Y., 1995, "Effects of Streamwise Convergence in Radius on the Laminar Forced Convection in Axisymmetric Ducts," Numer. Heat Transfer, Part A, **28**, pp. 19–38.
[5] Lee, S. H.-K., and Jaluria, Y., 1996, "Effects of Variable Properties and Viscous Dissipation During Optical Fiber Drawing," ASME J. Heat Transfer, **118**, pp. 350–358.
[6] Lee, S. H.-K., and Jaluria, Y., 1997, "Simulation of the Transport Process in the Neck-down Region of a Furnace Drawn Optical Fiber," Int. J. Heat Mass Transfer, **40**(4), pp. 843–856.
[7] Roy Choudhury, S., and Jaluria, Y., 1998, "Thermal Transport due to Material and Gas Flow in a Furnace for Drawing an Optical Fiber," J. Mater. Res., **13**(2), pp. 494–503.
[8] Roy Choudhury, S., and Jaluria, Y., 1998, "Practical Aspects in the Drawing of an Optical Fiber," J. Mater. Res., **13**(2), pp. 483–493.
[9] Roy Choudhury, S., Jaluria, Y., and Lee, S. H.-K., 1999, "A Computational Method for Generating the Free-surface Neck-down profile for Glass Flow in Optical Fiber Drawing," Numer. Heat Transfer, Part A, **35**, pp. 1–24.
[10] Kaminski, D. A., 1995, "Thermal Transport in Optical Fiber Manufacturing," *Proceedings of the Ist International Symposium on Radiative Heat Transfer*, Kusadasi, Turkey, M. P. Menguc, ed., Begell House, New York, pp. 667–681.
[11] Yin, Z., and Jaluria, Y., 1997, "Zonal Method to Model Radiative Transport in an Optical Fiber Drawing Furnace," ASME J. Heat Transfer, **119**(3), pp. 597–603.
[12] Yin, Z., and Jaluria, Y., 1998, "Thermal Transport and Flow in High-Speed Optical Fiber Drawing," ASME J. Heat Transfer, **120**, pp. 916–930.
[13] Wei, Z., Lee, K., Tchikanda, S. W., Zhou, Z., and Hong, S., 2004, "Free Surface Flow in High Speed Fiber Drawing With Large-Diameter Glass Preforms," ASME J. Heat Transfer, **126**, pp. 713–722.
[14] Okoshi, T., 1982, *Optical Fibers*, Academic, Orlando, Florida.
[15] International Engineering Consortium, 2006, "Fiber-Optic Technology Tutorial," http://www.iec.org/online/tutorials/fiber_optic/
[16] Izawa, T., and Sudo, S., 1987, *Optical Fibers: Materials and Fabrication*, KTK Scientific Publishers, Tokyo, Japan.
[17] Scholze, H., 1991, *Glass: Nature, Structure, and Properties*, Springer-Verlag, New York.
[18] Paek, U. C., 1999, "Free Drawing and Polymer Coating of Silica Glass Optical Fibers," ASME J. Heat Transfer, **121**, pp. 774–788.
[19] Yin, Z., 1997, "Numerical Investigation of Thermal Transport in Optical Fiber Drawing Processes," Ph.D. thesis, Rutgers University, New Brunswick, NJ.
[20] Landau, H. G., 1950, "Heat Conduction in a Melting Solid," Appl. Math. Q., **8**, pp. 81–94.
[21] Jaluria, Y., and Torrance, K., 2003, *Computational Heat Transfer*, 2nd ed., Taylor and Francis, NY.
[22] Chen, C., and Jaluria, Y., 2007 "Modeling of Radiation Heat Transfer in the

Drawing of an Optical Fiber with Multi-layer Structure" ASME J. Heat Transfer, **129**.

[23] Modest, M. F., 1993, *Radiative Heat Transfer*, McGraw–Hill, New York.

[24] Modest, M. F., 1988, "Radiative Shape Factors Between Differential Ring Elements on Concentric Axisymmetric Bodies," J. Thermophys. Heat Transfer, **2**(1), pp. 86–88.

[25] Yin, Z., and Jaluria, Y., 1998, "Thermal Transport and Flow in High-Speed Optical Fiber Drawing," ASME J. Heat Transfer, **120**, pp. 916–930.

[26] Hanafusa, H., Hibino, Y., and Yamamoto, F., 1985, "Formation Mechanism of Drawing-Induced E' Centers in Silica Optical Fibers," J. Appl. Phys., **58**(3), pp. 1356–1361.

[27] Vasilijev, V. N., Dulnev, G. N., and Naumchic, V. D., 1989, "The Flow of a Highly Viscous Liquid With a Free Surface," Glass Technol., **30**(2), pp. 83–92.

Numerical and Experimental Investigation of Melting in the Presence of a Magnetic Field: Simulation of Low-Gravity Environment

H. Zhang

M. Charmchi[1]
e-mail: majid_charmchi@uml.edu

Department of Mechanical Engineering,
University of Massachusetts Lowell,
Lowell, MA 01854

D. Veilleux
Raytheon Integrated Defense Systems,
1847 West Main Road,
Portsmouth, RI 02871

M. Faghri
Department of Mechanical Engineering,
University of Rhode Island,
Kingston, RI 02881
e-mail: faghrim@egr.uri.edu

In this paper, numerical and experimental studies are presented on melting behavior of a pure metal in the presence of a static magnetic field. When a transverse magnetic field is present and the working fluid is electrically conductive, the fluid motion in the magnetic field results in a force field (Lorentz forces) that will dampen the convective flows. Buoyancy driven flows are the focus of this study to simulate low-gravity conditions. Hartmann (Ha) number, a dimensionless parameter proportional to the strength of the magnetic field, dominates the convection flow suppression. The effects of the magnetic strength on melting rate and on the profile of the solid/melt interface are studied. The experiments are conducted with pure gallium as phase change material inside a rectangular test cell. The solid thickness at its side center position is measured by an ultrasound device and the solid/melt interface profile is captured via reflection florescent-light photography. Temperature measurements and volume expansion/contraction tracking are used to provide further details and to verify the numerical results. Magnetically induced low-gravity environments were extensively studied numerically, where the details of the flow field were obtained. The experimental and numerical results compare very well especially, at larger Hartmann numbers. The results showed that a magnetic filed could be used to simulate key melting characteristics found in actual low-gravity environments. However, under strong magnetic field, numerical simulations revealed a different three-dimensional flow structure in the melt region compared to the actual low-gravity flow fields where the flow circulations are smoothly curved. [DOI: 10.1115/1.2709961]

Keywords: magnetic field, magnetohydrodynamic (MHD), phase change, low gravity, natural convection

Introduction

Phase change process plays an important role in the industrial applications, such as crystal growth, welding, casting, heat storage, and material processing. It is well documented that the dynamics of the phase change processes are significantly influenced by natural (free) convection. Free convection flows diminish in a reduced gravity environment, and in some material processes this may lead to significant improvements in the finished products. Therefore, heat/mass transfer associated with phase change in reduced gravity environment has received considerable attention in recent years. The perfect micro gravity experiments can, of course, be conducted on the space laboratory. However, the resources for reaching the outer space environment are very limited—to this date, only 80 experiments have been performed on the International Space Station since the launch of Destiny Laboratory in February of 2001 [1]. Hence, producing low-gravity environment conditions on earth has been pursued by investigators seeking research opportunities in this field. With the current state of technology, several techniques are available for producing low-gravity environment on earth; such as, drop towers, parabolic flight paths, sounding rockets, and magnetic field. The drop towers as well as parabolic flights and sounding rockets have short time periods (order of seconds) and hence, they have limited application. Especially, they are not suitable for phase change experimentation where required time of completion is in order of minutes if not hours. Indeed, for some experimental studies, where the working fluid is electrically conductive, the required ground-based microgravity environment may be achieved by applying electromagnetic force field to counteract the effects of gravity as illustrated in a series of numerical work [2–6].

Typically magnetic fields are used to control the convective flows in the crystal growth industry and material processing [7–12]. It is well known that a magnetic field can significantly dampen the convective flows [13–15] and hence, in phase change cases, controlling the solid/melt interface shape and its propagation speed. In an earlier work, Dulikravich et al. [16] reported that the strength and the orientation of the magnetic field had profound influence on the solidification and melting rates by weakening the flow circulation in melt regions and causing distorted velocity profiles. Later, Dennis and Dulikravich [17] concluded that velocity within the melt could not be completely halted due to limitations of the applied magnetic field. They postulate that magnetic fields stronger than 1.0 T might be required to eliminate fluid motion within the melt. Flow suppression in melting and solidification has not been limited to applied magnetic field only; electro/magnetic fields have also been applied to control the flow field [18,19]. Ha et al. [18] used numerical simulations to compare the thermal flows and solidification of continuous steel casting while

---

[1] Corresponding author.

Contributed by the Heat Transfer Division of ASME for publication in the JOURNAL OF HEAT TRANSFER. Manuscript received March 7, 2006; final manuscript received December 12, 2006. Review conducted by Sumanta Acharya. Paper presented at the 2005 ASME International Mechanical Engineering Congress (IMECE2005), November 5–11, 2005, Orlando, FL, USA.

under the influence electro/magnetic fields. Harada et al. [19] concluded that the application of an electromagnetic field suppresses mixing of solute elements in clad casting. They also verified their numerical simulation predictions with actual clad casting experiments.

While many papers have addressed conducting fluids and the effects of magnetic and electro/magnetic fields, very few sought to study the effects of electro/magnetic fields on phase change problems as a facilitator for simulating low-gravity environments [2–6]. This series of numerical effort was initiated with the work of Asako et al. [2] where only the presence of a magnetic field was considered. Later, the authors expanded their work to include an applied electric field in combination with a magnetic field in such a way that the resulting Lorentz forces opposed the buoyancy flows [3,4]. In these numerical works the considered computational domain was a rectangular cavity having either the two sidewalls thermally active with other four walls insulated, or only the top wall was thermally conditioned and other five walls were insulated. Considering the front view of the cavity, in both thermal boundary conditions, a two-dimensional analysis seems reasonable and the solutions presented in Refs. [2–4] were indeed performed in the two-dimensional domain. Since the phase change material (PCM) was gallium, a fluid with low Prandtl number, the third dimension flow and gradients may not be negligible [14], and hence their effects need to be studied. Veilleux et al. [5,6] further expanded the previous works into three-dimensions and studied the resulting effects. They applied both transverse electric and magnetic fields to counteract the gravitational forces exerted on the system during the melting process. Their results showed that strong magnetic fields dampened the buoyancy driven flows and the overall melting rates and the solid/melt interface profiles resembled the low-gravity cases. However, the flow structures were significantly distorted [4]. When an electric field was applied, it substantially reduced the needed magnetic field intensity for halting the convective flows. However, in these cases the resulting Lorentz forces, produced by electro/magnetic fields, generated a flow field, opposite to the main flow direction, that is not present in actual low gravity. While these distortions in the flow field do exist, results showed that from a global phase change point-of-view, low-gravity environment can be simulated by magnetic and/or electro/magnetic fields.

The review presented in the last paragraph reveals that a substantial amount of numerical simulations have been performed. However, experimental data needed to verify the numerical results are severely limited. Computation of phase change processes in the presence of electro/magnetic fields is complicated and to manage the level of complexity, some assumptions were made. For example, the expansion/contraction of the material due to the change of phase density, the so-called phase change convection, is neglected and no mass is allowed to cross the computational boundary domain. Hence, the validity of assumptions and applicability of the simulations must be investigated. To achieve this, a series of experiments were performed to compare the test results with the computed data. Indeed, the focus of this paper is on the experimental validation of the numerical simulations. Here, the description of the applied numerical methods will be brief and the readers are referred to Refs. [3–6]; instead, more descriptions will be devoted to the experimental techniques and measurements, and the combined numerical and experimental results.

Most phase change experiments dealing with liquid metals address crystal growth issues. Due to the opaque nature of the liquid metals and alloys, experiments on liquid metals have been limited to the investigations of natural convection and diffusion, free surface flows, liquid/solid interface probing, and local temperature analysis [13,20]. Campbell and Koster [21] and Derebail and Oster [22] employed X rays or gamma rays to perform visualization studies of liquid/solid interface propagations, profile, and morphologies. The use of radiation rays, however, is expensive, requires a special facility for safety, and most importantly, is limited to thin layers of metal phase change processes. To measure the solid/melt interface positions continuously at some preselected locations, ultrasonic techniques can be employed [23–25]. This technique is used in this work; but because of the size of ultrasound probes, their use is limited to a very few locations at which the solid thickness can be measured. In addition to ultrasonic measurement, the profile of the solid/melt interface is captured through the transparent end windows by florescent-light reflection photography. In this work, special care is given to the volume expansion/contraction due to differences in phase densities. This volume change is tracked by an oil indicator traveling inside a calibrated vertical tube. Changes in interface profile as a function of time, the melting rate, and the influence of magnetic strength are analyzed and compared with the numerical results.

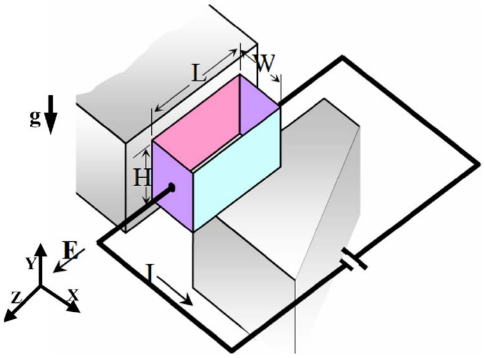

Fig. 1 **Schematic diagram of the experimental setup**

Problem Description

The geometry considered is a rectangular container, the test cell, of height (H), width (W), and length (L), which is filled with the phase change material (gallium) in its solid phase. The entire test cell is placed under a transverse magnetic field, where the magnetic field, B_0, is applied in the positive x direction as shown in Fig. 1. Initially the system is kept at the melting temperature, T_m. The left sidewall is suddenly raised to a uniform higher temperature ($T_h > T_m$), whereas the right sidewall of the test cell is kept at, or below, the melting temperature ($T_c \leqslant T_m$), and the remaining walls are adiabatic. Melting of the PCM begins and a free convection flow starts to develop in the melt region.

With reference to Fig. 1, the concept of magnetohydrodynamic (MHD) is briefly described. The applied electric/magnetic field results in an induced electromagnetic field. The strength and the effect of induced field, however, are negligible in the ranges being considered for this investigation. This assumption is valid when the magnetic Reynolds number remains much less than one ($\mathrm{Re}_m \ll 1$), as is the case for liquid metals and alloy [26] (in this investigation, the magnetic Reynolds number is about 6.5×10^{-6}). Therefore, the resulting Lorentz forces per unit volume could be represented as

$$\mathbf{F} = \mathbf{J} \times \mathbf{B} \tag{1}$$

where **B** is the magnetic field and **J** is the current density flux, which is expressed as

$$\mathbf{J} = \sigma(\mathbf{E} + \mathbf{U} \times \mathbf{B}) \tag{2}$$

Here, σ is the medium electrical conductivity and **U** is the velocity field vector. In this set of experiments, the electrical field, **E**, is turned off and only the magnetic field is active. Hence, the current density flux is expressed as

$$\mathbf{J} = \sigma[(U_x\vec{i} + U_y\vec{j} + U_z\vec{k})] \times (B_0\vec{i}) \tag{3}$$

or

Table 1 Electrical and thermophysical properties of gallium

Parameter	Symbol	Value	Unit
Melting point	T_m	29.78	°C
Density of solid	ρ_s	5907.0	$\mathrm{kg/m^3}$
Density of liquid	ρ_m	6094.7	$\mathrm{kg/m^3}$
Viscosity	μ	1.92×10^{-3}	kg/(m s)
Momentum diffusivity	ν	3.15×10^{-7}	$\mathrm{m^2/s}$
Electrical conductivity of solid	σ_s	6,644,518.0	1/m
Electrical conductivity of liquid	σ_m	3,846,154.1	1/m
Latent heat	h	89,160.0	J/kg
Melt thermal diffusivity	α_m	1.29×10^{-5}	$\mathrm{m^2/s}$
Thermal expansion coefficient	β	1.27×10^{-4}	1/K
Prandtl number	Pr	0.0244	

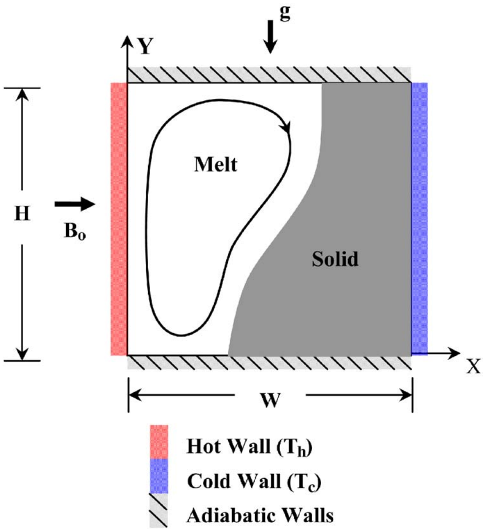

Fig. 2 Two-dimensional view of the computational domain

$$\mathbf{J} = \sigma(U_z B_0 \vec{j} - U_y B_0 \vec{k}) \tag{4}$$

By substituting Eq. (4) into Eq. (1); the Lorentz forces are expressed by

$$\mathbf{F} = \mathbf{J} \times \mathbf{B} = [\sigma(U_z B_0 \vec{j} - U_y B_0 \vec{k})] \times (B_0 \vec{i}) \tag{5}$$

or

$$\mathbf{F} = \sigma[(-U_y B_0^2)\vec{j} - (U_z B_0^2)\vec{k}] \tag{6}$$

It is shown in Eq. (6) that the magnetic force field counteracts the flow field and the force is proportional to B_0^2 in both y and z directions. For a specific physical length and material properties, the strength of the Lorentz forces is scaled by the Hartmann number, which is expressed in Eq. (7). Other dimensionless parameters that appear in the results are Stefan number, Prandtl number, Grashof number, and Rayleigh number, as well as time and temperature. They are defined as follows:

Hartmann number

$$\mathrm{Ha} = B_0 W \sqrt{\frac{\sigma_m}{\mu_m}} \tag{7}$$

Stefan number

$$\mathrm{Ste} = \frac{C(T_h - T_m)}{h} \tag{8}$$

Prandtl number

$$\mathrm{Pr} = \frac{\nu}{\alpha} \tag{9}$$

Grashof number

$$\mathrm{Gr} = \frac{g\beta(T_h - T_m)W^3}{\nu^2} \tag{10}$$

Rayleigh number

$$\mathrm{Ra} = \mathrm{Gr}\,\mathrm{Pr} \tag{11}$$

Dimensionless time

$$\tau = \frac{\alpha t}{W^2} \tag{12}$$

Dimensionless temperature

$$\theta = \frac{T - T_m}{T_h - T_m} \tag{13}$$

The thermophysical and electromagnetic properties of gallium are presented in Table 1.

Governing Equations

The computation domain considered in this work is shown in Fig. 2. The melting of an electroconductive phase change material in the presence of an electromagnetic field is governed by the conservation of mass, momentum, and energy, the induction equations, and the Poisson equation for electric potential. While this equation set can be solved numerically it possesses significant challenges to obtain a converged solution due to their highly coupled nature. In order to simplify the equation set, some assumptions are made.

As stated earlier, the induced electromagnetic field is negligible [26] and hence, the induction-free MHD approximation is employed. This approximation allows for the applied magnetic and electric fields be accounted for solely through the source terms in the conservation equations. In addition, the flow is assumed to be laminar, incompressible, and the thermophysical properties are constant in each phase (the properties are evaluated at the melting temperature, T_m). Furthermore, the densities of liquid and solid phases are assumed to be the same, $\rho_s = \rho_m$, except for the density that appears in the body force term which gives rise to the force imbalance between the solid and liquid phases. Therefore, material expansion and/or contraction due to phase change is not accounted for—since gallium has moderate volume change (about 3.5% volume contraction during melting), neglecting its effect may not produce significant error on the overall process simulation. The formulation is carried out as a single-domain problem, utilizing the enthalpy method developed by Cao and Faghri [27] where the same conservation equations are used for both the solid and liquid phases, by considering the solid region as a liquid with an infinite viscosity. Since both phases are present in the numerical domain and their volume fraction, their electro- thermophysical properties, and their appropriate force or energy source terms must be accounted for, the governing equation set is too prohibitively long to represent it here. A complete set of the equations can be found in Ref. [6]. Note that the presence of electric field, **E**, raises a new dimensionless parameter that is not introduced in this text, mainly the electromagnetic pressure number (Mp), defined as

$$\mathrm{Mp} = \frac{\rho_m \sigma_m B_0 E W^3}{\mu_m^2} \tag{14}$$

Since in this work electric field is off ($\mathbf{E}=0$), all terms associated with Mp are set to zero in the numerical solution [6].

Numerical Procedure

The governing equations were discretized using a control-volume based finite difference scheme. Patankar's SIMPLE algorithm was used to solve the coupled heat transfer and MHD flow problem [28]. The QUICK scheme of Hayase et al. [29], coupled

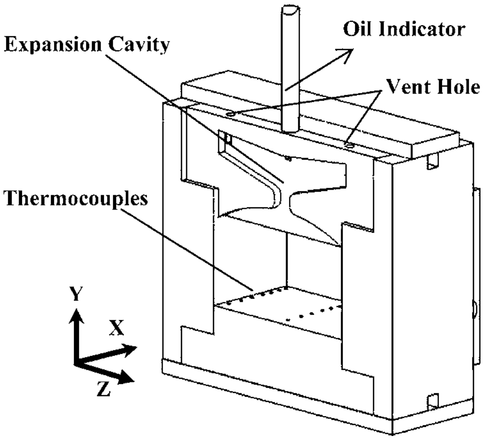

Fig. 3 The three-dimensional view of the test cell without its sidewalls

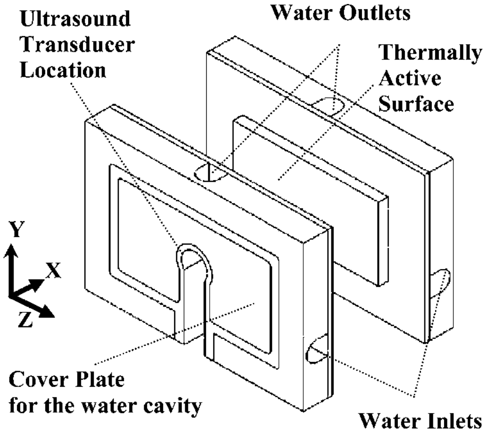

Fig. 4 Photograph of the copper walls

with a modified upwind method proposed by Cao et al. [27], were employed in the solution of the dimensionless enthalpy equation. The remaining dimensionless equations were solved utilizing the power law scheme [28].

The grid size dependency was examined for a series of three-dimensional grid systems. The mass circulation, solid/melt interface location (at the middle of the Y-Z planes), and the computer run time for the different grid systems were compared (see Table 2 in Ref. [6]). After careful examination, a $42 \times 42 \times 22$ grid system was selected for the numerical simulations. A similar practice was also exercised to determine a suitable time step. A value of 0.001 dimensionless time step yield results within 0.22% of the data obtained with 0.0001 time step but with 400% less CPU run time effort [6].

Experimental Apparatus

The experimental system consisted of: three heating/cooling water circulators, the test cell, the magnetic system, and the diagnostic system. A description of these components and the configurations will be presented in the following sections.

The heating/cooling circulators provided preset constant temperature water for the copper sidewalls of the test cell. A set of plumbing network was built to switch the sidewalls from one bath circulator to the next for rapid temperature conditioning. For example, suppose Tank 1, Tank 2, and Tank 3 are set at T_h (hot), T_c (cold), and T_m (melting temperature), respectively; by closing and opening a few valves, one can switch a sidewall temperature from initial T_m to higher temperature T_h—or in reverse—in a matter of seconds.

The three-dimensional (3D) view of the test cell, without its sidewalls, is shown in Fig. 3. The cavity had a cross-section dimension of 30 by 30 mm and it was 60 mm long. The sidewalls (shown in Fig. 4) were made of copper and the other four walls were fabricated from Plexiglas. The front and back walls were carefully polished to provide highly transparent windows for capturing the photographs. Three rows of fine-gauge type-E thermocouples were embedded on both top and bottom walls. One row was at the center and the other two rows were placed adjacent to the front and back windows, respectively. (The bottom rows can be seen in Fig. 3.)

Gallium was chosen as the working fluid, which has a moderate melting temperature of 29.78 °C. The density of liquid gallium is greater than that of solid phase. To accommodate the material expansion during solidification and subsequent contraction during melting, a streamlined auxiliary cavity was machined into the thick-Plexiglas-top wall near the “hot-copper sidewall.” As shown in Fig. 3, the two smaller vent holes were used for air evacuation and the larger vent hole connected the auxiliary cavity to the atmosphere through a transparent Plexiglas tube 3 mm in diameter (marked as “oil indicator”) was used as the gallium expansion/contraction volume indicator from which the melt volume fraction was obtained.

When copper walls were clean and free of nucleation sites, gallium remained at the liquid state even when the wall temperature dropped below the gallium melting temperature (subcooling effect). To prevent this, a small hole was drilled on the top surface, through the top wall, adjacent to the “cold-copper sidewall” for inserting a needle containing solid gallium seed.

Each copper sidewall, shown in Fig. 4, was secured to the test cell via eight 3 mm screws and sealed with a 1-mm-thick paper gasket soaked in vacuum grease. The dimension of each copper wall was 90 by 60 mm and 16 mm thick. A 10.7-mm-diameter burrow with depth of 14 mm was machined at the back center of each copper plate to house an ultrasound transducer. The first 5 mm length of each burrow was threaded to receive a penny cap to secure the transducer. A 10 mm wide slot provided passage for the transducer wire. The active surface of each copper wall, exposed to the gallium, had dimensions of 30 by 60 mm and both active surfaces were oxidized to prevent gallium attack. Constant-temperature water circulated in an 11 mm deep cavity, machined onto the back of each copper wall that was covered with a thin copper plate by soldering means (Fig. 4). The circulating water entered from two side inlets and exited from a single top outlet. Three thermocouples, strategically placed near the active surface of each copper wall, measured the surface temperature and verified its isothermal condition.

The magnetic system consisted of Walker Scientific electromagnet poles (model VF-7H), powered by the Walker Scientific dc power supply (model HS-1365-4SS), and the system was thermally conditioned by the Neslab Merlin series temperature bath (model M150). With the capacity of the power supply, 50 dc A, and within 65 mm air gap, the magnetic system provided an 0.88 T stable field. Best linear performance was achieved within the range of 0–0.6 T.

The magnetic field measurement was carried out by a Walker Scientific gauss meter (model MG-4D) equipped with a hall probe (model HP-3450S-20). Within the air gap, the field was measured at three different cross sections, (i.e., near each pole piece and at the center of the air gap). At each cross section, five measuring points were selected, one at the center of the pole and the other four were near the pole perimeter placed at a 90 deg incremental angle. The measurements were in Tesla and the probe had an accuracy of ±0.05% of reading. Frequent calibration measurements showed that the magnetic field uniformity was better than 99%.

The measuring system consisted of an ultrasound diagnostic system, temperature data acquisition, and image capturing system.

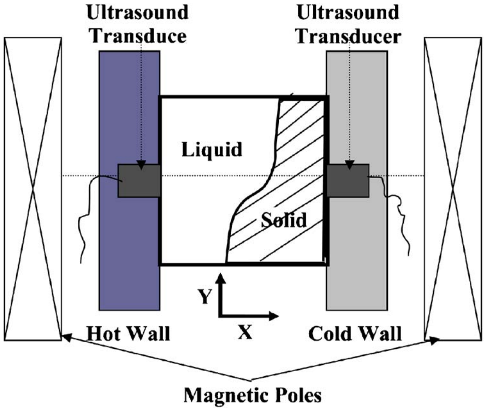

Fig. 5 Illustration of ultrasound diagnostic method

(*a*) **Melting at zero magnetic field (g)**

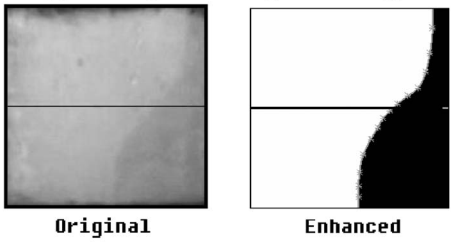

(*b*) **Melting under higher magnetic field**

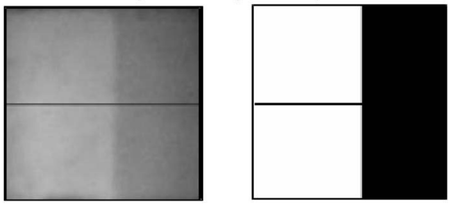

Fig. 6 Typical captured images and image enhancement

The thickness of the liquid (or solid) phase at the center of the sidewall was determined by the ultrasonic pulse propagation technique. The solid and liquid phases, separated by the interface, have different acoustic properties which can be used, with proper calibration, to measure the thickness of each phase within resolution proportional to the pulse wavelength. Ultrasonic pulses in the 5 MHz range are commonly utilized for these types of measurements. In practice, this diagnostic technique has been applied in pulse-echo mode, in transmission mode, or in angle beam shear wave mode [23,24]. Pulse-echo mode is simpler to use and was applied by McDonough and Faghri [25], but it has limitations. In the first stage of this work, the acoustic properties of gallium were documented and the effectiveness of each mode was evaluated. The angle beam configuration was impractical due to its requirement of near optimum transducers spacing. Both pulse-echo and through transmission modes were able to measure the solid thickness only when the interface was near flat (conduction controlled phase change). When natural convection was present in the melt region and the interface was curved, the reflected signal was lost and pulse-echo mode became useless. Only through transmission mode were we able to detect the interface position effectively.

The ultrasonic diagnostic system used in this work consisted of a computer-controlled pulser/receiver (Panametrics model 5800), a digital oscilloscope (HP model 54600A), a Pentium desktop computer with GPIB input-output (I/O) interface card, and a pair of 5 MHz videoscan ultrasonic transducers (Panametrics model V110-RM), configured in the through transmission mode as shown in Fig. 5. Exploratory tests revealed that the magnetic field had no effect on the ultrasound transducer outputs.

The thermocouple signals, 47 in total, were measured by a 14 bit National Instrument data acquisition system (NI PCI-6030E) and two thermocouple amplifiers (NI SCXI-1102). The 47 channels were scanned twice per second. The accuracy of temperature measurement was within ±0.2°C.

Three high-resolution cameras (creative PD1170) were used to capture the images of the front window, the back window, and the oil indicator level (i.e., volume expansion/contraction indicator), separately. Liquid gallium has slightly different emissivity than its solid phase and therefore, reflectivity. This difference in reflectivity can be augmented by using a florescent light source. As illustrated in Fig. 6, in the captured photos, the solid phase appears darker than the liquid region. (The horizontal lines indicate the center line where sound wave passed through.) Later, each photo was enhanced by IMAGE-Pro software, as shown in the right side of the captured image in a distinct black and white format. The processed images provided solid/melt interface profiles and solid/liquid volume fractions.

Experimental Procedure

Filling of Test Cell. Gallium, like most liquid metals, has large surface tension and thus can trap gas during filling. Here, first the test cell was filled with Meriam red oil fluid, a noncorrosive, low-surface-tension fluid, and degassed. Then, gas free warm gallium melt (at about 40°C) was slowly injected into the test cell while allowing for Meriam fluid to escape through the expansion cavity. Some Meriam fluid was allowed to remain inside the expansion cavity (also called the auxiliary volume) and was visible through the vertical glass "oil indicator." The presence of oil served two purposes: (a) it protected the gallium from air exposure; and (b) its column length inside the glass tube indicated the global rate of phase change due to expansion, during solidification, and contraction while PCM was melting.

Test Setup. After filling, the ultrasound transducers were placed on the copper walls at their prepared positions using a supplied thick honey as the coupling media. The transducers were secured in place by tightening the penny screws. The test cell was placed between the magnetic pole pieces and leveled. The water delivery tubes were connected to the copper walls. The thermocouples were connected to the data acquisition system and tested. The cameras were adjusted for best optical view and the ultrasound transducers were connected to the pulser/receiver device.

The three bath circulators were set for T_h, T_c, and T_m, respectively, for a typical test run. Both solidification and melting experiments were initiated from the melting temperature, T_m. During the initialization stage, both copper walls were thermally conditioned by a single water circulator maintained at T_m. When the temperature field reached the isothermal state, one of the copper walls was switched to a different circulator. To solidify, the cold side copper (opposite to the expansion cavity side) was switched to the circulator set at T_c while the hot sidewall was kept at T_m. When the solidification ended, the cold wall was switched back to T_m until an isothermal state was again established. The melting experiment initiated by switching the hot copper sidewall to T_h bath, while keeping the cold wall at T_m.

Due to the thermal inertia of the copper walls, there was a delay of about 2–3 min for the wall to reach its steady-state temperature. Figure 7 presents a typical wall temperature response to a sudden temperature change. The walls temperature responses were recorded and applied as the boundary condition into the numerical simulation.

As mentioned earlier, the images of the front and back windows were captured frequently (every 5 s) and analyzed to acquire the interface profile. The front and back images were very close; how-

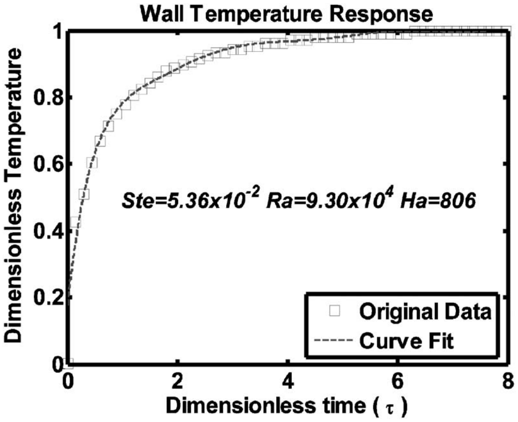

Fig. 7 Typical copper wall temperature response

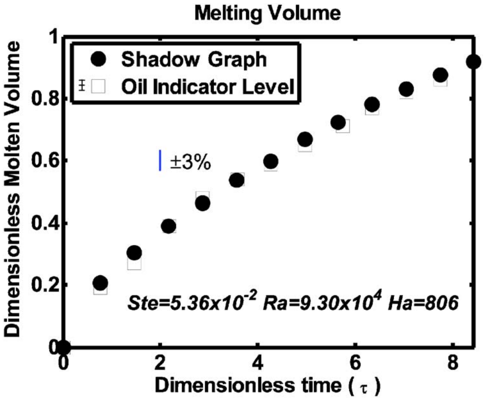

Fig. 9 Melt volume fraction: comparison of oil indicator and image data processing

ever, to compute the phase volume fractions, the phase surface fractions of both images were averaged and then from the averaged interface profile, the volume fraction of each phase was calculated as a function of time.

The ultrasound transducer continuously detected the solid/melt interface at the center of the sidewalls. These measured thickness values were compared with the thickness data obtained from images and the numerical results. One such comparison is shown in Fig. 8. As seen there, the agreement between the two sets of experimental data and the numerical results is astonishingly close.

The changes in the height of the oil column traveling in the vent tube are an excellent indicator of the changes in melt volume fractions. The melt (or solid) volume fractions were obtained from

$$V_m = \frac{\rho_m(\Delta V_{\text{oil}})}{(\rho_m - \rho_s)} = \frac{\rho_m A_{\text{tube}}(\Delta H_{\text{oil}})}{(\rho_m - \rho_s)} \tag{15}$$

Here, it is assumed that the interface profile is 2D (using the averaged values). This assumption was made after examining front and back images and reviewing the temperature data. (The thermocouples embedded in the top and bottom walls indicated that the temperature field was practically independent of the test cell depth z direction.) A comparison of melt volume fraction obtained by the oil level indicator and by image processing is presented in Fig. 9. As seen there, the agreement is within 3%. Similarly, for other experiments, the melting volume fraction was calculated from oil indicator levels and the images and the results compared very well, indicating that the test cell was leak free and working well.

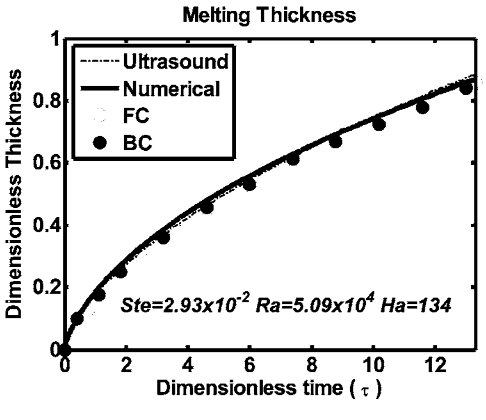

Fig. 8 A comparison of ultrasound, numerical, and image data: (FC) front window at center; (BC) back window at center

Experimental Uncertainty Analysis

The experimental results are presented by plotting the dimensionless thicknesses of the interface position at different temperature boundary conditions and magnetic strength versus the dimensionless time. The uncertainty is a product of the bias and precision errors in measuring temperature, magnetic strength, time, and processing captured images. The variable thermophysical properties and the heat losses through the assumed adiabatic walls are also sources of error. However, since the gallium melting temperature is close to the normal laboratory temperature, the heat loss/gain to/from the surrounding air is not large and may not affect the outcome substantially.

Stefan, Grashof, and Hartman numbers are the characteristic parameters of this work. Both Stefan and Grashof numbers are a function of wall temperature that is measured via embedded thermocouples. The temperature measurement system was calibrated to provide temperature data within ±0.2°C. This is less than 1% of the measuring temperature range. The magnetic strength measurement, which directly affects Hartman number, was accomplished within ±0.1%, but the magnetic field uniformity was about 99%. Hence, the overall uncertainty in magnetic field measurement was mainly influenced by its nonuniformity of 1%. Interface locations were obtained by analyzing the captured images taken at 5 s time intervals. Two cameras were triggered by two different computers. The computer internal clocks were synchronized before each experiment. The high-volume image-data transfer lead to a discrepancy between the two computer internal clocks at the end of each test (the accumulated error depended on the time period of the experiment). This error in time management may over- (or under-) estimate the melt thickness. Combining all said sources of errors, the measurement uncertainty of this system was estimated to be ±3%. Several experimental cases were repeated and in all cases the repeatability of acquired data was better than the uncertainty rate of 3%.

Results and Discussion

Experimental tests were carried out for three different categories: natural convection, solidification, and melting. In this paper natural convection will be briefly discussed followed by a discussion of the melting results. The influence of magnetic strength is investigated and compared with numerical results.

Natural Convection. In this set of tests, the temperatures of both copper walls were higher than the melting temperature of gallium, T_m. With a temperature difference corresponding to $\mathrm{Gr.Pr}^2 = 2\times10^3$, temperature profiles at different magnetic field are plotted in Fig. 10. The dimensionless parameters are as follows:

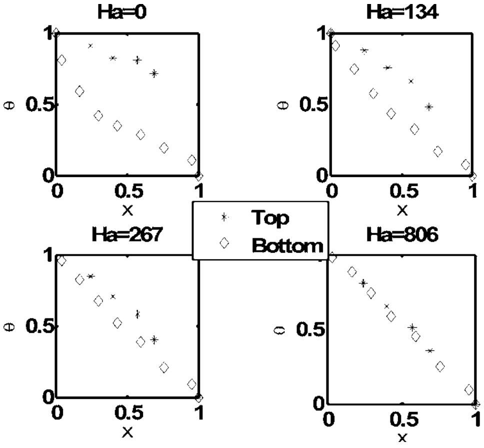

Fig. 10 Natural convection: effect of Hartmann number

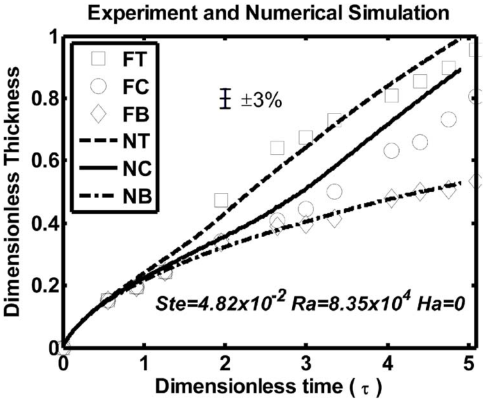

Fig. 11 Melt thickness at top, center, and bottom: comparison of experimental and numerical results (Ha=0)

$$X = \frac{x}{W} \tag{16}$$

$$\theta = \frac{T - T_c}{T_h - T_c} \tag{17}$$

As can be seen in Fig. 10, when magnetic field (represented by Ha) increases, the top and bottom surface temperature profiles become closer and finally merge into a single straight line. From Ha=0 to Ha=806, the dominating mode of heat transfer changes from a strong free convection to a simple heat conduction.

Unlike the previous results reported by authors for the painted copper walls [30], no noticeable thermal resistance was observed for the oxidized copper surface. The data presented in Fig. 10 are for the magnetic strength fields of 0 T, 0.1 T, 0.2 T, and 0.6 T, corresponding to Ha=0, 134, 267, and 806, respectively.

Melting Results. After the test cell was fully solidified, it was brought back to isothermal state at T_m. Then, the hot side copper wall was switched to a water bath having temperature $T_h > T_m$ and the melting process began. In the following sections, the melting results presented belong to cases with $\Delta T = T_h - T_m \approx 10°\mathrm{C}$ and the magnetic strengths of 0 T, 0.1 T, 0.25 T, and 0.6 T.

For each case, the hot-wall temperature history (similar to that shown in Fig. 7) was recorded and introduced to the numerical code as a boundary condition. The interface profiles obtained from the captured images were compared with the numerical results. (The time history of the center point on the interface profile of each case compared very well with the ultrasound data. Therefore, for clarity purposes, the curves belonging to the ultrasound were removed from these comparisons.)

Figures 11–14 present comparisons between numerical simulations and captured image results for cases of $\Delta T = T_h - T_m \approx 10°\mathrm{C}$, (i.e., Ste≈0.05 and Ra≈90,000), and for Ha=0, 134, 335, and 806, respectively. (Note: notations FT, FC, and FB mean front window, top, center, and bottom of images, respectively; and NT, NC, and NB mean the numerical profile at top, center, and bottom, respectively.) As illustrated in these four figures, the numerical simulations fit very well the results obtained from the images; the agreement is within (or better than) ±6%. Indeed, at larger Hartmann numbers the numerical results are very close to the experimental data, which means when natural convection is dampened and the melt/solid front is relatively flat, the enthalpy method used in the numerical code [6] predicts the test results quite accurately. On the other hand, when free convection is strong, the melting rate is comparatively large, and the interface is curved, the numerical model with approximations such as constant thermophysical properties in each phase, neglecting the volume contraction of the solid material undergoing the melting process, may affect the flow field in the melted region. Also, the grid resolution limitations, due to computation power, may contribute to small differences between experimental and numerical results at low Hartmann numbers when free convection flows are strong. In addition, when melting rate is large, the errors associated with time management of the captured images tend to overstate the differences existing between experimental and numerical results.

As shown in this work, two dimensionless parameters play major roles: they are Hartmann number (Ha) and Stefan number (Ste). The role of Stefan number in phase change processes has been well established, especially for conduction controlled melt-

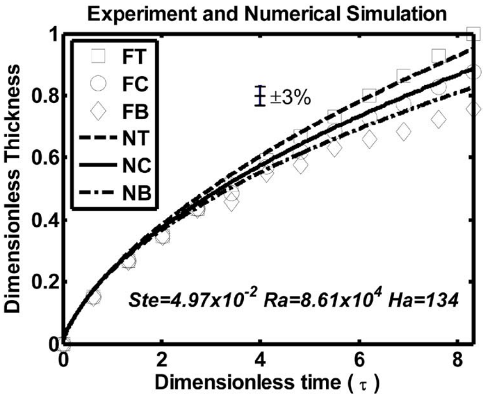

Fig. 12 Melt thickness at top, center, and bottom: comparison of experimental and numerical results (Ha=134)

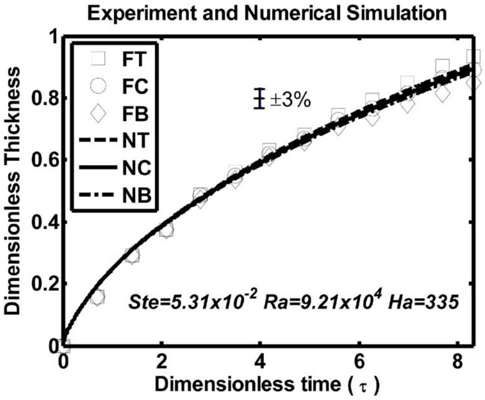

Fig. 13 Melt thickness at top, center, and bottom: comparison of experimental and numerical results (Ha=335)

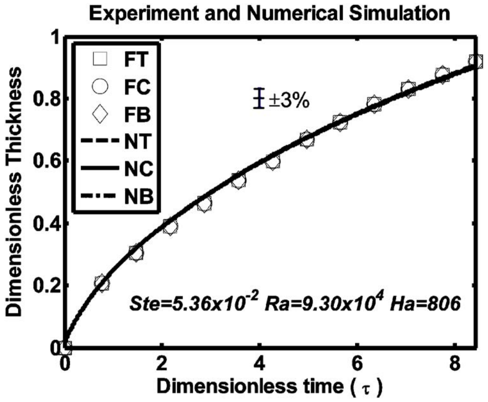

Fig. 14 Melt thickness at top, center, and bottom: comparison of experimental and numerical results (Ha=806)

ing and/or solidification. The role of Hartmann number is not yet clear on phase change rate. Indeed larger magnetic field will dampen the convective flows and will alter the shape of the melt/solid interface as illustrated in Fig. 6. However, its effect on overall melting rate is not overly remarkable as seen in this study. To examine this, the melting rates of the experiments reviewed in the previous discussion were computed and the results of all four tests are plotted in a single graph for comparison as shown in Fig. 15. As seen there, at shorter time periods where melt thickness is small, all melting rates are similar. As the melt thickness increases (at longer time periods), only the case of Ha=0 separates from the other three cases that were under magnetic influence. (Of course, as melt thickness increases, free convection will become stronger and melting rate should increase as the case of Ha=0 indicates.) It was expected that we would see a similar behavior for smaller Hartman numbers such as Ha=134 which did not exhibit such behavior.

Conclusion

The experimental results have illustrated that the melt/solid interface is significantly affected by the presence of a magnetic field. When a magnetic field is present, the overall melting rate decreases compared with zero field. However, the relation between the strength of the magnetic field and the melting rate is not yet clear. The experimental data compared very well with the numerical simulations, giving confidence that the assumptions made in the numerical modeling are valid.

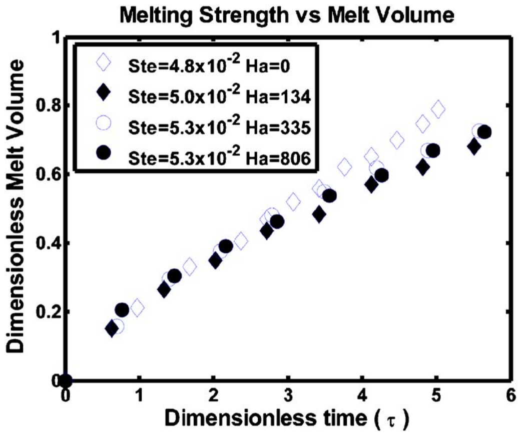

Fig. 15 Hartman number effect on the melting rate

Acknowledgment

Financial support for this work by NASA Microgravity Program (Grant No. NAF3-2426) is gratefully acknowledged.

Nomenclature

A_v = cross-section area of the venting hole, m^2
B = magnetic field, T
B_0 = applied magnetic field, T
C = specific heat, J/(kg K)
E = applied electric field, V
g = gravity acceleration, m/s^2
Gr = Grashof number
h = latent heat, J/kg
H = height of the test cell, m
Ha = Hartmann number
J = electrical current density, A/m^2
k = thermal conductivity, W/(m K)
L = depth of the test cell, m
Mp = electromagnetic pressure number
Pr = Prandtl number
Ra = Raleigh number
Re_m = magnetic Reynolds number
Ste = stefan number
t = time, s
T = temperature filed, K
U = velocity vector, m/s
V = melting volume fraction
W = width of the test cell, m
X = dimensionless interface front

Greek Symbols

α = thermal diffusivity, m^2/s
σ = electrical conductivity, 1/m
μ = viscosity, kg/(m s)
ν = kinematic viscosity, m^2/s
θ = dimensionless temperature
ρ = density, Kg/m^3
τ = dimensionless time
β = thermal expansion coefficient, 1/K

Subscripts

c = cold side
h = hot side
m = melting or liquid phase
o = oil indicator
s = solid phase
w = wall condition
x,y,z = system coordinates
X,Y,Z = dimensionless coordinates, (x/W, y/W, and z/W, respectively)

References

[1] Pellis, N. R., and North, R. M., 2004, “Recent NASA Research Accomplishments Aboard the ISS,” Acta Astronaut., **55**, pp. 589–598.
[2] Asako, Y., Gonçalves, E., Faghri, M., and Charmchi, M., 2002, “Numerical Solution of Melting Processes For Fixed and Unfixed Phase Change Material in the Presence of Magnetic Field—Simulation of Low-Gravity Environment,” Numer. Heat Transfer, Part A, **42**, pp. 1–19.
[3] Gonçalves, E., Faghri, M., Asako, Y., and Charmchi, M., 2004, “Numerical Solution of Melting Processes for Unfixed Phase Change Material in the Presence of Electromagnetically Simulated Low Gravity,” Numer. Heat Transfer, Part A, **46**, pp. 343–365.
[4] Gonçalves, E., Faghri, M., Asako, Y., and Charmchi, M., 2005, “Numerical Solution of Melting in Side-Heated Rectangular Enclosure Under Electromagnetically Simulated Low Gravity,” Numer. Heat Transfer, Part A, **47**, pp. 315–332.
[5] Veilleux, D. L., Gonçalves, E., Faghri, M., Asako, Y., and Charmchi, M., 2005, “Phase Change in a Three-Dimensional Rectangular Cavity Under Electromagnetically Simulated Low Gravity: Top Wall Heating with an Unfixed Material,” Numer. Heat Transfer, Part A, **48**, pp. 849–678.
[6] Veilleux, D. L., Gonçalves, E., Faghri, M., Asako, Y., and Charmchi, M., 2005,

"Phase Change in a Three-Dimensional Rectangular Cavity Under Electromagnetically Simulated Low Gravity: Sidewall Heating," Int. J. Numer. Methods Heat Fluid Flow, **15**(7), pp. 710–739.

[7] Baumgartl, J., and Müller, G., 1996, "The Use of Magnetic Fields for Damping the Action of Gravity Fluctuations (g-Jitter) During Crystal Growth Under Microgravity," J. Cryst. Growth, **169**(3), pp. 582–586.

[8] Yeckel, A., and Derby, J., 2004, "Dynamics of Three-Dimensional Convection in Microgravity Crystal Growth: g-Jitter With Steady Magnetic Fields," J. Cryst. Growth, **263**(1), pp. 40–52.

[9] Ganapathysubramanian, B., and Zabaras, N., 2004, "Using Magnetic Field Gradients to Control the Directional Solidification of Alloys and the Growth of Single Crystals," J. Cryst. Growth, **270**(1–2), pp. 255–272.

[10] Ramachandran, N., and Leslie, F. W., 2005, "Using Magnetic Fields to Control Convection During Protein Crystallization—Analysis and Validation Studies," J. Cryst. Growth, **274**(1–2), pp. 297–306.

[11] Li, K., and Hu, W. R., 2001, "Magnetic Field Design for Floating Zone Crystal Growth," J. Cryst. Growth, **230**(1–2), pp. 125–134.

[12] Colaco, M. J., Dulikravich, G. S., and Martin, T. J., 2005, "Control of Unsteady Solidification Via Optimized Magnetic Fields," Mater. Manuf. Processes, **20**(3), pp. 435–458.

[13] Okada, K., and Ozoe, H., 1992, "Experimental Heat Transfer Rates of Natural Convection of Molten Gallium Suppressed Under an External Magnetic Field in Either the X, Y, Z Direction," J. Heat Transfer, **114**, pp. 107–114.

[14] Ozoe, H., and Okada, K., 1989, "The Effect of the Direction of the External Magnetic Field on the Three-Dimensional Natural Convection in a Cubical Enclosure," Int. J. Heat Mass Transfer, **32**(10), pp. 1939–1954.

[15] Bertrand, O., Combeau, B. B., and Couturier, H., 1999, "Melting Driven by Natural Convection—A Comparison Exercise, Frist Results," Int. J. Therm. Sci., **38**, pp. 5–26.

[16] Dulikravich, G., Ahuja, V., and Lee, S., 1994, "Modeling Three-Dimensional Solidification With Magnetic Fields and Reduced Gravity," Int. J. Heat Mass Transfer, **37**(5), pp. 837–853.

[17] Dennis, B., and Dulikravich, G., 2002, "Magnetic Field Suppression of Melt Flow in Crystal Growth," Int. J. Heat Fluid Flow, **23**, pp. 269–277.

[18] Ha, M., Lee, H., and Seong, S., 2003, "Numerical Simulation of Three-Dimensional Flow, Heat Transfer, and Solidification of Steel in Continuous Casting Mold With Electromagnetic Brake," J. Mater. Process. Technol., **133**, pp. 322–339.

[19] Harada, H., Takeuchi, E., Zeze, M., and Tanaka, H., 1998, "MHD Analysis in Hydromagnetic Casting Process of Clad Steel Slabs," Appl. Math. Model., **22**, pp. 873–882.

[20] Botton, V., Lehmann, P., and Moreau, R., 2002, "A New Measurement Method of Solute Diffusivities Based on MHD Damping of Convection in Liquid Metals and Semi-Conductors," Energy Convers. Manage., **43**, pp. 409–416.

[21] Campbell, T. A., and Koster, J. N., 1994, "Visualization of Liquid–Solid Interface Morphologies in Gallium Subject to Natural Convection," J. Cryst. Growth, **140**, pp. 414–425.

[22] Derebail, R., and Oster, J. N. K., 1998, "Visualization Study of Melting and Solidification in Convecting Hypoeutectic Ga-In Alloy," Int. J. Heat Mass Transfer, **41**(16), pp. 2537–2548.

[23] Krautkramer, J., 1997, *Ultrasonic Testing of Materials*, Springer, New York.

[24] Hykes, D., Hedrick, W., and Starchman, D., 1985, *Ultrasound Physics and Instrumentation*, Churchill Livingstone, New York.

[25] McDonough, M., and Faghri, A., 1993, "Ultrasonic Measurement of Solid Liquid Interface for the Solidification of Water in Rectangular Enclosure," J. Heat Transfer, **115**, pp. 1075–1078.

[26] Davidson, P., 2001, *Introduction to Magnetohydrodynamic*, Cambridge University Press, Cambridge, UK.

[27] Cao, Y., and Faghri, A., 1989, "A Numerical Analysis of Stefan Problems for Generalized Multi-Dimensional Phase-Change Structures Using the Enthalpy Transforming Model," Int. J. Heat Mass Transfer, **32**(7), pp. 1289–1298.

[28] Patankar, S. V., 1980, *Numerical Heat Transfer and Fluid Flow*, Hemisphere, New York.

[29] Hayase, T., Humphrey, J. A. C., and Greif, R., 1992, "A Consistently Formulated QUICK Scheme for Fast and Stable Convergence Using Finite-Volume Iterative Calculation Procedures," J. Comput. Phys., **98**, pp. 108–118.

[30] Charmchi, M., Zhang, H., Li, W., and Faghri, M., 2004, "Solidification and Melting of Gallium in the Presence of Magnetic Field—Experimental Simulation of Low Gravity Environment," *Proceedings of IMECE 2004*, Anaheim, CA, November 14–19.

Journal of Heat Transfer

Technical Briefs

A Numerical Study of Energy Separation in a Jet Flow

Bumsoo Han[1]
e-mail: bhan@uta.edu

R. J. Goldstein

Department of Mechanical Engineering,
University of Minnesota,
Minneapolis, MN 55455

Redistribution of the total energy of a fluid in motion, which is called "energy separation," has been observed in various flow situations. Understanding the underlying mechanism of this interesting phenomenon has been limited due to lack of the temporal information on flow and temperature fields. In the present study, numerical simulation of a viscous circular jet was performed to provide detailed temporal information on pressure, vorticity, and total temperature fields. Nondimensionalized governing equations, including mass, momentum, and total energy conservation equations, were simultaneously solved by an equal-order linear finite element and fractional four-step method. The results show that the formation and transport of vortices induce a pressure fluctuation in the flow field. The fluid, which flows through the disturbed pressure field, exchanges pressure work with the surroundings, and gains or loses total energy. This work exchange leads to higher and lower total temperature regions than the surroundings. In addition to the presence and movement of the vortices, the results indicate that the vortex-pairing process significantly intensifies the pressure fluctuation and corresponding total temperature difference. This implies that the vortex-pairing process is a very important process in intensifying energy separation and might explain the enhancement of energy separation in a jet using acoustic excitation. [DOI: 10.1115/1.2709973]

Keywords: energy separation factor, jet flow, numerical analysis, vortex pairing, pressure fluctuation

Introduction

"Energy separation" is the redistribution of the total energy in a flowing fluid without external work or heat, so that some portion of the fluid has higher and other portion has lower total energy (temperature) than the remaining fluid. Since this interesting phenomenon was observed in a vortex tube (so-called Ranque-Hilsch tube) in the 1930s, many researchers have reported that energy separation could be observed in various flow situations including free jet [1–3], impinging jet [4], and flows across a circular cylinder [5–7]. Although theoretical and numerical models of energy separation in vortex tubes have been developed in several recent studies [8–10], those for flows with moving vortices are still limited.

Eckert [11] proposed a theoretical model of energy separation in a flow with moving vortices considering the significance of various terms in total energy conservation equation. He suggested the pressure fluctuation within a flow field caused by moving vortices was a key mechanism of total energy redistribution as well as the imbalance between the energy transport by viscous shear work and by heat conduction. Unlike the energy separation due to shear/conduction imbalance, the energy separation due to the pressure fluctuation has time-dependent characteristics associated with the movement of vortices. Kurosaka et al. [5] proposed a detailed model of total temperature variation around a transporting vortex in a vortex street. Though most previous studies were based on time-averaged temperature measurements, research on the instantaneous mechanism of energy separation is essential to understanding the phenomena due to the pressure fluctuation. A few numerical studies were performed to investigate the instantaneous mechanism. Fox et al. [1] performed a numerical analysis of energy separation in an inviscid and non-heat-conducting jet and investigated the mechanism of energy separation induced by vortex motion only. Han and Goldstein [12] carried out a numerical analysis for a plane shear layer by solving the two-dimensional Navier-Stokes equations.

In the present study, the mechanism of energy separation was numerically investigated in a viscous and heat-conducting circular jet flow. The energy separation by the pressure fluctuation as well as that by the shear/conduction imbalance was investigated with various Reynolds numbers (Re_D). The results provide physical insights on the instantaneous mechanism of energy separation.

Mathematical and Numerical Formulation

A jet with a very thin initial shear layer (δ_o) exited a circular nozzle with velocity of U_e and total temperature of $T_{t,o}$ into a stationary fluid at the same total temperature as shown in Fig. 1. The governing equations were mass conservation, unsteady Navier-Stokes equations, and total energy conservation equation. With the assumptions of axisymmetry, and incompressible and constant properties with viscosity ν and thermal diffusivity α, these equations were simplified and nondimensionalized based on U_e and the nozzle diameter D. For energy conservation, the energy separation factor, $S=(T_t-T_{t,o})/(U_e^2/2c_p)$, was introduced as a nondimensional temperature and the total energy conservation equation was rewritten in terms of S with $\mathrm{Re}_D=U_eD/\nu$ and $\mathrm{Pr}=\nu/\alpha$. Using the axisymmetry and boundary layer assumptions,

---

[1] Corresponding author's present address: Department of Mechanical and Aerospace Engineering, University of Texas at Arlington, Arlington, TX 76019.

Contributed by the Heat Transfer Division of ASME for publication in the JOURNAL OF HEAT TRANSFER. Manuscript received April 12, 2006; final manuscript received December 4, 2006. Review conducted by Sumanta Acharya. Paper presented at the HEFAT2002 Conference at Kruger Park, South Africa.

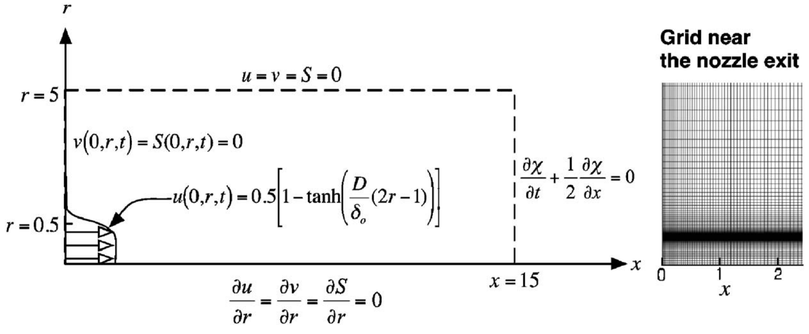

Fig. 1 Schematic diagram of the computational domain and grid near the inlet of the computational domain. χ at $x=15$ represents either u, v, or S.

the energy conservation equation was reduced as follows:

$$\frac{DS}{Dt} = \frac{1}{2}\frac{\partial p}{\partial t} + \frac{1}{\mathrm{Re}_D \mathrm{Pr}}\nabla^2 S + \frac{2}{\mathrm{Re}_D}\left[1 - \frac{1}{\mathrm{Pr}}\right]\frac{1}{r}\frac{\partial}{\partial r}\left(ru\frac{\partial u}{\partial r}\right) \qquad (1)$$

An equal-order finite element and fractional four-step method was adopted to discretize and solve the governing equations simultaneously. Detailed discretization and solution algorithm were described in [12,13]. Briefly, the Petrov-Galerkin weighted residual formulation was performed for each governing equation by multiplying weight functions and integrating over an arbitrary domain. These equations were applied to finite elements and discretized using the equal-order linear finite element method, where all variables of the elements were evaluated by the linear interpolation of all node values. Then, the equations were integrated in time using a fractional four-step method. For flow field calculation, the intermediate velocity ($\hat{u}_i$) was first calculated from the momentum equation. Then, the pressure was obtained from the mass conservation using the intermediate velocity, and the velocity (u_i^n) was corrected by the pressure. At all nodes, a convergence criterion ($|u_i^n - \hat{u}_i| < 1 \times 10^{-4}$) was satisfied at each time step. When the flow field was calculated, the discretized total energy equation was solved for the nondimensional total temperature.

At the inlet plane, a velocity profile with a thin initial shear layer was employed for the streamwise velocity as shown in Fig. 1. The ratio of initial shear layer thickness to the diameter of the jet, δ_o/D, was assumed to be 1/30, close to the value in experimental studies including Seol [14]. Within the initial shear layer, small disturbances were introduced in the radial velocity component. Through stability analysis of inviscid flow with the same velocity profile at $x=0$, the most unstable frequency and two subharmonic frequencies were selected as the disturbance frequencies. Along $r=0$, axisymmetric boundary conditions ($\partial/\partial r=0$) are adopted for all variables. At the outlet ($x=15$), a convective boundary condition is employed. This condition simulated convective transport due to vortices passing across the outlet plane as shown in Fig. 1. This condition was employed to minimize the distortion and perturbation by the reverse flow associated with vortices as described in [15]. The following conditions were imposed in the computational domain as initial conditions:

$$u(x,r,0) = 0.5\left[1 - \tanh\left(\frac{D}{\delta_o}(2r-1)\right)\right]$$

$$\text{and} \quad v(x,r,0) = S(x,r,0) = 0 \qquad (2)$$

A grid of 120 in the x-axis and 76 in the r-axis was used. For better results, more grid points were located along the axis of $r=0.5$ as shown in Fig. 1. The grid-dependence check was performed by comparing the calculated velocity fields of 120×76 and 240×152 grids when $\mathrm{Re}_D = 1.0 \times 10^3$. Calculations were performed with three different Reynolds numbers: 1.0×10^3, 2.0×10^3, and 1.0×10^4 with $\mathrm{Pr}=0.7$. The simulation was performed until all initial conditions were washed away and periodic velocity and pressure variations were confirmed.

The accuracy of the developed numerical code was tested for both flow velocity and total temperature calculation. The accuracy associated with the flow velocity calculation was checked by comparing the computational results to experimental measurements [16,17]. The total temperature calculation was validated by calculating the difference between total energy flow at given axial locations with that at the inlet of the computational domain. The calculation using time-averaged velocity and total temperature at several axial locations showed that the difference was 0.001% of the total energy at the inlet for $\mathrm{Re}_D = 1.0 \times 10^3$.

Results and Discussion

The instantaneous distributions of vorticity ($\omega = \partial v/\partial x - \partial u/\partial r$), pressure and total temperature for $\mathrm{Re}_D = 1.0 \times 10^3$ at two different time steps ($t=45$ and 46.5) are shown in Fig. 2. In the vorticity distributions, the "well-known" coherent ring vortical structure of a circular jet and corresponding interactions (i.e., the roll up and pairing of the vortices) are confirmed. At $t=45$, pairing of two neighboring vortices begins around $x=3$ so that the upstream vortex rolls the downstream one. At $t=46.5$, the roll up continues and the two vortices merge into a larger vortex near $x=4$. After the merge, the vorticity decreases downstream. In the pressure distributions, alternating local maxima and minima are observed—lower pressure near the center of vortices and higher pressure between the vortices. This alternating pressure variation is caused by the presence of the coherent vortical structure, and fluid flowing through this pressure field will be compressed or expanded along its path line. Through these compression and expansion processes, the fluid exchange pressure work with the surrounding fluid, which may result in redistributed total energy in the flow field.

The total temperature distributions clearly show the redistribution of total energy—higher total temperature in the lower half of the vortices and lower total temperature in the upper half of the vortices. This redistribution can be explained by considering the motion of fluid and the change of local pressure as proposed in [5,12]. When stationary fluid is entrained into the jet, it is entrained through the rear half of vortices and then flows through the lower half of the vortices. The local pressure at the lower half increases with time (i.e., $\partial p/\partial t \geqslant 0$) since fluid with higher-pressure approaches from the upstream. Thus, the fluid is compressed and gains energy from the surrounding fluid. On the contrary, the fluid entrained out through the front half of the vortices experiences pressure decrease and loses energy to the surrounding fluid.

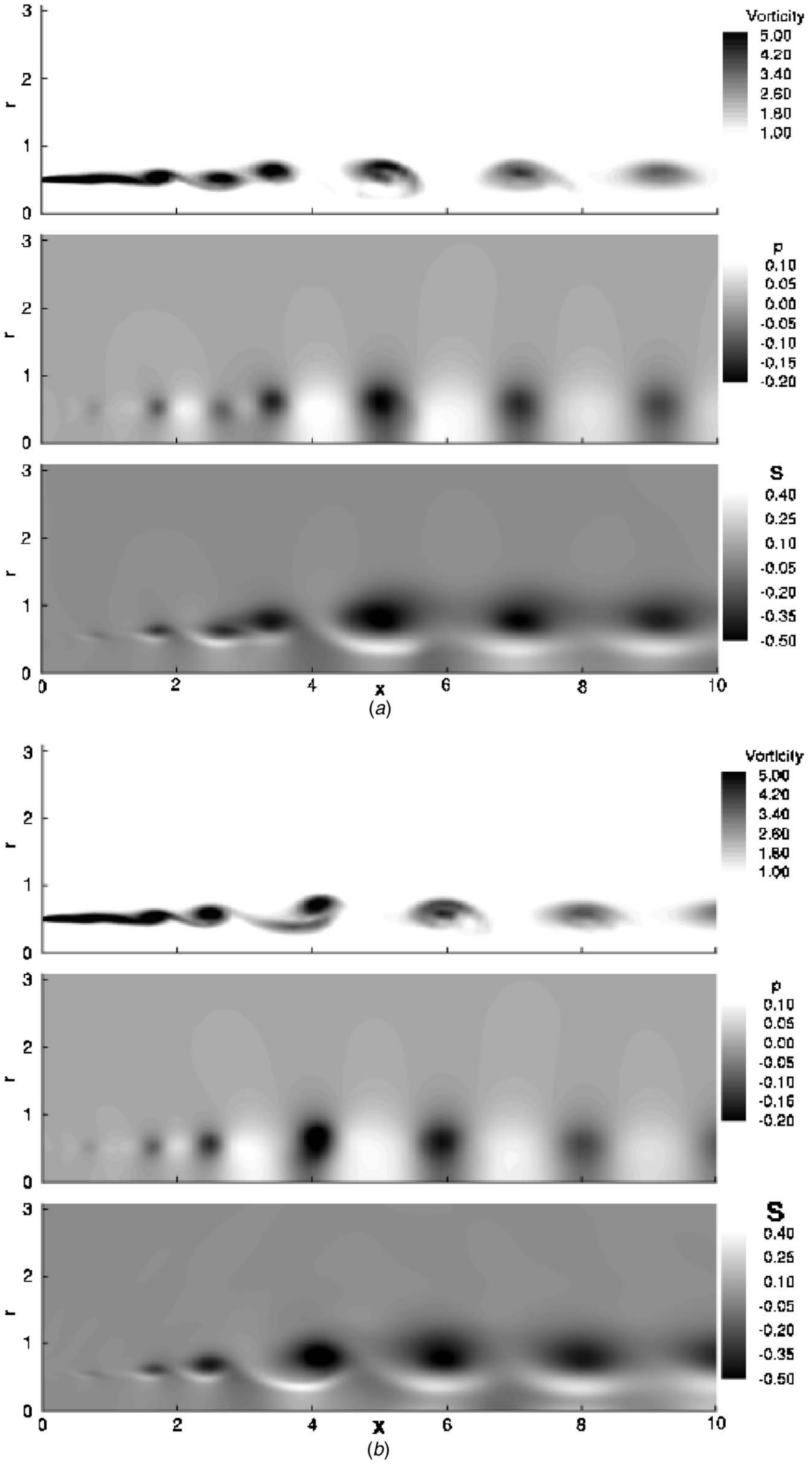

(a)

(b)

Fig. 2 Instantaneous vorticity, pressure, and energy separation factor distribution for $\mathrm{Re}_D=1.0\times10^3$: (*a*) at $t=45$ and (*b*) at $t=46.5$

Although the mechanism of the total energy redistribution is similar to that of a plane shear flow, the relative locations of high and low total temperature regions are different. As shown in Fig. 2, the axial locations of high and low total temperature regions are aligned. As shown in [12], however, hot and cold regions are axially staggered in a plane shear flow. This different axial alignment is thought to be caused by the difference in path lines of each flow situation, but further research is necessary to verify. In addition to the alternating pressure variation, the vortex merging process, which is observed near $x=4$, induces intensified pressure fluctuation as shown in the pressure contour at $t=46.5$. The corresponding total temperature difference between hot and cold re-

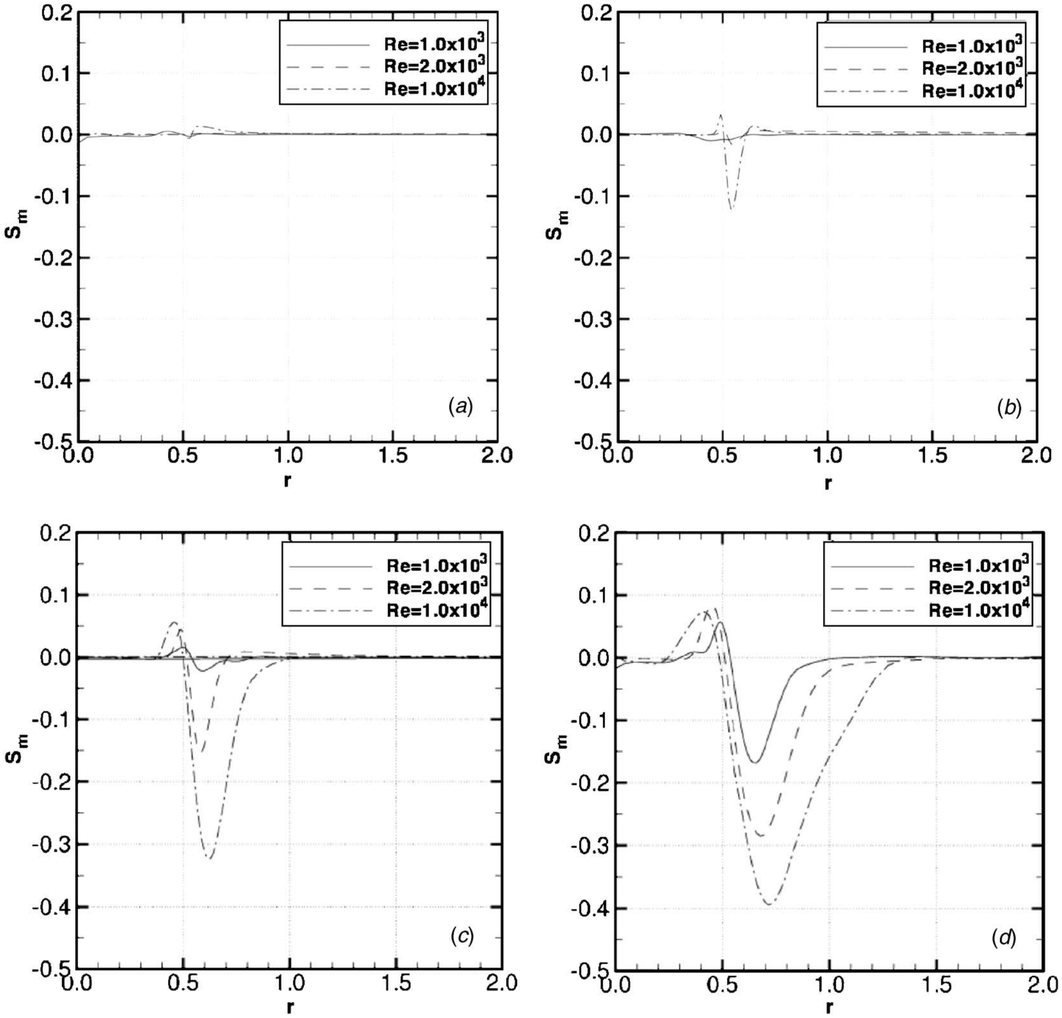

Fig. 3 Time-averaged energy separation factor distribution at four different axial locations: (*a*) at *x* =0.1, (*b*) *x*=0.5, (*c*) *x*=1.0, and (*d*) *x*=2.0

gions is also intensified after the pairing. Similar intensification was also observed in a numerical simulation of a plane shear flow [12].

Time-averaged energy separation factor profiles are presented at Fig. 3. At very near the nozzle exit (x=0.1), no significant energy separation is noted regardless of Reynolds numbers. At x =0.5, total temperature becomes higher than the surrounding at r=0.5 and lower near r=0.55 when $\mathrm{Re}_D=1.0\times 10^4$. This total energy redistribution patterns are observed in lower Reynolds number cases at further downstream. At x=1, higher total temperature near r=0.5, and lower total temperature around r=0.6 are predicted for all Reynolds numbers studied. This total energy redistribution pattern agreed with time-averaged experimental measurements in [1,2]. As observed in the experimental studies, the present simulation showed that the magnitude of energy separation in the lower total temperature region is much larger than that of the higher total temperature region. The calculated result also shows that the extent of energy separation is intensified with Re_D so that the time-averaged energy separation factor has a minimum of -0.3 when $\mathrm{Re}_D=1.0\times 10^4$. At x=2, the difference between higher and lower total temperature regions continues to increase.

Conclusion

A computational code using an equal-order finite element and four-step fractional step method was developed to study energy separation in an axisymmetric jet flow with three different Reynolds numbers: 1.0×10^3, 2.0×10^3, and 1.0×10^4. The result clearly illustrates the presence of instantaneous energy separation and provides insightful information to understand its mechanism. The result shows that the transport of vortical coherent structure induces pressure fluctuation in the flow field, a fluid flowing through the disturbed pressure field may exchange pressure work with the surrounding fluid, and, consequently, separates into higher and lower total energy regions. In addition to the movement of vortices, vortex pairing significantly increases the pressure fluctuation in the flow field and may intensify the energy separation.

Acknowledgment

This work was supported by the Engineering Research Program of the Office of Basic Energy Sciences at U.S. Department of Energy.

References

[1] Fox, M. D., Kurosaka, M., Hedges, L., and Hirano, K., 1993, "The Influence of Vortical Structure on Thermal Fields of Jets," J. Fluid Mech., **255**, pp. 447–472.

[2] Seol, W. S., and Goldstein, R. J., 1997, "Energy Separation in a Jet Flow," ASME J. Fluids Eng., **119**, pp. 74–82.

[3] Han, B., 2001, "Instantaneous Energy Separation in a Jet Flow," Ph.D. thesis, University of Minnesota, Minneapolis.

[4] Goldstein, R. J., Behbahani, A. I., and Heppelman, K. K., 1986, "Streamwise Distribution of the Recovery Factor and the Local Heat Transfer Coefficient to

an Impinging Circular Air Jet," Int. J. Heat Mass Transfer, **29**, pp. 1227–1235.

[5] Kurosaka, M., Gertz, J. B., Graham, J. E., Goodman, J. R., Sundaram, P., Riner, W. C., Kuroda, H., and Hankey, W. L., 1987, "Energy Separation in a Vortex Street," J. Fluid Mech., **178**, pp. 1–29.

[6] Goldstein, R. J., and He, B., 2001, "Energy Separation and Acoustic Interactions in Flow Across a Circular Cylinder," ASME J. Heat Transfer, **123**, pp. 682–687.

[7] Van Oudheusden, B. W., 2005, "Energy Separation in Steady Separated Wake Flow," ASME J. Fluids Eng., **127**, pp. 611–614.

[8] Shannak, B. A., 2004, "Temperature Separation and Friction Losses in Vortex Tube," Heat Mass Transfer, **40**, pp. 779–785.

[9] Aljuwayhel, N. F., Nellis, G. F., and Klein, S. A., 2005, "Parametric and Internal Study of the Vortex Tube Using a CFD Model," Int. J. Refrig., **28**, pp. 442–450.

[10] Piralishvili, S. A., and Fuzeeva, A. A., 2006, "Similarity of the Energy-Separation Process in Vortex Ranque Tubes," J. Eng. Phys. Thermophys., **79**, pp. 29–34.

[11] Eckert, E. R. G., 1987, "Cross Transport of Energy in Fluid Streams," Waerme- Stoffuebertrag., **21**, pp. 73–81.

[12] Han, B., and Goldstein, R. J., 2002, "Energy Separation in Shear Layers," Int. J. Heat Mass Transfer, **45**, pp. 47–55.

[13] Choi, H. G., Choi, H., and Yoo, J. Y., 1997, "A Fractional Four-Step Finite Element Formulation of the Unsteady Incompressible Navier-Stokes Equations Using SUPG and Linear Equal-Order Element Methods," Comput. Methods Appl. Mech. Eng., **143**, pp. 333–348.

[14] Seol, W. S., 1993, "Energy Separation in a Jet Flow," Ph. D. thesis, University of Minnesota, Minneapolis.

[15] Gresho, P. M., 1991, "Some Current CFD Issues Relevant to the Incompressible Navier-Stokes Equations," Comput. Methods Appl. Mech. Eng., **87**, pp. 201–252.

[16] Abramovich, G. N., 1963, *The Theory of Turbulent Jets*, MIT Press, Cambridge, MA.

[17] Rajaratnam, N., 1976, *Turbulent Jets*, Elsevier, New York.

Numerical Prediction of Fluid Flow and Heat Transfer in the Target System of an Axisymmetric Accelerator-Driven Subcritical System

---

K. Arul Prakash

G. Biswas[1]
e-mail: gtm@iitk.ac.in

Department of Mechanical Engineering,
Indian Institute of Technology Kanpur,
Kanpur-208 016, India

B. V. Rathish Kumar
Department of Mathematics,
Indian Institute of Technology Kanpur,
Kanpur-208 016, India

Thermal hydraulics related to the design of the spallation target module of an accelerator-driven subcritical system (ADSS) was investigated numerically using a streamline upwind Petrov-Galerkin (SUPG) finite element (FE) method. A large amount of heat is deposited on the window and in the target during the course of nuclear reaction between the proton beam and the molten lead-bismuth eutectic (LBE) target. Simulations were carried out to predict the characteristics of the flow and temperature fields in the target module with a funnel-shaped flow guide and spherical bottom of the container. The beam window was kept under various thermal conditions. The analysis was extended to the case of heat generation in the LBE. The principal purpose of the analysis was to trace the temperature distribution on the beam window and in the LBE. In the case of turbulent flows, the number of recirculation regions is decreased and the maximum heat transfer was found to take place downstream of the stagnation zone on the window. [DOI: 10.1115/1.2709972]

Keywords: ADSS, spallation target, finite element method, SUPG, thermal hydraulics

1 Introduction

In the near future, the accelerator-driven subcritical nuclear reactor system will play a significant role in nuclear power generation owing to its ability to enhance both the neutronics of reactors and safety physics [1]. The target system is the critical part of an accelerator-driven subcritical system (ADSS), which is shown in Fig. 1. In the target system, a high-energy proton beam from the accelerator irradiates a heavy metal target to produce spallation neutrons, which initiate fission reaction in the subcritical core. The protons are induced on the target through a vacuum pipe closed by a window at the end. Therefore, the beam window is exposed to a huge amount of thermal and mechanical load and suffers from radiation damage due to spallation neutrons. A lead-bismuth eutectic (LBE) is preferred as the target material owing to its high production rate of neutrons, effective heat removal rate, and very small amount of radiation damage. In addition, it can be used simultaneously as a reactor coolant. Hence, the spallation target module is the most innovative component of ADSS, which constitutes the physical interface between the accelerator and the subcritical core.

Although it is relatively easy to remove the total spallation heat by the LBE, what is crucial is that this has to be achieved without the target temperature exceeding the stipulated temperature in any region of the flow. There should not be any recirculation or stagnation zones leading to hot spots, inadequate window cooling, generation of vapors, etc. This necessitates detailed flow analysis in the spallation region, the flow region near the entrance of the annular zone along with the temperature distribution on the window.

There are two possibilities for examining the thermal-hydraulic behavior of a liquid-metal spallation region. The first option is to build a full-sized target and install it in a proton beam, suitably supplied with coolant under design conditions and instrumented. The second option is to simulate such a target using a state-of-the-art computational fluid dynamics (CFD) tool. This latter approach has been accomplished using a finite element (FE) streamline upwind Petrov-Galerkin (SUPG) technique [2]: axisymmetric time-dependent governing equations are solved.

Investigations concerning the development of the target system of an ADSS have been summarized by Maiorino et al. [3]. A review of the recent literature reveals that there have been few investigations focusing on the design of the target system of an ADSS. Dury et al. [4] analyzed the spallation zone near the beam window of the European Spallation source liquid-metal target facility numerically using CFX-4. They considered liquid mercury as the spallation target. Cho et al. [5] computed the heat transfer and flow characteristics in a simplified version of the target system model called HYPER using ANSYS and CFX packages. Whereas there is a circular flow guide in the target model considered by Dury et al. [4], there is no such flow guide in the model studied by Cho et al. [5]. Recently, window-based target modules, such as XADS [6], with funnel-shaped flow guides have been proposed. In this model, the downcomer part of the ADSS is separated from the riser part by using a flow guide. The flow takes a 180 deg turn around the tip of flow guide.

In this work, we consider the entire target system of ADSS with a funnel-shaped flow guide (see Fig. 1). Furthermore, we account for the high-energy proton beam impingement on the window surface by introducing appropriate thermal boundary conditions on the window. In view of the continuous proton beam impingement, the window surface may also be assumed to be isothermal for some situations. Also, we account for the heat generation in LBE based on FLUKA [7] data. The two-equation k-ϵ model with the wall-function approach is used for analyzing turbulent flows. An in-house SUPG-FE code based on the projection scheme of Chorin [8] was developed and validated. Simulations were carried out to analyze the flow and heat transfer characteristics in the target system of an ADSS for a wide range of Reynolds numbers.

2 Governing Equations and Boundary Conditions

2.1 Governing Equations. The flow is considered to be viscous, incompressible, and turbulent. The Reynolds analogy is applied to calculate the turbulent heat transfer. The geometry of interest is axisymmetric. The computational domain shown in Fig. 1 is discretized using small quadrilateral elements. All variables, including the velocity components, pressure, temperature, kinetic energy, and dissipation rate, are located at element nodes. The dimensionless equations governing the axisymmetric mean flow [9,10] are as follows:

Continuity Equation

$$\frac{1}{x^{\beta}}\frac{\partial}{\partial x}(x^{\beta}u)+\frac{\partial v}{\partial y}=0 \tag{1}$$

---

[1] Corresponding author.

Contributed by the Heat Transfer Division of ASME for publication in the JOURNAL OF HEAT TRANSFER. Manuscript received April 15, 2006; final manuscript received November 15, 2006. Review conducted by Sumanta Acharya.

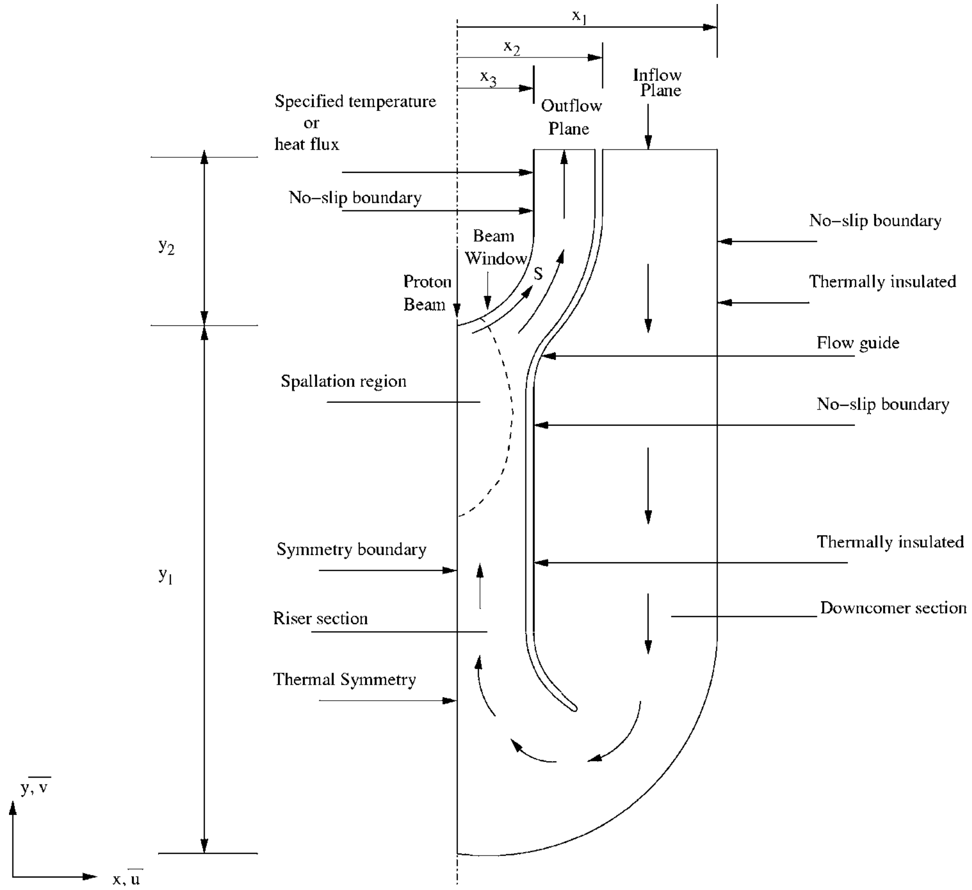

Fig. 1 Physical domain of the target system of an ADSS with boundary conditions

Momentum Equations

$$\frac{\partial u_j}{\partial \tau} + u_i\frac{\partial u_j}{\partial x_i} = -\frac{\partial p}{\partial x_i} + \frac{1}{\mathrm{Re}}\frac{1}{x^\beta}\left\{\frac{\partial}{\partial x_i}\left[x^\beta \nu_{\mathrm{eff}}\left(\frac{\partial u_i}{\partial x_j}+\frac{\partial u_j}{\partial x_i}\right)\right] - \frac{2\beta\delta_{1j}\nu_{\mathrm{eff}}u_j}{x_i}\right\} \qquad (2)$$

where p is the pressure, u_j are the radial and axial mean velocity components, respectively, and x_i the radial and axial coordinates, respectively. The index β is unity for the axisymmetric cases. The equations describing two-dimensional planar flows can be obtained from Eqs. (1) and (2) by setting $\beta=0$. The effective turbulent viscosity $\nu_{\mathrm{eff}}=(1+\nu_{t,n})$ is calculated using the (k-ϵ) model of turbulence [10,11]

$$\nu_{\mathrm{eff}} = 1 + c_\mu \mathrm{Re}\frac{k_n^2}{\epsilon_n} \qquad (3)$$

Transfer of the dimensionless turbulent kinetic energy k_n, its dissipation rate ϵ_n and the temperature distribution θ are modeled as follows:

***k* Equation**

$$\frac{\partial k_n}{\partial \tau} + u\frac{\partial k_n}{\partial x} + v\frac{\partial k_n}{\partial y} = \frac{1}{x^\beta}\frac{1}{\mathrm{Re}}\left[\frac{\partial}{\partial x}\left(x^\beta\frac{\nu_{t,n}}{\sigma_k}\frac{\partial k_n}{\partial x}\right) + \frac{\partial}{\partial y}\left(x^\beta\frac{\nu_{t,n}}{\sigma_k}\frac{\partial k_n}{\partial y}\right)\right] + G_n - \epsilon_n \qquad (4)$$

ϵ Equation

$$\frac{\partial \epsilon_n}{\partial \tau} + u\frac{\partial \epsilon_n}{\partial x} + v\frac{\partial \epsilon_n}{\partial y} = \frac{1}{x^\beta}\frac{1}{\mathrm{Re}}\left[\frac{\partial}{\partial x}\left(x^\beta\frac{\nu_{t,n}}{\sigma_\epsilon}\frac{\partial \epsilon_n}{\partial x}\right) + \frac{\partial}{\partial y}\left(x^\beta\frac{\nu_{t,n}}{\sigma_\epsilon}\frac{\partial \epsilon_n}{\partial y}\right)\right] + \frac{\epsilon_n}{k_n}(C_{1\epsilon}G_n - C_{2\epsilon}\epsilon_n) \qquad (5)$$

Energy Equation

$$\frac{\partial \theta}{\partial \tau} + u\frac{\partial \theta}{\partial x} + v\frac{\partial \theta}{\partial y} = \frac{1}{x^\beta}\frac{1}{\mathrm{Re}\,\mathrm{Pr}}\left[\frac{\partial}{\partial x}\left\{x^\beta(1+\alpha_{t,n})\frac{\partial \theta}{\partial x}\right\} + \frac{\partial}{\partial y}\left\{x^\beta(1+\alpha_{t,n})\frac{\partial \theta}{\partial y}\right\} + S_\theta\right] \qquad (6)$$

where S_θ is the heat generation source term and G_n is the turbulence production term.

Finally, $\nu_{t,n}$ and $\alpha_{t,n}$ can be written as

$$\nu_{t,n} = C_\mu \mathrm{Re}\frac{k_n^2}{\epsilon_n} \qquad \alpha_{t,n} = C_\mu \mathrm{Re}\frac{\mathrm{Pr}\,k_n^2}{\sigma_t\epsilon_n} \qquad (7)$$

where the model coefficients are $C_\mu=0.09$, $\sigma_k=1.0$, $\sigma_\epsilon=1.3$, $\sigma_t=0.9$, $C_{1\epsilon}=1.44$, and $C_{2\epsilon}=1.92$.

The pertinent nondimensional parameters are

$$\text{Reynolds number, } \mathrm{Re} = \frac{V_0 D}{\nu}$$

and

$$\text{Prandtl number, } \mathrm{Pr} = \frac{\nu}{\alpha}$$

where D is the characteristic length, ν is the kinematic viscosity, α is the thermal diffusivity, and V_0 is the mean inlet velocity.

2.2 Boundary Conditions. The detailed analysis of molten LBE flow in the laminar and turbulent regimes are considered. The boundary conditions of interest for the laminar flow are

- Inlet section: $u=0$, $v=v(x)$; $\theta=0$
- Symmetry boundary $u=0$, $\partial v/\partial n=0$; $\partial\theta/\partial n=0$
- No-slip wall $u=v=0$
  Along the beam window $\theta=1.0$ (constant temperature) or $\partial\theta/\partial n=1.0$ (constant heat flux)
  For other walls $\partial\theta/\partial n=0$ (thermally insulated)
- Outlet section: $\partial u/\partial n=\partial v/\partial n=0$; $\partial\theta/\partial n=0$
  where n represents the normal direction to the surface. Nondimensionalization of the energy equation for the constant heat flux case is applied with respect to the dimensional uniform heat flux on the beam window. However, the final form of the energy equation remains the same.

For the turbulent flows, the standard k-ϵ turbulence model has been used. The standard k-ϵ relies on the high Reynolds number assumption, which is not valid very near the wall where the viscous effects are predominant. The wall-function approach was followed to model the near-wall region [11]. In this approach, the flow near the solid boundaries is not solved for, but is assumed to obey the *law of the wall*. The tangential velocity and turbulence quantities are then specified. The estimation of wall shear stress based on the finite element method is adopted according to Benim and Zinser [12]. The conditions for velocity and temperature can be specified in the following way:

- Inlet plane

$$v = v(x); \quad u = 0$$

$$k_n = 1.5I^2; \quad \epsilon_n(x) = \frac{k_n^{3/2}C_\mu^{3/4}}{\chi x} \quad \text{for } x < (\lambda/\chi)$$

$$= \frac{k_n^{3/2}C_\mu^{3/4}}{\lambda x_p} \quad \text{for} \quad x > (\lambda/\chi)$$

$$\theta = 0 \tag{8}$$

where $v_{\tau,n}$ is nondimensional friction velocity, x^+ is given by xv_τ/ν, I is the turbulent intensity, $\chi=0.42$, which is known as the von Kármán constant, λ is a constant prescribing the ramp distribution of the mixing length in boundary layers and is equal to 0.09 and $E=9.743$. The boundary conditions at the outlet and the confining walls are given as follows:

- Symmetry boundary $u=0$, $\partial f/\partial n=0$; $f=(v,\theta,k_n,\epsilon_n)$
- Outlet section $\partial f/\partial n=0$; $f=(u,v,\theta,k_n,\epsilon_n)$

The wall functions due to Launder and Spalding [11] are used to mimic the near-wall region for the no-slip walls. For $x_p^+ \geqslant 11.63$,

$$\tau_{w,n}^{y} = \frac{v_p C_\mu^{1/4} k_{n,p}^{1/2} \chi}{\ln(Ex_p^+)} \tag{9}$$

where $x_p^+ = x_p \, \mathrm{Re} C_\mu^{1/4} \, k_{n,p}^{1/2}$. The subscript p refers to the first grid point adjacent to the wall. Efforts were made (grid size chosen) to retain x_p^+ closer to 20 in most of the computations.

Instead of using Eqs. (4) and (5) near the wall, k_n, ϵ_n at point p are computed from

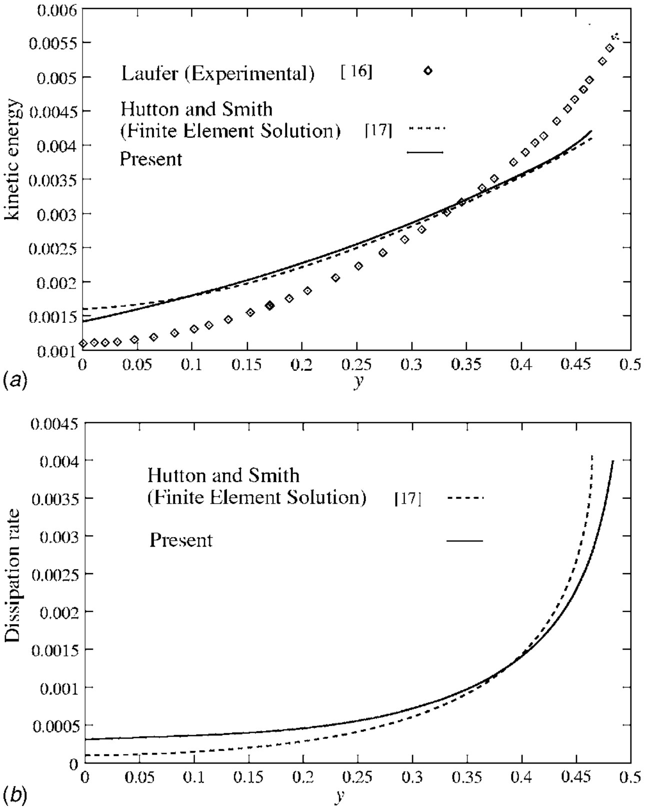

Fig. 2 (*a*) Fully developed pipe flow results (kinetic energy) for Re=500,000 and (*b*) fully developed pipe flow results (dissipation rate) for Re=500,000

$$k_{n,p} = \frac{v_{\tau,n}^2}{C_\mu^{1/2}}; \quad \epsilon_{n,p} = \frac{v_{\tau,n}^3}{\chi x_p} \tag{10}$$

where $v_{\tau,n}$ is the friction velocity is given as $v_{\tau,n} = C_\mu^{1/4} k_{n,p}^{1/2}$

3 Grid Generation, Solution Technique, and Code Validation

The computational grid of the target system is generated using an algebraic method, smoothed, and clustered by the elliptic partial grid generation technique using Poisson's equations. A SUPG finite element method [2] has been used to discretize and solve the governing conservation equations. The pressure-velocity iterations follow the method due to Harlow and Welch [13]. The entire procedure has been documented in Maji and Biswas [14] and in the recent work of Prakash et al. [15]. The code validation for the turbulent flow was accomplished through comparison of the predictions for fully developed pipe flow to experiment and to predictions of other investigations. The predicted turbulent kinetic energy and its dissipation rate were compared to the results of Laufer [16] and Hutton and Smith [17]. The results shown in Fig. 2 are in good agreement with the experimental [16] and numerical [17] results.

The following three meshes are considered for the grid sensitivity analysis: (i) 33 grid points in the cross-stream direction ×247 grid points in the streamwise direction having 8151 nodes and 7872 elements, (ii) 51 grid points in the cross-stream direction ×307 grid points in the streamwise direction with 15,657 nodes and 15,300 elements, and (iii) 69 grid points in the cross-stream direction ×367 grid points in the streamwise direction with 25,323 nodes and 24,888 elements.

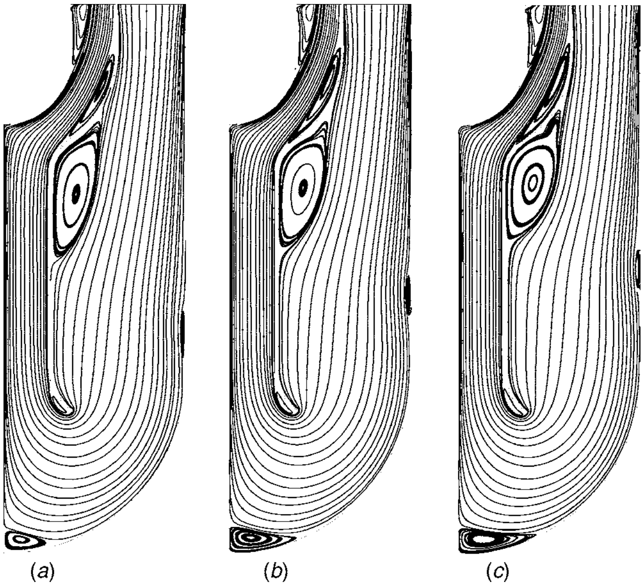
(*a*) (*b*) (*c*)

Fig. 3 Streamlines for (*a*) Re=500, (*b*) Re=700, and (*c*) Re =1000

As one moves from coarse grid to fine grid, the maximum deviation in the Nusselt number for Re=500 calculated along the beam window is found to be <1.01%. Hence in the present study, a grid consisting of (51×307) nodes was chosen for all computations.

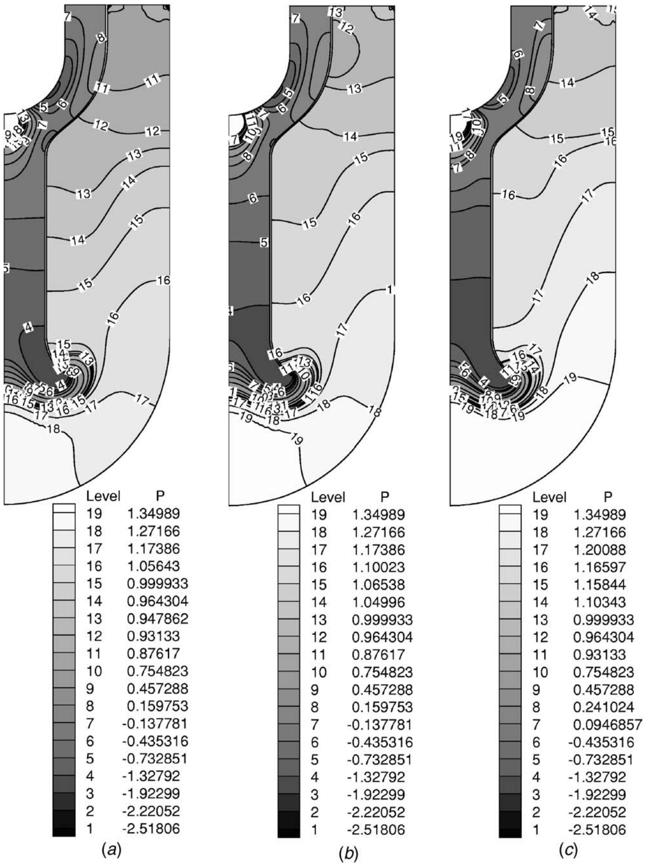

(*a*) (*b*) (*c*)

Fig. 4 Pressure contours for (*a*) Re=500, (*b*) Re=700, and (*c*) Re=1000

4 Results and Discussion

4.1 Flow and Heat Transfer Characteristics of Laminar Flows. Figure 3 shows streamline patterns for the flow field obtained with Re=500, 700, and 1000. At Re=500, a primary vortex is observed near the inlet section along the guide due to sudden expansion of the flow domain. In addition, there are recirculation regions near the 180 deg turn and also near the exit along both the beam window and the flow guide. Secondary recirculation zones are observed in the stagnation region at the bottom of the downcomer section of the target system along the axis of symmetry and along the solid wall prior to the first change of curvature in the geometry of the target system. At Re=700 and 1000, although the primary vortex bulges, the reattachment length decreases owing to the increasing velocity field. The pressure developed at the inner edge of the bend of the separating wall will decrease with increasing Reynolds number, which will influence the reattachment length. Also, with increasing velocity, while the secondary recirculation zone in the stagnation region becomes prominent, the secondary recirculation zone, along the solid wall, becomes shorter and drifts upstream. For all Reynolds numbers, pressure (Fig. 4) is seen to increase near the zone of sudden expansion immediately after the inlet. Subsequently, it decreases uniformly near the bend. The pressure drop, and thereby the pressure gradient, are very high in the stagnation zones. Thereafter, the pressure recovers up to the convex downstream of stagnation zone, where the secondary recirculation zone occurs, and finally attains atmospheric pressure at the exit plane. One of the assumptions in this work is the constant properties of the working fluid. The Prandtl number of this study is 0.02. The temperature contours on the beam window for the isothermal boundary for different Reynolds numbers are shown in Fig. 5. In the case of low-Prandtl-number fluids, the thermal boundary layer grows faster than the velocity boundary layer. The thermal diffusivity dominates over the molecular diffusivity. The thermal boundary layer, which is seen to manifest along the window, becomes sharper with increasing Reynolds number.

4.1.1 Calculation of Local Nusselt Number, Skin Friction Coefficient, and Coefficient of Pressure. The local skin friction coefficient and the local Nusselt number based on the inlet temperature of the stream are defined in nondimensional form as

$$C_{fs}=\frac{2}{\mathrm{Re}}\frac{\partial U}{\partial n}\qquad \mathrm{Nu}_S=-\frac{\partial\theta}{\partial n}$$

where n denotes the direction normal to the window, S is the streamwise distance along the beam window, U is the nondimensional velocity component tangential to the wall, and θ is the dimensionless temperature.

Figure 6 compares the Nusselt number distribution based on the inlet temperature (T_∞) along the beam window of the target system of an ADSS for the above-mentioned Reynolds numbers. It was observed that the Nusselt number increases initially and then decreases. This is in agreement with the observed trend of variation of the thermal boundary layer. Finally, the Nusselt number increases near the exit plane because of recirculation of flow in the window region near the exit. The Nusselt number increases with increasing Reynolds number. Figure 7 shows the $C_f\times\mathrm{Re}$ variation along the surface of the window. It is evident that $C_f\times\mathrm{Re}$ remains constant along the leading edge of the window and then decreases at the exit. The peak value of $C_f\times\mathrm{Re}$ increases with increasing Reynolds number. Also, the spatial location of the occurrence of peak values shifts toward the trailing edge of the beam window with increasing Reynolds number. These effects may be attributed to the combined influence of the curvature ef-

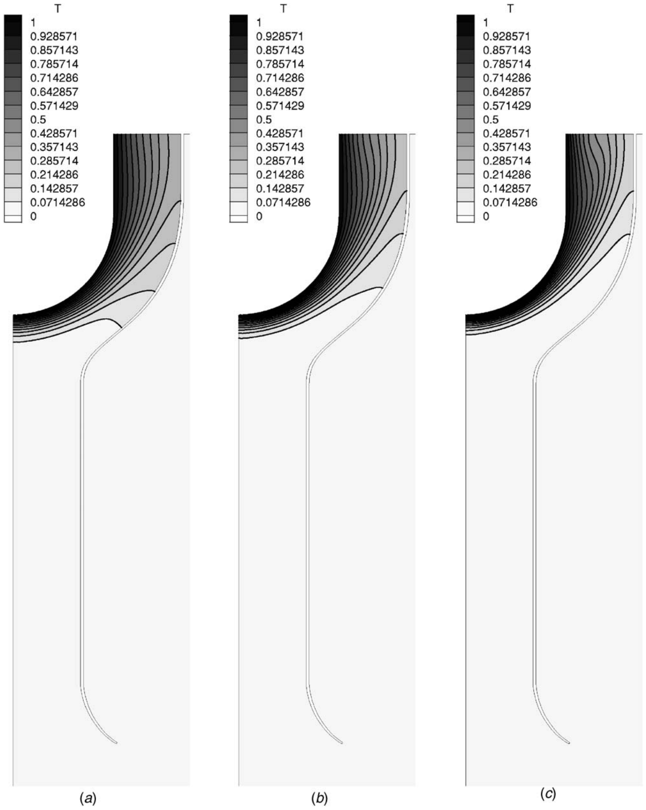

Fig. 5 Temperature contours for constant temperature along the beam window (enlarged view of beam window:) (*a*) Re =500, (*b*) Re=700, and (*c*) Re=1000

fect, the presence of a prominent vortex, and the change from free-slip to no-slip boundary from the leading edge of the window.

4.1.2 Calculation With Heat Generation. Initially, the simulations are carried out with the presumption that the liquid metal is nonabsorbing. Currently, the liquid metal (LBE) is considered to be energy absorbing with the heat generation, source term in Eq. (6) taken into account. The kinetic energy of the proton beam is converted into heat energy. The heat generation function on the liquid metal was developed using data from the FLUKA code for a 1 GeV proton beam [7]. The isotherms calculated, including heat generation in the LBE with constant window surface temperature along the beam window, are shown in Fig. 8. Unlike for the nonreacting case, here the influence of proton beam bombardment on the window is observed not only downstream of the window but also upstream of it as far as the tip of the flow guide. However, the peak temperature value lies along the beam window.

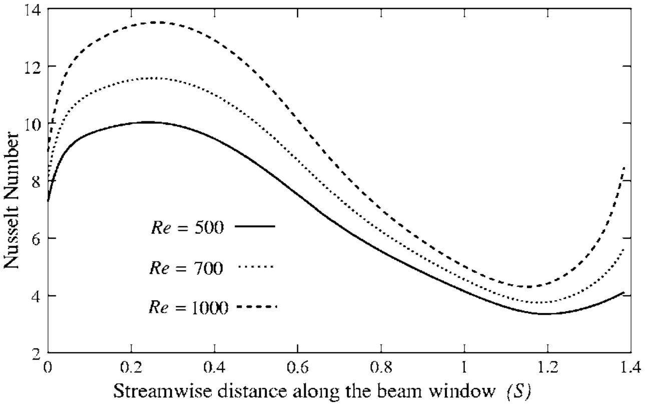

Fig. 6 Nusselt number for constant temperature along the beam window: (*a*) Re=500, (*b*) Re=700, and (*c*) Re=1000

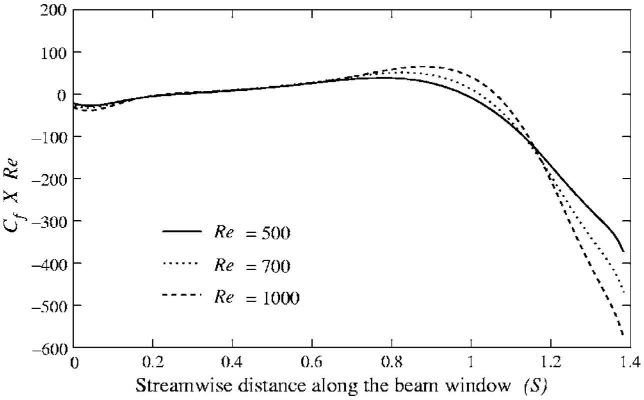

Fig. 7 $C_f \times$Re along the beam window: (*a*) Re=500, (*b*) Re =700, and (*c*) Re=1000

4.2 Flow and Heat Transfer Characteristics of Turbulent Flows. Figure 9 show the streamlines for three different Reynolds numbers: (a) Re=14,1340, (b) Re=282,690, and (c) Re =565,380. The velocities corresponding to Re=141,340, Re =282,690, and Re=565,380, are 0.1716 m/s, 0.3423 m/s, and 0.6823 m/s, respectively. These velocities are in the operational

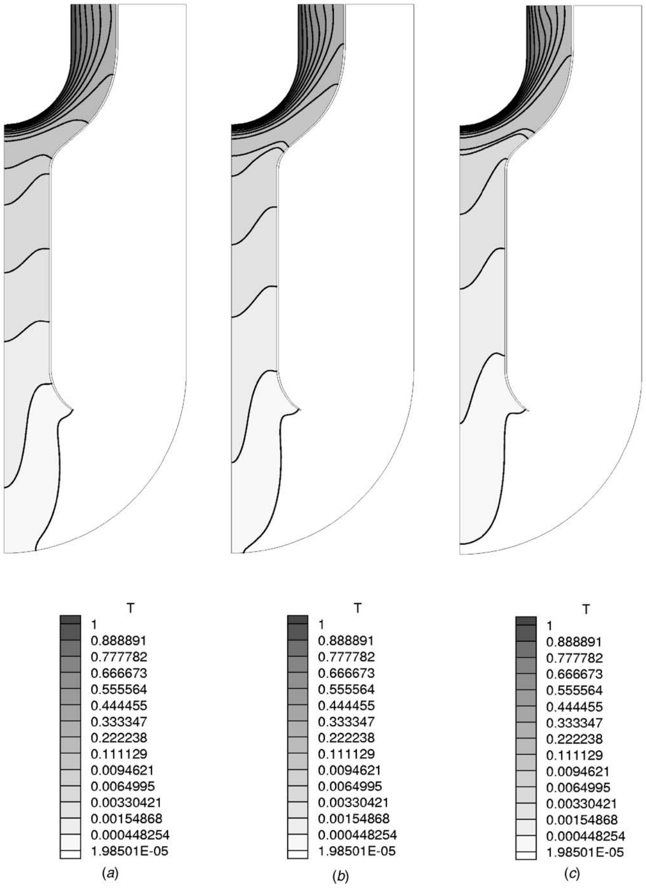

Fig. 8 Temperature contours for heat generation in LBE and constant window surface temperature along the beam window: (*a*) Re=500, (*b*) Re=700, and (*c*) Re=1000

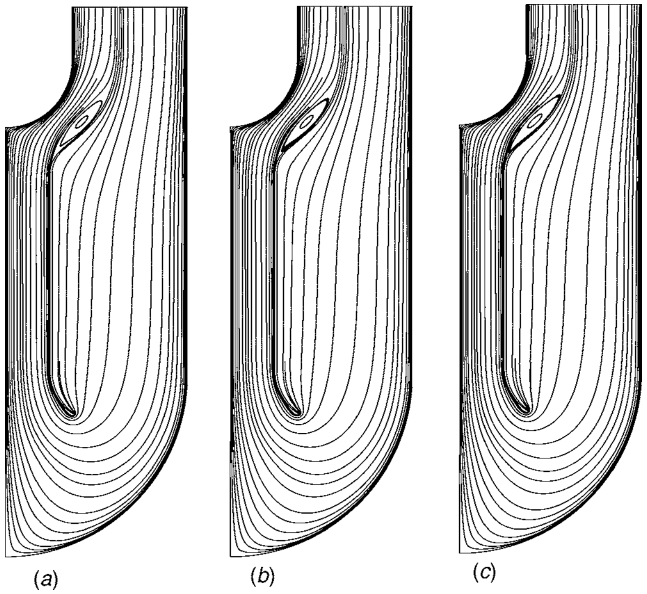

Fig. 9 Streamlines for (*a*) Re=141,340, (*b*) Re=282,690, and (*c*) Re=565,380

range of a class of target system. Streamline plots show that there is a flow separation and reattachment near the convex bend and the size of the separated eddy decreases with increase in the Reynolds number. Near the beam window, the fluid experiences convex flow followed by concave flow, whereas the opposite occurs for flow along the guide near the exit plane. It has been observed for flows with curvature the quantity $\overline{u'v'}$ first increases and then decreases in magnitude on the beam window, whereas the opposite occurs on the flow guide near the exit plane. Therefore, in the case of turbulent flows, the enhanced transverse momentum transport occurs toward the curved section of the beam window and the separation is delayed; in fact, it is prevented owing to the presence of fluid particles with higher kinetic energy. Separated flows are observed in the convex zone along the flow guide. Clearly, three Reynolds numbers give good qualitative consistency and the vortex formation appears to be well reproduced. Figure 10 presents the distribution of the time-mean temperature over the flow field for Re=565,380. At the bend on the window, Fig. 10 shows convection from the wall. The variation of the Nusselt number is shown in Fig. 11. The amount of heat diffusion toward the radial direction decreases with increase in Reynolds number because more heat energy is convected away from the wall with increasing velocity of LBE. The peak value of the Nusselt number occurs at the start of the window curvature and the peak value shifts along the streamwise direction for higher Reynolds numbers.

5 Concluding Remarks

A computational study using the SUPG-based finite element method was performed to determine the laminar and turbulent flow and heat transfer characteristics in the target module of an ADSS. Predictions were made for the velocity profile, pressure variation, and the temperature contours of the flowing liquid metal for the cases of a beam window under the constant temperature condition. The situations with heat energy generation in LBE and a constant temperature window boundary were also considered. In the laminar case, primary vortices are formed in the smooth step, along the guide, near the inlet. Also, secondary vortices are generated along the outer solid wall prior to convex curvature, at the tip of the guide near to the 180 deg turn, at the stagnation zone near the axis of symmetry and at the exit passage between the beam window and the flow guide. The reattachment length associated with the primary vortices decreases with an increase in Reynolds number, and the secondary vortices increase in size. The isotherms for the case of the LBE with energy generation indicate that the effect of the energy source is diffused upstream of the beam window until the tip of the flow guide. The computation is extended for turbulent flows, where the recirculation regions are

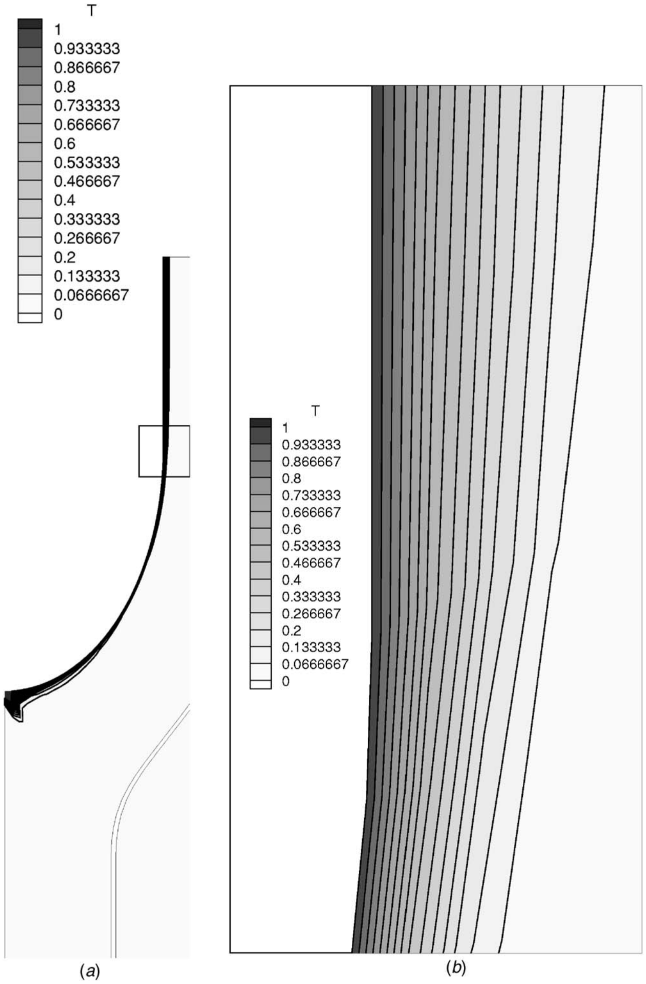

Fig. 10 (*a*) Temperature contours for constant temperature along the beam window (enlarged view of beam window) for Re=565,380, and (*b*) enlarged view of the rectangular portion shown in (*a*)

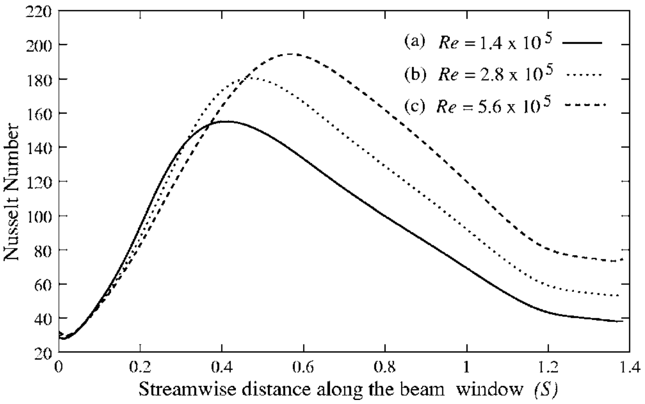

Fig. 11 Nusselt number for constant window temperature along the beam window for (*a*) Re=141,340, (*b*) Re=282,690, and (*c*) Re=565,380

observed only on the convex section along the flow guide downstream of the stagnation zone. Temperature contours reveal decreased diffusion of energy in the radial direction. It is evident that for turbulent flows, the number of recirculation regions is decreased and the maximum heat transfer takes place downstream of the stagnation zone where the proton beam impinges from the opposite side. The present simulation helps in understanding the basic convection problem. From this analysis, it is possible to find a rational basis for the selection of a suitable target system.

Acknowledgment

This investigation was sponsored by the Board of Research in Nuclear Sciences (BRNS), Grant No. 2002/34/6, India.

Nomenclature

C_f = skin friction coefficient
C_μ = coefficients in two-equation (k-ϵ) turbulence model
$C_{1\epsilon}$ = coefficients in two-equation (k-ϵ) turbulence model
$C_{2\epsilon}$ = coefficients in two-equation (k-ϵ) turbulence model
D = inlet hydraulic diameter
k_n = dimensionless turbulent kinetic energy ($=k/V_0^2$)
Nu = Nusselt number
p = dimensionless pressure ($=p/\rho V_0)^2$)
Re = Reynolds number
S = streamwise distance along the window
t = dimensional time
u_j = dimensionless velocity components ($=u_j/V_0$)
V_0 = mean inlet velocity
x_i = dimensionless coordinates along radial and axial direction ($=x_i/D$)
ϵ_n = dimensionless dissipation rate $[=\epsilon/(V_0)^3/(D)]$
θ = dimensionless temperature $[=(T-T_\infty)/(T_w-T_\infty)]$
$\nu_{t,n}$ = dimensionless turbulent kinematic viscosity (ν_t/ν)

Greek symbols

$\alpha_{t,n}$ = dimensionless thermal diffusivity (α_t/α)
τ = dimensionless time $[t/(D/V_o)]$
σ_k = coefficients used in the two (k-ϵ) equation turbulence model
σ_ϵ = coefficients used in the two (k-ϵ) equation turbulence model
σ_t = coefficients used in wall treatment for energy equation
$\Delta\tau$ = dimensionless time step

Subscripts

∞ = inflow condition

Superscripts

β = index for axisymmetry (=0 for planar and 1 for axisymmetric)

References

[1] Rubbia, C., Rubio, J. A., Buono, S., Carminati, F., Fietier, N., Galvez, J., Geles, C., Kadi, Y., Klapisch, R., Mandrillon, P., Revol, J. P., and Roche, Ch., 1995, "Conceptual Design of a Fast Neutron Operated High Power Energy Amplifier," CERN Report No. CERN-AT-95–44 (ET), Geneva.

[2] Brooks, A. N., and Hughes, T. J. R., 1980, "Streamline Upwind Petrov-Galerkin Formulations for Convection Dominated Flows With Particular Emphasis on the Incompressible Navier-Stokes Equations," Comput. Methods Appl. Mech. Eng. **32**, pp. 199–259.

[3] Maiorino, J. R., Santos, A. d., and Pereira, S. A., 2002, "The Utilization of Accelerators in Sub-Critical Systems for Energy Generation and Nuclear Waste Transmutation—the World Status and a Proposal of a National R&D Program," Braz. J. Phys. **33**(2), pp. 267–272.

[4] Dury, T. V., Smith, B. L., and Bauer, G. S., 1999, "Design of the European Spallation Source Liquid-Metal Target Using Computational Fluid Dynamics," Nucl. Technol., **127**, pp. 218–232.

[5] Cho, C. H., Song, T. Y., and Tak, N. I., 2004, "Numerical Design of a 20 MW Lead-Bismuth Spallation Target for an Accelerator-Driven System," Nucl. Eng. Des. **229**, pp. 317–327.

[6] Batta, A., Broeders, C. H. M., Cheng, X., Konobeyev, A., Neitzel, J., Tak, N., and Travleev, A., 2003, "Window Target Unit for the XADS Lead-Bismuth Cooled Primary System," *Proceedings of International Workshop on P and T and ADS Development*, Mol, Belgium, Oct. 6–8, SCK.CEN Club-House, Mol, Belgium, pp. 1–9.

[7] Buono, S., Kadi, Y., and Rubbia, C., 1997, "Energy Deposition of a Proton Beam in the Lead Target of the Energy Amplifier," CERN/ET Internal Note, pp. 97.1–97.11.

[8] Chorin, A. J., 1967, "A Numerical Method for Solving Incompressible Viscous Flow Problems," J. Comput. Phys. **2**, pp. 12–26.

[9] Reddy, J. N., and Gartling, D. K., 1994, *The Finite Element Method in Heat Transfer and Fluid Dynamics*, CRC Press, Boca Raton.

[10] Comini, G., and Del Giudice, S., 1985, "A k-ϵ Model of Turbulent Flow," Numer. Heat Transfer **8**, pp. 133–147.

[11] Launder, B. E., and Spalding, D. B., 1974, "The Numerical Computation of Turbulent Flows," Comput. Methods Appl. Mech. Eng. **3**, pp. 269–289.

[12] Benim, A. C., and Zinser, W., 1985, "Investigation Into the Finite Element Analysis of Confined Turbulent Flows Using a k-ϵ Model of Turbulence," Comput. Methods Appl. Mech. Eng. **51**, pp. 507–523.

[13] Harlow, F. H., and Welch, J. E., 1965, "Numerical Calculation of Time-Dependent Viscous Incompressible Flow of Fluid With Free Surface," Phys. Fluids **8**, pp 2182–2188.

[14] Maji, P. K., and Biswas, G., 1999, "Analysis of Flow in the Spiral Casing Using a Streamline Upwind Petrov Galerkin Method," Int. J. Numer. Methods Eng. **45**, pp. 147–174.

[15] Prakash, K. A., Biswas, G., and Rathish Kumar, B. V., 2006, "Thermal Hydraulics of the Spallation Target Module of an Accelerator Driven Sub-Critical System: A Numerical Study," Int. J. Heat Mass Transfer **49**, pp. 4633–4652.

[16] Laufer, J., 1954, "The Structure of Turbulence in Fully Developed Pipe Flow," NACA Report No. 1174.

[17] Hutton, A. G., and Smith, R. M., 1981, "On the Finite Element Simulation of Incompressible Turbulent Flow in General Two-Dimensional Geometries," *Numerical Methods in Laminar and Turbulent Flow*, Pineridge, Swansea, C. Taylor and B. A. Shrefler, eds., pp. 229–242.

Numerical Simulation for Under-Floor Air Distribution System With Swirl Diffusers

Xiuling Wang

Darrell W. Pepper[1]
Professor and Director
e-mail: dwpepper@nscee.edu

Nevada Center for Advanced Computational Methods,
University of Nevada Las Vegas,
Las Vegas, NV 89154-4027

A finite volume renormalization group (RNG) k-ε turbulent model was employed to simulate an under-floor air distribution (UFAD) system consisting of eight swirl diffusers. Mesh generation was conducted using PRO/E and GAMBIT. Computational fluid dynamics (CFD) results using FLUENT show both flow and thermal patterns for an instrumented laboratory room (Building Technology Laboratory-BTL) located at the University of Nevada Las Vegas. Simulation results are presented using symmetrical boundary settings for the BTL. Stratification heights and clear zones are discussed. The application of CFD simulation provides insightful analyses in UFAD design and placement.

[DOI: 10.1115/1.2709974]

Keywords: finite volume, RNG k-ε turbulent model, heat transfer, UFAD, swirl diffusers

1 Background

Ceiling air distribution (CAD), which supplies air to and removes air from conditioned spaces at ceiling levels, has been widely used in HVAC systems. As warm air near the ceiling of a room is introduced into conditioned air, the conditioned cool air temperature increases as it approaches the floor level. Under-floor air distribution (UFAD) systems are uniquely different, i.e., since conditioned air is introduced at floor level, no warm air is induced into the room. UFAD is more efficient than CAD for achieving the same cooling loads. The first introduction of an UFAD system occurred in West Germany during the 1950s to cool a computer room. Since its first introduction, interest in it has developed over the years as a promising technology to provide efficient cooling and good indoor air quality [1].

The advantages of the UFAD system can be summarized as follows [2]: (i) improved flexibility for building services; (ii) improved ventilation efficiency and indoor air quality; (iii) improved occupant comfort, productivity, and health; (iv) reduced energy use; (v) reduced life-cycle building costs; and (vi) reduced floor-to-ceiling height in new construction.

In order to capitalize on the advantages of UFAD, knowledge of the characteristics of UFAD systems are needed to help guide designers and building owners achieve a cooling system with high energy efficiency and thermal comfort. Bauman and Webster [1] state there is constant risk to designers and building owners in creating an efficient system due to the lack of objective information and standardized design guidelines. Computational fluid dynamics (CFD) is a powerful tool that is now being utilized in HVAC design studies. CFD provides fast and cost effective results that can be compared to experimental data. Many of the better CFD tools in use today are being used to simulate indoor air quality (IAQ), contaminant dispersion, and the performance of HVAC systems [3–14].

In this study, simulation results of an UFAD system containing eight swirl diffusers have been obtained using the commercial CFD program FLUENT. Preprocessing work was conducted using PRO/E and GAMBIT. Numerical results show both flow and thermal patterns for an instrumented laboratory room—the Building Technology Laboratory (BTL) at the University of Nevada Las Vegas. The BTL facility is a unique, one-of-a-kind instrumented laboratory; it is especially designed for measuring the airflow characteristics of grills, registers, diffusers, and other types of room ventilation. The room is 30 ft (9.14 m) (length) × 22 ft (6.71 m) (width) × 12 ft (3.66 m) (height), as shown in Fig. 1. The height of the room is adjustable. The BTL is used to measure the quality, efficiency, and effectiveness of different heating, ventilating, and air conditioning system components and configurations and their related effects on building occupants. Experimental data are currently being taken within the facility; this data will be compared to the numerical results in a follow-up paper.

Numerical results for flow and thermal patterns within the BTL are presented. Detailed simulation results of temperature and velocity distributions at several test planes are analyzed. Comparisons of temperatures and velocities within the BTL are made for a range of volume flow rates associated with eight swirl diffusers located within the floor. Stratification heights and clear zones are also discussed.

2 Preprocessing

Only a very limited number of papers can be found in the literature that deal with UFAD systems and their use in HVAC. To the best of our knowlege, no one has yet conducted a detailed numerical simulation of swirl diffusers for use in UFAD systems. Swirl diffuser geometry is complex, and the flow features are difficult to simulate.

In this study, three-dimensional (3D) geometrical modeling of the swirl diffuser was conducted using PRO/E; an IGES file was first created. 3D meshing was achieved using the commercial mesh generation package, GAMBIT, and accessing the IGES file as input.

2.1 Geometry Modeling. The 3D geometry for a floor swirl diffuser is shown in Figs. 2(*a*) and 2(*b*). The bottom part of the swirl diffuser was simplified when input to GAMBIT for meshing. The computational domain for the swirl diffuser includes the top section and a short cylinder, as shown in Fig. 2(*c*).

The layout of the testing space BTL with eight swirl diffusers is shown in Fig. 3. The dimensions for the test space with the swirl diffusers were set to 30 ft (9.14 m) × 20 ft (6.10 m) × 9 ft (2.74 m) with the coordinate origin in the center of the room.

2.2 Mesh Generation. The computational mesh for the BTL swirl diffusers was constructed using hexahedral cells. Since the room is symmetrical, only half of the BTL was discretized, utilizing symmetrical boundary conditions in the FLUENT simulation. Mesh-independent studies were made using three separate structured meshes with densities: (i) 797,140 (ii) 1,410,338, and (iii) 1,969,442 cells and one unstructured mesh (tetrahedral) with density 1,498,064 cells—negligible differences were observed in the results. The final mesh consisting of 797,140 cells, which is shown in Fig. 4, was selected and deemed sufficient for the set of the simulations.

---

[1] Corresponding author.

Contributed by the Heat Transfer Division of ASME for publication in the JOURNAL OF HEAT TRANSFER. Manuscript received July 31, 2006; final manuscript received December 6, 2006. Review conducted by Sumanta Acharya. Paper presented at the 2006 ASME International Mechanical Engineering Congress (IMECE2006), Chicago, IL, November 5–10, 2006.

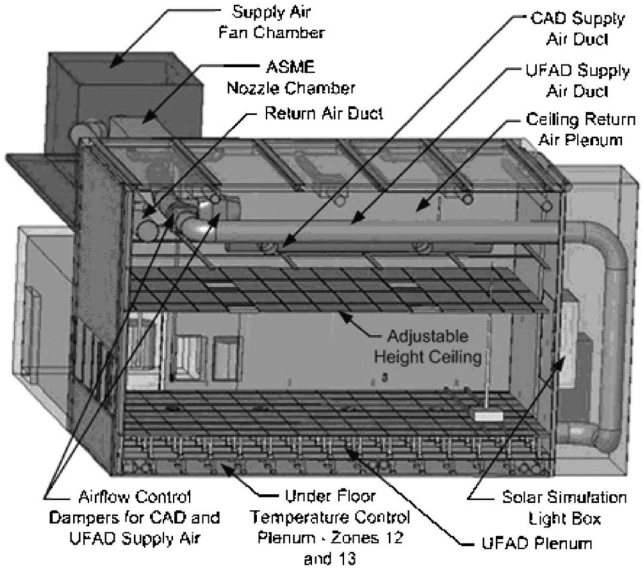

Fig. 1 Side-section view of the BTL (from Ref. [15])

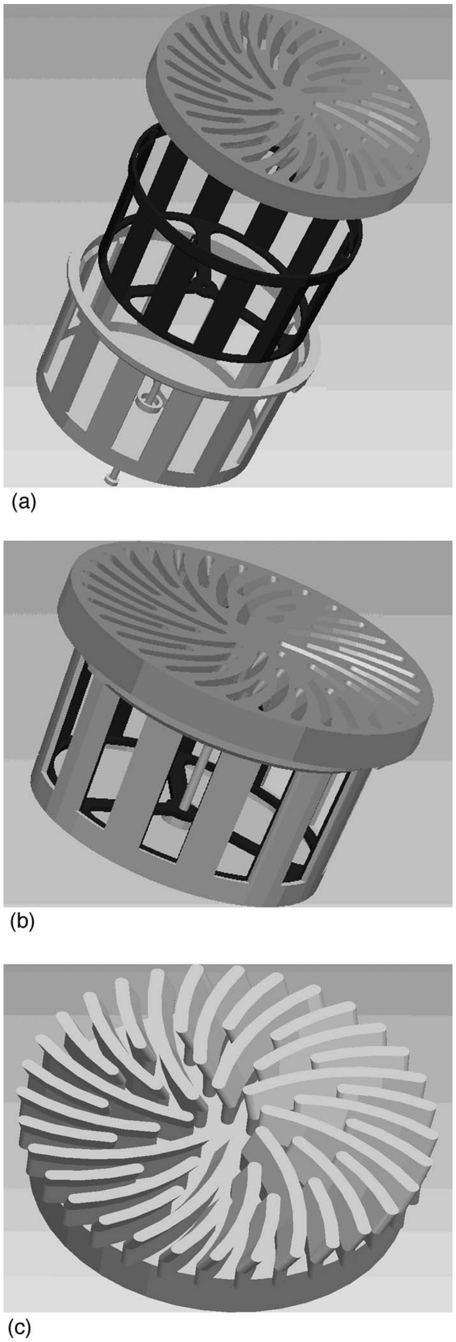

Fig. 2 3D geometry for swirl diffuser: (*a*) exploded view, (*b*) assembled view, and (*c*) computational domain

Figure 5 shows a close-up view of the computational mesh around a single swirl diffuser. The mesh surrounding the swirl diffuser was refined in order to capture fast changing flow features.

3 Numerical Simulation

Based on the supplied air volume flow rate, the airflow inside the computational domain (which includes the BTL and swirl diffusers) is turbulent. Various turbulent closure schemes exist and are well documented in the literature. For indoor air ventilation simulation, the two-equation k-ε model is the more popular and widely used scheme [4–14,16].

In 1995, Chen [6] compared the performance of five different models for simulating simple indoor airflows and found that the standard and RNG k-ε predicted flow patterns best. As one of the variants of the standard k-ε models, the RNG model was found to perform slightly better, especially in handling complex shear flows involving rapid strain, moderate swirl, vortices, and locally transitional flows [6,17], e.g., boundary layer separation, massive separation, and vortex-shedding behind bluff bodies, stall in wide-angle diffusers and room ventilation.

In this study, the RNG k-ε model was adopted. In the RNG model, equations and coefficients are analytically derived, where significant improvements in the ε equation formulation have enhanced the ability of FLUENT to model highly strained flows [17]. Additional options aid in predicting swirling flows, which is especially suitable in the UFAD simulation with swirl diffusers.

The SIMPLE algorithm, which was first introduced by Pantankar and Spalding [18] and Patankar [19] for resolving the coupling between pressure and velocity, was employed in this study. In this scheme, the same volume is employed for the integration of all conservation equations; all variables were stored at the control volume's cell center.

A nonstaggered grid was used in the simulation, and a second-order differencing scheme with a segregated solver were chosen. The nonlinear governing equations were linearized using an implicit technique with respect to a set of dependent variables. The algebraic equations were solved iteratively using an additive correction multigrid method with a Gauss-Seidel relaxation procedure [17].

3.1 Governing Equations. Flow is governed by the ensemble-averaged differential equations for the conservation of mass, momentum, and energy. The Reynolds stresses arising from the averaging process are modeled using the linear Boussinesq approximations. The stresses are commonly expressed in Cartesian tensor notation as

$$-\overline{\rho u_i' u_j'} = 2\mu_t\left(S_{ij}-\frac{1}{3}D\delta_{ij}\right)-\frac{2}{3}\rho\delta_{ij}k \tag{1}$$

where

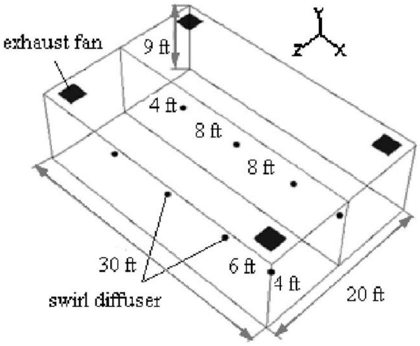

Fig. 3 Layout for testing space in BTL with eight swirl diffusers

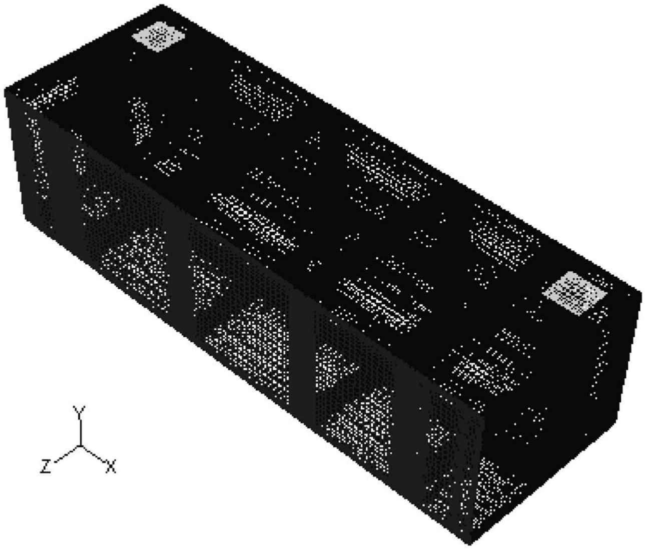

Fig. 4 Mesh for BTL with four swirl diffusers

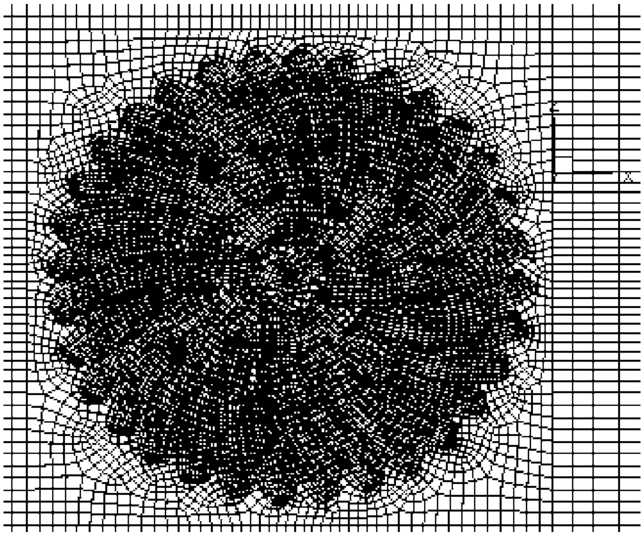

Fig. 5 Mesh for BTL around swirl diffusers

$$\delta_{ij} = \frac{1}{2}\left(\frac{\partial U_i}{\partial x_j} + \frac{\partial U_j}{\partial x_i}\right) \tag{2}$$

The conservation equations are

Continuity equation:

$$\frac{\partial}{\partial x_j}(\rho U_j) = 0 \tag{3}$$

Momentum equation:

$$\frac{\partial}{\partial x_j}(\rho U_j U_i) = -\frac{\partial p}{\partial x_i} + \frac{\partial}{\partial x_j}[2(\mu + \mu_T)S_{ij}] - \frac{2}{3}\frac{\partial}{\partial x_i}[(\mu + \mu_T)D + \rho k] \tag{4}$$

Energy equation:

$$\frac{\partial}{\partial x_j}(\rho u_j C_p T) = \frac{\partial}{\partial x_j}\left(\lambda \frac{\partial T}{\partial x_j} - \overline{\rho u_j' T'}\right) + S_i^T \tag{5}$$

Consistent with the idea of two-equation turbulence models, the turbulent viscosity in the above equations is defined as

$$\mu_T = C_\mu \rho \frac{k^2}{\varepsilon} \tag{6}$$

where the empirical constant C_μ is usually taken to be 0.09. The k-ε equations and related closure coefficients are listed as follows:

$$\frac{\partial(\rho k)}{\partial t} + \frac{\partial}{\partial x_j}(\rho U_j k) = \frac{\partial}{\partial x_j}\left[\left(\mu + \frac{\mu_T}{\sigma_k}\right)\frac{\partial k}{\partial x_j}\right] + 2\mu_T S_{ij} S_{ij} - \frac{2}{3}(\mu_T D^2 + \rho k D) - \rho\varepsilon \tag{7}$$

$$\frac{\partial(\rho \varepsilon)}{\partial t} + \frac{\partial}{\partial x_j}(\rho U_j \varepsilon) = \frac{\partial}{\partial x_j}\left[\left(\mu + \frac{\mu_T}{\sigma_\varepsilon}\right)\frac{\partial \varepsilon}{\partial x_j}\right] + C_1 \frac{\varepsilon}{k}\left[2\mu_T S_{ij} S_{ij} - \frac{2}{3}(\mu_T D^2 + \rho k D)\right] - C_2 \rho \frac{\varepsilon^2}{k} + C_3 \rho \varepsilon D - R \tag{8}$$

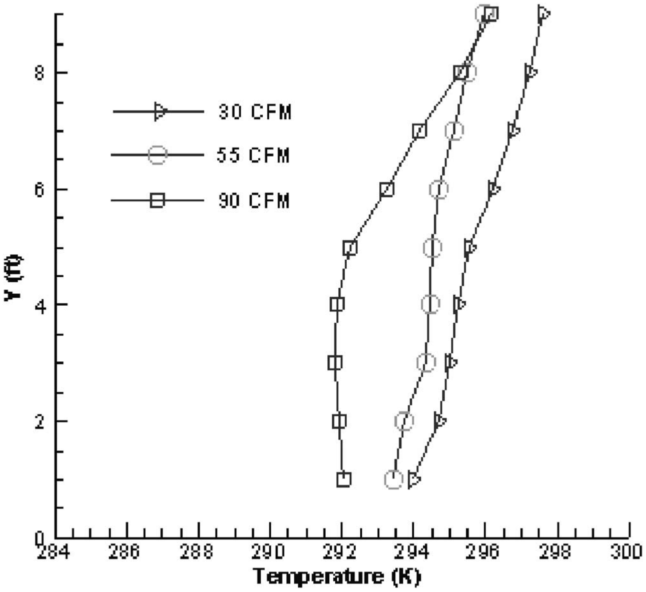

Fig. 6 Variation of average surface temperature versus height

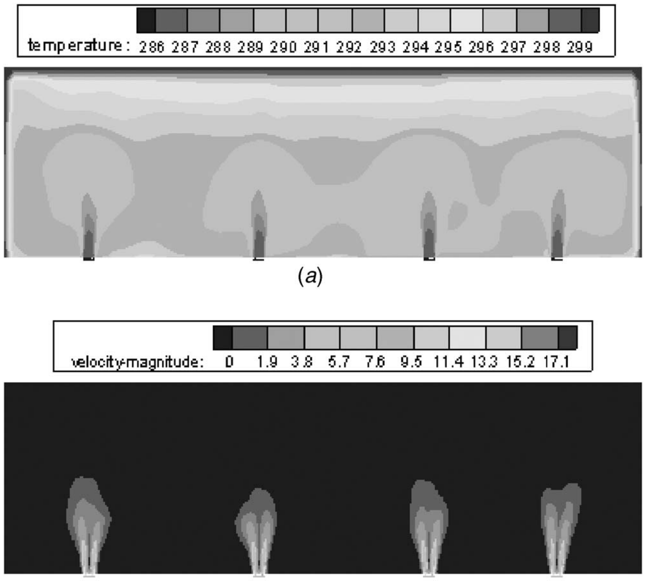

(*a*)

(*b*)

Fig. 7 Temperature and velocity distribution at $Z=5$ ft (1.52 m)

$$R = \rho C_\mu \frac{\eta^3\left(1 - \frac{\eta}{\eta_0}\right)}{1 + \beta\eta^3}\frac{\varepsilon^2}{k} \tag{9}$$

where

Table 1 Comparison between manufacturer's data and simulation results

Airflow at 90 cfm ($0.042\ \mathrm{m^3/s}$)	Vertical projection at 150 fpm (0.762 m/s)	Vertical projection at 50 fpm (0.254 m/s)	Horizontal spread at 50 fpm (0.254 m/s)
Manufacturer	1.6 ft (0.49 m)	4.4 ft (1.34 m)	3.7 ft (1.13 m)
Simulation	1.66 ft (0.51 m)	4.5 ft (1.37 m)	3.5 ft (1.07 m)

$$\eta_{ij} = \frac{k}{\varepsilon}S_{ij}; \quad \eta = \|\eta_{ij}\|; \quad C_1 = 1.42; \quad C_2 = 1.75;$$

$$C_3 = -0.373; \quad \sigma_k = 1.0; \quad \sigma_\varepsilon = 1.22;$$

$$\beta = 0.012; \quad \eta_0 = 4.38$$

3.2 Numerical Procedure and Boundary Setting.

Simulations were made according to the same experimental conditions that are currently underway within the BTL. Inlet volume flow rate for each swirl diffuser was 30 cfm ($0.014\ \mathrm{m^3/s}$), 55 cfm ($0.026\ \mathrm{m^3/s}$), and 90 cfm ($0.042\ \mathrm{m^3/s}$). The supply air temperature was set to 285.9 K (12.75°C). The BTL permits all six walls to be set to constant Dirichlet conditions with surface temperatures at 296.9 K (23.75°C).

Different volume flow rates were adopted in the simulation. Figure 6 shows the average surface temperature for three volume flow rates for the BTL. Volume flow rates 1, 2, and 3 correspond to 30 cfm ($0.014\ \mathrm{m^3/s}$), 55 cfm ($0.026\ \mathrm{m^3/s}$), and 90 cfm

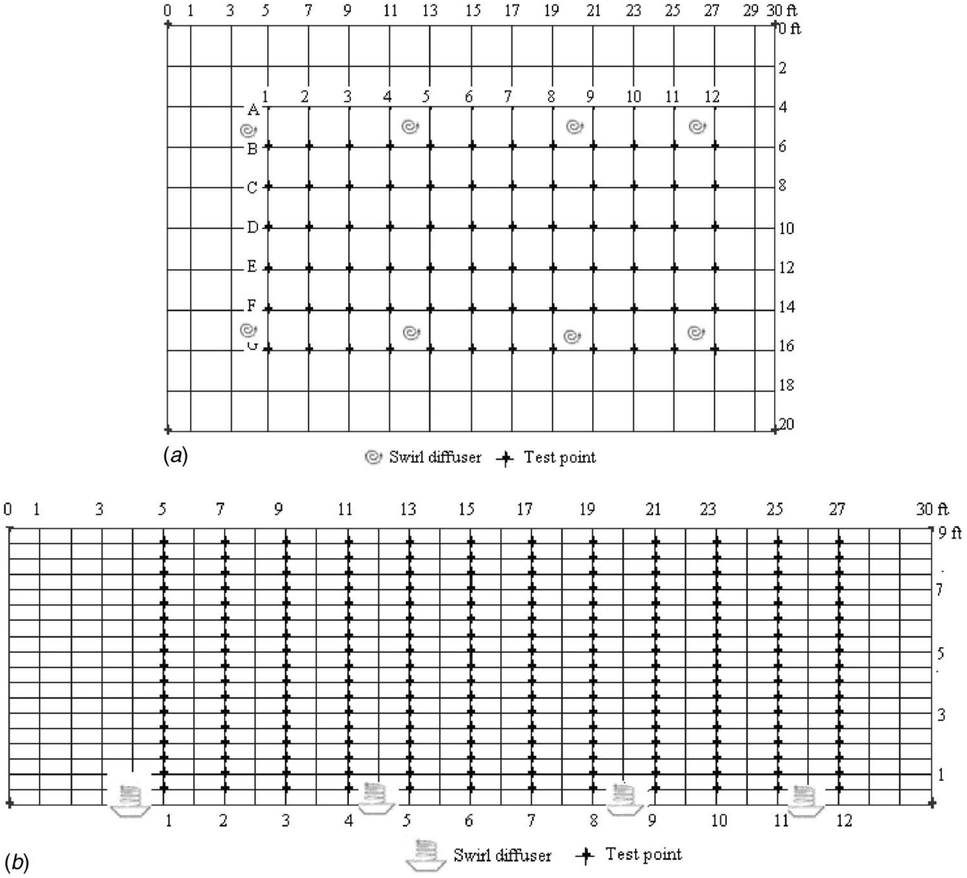

(*a*)

(*b*)

Fig. 8 Test grids in the BTL

($0.042\ \mathrm{m}^3/\mathrm{s}$). The average surface value is defined by area-weighted average surface integration value at different height levels in the room. The averaged surface temperature increases in value as the height Y increases.

Comparing the average surface temperature distributions of the three volume flow rates, volume flow rate 3 (90 cfm ($0.042\ \mathrm{m}^3/\mathrm{s}$)) appears the best—the best cooling results are obtained within the stratification height range. Therefore, all subsequent simulations were based on a volume flow rate of 90 cfm ($0.042\ \mathrm{m}^3/\mathrm{s}$).

There are two important regions, or zones, that develop in UFAD systems [1]: (i) clear zone and (ii) stratification height. A clear zone is defined as an imaginary cylinder of specified diameter around the center point of the diffuser. Clear zones are generally 3–6 ft (0.91–1.83 m) in diameter. In a displacement ventilation system, a horizontal interface, known as the stratification height, can divide the room into two zones (upper and lower) having distinct airflow conditions. The lower zone beneath the stratification level has no recirculation and is close to displacement flow. The upper zone above the stratification level is characterized by recirculating flow producing a fairly well mixed region. In a properly designed displacement ventilation system, the stratification height is maintained near the top of the occupied zone.

Figures 7(*a*) and 7(*b*) show the temperature and velocity distributions in the X-Y plane for four in-line diffusers and indicate that the air is well mixed by the effects of the swirl diffusers. Figure 7(*a*) shows that the stratification height is around 6 ft, and Fig. 7(*b*) shows that the clear zone is about 4.2 ft (1.28 m), which are common to UFAD systems [1,2]. At the lower height level, effects of the swirl diffuser are significant, as the height increases above the stratification height (for the current volume flow rate), the stratification height is around 6 ft (1.83 m), velocities become relatively stable and temperatures are high. Figure 7(*a*) indicates that the coolest and most well-mixed air is in the region within 6 ft (1.83 m) of the floor, where people reside.

A comparison of performance data provided by the manufacture and results from the numerical simulation are listed in Table 1. Overall good agreement is observed.

In an effort to provide additional information for design of UFAD systems, velocities and temperatures at a set of test points were also investigated. The locations of the test grids in the BTL are shown in Fig. 8. Data from test planes A, B, and D are presented, which correspond to planes at $Z=-6$ ft (1.83 m), -4 ft (-1.22 m), and 0 ft (0 m).

Figures 9(*a*)–9(*c*) show the variation of air velocity magnitude at the test planes as a function of height. Figure 9(*a*) shows that the velocity is more uniform than velocities in Figs. 9(*b*) and 9(*c*); this is due to the test plane being far away from the swirl diffusers. Below 6 ft (1.83 m), the variation of the velocity magnitude in Fig. 9(*a*) is <0.5 ft/s (0.15 m/s) while the largest variation in Figs. 9(*b*) and 9(*c*) can reach as high as 1.25 ft/s (0.38 m/s).

Figures 10(*a*)–10(*c*) show the variation of the temperature at the test planes as a function of height. The temperature is more uniformly distributed in Fig. 10(*a*), as test plane $Z=0$ is furthest from the swirl diffusers. Temperatures below 6 ft (1.83 m), the stratification height, do not change significantly for all three test planes. People positioned within these ranges should feel more comfortable.

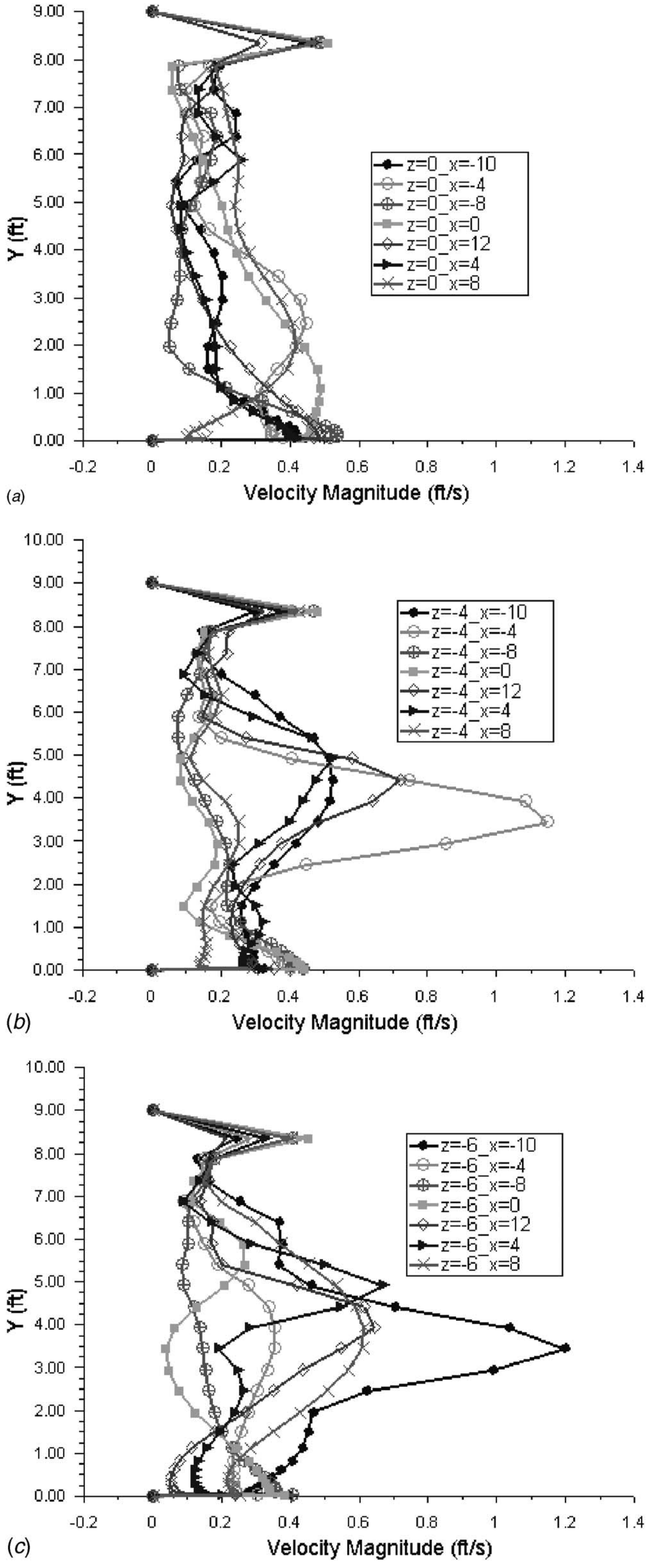

Fig. 9 Velocity magnitude at three test planes

4 Conclusions

Simulation results of an UFAD system containing eight swirl diffusers have been obtained using FLUENT, a popular finite volume commercial code, employing a RNG k-ε turbulent model. Utilizing symmetrical boundary conditions, only one-half of the room containing four diffusers was modeled. Results show both expected flow and thermal patterns for the instrumented laboratory room. Calculations were obtained for three volume flow rates. Velocity and temperature distributions at specified test planes were investigated.

UFAD systems are uniquely different from traditional CAD systems: conditioned air is introduced at floor level, i.e., no warm air is introduced into the room. In a CAD system, warm air near the ceiling of a room is introduced into the conditioned air. The

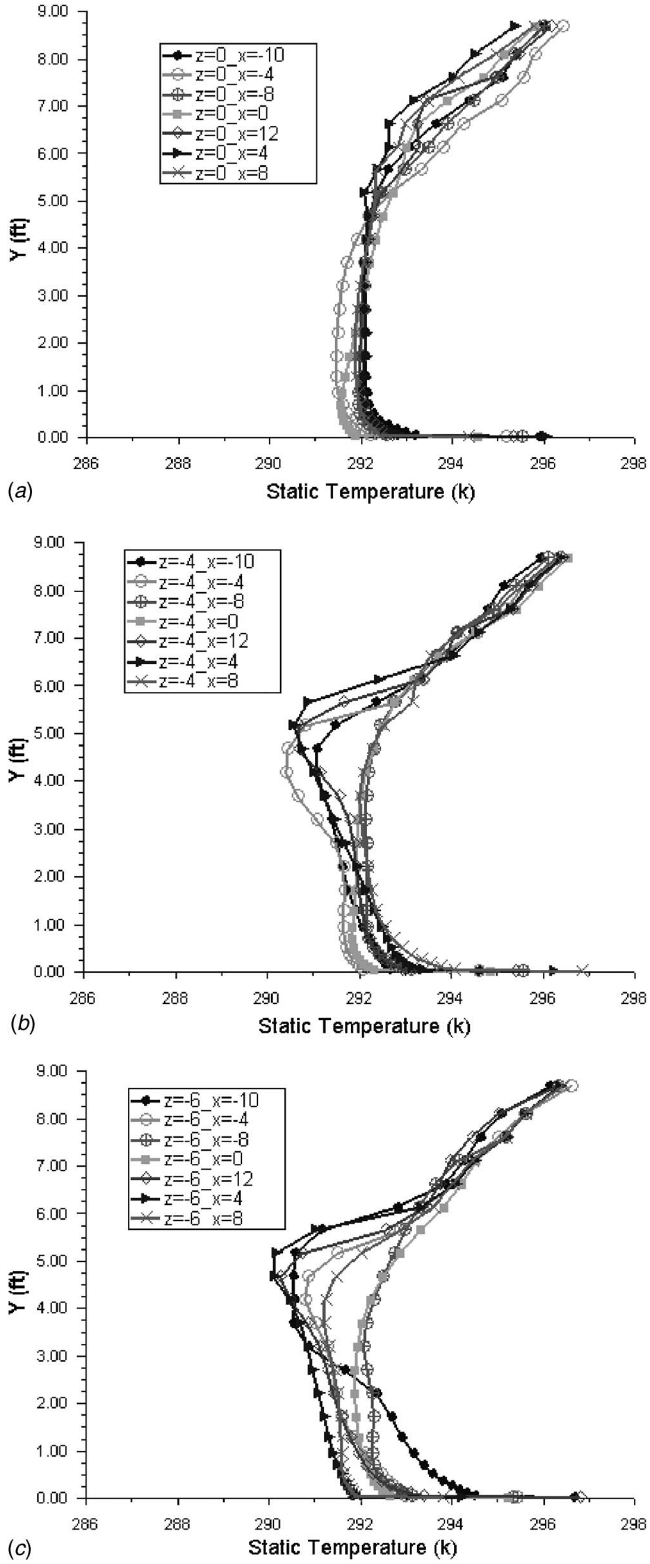

Fig. 10 Temperature at three test planes

stratification heights in the UFAD system indicate that most of the conditioned air will reach those regions where occupants exist. Clear zones are regions with high-velocity movement, which can lead to human discomfort. Additional simulations and subsequent verification studies should ultimately result in a data set that will be useful in guiding future UFAD design and installation. The application of FLUENT was particularly helpful in assessing the complex flow and thermal distributions associated with swirl diffusers.

Nomenclature

ρ = density
μ = viscosity
μ_t = turbulent viscosity
p = pressure
ε = turbulent dissipation
C_p = specific heat capacity
U = mean velocity
u' = fluctuating velocity
T = mean temperature
T' = fluctuating temperature
S = source term
x = space

References

[1] Bauman, F. S., and Webster, T., 2001, "Outlook for Under Floor Air Distribution," ASHRAE J., **43**(6), pp. 18–27.
[2] Bauman, F. S., 2003, "Under Floor Systems: Shedding Light on Common Myths," Heat./Piping/Air Cond. Eng., **4**, pp. 26–39.
[3] Posner, J. D., Buchanan, C. R., and Dunn-Rankin, D., 2003, "Measurement and Prediction of Indoor Air Flow in a Model Room," Energy Build., **35**, pp. 515–526.
[4] Huang, X., Dai, Y., and Mei, Q., 2003, "Numerical Simulation of Air Flow in Air-Conditioned Room," J. Nanjing Univ. Sci. Technol., **27**(4), pp. 355–358.
[5] Xue, R., Wang, G., and Fang, L., 2005, "Numerical Simulation of Thermal Comfort Degree in Air Conditioning Room," J. Harbin Inst. Technol., **37**(8), pp. 1145–1147.
[6] Chen, Q., 1995, "Comparison of Different k-ε Models for Indoor Air Flow Computations," Numer. Heat Transfer, Part B, **28**, pp. 353–369.
[7] Fan, Y., 1995, "CFD Modeling of Air and Contaminant Distribution in Rooms," Energy Build., **23**, pp. 33–39.
[8] Tang, Z., and Zhan, J., 2003, "Application of CFD to the Research of Air Flow in Room," *Proc. of 2003 17th National Conference on Hydrodynamics and the 16th National Congress on Hydrodynamics (2003–2004)*, Hong Kong Polytechnic University, Hong Kong, pp. 330–337.
[9] Chen, Q., 1996, "Prediction of Room Air Motion by Reynolds-Stress Models," Build. Environ., **31**(3), pp. 233–244.
[10] Ma, L., Tao, W., Dai, Y., and Sun, D., 2005, "Numerical Simulation of Temperature Distribution and Turbulent Flow in the Radiant Floor Heating Room," J. Eng. Thermophys., **26**(3), pp. 501–503.
[11] Tibaut, P., and Basara, B., 2003, "Advanced Turbulence Models for Indoor Thermal Comfort Simulation Operating Room," *Proc. of 2003 4th International Symposium on Heating, Ventilating and Air Conditioning*, Tsinghua University, Beijing, China, pp. 214–220.
[12] Murakami, S., and Kato, S., 1989, "Numerical and Experimental Study on Room Airflow—3-D Predictions Using the Kappa-E Turbulence Model," Build. Environ., **24**(1), pp. 85–97.
[13] Nielsen, P., 1998, "Selection of Turbulence Models for Prediction of Room Airflow," ASHRAE Trans., **104**(1B), pp. 1119–1127.
[14] Oh, M., Lim, H., and Lee, Y., 1990, "Unsteady Propagation of Contamination Particles in the Turbulent Flow Field for the Dynamic Analysis of Clean Rooms," *Proc. of Annual Technical Meeting—Institute of Environmental Sciences*, Inst. of Environmental Sciences, New Orleans, LA, pp. 283–289.
[15] Reynolds, D., personal communication.
[16] Baratta, M., and d' Ambrosio, S., 2004, "Further Investigation of RNG k-ε Model Capabilities in the Simulation of In-Cylinder Turbulent Flows," The Sixth International Symposium on Diagnostics and Modeling of Combustion in Internal Combustion Engines, Yokohama, Japan.
[17] Fluent, 2005, *FLUENT User Guide*, Version 6.2, Fluent Inc., Lebanon, NH.
[18] Patankar, S. V., and Spalding, D. B., 1972, "A Calculation Procedure for Heat, Mass and Momentum Transfer in Three-Dimensional Parabolic Flows," Int. J. Heat Mass Transfer, **17**, pp. 1787–1806.
[19] Patankar, S. V., 1980, *Numerical Heat Transfer and Fluid Flow*, McGraw Hill, New York.

Analysis of Interfacial Heat Transfer Coefficient of Green Sand Mold Casting for Aluminum and Tin-Lead Alloys by Using a Lump Capacitance Method

Hsien-Chi Sun

Long-Sun Chao[1]
e-mail: lschao@mail.ncku.edu.tw

Department of Engineering Science,
National Chen Kung University,
No. 1, Ta-Hsueh Road, 701,
Tainan, Taiwan, R.O.C.

During the casting process of green sand mold, air gaps will form between the metal and sand mold. The air gaps will make it difficult to analyze the heat transfer at the mold/metal interface. Generally, an interfacial heat transfer coefficient is employed to evaluate the heat flux transferred across the air gaps. Though the interfacial heat transfer coefficient is highly important, its value is not easily obtained by using the direct experimental or theoretical method. With temperature-measured data, some inverse methods can be used to predict the coefficient. However, the latent heat released and undercooling during the solidification of the molten metal and the moisture of the green sand mold complicate the associated temperature calculations. To overcome this difficulty, a lump capacitance method is proposed in this study to calculate the interfacial heat transfer coefficient for the casting process in green sand mold. Thermalcouples are utilized to measure the temperatures of sand mold and metal. The geometry of casting is cylindrical and the castings are A356 alloy and Sn-20 wt. % Pb alloy. With the predicted interfacial coefficients, the temperature field of the metal was solved numerically. Based on the solidification time, the numerical results are in good agreement with the experimental ones. This verified the feasibility of the proposed method and it can be applied in the future study or design of a casting process. [DOI: 10.1115/1.2709975]

Keywords: interfacial heat transfer coefficient, lump capacitance method, mold/metal interface, air gap

1 Introduction

In the beginning of the green sand mold casting, the molten metal cools down and a thin solidified layer forms at the mold/metal interface. As the temperature of the metal decreases, the layer shrinks and the sand mold expands due to the heating from the casting, which induces air gaps between the metal and the mold. In the heat-transfer analysis, an interfacial heat transfer coefficient is generally used to evaluate the heat flux transferred across the air gaps. The value of the coefficient is very important to the casting designers and analysts [1,2] but is not easily obtained. Consequently, the purpose of this study is to investigate the interfacial heat transfer coefficient for the green sand mold casting with a simple and feasible method.

In an early investigation of the heat transfer between metal and mold, Ho and Pehlke [3] first used the Beck's nonlinear inverse method to calculate the interfacial heat transfer coefficient. Second, two linear transducers were employed to measure the size of the air gap directly. According to the gap size, the heat flux across the gap and then the interfacial heat transfer coefficient were calculated by counting the effects of radiation and conduction heat transfers. In 1985, Ho and Pehlke [4] calculated the heat flux at the metal/mold interface by using the Beck's method, from which the interfacial heat transfer coefficient could be computed. Zeng and Pehlke [5] established two models, with and without macrogap formation at the interface. The interfacial heat transfer coefficient of not having macrogap is estimated by utilizing the calculation method of contact resistance [6], and the coefficient of having gap is predicted by using the similar method of Ho and Pehlke [3].

With the guessed or modified heat transfer coefficient, Nishida et al. [7] used the explicit finite difference method to compute the temperature distribution. The heat transfer coefficient was corrected iteratively by comparing the computing temperature to the measured one until a convergent coefficient was obtained. He also utilized an extrapolation method to calculate the metal and mold temperatures at the metal/mold interface from the measured temperatures near the interface. With the extrapolated interface temperatures, the heat flux and heat transfer coefficient were computed.

In 1970, Beck [8] reported that the temperature response inside a heated body lagged behind the temperature change at the body surface. Accordingly, he proposed a "future temperature" concept to solve the lagged problem involved in evaluating the surface heat flux or the surface temperature from the internally measured temperatures. In 1982, Beck et al. [9] used a sensitivity coefficient to improve the accuracy and stability of the computational results. Combined the derivative scheme with the integral one, Browne and O'Mahoney [10] and O'Mahoney and Browne [11] developed a new inverse method to calculate the temperatures at the metal/mold interface and then the interface heat transfer coefficient.

Hwang et al. [12] employed two methods to calculate the interfacial heat transfer coefficient. In the first method, the measured gap size was used to calculate the interfacial heat coefficient directly [3,4], whereas in the second one, Beck's inverse method was applied to calculate the interfacial heat coefficient from the temperature data measured near the mold/metal interface. Narayan Prabhu and Griffiths [13] proposed a model to compute the interfacial heat transfer coefficient. The model considered the effects of both conduction and radiation, based on the roughness characteristics of the casting and mold surfaces.

Kim et al. [14] computed the heat flux and the temperature of metal/mold interface by using the Beck's inverse method, and then the interfacial heat transfer coefficient could be computed. The interfacial coefficients were analyzed based on three regimes: liquid, solidification, and solid states. The effects of the coating applied to the mold surface were also investigated. Kobryn and Semiatin [15] investigated the interfacial heat transfer coefficients for the shrink-off and shrink-on casting geometries with the finite element method and an iterative calibration-curve technique. Uticard et al. [16] have used the concept of lump capacitance for computing the heat transfer coefficients between the high-temperature liquids ($NaNO_3$, NaCl, Na_3AlF, and $2FeO \cdot SiO_2$) and the solid surfaces of Ni and Cu. However, the solidification phenomenon was not involved in this work.

The discussions above have indicated that the interfacial heat flux and heat transfer coefficient cannot be easily obtained simply by using an experimental or theoretical method. With an inverse method, the released latent heat, the undercooling occurred during solidification, and the moving moisture of sand mold complicate the calculations. Consequently, a lump capacitance method was proposed in this paper to calculate the interfacial heat transfer coefficients for the casting processes of A356 aluminum alloy and

---

[1] Corresponding author.

Contributed by the Heat Transfer Division of ASME for publication in the Journal of Heat Transfer. Manuscript received February 27, 2006; final manuscript received December 31, 2006. Review conducted by Jayathi Murthy.

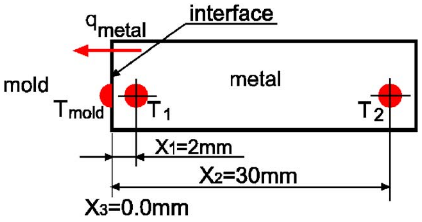

Fig. 1 Schematic illustration of temperature-measured points used to investigate the interfacial heat transfer coefficient at the mold/metal interface

Sn-20 wt.% Pb alloy in a green sand mold. Thermocouples are used to measure the internal temperatures of the metal casting at two different locations and the temperature of the sand mold at the interface during the solidification process. To confirm the validity of the proposed method, the value of the interfacial heat transfer coefficient obtained for the A356 aluminum alloy was put into a finite element commercial program, FIDAP, and the computed solidification time was compared to the experimental one.

2 Experimental Method

This paper investigates the interfacial heat transfer coefficient at the mold/metal interface in a casting process of green sand mold. The casting is cylindrical with 15 cm in length and 4.4 cm diam. In the casting process, molten metal was poured into the cylindrical cavity of sand mold via a gate located at the center of the cavity. The composition of the sand is SiO_2-94.2%, Al_2O_3-1.7%, Na_2O-1.6%, CaO-0.2%, K_2O-0.2%, and TiO_2-0.3%. The sand mold had a moisture content of 8% and a hardness value of 51. In this study, the interfacial heat transfer coefficient was calculated based on the temperature data measured in the experiment. Figure 1 shows the positions of three temperature-measured points; q_{metal} denotes the heat flux transferred from the metal to the sand mold. T_1 and T_2 are internal temperatures within the casting that are measured at distances from the mold/metal interface of 2 mm and 30 mm, respectively. T_{mold} and T_{metal} are the temperatures of the sand mold and the metal at the mold/metal interface. In practice, embedding a thermocouple at the interface to measure T_{metal} is difficult. Therefore, in this paper, it is assumed that the measured temperature T_1, located at a position very close to the mold/metal interface, is regarded as T_{metal}. The value of q_{metal} is unknown, since it is not easy to measure the value by using a simple experimental method. In this study, a lump capacitance method is proposed to calculate q_{metal} with the temperature data measured from the casting experiment. As q_{metal} is obtained, the heat transfer coefficient at the interface can be computed.

3 Theoretical Aspect

3.1 Interfacial Heat Flux and Heat Transfer Coefficient. Since the contact between the casting and the mold wall is not perfect during the solidification process, the interfacial heat transfer coefficient h is used to calculate q_{metal}. The present study employs two ways to calculation this coefficient:

1. The heat transfer at the mold/metal interface is assumed to be a quasi-steady problem. Accordingly, the heat flux transferred out from the metal is equal to the heat flux entering the sand mold, and then the interfacial heat transfer coefficient, h_1, can be expressed as

$$h_1 = \frac{q_{\text{metal}}}{T_{\text{metal}} - T_{\text{mold}}} \tag{1}$$

2. Because the thermal conductivity of sand mold is low, the solidification process of the casting can be analogous to the cooling of a high-temperature object in air. Therefore, the present study imitates the Newton's cooling law and proposes a new interfacial heat transfer coefficient, h_2, which can be expressed as

$$h_2 = \frac{q_{\text{metal}}}{T_{\text{metal}} - T_\infty} \tag{2}$$

where T_∞ represents the temperature of the sand mold at a position far from the mold/metal interface, which can be the room temperature [17].

3.2 Lump Capacitance Method. Since the conductivity of metal is high, in analyzing the heat transfer of the casting process, it can be assumed that the temperature of the metal is uniformly distributed throughout the whole casting and varies only with time. Consequently, the metal can be regarded as a lumped system and with the concept of the effective specific heat, the thermal energy variation of the system ΔQ from t to $t+\Delta t$ can be written as

$$\Delta Q = \int_{T(t)}^{T(t+\Delta t)} \rho V Cp^{\text{eff}} dT \tag{3}$$

where V is the volume of the casting and ρ is the density. Cp^{eff} is the effective specific heat, which also includes the effect of latent heat. In Eq. (3), $T(t)$ and $T(t+\Delta T)$ are taken from the temperature data of measured point T_2 (shown in Fig. 1). ΔQ is transferred to the sand mold through the metal/mold interface. Accordingly, q_{metal} can be expressed as

$$q_{\text{metal}} = \frac{\Delta Q}{A \Delta t} \tag{4}$$

where A is the area of the casting surface.

To specify the effective specific heat Cp^{eff}, it has three regions: the solid, liquid, and solidification regions. In the solid region, $Cp^{\text{eff}} = Cp_S$ and in the liquid one, $Cp^{\text{eff}} = Cp_L$, where Cp_S and Cp_L are the specific heats of solid and liquid, respectively. In the solidification region, the Sn-20 wt.% Pb alloy has two different stages, i.e., proeutectic and eutectic stages. The A356 aluminum alloy also has two solidification stages, i.e., primary phase and eutectic stages. In the solidification region, the effective specific heat can be expressed as

$$Cp^{\text{eff}} = f_S Cp_S + (1 - f_S) Cp_L - L_f \frac{df_S}{dT} \tag{5}$$

where f_S is the solid fraction and L_f is the latent heat. Since the heat transfer behavior in the eutectic region of lead-tin alloy is similar to that of pure substance, the effective specific heat can be written as

$$Cp^{\text{eff}} = \frac{1}{2}\left(\frac{L_f^*}{\Delta T} + Cp_S + Cp_L \right) \tag{6}$$

$$L_f^* = [1 - (f_S)_{\text{eutectic}}] L_f \tag{7}$$

where $(f_S)_{\text{eutectic}}$ is the solid fraction at the eutectic temperature.

As shown below, the methods employed to calculate the solid fractions of the A356 aluminum alloy and the Sn-20 wt.% Pb alloy are different.

3.2.1 356 Aluminum Alloy. The empirical formulations of f_S for these two solidification stages of A356 aluminum alloy [18] are used and their expressions can be written as

a. Primary phase solidification

$$f_s = \left(\frac{T_L - T}{T_L - T_{\text{eut}}} \right)^{n_p} f_p \tag{8}$$

$$\frac{df_s}{dT} = \frac{-f_p n_p}{T_L - T_{\text{eut}}} \left(\frac{T_L - T}{(T_L - T_{\text{eut}})} \right)^{n_p - 1} \tag{9}$$

Table 1 Thermal properties of A356 alloy

Specific heat of solid Cp_S	877.8 J/kg °C
Specific heat of liquid Cp_L	1045 J/kg °C
Density ρ	2700 kg/m^3
Latent heat L_f	3,888,740 J/kg

b. Eutectic solidification

$$f_s = f_p + \left(\frac{T - T_{\text{eut}}}{T_s - T_{\text{eut}}}\right)^{n_e}(1 - f_p) \tag{10}$$

$$\frac{df_s}{dT} = \frac{(1 - f_p)n_e}{T_s - T_{\text{eut}}}\left(\frac{T - T_{\text{eut}}}{T_s - T_{\text{eut}}}\right)^{n_e - 1} \tag{11}$$

where T_L is the liquidus temperature, T_{eut} is the eutectic temperature, and f_P is the solid fraction of the primary phase at the eutectic temperature, whose value is 0.551. n_p is a nonlinear factor with a value of 0.48217, and n_e is another nonlinear factor with a value of 0.09544. The thermal properties of A356 alloy are given in Table 1 [19].

3.2.2 Sn-20 wt.% Pb *Tin-Lead Alloy*. During the proeutectic stage, the equilibrium lever rule is used to calculate the solid phase ratio, i.e.,

$$f_s = \frac{T - T_L}{(T - T_0)(1 - k_0)} \tag{12}$$

$$\frac{df_s}{dT} = \frac{T_L - T_0}{(T - T_0)^2(1 - k_0)} \tag{13}$$

where T_L is the liquidus temperature, k_0 is the equilibrium distribution coefficient, and T_0 is the melting temperature of tin. The thermal properties of Sn-20 wt.% Pb alloy are listed in Table 2 [19].

4 Results and Discussion

In this paper, the heat transfer between the metal and the sand mold in a casting process of green sand mold was investigated. The results of the study can be divided into two parts: (i) the cooling curves of the measured points in the metal and (ii) the heat flux q_{metal} and the heat transfer coefficient h at the metal/mold interface.

4.1 Cooling Curves of the Measured Points in the Metal.

4.1.1 A356 Aluminum Alloy. Figure 2 presents the cooling curves obtained at measured points T_1 and T_2 (shown in Fig. 1) within the metal during a casting process. As shown in Fig. 2, immediately after the molten metal is poured into the mold cavity, the temperature descends rapidly toward the liquidus temperature of 618°C. It can be seen that the temperature then increases slightly, which is the recalescence phenomenon. The phenomenon at T_2 is more obvious than that at T_1. This marks the onset of primary phase solidification of A356 alloy. As the temperature reduces to approximately 570°C, an obvious plateau is observed. The temperature of T_2 stays there for ~95 s. This stage corresponds to the eutectic solidification. As the temperature reaches the solidus temperature of 548.6°C, the solidification process is complete. From Fig. 2, it can be found that the cooling curves of T_1 and T_2 are broadly similar over the course of the solidification process. This is particularly true when they are both in liquid or solid state. The cooling trend throughout the metal is similar to those observed at T_1 and T_2. Consequently, the present study is justified in employing the lump capacitance method.

Table 2 Thermal properties of Sn-20 wt.% Pb alloy

Specific heat of solid Cp_S	891.626 J/kg °C
Specific heat of liquid Cp_L	1014.07 J/kg °C
Density ρ	7860 kg/m^3
Latent heat L_f	52,906 J/kg

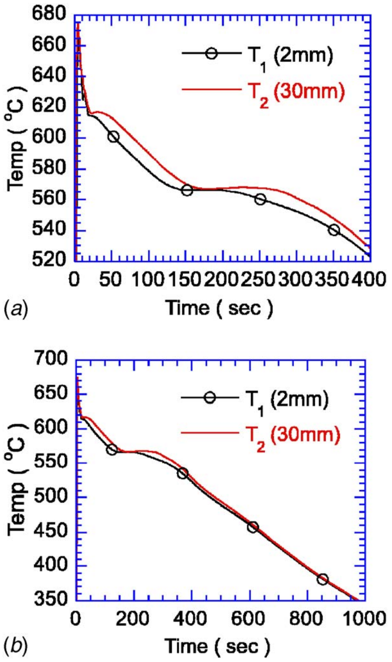

Fig. 2 Cooling curves of A356 alloy measured at the locations of x=2 mm (T_1) and 30 mm (T_2) from the mold/metal interface

4.1.2 Sn-20% Pb Alloy. Figure 3 illustrates the cooling curves of Sn-20% Pb alloy measured at T_1 and T_2. This figure clearly

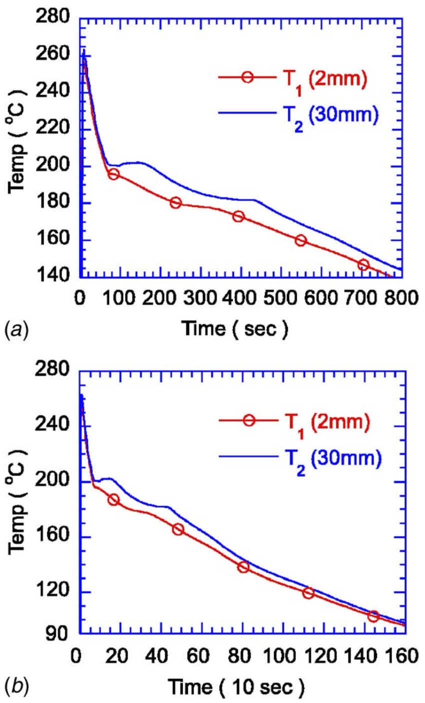

Fig. 3 Cooling curves of Sn-20 wt.% Pb alloy measured at distances of x=2 mm and 30 mm from mold/metal interface

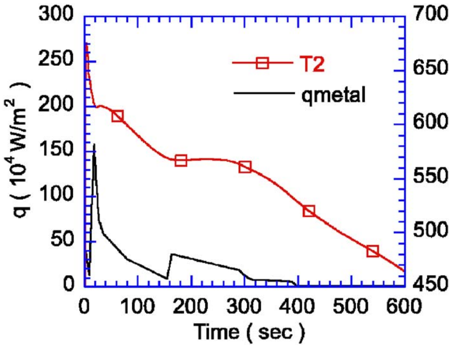

Fig. 4 Computed interfacial heat flux and T_2 versus time for A356 alloy

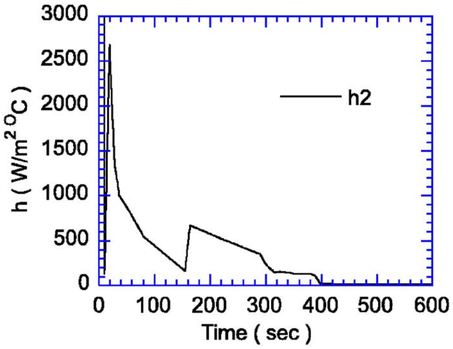

Fig. 6 Interfacial heat transfer coefficient h_2 for A356 alloy

reveals the presence of two distinct growth stages, i.e., the proeutectic and eutectic stages. When the temperature reaches a value of ~200°C, the recalescence phenomenon occurs. This signifies the appearance of equiaxed grains of proeutectic phase in the melt. As the molten metal cools toward a temperature of ~183°C, a eutectic mixture of α and β phase is generated, indicating the stage of eutectic solidification.

4.2 Interfacial Heat Flux and Heat Transfer Coefficient. In this study, the interfacial heat flux was calculated by using the lump capacitance method. Figure 4 shows the heat flux and the measured T_2 varying with time for A356 aluminum alloy. Within ~20 s after pouring, the interfacial heat flux rises steeply to a very high peak value, corresponding to the initiation of primary phase. After ~150 s, q_{metal} reduces to a local minimum value, which marks the completion of the primary phase solidification. As it enters the eutectic solidification, the heat flux reaches the other peak at 160 s. As further time elapses, the value of q_{metal} decays gradually. At 400 s, the eutectic solidification stage is completed and q_{metal} decreases to a very low value.

Figures 5 and 6 illustrate the interfacial heat transfer coefficients, h_1, and, h_2, varying with time. In Fig. 6, it is apparent that the h_2 curve follows the same trend as that of q_{metal}, i.e., a high peak value is located at the beginning of primary phase solidification and a second peak is at the start of eutectic solidification. q_{metal} is calculated based on the measured temperature of T_2. The variation trend of $T_{\mathrm{metal}}(=T_1)$ is similar to that of T_2, and so is the trend of $T_{\mathrm{metal}}-T_{\mathrm{air}}$ ($T_{\mathrm{air}}=28$°C). Consequently, the variation of h_2 is broadly similar to that of q_{metal}. However, in computing h_1, T_{mold} is used instead of T_{air}. The variation trend of T_{mold} (Fig. 7) is different from that of T_2. Therefore, the trend of h_1 differs slightly from that of q_{metal}. Specifically, the comparison of Figs. 4 and 5 shows that the value of h_1 does not decrease as rapidly as q_{metal} during primary phase solidification, from 30 s to 80 s.

Figure 8 illustrates the interfacial heat flux and temperature T_2 varying with time for Sn-20%Pb alloy. After molten metal is poured into the mold, the contact is first tight between the metal and the mold wall, and hence, the value of q_{metal} is very large. After ~50 s, q_{metal} reduces to a local minimum value, where it is the beginning of the proeutectic solidification stage. Because of the release of latent heat in this stage, the heat flux flowing across the interface increases and rises to a peak value at ~200 s. Subsequently, the heat flux decays and after ~325 s, q_{metal} reaches another local minimum, where it corresponds to the eutectic temperature of 183°C. This point marks the completion of the proeutectic stage. The solidifying metal then enters the eutectic solidification stage, as indicated by the final q_{metal} peak. At ~575 s, the eutectic solidification stage is completed. Afterward, q_{metal} remains at a small and relatively stable value.

Figures 9 and 10 show the interfacial heat transfer coefficients,

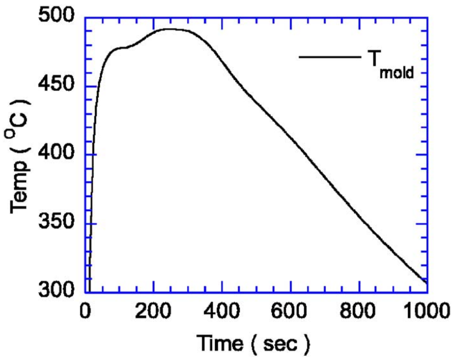

Fig. 7 Sand mold temperature at the metal/mold interface versus time for A356 alloy

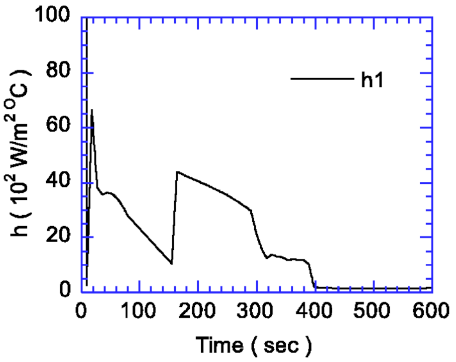

Fig. 5 Interfacial heat transfer coefficient h_1 for A356 alloy

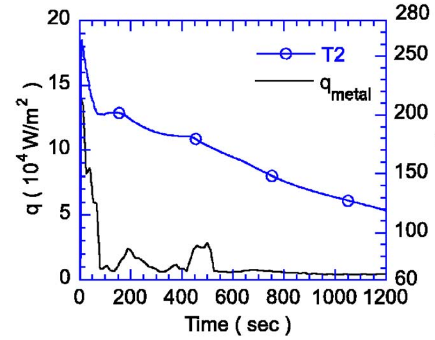

Fig. 8 Computed interfacial heat flux and T_2 versus time for Sn-20 wt.% Pb alloy

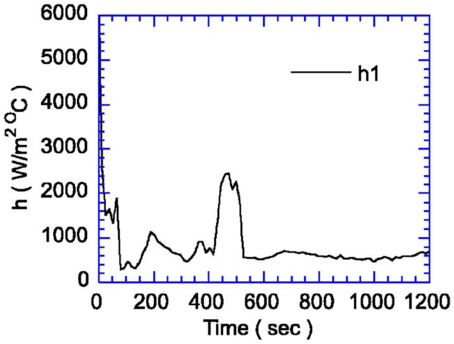

Fig. 9 Interfacial heat transfer coefficient h_1 for Sn-20 wt.% Pb alloy

h_1 and h_2, for the Sn-20%Pb alloy. The variation trends of these two coefficients are similar to that of interfacial heat flux, shown in Fig. 8. Because the pouring temperature and conductivity of the Sn-20%Pb alloy are not high, the temperature variation of T_{mold} (Fig. 11) is not very large. Accordingly, the variation trends of h_1 and h_2 are almost identical and are distinguished only by the fact that $h_2 < h_1$ since the former is calculated on the basis of T_{air}.

To check the validity of the lump capacitance method, an effective Biot number is applied and it can be written as

$$\mathrm{Bi} = \frac{(h_2)_{\mathrm{ave}} L}{k} \tag{14}$$

where $(h_2)_{\mathrm{ave}}$ is the average of h_2 over the whole solidification process. L and k are the length and the thermal conductivity of the casting, respectively. The Bi numbers for A356 and Sn-20 wt.% Pb alloys are shown in Table 3, where it can be found that the Bi numbers are very small. Consequently, the application of the lump capacitance method in this paper is reasonable.

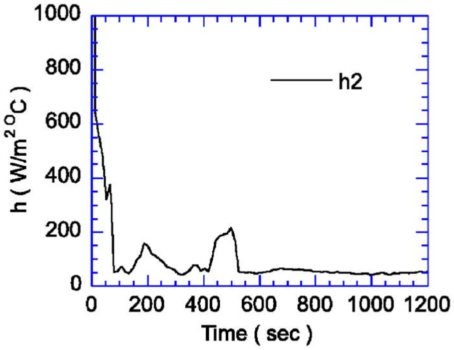

Fig. 10 Interfacial heat transfer coefficient h_2 for Sn-20 wt.% Pb alloy

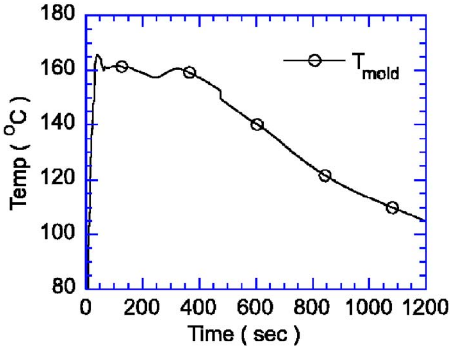

Fig. 11 Sand mold temperature at the metal/mold interface for Sn-20 wt.% Pb alloy

Table 3 Effective Biot numbers of A356 and Sn-20 wt.% Pb alloys

Metal	A356 alloy	Sn-20 wt.% Pb alloy
Bi	0.0094	0.0633

4.3 Simulation by FIDAP Software. To further justify the use of the lump capacitance method in the present study, the interfacial heat transfer coefficient, h_2, of the A356 aluminum alloy was put into a finite element commercial program FIDAP to simulate the casting process. The solidification time of the casting at the point T_2 was measured experimentally and was then compared to that predicted numerically. The experimental solidification time was found to be 378 s, whereas the time calculated by the numerical simulation was 351.4 s. The relative error between these two results is just 7%. Therefore, the feasibility of using the lump capacitance method to calculate the interfacial heat transfer coefficient is verified.

5 Conclusions

This study proposed a lump capacitance method to investigate the heat flux and heat transfer coefficient at the metal/mold interface in the green sand mold casting of A356 and Sn-20 wt.% Pb alloys. The following conclusions can be drawn from the foregoing results:

1. During the solidification of the molten metal, the cooling curves obtained at different positions within the casting are broadly similar. The A356 and Sn-20 wt.% Pb alloys have two solidification stages, the primary (or proeutectic) phase and the eutectic phase, and both exhibit the recalescence phenomenon. The release of latent heat energy during these two stages increases the computed heat flux across the air gap at the mold/metal interface.
2. Since the thermal conductivity and pouring temperature of Sn-20 wt.% Pb alloy are lower than those of A356 alloy, the variation of T_{mold} with time is less significant than that of A356 alloy. Consequently, the variation trends of h_1 and h_2 with time for Sn-20 wt.% Pb alloy are similar, and they are slightly different for A356 alloy.
3. The h_1 and h_2 curves exhibit peak values, corresponding to the release of latent heat, and troughs, corresponding to the conclusion of the proeutectic (primary phase) or eutectic solidification stages.
4. The h_2 curves for the A356 aluminum alloy and the Sn-20 wt.% Pb alloy are both similar to their own q_{metal} curves. In practice, it is not easy to measure the temperature of the mold/metal interface. The interfacial heat transfer coefficient h_2 is calculated on the basis of the room temperature rather than the sand mold temperature and therefore provides a more convenient approach to obtain the heat transfer coefficient.
5. The resulting Biot numbers are very small for A356 and Sn-20 wt.% Pb alloys. With the h_2 data of the A356 alloy, the numerically predicted solidification time differs from that obtained experimentally by only 7%. These could verify the feasibility of using the proposed lump capacitance method to calculate the interfacial heat transfer coefficient.

Nomenclature

Cp^{eff} = effective specific heat
Cp_s = specific heat of solid
Cp_L = specific heat of liquid
f_s = solid fraction

h = interfacial heat transfer coefficient
k_0 = equilibrium distribution coefficient
L_f = latent heat
q_{metal} = the heat flux transferred from the metal to the sand mold at the mold/metal interface
T_{eut} = eutectic temperature
T_L = liquidus temperature
T_{mold} = the sand-mold temperature at the mold/metal interface
T_{metal} = the metal temperature at the mold/metal interface
T_0 = melting temperature of tin
T_1 = the measured temperature of metal at the location shown in Fig. 1
T_2 = the measured temperature of metal at the location shown in Fig. 1
V = volume of casting
ΔQ = the thermal energy variation of metal from t to $t+\Delta t$
ρ = density

References

[1] Ruhul Amin, M., and Gawas, Nikhil L., 2003, "Conjugate Heat Transfer and Effects of Interfacial Heat Flux During the Solidification Process of Continuous Castings," ASME J. Heat Transfer, **125**, pp. 339–348.
[2] Wei, P. S., and Yeh, F. B., 2000, "Heat Transfer Coefficient in Rapid Solidification of a Liquid Layer on a Substrate," ASME J. Heat Transfer, **122**, pp. 792–800.
[3] Ho, K., and Pehlke, R. D., 1983, "Transient Methods for Determination of Metal-Mold Interfacial Heat Transfer," AFS Trans., **91**, pp. 689–698.
[4] Ho, K., and Pehlke, R. D., 1985, "Metal-Mold Interfacial Heat Transfer," Metall. Trans. B, **16B**, pp. 585–594.
[5] Zeng, X. C., and Pehlke, R. D., 1985, "Analysis of Heat Transfer at Metal-Sand Mold Boundaries and Computer Simulation of Solidification of a Gray Iron Casting," AFS Trans., **93**, pp. 275–282.
[6] Holman, J. P., 2002, *Heat Transfer*, McGraw-Hill, New York.
[7] Nishida, Y., Droste, W., and Engler, S., 1986, "The Air-Gap Formation Process at the Casting Mold Interface and the Heat Transfer Mechanism Through the Gap," Metall. Trans. B, **17B**, pp. 833–844.
[8] Beck, J. V., 1970, "Nonlinear Estimation Applied to the Nonlinear Inverse Heat Conduction Problem," Int. J. Heat Mass Transfer, **13**, pp. 703–716.
[9] Beck, J. V., Litkouhi, B., and Clair, C. R. St., 1982, "Efficient Sequential Solution of Nonlinear Inverse Heat Conduction Problem," Numer. Heat Transfer, **5**, pp. 275–286.
[10] Browne, D. J., and O'Mahoney, D., 2001, "Interface Heat Transfer in Investment Casting of Aluminum Alloys," Metall. Mater. Trans. A, **32A**, pp. 3055–3063.
[11] O'Mahoney, D., and Browne, D. J., 2000, "Use of Experiment and an Inverse Method to Study Interface Heat Transfer During Solidification in the Investment Casting Process," Exp. Therm. Fluid Sci., **22**, pp. 111–122.
[12] Hwang, J. C., Chuang, H. T., Jong, S. H., and Hwang, W. S., 1994, "Measurement of Heat Transfer Coefficient at Metal/Mold Interface During Casting," AFS Trans., **102**, pp. 877–884.
[13] Narayan Prabhu, K., and Griffiths, W. D., 2002, "One-Dimensional Predictive Model for Estimation of Interfacial Heat Transfer Coefficient During Solidification of Cast Iron in Sand Mould," Mater. Sci. Technol., **18**, pp. 804–810.
[14] Kim, H. S., Cho, I. S., Shin, J. S., Lee, S. M., and Moon, B. M., 2005, "Solidification Parameters Dependent on Interfacial Heat Transfer Coefficient Between Aluminum Casting and Copper Mold," ISIJ Int., **45**(2), pp. 192–198.
[15] Kobryn, P. A., and Semiatin, S. L., 2001, "Determination of Interface Heat-Transfer Coefficients for Permanent Mold Casting of Ti-6Al-4V," Metall. Mater. Trans. B, **32B**, pp. 685–695.
[16] Uticard, T. A., Warczok, A., and Desclaux, P., 1994, "The Measurement of the Heat-Transfer Coefficient Between High-Temperature Liquids and Solid Surfaces," Metall. Mater. Trans. B, **25B**, pp. 43–51.
[17] Dantzig, J. A., and Lu, S. C., 1985, "Modeling of Heat Flow in Sand Castings: Part I: The Boundary Curvature Method," Metall. Trans. B, **16B**, pp. 195–202.
[18] Chen, Y. F., Jong, S. H., and Hwang, W. S., 1996, "Effects of Cooling Rate on Latent Heat Released Mode of Near Pure Aluminium and Aluminium-Silicon Alloys," Mater. Sci. Technol., **12**(7), pp. 539–544.
[19] Lin, L. S., 2005, "Prediction of Thermal Properties of Solidification," Master's thesis, National Cheng Kung University, Taiwan.

Use of Streamwise Periodic Boundary Conditions for Problems in Heat and Mass Transfer

Steven B. Beale
Mem. ASME
National Research Council,
Montreal Road,
Ottawa, K1A 0R6,
Canada
e-mail: steven.beale@nrc-cnrc.gc.ca

Fully developed periodic boundary conditions have frequently been employed to effect performance calculations for heat and mass exchange devices. In this paper a method is proposed, which is based on the use of primitive variables combined with the prescription of slip values. Either pressure difference or mass flow rate may be equivalently prescribed. Both constant wall temperature (Dirichlet) and constant heat flux (Neumann) conditions may be considered, as well as the intermediate linear (Robin) boundary condition. The example of an offset-fin plate-fin heat exchanger is used to illustrate the application of the procedure. The mathematical basis by which the method may be extended to the consideration of mass transfer problems with arbitrary boundary conditions, and associated continuity, momentum, and species sources and sinks is discussed. [DOI: 10.1115/1.2709976]

Keywords: computational fluid dynamics, periodic boundary conditions, primitive variables, heat and mass transfer

Introduction

In the application of computational fluid dynamics (CFD) to the analysis of heat and mass exchange devices, much computational effort may be avoided by considering elements deep within the design where the flow-field is "fully developed," [1–3]. Let it be assumed the domain has been tessellated with a structured mesh with associated finite-volume equations [4],

$$\sum a_{\mathrm{NB}}(\phi_{\mathrm{NB}} - \phi_P) + S = 0 \qquad (1)$$

where $\phi = p', u, v, w, T, m$, and the compass notation [4] is employed for the neighbor values, NB = W (west), E (east), S (south), N (north), L (low), and H (high). The source term in Eq. (1) is frequently linearized according to

$$S = C(V - \phi_P) \qquad (2)$$

where C is a source-term coefficient and V is a source-term value. If the flow is fully developed

$$\boldsymbol{u}(0,y,z) = \boldsymbol{u}(l,y,z) \qquad (3)$$

$$p(0,y,z) = p(l,y,z) + \Delta p_0 \qquad (4)$$

For constant heat flux, the temperature field is piecewise linear, $T(0,y,z) = T(l,y,z) + c$, whereas for constant wall temperature $\theta(0,y,z) = \theta(l,y,z)$, where $\theta = (T - T_w)/(T_0 - T_w)$, and T_0 is a reference temperature, often chosen as the bulk value. These may be combined to obtain [5]

$$T(0,y,z) = c_1 T(l,y,z) + c_2 \qquad (5)$$

$$c_1 = \begin{cases} \dfrac{T_0(0) - T_w}{T_0(l) - T_w} & \text{constant } T_w \\ 1 \quad \text{constant } \dot{q}''_w \end{cases} \qquad (6)$$

$$c_2 = \begin{cases} T_w(1 - c_1) & \text{constant } T_w \\ T_0(l) - T_0(0) & \text{constant } \dot{q}''_w \end{cases} \qquad (7)$$

Patankar Liu and Sparrow [6] transformed the state variables to obtain a set of cyclic equations

$$\phi(x,y,z) = \phi(x + l,y,z) \qquad (8)$$

This was achieved by defining a reduced pressure, $\tilde{p} = p - \beta x$. Murthy and Mathur [7] proposed a rationale whereby β is adjusted until a desired mass flux is obtained. For constant wall flux, a reduced temperature, $\tilde{T} = T - \gamma x$ may also be defined. The reduced-variable approach was subsequently adopted by numerous researchers, for example Patankar and Prakash [8]. The user must introduce volumetric sources into the transformed equations, and also modify the wall boundary conditions. For constant T_w, the nondimensional temperature, θ, is the state variable. The θ system of equations is, however, complex as it involves the solution for the local reference temperature. Kelkar and Patankar [9] subsequently proposed a primitive-variable formulation in temperature (only) for the constant T_w problem. The present author also worked with primitive variables, p, T (not $\tilde{p}$, $\tilde{T}$, θ) in previous work [5,10,11]. Periodic boundary conditions were implemented by the addition of a slab of halo cells downstream [12–14].

Present Approach

The problem to be addressed is the means whereby periodic boundary conditions may be reduced to cyclic conditions in the primitive-variable formulation, without the introduction of either transformed variables or halo cells. This is achieved by imposing slip conditions in the x direction.

Fluid Flow. For streamwise u momentum, an impulse or pressure "shock" condition is imposed

$$S = A_P \Delta p_0 \qquad (9)$$

along a single y-z plane of cells. Figure 1(a) illustrates the notion

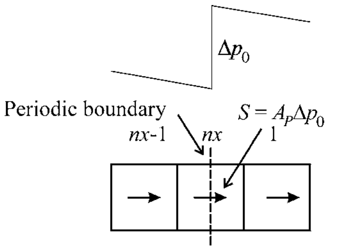

(a) Pressure

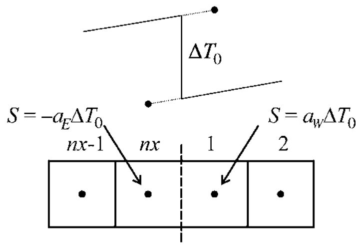

(b) Temperature

Fig. 1 Slip boundary conditions for a staggered scheme, constant wall flux

---

Contributed by the Heat Transfer Division of ASME for publication in the Journal of Heat Transfer. Manuscript received March 28, 2006; final manuscript received December 18, 2006. Review conducted by Jayathi Murthy. Paper presented at the 2005 ASME Heat Transfer Summer Conference (HT2005), San Francisco, CA, USA, July 15–22, 2005.

schematically. If it is desired that the bulk velocity, u_0, or Reynolds number be prescribed, Δp_0 may be corrected according to $\Delta p_0 = \Delta p_0^* + \Delta p_0'$, where Δp_0^* is the value at the previous iteration, and $\Delta p_0'$ is a correction factor. Neglecting streamwise diffusion and applying an order-of-magnitude analysis yields

$$\Delta p_0' = \rho |u_0| (u_0 - u_0^*) \tag{10}$$

which is similar to, but simpler than that given in Ref. [7].

Heat Transfer. For the temperature field there is a slip in the values across the boundary faces, and it is necessary to prescribe a source/sink pair. The slip values are the differences between actual and apparent temperatures that would arise if the field were truly periodic. They are not necessarily equal and opposite. If the user has access to the neighbor values, ϕ_{NB} in Eq. (1), in the CFD solver, it is possible to directly add/subtract the ΔT slip values from the neighbors, T_E and T_W. If the user does not have access to the solver, it is more convenient to introduce a pair of source terms say, $S = a_W \Delta T_W$ at $i=1$, and $S = a_E \Delta T_E$ at $i = nx$. For the constant $\dot{q}_w''$ (Neumann) condition, $\Delta T_W = -\Delta T_E = \Delta T_0$. Figure 1(*b*) illustrates schematically the source–sink pair. Although it is possible to directly set $\Delta T_0 = \dot{q}_w / \dot{m} c_p$ [6], as a fixed flux (source), the author chooses to adjust the source term iteratively, until the upstream in-cell temperature reaches a desired reference value, $T_0(0)$, with

$$\Delta T_0 = T_0(0) - T_0(l) \tag{11}$$

where $T_0(l)$ is a fetched value, e.g., the bulk downstream value, and $T_0(0)$ is a prescribed value. This rationale works well under most circumstances, however, situations can arise where the choice of $T_0(0)$ is not arbitrary, but is a function of the boundary values.

For the constant T_w (Dirichlet) condition, the implementation is similar to that in Ref. [9]. The source terms are $a_W[(c_1 - 1)T_W + c_2]$ at $i=1$ and $a_E[(1 - c_1)T_E - c_2]$ at $i = nx$, where T_W is the west neighbor at $i=1$ i.e., T_P at $i = nx$, and T_E is the east neighbor at $i = nx$, i.e., T_P at $i=1$, and $\Delta T_E \neq -\Delta T_W$. The boundary conditions for both Dirichlet and Neumann problems may be written as

$$S = \pm a_{\mathrm{NB}}[(c_1 - 1)T_{\mathrm{NB}} + c_2] \tag{12}$$

where c_1 and c_2 are specified in Eqs. (6) and (7), the subscript NB refers to the east or west neighbor, and the linking coefficients a_E and a_W must be computed by the same scheme employed in the CFD solver.

Mass Transfer. The unit cell approach has also been applied to mass transfer problems [15–17], and may be used in heat transfer problems with injection/suction at the boundaries, where temperature (or enthalpy) replaces mass fraction, denoted here by ϕ. A constant transformed substance state (Robin) boundary condition is appropriate

$$S = \dot{m}(\phi_\infty - \phi_w) \tag{13}$$

where ϕ_∞ denotes ϕ in the transferred substance state [18,19]. Comparison of Eqs. (2) and (13) reveal that if $\phi_w \approx \phi_P$, the mass transfer problem is another instance of the linearized source term with $C = \dot{m}$ and $V = \phi_\infty$. Differences between nodal and wall values are easily dealt with using harmonic averaging of the coefficients; e.g., with $S = a_w(\phi_w - \phi_P)$, Eq. (2) is enumerated with $C = \dot{m} a_w / (\dot{m} + a_w)$, and $V = \phi_\infty$. For low Péclet numbers $a_w = \Gamma A / |P - w|$; while at high Péclet numbers both convection and diffusion must be accommodated [17]. The constant transferred substance state boundary condition differs from constant value or flux. However in the limit $\dot{m} \to 0$, it reduces to a Neumann condition and in the limit $\dot{m} \to \infty$, it reduces to a Dirichlet condition. The reader will note that the linear wall condition does not necessarily have to assume the form, Eq. (13), but could also be expressed as

$$S = g_\infty A(\phi_\infty - \phi_w) \tag{14}$$

where g_∞ is a heat/mass transfer coefficient.

Equations (5)–(7) may thus be conveniently generalized for the linear boundary condition

$$\phi(0) = c_1 \phi(l) + c_2 \tag{15}$$

$$c_1 = \frac{\phi_0(0) - \phi_w(0)}{\phi_0(l) - \phi_w(l)} \tag{16}$$

$$c_2 = \phi_0(0) - c_1 \phi_0(l) \tag{17}$$

The upstream wall value must be computed

$$\phi_w(0) = \frac{\phi_0(0) + B(l)\phi_\infty}{1 + B(l)} \tag{18}$$

$$B(x) = \frac{\phi_0(x) - \phi_w(x)}{\phi_w(x) - \phi_\infty} \tag{19}$$

and it is tacitly assumed that the driving force [18,19] is cyclic, $B(l) = B(0)$.

For low mass flow rates, no continuity modifications are required. At higher mass flow rates, injection/suction rates have a significant impact on the crosswise v velocity, pressure gradients, and scalar transport, and these can be captured only by including continuity changes. A similarity velocity profile, $u(0) = cu(l)$, may be presumed [17]. In the continuity/pressure–correction equation, a mass sink equal and opposite to the source at the wall (or vice-versa) is required, $S = -\rho A_P (c-1) u(l)$. In the u momentum equations it is also necessary to introduce momentum slip terms, $V = \pm a_{\mathrm{NB}}(c-1)u_{\mathrm{NB}}$. The equations are further complicated because the a_{NB} coefficients include convection terms and must also be modified. High mass transfer rate problems will be considered in future work.

Example: Offset-Fin Heat Exchanger

The problem considered is conjugate laminar-flow heat transfer in a three-dimensional offset-fin plate-fin heat exchanger as illustrated in Fig. 2. Solutions to this problem were provided in Refs. [5,10] together with details of the geometry and fluid properties. A domain of $2l \times p/2 \times b$ was tessellated with a mesh of $56 \times 37 \times 57$ (118, 104) cells. Calculations were performed with a segregated solver, staggered grid, and hybrid scheme [4], using the CFD code PHOENICS [20]. Figure 3 shows velocity vectors for plan and elevation views of the heat exchanger design midway between the fins at $y = p/4$ and the plates at $z = b/2$, respectively. Figures 4 and 5 are contours of pressure, p, and temperature, T,

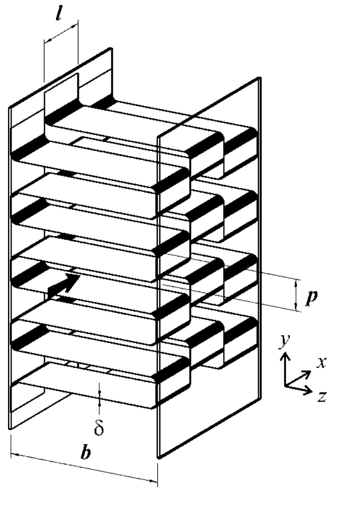

Fig. 2 Offset-fin plate-fin geometry

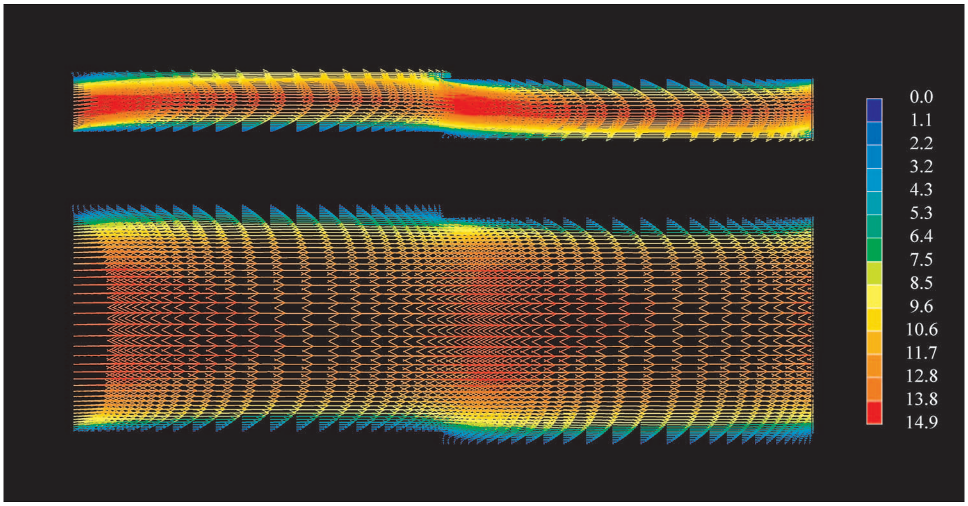

Fig. 3 Velocity vectors (m/s) for Re=500

Fig. 4 Pressure (Pa) distribution for Re=500

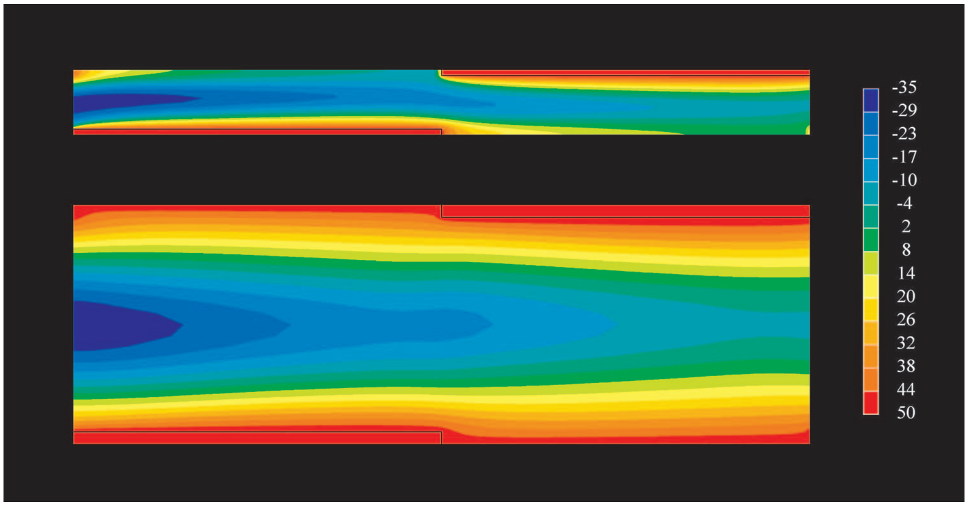

Fig. 5 Temperature (°C) distribution for Re=500

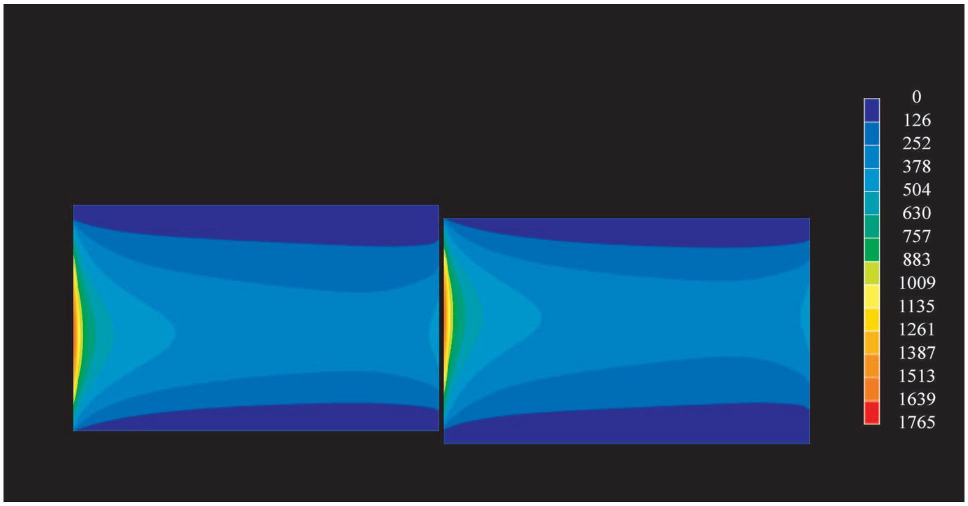

Fig. 6 Local Nusselt number for Re=500

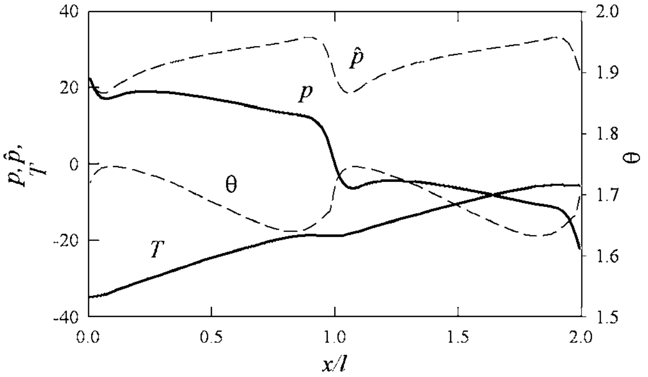

Fig. 7 Dimensional pressure p (Pa) and temperature T (°C), as well as reduced pressure $\tilde{p}$ (Pa) and nondimensional temperature θ, for Re=500 along the symmetry line $y=p/4$, $z=b/2$

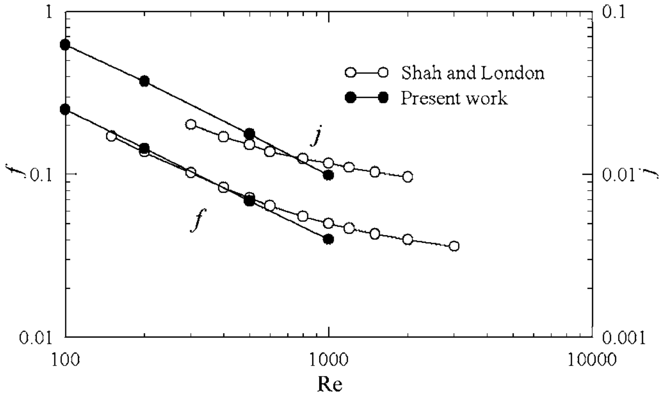

Fig. 8 Friction and heat transfer factors compared with experimental data

respectively, in the symmetry planes. Figure 6 shows the local Nusselt number on the fin surface. It is a maximum at the front center of the fin, where shear is greatest and decreases rapidly as the boundary layer develops. Figure 7 shows a comparison of p and T with values of $\tilde{p}$ and θ, computed at the end of the calculations, along the center line $y=p/4$, $z=b/2$. It can readily be seen that these are cyclic. Overall friction and heat transfer factors were also computed [5,10], and are compared to experimental values in Fig. 8. It can be seen that agreement is good for friction factor, f, with some error apparent in heat transfer factor, j, consistent with values in Refs. [5,10].

Discussion and Conclusions

Periodic boundary conditions may readily be prescribed for problems in fluid mechanics, heat, and mass transfer, in primitive form with cyclic boundary conditions, by associating periodic boundary conditions with the slip values, introduced as source terms. No equation transformations or new field variables are required, and standard wall boundary conditions may readily be employed. Either the mean pressure gradient, or the reference velocity/flow Reynolds number may be prescribed. The method devised to adjust the pressure jump based on a desired reference bulk velocity or Reynolds number, Eq. (10), was found to work well. The formulation is advantageous, not only for the constant T_w (Dirichlet) condition, but also for the generalized heat/mass transfer (Robin) problem. Equations (15)–(19) are quite general and can be applied to problems containing a mix of different linear coefficients and values. If two or more different conditions are prescribed on different wall sections, driving force and upstream wall values are simply computed individually using Eqs. (18) and (19). Thus, cell-by-cell variations in the boundary values and coefficients across the domain may be accommodated. A method for modifying the continuity and momentum equations for high rates of mass transfer was detailed, and will be implemented in the future. Although the work presented here is based on a finite-volume method, with structured mesh and staggered velocity scheme, the technique is quite general and may be readily extended to situations where unstructured meshes, co-located variables, and finite-element analysis techniques are used to perform flow-field calculations.

Acknowledgment

The author wishes to thank both John Ludwig at CHAM Ltd. and Ron Jerome at NRC for providing technical support.

Nomenclature

A = area, m^2
a = coefficient in finite-volume equations
B = driving force
b = heat exchanger plate width, m
C = source term coefficient
C_p = specific heat, J/kg K
f = friction factor

g = heat/mass transfer coefficient, $\mathrm{W/m^2\,K}$ or $\mathrm{kg/m^2\,s}$
j = heat transfer factor
l = streamwise characteristic length, pitch, m
$\dot{m}$ = mass flow rate, kg/s
T = temperature, K
$\dot{q}$ = heat transfer rate, W
$\dot{q}''$ = heat flux rate, $\mathrm{W/m^2}$
u = streamwise velocity component, m/s
v = crosswise velocity component, m/s
w = crosswise velocity component, m/s
p = pressure, Pa, fin pitch, m
$\hat{p}$ = reduced pressure, Pa
Re = Reynolds number
V = source term value
V_p = volume of cell P, $\mathrm{m^3}$
T = temperature, K
$\hat{T}$ = reduced temperature, K
x = streamwise displacement component, m
y = crosswise displacement component, m
z = crosswise displacement component, m

Greek Symbols

β = volumetric term, Pa/m
Γ = exchange coefficient, kg/m s
γ = volumetric term, K/m
δ = fin thickness, m
θ = nondimensional temperature
ρ = density, $\mathrm{kg/m^3}$
ϕ = generalized state variable

References

[1] Thom, A., and Apelt, C. J., 1961, *Field Computations in Engineering and Physics*, Van Nostrand, London.
[2] Le Feuvre, R. F., 1973, “Laminar and Turbulent Forced Convection Processes through in-Line Tube Banks,” Ph.D. thesis, Imperial College of Science and Technology, University of London, London, UK.
[3] Massey, T. H., 1976, “The Prediction of Flow and Heat-Transfer in Banks of Tubes in Cross-Flow,” Ph.D. thesis, Council for National Academic Awards, U.K.
[4] Patankar, S. V., 1980, *Numerical Heat Transfer and Fluid Flow*, Hemisphere, New York.
[5] Beale, S. B., 1993, “Fluid Flow and Heat Transfer in Tube Banks,” Ph.D. thesis, Imperial College of Science, Technology and Medicine, London, UK.
[6] Patankar, S. V., Liu, C. H., and Sparrow, E. M., 1977, “Fully-Developed Flow and Heat Transfer in Ducts Having Streamwise-Periodic Variations of Cross-Sectional Area,” ASME J. Heat Transfer, **99**, pp. 180–186.
[7] Murthy, J. Y., and Mathur, S., 1997, “Periodic Flow and Heat Transfer Using Unstructured Meshes,” Int. J. Numer. Methods Fluids, **25**, pp. 659–677.
[8] Patankar, S. V., and Prakash, C., 1981, “An Analysis of the Effect of Plate Thickness on Laminar Flow and Heat Transfer in Interrupted Plate Passages,” Int. J. Heat Mass Transfer, **24**, pp. 1801–1810.
[9] Kelkar, K. M., and Patankar, S. V., 1987, “Numerical Prediction of Flow and Heat Transfer in a Parallel Channel With Staggered Fins,” ASME J. Heat Transfer, **109**, pp. 25–30.
[10] Beale, S. B., 1990, “Laminar Fully Developed Flow and Heat Transfer in an Offset Rectangular Plate-Fin Surface,” The PHOENICS Journal of Computational Fluid Dynamics and its Application, 3, pp. 1–19.
[11] Beale, S. B., and Spalding, D. B., 1998, “Numerical Study of Fluid Flow and Heat Transfer in Tube Banks With Stream-Wise Periodic Boundary Conditions,” Trans. Can. Soc. Mech. Eng., **22**, pp. 394–416.
[12] Antonopoulos, K. A., 1979, “Prediction of Flow and Heat Transfer in Rod Banks,” Ph.D. thesis, Imperial College, University of London, London, UK.
[13] Antonopoulos, K. A., 1985, “Heat Transfer in Tube Assemblies under Conditions of Laminar, Axial, Transverse and Inclined Flow,” Int. J. Heat Fluid Flow, **6**, pp. 193–204.
[14] Antonopoulos, K. A., 1987, “The Prediction of Turbulent Inclined Flow in Rod Banks,” Comput. Fluids, **14**, pp. 361–378.
[15] Baier, G., Grateful, T. M., Graham, M. D., and Lightfoot, E. N., 1999, “Prediction of Mass Transfer in Spatially Periodic Flows,” Chem. Eng. Sci., **54**, pp. 343–355.
[16] Comini, G., and Croce, G., 2001, “Convective Heat and Mass Transfer in Tube-Fin Exchangers under Dehumifying Conditions,” Numer. Heat Transfer, Part A, **40**, pp. 579–599.
[17] Beale, S. B., 2005, “Mass Transfer in Plane and Square Ducts,” Int. J. Heat Mass Transfer, **48**, pp. 3256–3260.
[18] Spalding, D. B., 1960, “A Standard Formulation of the Steady Convective Mass Transfer Problem,” Int. J. Heat Mass Transfer, **1**, pp. 192–207.
[19] Spalding, D. B., 1963, *Convective Mass Transfer; An Introduction*, Edward Arnold, London, UK.
[20] Spalding, D. B., 2004, *Phoenics Overview*, CHAM Ltd., London, UK.

Journal of
Heat Transfer

Erratum

Erratum: “Thermal Conductivity of Metal-Oxide Nanofluids: Particle Size Dependence and Effect of Laser Irradiation” and “The Role of the Viscous Dissipation in Heated Microchannels”
[Journal of Heat Transfer, 2007, 129(3)]

The two papers entitled “Thermal Conductivity of Metal-Oxide Nanofluids: Particle Size Dependence and Effect of Laser Irradiation” and “The Role of the Viscous Dissipation in Heated Microchannels” should have been placed under the category *Micro/Nanoscale Heat Transfer*.